Springer Protocols

Celeste M. Nelson *Editor*

Tissue Morphogenesis

Methods and Protocols

VIDEOS
springerimages.com

Humana Press

METHODS IN MOLECULAR BIOLOGY

For further volumes:
http://www.springer.com/series/7651

Tissue Morphogenesis

Methods and Protocols

Edited by

Celeste M. Nelson

Chemical and Biological Engineering, Princeton University, NJ, USA

☼ Humana Press

Editor
Celeste M. Nelson
Chemical and Biological Engineering
Princeton University
NJ, USA

Videos to this book can be accessed at http://www.springerimages.com/videos/978-1-4939-1163-9

Printed on acid-free paper

Preface

Tissue morphogenesis encompasses a diverse array of processes that transforms unpatterned populations of cells into the distinct tissue structures of the mature organism. The creation of complex, multicellular tissue architectures is critical for organ formation and eventual function. The study of tissue morphogenesis is a rich one, with key conceptual advances emerging from several model organisms. Recent advances have benefited from collaborations between developmental biologists and physicists and engineers, who bring sophisticated analysis techniques as well as theoretical paradigms. This volume highlights the major techniques, both experimental and computational, for the study of tissue morphogenesis, divided into several sections, with specific focus on techniques to image, manipulate, model, and analyze tissue morphogenesis.

This book comprises 22 chapters authored by 68 leading experts from institutions in the USA, Canada, Puerto Rico, France, Austria, the Netherlands, Hungary, Switzerland, Turkey, and Taiwan. This diverse group includes developmental biologists, cell biologists, engineers, and systems biologists working on a large variety of both classical and innovative model systems.

We have divided the book into five parts, based on either methodology or model system. Given that tissue morphogenesis is a dynamic process, and given the seemingly enormous advances in imaging technologies over the past 5 years, the first part (Chapters 1–9) comprises nine chapters devoted to imaging analysis of tissue morphogenesis. This part includes chapters on using imaging techniques to measure the mechanical properties of morphogenetic tissues, the forces that they either exert or experience, or the corresponding changes in cell dynamics or gene expression. The second part (Chapters 10–13) comprises four chapters focused on culture models of tissue morphogenesis, including both cell-based and organ explant models. The third part (Chapters 14–17) comprises an additional four chapters that describe techniques for manipulating cells and tissues in vivo, including classical tissue recombination experiments as well as more recently developed laser-based tissue ablation approaches. The fourth part (Chapters 18–19) contains two chapters describing novel model systems to investigate tissue morphogenesis. The fifth and final part (Chapters 20–22) comprises three chapters that describe the use of computational models in understanding tissue morphogenesis.

This book is intended to serve as a primary resource for both fundamental and practical understanding of the techniques used to uncover the basis of tissue morphogenesis. The book is intended to be a primary source for academics and professionals working in developmental biology, tissue engineering, and medicine.

NJ, USA   *Celeste M. Nelson*

Contents

Contributors

RICARDO J. ABREU-IRIZARRY • *Biology Department, University of Puerto Rico, San Juan, Puerto Rico*

SINU JASRAPURIA AGRAWAL • *Rice University, Houston, TX, USA*

ANASTASIIA ALEKSANDROVA • *Department of Anatomy and Cell Biology, University of Kansas Medical Center, Kansas City, KS, USA*

PATRICK W. ALFORD • *Department of Biomedical Engineering, University of Minnesota-Twin Cities, Minneapolis, MN, USA*

FERNANDO AMAT • *Howard Hughes Medical Institute, Janelia Farm Research Campus, Ashburn, VA, USA*

JENNIFER N. BECK • *Department of Cell Biology, Center for Cell Dynamics, Johns Hopkins School of Medicine, Baltimore, MD, USA; Department of Oncology, Center for Cell Dynamics, Johns Hopkins School of Medicine, Baltimore, MD, USA*

MARTIN BEHRNDT • *Institute of Science and Technology Austria, Klosterneuburg, Austria*

SAMIR A. BELLO • *Biology Department, University of Puerto Rico, San Juan, Puerto Rico*

STEPHANIE L.K. BOWERS • *Department of Medical Pharmacology and Physiology, University of Missouri School of Medicine and Dalton Cardiovascular Research Center, Columbia, MO, USA*

JONATHAN T. BUTCHER • *Department of Biomedical Engineering, Cornell University, Ithaca, NY, USA*

PEDRO CAMPINHO • *Institute of Science and Technology Austria, Klosterneuburg, Austria*

WELLINGTON V. CARDOSO • *Department of Medicine, Columbia University Medical Center, New York, NY, USA*

SOPHIA N. CARRELL • *Department of Chemical and Biomolecular Engineering, North Carolina State University, Raleigh, NC, USA*

CHIA-YUAN CHEN • *Department of Mechanical Engineering, National Taiwan University of Science and Technology, Taipei, Taiwan*

FELICIA CHEN • *Pulmonary Center, Boston University School of Medicine, Boston, MA, USA*

KEVIN J. CHEUNG • *Department of Cell Biology, Center for Cell Dynamics, Johns Hopkins School of Medicine, Baltimore, MD, USA; Department of Oncology, Center for Cell Dynamics, Johns Hopkins School of Medicine, Baltimore, MD, USA*

LILY S. CHEUNG • *Department of Chemical and Biological Engineering, Princeton University, Princeton, NJ, USA*

ANDRÁS CZIRÓK • *Department of Anatomy and Cell Biology, University of Kansas Medical Center, Kansas City, KS, USA; Department of Biological Physics, Eotvos University, Budapest, Hungary*

GEORGE E. DAVIS • *Department of Medical Pharmacology and Physiology, University of Missouri School of Medicine and Dalton Cardiovascular Research Center, Columbia, MO, USA*

MATTHEW T. DAVIS • *Department of Medical Pharmacology and Physiology, University of Missouri School of Medicine and Dalton Cardiovascular Research Center, Columbia, MO, USA*

DANIEL J. DICKINSON • *Department of Biology, University of North Carolina, Chapel Hill, NC, USA*

ANDREW J. EWALD • *Department of Cell Biology, Center for Cell Dynamics, Johns Hopkins School of Medicine, Baltimore, MD, USA; Department of Oncology, Center for Cell Dynamics, Johns Hopkins School of Medicine, Baltimore, MD, USA*

RODRIGO FERNANDEZ-GONZALEZ • *Institute of Biomaterials and Biomedical Engineering, University of Toronto, Toronto, ON, Canada; Department of Cell and Systems Biology, University of Toronto, Toronto, ON, Canada*

BENJAMEN A. FILAS • *Department of Ophthalmology and Visual Sciences, Washington University, St. Louis, MO, USA*

RAMSEY A. FOTY • *Department of Surgery, UMDNJ-Robert Wood Johnson Medical School, New Brunswick, NJ, USA*

PATRICK FRIED • *Department for Biosystems Science and Engineering, ETH Zurich, Basel, Switzerland*

JOSE E. GARCIA-ARRARAS • *Biology Department, University of Puerto Rico, San Juan, Puerto Rico*

PHILIPP GERMANN • *Department for Biosystems Science and Engineering, ETH Zurich, Basel, Switzerland*

NIKOLCE GJOREVSKI • *Department of Chemical and Biological Engineering, Princeton University, Princeton, NJ, USA*

JACKY G. GOETZ • *Institute of Genetics and Molecular and Cellular Biology, Illkirch, France*

SELDA GOKTAS • *Department of Mechanical Engineering, Koc University, Istanbul, Turkey*

CHELSEA L. GREGG • *Department of Biomedical Engineering, Cornell University, Ithaca, NY, USA*

CARL-PHILIPP HEISENBERG • *Institute of Science and Technology Austria, Klosterneuburg, Austria*

ROBERT J. HUEBNER • *Department of Cell Biology, Center for Cell Dynamics, Johns Hopkins School of Medicine, Baltimore, MD, USA; Department of Oncology, Center for Cell Dynamics, Johns Hopkins School of Medicine, Baltimore, MD, USA*

DAGMAR IBER • *Department for Biosystems Science and Engineering, ETH Zurich, Basel, Switzerland*

PHILIPP J. KELLER • *Howard Hughes Medical Institute, Janelia Farm Research Campus, Ashburn, VA, USA*

KHALED KHAIRY • *Howard Hughes Medical Institute, Janelia Farm Research Campus, Ashburn, VA, USA*

WILLIAM J. KOWALSKI • *Department of Biomedical Engineering, Carnegie Mellon University, Pittsburgh, PA, USA*

WILLIAM C. LEMON • *Howard Hughes Medical Institute, Janelia Farm Research Campus, Ashburn, VA, USA*

P.-F. LENNE • *Institut de Biologie du Developpement de Marseille Luminy, Marseille, France*

CHUN YIN BOSCO LEUNG • *Institute of Biomaterials and Biomedical Engineering, University of Toronto, Toronto, ON, Canada; Department of Cell and Systems Biology, University of Toronto, Toronto, ON, Canada*

CHARLES D. LITTLE • *Department of Anatomy and Cell Biology, University of Kansas Medical Center, Kansas City, KS, USA*

PETER Y. LWIGALE • *Rice University, Houston, TX, USA*

CHUN-XIA MENG • *Department of Medical Pharmacology and Physiology, University of Missouri School of Medicine and Dalton Cardiovascular Research Center, Columbia, MO, USA*

DENIS MENSHYKAU • *Department for Biosystems Science and Engineering, ETH Zurich, Basel, Switzerland*

ROELAND M.H. MERKS • *Centrum Wiskunde & Informatica, Amsterdam, The Netherlands; Netherlands Consortium for Systems Biology/Netherlands Institute for Systems Biology, Amsterdam, The Netherlands*

FABIEN MONDUC • *Institute of Genetics and Molecular and Cellular Biology, Illkirch, France*

CELESTE M. NELSON • *Department of Chemical and Biological Engineering, Princeton University, Princeton, NJ, USA; Department of Molecular Biology, Princeton University, Princeton, NJ, USA*

W. JAMES NELSON • *Program in Cancer Biology, Stanford University, Stanford, CA, USA; Department of Biology, Stanford University, Stanford, CA, USA; Department of Molecular and Cellular Physiology, Stanford University, Stanford, CA, USA*

KIM-VY NGUYEN-NGOC • *Department of Cell Biology, Center for Cell Dynamics, Johns Hopkins School of Medicine, Baltimore, MD, USA; Department of Oncology, Center for Cell Dynamics, Johns Hopkins School of Medicine, Baltimore, MD, USA*

MARGRIET M. PALM • *Centrum Wiskunde & Informatica, Amsterdam, The Netherlands; Netherlands Consortium for Systems Biology/Netherlands Institute for Systems Biology, Amsterdam, The Netherlands*

KEREM PEKKAN • *Department of Mechanical Engineering, Carnegie Mellon University, Pittsburgh, PA, USA; Department of Biomedical Engineering, Carnegie Mellon University, Pittsburgh, PA, USA*

ALEXANDRA S. PIOTROWSKI • *Department of Chemical and Biological Engineering, Princeton University, Princeton, NJ, USA*

M. RAUZI • *Institut de Biologie du Developpement de Marseille Luminy, Marseille, France*

ANDREW K. RECKNAGEL • *Department of Biomedical Engineering, Cornell University, Ithaca, NY, USA*

GREGORY T. REEVES • *Department of Chemical and Biomolecular Engineering, North Carolina State University, Raleigh, NC, USA*

BRENDA J. RONGISH • *Department of Anatomy and Cell Biology, University of Kansas Medical Center, Kansas City, KS, USA*

VERENA RUPRECHT • *Institute of Science and Technology Austria, Klosterneuburg, Austria*

YANNICK SCHWAB • *Institute of Genetics and Molecular and Cellular Biology, Illkirch, France*

ELIAH R. SHAMIR • *Department of Cell Biology, Center for Cell Dynamics, Johns Hopkins School of Medicine, Baltimore, MD, USA; Department of Oncology, Center for Cell Dynamics, Johns Hopkins School of Medicine, Baltimore, MD, USA*

STANISLAV SHVARTSMAN • *Department of Chemical and Biological Engineering, Princeton University, Princeton, NJ, USA; Lewis-Sigler Institute for Integrative Genomics, Princeton University, Princeton, NJ, USA*

MICHAEL SMUTNY • *Institute of Science and Technology Austria, Klosterneuburg, Austria*

LARRY A. TABER • *Department of Biomedical Engineering, Washington University, St. Louis, MO, USA*

SIMON TANAKA • *Department for Biosystems Science and Engineering, ETH Zurich, Basel, Switzerland*

VICTOR D. VARNER • *Department of Chemical and Biological Engineering, Princeton University, Princeton, NJ, USA*

JULIEN VERMOT • *Institute of Genetics and Molecular and Cellular Biology, Illkirch, France*

WILLIAM I. WEIS • *Program in Cancer Biology, Stanford University, Stanford, CA, USA; Department of Molecular and Cellular Physiology, Stanford University, Stanford, CA, USA; Department of Structural Biology, Stanford University, Stanford, CA, USA*

GANG XU • *Department of Engineering and Physics, University of Central Oklahoma, Edmond, OK, USA*

Part I

Imaging Morphogenesis

Chapter 1

Probing Regional Mechanical Properties of Embryonic Tissue Using Microindentation and Optical Coherence Tomography

Benjamen A. Filas, Gang Xu, and Larry A. Taber

Abstract

Physical forces regulate morphogenetic movements and the mechanical properties of embryonic tissues during development. Such quantities are closely interrelated, as increases in material stiffness can limit force-induced deformations and vice versa. Here we present a minimally invasive method to quantify spatiotemporal changes in mechanical properties during morphogenesis. Regional stiffness is measured using microindentation, while displacement and strain distributions near the indenter are computed from the motion of tissue labels tracked from 3-D optical coherence tomography (OCT) images. Applied forces, displacements, and strain distributions are then used in conjunction with finite-element models to estimate regional material properties. This method is applicable to a wide variety of experimental systems and can be used to better understand the dynamic interrelation between tissue deformations and material properties that occur during time-lapse studies of embryogenesis. Such information is important to improve our understanding of the etiology of congenital disease where dynamic changes in mechanical properties are likely involved, such as *situs inversus* in the heart, hydrocephalus in the brain, and microphthalmia in the eye.

Key words Morphogenesis, Development, Dynamic imaging, Mechanical testing, Contrast agents, Ballistic labeling, Strain, Computational modeling

1 Introduction

Embryos undergo dramatic changes in size, shape, and material properties during development. To understand the evolution of these quantities, noninvasive imaging and micromechanical testing techniques are often used (reviewed in [1–5]). The purpose of this chapter is to show how tissue labeling, microindentation, and noninvasive imaging can be combined to probe spatiotemporal distributions in mechanical properties in the developing chicken embryo.

Benjamen A. Filas and Gang Xu are contributed equally to this chapter.

Optical coherence tomography (OCT) has emerged as a useful tool for subsurface imaging of living biological samples (up to 2 mm deep; for comparison, confocal microscopes usually only reach depths of less than half a millimeter [6]) with high spatial resolution (10 μm or less) in three dimensions [7]. OCT has proven useful in reconstructing three-dimensional tissues during time-lapse imaging studies of the chicken embryo [8–10], with applications for in utero imaging recently demonstrated in mammalian embryos [11, 12]. To quantify such changes in morphology, we have developed an OCT-based label tracking technique to measure morphogenetic strains in 3-D [8, 13].

We have also used a cantilever-based microindentation method to probe the regional material properties of developing epithelia in the chicken embryo [14–16]. This technique is based on the same principles used in atomic force microscopy [17] and cell indentation [17, 18]. In our approach, the applied force and deformation at the indenter tip are measured from bright-field microscopy recordings of the experiment [14]. Resulting force-displacement data are then supplemented with a computational model to estimate nonlinear material properties in the indented region [14, 16]. These properties can be determined more accurately by also including in the analysis data on tissue deformation in the vicinity of the indenter tip [15].

Here, we illustrate how combining microindentation and OCT imaging can be used to estimate material properties in the embryo. In our current configuration, the cantilever introduces a small, localized indentation at specific regions, while the OCT system is used to determine the deformation profile near the indentation site from the recorded motions of high-contrast fiducial markers injected into the tissue using a gene gun. When supplemented with a computational model, force-deflection and deformation data can be used to estimate regional material properties, as well as residual stress, in the tissue.

Some limitations of previous methods are overcome with this approach. First, OCT permits 3-D surface shapes and strains to be determined during indentation, deformations that were previously only analyzed in 2-D due to inherent limitations in bright-field microscopy [14]. This information can then be used to inform more accurate 3-D distributions of material properties. Second, instead of an adherence-based marker attachment approach [8, 15], we use a gene gun to securely embed beads in the tissue, thereby eliminating measurement artifacts due to bead drift and detachment. Third, because of the minimally invasive and relatively high-throughput nature of the technique, changes in material properties can be more readily assessed with better spatiotemporal resolution during dynamic studies of morphogenesis.

2 Materials

2.1 Chicken Embryo Preparation, Labeling, and Culture

1. Preparation supplies:
   (a) Egg incubator (Hova-Bator, Georgia Quail Farms).
   (b) Fine forceps (#5, stainless steel, Fine Science Tools).
   (c) Blunt forceps (straight, broad, 11.5 cm, Fine Science Tools).
   (d) Microscissors (curved, 9 mm, Fine Science Tools).
   (e) Whatman filter paper (#2, 9 cm circles, Fisher Scientific).
   (f) Stainless steel rings (0.68 in. outer diameter, McMaster Carr).
   (g) Single-hole punch.
   (h) 35 mm culture dishes (one per embryo), two 150 mm dishes.
   (i) Dissecting microscope (M80, Leica).
2. Labeling supplies:
   (a) Polystyrene microspheres (6–10 μm diameter, Biosciences). *See* **Note 1** for bead selection rationale.
   (b) Tefzel tubing (3.175 mm outer diameter, Biorad) for gene gun bullet preparation.
   (c) Helios gene gun (Biorad) attached to helium gas supply (*see* **Note 2** for alternatives).
3. Culture supplies:
   (a) 95 % oxygen, 5 % carbon dioxide gas supply.
   (b) Small plastic bag (1 quart).
4. Solutions:
   (a) Ethanol (95 %) for bullet preparation.
   (b) PBS with calcium and magnesium (Sigma Aldrich).
   (c) DMEM culture medium (4.5 g/L glucose, sodium bicarbonate, and L-glutamine) supplemented with chick serum (10 %) and penicillin/streptomycin/neomycin antibiotics (1 %) (Sigma Aldrich).

2.2 Optical Coherence Tomography (OCT) and Microindentation

1. OCT supplies:
   (a) Laser viewing card (VR2, Thorlabs; the specific viewing card depends on the wavelength of the laser light source of the OCT system).
   (b) OCT imaging system (OCT1300SS, Thorlabs).
   (c) Black membrane disk filters (VWR).
   (d) Transfer pipette (3.2 mL, Sigma Aldrich).

2. Microindentation supplies (for an alternative method to microindentation, *see* **Note 3**).
   (a) Micropipette puller (PC-10, Narishige).
   (b) Glass micropipettes (1 mm diameter, World Precision Instruments).
   (c) Micromanipulator (MM33, Sutter Instruments).
   (d) Piezoelectric motor (PZS-200, Burleigh Instruments).

2.3   Analysis   Computer software (programs we use listed first; possible open-source alternatives listed thereafter):

(a) 3-D image analysis (Volocity, PerkinElmer; open source: Fiji, www.fiji.sc).
(b) Programming (Matlab, Mathworks; open source: Python, www.python.org).
(c) Finite element modeling (Comsol Multiphysics; Abaqus, Dassault Systèmes; open source: FEBio, http://mrl.sci.utah. edu/software/febio).

3   Methods

3.1   Chicken Embryo Preparation, Labeling, and Culture

1. Place fertile eggs in a humidified incubator at 38 °C to yield embryos at desired stages. See Hamburger and Hamilton [19] for incubation times and developmental stages.

2. Extract embryos from the eggs. Gently crack the egg open and place the contents into a 150 mm Petri dish. The embryo (a small white disk) will be positioned on top of the yolk. Using blunt forceps, remove the thicker albumen around the yolk. Trim two pieces of Whatman #2 filter paper to an approximate 2 cm diameter circular disk and create at least two intersecting holes in the middle using a paper hole puncher. Place one of the papers on the yolk, centering the embryo in the holes, and let sit for a minute. Cut around the perimeter of the filter paper with microscissors and remove the embryo (now attached to the filter paper via extraembryonic membranes) from the yolk with fine forceps. Gently rinse the embryo in PBS in a 150 mm Petri dish. Transfer the washed embryo to a 35 mm culture dish, sandwich the attached membranes with the second piece of filter paper, and use a 0.68 in. diameter steel ring to stabilize the construct at the bottom of the dish (Fig. 1a). Add PBS (1.5 mL) to hydrate the embryo and verify normal morphology under a dissecting microscope. This step is demonstrated in its entirety in [20].

3. Label tissue for deformation tracking. Using microscissors, remove membranes covering the tissue of interest (e.g., for the heart on the ventral side of the embryo, remove the splanchnopleure; for the brain on the dorsal side, cut away
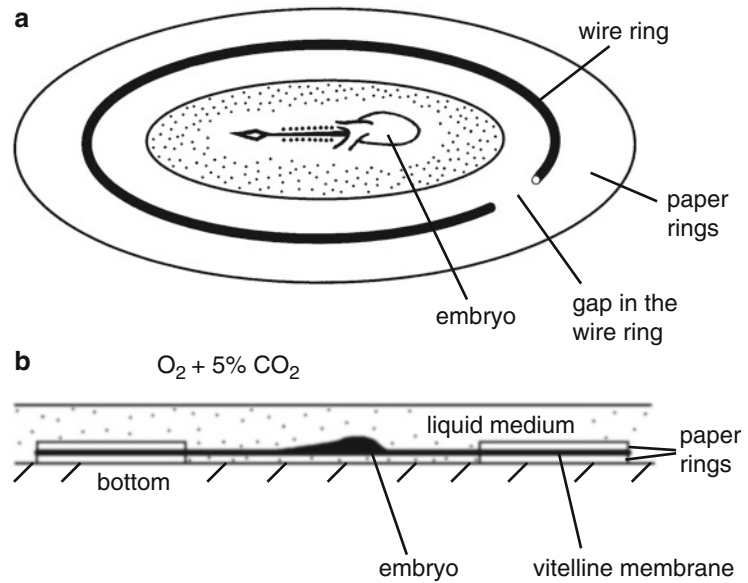
Fig. 1 Schematic for chicken embryo culture (adapted with permission from [21]). (**a**) Embryos are removed from the yolk using a filter paper carrier. A wire ring is placed on top of the filter paper to prevent the embryo from floating. (**b**) The embryo (here: ventral side up) is submerged in liquid medium (*see* Subheading 3.1) and a 95 % O_2, 5 % CO_2, atmosphere is used for culture

the vitelline membrane). Remove all PBS from the culture dish and inject polystyrene microspheres from previously prepared "bullets" (diameter = 10 μm; *see* **Notes 1** and **4**) at 60–100 psi (*see* **Note 5**) using a gene gun (Fig. 2a). Rehydrate the embryo in culture medium (89 % DMEM, 10 % chicken serum, 1 % antibiotics; ≈1.5 mL). To eliminate potential artifacts due to surface tension, submerge the embryo completely to a depth of about 0.5 mm (Fig. 1b) [21].

4. Verify sparse labeling in the tissue using a dissecting microscope. If bead number is insufficient for future strain analysis (<8 beads near the region of interest, *see* Fig. 4), repeat gene gun labeling procedure in the previous step.

5. Place up to seven culture dishes in a 150 mm Petri dish, load samples into a plastic bag filled with 95 % O_2 and 5 % CO_2, and place in the incubator (Fig. 1b, *see* **Note 6** for atmosphere rationale and alternative culture methods).

3.2 Optical Coherence Tomography and Microindentation

1. Remove the culture dish containing the embryo from the incubator and place on the stage of the OCT system. Verify that a layer of liquid media is present over the embryo. This layer should be shallow enough to maintain a strong image signal, but deep enough to submerge the cantilever beam so that surface tension forces will not affect the measurements.
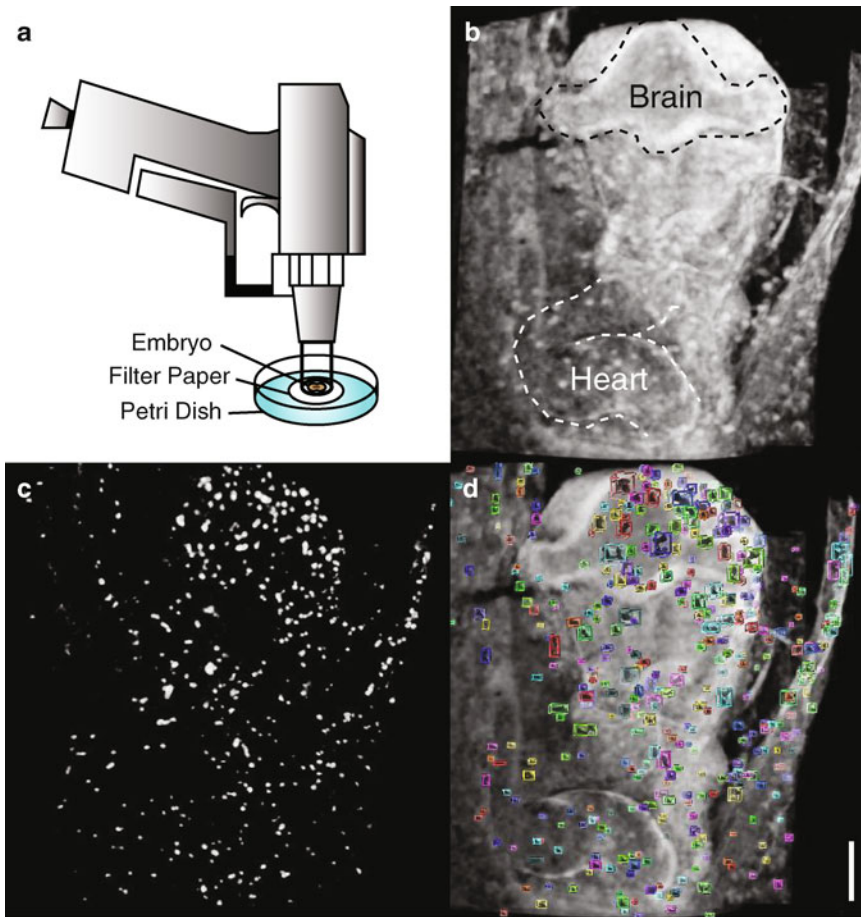
Fig. 2 Embryo labeling. (**a**) Gene gun for ballistic embryo labeling with polystyrene microspheres. (**b**) 3-D rendering of HH12 chick embryo, ventral side up. The c-looped heart and ventral forebrain are outlined. (**c**) Contrast, grayscale, and brightness are adjusted to highlight injected microspheres. (**d**) Microspheres are segmented and overlaid on original rendering to assess label locations and density. Scale bar: 200 μm

This layer of fluid is also required to prevent the embryo from drying out during the experiment and is critical to avoid OCT imaging artifacts that occur at tissue-gas interfaces.

2. Turn on the near-infrared laser for the OCT system and locate the desired region for indentation in the cross-sectional imaging window. For small samples that are difficult to locate, we recommend using a laser viewing card for preliminary sample alignment prior to image inspection. If necessary, place a dark membrane disk underneath the embryo to limit reflection artifacts that arise from the bottom of the culture dish. Upon locating your region of interest, verify that microspheres (local, bright, high-contrast markers, Fig. 2b–d) are embedded in the tissue.
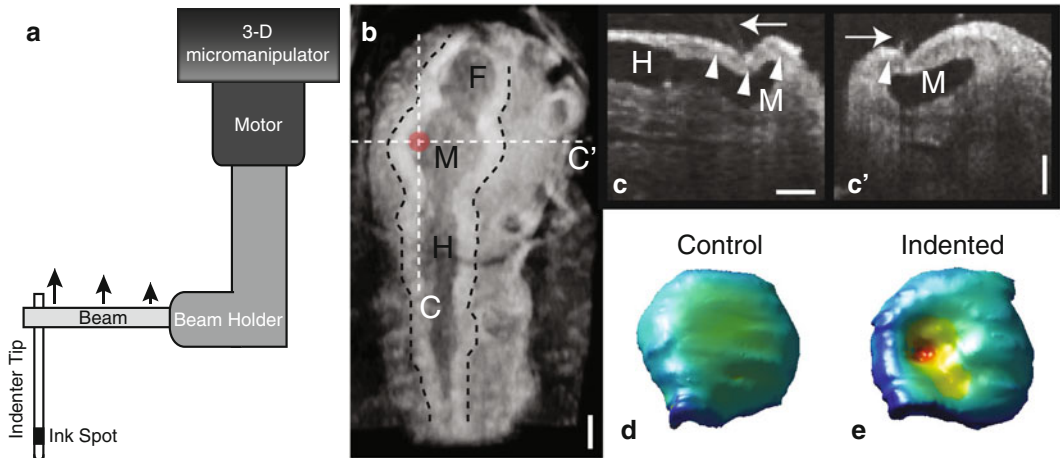
Fig. 3 OCT imaging during microindentation. (**a**) Schematic for microindenter as described in Subheading 3.2. *Arrows* indicate direction of cantilever beam deflection. (**b**) HH12 chick embryo dorsal side up with overlying vitelline membrane removed. Brain tube outlined for clarity (F = forebrain; M = midbrain; H = hindbrain). Cross-sectional locations for microindentation planes (**c** and **c′**) are indicated. *Red circle* indicates location for microindentation. (**c** and **c′**) Longitudinal and transverse cross sections of the brain, respectively, during indentation. Microindenter tip (*arrows*) and microspheres (*arrowheads*, only some are denoted) are apparent. (**d** and **e**) 3-D reconstructions of the control and indented midbrain. Color map is surface curvature to show indentation location. Scale bars: 100 μm

3. Perform an initial 3-D scan around the region of interest (Figs. 2b–d and 3b). Optimize scanning window size based on the size of the tissue and sampling frequency based on the resolution of the OCT system. Note that oversampling will lead to more cumbersome image analysis later. For the early chicken embryo, we have found success with a 3 × 3 mm scanning window with transverse resolution near that of the diameter of the microspheres used to label the embryo.

4. Prepare the microindenter. (For clarity, some of the structural components used in this step are shown in schematic form in Fig. 3a. These items are indicated in **bold** in the text.) Make a microindenter from a glass micropipette using a pipette puller set near the maximum temperature setting to yield a small **indenter tip** (10–30 μm diameter, 0.5–1 cm length). Place a small **ink spot** on the tip to aid in motion tracking (*see* Subheading 3.3, **step 1**). This tip is connected at a right angle via superglue to a slightly wider cantilever **beam** (60–80 μm diameter, 4–5 cm length), which is obtained by using the pipette puller at slightly lower temperature. This beam is connected at its other end to a rigid **beam holder** (1 mm diameter pipette, 6–8 cm length, pre-bent at a right angle using a torch) which is attached to a pipette holder controlled by a piezoelectric

motor and three-dimensional **micromanipulator**. For advice on calibrating the cantilever beam prior to beginning the experiment, *see* **Note 7**.

5. Using visual inspection, position the indenter tip close to the region of interest in the embryo. Carefully control the micromanipulator to move the indenter tip into the focal view of the OCT (Fig. 3c, c′).

6. Begin periodic indentation of the tissue. Record a series of indentations (at least three) while constantly scanning in 2-D cross section using the OCT system (*see* **Note 8** for comments on cross-sectional versus volumetric image acquisition rates using OCT) (Fig. 3c, c′). Following periodic indentation, stop the indenter tip at various indentation depths (including the maximum) and perform a 3-D scan around the indentation site to record the deformed tissue profile (Fig. 3d, e). Volumetric scanning time should be optimized for image clarity, but also to prevent viscoelastic effects from complicating later deformation analyses as described in **Note 9**.

7. When the indenter is retracted from the tissue, move the tissue away from the indenter using micrometer controls on the OCT stage. Now, repeat the periodic indentation and cross-sectional imaging described in the previous step in fluid alone. These control data will be used to calculate cantilever beam deflection. Volumetric scans are not necessary in this step.

3.3 Stiffness and Displacement Analysis

1. Using thresholding algorithms in three-dimensional image analysis software (e.g., Fiji or Volocity), record indentation depth (w) from the displacement of the indenter tip, which can often be visualized directly in OCT cross sections. Due to light scattering, a dark ink spot applied on the tip (Fig. 3a) is also useful for tracking. Repeat for all tissue and control indentations.

2. Calculate cantilever beam deflection (which is not tracked directly) from the difference in tip displacement between the control and tissue indentations. Convert this deflection to applied force using data from the calibration step described in **Note 7**. *See* ref. 14 for more details.

3. Compute stiffness from the slope of the resulting force-displacement curve at a particular indentation depth. Stiffness at small indentation depths (5–10 μm) can usually be approximated using a simple linear regression. Larger indentation depths, however, often result in nonlinear force-displacement curves, as tissues tend to stiffen with increasing deformation. In this case, we have found the following four-parameter function to be useful for curve fitting:

$$P = aw + \frac{b}{2}w^2 + \frac{c}{d}\exp^{(dw)}, \tag{1}$$
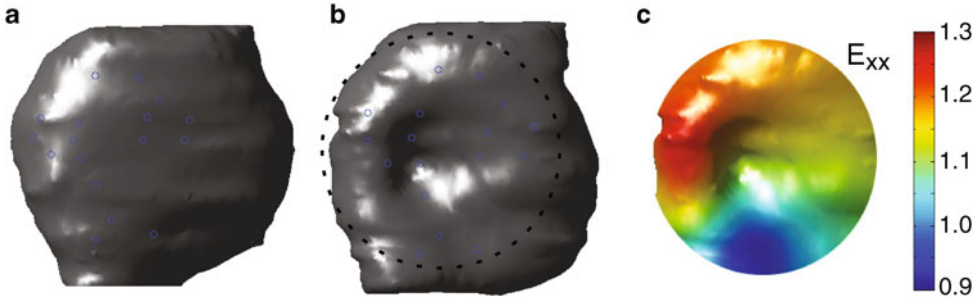
Fig. 4 Indentation strain. (**a**) Undeformed and (**b**) indented midbrain. Tracked marker positions ($n = 17$) indicated with *open circles* (shifted above the surface for visualization purposes). *Dashed circle* indicates region for strain analysis. (**c**) Lateral normal strain (E_{xx}) is computed from marker centroids and mapped to the indented surface. Strain is generally positive and is highest adjacent to the indentation site where gradients in tissue curvature are most prominent

where a, b, c, and d are regression parameters determined through nonlinear least-squares analysis (performed in Matlab or a similar statistics program) and P is the applied force. Tissue stiffness is then given by

$$k(w) = \frac{\mathrm{d}P}{\mathrm{d}w} = a + bw + c\exp^{(\mathrm{d}w)}. \qquad (2)$$

3.4 Deformation Analysis (Strains)

1. Use thresholding algorithms to determine centroids of fiducial markers (at least 8) near the indenter tip in the control and fully indented configurations (Fig. 4a, b). Since the beads are embedded in the epithelium, the indenter tip will not dislodge the beads.

2. Compute Lagrangian strains from the bead coordinates (X,Y,Z) and (x,y,z) in the undeformed and deformed configurations, respectively (Fig. 4c) [22]. Use standard routines (Matlab or similar) to fit 2-D surfaces (appropriate for most thin epithelia, *see* **Note 10**) to marker coordinates near the indenter tip to generate $x(X,Y)$, $y(X,Y)$, and $z(X,Y)$ with the undeformed surface given by $Z = Z(X,Y)$ (see appendix of [8]).

3. Next, compute two-dimensional surface strains (E_{ij}) on a 3-D surface using the following equations (*see* ref. 8):

$$E_{xx} = \frac{\left[\left(\frac{\partial x}{\partial X}\right)^2 + \left(\frac{\partial y}{\partial X}\right)^2 + \left(\frac{\partial z}{\partial X}\right)^2 - 1 - \left(\frac{\partial Z}{\partial X}\right)^2\right]}{2\left[1 + \left(\frac{\partial Z}{\partial X}\right)^2\right]}$$
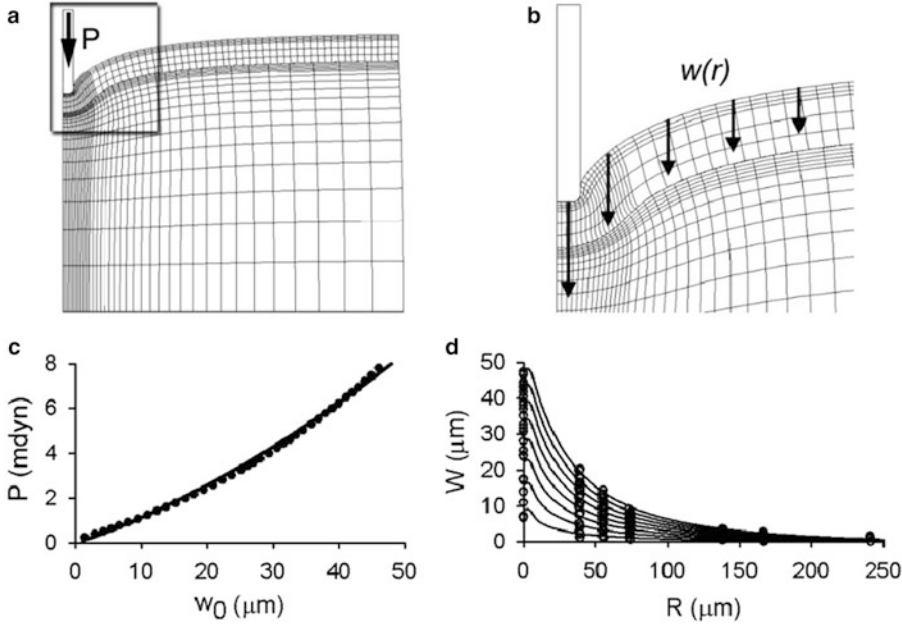
Fig. 5 Experiments and modeling to determine material properties (adapted with permission from [15]). (**a**) Finite element model for indentation. (**b**) Close-up of mesh near the indenter. Vertical displacements $w(r)$ of several surface nodes are recorded during indentation. (**c** and **d**) Force-indentation (**c**) and surface marker displacement (**d**) curves from a representative sample. *Circles* (experiment) and best-fit model solutions (*curve*) are shown. Good agreement suggests that material properties used in the model are sufficient to capture experimental behavior

$$E_{yy} = \frac{\left[\left(\frac{\partial x}{\partial Y}\right)^2 + \left(\frac{\partial y}{\partial Y}\right)^2 + \left(\frac{\partial z}{\partial Y}\right)^2 - 1 - \left(\frac{\partial Z}{\partial Y}\right)^2\right]}{2\left[1 + \left(\frac{\partial Z}{\partial Y}\right)^2\right]} \quad (3)$$

$$E_{xy} = \frac{\left(\frac{\partial x}{\partial X}\frac{\partial x}{\partial Y} + \frac{\partial y}{\partial X}\frac{\partial y}{\partial Y} + \frac{\partial z}{\partial X}\frac{\partial z}{\partial Y} - \frac{\partial Z}{\partial X}\frac{\partial Z}{\partial Y}\right)}{2\sqrt{\left[1 + \left(\frac{\partial Z}{\partial X}\right)^2\right]\left[1 + \left(\frac{\partial Z}{\partial Y}\right)^2\right]}}.$$

Practical details to consider in a strain analysis, including marker density and noise in experimental data, are described in **Note 11**.

3.5 Material Properties

1. Establish a 3-D finite element model (e.g., using Comsol Multiphysics, Abaqus, or similar) with a geometry approximating the indented tissue region (Fig. 5a, b). (In more complex cases, the 3-D geometry of the control surface can be imported directly into the modeling program using appropriate geometry interconversion files.) Postulate a suitable strain-energy

density function W and use the model to simulate the indentation experiment. It is important to include residual stress in this procedure as discussed in **Note 12**.

2. Use the following objective function (Ω) and a standard non-linear least-squares optimization procedure (e.g., Levenberg-Marquardt algorithm) to minimize differences between experimental ($^{\text{EXP}}$) and model ($^{\text{FE}}$) forces, displacements, and strains (Fig. 5c, d). For optimization, an objective function (Ω) of the form

$$\Omega = P + U + E \qquad (4)$$

is useful, where

$$P = \sum_k \left(P^{\text{FE}} - P^{\text{EXP}} \right)_k^2$$

$$U = \sum_{i=1}^{3} \sum_k \sum_l \left(u_i^{\text{FE}} - u_i^{\text{EXP}} \right)_{lk}^2$$

$$E = \sum_{i=1}^{3} \sum_{j=1}^{3} \sum_k \sum_l \left(E_{ij}^{\text{FE}} - E_{ij}^{\text{EXP}} \right)_{lk}^2. \qquad (5)$$

In these equations, P is indentation force, u_i are tissue displacements, E_{ij} are Lagrangian strains, k indicates the tip displacement step, and l is the grid point. Perform an initial optimization and then repeat the procedure with each function in Eq. 5 scaled by the mean value from the previous solution [23]. When the scaling parameters converge, the global minimum is obtained, thus giving the material properties in W[24]. If convergence issues are encountered when varying material parameters in W, a semiautomated weighted grid-averaging method can be used as an alternative to this step [15].

4   Notes

1. We have found that smaller microspheres (<6 μm) are difficult to discern from surrounding tissue using OCT imaging. While we have been able to visualize other colors, dark microspheres (blue, black) scatter more light and act as ideal contrast agents. Larger microspheres (>10 μm) are more likely to cause damage during ballistic labeling and may span multiple cell lengths, potentially complicating strain analysis.

2. Ballistic labeling with a gene gun is a simple, high-throughput tissue labeling method for embryonic tissues. In some cases, such labeling may be impractical, however, such as labeling

epithelia buried deep within other tissue layers. In this case, readers are directed to microinjection methods using glass micropipettes [13, 20].

3. An alternative indentation method is to use magnetic microspheres under a strong magnetic field to apply forces [6]. For very small beads, however, the force may be too small to sufficiently deform the tissue.

4. To prepare gene gun bullets, mix 50 μL of stock bead solution with 200 μL of 95 % ethanol and pull this solution into Tefzel tubing using a microsyringe. Allow the beads to sediment for 15 min and suction off excess ethanol. Let sit for an additional 15–30 min so that the beads dry and adhere to the surface of the tubing. Strike the tubing against a hard surface to help achieve a more uniform bead distribution. Cut the tubing into small pieces (<1 cm in length) to generate "bullets" to load into the gene gun. Dilute or concentrate the initial bead solution as necessary to yield a sparser or a denser final bead distribution.

5. Bead injection pressure depends on the thickness, location, and stiffness of the tissue, as well as the size and composition of the injected labels. With early-stage chicken embryos, we have found that injection pressures above 100 psi can tear the extra-embryonic membranes that adhere the embryo to the filter paper. Lower injection pressures (40–60 psi) have proven successful in thinner, softer epithelia (e.g., the myocardium relative to the neuroepithelium) at these stages.

6. Because the embryo is submerged in this culture method, relatively high oxygen levels are necessary to achieve normal development [21]. For more traditional surface-based culture methods on albumen or DMEM gels [25], proceed with a standard 5 % CO_2, 21 % O_2, balance N_2 atmosphere. Note that the embryo must be submerged prior to the microindentation experiment, however, for the reasons given in **step 1** of Subheading 3.2.

7. The spring constant of the cantilever beam can be calibrated by adding several known weights (e.g., small pieces of wire) to the free end and measuring resulting deflections. Beam stiffness should be similar to that of the tissue being studied to optimize measurement sensitivity. Using the size and length guidelines for the cantilever beam described in **step 4** of Subheading 3.2, we can measure indentation forces at the level of nanonewtons (for comparison, atomic force microscopy measures in the range of piconewtons) [14].

8. The frame acquisition rate of most OCT systems is not sufficient to record volumetric scans of the microindentation experiment in real time. Because of this limitation, we recommend

recording periodic indentations in 2-D cross section (easily visualized in real time), followed by stationary 3-D scans at selected indentation depths.

9. Volumetric scans during indentation should be optimized such that imaging time is minimized, yet image quality is still sufficient to accurately measure bead locations in later analyses. Fast scan times are important to prevent stress relaxation (viscoelastic) effects from affecting sample geometry. We recommend limiting the size of the imaging window to that of the tissue of interest to decrease acquisition time (often improving stack acquisition speed near an order of magnitude). Repeated 3-D scans over an extended time interval will also help in determining when, or if, stress relaxation effects become significant in the indented tissue.

10. Implicit in our strain analysis is that beads are embedded in a thin epithelium with coordinates well approximated by a surface. For thick tissue this assumption may not be appropriate, in which case approaches that quantify transmural strain distributions from marker arrays can be used [26].

11. The accuracy of the strain algorithm is directly tied to the accuracy of the surface fitting performed in **step 2** of Subheading 3.4. We have found that the density and distribution pattern of surface markers, the overall geometry of the fitted surface, and noise in the data can all affect the accuracy of strain analysis. Some guidelines for navigating these effects are as follows. We have found a well-spaced grid of 8+ markers near the indentation site to be sufficient to capture local variations in strain, with care taken not to over-extrapolate to outlier marker positions. Noise in the data can be accounted for by adjusting, for example, the "stiffness" of a thin plate spline used in the surface fits, although it is also important not to oversmooth the data. Test cases can often be useful in discerning these effects [13].

12. Constitutive equations need to be referred to the stress-free state of the tissue, which can be assessed using residual stress estimates [15]. From these data, residual stretch ratios can be incorporated as additional material parameters in the finite element model via the fitting steps described in Subheading 3.5.

Acknowledgements

References

1. Gregg CL, Butcher JT (2012) Quantitative in vivo imaging of embryonic development: opportunities and challenges. Differentiation 84:149–162

2. Trier SM, Davidson LA (2011) Quantitative microscopy and imaging tools for the mechanical analysis of morphogenesis. Curr Opin Genet Dev 21:664–670

3. Davidson L, Keller R (2007) Measuring mechanical properties of embryos and embryonic tissues. Methods Cell Biol 83:425–439

4. Davidson L, von Dassow M, Zhou J (2009) Multi-scale mechanics from molecules to morphogenesis. Int J Biochem Cell Biol 41:2147–2162

5. Wozniak MA, Chen CS (2009) Mechanotransduction in development: a growing role for contractility. Nat Rev Mol Cell Biol 10:34–43

6. Lee SJ, Sun J, Flint JJ et al (2011) Optically based-indentation technique for acute rat brain tissue slices and thin biomaterials. J Biomed Mater Res B 97:84–95

7. Fujimoto JG (2003) Optical coherence tomography for ultrahigh resolution in vivo imaging. Nat Biotechnol 21:1361–1367

8. Filas BA, Efimov IR, Taber LA (2007) Optical coherence tomography as a tool for measuring morphogenetic deformation of the looping heart. Anat Rec 290:1057–1068

9. Jenkins MW, Watanabe M, Rollins AM (2012) Longitudinal imaging of heart development with optical coherence tomography. IEEE J Select Top Quantum Electron 18:1166–1175

10. Rugonyi S, Shaut C, Liu A et al (2008) Changes in wall motion and blood flow in the outflow tract of chick embryonic hearts observed with optical coherence tomography after outflow tract banding and vitelline-vein ligation. Phys Med Biol 53:5077–5091

11. Syed SH, Larin KV, Dickinson ME et al (2011) Optical coherence tomography for high-resolution imaging of mouse development in utero. J Biomed Opt 16:046004

12. Larina IV, Larin KV, Justice MJ et al (2011) Optical coherence tomography for live imaging of mammalian development. Curr Opin Genet Dev 21:579–584

13. Filas BA, Knutsen AK, Bayly PV et al (2008) A new method for measuring deformation of folding surfaces during morphogenesis. J Biomech Eng 130:61010

14. Zamir EA, Srinivasan V, Perucchio R et al (2003) Mechanical asymmetry in the embryonic chick heart during looping. Ann Biomed Eng 31:1327–1336

15. Zamir EA, Taber LA (2004) Material properties and residual stress in the stage 12 chick heart during cardiac looping. J Biomech Eng 126:823–830

16. Xu G, Kemp PS, Hwu JA et al (2010) Opening angles and material properties of the early embryonic chick brain. J Biomech Eng 132:011005

17. Zahalak GI, McConnaughey WB, Elson EL (1990) Determination of cellular mechanical properties by cell poking, with an application to leukocytes. J Biomech Eng 112:283–294

18. Lam V, Wakatsuki T (2011) Hydrogel tissue construct-based high-content compound screening. J Biomol Screen 16:120–128

19. Hamburger V, Hamilton HL (1951) A series of normal stages in the development of the chick embryo. J Morph 88:49–92

20. Filas BA, Varner VD, Voronov DA et al (2011) Tracking morphogenetic tissue deformations in the early chick embryo. J Vis Exp e3129

21. Voronov DA, Taber LA (2002) Cardiac looping in experimental conditions: the effects of extraembryonic forces. Dev Dyn 224:413–421

22. Hashima AR, Young AA, McCulloch AD et al (1993) Nonhomogeneous analysis of epicardial strain distributions during acute myocardial ischemia in the dog. J Biomech 26:19–35

23. Guccione JM, McCulloch AD, Waldman LK (1991) Passive material properties of intact ventricular myocardium determined from a cylindrical model. J Biomech Eng 113:42–55

24. Humphrey JD (2002) Cardiovascular solid mechanics: cells, tissues, and organs. Springer, New York

25. Chapman SC, Collignon J, Schoenwolf GC et al (2001) Improved method for chick whole-embryo culture using a filter paper carrier. Dev Dyn 220:284–289

26. Kindberg K, Karlsson M, Ingels NB et al (2007) Nonhomogeneous strain from sparse marker arrays for analysis of transmural myocardial mechanics. J Biomech Eng 129:603–610

Chapter 2

Hemodynamic Flow Visualization of Early Embryonic Great Vessels Using μPIV

Selda Goktas, Chia-Yuan Chen, William J. Kowalski, and Kerem Pekkan

Abstract

Microparticle image velocimetry (μPIV) is an evolving quantitative methodology to closely and accurately monitor the cardiac flow dynamics and mechanotransduction during vascular morphogenesis. While PIV technique has a long history, contemporary developments in advanced microscopy have significantly expanded its power. This chapter includes three new methods for μPIV acquisition in selected embryonic structures achieved through advanced optical imaging: (1) high-speed confocal scanning of transgenic zebrafish embryos, where the transgenic erythrocytes act as the tracing particles; (2) microinjection of artificial seeding particles in chick embryos visualized with stereomicroscopy; and (3) real-time, time-resolved optical coherence tomography acquisition of vitelline vessel flow profiles in chick embryos, tracking the erythrocytes.

Key words Tissue morphogenesis, Particle image velocimetry, Hemodynamics, Cardiovascular development, Aortic arch, Congenital heart defects, Confocal microscopy, Chick embryo, Zebrafish, Optical coherence tomography

1 Introduction

Increasing number of patients suffering from cardiac diseases, particularly congenital heart defects [1] and emphasis on mechanotransduction during cardiac development [2], has urged the exploration of experimental tools for rapid and accurate quantification of cardiac flows. Syndromes and abnormalities influencing cardiac function start during early embryonic development, where the direct assessment of hemodynamics is even more challenging due to microfluidic scales [3]. Thus, advanced imaging and visualization methods need to be employed to precisely detect the malformations of the embryonic cardiac vessel systems and guide towards the necessary fetal treatments.

Various techniques have been utilized in order to noninvasively quantify the blood flow dynamics of embryonic cardiovascular structures, such as the Doppler ultrasound [4], Doppler optical

coherence tomography (Doppler-OCT) [5], and traditional microparticle image velocimetry (μPIV) [6, 7]. This chapter focuses on the use of μPIV technology for two model systems, namely the chick and zebrafish embryos. These model organisms have been widely examined for investigating vertebrate cardiovascular development and are well documented [8, 9]. μPIV is most applicable to chick embryos at stage 24 (approximately 4 days after the start of incubation) when the cardiac looping transforms the heart into a looped tube [10]. In the case of the zebrafish, embryos raised to 32 and 48 h post-fertilization periods can be utilized for predicting flow patterns [11]. μPIV technique requires the labeling of flowing fiducial fluid elements. However, injecting artificial particles to the microcirculation of the zebrafish embryos and subsequent long-duration time-lapsed imaging are practically difficult due to bleeding. Furthermore, particles will interfere with normal cardiac physiology. Major remedy is to utilize transgenic zebrafish embryos [12] or the OCT-μPIV.

2   Materials

2.1 Transgenic Embryo Sources and Staging

1. Fertile white Leghorn chicken eggs are from a local farm. Eggs should be placed in an incubator of 37 °C and 50–60 % relative humidity (*see* **Note 1**). To facilitate experimental work, eggs should be incubated blunt end up.

2. Zebrafish (*Danio rerio*) were maintained according to standard protocols [13]. *chrna1b*107/*b*107 [14], *Tg*(*kdrl:GFP*)*la*116 [15], *Tg*(*gata1:DsRed*)*sd*2 [16] zebrafish embryos were raised to 32 and 48 h post-fertilization (hpf) for hemodynamic quantification.

2.2 Solutions and Seeding Particles

1. Zebrafish anesthetic: 400 mg Tricaine powder (Sigma-Aldrich Corp., St. Louis, MO, USA), 97.9 mL deionized water, 1 M Tris-HCL (Sigma-Aldrich Corp., St. Louis, MO, USA), pH 7.

2. Chick Ringer's solution: 135 mM NaCl, 4 mM KCl, 10 mM Tris–HCl, 10 mM Tris base, 11 mM dextrose, pH 7.4 (*see* **Note 2**).

3. Fluorescent particles: 0.5 μm fluorescent polystyrene microspheres (Thermo Scientific Fluoro-Max Red Aqueous Fluorescent Particles, Waltham, MA, USA). Dilute the 1 % solid stock particle solution to 0.05 % solids with Ringer's solution. Add 150 μL of the 1 % solid solution to 2.85 mL Ringer's solution and vortex. The diameter and seeding concentration of artificial particles should be optimized for the specific PIV equipment (*see* **Note 3**).

2.3 Zebrafish Confocal Microscopy and Microfluidic Platform

1. SU8 2075 photoresist and developer (MicroChem Corp., Newton, MA, USA).

2. Polydimethylsiloxane (PDMS) (Dow Corning Corp., Midland, MI, USA).

3. Acetone and Isopropanol (Sigma-Aldrich Corp., St. Louis, MO, USA): As an alternative, agarose gel (Sigma-Aldrich Corp., St. Louis, MO, USA) can be used to mount embryos during imaging (*see* ref. 12).

4. Hot plate.

5. Micro-poker.

6. Spin coater (Solitec Photoresist Spinner, WT Services, Inc., Fitchburg, MA, USA).

7. Silicon wafer.

8. Plasma cleaner.

9. Vacuum oven.

10. N_2 gun.

11. Petri dishes of 14 cm diameter (Fisher Scientific International Inc., Hampton, NH, USA).

12. Curing agent (Dow Corning Corp., Midland, MI, USA).

13. DaVis 7.2 PIV (LaVision, Inc., Goettingen, Germany) software is adopted for quantification of hemodynamics in blood vessels.

14. A Leica TCS SP5 confocal microscope with resonant scanner (Leica Microsystems GmbH, Wetzlar, Germany) is used for fluorescent imaging.

2.4 Chick Embryo Microscopy and Instrumentation

1. Leica MZ 16FC stereomicroscope with external Leica EL6000 mercury halide light source coupled through the collimator for episcopic fluorescence (Leica Microsystems GmbH, Germany) (*see* **Note 4**). The microscope binocular includes a beam splitter to direct light to both eyepieces or one eyepiece and a mounted camera.

2. Leitz 3-axis micromanipulator.

3. Dumont #55 and 5MS tweezers (WPI, Sarasota, FL, USA).

4. Vannas microscissors, 8 cm length with 5 mm blades and 0.1 mm tips (WPI, Sarasota, FL, USA).

5. 28 gauge MicroFil needle (WPI, Sarasota, FL, USA).

6. 10 μL Hamilton gastight syringe with Luer tip.

7. 20 gauge blunt tip needle.

8. PE-60 tubing (Braintree Scientific, Braintree, MA, USA).

9. PC-10 puller and EG-44 microgrinder (Narishige Inc., Japan) for generating 20–30 μm microneedles used for injection (*see* **Note 5**).

10. Photron SA4 high speed camera, Leica FX350 high speed camera.

2.5 Chick Embryo Optical Coherence Tomography

1. Thorlabs Ganymede Spectral Domain Optical Coherence Tomography (OCT) system: The OCT light source is a 930 nm superluminescent diode with a 100 nm spectral bandwidth. Axial resolution is 5.8 μm in air (4.3 μm in water) and lateral resolution is 8 μm. The maximum A-scan rate is 29 kHz (*see* **Note 6**). The spectrometer consists of a 12-bit high-sensitivity CCD camera with 2.0 μm pixel spacing. Data is transferred in real time over a GigE connection to a PC with a 3.3 GHz processor. A refraction index of 1.33 is used for the aqueous environment of the chick embryo. The OCT stage includes an XY-axis manipulator for fine adjustment of the embryo position. The position of the scanning plane can be further adjusted by shifting the Galvo mirrors enclosed in the probe.

2. A custom-built enclosed clear plastic chamber surrounding the OCT imaging probe and egg to maintain a 37 °C and 60 % humidity environment. Important features include a 250 W heat lamp connected to a temperature controller and a drug-store humidifier. Adjustable vents on opposing sides and a computer fan create adequate air circulation.

3 Methods

3.1 Embryo Staging

This protocol is designed to quantify microcirculation of embryos at selected developing stages. To ensure the healthy growth of the tested developing zebrafish, a zebrafish breeding protocol is followed (*see* ref. 13). The morphological changes of zebrafish embryos during this time window are quantified and described in Table 1. Chick embryos are staged according to Hamburger and Hamilton [17]. For early embryos (prior to stage 26), the number of somites and angle between the axial and cranial axes are primary indicators of the development stage. Blood flow begins between stages 11 and 12 (40–45 h).

3.2 Microfluidic Platform Fabrication

To immobilize zebrafish embryos during time-lapse confocal-μPIV imaging, a biocompatible polydimethylsiloxane (PDMS) platform is fabricated through a microfabrication procedure as described below:

1. Rinse a 4-in. silicon wafer and a 5-in. transparency (which defines the geometry of the platform) with acetone and

Table 1
Dimensions of zebrafish embryos during 24–48 hpf (hours post-fertilization)

(mm)				
28 hpf	0.56	0.60	1.07	1.78
36 hpf	0.47	0.55	1.38	2.14
48 hpf	0.34	0.39	1.30	1.94

isopropanol. Blow-dry the wafer and the transparency with N_2 gun after the rinse.

2. Place the wafer onto a spin-coater stage for SU8 2075 film spinning. The set spinning parameters are 10 s at 500 rpm and subsequent 30 s at 2,000 rpm.

3. Place the wafer with SU8 film (~150 μm thick) on top of a hot plate for 60 min at 65 °C (see **Note 7**).

4. Allow the wafer to cool to room temperature and harden after heating. Expose the wafer with a 365 nm ultraviolet (UV) light source for 145 s.

5. Heat the wafer for 22 min at 65 °C. Allow the wafer to cool to room temperature again.

6. Develop the exposed SU8 film using an SU-8 developer for approximately 20 min. Apply a 10-s rinse with isopropanol. Dry the wafer with N_2 gun and inspect it with a profilometer to examine the features of the SU8 mold.

7. To make a corresponding PDMS platform replica using the SU8 mold, firstly place the SU8 mold in a petri dish (*see* **Note 8**).

8. Mix PDMS base and curing agent in a 10:1 (base:agent) ratio of mixture by weight (example 30 g base, 3 g agent).

9. Place the mixture in a centrifuge tube and centrifuge for about 20 s to remove bubbles.

10. Bring a cup of PDMS mixture close to the surface of the SU8 mold. Pour it onto the center of the mold and spread around it (*see* **Note 9**).

11. Place the SU8 mold filled with PDMS in a vacuum oven. Wait for 2 min and then release the vacuum quickly. Repeat this procedure until the majority of small bubbles have been dispersed.
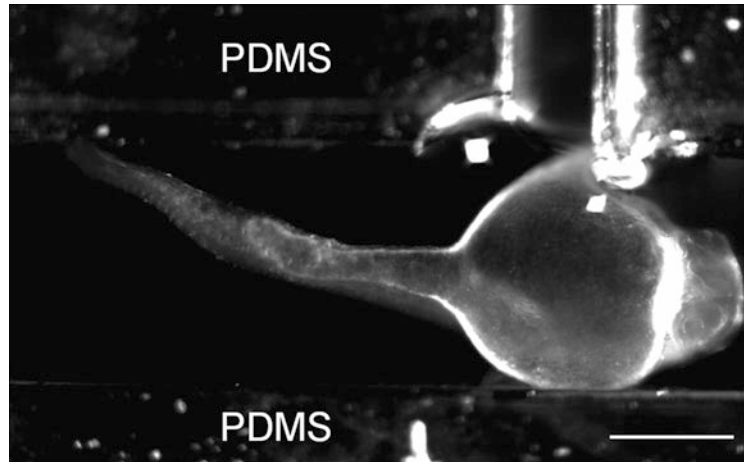
Fig. 1 A zebrafish embryo is immobilized in a PDMS microfluidic platform to facilitate the time-lapse imaging. Scale bar: 400 μm

12. Heat PDMS for 120 min at 60 °C. Remove cured PDMS from the SU8 mold by loosening edges with a scraping tool. Continue with plasma cleaning of the PDMS microfluidic platform (Fig. 1) [18].

3.3 Volumetric Confocal Microscopy Imaging of Zebrafish

1. Position embryos laterally on the stage of a confocal microscope to have a visual of erythrocyte flows.

2. Record time-lapse images (256×64 pixels) using a $20\times$ oil objective on a confocal microscope fitted with Ar and HeNe lasers (488 and 543 nm) (*see* **Note 10**).

3. Acquire images using 8,000 Hz (phase-matched bidirectional resonant scanner). Set the full-frame acquisition rate at 175 frames per second (4,000 frames can be recorded per dataset). Record at least 20 cardiac cycles, with 60–90 data points sampled in each cardiac cycle.

3.4 Microinjection of Seeding Particles into the Chick Embryo

1. Candle the egg by holding it in front of a bright white light source to view the position of the air sac. Place the egg in a holder made from an empty scotch tape ring, round bottom flask holder, or other stable platforms. Using the blunt end of the tweezers, gently crack the shell above the air sac and peel away to create a small window around 1 cm². Remove any underlying shell membrane blocking the embryo. With the tweezers, gently peel away the slightly opaque membrane covering the embryo and surrounding vitelline circulation. Only peel away enough to expose the embryo and area planned for injection and PIV acquisition (*see* **Note 11**). The embryo should appear right side up. Left side up or otherwise

dysmorphic embryos should be discarded unless the experiment calls for them. The window can be covered with Parafilm and the egg is placed back in the incubator if necessary.

2. Thread about 18 cm of PE-60 tubing onto the 20 gauge blunt-tip needle and connect to the Hamilton syringe. Attach the Hamilton syringe to the body of the micromanipulator with scotch tape. Prime the syringe and tubing with Ringer's solution using the MicroFil to perfuse from the syringe to the tubing. Replace the syringe plunger when done. Using the MicroFil, prime the microneedle with Ringer's solution. Attach the microneedle to the end of the tubing, being sure to avoid the introduction of air bubbles (*see* **Note 12**). Fix the microneedle to the end of the micromanipulator using a clamp or other devices, being sure to give enough length to reach the egg.

3. Put a small amount (3 µL) of the fluorescent dye solution in a shallow dish (the cap cut from a 2 mL centrifuge tube works well) and place on the microscope stage. Using the micromanipulator, carefully position the tip of the microneedle into the drop of solution. Draw the fluorescent particles into the tip of the microneedle by retracting the plunger of the Hamilton syringe. Verify that the microneedle has taken up some solution by examining with the microscope.

4. Place the windowed egg under the microscope. If the embryo is stage 18 or older, dissect away any additional membranes covering the desired injection site using the tweezers and microscissors. Do not remove more membrane than necessary.

5. Using the micromanipulator, position the microneedle at the desired injection site and gently advance to puncture the vascular tissue (*see* **Note 13**). Blood cells should be observed within the tip of the microneedle to ensure penetration into the lumen. Bleeding should not be observed, as it indicates a complete puncture through the vessel. If bleeding is observed, the microneedle is withdrawn and the embryo is discarded. Figure 2 shows a stage 21 (3.5-day) embryo with the needle in place.

6. Turn on the external fluorescent light source and rotate the filter carriage to the appropriate set. At this time, switch to a higher objective if possible (*see* **Note 4**).

7. Inject the desired volume of solution by depressing the plunger of the Hamilton syringe. Light pressure should be applied not to burst the delicate embryo. Injection volumes of up to 0.5 µL have been shown to minimally affect normal hemodynamics (<10 % change in stroke volume and mean arterial pressure) [19]. A section of the vitelline vasculature with seeded particles is shown in Fig. 3.
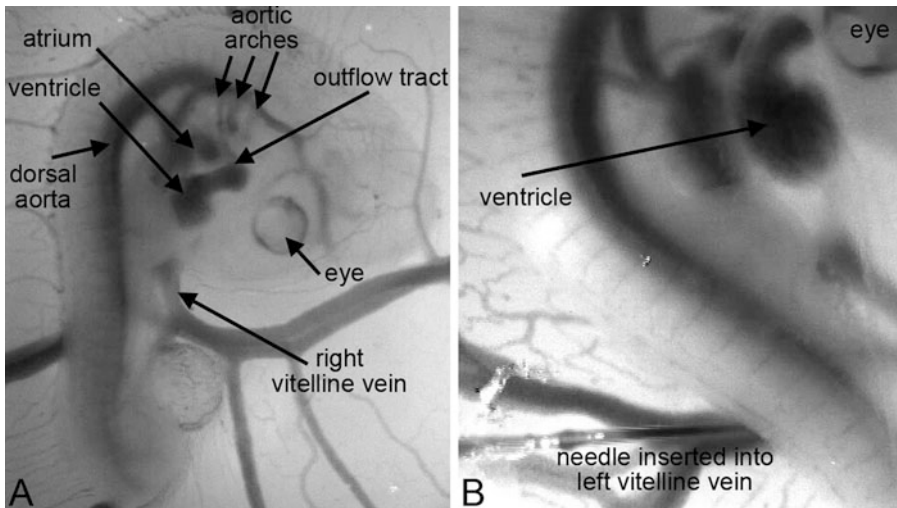
Fig. 2 A stage 21 (3.5-day) chick embryo. (**a**) The embryo vas viewed under a stereomicroscope with major cardiovascular structures labeled. (**b**) A microneedle is inserted into the left vitelline vein to facilitate injection of microparticles

Fig. 3 A section of the extraembryonic vitelline vascular network with seeded half micron microparticles after injection. Blood flow is right to left in the large vessel. The sparse background is due to particles within the smaller vessels and capillaries

8. Record the circulation of particles for PIV post-processing. The embryonic heart rate between stages 18 and 24 ranges from 1 to 3 Hz and peak dorsal aortic blood velocity is approximately 30 mm/s. Velocities in the primary vitelline veins range from 1 to 10 mm/s. Data acquisition at 100 frames per second is therefore required for vessels such as the dorsal aorta, while 30 frames per second is sufficient for the extraembryonic regions.
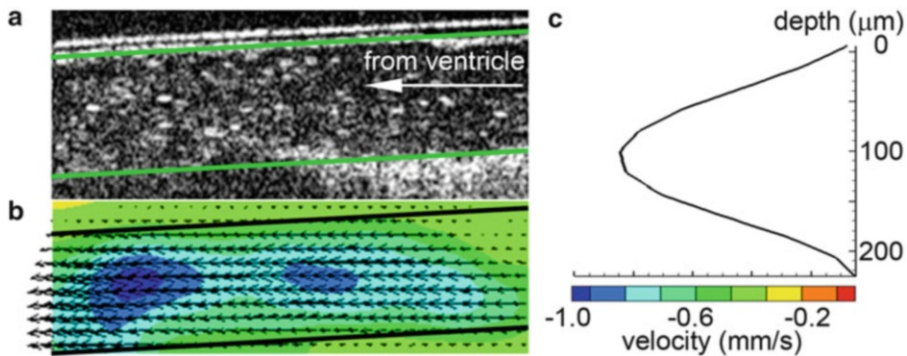
Fig. 4 Velocity vectors in the right vitelline vein of a stage 18 (3-day) embryo computed from OCT data. (**a**) Sample frame from a 2D OCT image sequence. *Green lines* mark the vessel boundaries. (**b**) Cycle-averaged velocity vectors computed from PIV of erythrocytes. *Black lines* mark vessel boundaries. (**c**) The velocity profile along the *dotted line* in **b** (Color figure online)

3.5 Optical Coherence Tomography Acquisition for PIV

1. Turn on the incubation chamber and allow it to stabilize temperature and humidity.

2. Window the egg to expose the embryo as described previously (*see* Subheading 3.4, **step 1**).

3. Place the egg on the OCT stage. Turn on the OCT system and apply appropriate settings, including scan width, number of A-lines, and index of refraction.

4. Begin acquiring 2D B-scans with live streaming. Position and rotate the embryo such that the scanning plane intersects the vessel longitudinally. Use the OCT Galvo controls to finely adjust the scanning plane angle and position. Ensure that the scanning direction and blood flow direction are the same.

5. Adjust the scanning width and number of A-lines to achieve the desired frame rate (*see* **Note 14**).

6. Stop live streaming and set the record options for the application. Record a set number of B-scans or for a set number of seconds.

7. Restart the scan and record the data (*see* **Note 15**). Figure 4 shows a sample processed dataset of blood flow in the stage 18 right vitelline vein.

3.6 Time-Lapse Flow Velocity Measurement

1. Calculate velocity vectors of blood flows using a fast Fourier transform cyclic algorithm with second-order correlation from the PIV software (*see* **Note 16**).

2. Employ Gaussian peak fit as a three-point estimator to obtain sub-pixel accuracy measurement. Apply a multi-pass post-processing median filter to remove bad vectors >2 root mean square (rms) velocity, and reinserted if <3 rms of neighboring vectors (Fig. 5).
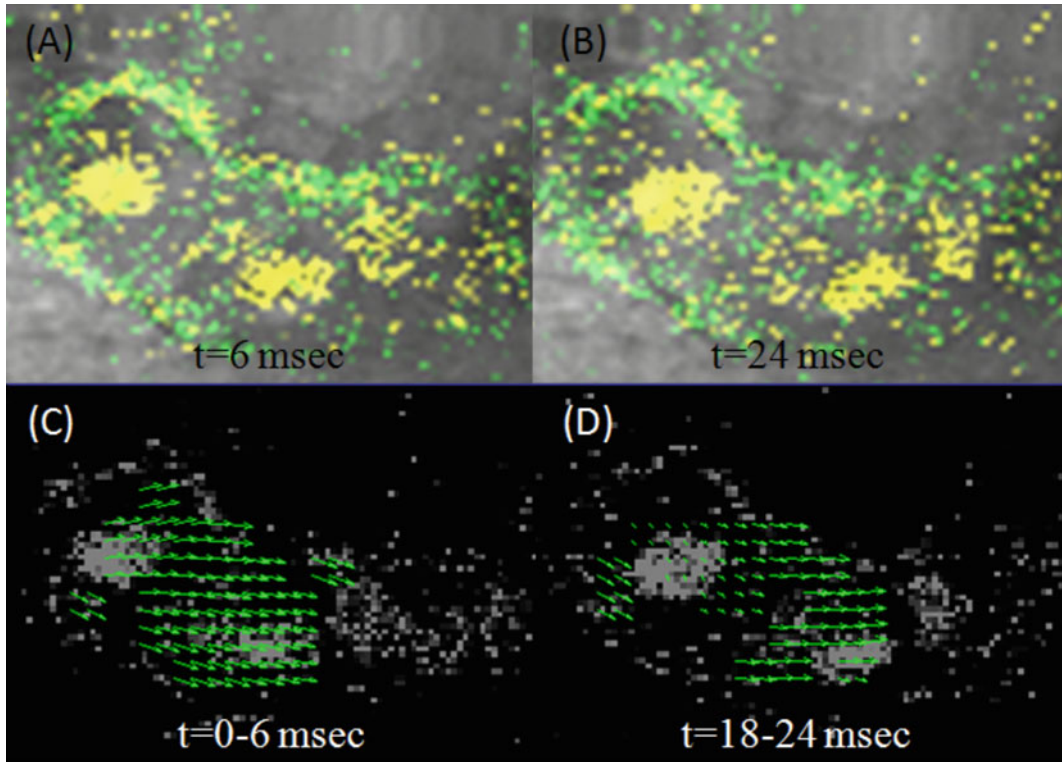
Fig. 5 An example of calculated velocity vectors of a blood flow in a zebrafish embryo at two instants. (**a**) and (**b**) show raw single-scan confocal images; (**c**) and (**d**) show velocity vectors (adapted from [11]) (reproduced with permission from IOS Press, The Netherlands)

3.7 Wall Shear Stress (WSS) Calculation

1. Extract instantaneous streamwise velocity from a 50×30 pixel window within a two-dimensional time-lapse PIV velocity map.

2. Integrate the streamwise velocity component along the vessel cross section to provide the instantaneous average blood flow rate (*see* **Note 17**).

3. Calculate the averaged diameters of the vessel using the average of systolic and diastolic diameters throughout three cardiac cycles.

4. Orient embryos to access a region of unidirectional flow.

5. Estimate the instantaneous WSS values from Eq. 1, as follows (*see* **Note 18**):

$$\tau = \mu \frac{\partial u}{\partial r} \tag{1}$$

$\frac{\partial u}{\partial r}$ represents the streamwise normal velocity gradient along the diameter of a blood vessel of interest (*see* ref. 11).

4   Notes

1. Embryos will not begin development until the egg is placed in the incubator. To have the correct stage embryo for experiment, it is important to coordinate the start time of the incubation. Eggs that are not incubated soon after laying generally show delayed developmental stages, and this delay increases with the amount of time waited before incubation begins. Starting incubation more than 3 days after laying results in a low yield (<50 %).

2. Weigh 7.89 g NaCl, 0.30 g KCl, 1.58 g Tris–HCl, 1.21 g Tris base, and 1.98 g dextrose and transfer to the vessel. Dilute to a total volume of 900 mL with distilled water and mix until clear. Adjust the pH with 1 N HCl. Dilute to 1 L with distilled water. Store the solution in a closed container at 4 °C.

3. Keane and Adrian demonstrated an optimal particle seeding concentration depending on the PIV optics [20]. For volumetric illumination, the depth of correlation (thickness that influences the correlation result) is related to particle diameter [21].

4. A stereomicroscope is useful for work with *in ovo* chick embryos, given the long working distance of the objective lens. It is helpful to have an external white light source. A gooseneck illuminator is preferable, as it allows for easy positioning and minimally obstructs access to the embryo. A 1.0× objective (working distance of 60 mm) can be used for embryo manipulation, including injection, while a 5.0× objective can be used for PIV data acquisition. The Leica MZ 16FC can be equipped with rotating objective turret (FluoCombi III) for this purpose. The Leica MZ 16FC uses a floating lens to adjust the zoom level, ranging between 0.63× and 11.5×. The focus can be controlled digitally and locked to preserve the focal plane. A variety of dichroic filter sets are manufactured for use with the fluorescence module.

5. The microneedle is pulled from a 1.0 mm inner diameter glass capillary tube. After pulling, the microneedle is beveled to a 30° tip angle using a microgrinder for about 30 min. The microneedle should be inspected for chips prior to use. The same microneedle can be used for up to four injections unless it is broken or blocked between the injections. Fluorescent particles tend to aggregate and block the microneedle. They can be flushed with distilled water using the MicroFil.

6. The maximum A-scan rate cannot be achieved due to data transfer from the OCT engine to the PC. Live streaming of the B-scan further degrades the actual scan rate. In the case of live streaming, frame rates of 25.1 fps and 17.1 fps are achieved for a 512 and 757 A-line image, respectively.

7. During the baking of the SU8 film, use a micro-poker (small sharp glass rod) to pop bubbles while heating.

8. A paperboard dam around the platform area can be prepared to reduce the amount of PDMS needed.

9. When pouring PDMS into SU8 mold, be sure to pour the mixture slowly and close to the mold in order to reduce the formation of bubbles.

10. Set high-sensitive photomultiplier (PMT) detection in the range of 495–536 nm and 555–640 nm for green fluorescent protein (GFP) and red fluorescent protein (DsRed) signals, respectively.

11. To peel away the extraembryonic membrane, it is easiest to find a place where the membrane has buckled, grab with the tweezers, and pull gently. Pulling in a circular pattern may help to bring as much membrane away as possible. It is important not to break any vessels, as the embryos cannot clot until day 8.

12. The outer diameter of the glass capillary is slightly larger than the inner diameter of the tubing to ensure a tight seal. It helps to expand the end of the tubing using the tweezers or a heated metallic probe.

13. Typical injection sites include the large vitelline veins. These vessels are external to the embryo and close to the surface, allowing easy access. If the embryo is stage 18 or older, remove the overlying vitelline membrane using the tweezers and microscissors. Vitelline vessels are around 300 μm at stage 18. The microneedle tip should be 1/10th the vessel diameter. Position the embryo such that the microneedle and vessel are parallel. If the microneedle pushes the vessel and does not puncture, it is likely dull and should be replaced.

14. The lateral scanning width and number of A-lines should be optimized to allow the fastest frame rate without sacrificing lateral pixel resolution. These parameters will set the maximum velocity that can be acquired. A faster frame rate and larger scanning width will increase the number of frames that contain the same particles, allowing higher velocities. However, increasing the frame rate, by reducing the number of A-lines, and expanding the scanning width quickly reduce the lateral pixel resolution (scan width divided by number of A-lines). In general, the maximum velocity that can be measured is slightly less than the scan width multiplied by the frame rate.

15. The Thorlabs OCT software writes data to a propriety file type. These files can be read easily with programs developed in MATLAB or another language. Each frame is exported as a TIFF image for use with the PIV processing software.

16. 16×16 pixel with 50 % overlap for two iterations is used as the first-pass interrogation window. The second pass is selected as 12×12-pixel interrogation size with 50 % overlap for two iterations.

17. The Womersley numbers of the embryonic microcirculation are generally low (<1). As such, an assumption of a quasi-steady parabolic plasma velocity profile is justified.

18. Equation 1 is applied with the assumptions of conservation of mass as well as the no-slip boundary conditions at the vessel walls. Embryos with significant out-of-plane velocity components at the imaging plane should be discarded.

Acknowledgement

References

1. Pekkan K, Keller BB (2013) Developmental fetal cardiovascular biomechanics in the 21st century: another tipping point. Cardiovasc Eng Technol 4:231–233

2. Buskohl PR, Jenkins JT, Butcher JT (2012) Computational simulation of hemodynamic-driven growth and remodeling of embryonic atrioventricular valves. Biomech Model Mechanobiol 11:1205–1217

3. Kowalski WJ, Dur O, Wang Y, Patrick MJ, Tinney JP, Keller BB, Pekkan K (2013) Critical transitions in early embryonic aortic arch patterning and hemodynamics. PLoS One 8: e60271

4. Oosterbaan AM, Ursem NT, Struijk PC, Bosch JG, van der Steen AF, Steegers EA (2009) Doppler flow velocity waveforms in the embryonic chicken heart at developmental stages corresponding to 5–8 weeks of human gestation. Ultrasound Obstet Gynecol 33:638–644

5. Gu S, Jenkins MW, Peterson LM, Doughman YQ, Rollins AM, Watanabe M (2012) Optical coherence tomography captures rapid hemodynamic responses to acute hypoxia in the cardiovascular system of early embryos. Dev Dyn 241:534–544

6. Chen C, Menon PG, Kowalski W, Pekkan K (2013) Time-resolved OCT-µPIV: a new microscopic PIV technique for noninvasive depth-resolved pulsatile flow profile acquisition. Exp Fluids 54:1426

7. Vennemann P, Kiger KT, Lindken R, Groenendijk BC, Stekelenburg-de Vos S, ten Hagen TL, Ursem NT, Poelmann RE, Westerweel J, Hierck BP (2006) In vivo micro particle image velocimetry measurements of blood-plasma in the embryonic avian heart. J Biomech 39:1191–1200

8. Martinsen BJ (2005) Reference guide to the stages of chick heart embryology. Dev Dyn 233:1217–1237

9. Bakkers J (2011) Zebrafish as a model to study cardiac development and human cardiac disease. Cardiovasc Res 91:279–288

10. Manner J (2000) Cardiac looping in the chick embryo: a morphological review with special reference to terminological and biomechanical aspects of the looping process. Anat Rec 259:248–262

11. Chen CY, Patrick MJ, Corti P, Kowalski W, Roman BL, Pekkan K (2011) Analysis of early embryonic great-vessel microcirculation in zebrafish using high-speed confocal muPIV. Biorheology 48:305–321

12. Corti P, Young S, Chen CY, Patrick MJ, Rochon ER, Pekkan K, Roman BL (2011) Interaction between alk1 and blood flow in the development of arteriovenous malformations. Development 138:1573–1582

13. Westerfield M (2000) The Zebrafish book. University of Oregon Press, Eugene

14. Sepich DS, Wegner J, O'Shea S, Westerfield M (1998) An altered intron inhibits synthesis of the acetylcholine receptor alpha-subunit in the paralyzed zebrafish mutant nic1. Genetics 148:361–372

15. Choi J, Dong L, Ahn J, Dao D, Hammerschmidt M, Chen JN (2007) FoxH1 negatively modulates flk1 gene expression and vascular formation in zebrafish. Dev Biol 304:735–744

16. Traver D, Paw BH, Poss KD, Penberthy WT, Lin S, Zon LI (2003) Transplantation and in vivo imaging of multilineage engraftment in zebrafish bloodless mutants. Nat Immunol 4:1238–1246

17. Hamburger V, Hamilton HL (1951) A series of normal stages in the development of the chick embryo. J Morphol 88:49–92

18. Patrick MJ, Chen C, Frakes DH, Dur O, Pekkan K (2011) Cellular-level near-wall unsteadiness of high-hematocrit erythrocyte flow using confocal μpIV. Exp Fluids 50:887–904

19. Wagman AJ, Hu N, Clark EB (1990) Effect of changes in circulating blood volume on cardiac output and arterial and ventricular blood pressure in the stage 18, 24, and 29 chick embryo. Circ Res 67:187–192

20. Keane RD, Adrian RJ (1990) Optimization of particle image velocimeters. 1. Double pulsed systems. Meas Sci Technol 11:1202–1215

21. Olsen MG, Adrian RJ (2000) Out-of-focus effects on particle image visibility and correlation in microscopic particle image velocimetry. Exp Fluids 29:S166–S174

Chapter 3

Using Correlative Light and Electron Microscopy to Study Zebrafish Vascular Morphogenesis

Jacky G. Goetz, Fabien Monduc, Yannick Schwab, and Julien Vermot

Abstract

Live imaging is extremely useful to characterize the dynamics of cellular events in vivo, yet it is limited in terms of spatial resolution. Correlative light and electron microscopy (CLEM) allows combining live confocal microscopy with electron microscopy (EM) for the characterization of biological samples at high temporal and spatial resolution. Here we describe a protocol allowing extracting endothelial cell ultrastructure after having imaged the same cell in its in vivo context through live confocal imaging during zebrafish embryonic development.

Key words Zebrafish, Embryo, Morphogenesis, Angiogenesis, Live confocal microscopy, Electron microscopy, Electron tomography, Laser etching, Targeted ultramicrotomy, Serial sectioning

1 Introduction

Embryo morphogenesis is a fundamental process allowing a growing organism to develop functional organs. Often in this context, cell motion is highly dynamic and depends on its cellular and molecular environment. These latest years, the use of photon and electron microscopy significantly accelerated our understanding of morphogenesis. A challenge in the field is that tissue morphogenesis occurs at many different spatial and temporal scales (from several millimeters to few nanometers and hours to milliseconds, respectively). A classical example is the development of the vascular system, where blood vessel formation depends on blood cell movements generated by the beating heart. As a consequence, vascular development is driven by events spanning several time scales: the slow migration of endothelial cells (few microns/hour) and the high velocities of circulating blood cells (few millimeters/second).

Continuous progresses in light microscopy are pushing the limits of resolution. On one hand, super-resolution fluorescence microscopy (PALM, STORM, OMX) has dramatically increased the spatial resolution of photonic imaging techniques (in the
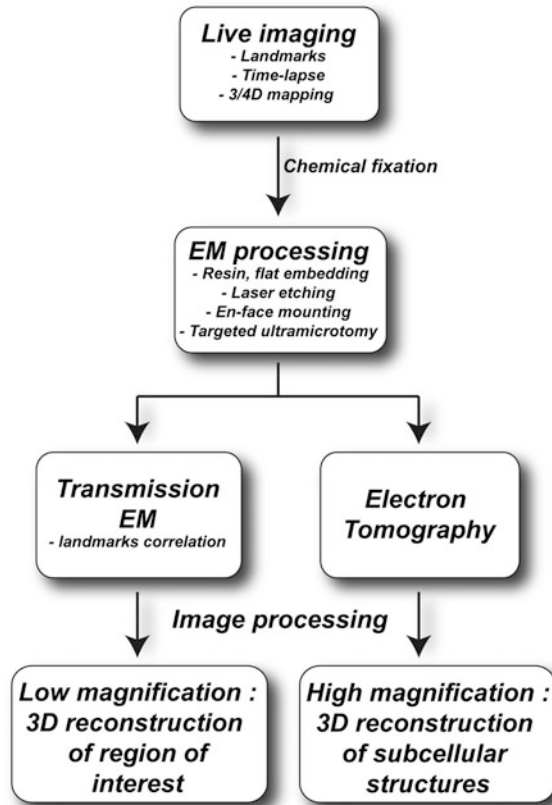
Fig. 1 CLEM pipeline. Drawing depicting the main steps of CLEM

order of a few tens of nanometers). On the other hand, progresses in confocal, two-photon, and light sheet microscopy have allowed pushing the time resolution limits extensively [1–3].

Furthermore, there have also been major breakthrough in the field of electron microscopy, which now can address three-dimensional ultrastructural analysis of large biological volumes. With serial electron tomography, one can now study with great details the 3D architecture of complete cells [4, 5]. This technique consists of acquiring tilt series from semi-thin resin sections. If the same structure is followed through consecutive sections, one can retrace the volume of large structures spanning several microns.

However, these techniques are still heavily compartmentalized and methods have been developed to combine them by correlating images obtained with different imaging modalities [4]. Specific protocols now permit a very precise correlation between light and electron microscopy images of the same biological sample and combine the advantages of each imaging approaches.

Here, we describe a protocol allowing to image vascular morphogenesis in a living zebrafish embryo and to correlate the observed events to electron micrographs and 3D electron tomograms (Fig. 1). Light microscopy is used to image the event of

interest to obtain a 4D (x,y,z,t) mapping of the region of interest (ROI) and to identify anatomical landmarks that can be used to track back the ROI using EM. Furthermore, we describe how to exploit thick EM sections (in the order of 250 nm) for dissecting cell ultrastructure through electron tomography after correlation. As an example, we provide here the correlative imaging of a budding endothelial cell located in the dorsal aorta of a 28-hpf zebrafish embryo and describe the consecutives steps we have used for this purpose.

2 Materials

2.1 Zebrafish (ZF) Embryo Anesthesia, Live Imaging, and Image Reconstruction (Fig. 2)

1. Petri dish (35 or 60 mm diameter).

2. 0.3× Danieau solution: Danieau's solution recipe (30×): Mix NaCl (101.7 g, final concentration = 1,740 mM), KCl (1.56 g, final concentration = 21 mM), MgSO$_4$, 7H$_2$O (2.96 g, final concentration = 12 mM), Ca(NO$_3$)$_2$ (4.25 g, final concentration = 18 mM), and HEPES buffer (35.75 g, final concentration = 150 mM) in 1 L of water and stir until dissolved. 30× solution can be stored at 4 °C; the pH is 7.6 (*see* **Note 1**).
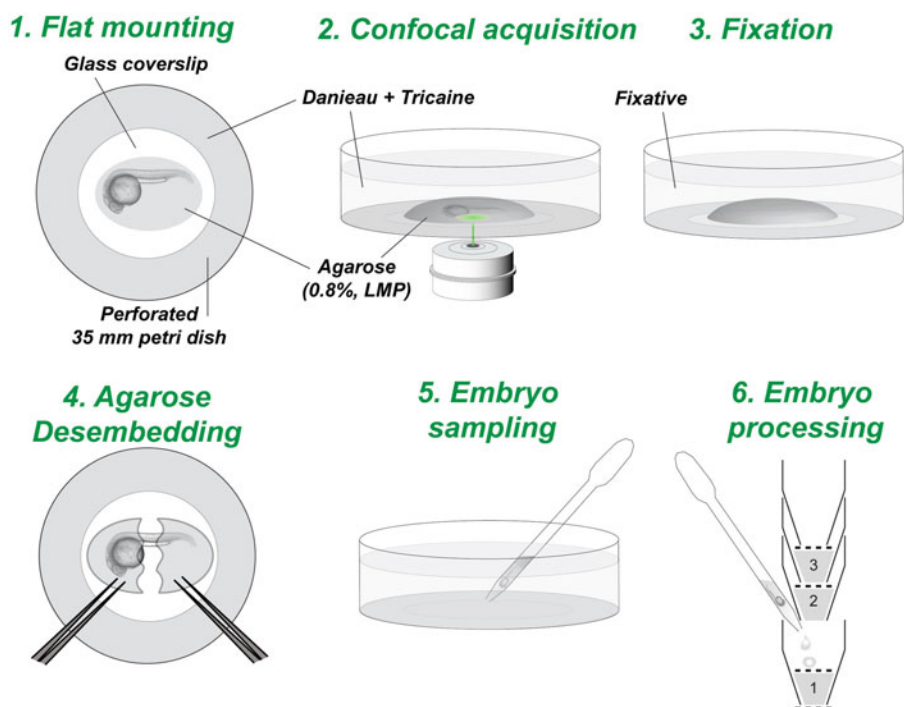
Fig. 2 Light microscopy and fixation. Drawings representing the six steps necessary to process the sample from the mounting (step 1), imaging (step 2), fixation after imaging (step 3), recollection of the imaged embryo (steps 4 and 5), and embryo processing for embedding

3. Air incubator preheated at 28 °C.

4. Danieau solution supplemented with 0.003 % 1-phenyl-2-thiourea (0.2 mM) to stop skin pigmentation a few hours after fertilization.

5. Forceps n°5 (FST, Dumont).

6. 0.3× Danieau solution supplemented with 0.003 % 1-phenyl-2-thiourea (0.2 mM) and with 0.02 mg/ml Tricaine (Sigma-Aldrich).

7. 0.8 % low-meting-point agarose supplemented with 0.02 mg/ml tricaine (*see* **Note 2**).

8. A water bath set at 40 °C.

9. A perforated 35 mm petri dish (Falcon, Becton Dickinson) with a glass coverslip (Thermo Scientific, thickness 1, 30 mm) glued with grease (Dow Corning, GMBH) (*see* **Note 3** and Fig. 7).

10. A Pasteur pipette.

11. A stereomicroscope (Leica M250F).

12. A confocal microscope equipped with a heating chamber set at 28 °C and equipped with a high NA 20× objective as well as with a resonant scanner (800 Hz) for fast acquisition (*see* **Note 4**).

13. A computer equipped with ImageJ and Imaris software (*see* **Note 5**).

2.2 Fixation, Post-fixation, En Bloc Staining (Figs. 3 and 4)

1. Flow-through chamber stacks for parallel sample processing: 1 ml pipette tips, plastic mesh from Cellsafe biopsy capsules (Leica).

2. 2.5 % Glutaraldehyde, 0.05 % malachite green oxalate, in 0.1 M sodium cacodylate (*see* **Note 6**).

3. 0.1 M sodium cacodylate buffer.

4. Reduced osmium: 0.8 % potassium ferrocyanide, 1 % osmium tetroxide in 0.1 M cacodylate buffer.

5. 1 % tannic acid.

6. 0.5 % uranyl acetate.

2.3 Resin Embedding, Laser Etching, and Serial Sectioning (Fig. 5)

1. Graded series of acetone (25, 50, 75, 95, and 100 %).

2. Resins: Araldite M 18.2 % (Sigma 10951), epon 812 22.7 % (Sigma 45345), Hardener DDSA 54.5 % (Sigma 45346), DMP-30 4.5 % (Sigma 93331).

3. Material for flat embedding/remounting: Aclar films, 7.8 mil (EMS), glass slides.

4. Oven set at 60 °C.

5. Laser microdissection microscope, Leica LMD6000.
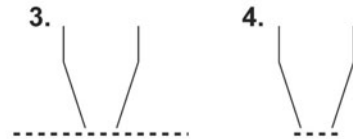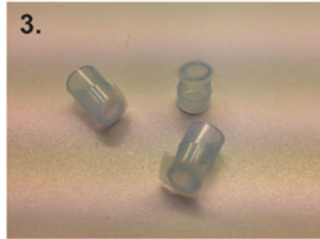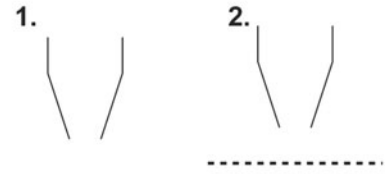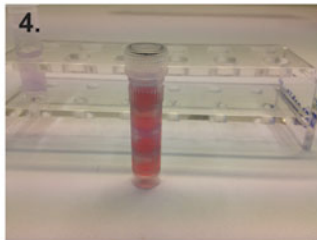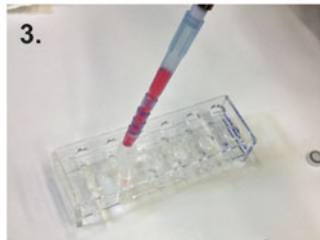
Fig. 3 Preparation of flow-through multicell incubation chamber. The multicell incubation chamber permits to perform the washes with several embryos while keeping them separated for subsequent embedding

A. Preparation of aclar films and spacer

glass slide   aclar film   spacer   aclar film   glass slide
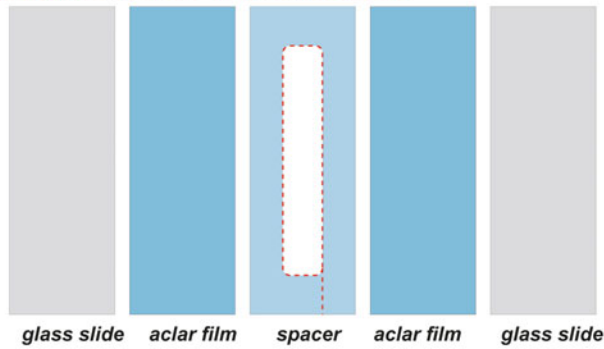
B. Montage for flat embedding
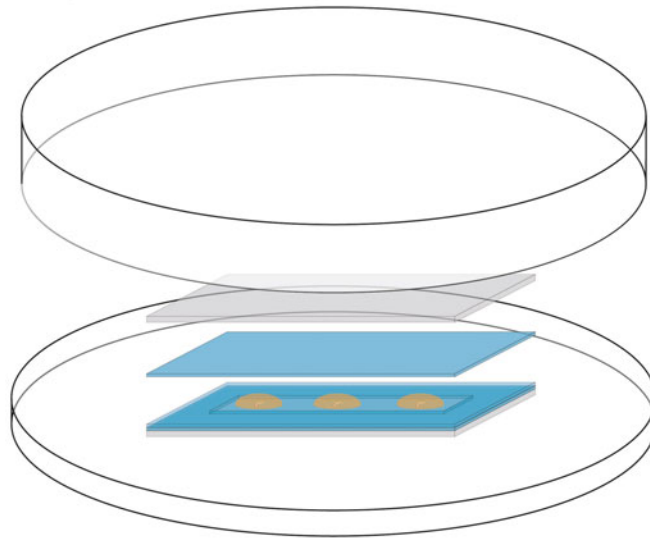
Fig. 4 Flat embedding in epoxy resins. Drawing representing the montage used to flat embed the embryo within the epoxy resins

6. Ultramicrotome, Ultracut UCT.

7. Diamond knives: Cryotrim 20, Histo diamond, and Ultra35.

8. EM grids: Maxtaform, copper-rhodium slot grids.

9. Grid box.

10. Grid datasheet.

2.4 Contrasting Agents (See Note 7)

1. Uranyl acetate.

2. Lead citrate.

2.5 Electron Microscopes

1. Philips CM12, with Orius 1000 CCD camera (Gatan).

2. Tecnai F30 for electron tomography.
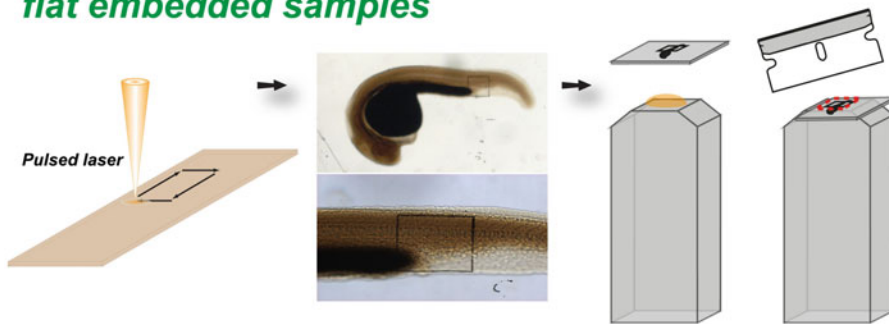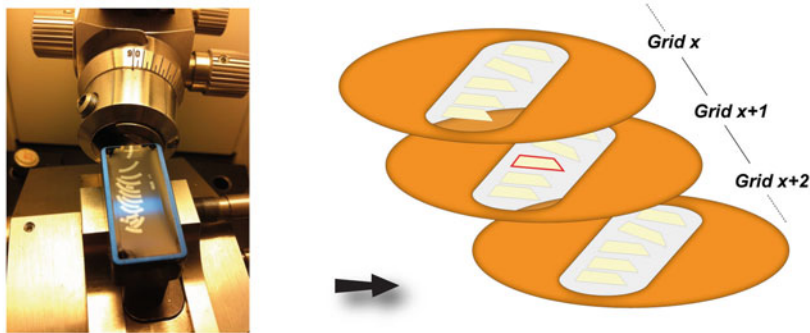
Fig. 5 Laser etching and sectioning. The laser etching step permits to localize the embryo before serial sectioning

2.6 Software for Image Processing	1. iMOD package (http://bio3d.colorado.edu/imod/). 2. Fiji (http://fiji.sc/Fiji). 3. Imaris (Bitplane).

3 Methods

3.1 Zebrafish Embryo: Need for Fluorescent Lines Compatible with Live Imaging	1. Our protocol is based on the use of fluorescent zebrafish transgenic lines. The tissue-specific expression of fluorescent proteins renders the correlative analysis easier. Herein, we used the *Tg(flk1:mcherry)* line where the endothelial cells express the red fluorescent protein (mCherry) through the control of the endothelial specific *flk1* promoter (Fig. 6). 2. Combination of double-transgenic lines will ease the localization of the biological events as well as the correlation between photonic and electronic microscopy. 3. This method is compatible with embryos of various stages.
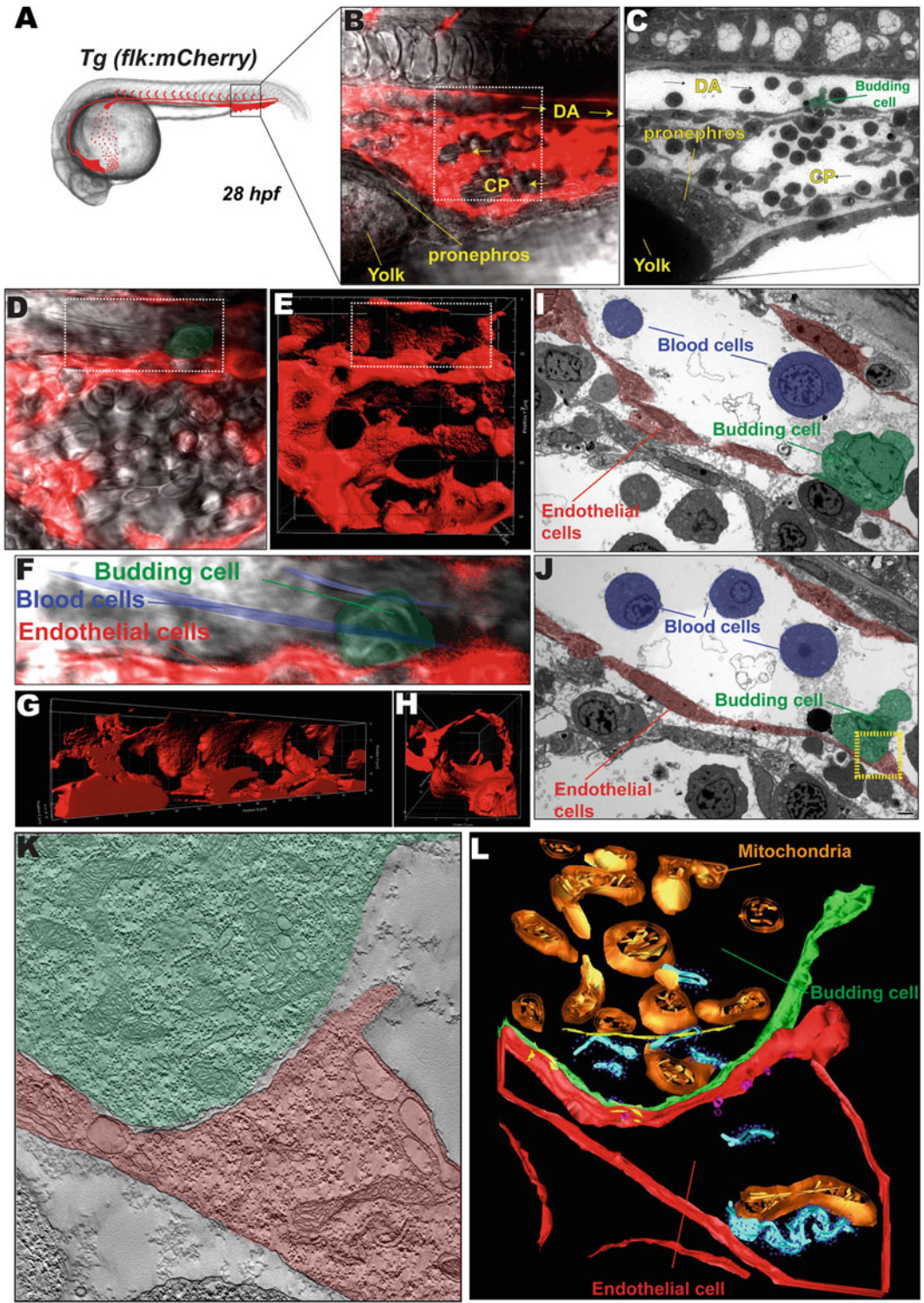
Fig. 6 CLEM experiment. (**a**) Scheme of a 28-hfp ZF embryo and its vasculature. (**b**) Confocal and transmitted image of a *Tg*(*flk1:mCherry*) embryo showing its vasculature (*red*) and anatomy (*gray* levels). Yolk, pronephros, dorsal aorta (DA), and caudal plexus (CP) are highlighted. Blood flow direction is indicated. (**c**) Transmission

3.2 Embryo Anesthesia and Montage (Fig. 2)

1. Collect ZF embryos after mating and transfer them into a petri dish containing 0.3× Danieau solution (*see* **Note 1**).

2. Place the plates in an air incubator preheated at 28 °C.

3. Transfer embryos into a petri dish containing Danieau solution supplemented with 0.003 % 1-phenyl-2-thiourea (0.2 mM) to stop skin pigmentation a few hours after fertilization. This treatment is needed if imaging is performed 20 h post-fertilization, as pigments start to form at these stages making the embryo more opaque and sensitive to light.

4. Remove embryo's chorion using forceps (*see* **Note 8**).

5. Transfer the embryos into a clean petri dish containing 0.3× Danieau solution supplemented with 0.003 % 1-phenyl-2-thiourea (0.2 mM) and with 0.02 mg/ml tricaine in order to anesthetize the embryos.

6. Prepare a solution of 0.8 % low-meting-point agarose, supplemented with 0.02 mg/ml tricaine, and store it in a water bath set at 40 °C to avoid polymerization (*see* **Note 2**).

7. Prepare a perforated 35 mm petri dish with a glass coverslip (Thermo Scientific, thickness 1, 30 mm) glued with grease (Dow Corning, GMBH) necessary for inverted confocal microscopy (*see* **Note 3** and Fig. 7).

8. Transfer the embryos into a petri dish filled with the warm, low melting point agarose you prepared using a Pasteur pipette. Avoid agarose dilution by transferring the smallest quantity of liquid in the process (*see* **Note 9**).

9. Collect the embryo using a Pasteur pipette with a small volume of agarose (200 μl approx.).

10. Dispose the embryo onto the perforated petri dish containing the glass coverslip in a drop of agarose.

11. Mount the embryos under a stereomicroscope (Leica M250F) by orienting it on its flank and make sure that the embryo is as

---

Fig. 6 (continued) electron microscopy image of the same ROI (**b**). The budding cell is visible in the DA and color-coded in *green*. (**d**) Higher magnification image of the region in **b** (*dashed lines*). The budding cell is visible in the DA and color-coded in *green*. (**e**) 3D reconstruction of the same region (red fluorescence, vasculature) showing vessel topography. (**f**) Higher magnification image of the region in **d** (*dashed lines*). The budding cell is visible in the DA and color-coded in *green*. Blood and endothelial cells are visible and color-coded, respectively, in *blue* and *red*. (**g–h**) 3D reconstruction of the same region (red fluorescence, vasculature) showing vessel topography. (**i–j**) TEM images of the *boxed region* in **d–e**. The budding cell is visible in the DA and color-coded in *green*. Blood and endothelial cells are visible and color-coded, respectively, in *blue* and *red*. (**k**) Electron tomogram of the *boxed region* in **j** (*yellow dashed lines*). (**l**) 3D segmented model of the electron tomogram showing cell contour and mitochondria
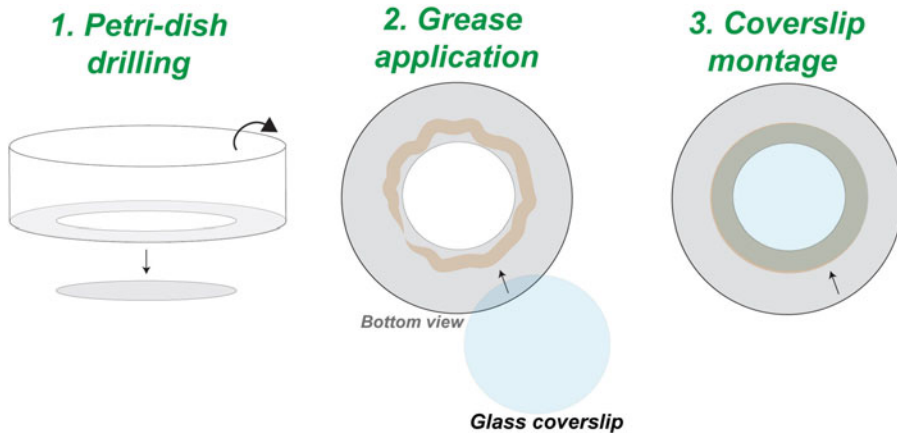
Fig. 7 Creating a live imaging chamber. The imaging chamber consists in a petri dish whose bottom is perforated so that we can seal a round coverslip in place to perform the confocal imaging. Grease is used to seal the coverslip with the petri dish

close as possible to the glass by gently pushing with forceps or an eyelash.

12. Cover the gel with tricaine-containing Danieau's solution once the agarose is polymerized, in order to avoid agarose shrinkage and embryo movements, respectively (*see* **Note 10**).

13. Place the embryo-containing petri dish under the microscope and image the embryo.

3.3 Live Imaging and Image Processing: Capturing the Event of Interest Together with Anatomical Landmarks

1. Localize the region of interest and perform z stacks with a large field of view (*see* **Note 11**). Here, we decided to image the embryo in a region localized in the ZF dorsal aorta (DA) (visible through the red fluorescence), which is very close to both the ZF pronephros (right above the yolk) and the associated venous caudal plexus (CP) (Fig. 6). This particular region contains thus many anatomical landmarks, which renders the correlation with electron microscopy more amenable. Here, we imaged one single endothelial cell budding out of the endothelium, towards the vessel lumen (dorsal aorta, Fig. 6). This particular phenomenon was imaged using red fluorescence from the endothelium, as well as transmitted light (blood cell movement—*see* **Note 12**).

2. Process images using ImageJ (Fiji) freeware and Imaris software.

3. Build a 3D map of the vessel, allowing precise measurement of the structure of interest localizations.

3.4 Sample Preparation for Electron Microscopy

3.4.1 Design of a Multi-Flow-Through Chamber Stack (Fig. 3)

1. Cut 1 ml pipette tips as shown in Fig. 3.
2. Approach the pipette tip to the flame of a Bunsen burner to melt the plastic.
3. Quickly snap the tip to the plastic mesh.
4. Section the mesh around the tip and remove the excess of plastic to produce a smooth edge.
5. Repeat the procedure to produce several baskets that can then be piled up.

3.4.2 Fixation/ Dehydration/Infiltration

1. Transfer the embryos in fixative (2.5 % glutaraldehyde in 0.1 M cacodylate buffer) and remove from the agarose. In order to allow better fixation and osmium penetration, head and tail tip can be cut using fine forceps.
2. Transfer the tissue to a basket and close it with an empty basket (*see* **Note 13**).
3. Transfer the samples in fixative with malachite green (*see* **Note 14**).
4. Incubate for 1 h on ice.
5. Wash four times for 5 min with 1 ml cacodylate buffer.
6. Post-fix with 1 ml of reduced osmium (0.8 % potassium ferro-cyanide/1 % osmium tetroxide) for 1 h on ice (*see* **Note 15**).
7. Wash four times for 5 min with 1 ml cacodylate buffer.
8. Stain with 1 ml 1 % tannic acid for 1 h on ice.
9. Wash one time for 5 min with 1 ml cacodylate buffer and three times with distilled water.
10. Stain with 1 ml 0.5 % uranyl acetate for 1 h at room temperature (protect from light).
11. Wash four times for 5 min with water.
12. Incubate in 25 % acetone for 10 min on ice.
13. Incubate in 50 % acetone for 10 min on ice.
14. Incubate in 75 % acetone for 10 min on ice.
15. Incubate in 95 % acetone for 10 min on ice. Repeat two times.
16. Incubate three times in 100 % acetone for 10 min on ice.
17. Infiltrate in 25 % resin (in acetone) for at least 2 h.
18. Infiltrate in 50 % resin (in acetone) for at least 2 h.
19. Infiltrate in 75 % resin (in acetone) for at least 2 h.
20. Infiltrate in 100 % resin overnight in the hood (cap off).

3.4.3 Flat Embedding (Fig. 4) (See Also Refs. 6, 7)

1. Prepare three aclar films, 7.8 mil (200 μm thick), 76 × 26 mm.
2. Cut a central rectangular hole in one of them, 155 × 10 mm; this is the spacer.
3. Place the first aclar film on a glass slide installed in the lid of a 10 cm petri dish.

4. Place the spacer.

5. Place the infiltrated samples on the montage and add drops of fresh epon to them (*see* **Note 16**).

6. Carefully place the top Aclar film, avoiding any air bubble (*see* **Note 17**).

7. Cover with a glass slide.

8. Cover with the bottom part of the petri dish and place some weight to it (for example an empty glass bottle).

9. Transfer to the oven, for a 2-day polymerization at 60 °C.

3.4.4 Laser Etching
(Fig. 5) (See Also Refs. 6, 7)

1. Remove the Aclar films and spacer from the sample (*see* **Note 18**).

2. Place the bloc on a glass slide and transfer it to a laser micro-dissecting microscope.

3. Create landmarks by etching the bloc surface (*see* **Note 19**).

3.5   Remounting of the Bloc for Parallel Serial Sectioning (Fig. 5)

1. With fine grain sand paper, scratch the surface of the bloc that was not etched by laser microdissection.

2. Add a drop of fresh resin.

3. Place a dummy bloc onto the drop of resin.

4. Let polymerize overnight at 60 °C.

5. With a razor blade, cut the resin around the region of interest.

3.6   Serial Thick Sectioning (Fig. 5)

1. Mount the bloc in the sample holder of the ultramicrotome.

2. Coarsely trim the bloc with a razor blade to approach the etched landmarks.

3. Finish the trimming with a trimming diamond.

4. Knowing the anatomy of the zebrafish embryo for each specific stage of development, we knew the approximate location of the dorsal aorta (DA). Coarse parasagittal trimming was therefore performed to reach the region containing the DA, using the feed of the ultramicrotome to evaluate the depth of trimming. Trimming was stopped approximately 5 μm before the putative position of the DA, and serial sections were collected. For serial sectioning details, please *see* ref. 6.

5. Collect the serial sections on slot grids.

6. Record the position on order of the sections on a separated datasheet.

7. For EM tomography, 200 nm serial thick sections are collected (*see* **Note 20**).

3.7 EM Acquisition, Electron Tomography, and Image Processing	1. Track the region of interest using a transmission electron microscope (Philips CM12, operated at 80 kV) (*see* **Note 21**).

1. Track the region of interest using a transmission electron microscope (Philips CM12, operated at 80 kV) (*see* **Note 21**).

2. Perform electron tomography in a chosen ROI (Fig. 6j–l) (*see* **Note 22**).

3. Segment the tomograms using Imod software.

4. Assemble a 3D model using Imod.

4 Notes

1. We recommend storing the danieau solution as a $30\times$ stock and make a $0.3\times$ solution for day-to-day experiments.

2. We recommend preparing this solution freshly for everyday experiments.

3. In order to seal glass coverslips onto 35 mm plastic petri dish, we apply a low amount of grease and stick the coverslip applying moderate load (Fig. 7).

4. Acquisition speed can be increased when using a 64×254 pixel imaging window.

5. Imaris is used for the renderings. Other software are available on the market and can be used for the same purpose.

6. Malachite green is a triarylmethane dye which was shown, when combined with aldehyde fixation, to prevent lipid extraction during the sample preparation for EM [8]. By preventing lipid extraction, the osmium fixation is greatly improved. As a consequence, we observed a lower penetration efficiency of the osmium in the depth of the specimen. Dissecting the sample close to the region of interest ensures a proper fixation and good contrast. Interestingly, the enhanced contrast given by this protocol allows for direct observation of the sections at the TEM, without contrasting further with heavy metals.

7. On sections, staining is not needed when using malachite green.

8. Use one forceps to immobilize the chorion (by pinching it) and the other forceps to pull the chorion out.

9. After pipetting the embryo into the Pasteur pipette, keep the pipette vertical and wait until the embryo reaches the tip of the capillary by gravity. Once at the bottom, generate a small drop containing the embryo and transfer into the agarose by capillarity.

10. For short-time experiments (few minutes), this step is not necessary as the agarose does not shrink over a short period of time. Gently touch the agarose with a forceps to check if the agarose is cured before pulling the water.

11. Since the method is mainly based on anatomical landmarks, it is important to have a good overview of the anatomy at the confocal imaging step.

12. Imaging of blood cell movement in zebrafish embryos can be easily performed using fluorescence in the *Tg(gata1:dsRed)* transgenic line.

13. It is possible, at this step, to pile up several baskets, for simultaneous processing of several types of embryos.

14. The new solution can be pipetted through the baskets, as shown in Fig. 3. This procedure enables an efficient solution exchange and is used throughout the whole experiment.

15. The tubes are closed at the stage to avoid osmium dissemination. Microtubes with screw caps are preferred here (reference: Sarstedt microtubes type G).

16. You can make sure that the samples reach the bottom of the resin drop by gently pushing the embryo with an eyelash; this will prevent them from drifting when installing the top Aclar sheet.

17. If too much resin is deposited, it will be drained from the montage resulting in resin-free spaces around the sample. If the samples are thicker than 200 µm, two spacers can be used.

18. If the resin has spilled over, the use of a razor blade is necessary to dismount the sandwich as the glass slide and the aclar film will be tightly glued together. When removing the Aclar films, place the montage flat on the bench and peal off the Aclar film keeping the block of resin flat. If bended, the block can break, resulting in sample damages.

19. Make sure that the sample is oriented consistently to the confocal imaging plan. The etched frame should correspond to the imaged frame, at low magnification, performed in the confocal microscope.

20. The fixation protocol gives enough contrast to the cell; hence post-staining of the sections is not necessary.

21. Here, using the anatomic landmarks (DA, CP, pronephros, yolk), we tracked the budding endothelial cell (green) in the DA (Fig. 6). This ROI was thus easily found on several consecutive sections. Such an anatomical landmark can be used (using a coordinate system) to track back several events of interests all over the ZF embryo.

22. Here, we focused the study on contact zones between the budding cell and its original endothelium. For this purpose, automated data acquisition of tilt series through an angular range of about $-70°$ to about $+70°$ (depending on the sections) with $1°$ increments was performed using a field emission gun electron microscope operating at 300 kV (Tecnai F30; FEI Company, Eindhoven, The Netherlands).

5   Additional Remarks

1. HPF is the method of choice to preserve the ultrastructure of biological specimen in a close to native state. But it is limited to samples thinner than 200 μm. The ZF embryo, at least in its anterior part, is thick and does not fit the HPF carrier of the EMPACT2. Moreover, we wanted minimal anatomical changes of the sample between the LM acquisition and the flat embedding, in order to precisely retrace the position of the ROI. When trying to fit the embryos into the HPF carrier of the EMPACT2, the sample is necessarily compressed and folded [9].

2. We decided to chemically fix the ZF embryos. As they do not breathe at this stage, and as their skin is already an efficient barrier to the external medium, immersion fixation is not efficient and can take minutes to be achieved. It is therefore preferable to cut the specimen while in fixative, to allow quick penetration of the chemicals and efficient fixation.

3. There is no need to perform thick sectioning if electron tomography is not needed.

4. Aclar is a Teflon polymer [10] that we use for its lower adherence to the epon resin. It is a perfect material for flat embedding as it is easily removed from the cured resin. Furthermore, it produces flat and smooth block faces, allowing for LM imaging of the embedded blocks.

Acknowledgements

References

1. Truong TV, Supatto W (2011) Toward high-content/high-throughput imaging and analysis of embryonic morphogenesis. Genesis 49 (7):555–569. doi:10.1002/dvg.20760

2. Weber M, Huisken J (2011) Light sheet microscopy for real-time developmental biology. Curr Opin Genet Dev 21(5):566–572. doi:10.1016/j.gde.2011.09.009

3. Vermot J, Fraser SE, Liebling M (2008) Fast fluorescence microscopy for imaging the dynamics of embryonic development. HFSP J 2(3):143–155. doi:10.2976/1.2907579

4. Kolotuev I, Hyenne V, Schwab Y, Rodriguez D, Labouesse M (2013) A pathway for unicellular tube extension depending on the lymphatic vessel determinant Prox1 and on osmoregulation. Nat Cell Biol 15 (2):157–168. doi:10.1038/ncb2662

5. Hoog JL, Antony C (2007) Whole-cell investigation of microtubule cytoskeleton architecture by electron tomography. Methods Cell Biol 79:145–167. doi:10.1016/S0091-679X(06)79006-9

6. Kolotuev I, Bumbarger DJ, Labouesse M, Schwab Y (2012) Targeted ultramicrotomy: a valuable tool for correlated light and electron microscopy of small model organisms. Methods Cell Biol 111:203–222. doi:10.1016/B978-0-12-416026-2.00011-X, B978-0-12-416026-2.00011-X [pii]

7. Kolotuev I, Schwab Y, Labouesse M (2010) A precise and rapid mapping protocol for correlative light and electron microscopy of small invertebrate organisms. Biol Cell 102 (2):121–132. doi:10.1042/BC20090096, BC20090096 [pii]

8. Hayat MA (1986) Basic techniques for transmission electron microscopy (chapter 1). Academic, New York, p 18

9. Nixon SJ, Webb RI, Floetenmeyer M, Schieber N, Lo HP, Parton RG (2009) A single method for cryofixation and correlative light, electron microscopy and tomography of zebrafish embryos. Traffic 10(2):131–136. doi:10.1111/j.1600-0854.2008.00859.x

10. Jimenez N, Van Donselaar EG, De Winter DA, Vocking K, Verkleij AJ, Post JA (2010) Gridded Aclar: preparation methods and use for correlative light and electron microscopy of cell monolayers, by TEM and FIB-SEM. J Microsc 237(2):208–220. doi:10.1111/j.1365-2818.2009.03329.x

Micro/Nano-Computed Tomography Technology for Quantitative Dynamic, Multi-scale Imaging of Morphogenesis

Chelsea L. Gregg, Andrew K. Recknagel, and Jonathan T. Butcher

Abstract

Tissue morphogenesis and embryonic development are dynamic events challenging to quantify, especially considering the intricate events that happen simultaneously in different locations and time. Micro- and more recently nano-computed tomography (micro/nanoCT) has been used for the past 15 years to characterize large 3D fields of tortuous geometries at high spatial resolution. We and others have advanced micro/nanoCT imaging strategies for quantifying tissue- and organ-level fate changes throughout morphogenesis. Exogenous soft tissue contrast media enables visualization of vascular lumens and tissues via extravasation. Furthermore, the emergence of antigen-specific tissue contrast enables direct quantitative visualization of protein and mRNA expression. Micro-CT X-ray doses appear to be non-embryotoxic, enabling longitudinal imaging studies in live embryos. In this chapter we present established soft tissue contrast protocols for obtaining high-quality micro/nanoCT images and the image processing techniques useful for quantifying anatomical and physiological information from the data sets.

Key words Tissue morphogenesis, Embryonic development, Morphogenesis, Soft tissue, Micro/nanoCT images

1 Introduction

Growth, differentiation, and organization represent the fundamental stages of embryogenesis [1]. Heterogeneous patterning of multiple cell types with complex orchestration has necessitated the development of new imaging strategies for capturing this dynamic process. Parallel advancements in experimental and imaging technologies have enabled dynamic, quantitative studies of morphogenesis and dysmorphogenesis. Three-dimensional imaging modalities offer unique insights and provide quantitative information on the dynamic tissue fate changes during development.

Micro/nano-computed tomography (micro/nanoCT) has been used for the past 15 years to characterize tortuous spatial geometries at high resolutions [2]. A gamma source emits

high-powered X-ray energy whose attenuation through the sample is registered by a gamma camera opposite the emitter relative to a bone standard [3]. Through a back projection analysis from 360° discrete angle measurements, the image is fully registered into a series of planar slices which can be interpolated into a three-dimensional reconstruction [2]. Scans lasting for a few minutes or less can achieve resolution at 50–25 µm [4] but longer exposure times can yield resolution into the submicron range [5].

Micro/nanoCT has become an important imaging technology for dynamic and quantitative imaging of embryonic development. Johnson and colleagues imaged transgenic mouse embryos using microCT for virtual histology. With an 8 µm scan of wild-type mice stained with osmium tetroxide, virtual histology from the microCT scan is compared to that of paraffin histology of E11.5 embryos (Fig. 1, [6]). Using a 27 µm scan and osmium tetroxide staining, segmentation and screening of developmental defects found in the rostral neural tube of *Pax3:Fkhr* E11.5 transgenic mouse embryos were seen with microCT imaging [6]. Through virtual histology segmentation, the cephalic forebrain, midbrain, and hindbrain vesicles, the heart wall and cardiac ventricles, and the liver were visualized [6]. Furthermore, the incomplete neural crest closure, overgrowth of the mesenchyme, and hypotrophy of the telencephalic vesicles are seen with the 27 µm microCT scan. Furthermore, Degenhardt and colleagues used microCT to image *PlexinD1* mutant mouse embryos at 16 µm resolution for visualizing cardiac defects stained with Lugol's solution [7]. E17.5 *PlexinD1* mutant embryos were compared to wild-type embryos and multi-planar reconstructions were used to determine the planes that best reveal the defects, showing intracardiac and extracardiac defects that are clearly seen with the microCT scans (Fig. 1, [7]).

In HH24 chick embryos, Metscher compared different soft tissue staining techniques imaged at 12 µm resolution (Fig. 2, [5]). Butcher et al. scanned embryonic chick hearts from HH15 to HH36 perfused with Microfil™, a radiopaque casting polymer, through microinjection. The hearts were scanned at 10.5 µm resolution and three-dimensional volumetric reconstructions were rendered and compared to serial reconstructions and scanning electron micrographs. Volume changes of the atria, ventricles, outflow tract, and atrioventricular canal were quantified throughout development. The general microinjection setup and microCT volume rendering as compared to the serial sections and scanning electron micrograph are given in Fig. 3 [2]. Kim and colleagues stained chick embryos with osmium tetroxide and characterized organ development with isosurface three-dimensional renderings of chicks spanning days 4–10 of embryogenesis (Fig. 3, [4]).

Using the high-resolution capabilities in nanoCT, Metscher et al. demonstrated scan resolutions of 0.97 µm of the developing chick embryo stained with Lugol's solution where neural crest cells
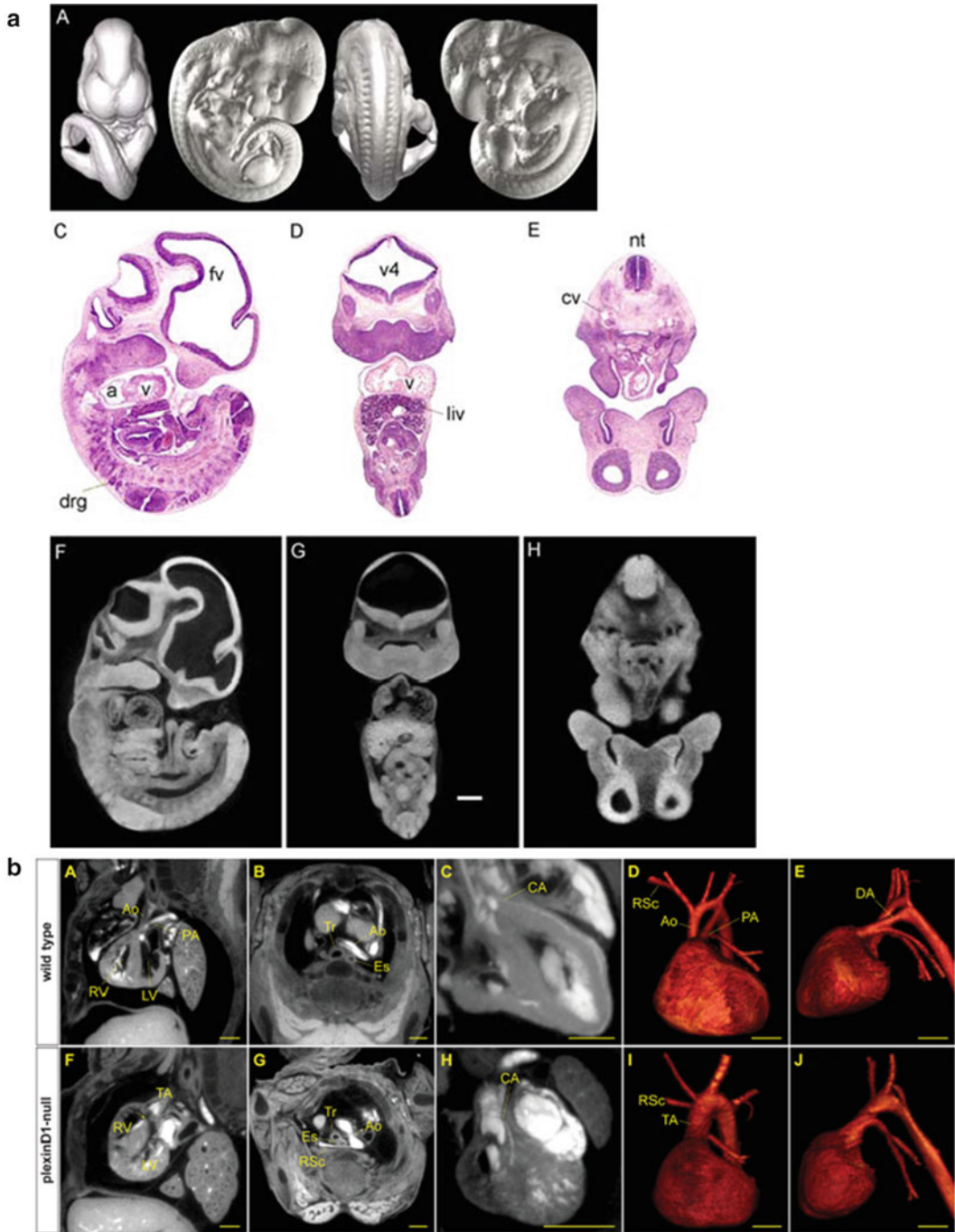
Fig. 1 (**a**) Comparison of paraffin and virtual histology of E11.5 mouse embryos scanned at 8 μm with isosurface renderings in the *top row*, traditional histology sections from a littermate in the *middle row*, and the virtual histology via microCT in the *bottom row* [6]. (**b**) Multi-planar reconstructions of E17.5 wild-type mice and PlexinD1 mutant mice in the *black* and *white images* of the *top* and *bottom rows*, respectively. The *red images* illustrate volumetric reconstructions of the wild-type (*top row*) and mutant mice (*bottom row*) demonstrating the malformation of the aorta and pulmonary artery [7]. Scale bars: (**a**) 400 μm, (**b**) 500 μm
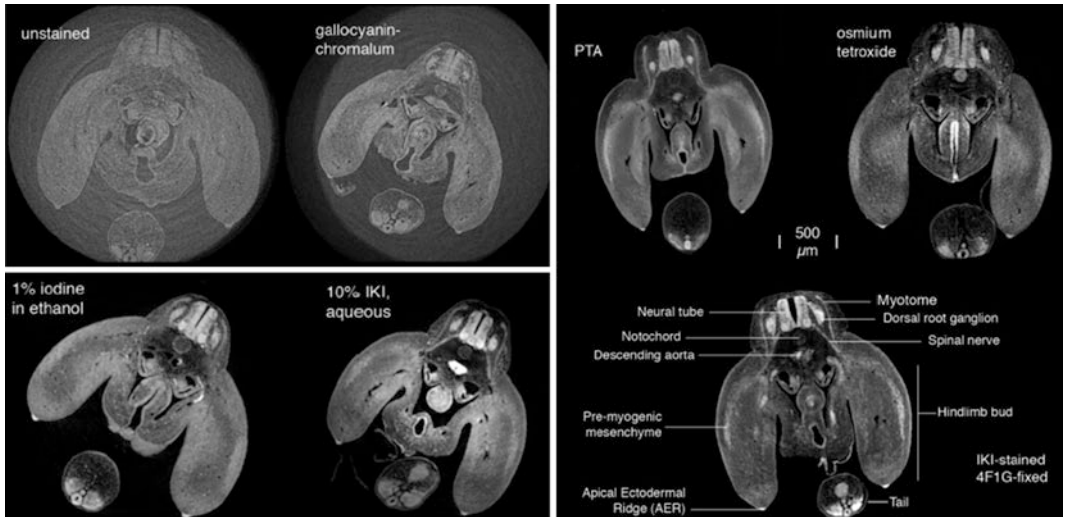
Fig. 2 Comparison of common contrast stains denoted on the image with resolution ranging from 4.6 to 5.1 μm [5]. Scale bar is 500 μm
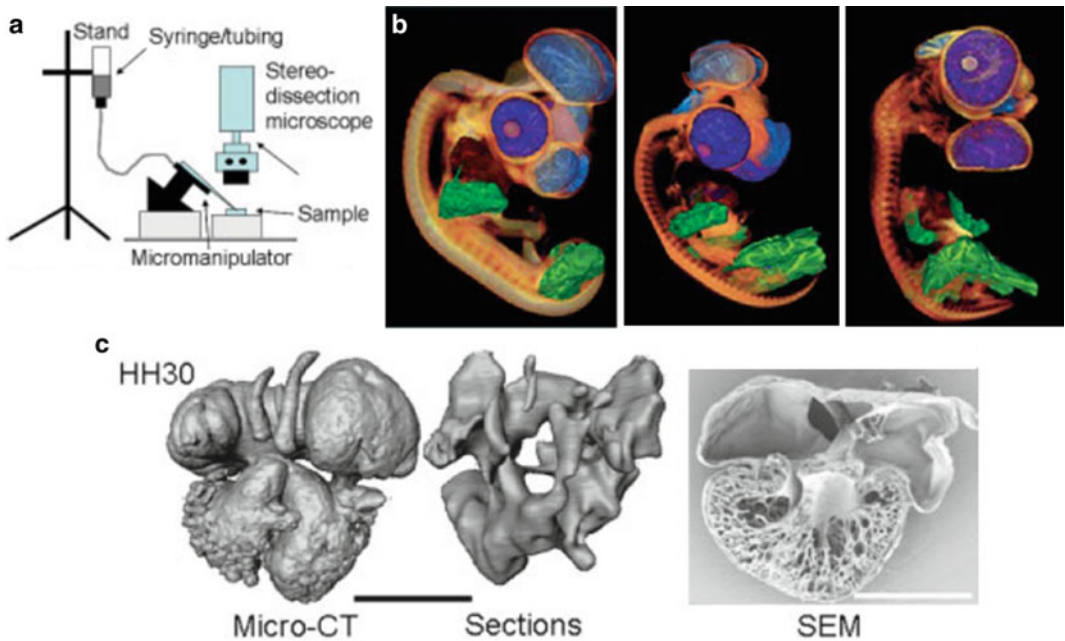
Fig. 3 (**a**) Microinjection setup [2]. (**b**) Isosurface renderings of days 4, 7, and 10 (*left* to *right*) chick embryos with colorized segments showing the cranial neural crest (*light blue*), eye (*purple*), limb (*green*), cardiac muscle (*brown*), and conotruncal cavity (*dark blue*) [4]. (**c**) MicroCT image of an HH30 chick heart (*left*) as compared to the serial reconstruction (*middle*), and the scanning electron micrograph (*right*) [2]. Scale bar is 1 mm
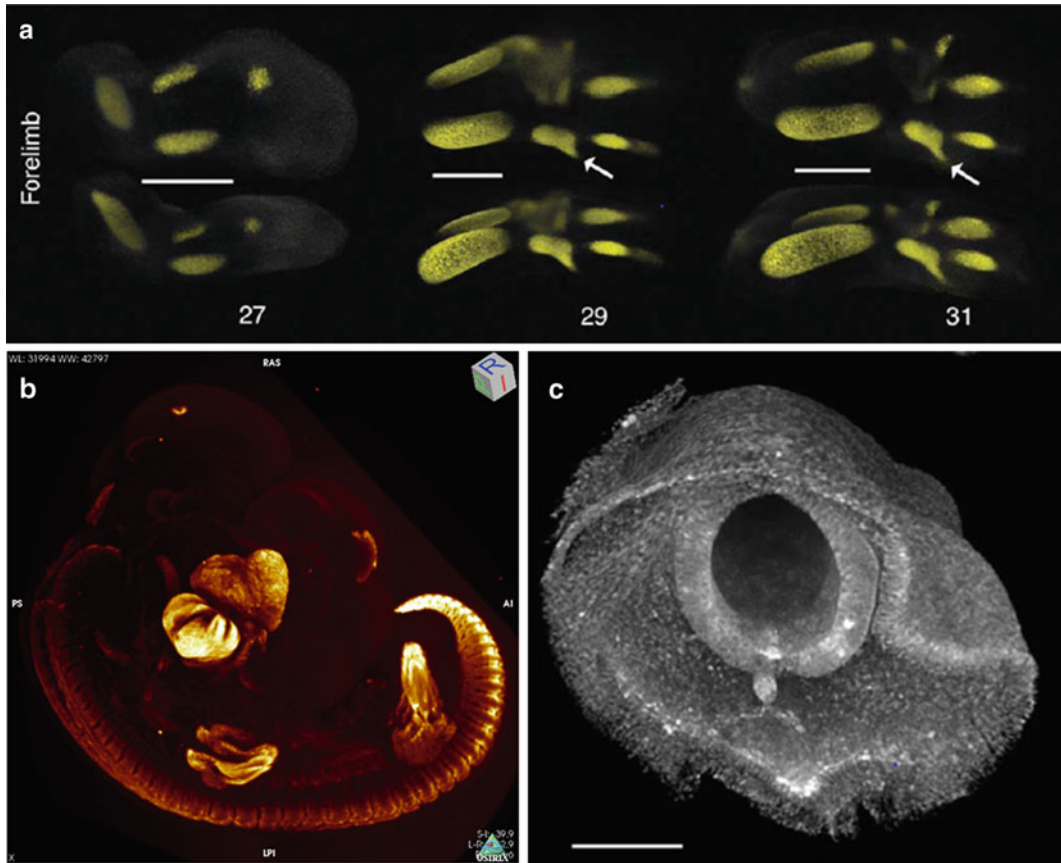
Fig. 4 (**a**) Volumetric reconstruction from a microCT image of limb cartilage patterning over development at HH27, -29, and -31 of the chick embryo with antigen-specific staining of type II collagen at resolutions between 3.8 and 4.8 μm [8]. The *arrow* indicates the vestigial anlage of digit 5 in the forelimb. Scale bar is 500 μm. (**b**) Alpha myosin heavy chain antigen-specific staining in the chick embryo. (**c**) High-magnification image of a stage 12 chick embryo with resolution at 0.97 μm where neural crest cells are visualized [5]. Scale bar is 100 μm

can be seen (Fig. 4, [5]). Extending past general soft tissue staining, Metscher and colleagues have demonstrated antigen-specific tissue staining with whole-mount imaging of antibody probes with metal-based immunodetection [8]. In Fig. 4, antigen-specific immunos-taining for alpha myosin heavy chain (aMHC) and type II collagen distribution in the developing limb is given. Henning and colleagues demonstrated the first in vivo live embryonic study using microCT imaging. Henning et al. quantified the level of contrast, biodistribution, and organ volume of developing chick embryos (Fig. 5, [9]). Furthermore, Henning and colleagues demonstrated that radiation from the scan up to 798mGray did produce any morphological defects up to day 10 of chick development when the experiment was ended [9]. Visipaque™ (VP) and Omnipaque™ (OP) were used as exogenous soft tissue contrast.
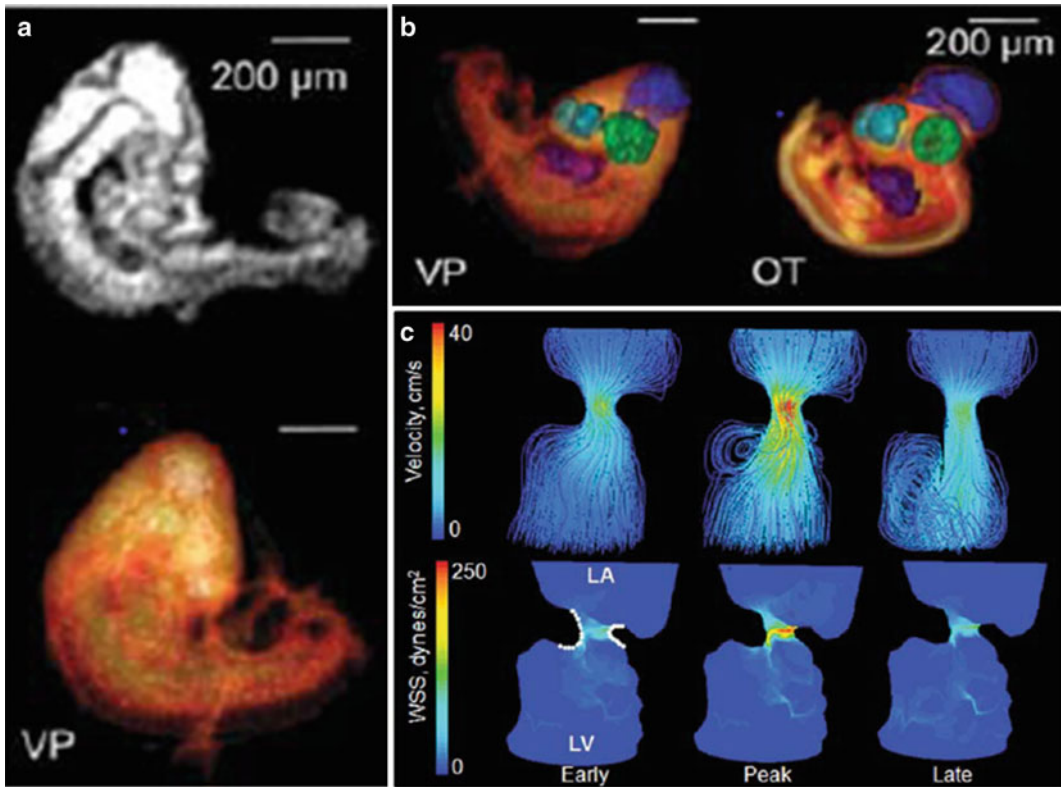
Fig. 5 (**a**) 2D and 3D rendered 50 μm microCT images of live day-3 embryonic chicks injected with VP [9]. (**b**) Quantitative volumetric analysis of day-4 chick embryos imaged at 50 μm [9]. *Dark blue* represents the hindbrain, *light blue* is the forebrain, *green* is the eye, and *purple* is the heart. (**c**) 3D hemodynamic environment of the atrioventricular canal in an HH27 chick embryo [10]. Scale bar is 200 μm

OP was found to be embryotoxic within 24 h postinjection due to being hyperosmotic whereas iso-osmotic VP was nontoxic up to day 10 of development [9]. Additionally, VP produced 1060 Hounsfield units of contrast with a 50 μm resolution microCT scan [9].

Micro/nanoCT imaging is a powerful tool for quantifying dynamic anatomical changes throughout development and it enables physiological changes to be measured as well. Using the image data, three-dimensional models can be generated and used for computational analysis and simulation of physiological events. Yalcin and colleagues analyzed the hemodynamic patterning of the atrioventricular canal in the embryonic chick using three-dimensional data obtained by microCT and flow parameters acquired from ultrasound imaging. The averaged wall shear stress was found at early, peak, and late stages of the cardiac cycle characterizing the inflow and outflow patterns seen in development (Fig. 5, [10]).

Micro/nanoCT imaging is a powerful tool for studying embryonic development and quantifying anatomical and physiological changes. Through the wide variety of tissue staining techniques, high-contrast, high-resolution multi-scale three-dimensional images are easily attained and with the emerging antigen-specific staining, localized expression changes can be differentiated and quantified. Furthermore, with the advancement into live embryonic imaging, longitudinal embryonic studies have become a tangible reality. In this chapter we introduce some of the most common protocols for imaging with micro/nanoCT and the image processing techniques needed to quantify the information observed within the image.

2 Materials

2.1 General Soft Tissue Contrast Agents

The most prominently used methods for nonspecific embryonic soft tissue contrast are given below. This information is summarized in Table 1 (*see* **Note 1**).

2.1.1 Lugol's Solution

1. 1 % weight/volume of elemental iodine (I_2, Sigma).
2. 2 % potassium iodide in water (KI, Sigma).

2.1.2 Phosphotungstic Acid (PTA)

1. 1 % weight/volume of phosphotungstic acid (Mallinckrodt Stains) in water.
2. Absolute ethanol.

2.1.3 Osmium Tetroxide

1. 1–2 % osmium tetroxide in phosphate buffer (OsO_4).

2.1.4 Gallocyanin-Chromalum

1. 5 % weight/volume in water of gallocyanin-chromalum (Chroma 1A).

2.1.5 Microfil TM

1. Standard petri dish.
2. Earl's Balanced Salt Solution (EBSS, Sigma).
3. Microinjection protocol (*see* Subheading 2.3).
4. Polymerizing contrast agent (Microfil, Flow-Tech, Inc.).

2.1.6 Omnipaque™

1. Omnipaque is administered to a live specimen but it is lethal within 24 h making it ineffective for longitudinal studies [9].
2. Omnipaque™ (iohexol, GE Healthcare) with a concentration of 350 mg/mL of iodine.

2.1.7 Visipaque™

1. Visipaque is administered to a live specimen and has shown to be nonembryotoxic [9].
2. Visipaque™ (iodixanol, GE Healthcare) with a concentration of 320 mg/mL of iodine.

Table 1
General exogenous soft tissue contrast for CT imaging (adapted from [5]) (*See* Notes 2 and 3)

Contrast stain	Lugol's solution	Phosphotungstic acid	Osmium tetroxide	Gallocyanin-chromalum	Microfil™	Omnipaque™	Visipaque™
Stain solution	$1\%\ I_2 + 2\%$ KI	1% PTA in H_2O Mix 30% PTA $+\ 70\%$ absolute EtOH	1–$2\%\ OsO_4$ in phosphate buffer	5% dissolved in billing water, cooled, and filtered	Mix in a ratio of 80:15:5 diluent:agent:catalyst	N/A	N/A
Staining protocol	Stain for 30 min to overnight Wash in H_2O, dehydrate in EtOH	Stain for 2 h to overnight Wash in EtOH Scan in 70–100 % EtOH	Stain for 1–2 h Wash in phosphate buffer Dehydrate in EtOH	Stain overnight, wash in water, and dehydrate in EtOH	Inject into structure being imaged, polymerizes in approximately 10 min	Microinject into vascular system of specimen, specimen is alive for imaging	Microinject into vascular system of specimen, specimen is alive for imaging
Advantages	Rapid, deep penetration, cheap, robust, stock solution stable for months	High levels of contrast, stock solution is stable for months, sharp tissue differentiation	Combines with extracellular matrix, high contrast	Allows for cell densities and individual cells to be visualized	Imaging negative spaces, remains isolated once polymerized, high level of contrast	Allows for short-term live imaging	Allows for long-term live imaging
Limitations	Overstain some mineralized tissues, intensity can vary	Slow tissue penetration (few millimeters)	Toxic with expensive disposal, limited penetration, cannot be used with alcohol-stored tissues	Overall low level of contrast	Complicated staining protocol, requires microinjections	Embryotoxic within 24 h, requires microinjection, low residence time	Requires microinjection, low residence time

2.2 Antigen-Specific Contrast	1. A primary antibody is chosen for immunostaining.
	2. Secondary antibody for immunostaining (goat anti-mouse IgG HRP conjugate, Invitrogen) (*see* **Note 6**).
2.2.1 Enzyme Metallography Immunostaining (Adapted from [8])	3. Glyoxal-based fixative (Shandon Glyo-Fixx, Thermo Scientific).
	4. 100 % methanol.
	5. Dimethylsulfoxide.
	6. Hydrogen peroxide.

7. Solution of 100 mM maleic acid, 150 mM NaCl, 0.1 % Triton X-100 pH 7.4 (MABT).

8. Blocking solution of MABT with 0.1 % saponin, 10 % sheep serum, 0.5 % Roche Blocking Reagent, DMSO.

9. Nanoprobes EnzMet 6010 Enzyme Metallography Kit (Yaphank, NY).

   (a) The EnzMet kit from Nanoprobes comprises three different solutions based on the chemical reduction reaction in peroxidase to reduces silver ions (Ag+) to insoluble metallic silver (Ag0), precipitating in the immediate vicinity of the enzyme conjugate.

   (b) Using a peroxidase-conjugated secondary antibody and following the EnzMet kit instructions, the silver precipitate acts as the tissue-specific contrast agent for CT imaging of the specimen.

2.3 Microinjection

1. Borosilicate glass capillary tubes (Sutter Instrument Co, OD 1.0 mm, ID 0.75 mm).
2. Small-diameter silicone tubing (VWR).
3. 3 mL plastic syringe (BD).
4. Laboratory stand.
5. Micromanipulator.

2.4 Micro/NanoCT Imaging

1. eXplore CT series scanners (GE Healthcare).
2. Xradia CT series scanners (Xradia Inc.).

2.5 Image Filtering, Rendering, and Analysis

1. Useful software platforms for image processing (*see* **Note 7**):
   (a) OsiriX (Rosset et al. 2004) (*see* **Note 8**).
   (b) MicroView (GE Healthcare).
   (c) ImageJ (National Institutes of Health) (*see* **Note 10**).
   (d) GAMBIT (ANSYS Inc.).

3   Methods

3.1   General Soft Tissue Contrast Agents

3.1.1   Lugol's Solution

1. In deionized water, combine the iodine metal and the potassium iodide and then aliquot out the necessary amount needed for the sample.

2. Prior to staining the sample, the solution should be diluted to 10 % of its initial concentration with deionized water.

3. Using samples that have been stored in aqueous solution, the specimen is stained for a minimum of 30 min to overnight depending on the size and density of the sample being stained.

4. Once the staining process is complete, the sample should be washed with water prior to imaging and once the imaging is complete the sample is dehydrated in ethanol and stored.

5. Lugol's solution is stable for several months.

3.1.2   Phosphotungstic Acid

1. The stock solution is a 1 % weight/volume solution of phosphotungstic acid in water.

2. For staining samples, mix 30 % of phosphotungstic acid stock solution with 70 % absolute ethanol.

3. For this staining protocol, samples should be dehydrated in 7 % ethanol prior to staining. For staining the specimens, suspend the sample in the above solution for 2 h to overnight depending on the size and density of the sample.

4. Prior to imaging, wash the samples with 70 % ethanol and scan in 70–100 % ethanol.

5. This solution is stable for several months.

3.1.3   Osmium Tetroxide (see Note 2)

1. Using samples that are in an aqueous solution, stain the sample for 1–2 h with 1–2 % OsO_4 in phosphate buffer.

2. Once the staining is complete, the sample should be washed in phosphate buffer and dehydrated in ethanol for storage.

3.1.4   Gallocyanin-Chromalum

1. Working with 5 % weight/volume gallocyanin-chromalum in water, the solution should be boiled to dissolve all of the gallocyanin-chromalum generating the working contrast agent.

2. Once the gallocyanin-chromalum has been dissolved, allow the solution to cool and then filter the solution.

3. The samples should start in an aqueous solution medium prior to staining and before exposing the samples to the gallocyanin-chromalum stain they should be washed in water.

4. For the optimal contrast, the samples should be stained overnight and then re-washed with water prior to imaging.

5. Once imaging has been completed, the samples can be dehydrated in ethanol and stored.

6. The solution is stable for 1–2 weeks.

3.1.5 Microfil™

1. Begin by placing the sample in a culture dish with a small amount of buffered saline.

2. Microfil is perfused at a ratio of 80:15:5 diluent:agent:catalyst (Microfil, Flow-Tech Inc.) in the desired location for imaging via microinjection introduced in Subheading 3.3.

3. Perfusion requires approximately 10 min before it is complete.

4. After perfusion, embryos should be fixed in whichever method the investigator prefers and is then stored.

3.1.6 Omnipaque™

1. Omnipaque™ is microinjected into the specimen via the protocol introduced in Subheading 3.3.

2. The specimen should be imaged immediately postinjection, especially if the cardiovascular system is of particular interest in the study due to the quick extravasation of OP from the vessels.

3.1.7 Visipaque™

1. Visipaque™ is microinjected into the specimen via the protocol introduced in Subheading 3.3.

2. The specimen should be imaged immediately postinjection, especially if the cardiovascular system is of particular interest in the study due to the quick extravasation of VP from the vessels.

3. Previous studies demonstrate the biodistribution kinetics of Visipaque and the large organ systems that the contrast agent resides in past injection [9].

3.2 Antigen-Specific Contrast

3.2.1 Enzyme Metallography Immunostaining (Adapted from [8])

1. The embryos should be fixed in the glyoxal-based fixative. After fixation the sample is rinsed with 100 % methanol and stored.

2. Incubate the embryos in a solution of methanol, DMSO, and hydrogen peroxide for 12 h.

3. The specimen should be washed twice in 50 % methanol and rehydrated through a methanol series to MABT solution.

4. Wash the samples in the MABT solution (described in Subheading 2.2) + 0.1 % saponin for 10 min followed by blocking the sample at room temperature with the blocking solution (given in Subheading 2.2).

5. Incubate the sample with the primary antibody in a ratio of 1:500 in blocking solution for 2–3 days and then wash the sample in the blocking solution overnight.

6. Incubate the sample with the secondary antibody in a ratio of 1:500 blocking solution for 2–3 days.

7. Once primary and secondary antibody steps are complete, the sample should be washed several times in the MABT solution with a final MABT wash overnight.

8. Postfix the specimen in 10 % formalin in MABT for 20 min and then wash in double-distilled water three times for 10 min during each wash.

9. Change the solution that the samples are in to a solution of 0.1 % Triton X-100 in distilled water.

10. Transfer the immunolabeled specimens in 0.1 % Triton X-100 to clean tubes and remove the Triton X-100 solution.

11. Once all steps to this point have been completed, the reagents suppled by Nanoprobes Inc. EnxMet 6010 kit will be used for the remaining procedure.

   (a) 300–400 μL of solution A should be added and mixed gently for 4 min.

   (b) Repeat the above step for solution B and solution C supplied by Nanoprobes Inc.

   (c) Once all reagents have been added and thoroughly mixed, monitor the specimen under a dissecting microscope for 20–40 min with gentle agitation.

   (d) Change to the stop solution just as the solution begins to appear gray and then rinse in distilled water.

12. Complete a methanol series by first washing the samples in 75 % methanol followed by 100 % methanol.

3.3 Microinjection (see Note 5)

1. Pull borosilicate glass capillary tubes into microneedles.

2. The needles should be cut to the desired diameter and beveled to 45° with a microforge.

3. The assembly of the microinjection apparatus is as follows:

   (a) The silicone tubing is attached to the 3 mL syringe via a pipette tip.

   (b) The agent being injected is loaded into the silicon tubing and the needle is attached to the end of the tubing.

   (c) A gravity-driven pressure gradient is established with the micromanipulator attached to a laboratory stand.

   (d) The soft tissues of the embryo are visualized through a dissection microscope.

   (e) The needle is positioned into the vessel of the embryo and pressure through the syringe is applied, injecting the agent into the specimen.

3.4 Micro/NanoCT Imaging

1. For live embryonic imaging, a scanner that only rotates the gantry and not the sample is necessary; this type of scan is typical for a microCT scanner such as the GE eXplore but not for the Xradia scanner.

2. Resolution of the image is largely dependent on the field of view; for live studies 25 μm voxels have been reported [4] but for fixed embryonic studies resolutions have been reported to be as small as 0.97 μm voxels on an Xradia imaging system (Metscher 2009).

3.5 Image Filtering, Rendering, and Analysis

3.5.1 Image Filtering

(a) The first step for image processing is to determine the structure of interest in the image. Contrast levels can be changed in OsiriX along with basic filtering techniques such as thresholding for segmenting out structures based on defined contrast levels. Additionally, ImageJ is easy to use and open source for basic filtering techniques (i.e., thresholding) and the image file type is readily changed in ImageJ which is convenient for opening the image in a separate software platforms.

(b) Furthermore the level of contrast, measured in Hounsfield units, can be analyzed through virtual cross sections within the image and displayed with a contrast vs. spatial location plot to understand the contrast enhancement of the desired anatomical structure. MicroView easily plots this information through the use of its line tool feature. Absolute Hounsfield unit measurements are indicative of relative contrast biodistribution at the given time when the image was taken.

(c) Image data sets, either in TIF or DICOM format, can be easily reconstructed through volumetric rendering, maximum intensity projections, and multi-planar reconstruction through OsiriX.

(d) Region growing algorithms are established through user-defined seed points positioned in the region of interest (ROI), typically a single anatomical segment or organ. The local gradient magnitude is used to find the standard deviation to segment out the single structure of interest. This is done effectively by setting pixel values in the ROI to zero and then propagating this negative space based on the user-defined seed point through the Z plane [4].

3.5.2 Rendering

(a) Image data sets, either in TIF or DICOM format, can be easily reconstructed through volumetric rendering, maximum intensity projections, and multi-planar reconstruction, most easily achieved in OsiriX.

(b) Region growing algorithms are established through user-defined seed points positioned in the region of interest (ROI), typically a single anatomical segment or organ. The local gradient magnitude is used to find the standard deviation to segment

out the single structure of interest. This is done effectively by setting pixel values in the ROI to zero and then propagating this negative space based on the user-defined seed point through the Z plane [4]. Segments from the image based on region growing or user-defined regions of interest can be reconstructed through volumetric renderings, maximum intensity projections, and multi-planar reconstructions.

3.5.3 Analysis

(a) For anatomical analysis, renderings obtained from the images can be used to make basic measurements such as surface area and volume. OsiriX is an easy software to make these measurements in. Additionally, for simple measurements ImageJ is ideal for user-defined line segmenting where small measurements can be made.

(b) For physiological simulations, geometries obtained from the renderings described in the section above can be imported into computational analysis software such as GAMBIT and meshed optimizing tetrahedral elements for analysis by varying the surface and volume.

(c) ANSYS 12 FLUENT is a well-known computational fluid dynamics solver designed for second-order double-precision 3D pressure-driven complex flows based on the meshed geometries from GAMBIT. From user-defined flow conditions, fluid simulations can be performed based on the anatomical geometry from the microCT image. It is reasonable to have 30–50 time steps and 1,000 iterations of each simulation for analyzing regions of flow [10] (*see* **Note 10**).

4   Notes

1. General soft tissue contrast agents all vary in the time for staining and if the sample should be in an aqueous or an alcohol medium, be sure to make note of that when considering which contrast agent is the most appropriate for the given study.

2. Osmium tetroxide produces excellent contrast but it is toxic and disposal can be expensive.

3. Be aware of how dense your embryonic sample is based on its age in development and make sure to adjust the staining time accordingly, err on the side of longer rather than shorter staining times.

4. The whole-embryo staining options will begin to leach out of the tissues once the staining procedure has ended; therefore, the sample should be imaged as soon as possible for maximum contrast.

5. Microfil™, Omnipaque™, and Visipaque™ contrast agents are injected into the specimen; microinjections are time consuming to master and these stains take additional considerations given this requirement.

6. The antigen-specific staining works on the principle of the secondary antibody reacting through a reduction reaction of the silver ions to insoluble metallic silver which acts as the contrast agent. This reaction happens when a peroxidase is present; therefore, it must be inherent to the secondary antibody; otherwise the reaction will not take place and the silver precipitation will not occur.

7. Many different software platforms exist for image processing and the few mentioned in this chapter is not an exhaustive list but simple suggestions based on experience; several different software options are available and most of the time it is simply based on accessibility and preference to the investigator.

8. OsiriX is capable of many different image processing tasks and has proved itself to be a valuable tool but it is only available for Macintosh computers; there is no PC alternative for OsiriX.

9. ImageJ is an initial place to start with image processing, thresholding is easy in ImageJ and slices of the image stack can be eliminated which can significantly reduce the file size.

10. For the input parameters in fluid simulation studies, if literature values are not available then Doppler ultrasound imaging produces excellent flow information that can be used in the simulations.

References

1. Dehaan RL, Ebert JD (1964) Morphogenesis. Annu Rev Physiol 26:15–46

2. Butcher JT, Sedmera D et al (2007) Quantitative volumetric analysis of cardiac morphogenesis assessed through micro-computed tomography. Dev Dyn 236(3):802–809

3. Gregg CL, Butcher JT (2012) Quantitative in vivo imaging of embryonic development: opportunities and challenges. Differentiation 84(1):149–162

4. Kim JS, Min JH et al (2011) Quantitative three-dimensional analysis of embryonic chick morphogenesis via microcomputed tomography. Anat Rec 294(1):1–10

5. Metscher BD (2009) MicroCT for developmental biology: a versatile tool for high-contrast 3D imaging at histological resolutions. Dev Dyn 238(3):632–640

6. Johnson JT, Hansen MS et al (2006) Virtual histology of transgenic mouse embryos for high-throughput phenotyping. PLoS Genet 2(4):471–477

7. Degenhardt K, Wright AC et al (2010) Rapid 3D phenotyping of cardiovascular development in mouse embryos by micro-CT with iodine staining. Circ Cardiovasc Imaging 3 (3):314–322

8. Metscher BD, Muller GB (2011) MicroCT for molecular imaging: quantitative visualization of complete three-dimensional distributions of gene products in embryonic limbs. Dev Dyn 240(10):2301–2308

9. Henning AL, Jiang MX et al (2011) Quantitative three-dimensional imaging of live avian embryonic morphogenesis via microcomputed tomography. Dev Dyn 240 (8):1949–1957

10. Yalcin HC, Shekhar A et al (2011) Hemodynamic patterning of the avian atrioventricular valve. Dev Dyn 240(1):23–35

11. Rosset A, Spadola L et al (2004) OsiriX: An Open-Source Software for Navigating in Multidimensional DICOM Images. J Digit Imaging 17(3):205–216

Chapter 5

Imaging the Dorsal-Ventral Axis of Live and Fixed *Drosophila melanogaster* Embryos

Sophia N. Carrell and Gregory T. Reeves

Abstract

Optimal imaging conditions are of critical importance in developmental biology, as much of the data in the discipline is acquired through microscopy. However, imaging deep sections of tissue, especially live tissue, can be a technical challenge due to light scattering and difficulties in mounting the sample. In particular, capturing high-quality images of dorsal-ventral cross sections requires "end-on" mounting to orient the anterior-posterior axis vertically. Here we present methods to mount and image dorsal-ventral cross sections of both live and fixed *Drosophila melanogaster* embryos. Our methods have the advantages of being rapid, allowing deep optical sections, and not requiring expensive, specialized equipment.

Key words *Drosophila melanogaster*, Embryo, Imaging, Dorsal-ventral cross section, Confocal microscopy, Dorsal gradient

1 Introduction

Confocal microscopy has become the gold standard in high-quality imaging, as researchers have begun to rely on fluorescent detection methods for quantitative imaging of molecular species in situ. However, confocal microscopy is light limited, making it difficult to image deep into tissues with a sufficiently high signal-to-noise ratio due to scattering of light through the tissue. This problem is particularly challenging when studying phenomena with spatial variations along the dorsal-ventral (DV) axis, such as the Dorsal (dl) nuclear gradient or mesoderm spreading in the *Drosophila* embryo [1–3].

To capture the entire DV axis in a single image, a form of "end-on" mounting is required, in which the anterior-posterior axis is aligned with the *z*-axis of the microscope [4–8]. However, this orientation can prove difficult to achieve due to geometry constraints (fruit fly embryos are egg shaped). Previous work has circumvented this problem by imaging *z*-stacks of laterally mounted embryos and computationally reconstructing the DV axis view

[9–12]. However, this technique was time intensive (approximately 45 min of imaging time per embryo [9]), light scattering problems beyond approximately 100 μm deep into the embryo degraded fluorescent signal, and image quality along the DV was lost at the midsagittal plane of the embryo due to poor *z*-axis resolution.

While many methods do exist for mounting *Drosophila* embryos to capture the full DV axis, they tend to be disadvantageous for several reasons (e.g., requiring lengthy time commitments and/or specialized equipment). For fixed embryos, microtome sections of plastic-embedded embryos provide precise cross sections, but require more than a day's worth of preparation (for example, *see* [13, 14]) and a good deal of manual carving with a razor blade. Recently, a microfluidic device has been developed to orient embryos end-on in a high-throughput fashion [6]. This method is extremely advantageous in that it allows users to quickly generate a large data set (>100 embryos in one experiment) [15], and the imaging can be automated with a programmable xy stage. However, this method is not available to most fly biologists, as highly customized microfluidic equipment is required. Another potential drawback is the depth of tissue penetration: imaging deeper than 75 μm (~15 %) into the embryo has not been demonstrated with this device [6, 15–18], yet DV patterns have been reported to change significantly up to 150 μm in depth [8, 15]. Fixed embryos have also been embedded in a gel that solidifies near room temperature, allowing for upright orientation of the embryos [19]. This technique allows for approximately ten embryos to be mounted simultaneously, and has the advantage of not requiring specialized equipment. While a minimum of 20 min is needed to solidify the jelly layer, an overnight incubation leads to better results. The maximum allowed depth of optical section with this technique is not clear.

There are also several techniques available for end-on mounting of embryos for live imaging. Witzberger and colleagues devised a polyacrylamide gel device to hold embryos upright (and also coined the term "end-on imaging") [4]. This technique produced high-quality images of live embryos at a temporal resolution of 30 s. This technique had a further advantage in that approximately 20 embryos could be mounted simultaneously in the device. However, device fabrication may prove a barrier to widespread use. Furthermore, the authors reported a loss in image quality past ~75 μm in tissue depth. Alternatively, embryos have been mounted upright on silicone-coated glass [5, 20–22]. However, this technique is fragile, in that small perturbations cause the embryo to tip over. Because of this, only one embryo can be realistically mounted at once. The microfluidic array, and possibly the gel-embedding techniques may also be used to image live embryos, but are subject to the same drawbacks as described above [6, 19].

Here we present two methods to mount *Drosophila* embryos for direct DV axis imaging. For fixed embryos, we describe in detail a manual cross-sectioning technique, which has been used previously [7, 8, 23]. This method has several advantages as compared to those described above. First, the manual cross-sectioning method is less time intensive than previous fixed-embryo methods. Once a researcher is familiar with the technique, up to 75 embryos may be prepared in an hour. Second, the method requires no equipment or special reagents beyond those which most *Drosophila* labs already have on hand. For live embryos, we describe a technique to adhere embryos to an upright, solid surface, similar to the mounting strategy used previously for imaging the DV axis using selective plane illumination microscopy [8]. This method allows for imaging up to 200 μm into the embryo without prohibitive loss of fluorescent signal. The method has further advantages in that it requires very little manual skill, it is rapid (taking less than 30 min), and it allows for mounting several embryos in the same dish.

2   Manual Cross Sectioning

1. 70 % glycerol: Combine 7 mL glycerol with 3 mL DI water in a 15 mL conical tube. Rock on a nutator for 10 min to ensure proper mixing. Alternatively, vortex for 1 min or until the viscosity appears consistent throughout the whole tube.

2. Hair loop: Attach a human hair in a small (2 mm diameter) loop to a 1,000 μL pipette tip with tape (Fig. 1).

3. Razor blade: Single edge industrial no. 9.
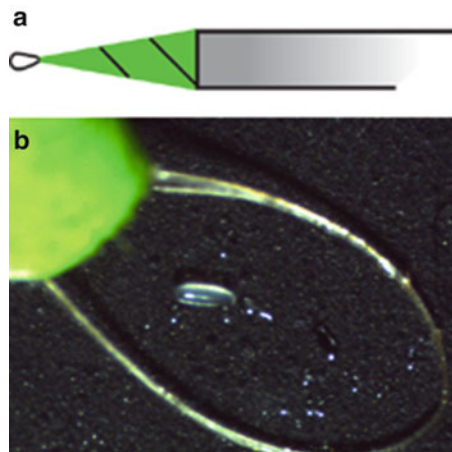
Fig. 1 Hair loop. (**a**) Schematic of the hair loop. Tape is *green* for contrast. (**b**) Image of a loop around a *Drosophila* embryo for scale

    4. 22 mm cover slips.

    5. Dissecting microscope with black plate.

    6. 9-Well glass dish.

    7. Double-sided tape.

2.1 Mounting Living Embryos

The methods presented here are for use with an inverted confocal microscope. The mounting block has been optimized for use with a Zeiss LD C-Apochromat 40× *NA* 1.1 water immersion objective, with a working distance of 620 μm. However, the general technique of adhering embryos to a cover slip can also be applied to an upright microscope, or a light sheet microscope [8] (*see* **Note 1**).

1. Mesh basket.

2. Bleach.

3. Hair loop.

4. Double-sided tape.

5. Glass-bottom petri dish: 35 mm diameter, 20 mm glass diameter, cover slip thickness #1.5 (or as recommended by the objective manufacturer).

6. Mounting block: Have a machinist create a mounting block that fits the following parameters (Fig. 2).

   Constraints:

   (a) The height must be highly precise: short enough to bring the embryos within the working distance of the objective but not so short that the embryos are smashed against the cover slip. For a 22 mm cover slip, a mounting block height of 21.5 mm is recommended (*see* **Note 2**).

   (b) One surface must be perfectly flat to allow a cover slip to be taped to it.

   (c) Material must be dense enough not to tip over when partially immersed in water.

   (d) Size must be small enough to sit inside petri dish.

   (e) Once inside the petri dish, the geometry must be such that at least part of the flat side is above the well formed by the glass cover slip on the bottom of the petri dish, so that the cover slip can hang down into the well (Fig. 2).

   (f) Material must be such that it is easy to attach and remove double-sided tape.

7. Heptane glue: Cut several short pieces (5–10 cm) of double-sided tape and add them to a 200 mL bottle. Cover with heptane (approximately 1 mL per cm of tape) and shake the bottle gently overnight at room temperature to dissolve the adhesive from the tape [24].
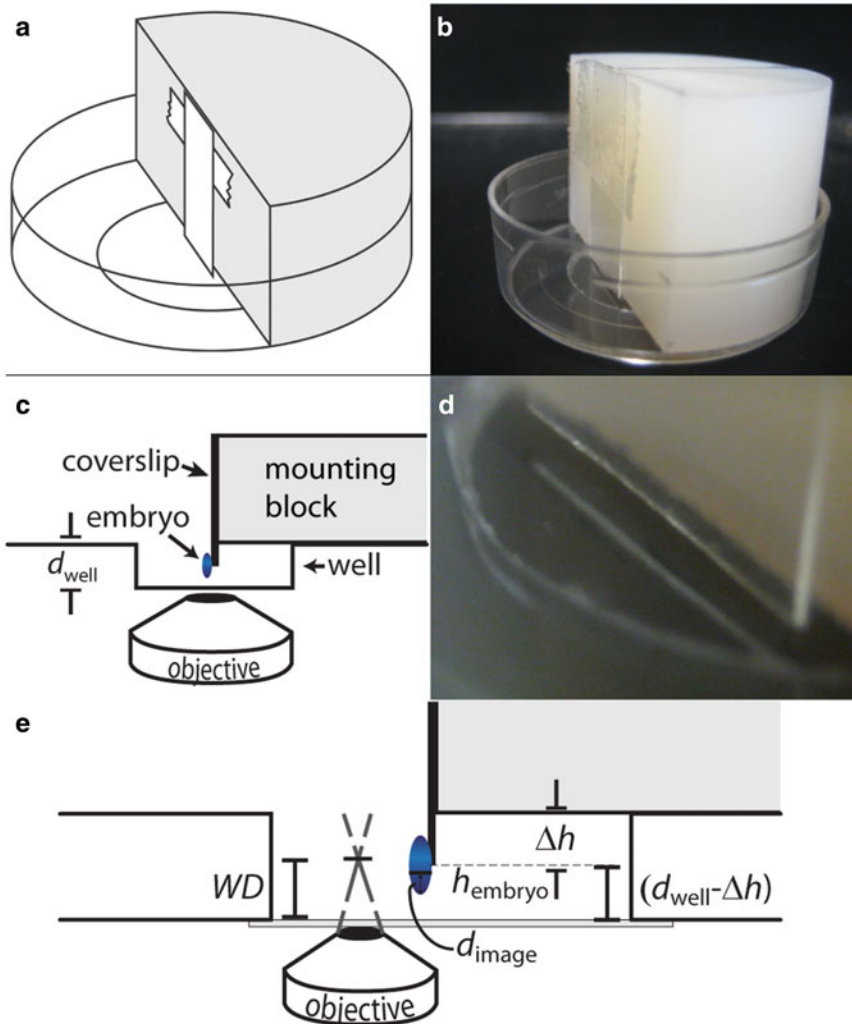
Fig. 2 Live imaging mounting block. (**a**) Schematic of the mounting block. The cover slip is attached with a piece of double-sided tape. (**b**) Image of the mounting block/cover slip in a glass-bottom petri dish. (**c**) Imaging schematic. The cover slip should be precisely aligned with the top of the mounting block, suspending the embryos in the well. (**d**) Close-up of the cover slip in the well. Note that the cover slip should not touch the bottom of the well. (**e**) Close-up schematic of the well, with each of the heights required for calculating the height of the mounting block labeled

8. Diamond scribe for glass etching.

9. Sticky cover slip: Using a diamond scribe, cut a 22 mm square cover slip roughly in half (*see* **Note 3**). Cover the bottom half of each half with about 10 μL of heptane glue and allow to dry for a minimum of 10 min.

3   Methods

3.1   Manual Cross Sectioning

Carry out all steps at room temperature (*see* **Note 4**). This procedure is written for a right-handed user. Left-handed users should use mirror-image orientations.

1. Prepare fixed embryos via immunostaining (*see* **Note 5**).

2. Transfer about 70 μL of embryos to one well of a glass dish (*see* **Notes 6** and **7**).

3. Under the microscope (using the black plate), select embryos that are appropriately aged for your application (approximately 100 embryos), and transfer them to the top left of a 22 mm cover slip using a clipped pipette tip (*see* **Note 8**).

4. Using an unmodified pipette tip, remove as much of the glycerol as possible, and return it to the glass well (*see* **Note 9**).

5. Use a rolled-up corner of a Kimwipe to remove as much of the remaining glycerol as possible (*see* **Note 10**).

6. Use a hair loop to manipulate an embryo away from the group (*see* **Note 11**) and orient it at a 20° angle (*see* **Note 12**) (Fig. 3).

7. Use a razor blade to remove approximately 150 μm of tissue from the right end of the embryo (Fig. 4). Be careful to ensure that the razor blade cuts straight down and entirely separates the two sections of tissue (*see* **Note 13**).

8. Reorient the embryo if it moved during **step 7** and remove about 150 μm of tissue from the left end (*see* **Note 14**).

9. Carefully manipulate the cross section away from the cut off sections and to the bottom right corner of the cover slip, at least 2 mm from the bottom and right edges (*see* **Note 15**).
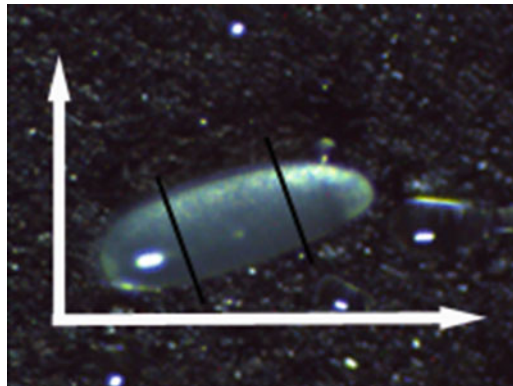
Fig. 3 Angle for orienting the embryo for cross sectioning. *Black lines* indicate where cuts should be made
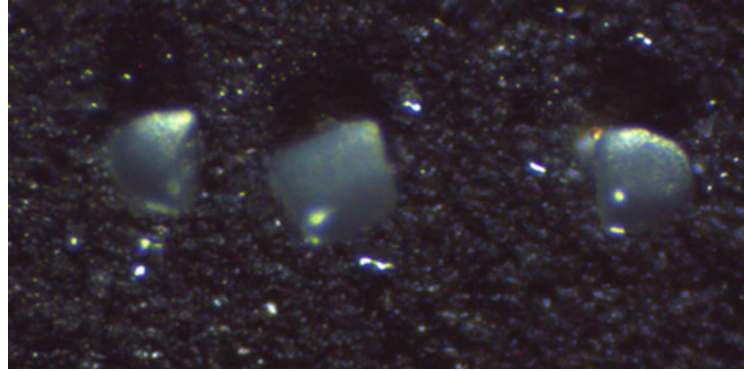
Fig. 4 Properly cross-sectioned embryo. Each end is ~150 μm long, leaving 200 μm in the *middle*. Notice how the middle section is roughly *square*. Although one side of the cross section is not perfectly perpendicular, this is an acceptable section. Simply orient the section so that the perpendicular side is down on the cover slip (*see* **Note 13**)
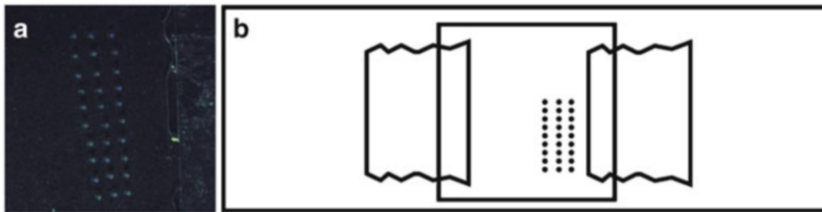
Fig. 5 Mounted cross sections. (**a**) Properly mounted cross sections. (**b**) Schematic of the whole slide

10. Using a hair loop, manipulate the cross section so that it is standing straight up.

11. Repeat until all embryos are cross-sectioned, aligning them in three columns, approximately 0.5 mm apart from one another (Fig. 5) (*see* **Note 16**).

12. Put two layers of double-sided tape down on a microscope slide. Put another two layers of double-sided tape down about 2 cm apart from the first set (*see* **Note 17**).

13. Carefully pick up the cover slip with the cross-sectioned embryos on it. Place it embryo-side down on the double-sided tape so that both edges are adhered to the tape but none of the cross sections are in the tape (Fig. 5). Press down on the sides to ensure proper adhesion (*see* **Note 18**).

14. Pipette 50–70 μL of 70 % glycerol under the cover slip, adding it slowly and all from one edge. Add enough to fill the space between the slide and the cover slip but no more (*see* **Note 19**).

15. While imaging cross sections, be sure to focus below the level of tissue that has been damaged by the razor blade (Fig. 6). Typical images obtained from this technique are shown in Fig. 7.
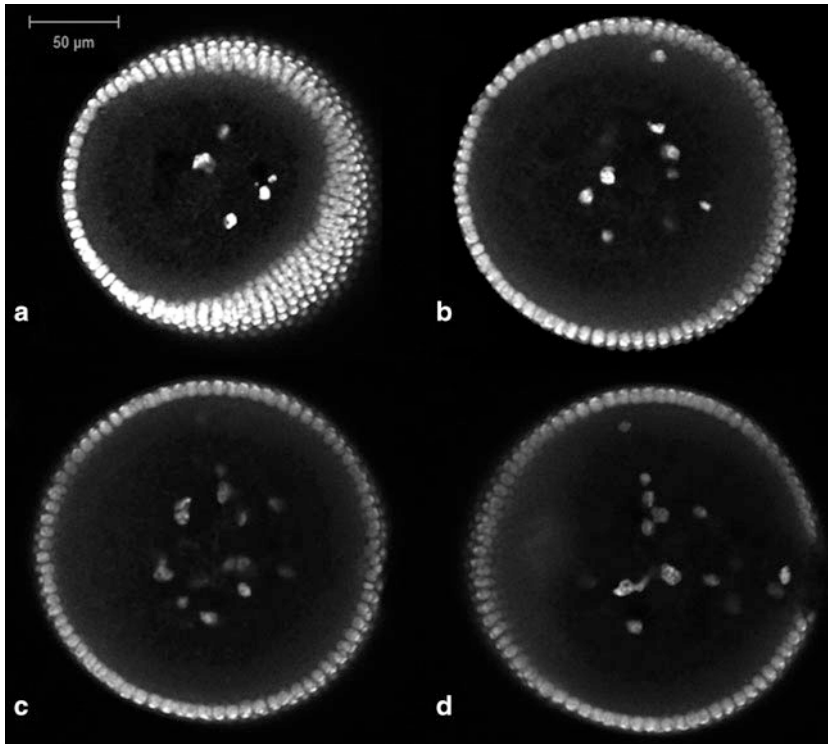
Fig. 6 Manual cross sectioning damages the tissue. Images should be taken at a z depth in between the damaged portions of tissue. (**a**) The portion closest to the cover slip shows evidence of crushing by the razor blade, as evidenced by the visibility of more than one row of nuclei. (**b**) Tissue further from the cover slip still shows some signs of damage, particularly in the double row of nuclei visible on the *right side*. (**c**) When at an appropriate z depth, the tissue will appear circular and have no visible marrings. (**d**) The portions furthest from the cover slip also show signs of damage from the razor blade. Nuclei stained with DAPI
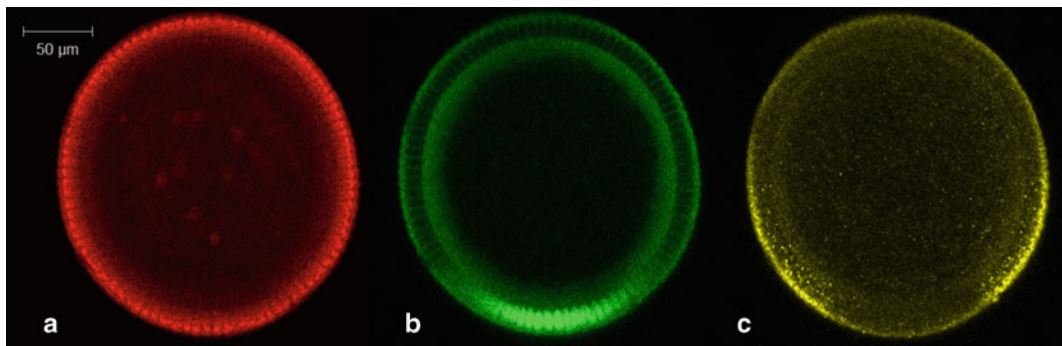
Fig. 7 Typical images of a cross-sectioned embryo. (**a**) Nuclei are marked with anti-histone. (**b**) The protein Dorsal appears in a nuclear gradient that peaks at the ventral midline. (**c**) *sog* mRNA appears in the ventrolateral portion of the embryo. Images are oriented so that ventral is down

3.2 Mounting Live Embryos

This method has been optimized for a $40\times$ *N.A.* 1.1 water immersion objective mounted on a Zeiss LSM 710 inverted confocal microscope.

1. Anesthetize an appropriate number of flies and transfer them to a collection cage several days before imaging will take place (*see* **Note 20**). Streak a small amount of yeast paste onto a grape juice plate, and change the plate daily until ready for imaging.

2. Anesthetize the flies in the cage and allow them to lay embryos for 1–2 h (*see* **Note 21**).

3. Introduce a new plate streaked with yeast paste to the cage, and allow the flies to lay embryos for 30–45 min (*see* **Note 22**). Age the embryos to 30 min shy of the desired developmental stage (*see* **Note 23**).

4. Brush embryos from grape juice agar plate into a mesh basket using a paintbrush and DI water (*see* **Note 24**).

5. Dechorionate embryos using either **step (A)** (dechorionation in bleach) or **step (B)** (manual dechorionation) [24].

    (A) *Dechorionation with bleach and embryo selection*:
    - Submerge the basket of embryos in 100 % bleach for 30 s (*see* **Note 25**).
    - Rinse well with DI water.
    - Remove mesh from basket. Place the mesh onto the now-clean grape juice agar plate (*see* **Note 26**).
    - Select embryos of the desired stage for mounting (*see* **Note 27**).

    (B) *Manual dechorionation and embryo selection*:
    - Using a brush, transfer embryos from mesh onto a plate with transparent agar or agarose. Cover embryos with a small amount of halocarbon oil (*see* **Note 28**).
    - Using transmitted illumination, select approximately 10–15 embryos of the appropriate stage.
    - Using a brush, transfer the selected embryos to a clean agar gel plate, transferring as little oil as possible.
    - With a hair loop, roll embryos on the clean agar gel to remove as much oil as possible.
    - Place a strip of double-sided tape on a microscope slide.
    - Using a brush, transfer embryos one by one to the double-sided tape.
    - With the hair loop, gently roll each embryo until the chorion is removed by the tape.

- After the chorion is removed from an embryo, transfer it back to a clean agar gel plate to keep it in a moist environment (*see* **Note 29**).

6. Using a hair loop, transfer embryos from agar plate to sticky cover slip (*see* **Note 30**). Embryos will naturally cling to the hair loop, although it may take several tries to pick one up. Orient each embryo perpendicular to the bottom of the cover slip. Place each embryo so that approximately half of the embryo is on the cover slip and half is hanging off (*see* **Note 31**). Repeat until the desired number of embryos has been mounted (*see* **Note 32**).

7. Carefully adhere a piece of double-sided tape to the back of the cover slip (the side without the embryos).

8. Adhere the cover slip to the mounting block such that the top of the cover slip is exactly in line with the top of the mounting block (*see* **Note 33**). The embryos will be hanging off the bottom. *See* Subheading 2 for a description of how to design the mounting block.

9. Put a small amount of DI water into a glass-bottom petri dish (*see* **Note 34**). Gently place the mounting block into the water so that the embryos are submerged.

10. Carefully transfer the glass-bottom dish/mounting block to the microscope and begin collecting images. *See* Figs. 8 and 9 for example images obtained using this method.
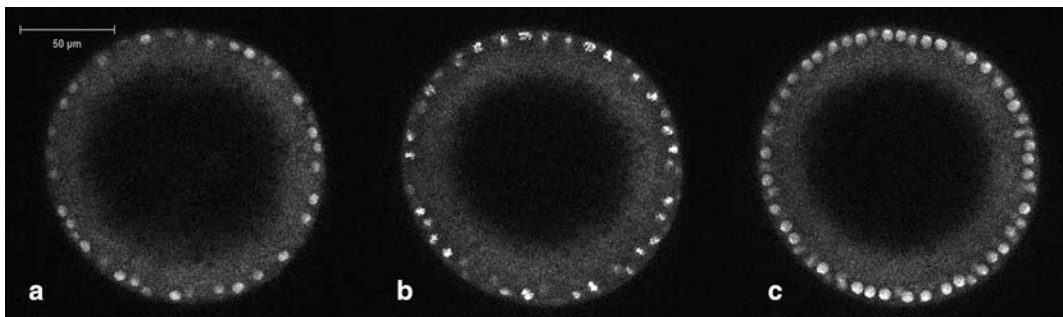
Fig. 8 Sample images obtained from a live embryo expressing a histone::RFP fusion protein. (**a**) Nuclear cycle 11. (**b**) Mitosis between nuclear cycles 11 and 12. (**c**) Nuclear cycle 12. Images are taken 10 min apart and ~100 μm from the tip of the embryo
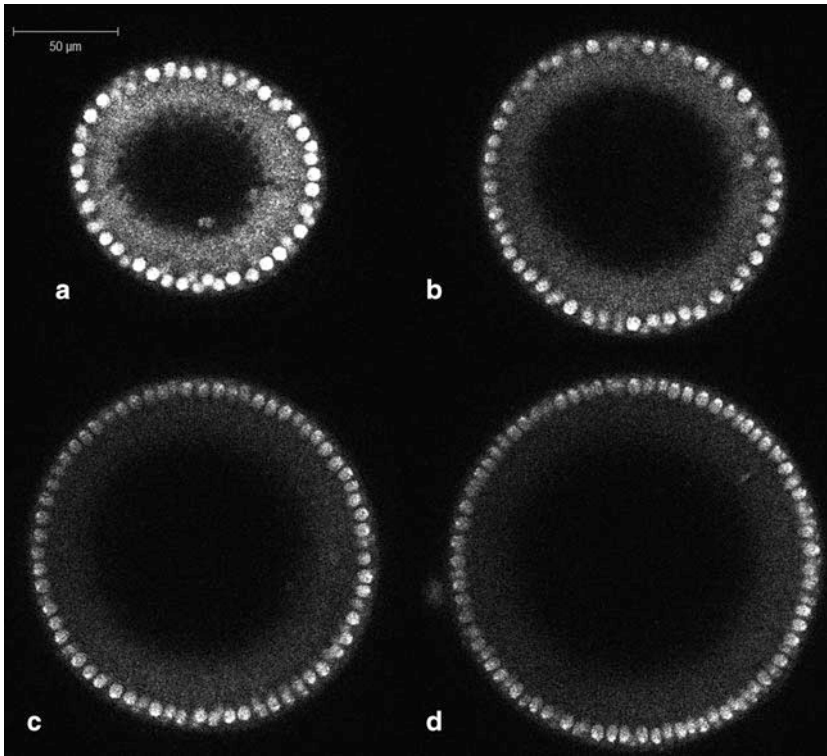
Fig. 9 Sample images obtained from a live embryo expressing a histone::RFP fusion protein at a depth of (**a**) 50 μm, (**b**) 100 μm, (**c**) 150 μm, and (**d**) 200 μm from the tip of the embryo

4   Notes

1. For other microscope geometries, using heptane glue to adhere embryos to a cover slip is still a useful technique. For upright microscopes, the cover slip must be shorter than the depth of the petri dish used (so that the embryos are covered with water), and it must be adhered to a short mounting block (so that the cover slip is vertical). The design of the mounting block has very little constraint: it just must be small enough to fit in the dish, it must be dense enough not to tip over when fully submerged in water, and it must have a flat surface for the cover slip to be adhered to. Also, the embryos must be oriented facing up off of the cover slip, and a water-dipping objective is necessary. For light sheet microscopes, the cover slip can be adhered to a block attached to the mounting rod, and embryos should face horizontally off of the cover slip with their AP axis aligned with the z-axis of the imaging objective.

2. The two tightest constraints are (1) that one side must be perfectly flat, and (2) that its height must be a precise amount

shorter than the height of the cover slip so that aligning one end of the cover slip with the top of the mounting block causes the embryos to hang down into the well far enough to be imaged (Fig. 2). The bounds on the height of the mounting block (h_{block}) are determined by a combination of the height of the cover slip ($h_{coverslip}$), the depth of the well (d_{well}), the portion of the embryo that hangs off the cover slip (h_{embryo}), the desired depth of imaging (d_{image}), and the working distance of the objective lens (WD). If $\Delta h \equiv h_{coverslip} - h_{block}$, then

$$d_{well} - \Delta h > h_{embryo}, \text{ and}$$
$$d_{well} - \Delta h - h_{embryo} + d_{image} < \text{WD}.$$

For our purposes, we had $d_{well} = 1$ mm, h_{embryo} ~250 μm, d_{image} ~200 μm, and WD = 620 μm. For those numbers, $\Delta h = 0.5$ mm worked well, and since $h_{coverslip} = 22$ mm, we had the mounting block machined to a height of $h_{coverslip} = 21.5$ mm.

3. A half cover slip is used so that it will fit into the 20 mm diameter well. If the imaging dish has a larger well, or smaller cover slips are available, a whole cover slip may be used.

4. Some researchers find the embryos easier to see in a darkened room.

5. Immunostaining is performed according to an established procedure, omitting the Proteinase K step [25]. Embryos not being prepared should be stored at −20 °C and in the dark to prevent loss of fluorescence.

6. To prevent damaging embryos while transferring them, it may be helpful to clip a pipette tip (using scissors) to make a wider opening.

7. This step is optional. Some researchers find that this step limits the amount of glycerol that gets placed on the cover slip. It also enables researchers to more accurately select embryos that are of the desired age.

8. Embryos are cross-sectioned on the cover slip so that the tissue is as close to the objective as possible due to variability in the height of the cross sections produced.

9. Some embryos may be removed with the glycerol. This is not an issue. Simply return them to the glass plate with the glycerol. Cover the glass plate with something (an empty pipette tip box works well) to protect the leftover embryos from light while you cross-section the others.

10. Depending on how much glycerol remains on the cover slip, all four corners of a Kimwipe may be necessary. Excess glycerol allows the embryo to slide on the glass, which can cause the razor blade to slide off the embryo, so it helps to remove as much as possible before attempting to cross-section. However,

Kimwipes can leave fibers on the cover slip that can lead to errors in image analysis. If any fibers appear, ensure that they are removed from the area closest to the cross-sectioned embryos.

11. Two or even three similarly sized embryos may be cross-sectioned at the same time.

12. The angle at which the embryo is oriented is up to the user, so long as it is comfortable to hold the blade perpendicular to the embryo. Embryos are not aligned horizontally because the razor blade blocks the view of the embryo during the cross-sectioning process. If it is difficult to manipulate the embryo, the cover slip may also be rotated, taking care to prevent any previously cross-sectioned embryos from being in line with where the cuts will be made.

13. Straight edges are important for proper imaging. If the tissue sticks to the razor blade, gently set the blade down on the cover slip and use a hair loop to slide it off. It may be easier to cut a straight edge by resting the far edge of the razor blade on the cover slip, and then pressing forward towards the embryo. If a cross section has one side that is perfectly perpendicular to the axis of the embryo but the other is not (as seen in Fig. 4), orient the embryo so that the perpendicular side is down on the cover slip so that images taken are from a proper DV cross section.

14. Due to the variance in some gradients, particularly the nuclear gradient of Dorsal, that occurs at the anterior and posterior ends, the desired size of a cross section is 200 μm, a little bigger than the middle third. The cross section should look similar to a square at this point, since the diameter of the embryo is also ~200 μm. Sections that are "too tall" will be smashed by the cover slip. Sections that are too short may not have a sufficient amount of undamaged tissue for imaging.

15. The unwanted sections of embryo tissue can be moved to the lower left corner of the cover slip (the "graveyard"), along with any embryos that are not suitable for cross sectioning due to age or other defects.

16. Any configuration will do, but it is easier to image the embryos when they are neatly arranged.

17. Each layer of double-sided tape is approximately 100 μm thick, so two layers of tape will prevent the cover slip from crushing the 200 μm tall cross sections.

18. Ensure that the double-sided tape layers lay flat on the microscope slide; any unevenness in the tape layers can cause irregular adherence of the cover slip and subsequent loss of the cross sections during the next step. The blunt end of a paintbrush works particularly well to adhere the cover slip to the tape. The "graveyard" can be put on the tape.

19. Be careful not to add too much glycerol. If cross sections "float away" during this step, they may be too short. If many of the cross sections have been knocked over or appear compressed in the z direction, they may be too tall.

20. Allowing the flies time to acclimate to the cage seems to lead to better laying.

21. Anesthetizing the flies and allowing them to lay embryos for a short period of time clears the females of any embryos they have not yet laid, ensuring that the collection will consist of more precisely aged embryos.

22. The length of the embryo collection period can vary depending on how many flies are present in the cage and the window of desired initial developmental stage of the embryos to be imaged.

23. The remaining steps require about 30 min to complete by a researcher who is comfortable with the technique. For new users, it is recommended to allow 45 min–1 h, since it is better to have to wait for some time for the desired developmental stage than to miss it completely.

24. Flies often lay embryos in the yeast paste, so it is important to rinse the yeast paste into the basket as well.

25. The amount of time can vary from 10 to 40 s. Start with the shortest time possible; if the chorion is still present on most embryos, increase this time by 10 s intervals until most embryos appear fully dechorionated. Bleaching the embryos for too long can lead to decreased viability. We find that 30 s is the optimal time.

26. The embryos need to be kept moist to ensure survival; however, embryos will be difficult to manipulate if the surface of the plate is too damp. If DI water remains after the previous step, remove it with a paper towel.

27. After dechorionation, some embryo morphology can be seen, allowing for selection of the proper stage.

28. The halocarbon oil clarifies the chorion. With transmitted light, some embryo morphology can be seen, allowing for selection of the proper stage.

29. As an alternative to using several agar gel plates, one can cut out several sections (one for the halocarbon oil, one for removing the oil, and one for keeping embryos moist after dechorionation) of one plate.

30. This step is critical to the success of the live imaging experiment, so pay careful attention while carrying it out. It will likely take several tries before one is fully comfortable with the method of transferring and orienting embryos. It may be

helpful in moving embryos to coat the hair loop in a small amount of heptane glue by rolling it over the surface of the coated cover slip. We find it easier to pick up an embryo with the hair loop so that part of the embryo extends outside the hair loop to allow for proper positioning on the cover slip.

31. It is possible to reorient the embryos once they have been placed on the cover slip, but due to the sticky nature of the heptane glue, they may burst if moved too much. Up to 2/3 of the embryo length may be suspended off the end of the cover slip.

32. The number of embryos mounted is dependent on the user, keeping in mind that it is only possible to image one embryo at a time. It is recommended to mount an excess of embryos to ensure that at least one is of the appropriate age and in the appropriate (precisely upright) position.

33. Because the tape is more strongly adhered to the cover slip, it is possible to reorient the cover slip on the device if it is not perfectly straight. Also, depending on the size of the well, it may be necessary to ensure that the cover slip is attached precisely in the middle of the device.

34. Be careful not to overfill the petri dish, as the mounting block will take up a lot of volume.

Acknowledgements

References

1. Moussian B, Roth S (2005) Dorsoventral axis formation in the Drosophila embryo–shaping and transducing a morphogen gradient. Curr Biol 15:R887–R899

2. Reeves GT, Stathopoulos A (2009) Graded dorsal and differential gene regulation in the Drosophila embryo. Cold Spring Harb Perspect Biol 1:a000836

3. Leptin M (2005) Gastrulation movements: the logic and the nuts and bolts. Dev Cell 8:305–320

4. Witzberger MM, Fitzpatrick JAJ, Crowley JC et al (2008) End-on imaging: a new perspective on dorsoventral development in Drosophila embryos. Dev Dyn 237:3252–3259

5. DeLotto R, DeLotto Y, Steward R et al (2007) Nucleocytoplasmic shuttling mediates the dynamic maintenance of nuclear Dorsal levels during Drosophila embryogenesis. Development 134:4233–4241

6. Chung K, Kim Y, Kanodia JS et al (2011) A microfluidic array for large-scale ordering and orientation of embryos. Nat Methods 8:171–176

7. Trisnadi N, Altinok A, Stathopoulos A et al (2012) Image analysis and empirical modeling of gene and protein expression. Methods 62 (1):68–78

8. Reeves GT, Trisnadi N, Truong TV et al (2012) Dorsal-ventral gene expression in the

Drosophila embryo reflects the dynamics and precision of the dorsal nuclear gradient. Dev Cell 22:544–557

9. Liberman LM, Reeves GT, Stathopoulos A et al (2009) Quantitative imaging of the Dorsal nuclear gradient reveals limitations to threshold-dependent patterning in Drosophila. Proc Natl Acad Sci U S A 106:22317–22322

10. Luengo Hendriks CL, Keränen SVE, Fowlkes CC et al (2006) Three-dimensional morphology and gene expression in the Drosophila blastoderm at cellular resolution I: data acquisition pipeline. Genome Biol 7:R123

11. Keränen SVE, Fowlkes CC, Luengo Hendriks CL et al (2006) Three-dimensional morphology and gene expression in the Drosophila blastoderm at cellular resolution II: dynamics. Genome Biol 7:R124

12. Fowlkes CC, Hendriks CLL, Keränen SVE et al (2008) A quantitative spatiotemporal atlas of gene expression in the Drosophila blastoderm. Cell 133:364–374

13. Hemavathy K, Meng X, Ip YT (1997) Differential regulation of gastrulation and neuroectodermal gene expression by Snail in the Drosophila embryo. Development 124:3683–3691

14. McMahon A, Supatto W, Fraser SE et al (2008) Dynamic analyses of Drosophila gastrulation provide insights into collective cell migration. Science 322:1546–1550

15. Kanodia JS, Kim Y, Tomer R et al (2011) A computational statistics approach for estimating the spatial range of morphogen gradients. Development 138:4867–4874

16. Kim Y, Andreu MJ, Lim B et al (2011) Gene regulation by MAPK substrate competition. Dev Cell 20:880–887

17. Kanodia JS, Liang H-L, Kim Y et al (2012) Pattern formation by graded and uniform signals in the early Drosophila embryo. Biophys J 102:427–433

18. Helman A, Lim B, Andreu MJ et al (2012) RTK signaling modulates the Dorsal gradient. Development 139:3032–3039

19. Belu M, Javier M, Ayasoufi K et al. (2010) Upright imaging of Drosophila embryos. J Vis Exp (43): 2175

20. Kanodia JS, Rikhy R, Kim Y et al (2009) Dynamics of the Dorsal morphogen gradient. Proc Natl Acad Sci U S A 106: 21707–21712

21. Mavrakis M, Rikhy R, Lilly M et al (2008) Fluorescence imaging techniques for studying Drosophila embryo development. In: Bonifacino JS et al (eds) Current protocols in cell biology. Wiley, New York, NY, Chapter 4, Unit 4.18

22. Daniels BR, Rikhy R, Renz M et al (2012) Multiscale diffusion in the mitotic Drosophila melanogaster syncytial blastoderm. Proc Natl Acad Sci U S A 109:8588–8593

23. Grosshans J, Wieschaus E (2000) A genetic link between morphogenesis and cell division during formation of the ventral furrow in Drosophila. Cell 101:523–531

24. Supatto W, McMahon A, Fraser SE et al (2009) Quantitative imaging of collective cell migration during Drosophila gastrulation: multiphoton microscopy and computational analysis. Nat Protoc 4:1397–1412

25. Kosman D, Mizutani CM, Lemons D et al (2004) Multiplex detection of RNA expression in Drosophila embryos. Science 305:846

Chapter 6

Light Sheet-Based Imaging and Analysis of Early Embryogenesis in the Fruit Fly

Khaled Khairy, William C. Lemon, Fernando Amat, and Philipp J. Keller

Abstract

The fruit fly is an excellent model system for investigating the sequence of epithelial tissue invaginations constituting the process of gastrulation. By combining recent advancements in light sheet fluorescence microscopy (LSFM) and image processing, the three-dimensional fly embryo morphology and relevant gene expression patterns can be accurately recorded throughout the entire process of embryogenesis. LSFM provides exceptionally high imaging speed, high signal-to-noise ratio, low level of photoinduced damage, and good optical penetration depth. This powerful combination of capabilities makes LSFM particularly suitable for live imaging of the fly embryo.

The resulting high-information-content image data are subsequently processed to obtain the outlines of cells and cell nuclei, as well as the geometry of the whole embryo tissue by image segmentation. Furthermore, morphodynamics information is extracted by computationally tracking objects in the image. Towards that goal we describe the successful implementation of a fast fitting strategy of Gaussian mixture models.

The data obtained by image processing is well-suited for hypothesis testing of the detailed biomechanics of the gastrulating embryo. Typically this involves constructing computational mechanics models that consist of an objective function providing an estimate of strain energy for a given morphological configuration of the tissue, and a numerical minimization mechanism of this energy, achieved by varying morphological parameters.

In this chapter, we provide an overview of in vivo imaging of fruit fly embryos using LSFM, computational tools suitable for processing the resulting images, and examples of computational biomechanical simulations of fly embryo gastrulation.

Key words Light sheet microscopy, Computational modeling, Tissue biomechanics, Live imaging, Quantitative developmental biology, *Drosophila melanogaster*, Embryonic development, Image processing

1 Introduction

Morphogenesis is a dynamic—inherently three dimensional—process, through which tissues and organs take their shape. In particular, the basic body plan of the developing organism is determined during gastrulation, which can be regarded as a sequence of epithelial tissue invaginations. Such folds are

ubiquitous in metazoans and uncovering their mechanisms is of wide-reaching importance. For the study of epithelial invaginations, the fruit fly is highly suitable because of its amenability to genetic manipulation. However, our understanding of gastrulation, and morphogenetic processes in general, is limited by the quality and spatial resolution of images we are able to acquire of the process (for both wild type and mutants), the invasiveness and speed of image acquisition techniques, the accuracy by which we can extract phenotypic and dynamic features from the images, and the predictive power of computer simulations that challenge morphogenetic hypotheses.

Compared to conventional microscopy techniques, such as confocal laser scanning microscopy, light sheet fluorescence microscopy (LSFM) is in an excellent position to address the challenges related to image quality, acquisition speed, and invasiveness of the recording process. The key concept behind LSFM is sample illumination in a thin volume section orthogonal to fluorescence detection. Through this arrangement (Fig. 1a, b), LSFM illuminates only the in-focus plane, thus providing intrinsic optical sectioning. This means that it enables simultaneous detection of the fluorescence signal from an entire plane. As a result of this microscope design, LSFM provides high acquisition speed, high signal-to-noise ratio, minimal levels of photo-bleaching, and good penetration depth. The sample typically resides in a low-concentration agarose cylinder (Fig. 1c), which represents a low-stress environment compared to the conventional glass slide/coverslip systems. All of these properties make LSFM particularly suitable for in vivo imaging applications. In the following, we discuss in particular opportunities in the live imaging and study of embryonic development of the fruit fly (Fig. 1d).

The images provided by LSFM contain information on the fluorescently labeled structures in three dimensions and over time, and must typically be appropriately processed before further quantitative analyses are possible. Common requirements are the extraction of nuclear positions, cell boundaries, tissue outlines, cell tracks, and relative label expression levels. The main computational tasks are accordingly image pre-processing, image segmentation, and cell tracking.

Here, we provide an overview of an advanced LSFM system (with simultaneous multiview imaging capability) as applied to the live imaging of fly embryos, and the challenges met for that specific system. We also describe computational tools suitable for processing the resulting LSFM data. Finally, we describe efforts at modeling the mechanics of fly embryogenesis, highlighting current challenges and directions.
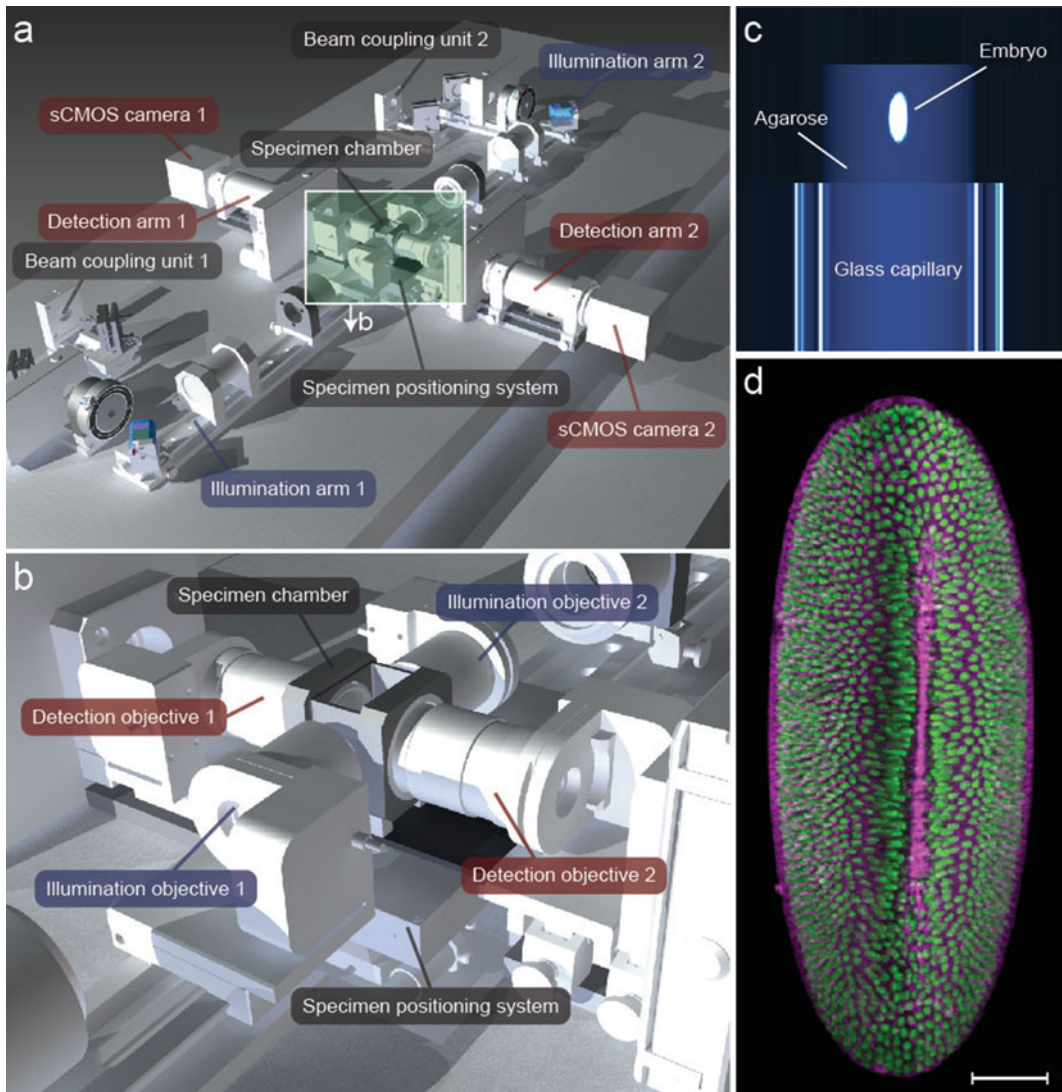
Fig. 1 Multiview light sheet microscopy of fruit fly embryo. (**a**) Layout of SiMView microscope. Two illumination arms generate the scanned laser light sheets used to excite fluorescence in the specimen located in the center of the water-filled specimen chamber. The two detection arms image the emitted fluorescent light onto the chips of high-speed sCMOS cameras. (**b**) Close-up of the specimen chamber in (**a**). (**c**) *Drosophila* embryos are held in the specimen chamber in a vertically oriented cylinder of 1 % agarose. (**d**) Maximum-intensity projection of a SiMView recording of a *Drosophila* embryo (ventral view). Fluorescent labels: nuclei (*green*) and membrane (*magenta*). The snapshot represents one time point of a 24-h long time-lapse recording. Scale bar = 50 μm. Panels (**a**) and (**b**) reprinted from Tomer et al. [14] with permission from Macmillan Publishers Ltd.

2 Materials

2.1 Materials for Fly Embryo Collection and Embedding

1. Grape juice plates (60 mm plastic tissue-culture dishes containing 3 % agar in 50 % grape juice).

2. Yeast paste (1 g of yeast mixed with 1.3 mL of tap water).

3. *Drosophila* mating cages (59-100, Genesee Scientific, Inc.).

4. Mesh basket (46-101, Genesee Scientific, Inc.).

5. Bleach (Sodium Hypochlorite, 425044-1L, Sigma-Aldrich).

6. 1 % low melting temperature agarose (Type VIIa, A0701, Sigma-Aldrich) in tap water.

7. Glass capillary, 20 mm long, 1.5/2.0 mm inner/outer diameter.

8. Scalpel.

3 Methods

3.1 Light Sheet Microscopy for Simultaneous Multiview Imaging

The last decade has seen many advances in light microscopy. Notably, light sheet microscopy has emerged as a powerful new technique that addresses the fundamental limitations arising from the intrinsic performance trade-offs encountered in conventional methods. In many in vivo imaging experiments, several conflicting key parameters need to be carefully balanced. It is usually desirable to achieve high temporal resolution (i.e., imaging speed), high spatial resolution, high signal-to-noise ratio, low photo-bleaching/toxicity, and good spatial coverage of the specimen [1].

Some implementations of light microscopy provide good overall performance, whereas others excel in one parameter, usually by trading off performance in other parameters. Conventional widefield fluorescence microscopes provide high imaging speed and good signal-to-noise ratio, but lack optical sectioning capability and are therefore unsuited for three-dimensional imaging. Point-scanning confocal fluorescence microscopes provide good spatial resolution and the intrinsic capability to eliminate scattered light [2], but perform poorly with respect to imaging speed, signal-to-noise ratio, photo-bleaching/toxicity, and penetration depth. Point-scanning two-photon microscopes improve over confocal fluorescence microscopes with respect to penetration depth and usually also photo-bleaching/toxicity [3, 4], but further reduce signal-to-noise ratio and imaging speed. Spinning disk confocal microscopes, which use multiple pinholes simultaneously, provide higher imaging speed than (single-)point-scanning confocal fluorescence microscopes [5], but reduce image quality.

Light sheet microscopes combine an intrinsic optical sectioning capability with high imaging speeds, good signal-to-noise ratio, and

low light exposure of the specimen, and are thus particularly well suited for biological live imaging [6–9]. A strength of this unique combination of capabilities is the possibility to study embryonic development at the system level while preserving the ability to follow cellular processes at the high spatiotemporal resolution required for global cell tracking [1].

In contrast to conventional and confocal epi-fluorescence microscopes, which employ the same lens for fluorescence excitation and detection, light sheet microscopes rely on the principle of sample illumination with a planar light sheet perpendicular to the axis of fluorescence detection [10–12]. The light sheet is coplanar with the focal plane of the fluorescence detection system. Fluorescent molecules are only excited in the illuminated plane, which is recorded in a single step with a camera-based detection system. As a result of this intrinsic optical sectioning capability, photo-bleaching and other types of photoinduced damage are avoided outside the thin, illuminated specimen section. This circumstance gives light sheet microscopes a decisive advantage in the fast imaging of sensitive biological specimens as well as in long-term in vivo imaging experiments [12–16]. Light sheet microscopes are furthermore particularly well suited for "multiview imaging," which refers to the strategy of observing the same specimen along multiple different directions. Thereby, parts of the specimen become visible that would otherwise be hidden or obscured in the observation along a single direction, owing to the limited penetration depth of the light microscope [17].

Basic light sheet microscopy implementations typically use a single light sheet and a single detection arm, oriented at a right angle to the light sheet. As in other forms of light microscopy, this single-view imaging arrangement only reveals a significant fraction of large specimens if these are sufficiently transparent. Unfortunately, most multicellular biological specimens are fairly opaque and thus absorb and scatter significant amounts of light when attempting to penetrate deeper than a few cell layers below the surface. For example, at most 30 % of the volume of an early *Drosophila* embryo is visible in high quality from a single view with this basic imaging strategy [14]. The lipid-rich yolk of the *Drosophila* embryo quickly degrades the profile of the light sheet as it passes through the embryo and also makes it impossible to acquire high-quality images from the far side (with respect to the detection axis) of the embryo. In order to improve physical coverage for whole-embryo imaging experiments, multiple views can be recorded sequentially, by simply turning the specimen in the microscope using a rotary stage. In this sequential multiview imaging mode, several complementary three-dimensional image stacks are acquired and subsequently computationally registered and combined [12, 13].

However, sequential multiview imaging only partially addresses the challenge of imaging a large living biological specimen. Since each sequential acquisition and rotation step takes a certain amount of time—during which development of the specimen continues—the resulting multiview image data set cannot usually be correctly registered. Cells are often highly dynamic and are thus captured in different locations and in different states in the respective overlap regions of the recorded multiview stacks. The resulting registration artifacts lead to mistakes and uncertainty in the subsequent data analysis, in particular when automated segmentation and tracking approaches are involved.

The above limitations are overcome by simultaneous multiview imaging: the SiMView light sheet microscopy platform for simultaneous multiview imaging allows simultaneous acquisition of four complementary views of the specimen for optimal physical coverage and furthermore provides exceptionally high imaging speeds [14]. In order to realize simultaneous multiview imaging, SiMView uses an orthogonal arrangement of four independently operated optical arms (Fig. 1a, b). One pair of these opposite arms is used for bidirectional light sheet illumination with two long-working distance air objectives, similar to the illumination arrangement used in earlier light sheet microscopes [18–20]. The other pair, arranged at a right angle to the first, is used for bidirectional fluorescence detection with high numerical aperture water-dipping objectives and fast scientific complementary metal–oxide semiconductor (sCMOS) cameras.

In SiMView experiments, the time delay of multiview image acquisition is on the order of a few tens of milliseconds when using one-photon excitation (owing to the sequential application of bidirectional illumination) and zero when using multiphoton excitation (owing to the simultaneous application of bidirectional illumination). The truly simultaneous operation of all four optical subsystems of the SiMView microscope is possible when using two-photon excitation, since fluorescence excitation is spatially confined to the focal volume. However, in both scenarios (one-photon and multiphoton SiMView imaging), the time delay of multiview image acquisition is by several orders of magnitude shorter than the time required for cells to move or change their shape on a spatial scale comparable to the spatial resolution of the microscope. SiMView is thus particularly well suited for quantitative live imaging of large developing specimens such as entire *Drosophila* embryos [14].

3.2 Methods for Fly Embryo Imaging   Light sheet-based microscopes often rely on long-working distance water-dipping objectives for fluorescence detection and therefore require sample immersion in an aqueous environment. Moreover, if specimens are subjected to multiview imaging, they must be optically accessible for light sheet illumination and fluorescence

detection from multiple angles. These two requirements often introduce challenges in the sample preparation. We developed protocols for live imaging of the entire fruit fly embryos embedded in agarose gels that fulfill these requirements and allow time-lapse data acquisition in a physiologically relevant context over long periods of time.

3.2.1 Embryo Collection and Embedding

To collect several embryos that are at the same developmental stage, it is necessary to begin with a large population of breeding adults (50–100 females). Placing flies of the correct genotype into a mating cage for 1 h should produce a number of synchronized embryos that are suitable for imaging. The adult flies are briefly anesthetized with CO_2 and placed into the mating cage. The open end of the mating cage is covered with a 60 mm tissue culture plate filled with grape juice agar. The grape juice plate should have a small streak of yeast paste in the center to induce the adult females to lay eggs. The flies are left undisturbed for an hour while embryos are being deposited. After an hour the adult flies are removed, leaving the embryos attached to the grape juice agar.

In order to improve the transparency of the embryos for imaging, the outermost embryonic membrane, the chorion, must be removed. The embryos are dechorionated by briefly exposing them to a 50 % solution of bleach in tap water, which causes the chorion to rupture and releases the embryo into the dilute bleach solution. The bleach solution is added directly to the grape juice agar plate and left for 30 s. The solution containing the dechorionated embryos is then poured into an egg collection basket where the embryos are retained by the fine mesh. The embryos are rinsed with copious amounts of water to remove the bleach. The embryos can be transferred to a clean tissue culture dish by inverting the egg collection basket and rinsing them with a small amount of water.

The SiMView light sheet microscope illuminates the embryo from two opposite directions and acquires images orthogonally with two synchronized detection systems (Fig. 1a, b). This requires that the embryo be optically accessible from all sides, which is accomplished by embedding the embryo in a transparent matrix of low-concentration agarose. For *Drosophila* embryos, a 1 % concentration of low-melting-point agarose provides enough mechanical stability to hold the embryo in place while remaining virtually transparent when submerged in the water-filled recording chamber of the microscope.

Embryos are embedded by filling a 20 mm long glass capillary (1.5/2.0 mm inner/outer diameter) with liquid 1 % agarose at 37 °C. The embryos must be gently lifted from the water-filled tissue culture dish on one tine of sharp dissecting forceps and placed into the agarose through one open end of the glass capillary. The agarose will polymerize quickly as it cools to 32 °C, but while the agarose is still liquid the embryo can be gently moved to orient

it appropriately for imaging. The embryos used for the imaging of gastrulation were oriented with the anterior-posterior axis of the animal parallel to the long axis of the capillary. An effort was also made to keep the embryo in the center of the agarose cylinder so that the optical path length through the agarose was approximately equal for the two illumination objectives and the two detection objectives. As the agarose begins to polymerize, the embryo should be left undisturbed so that it is not damaged by mechanical stresses caused by movement through the solidifying matrix.

Before imaging, the polymerized agarose cylinder is extruded out of the end of the capillary until the entire embryo is outside of the glass capillary. The glass causes substantial reflection and refraction of the light passing through it, so the imaging must be performed through agarose only. The agarose cylinder is pushed out of the glass capillary by filling the end opposite the embryo with a small plug of paraffin film or with a plug of plasticine. As the agarose cylinder is extruded, any excess agarose above the embryo can be removed by cutting it off with a scalpel. Then the cylinder is extruded more, just enough to expose the embryo (Fig. 1c). The result is the shortest possible cylinder of agarose exposed outside the glass that provides a clear optical path to the embryo. This maintains the most mechanical stability that can be provided by the low-concentration agarose. The glass capillary with the extruded agarose cylinder is carefully transferred to the water-filled recording chamber of the light sheet microscope and placed vertically into the capillary holder that is attached to the mechanical stages.

3.2.2 *Image Acquisition*   The details of the design of the SiMView light sheet microscope have been described elsewhere [14]. In brief, the specimen is held in a water-filled chamber surrounded by four microscope objective lenses (Fig. 1a, b). Two illumination lenses focus scanned laser light sheets onto the specimen from opposite sides. At right angles to these lenses are two long-working distance, water-dipping detection objectives that focus the emitted fluorescence onto the chips of two sCMOS cameras. All of the objectives are carried on piezoelectric stages so that their planes of focus can be adjusted with submicron accuracy. The focal planes of the detection arms are adjusted so that they are coplanar with the scanned light sheets and provide two complementary views of the illuminated plane of the specimen. The specimen, carried on mechanical four-axis stages, is stepped through the light sheets. The fluorescent light emitted by the specimen at each plane is detected simultaneously by the cameras and the images are acquired by custom software. After images for each plane are acquired, the stack can be assembled into a three-dimensional representation of the entire specimen.

The SiMView microscope offers several advantages for live imaging of animal development (*see* Subheading 3.1) and has

been applied to live imaging of *Drosophila* embryogenesis at 30-s intervals for 24 h [14]. SiMView microscopy enables the acquisition of time-lapse images with subcellular spatial resolution over a duration that is long enough to encompass the entirety of important developmental events and with the temporal resolution to follow the movements of individual cells.

During the early stages of *Drosophila* embryonic development, the cell cycle is very short and interesting morphogenetic events occur rapidly. For these types of specimens, the SiMView microscope is configured to acquire three-dimensional image stacks at 30-s intervals. The specimen volume is recorded with a lateral resolution of approximately 0.5 μm and an axial resolution of approximately 2.0 μm. At each time point of the time-lapse experiment, SiMView acquires four complementary views of the entire specimen. In many cases, the embryo expresses two different fluorescent proteins (e.g., a nuclear red fluorescent protein and a membrane-bound green fluorescent protein) and the image acquisition must be repeated twice in order to image the two colors separately. This increases the time interval between successive images to 1 min. Alternatively, two types of fluorescent proteins can also be imaged simultaneously by separating the fluorescence emission bands with an appropriate dichroic mirror and recording both spectral bands simultaneously with a pair of cameras in each detection arm [13]. Finally, the specimen can also be rotated so that different surfaces of the embryo (e.g., dorsoventral or lateral) face the cameras, and then the entire image acquisition protocol is repeated. This approach allows rotating the microscope's anisotropic point-spread function relative to the specimen, but further increases the time interval between images. In these most complex studies of early *Drosophila* embryo development, images are typically acquired at 2-min intervals. Each time point comprises two-color z stacks recorded from four orthogonal optical views for two different physical orientations (dorsoventral and lateral), encompassing the entire volume of the embryo with an axial step size of approximately 2 μm (Fig. 1d). Recordings typically terminate when the embryo hatches and the larva crawls out of the field of view. The larva can be transferred to a standard vial of fly food and raised to adulthood.

3.3 Image Processing

Before any analysis of morphogenetic mechanisms can be performed, either at the tissue or the cell levels, basic information such as nuclear positions, membrane boundaries, or gene expression levels need to be estimated from the stacks using image processing techniques. Figure 2a shows a standard pipeline suitable for many types of experiments.

3.3.1 Image Pre-processing

Image pre-processing refers to any image filtering or registration technique that needs to be performed in order to facilitate the extraction of information from the image. In this context, it is
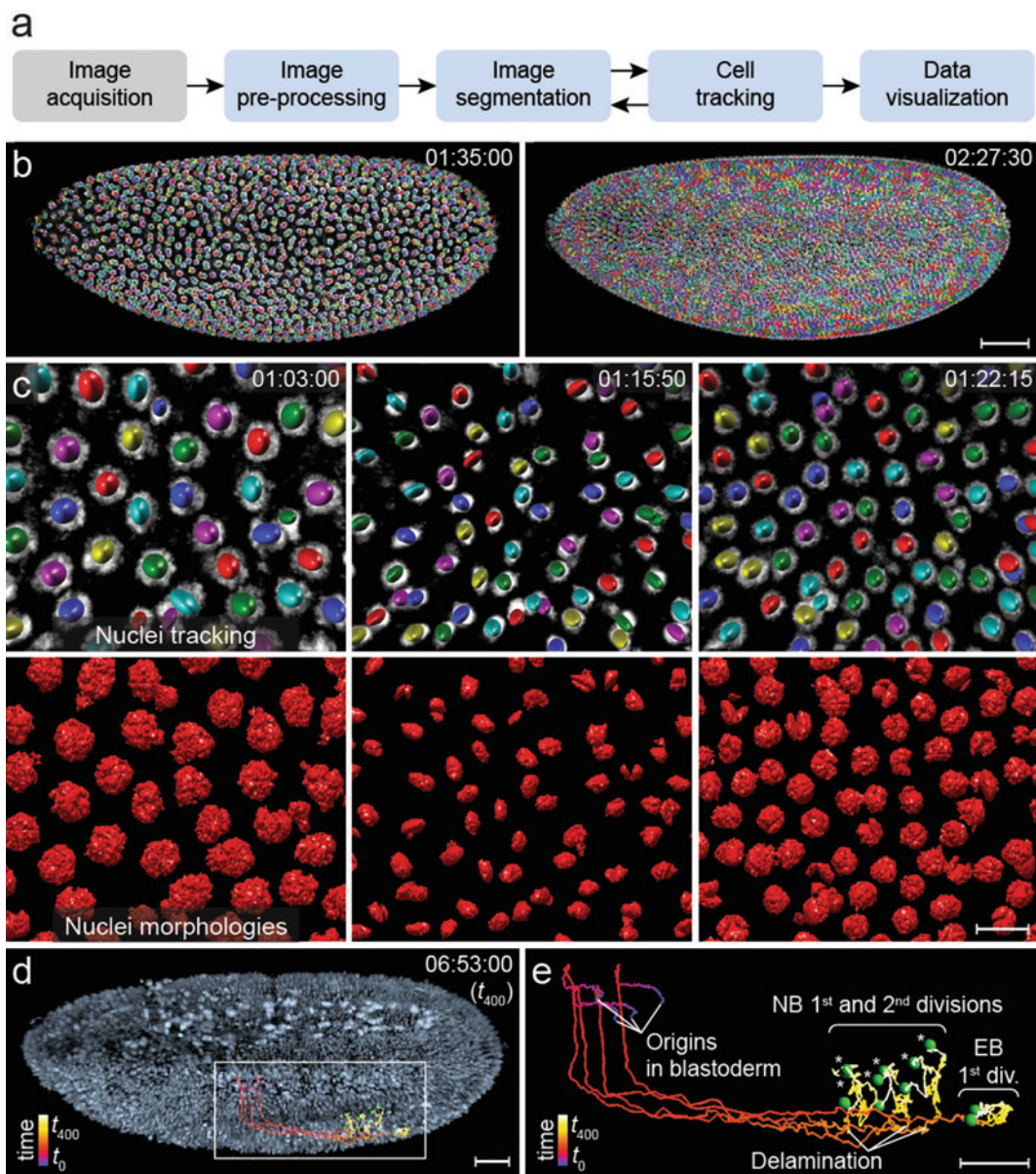
Fig. 2 Image-processing pipeline for SiMView recordings of *Drosophila* embryogenesis. (**a**) Block diagram describing the main steps of a pipeline for obtaining cell lineage information from time-lapse microscopy data. (**b**) Global nuclei tracking in the entire *Drosophila* syncytial blastoderm. Raw image data from light sheet microscopy was superimposed with automated tracking results using a sequential Gaussian mixture model approach. Images show snapshots before the 12th mitotic wave and after the 13th mitotic wave (using a random color scheme in the first time point), which is propagated to daughter nuclei using tracking information. (**c**) Enlarged view of a reconstructed embryo in panel (**a**) with nuclei-tracking information (*left*) and morphological nuclei segmentation (*right*). (**d**) One-photon SiMView recording of a histone-labeled *Drosophila* embryo superimposed with manually reconstructed lineages of three neuroblasts and one epidermoblast for 120–353 min after fertilization (time points 0–400 min); track color encodes time. (**e**) Enlarged view of tracks highlighted in (**c**). *Green spheres* show cell locations at time point 400. *Asterisks* mark six ganglion mother cells produced in two rounds of neuroblast division. *NB* neuroblast, *EB* epidermoblast. Scale bars: 50 μm (**a**), 10 μm (**b**), 30 μm (**c**, **d**). Panels (**b**)–(**e**) reprinted from Tomer et al. [14] with permission from Macmillan Publishers Ltd.

important to take measures to prevent data loss. The choice of specific filters and of the sequence in which they are applied depends on the given task. In the case of multiview image acquisition, the first step is usually to register and fuse all views. Well-tested and freely available tools exist to perform this task automatically and routinely for large-scale LSFM data sets [14, 21, 22]. For visualization purposes, a background subtraction filter is often applied in order to reduce autofluorescence levels and enhance contrast. In cases where dimmer nuclei are located close to more intensely fluorescent ones, median or anisotropic diffusion [23] filtering may be needed to reduce Poisson noise while preserving edges. Finally, it is also common to apply deconvolution algorithms to improve image quality. For this purpose, the Lucy-Richardson algorithm has been shown to be suitable for LSFM data [24]. Care must be taken to prevent the introduction of image artifacts that result from imprecise estimations of the local point-spread function (which can vary substantially across the volume of a large specimen).

Following pre-processing, two key image-processing tasks are frequently performed on time-lapse images of morphogenesis: segmentation and tracking. The former refers to grouping pixels in the same image that correspond to the same object. The latter refers to grouping pixels between images (in time) that correspond to the same objects. These two tasks are classical image processing procedures found in a broad spectrum of problems. They are accordingly strongly represented in the literature. The reader is referred to Khairy and Keller [1] for a survey on recent applications to developmental processes. For imaging fruit fly development, it often suffices to focus on methods for nuclei and membrane markers (Figs. 2a–c). As segmentation and tracking methods group pixels belonging to the same object (one in time and the other in space), these two processes can in principle be interleaved. In other words, a good segmentation makes tracking easier and vice versa.

| 3.3.2 Nuclei Segmentation | The segmentation of fluorescently labeled nuclei is a blob detection problem, because nuclei morphology is well approximated by an ellipsoid, despite variations in different cell cycle stages. There are four elements that determine the quality of the segmentation and the choice of methodology: the amount of background or autofluorescence present in the sample, the signal-to-noise ratio (SNR), the nuclear size distribution, and nuclear density (number of nuclei per unit image volume). |

In that regard, and specifically for *Drosophila*, the yolk core is highly autofluorescent (more so when using GFP, which is excited at around 488 nm), especially in the early stages of development. Therefore, the use of red fluorescent markers is recommended whenever possible. Also image segmentation algorithms need to be tuned to adapt to the different levels of segmentation difficulty

even within one LSFM time-lapse recording. Early in development, nuclei are well separated, but the background (yolk autofluorescence) is high, whereas towards the later stages, the nuclei are more closely packed, with less background signal.

We briefly describe two methods for nuclear segmentation that have been successful for LSFM data and that are freely available. Santella et al. [25] use a difference of Gaussians (Mexican hat) filtering to enhance blobs of pre-specified size. The algorithm assumes that every local maximum from the filter response is the center of a nucleus and uses a machine-learning classifier to remove false detections based on shape features. This approach is very fast and has been tested across different species. In particular, the authors report accuracy rates between 96 and 98 % for different developmental stages of *Drosophila*. However, its performance decreases when nucleus sizes vary significantly and the machine-learning classifier might need retraining to adjust for different image qualities. Moreover, the algorithm returns nuclei centers and radii, instead of a pixel-level segmentation mask. Li et al. [26] presented a method based on diffusion gradient vector flow [27], followed by gradient flow tracking specifically designed to handle scenarios where the nuclei are touching each other. The method returns detailed pixel-level segmentation, but tends to be considerably slower for large 3D datasets. This method has been successfully applied to segmenting fluorescently labeled nuclei in *Drosophila* embryo (Fig. 2c, bottom row).

3.3.3 Membrane Segmentation

The goal of membrane segmentation is to find the boundaries of cells. In images of entire multicellular specimen, cells are touching each other and form a dense network. In general, membrane segmentation is harder than nuclei segmentation due to unevenness in the marker levels across the length of the membrane and the fact that neighboring cells are in direct contact with each other.

There are two common approaches: watershed [28] and active contours (snakes) [29]. The first method is a classical segmentation algorithm that groups "basins" of intensity regions separated by high-intensity contours. Unfortunately, membrane staining tends to be uneven and allows watershed "leaking," which results in merging adjacent cells. Moreover, the watershed method tends to be sensitive to noise. It is thus important to design a good pre-processing strategy to avoid over-segmentation.

The active contour strategy fits a contour by minimizing an energy function with two opposing components: an external and an internal force. The external force comes from the image in the form of edges or intensity gradients. The internal forces regularize the solution in places where the signal is not strong enough or too noisy, thereby preventing the "leakage" effect seen in the watershed algorithm. The regularization is implemented in the form of curvature smoothness, shape constraints, or physical properties of the

tissue. However, it is not straightforward to implement this concept efficiently in 3D images with thousands of connecting active contours.

It is also possible to combine information from both nuclei and membrane channels in order to improve results [30]. For example, a very useful constraint is the fact that only one nucleus can be located per cell. Thus, the nuclei detected can be used to initialize the membrane segmentation using a Voronoi tessellation. Leakage can also be detected if a segmented cell membrane encompasses two nuclei. An important point to consider when using this strategy is that all chromatic aberrations have to be corrected to guarantee proper spatial correspondence between channels.

3.3.4 Tracking

The selection of tracking algorithm depends on the four factors previously discussed in the segmentation scenario (SNR, background intensity, cell density, and size distribution) as well as the temporal resolution of the recording and the spatiotemporal scales of the observed biological process. As a rule of thumb, one should acquire at a rate which guarantees that the structure to be tracked (usually a cell nucleus or a whole cell) has not moved more than half its diameter between consecutive images. Otherwise, accurate tracking and cell division detection can become impossible even for human annotators. For example, during *Drosophila* ventral furrow formation this condition requires acquisition rates faster than 20 s per image stack. Current tracking accuracy rates vary significantly depending on species, imaging technology, and development stage.

Tracking methods can be divided into three categories: contour evolution, state-space models, and data association. Contour evolution is in principle a sequential segmentation in time. The solution at time t is used to initialize a segmentation method, such as snakes, at time $t + 1$. If the temporal sampling is high enough, both time points are similar and the initialization is good enough to allow the segmentation to converge to a good solution. This represents a direct way of combining segmentation and tracking in a single step. Tomer et al. [14] used this approach to track over 3,000 cells in the *Drosophila* blastoderm with 94 % accuracy (Fig. 2b). In this case, the nuclear contours were modeled by ellipsoids forming a Gaussian mixture model on the image intensity that can be propagated in time.

The most common example of state-space models is particle filtering [31]. The user defines a set of parameters that need to be tracked for each nucleus (center, intensity, size, etc.). Given the solution at time t, the tracking algorithm tries to predict the position at time $t + 1$ using a motion model. This prediction is then corrected with the information contained in the image at $t + 1$. A key difference of these methods is that for each parameter a probabilistic distribution is maintained, which returns an estimation of

the uncertainty during the tracking. However, this feature comes at the expense of higher computational complexity, which tends to preclude the use of such approaches in images containing more than a few hundred cells.

Finally, data association methods try to match segmented objects from two time points. Each possible match is given a score based on some similarity measure (size, displacement, etc.). Then the optimal assignment is calculated by generating all matches with maximum score that do not merge tracks. In these cases, the similarity measure is critical to obtain a good solution, as well as a good segmentation method. Kausler et al. [32] presented a data association method specifically tailored to deal with developmental stages presenting many false detections due to background. They showed results in over 256 cells in early *Drosophila* stages with 96 % accuracy rate.

If perfect tracking and segmentation are required, different visualization and editing tools exist to verify results and correct them when necessary. McMahon et al. [33] used Imaris, a commercially available solution, to perform a dynamic analysis of collective cell migrations during gastrulation in *Drosophila*. Tomer et al. [14] also used Imaris to track neuroblast lineages in *Drosophila* (Fig. 2d, e). In addition, Megason [34] and Giurumescu et al. [35] presented freely available tools for cell lineage editing.

3.4 Computational Modeling of the Mechanics of Embryogenesis in the Fruit Fly

To fully understand morphogenesis a thorough investigation of the forces and mechanical responses in the context of the biological tissue must be conducted. Efforts towards this goal meet the challenges of (a) obtaining high spatial and temporal resolution images of fly embryos and relevant gene expression patterns with sufficient spatial coverage and over an adequate time span, (b) obtaining reliable morphological descriptors of the embryo tissue and all cells together with their spatial dynamics through image processing, (c) inferring/uncovering the mechanical effect of action of gene products as well as the mechanical induction of gene expression [36], (d) measuring passive mechanical properties of the tissues, and finally (e) computational modeling to challenge hypotheses. In this section we focus on point (e): the efforts undertaken to model developmental mechanics on a computer, in the context of the fly embryo.

In general, simulations of biomechanical processes require (a) a mathematical morphological description that provides an accurate measure of deformation from a reference shape, (b) a mechanism of applying loads locally to the tissue in accord with the hypothesis under testing, (c) a material constitutive model that represents the mechanical response of the tissue to loads (and together with the extent of deformation provides a shape energy), (d) a method to detect and handle boundaries, and (e) a numerical optimization process to vary the morphological parameters until a minimum energy (predicted) shape is attained.

There is a growing body of literature concerned with modeling the mechanics of morphogenesis. For an excellent recent review the reader is referred to Wyczalkowski and Taber [37]. However, only a small number of works have attempted the simulation of fly embryo mechanics. This is attributed to the difficulty of obtaining high-quality three-dimensional images of developing fly embryos using conventional techniques, and the complete lack of material parameters for epithelial tissues in this system. Those works that considered the mechanics of fly development focused mainly on the process of formation of the ventral furrow invagination, i.e., the sequence of events that leads to the internalization of the future mesoderm cells (the mesoderm primordium). These cells undergo a number of shape changes [38] (Fig. 3a); they constrict apically, and elongate to form an initial furrow. This is followed by cell shortening (at constant cell volume [39]) leading to wedging of the cells at the basal end, i.e., towards the yolk, and the formation of a tubelike structure. The process is known to be driven by the contractility of an actin-myosin meshwork, due to the action of the transcription factors *snail* and *twist* in a ratchet-like mechanism [40].

In a two-dimensional study, Munoz et al. [41, 42] assumed the tissue to be neo-Hookean (i.e., a model that approximates the response of a rubberlike material), consisting of a passive region (located dorsally and laterally), in addition to an active region (ventrally) in which contractile forces are generated. Their finite element numerical treatment is based on an idea of decomposing the deformation gradient tensor (the numerical entity that measures the extent of deformation for all considered deformation modes at a specific material point) into an active and a passive component, and the problem was formulated in terms of strain energy, which was then minimized to obtain predicted shapes. Their continuum model confirmed the notion that several mechanisms act together to provide the necessary robustness to the furrow formation process, and that there exists a set of allowed ratios of apical constriction vs. apicobasal elongation that favor the formation of the furrow as observed in experiments. The extension of this work to three spatial dimensions [43] predicts additional robustness, and the presence of an accordion-like global compression and expansion wave that moves through the embryo due to yolk flow. Both studies underline the importance of the vitteline membrane as a constraint, as well as the yolk volume. In addition the model makes the assumption that cells in the dorsal and lateral regions of the embryo epithelium shorten along their apicobasal axis. This is equivalent to the ectoderm "pushing," thereby facilitating the formation of the invagination. The major numerical difficulty that was overcome in these simulations is the "chatter" that occurs during optimization calculations involving discretized constraint surfaces. This was solved by approximating the vitteline membrane
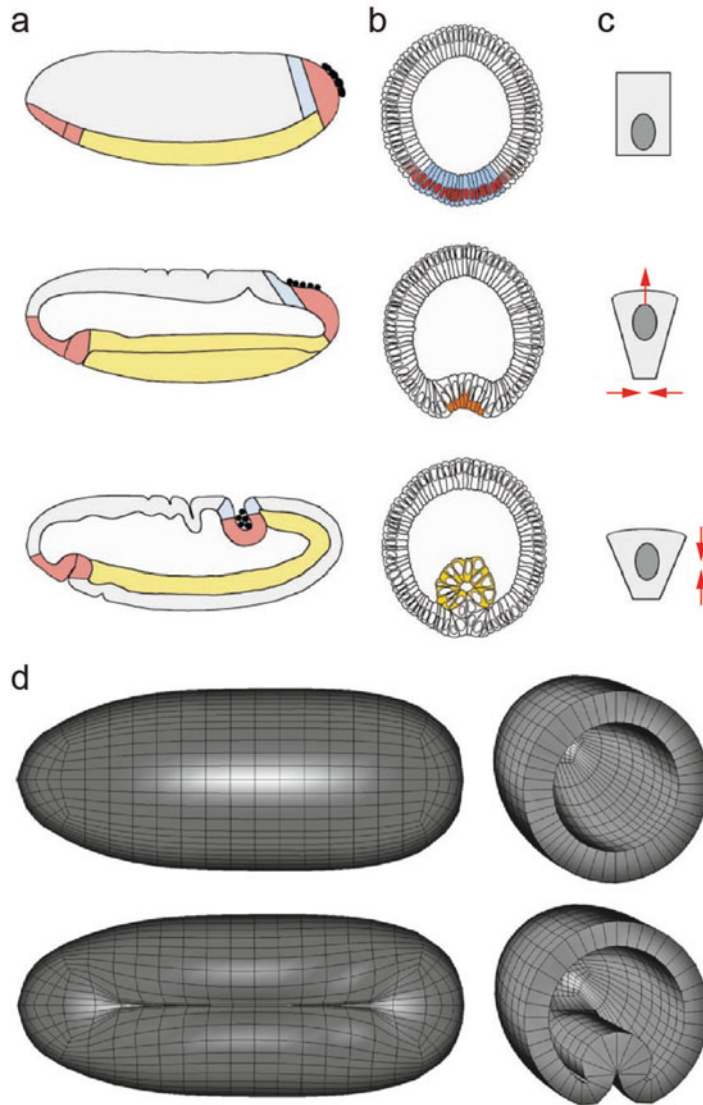
Fig. 3 Cell shape changes during ventral furrow formation and mechanical simulation. (**a**) Drawings of whole embryos indicating the regions of the mesodermal (yellow), endodermal (red), and ectodermal (grey, blue) primordia. At the cellular blastoderm stage (~3 h of development at 25 °C) the primordia lie at the surface of the embryo (*top*). Fifteen minutes later, the prospective mesoderm has formed a furrow on the ventral side of the embryo (*second embryo*). A few minutes later, the posterior part of the endoderm has invaginated and the germ band has begun to extend onto the dorsal side of the embryo (*third embryo*). (**b**) Diagrams of cross sections of embryos at the same stages as those shown in (**a**). Colors mark regions or cells in which events relevant for gastrulation occur. (**c**) Sketch of changes in a mesodermal cell in the embryos shown on the left. (**d**) Finite element simulation of ventral furrow invagination. *Top row*: starting shape. *Bottom row*: computational model result. Panels (**a**)–(**c**) reproduced from Leptin [38] with permission from Nature Publishing Group. Panel (**d**) reproduced from Conte et al. [43] with permission from Elsevier

using cubic B-splines, and incorporating this sliding contact tightly in the optimization iterations [44].

In another study, also using finite elements, the embryo was parameterized by a system of curvilinear coordinates, adopted from potential theory [45], that facilitated its treatment as a thick shell [46]. The authors simulated both the formation of the cephalic furrow and the simultaneous formation of cephalic and ventral furrows.

Ultimately, it is desirable to connect the data collected from microscopy to the mechanics of the underlying tissue. Towards this goal, we mention a strategy that infers forces involved in the ventral furrow formation from fluorescence microscopy images. Brodland et al. [47] used a mechanical model into which strains are input by using segmented images of a section through the embryo to estimate relative forces needed for the induction of such strain using mathematical inverse methods. Forces are assumed to be decomposed into active and passive components. Within a finite element framework, they relied on a general cell-based model [48], in which cell-cell interactions are represented by rod elements (loci for active forces), and the viscosity of the cytoplasm by orthogonal dashpots (passive force components). This approach solves a stiffening artifact that arises when space-filling viscous elements are used to model the cytoplasm. Although their work was conducted on two-dimensional images, it is pioneering in the sense that it analyzes the image data directly in the context of the mechanics of the underlying tissue.

Many of the challenges in embryo mechanics simulations are numerical in nature. The studies above were made possible by meeting (one or more of) these challenges, treating boundary conditions smoothly, choosing the best energy optimization strategy, mathematically representing the embryo morphology adequately, and/or avoiding problem formulations that lead to numerical artifacts and prevent convergence. Overcoming these computational and numerical challenges will open the door to more efficient simulations. However, it must be kept in mind that improvements in the predictive power of embryogenesis mechanics computer simulations in the future will also critically depend on the ability to record higher quality three- and four-dimensional live image data of all relevant structures, accurate estimation of morphology through improved image segmentation and tracking, more realistic biological material models, and accurate experimental material parameter measurements, which are currently lacking for the fly embryo.

Acknowledgments

References

1. Khairy K, Keller PJ (2011) Reconstructing embryonic development. Genesis 49(7): 488–513

2. Pawley JB (2006) Handbook of biological confocal microscopy. Springer, New York, NY

3. Diaspro A, Chirico G, Collini M (2005) Two-photon fluorescence excitation and related techniques in biological microscopy. Q Rev Biophys 38(2):97–166

4. Helmchen F, Denk W (2005) Deep tissue two-photon microscopy. Nat Methods 2 (12):932–940

5. Graf R, Rietdorf J, Zimmermann T (2005) Live cell spinning disk microscopy. Adv Biochem Eng Biotechnol 95:57–75

6. Keller PJ, Dodt HU (2011) Light sheet microscopy of living or cleared specimens. Curr Opin Neurobiol 22(1):138–143

7. Tomer R, Khairy K, Keller PJ (2011) Shedding light on the system: studying embryonic development with light sheet microscopy. Curr Opin Genet Dev 21(5):558–565

8. Weber M, Huisken J (2011) Light sheet microscopy for real-time developmental biology. Curr Opin Genet Dev 21(5):566–572

9. Mertz J (2011) Optical sectioning microscopy with planar or structured illumination. Nat Methods 8(10):811–819

10. Siedentopf H, Zsigmondy R (1903) Über Sichtbarmachung und Größenbestimmung ultramikroskopischer Teilchen, mit besonderer Anwendung auf Goldrubingläser. Ann Phys 315(1):1–39

11. Voie AH, Burns DH, Spelman FA (1993) Orthogonal-plane fluorescence optical sectioning: three-dimensional imaging of macroscopic biological specimens. J Microsc 170(3): 229–236

12. Huisken J et al (2004) Optical sectioning deep inside live embryos by selective plane illumination microscopy. Science 305 (5686):1007–1009

13. Keller PJ et al (2008) Reconstruction of zebrafish early embryonic development by scanned light sheet microscopy. Science 322(5904): 1065–1069

14. Tomer R et al (2012) Quantitative high-speed imaging of entire developing embryos with simultaneous multiview light-sheet microscopy. Nat Methods 9(7):755–763

15. Arnaout R et al (2007) Zebrafish model for human long QT syndrome. Proc Natl Acad Sci U S A 104(27):11316–11321

16. Scherz PJ et al (2008) High-speed imaging of developing heart valves reveals interplay of morphogenesis and function. Development 135(6):1179–1187

17. Swoger J et al (2007) Multi-view image fusion improves resolution in three-dimensional microscopy. Opt Express 15(13):8029–8042

18. Truong TV et al (2011) Deep and fast live imaging with two-photon scanned light-sheet microscopy. Nat Methods 8(9):757–760

19. Huisken J, Stainier DY (2007) Even fluorescence excitation by multidirectional selective plane illumination microscopy (mSPIM). Opt Lett 32(17):2608–2610

20. Dodt HU et al (2007) Ultramicroscopy: three-dimensional visualization of neuronal networks in the whole mouse brain. Nat Methods 4 (4):331–336

21. Preibisch S et al (2010) Software for bead-based registration of selective plane illumination microscopy data. Nat Methods 7 (6):418–419

22. Rubio-Guivernau JL et al (2012) Wavelet-based image fusion in multi-view three-dimensional microscopy. Bioinformatics 28 (2):238–245

23. Perona P, Malik J (1990) Scale-space and edge detection using anisotropic diffusion. IEEE Trans Pattern Anal Mach Intell 12(7):629–639

24. Lucy LB (1974) An iterative technique for the rectification of observed distributions. Astron J 79(6):745–754

25. Santella A et al (2010) A hybrid blob-slice model for accurate and efficient detection of fluorescence labeled nuclei in 3D. BMC Bioinformatics 11:580

26. Li G et al (2007) 3D cell nuclei segmentation based on gradient flow tracking. BMC Cell Biol 8:40

27. Xu C, Prince J (1998) Snakes, shapes, and gradient vector flow. IEEE Trans Image Proc 7(3):359–369

28. Lin G et al (2003) A hybrid 3D watershed algorithm incorporating gradient cues and object models for automatic segmentation of nuclei in confocal image stacks. Cytometry A 56(1):23–36

29. Dufour A et al (2005) Segmenting and tracking fluorescent cells in dynamic 3-D microscopy with coupled active surfaces. IEEE Trans Image Process 14(9):1396–1410

30. Pop S et al (2013) Extracting 3D cell parameters from dense tissue environments:

application to the development of the mouse heart. Bioinformatics 29(6):772–779

31. Smal I et al (2008) Multiple object tracking in molecular bioimaging by Rao-Blackwellized marginal particle filtering. Med Image Anal 12(6):764–777

32. Kausler BX et al (2012) A discrete chain graph model for 3D + t cell tracking with high misdirection robustness. In: Fitzgibbon A et al (eds) Computer vision - ECCV 2012. Springer, Berlin, pp 144–157. doi:10.1007/978-3-642-33712-3_11

33. McMahon A et al (2008) Dynamic analyses of Drosophila gastrulation provide insights into collective cell migration. Science 322 (5907):1546–1550

34. Megason SG (2009) In toto imaging of embryogenesis with confocal time-lapse microscopy. Methods Mol Biol 546:317–332

35. Giurumescu CA et al (2012) Quantitative semi-automated analysis of morphogenesis with single-cell resolution in complex embryos. Development 139(22):4271–4279

36. Farge E (2003) Mechanical induction of Twist in the Drosophila foregut/stomodeal primordium. Curr Biol 13(16):1365–1377

37. Wyczalkowski MA et al (2012) Computational models for mechanics of morphogenesis. Birth Def Res C Emb Today 96(2):132–152

38. Leptin M (1999) Gastrulation in Drosophila: the logic and the cellular mechanisms. EMBO J 18(12):3187–3192

39. Gelbart MA et al (2012) Volume conservation principle involved in cell lengthening and nucleus movement during tissue morphogenesis. Proc Natl Acad Sci U S A 109(47): 19298–19303

40. Martin AC, Kaschube M, Wieschaus EF (2009) Pulsed contractions of an actin-myosin network drive apical constriction. Nature 457 (7228):495–499

41. Munoz JJ, Barrett K, Miodownik M (2007) A deformation gradient decomposition method for the analysis of the mechanics of morphogenesis. J Biomech 40(6):1372–1380

42. Conte V et al (2009) Robust mechanisms of ventral furrow invagination require the combination of cellular shape changes. Phys Biol 6 (1):016010

43. Conte V, Munoz JJ, Miodownik M (2008) A 3D finite element model of ventral furrow invagination in the Drosophila melanogaster embryo. J Mech Behav Biomed Mater 1 (2):188–198

44. Munoz JJ (2008) Modelling unilateral frictionless contact using the null-space method and cubic B-Spline interpolation. Comput Methods Appl Mech Eng 197:979–993

45. Kellog OD (1953) Foundations of potential theory. Springer, Berlin

46. Allena R, Aubry D (2012) An extensive numerical simulation of the cephalic furrow formation in Drosophila embryo. Comput Methods Biomech Biomed Engin 15(5): 445–455

47. Brodland GW et al (2010) Video force microscopy reveals the mechanics of ventral furrow invagination in Drosophila. Proc Natl Acad Sci U S A 107(51):22111–22116

48. Viens D, Brodland GW (2007) A three-dimensional finite element model for the mechanics of cell-cell interactions. J Biomech Eng 129(5):651–657

Chapter 7

Quantitative Image Analysis of Cell Behavior and Molecular Dynamics During Tissue Morphogenesis

Chun Yin Bosco Leung and Rodrigo Fernandez-Gonzalez

Abstract

The cell behaviors that drive tissue morphogenesis, such as division, migration, or death, are regulated at the molecular scale. Understanding how molecular events determine cell behavior requires simultaneous tracking and measurement of molecular and cellular dynamics. To this end, we have developed SIESTA, an integrated tool for Scientific ImagE SegmenTation and Analysis that enables quantification of cell behavior and molecular events from image data. Here we use SIESTA to show how to automatically delineate cells in images (segmentation) using the watershed algorithm, a region-growing method for boundary detection. For images in which automated segmentation is not possible due to low or inappropriate contrast, we use a minimal path search algorithm to semiautomatically delineate the cells. We use the segmentation results to quantify cellular morphology and molecular dynamics in different subcellular compartments, and demonstrate the whole process by analyzing cell behavior and the dynamics of the motor protein non-muscle myosin II during axis elongation in a *Drosophila* embryo. Finally, we show how image analysis can be used to quantify molecular asymmetries that orient cell behavior, and demonstrate this point by measuring planar cell polarity in *Drosophila embryos*. We describe all methods in detail to allow their implementation and application using other software packages. The use of (semi) automated quantitative imaging enables the analysis of a large number of samples, thus providing the statistical power necessary to detect subtle molecular differences that may result in differences in cell behavior.

Key words Image analysis, Segmentation, Watershed, Minimal path search, Cell morphology, Molecular dynamics, Planar cell polarity, Cytoskeleton

1 Introduction

An outstanding question in tissue morphogenesis is how signals at the molecular scale orchestrate cell behaviors. Modern live imaging technologies allow simultaneous visualization of events at the molecular and the cellular scales. For instance, multi-view selective plane illumination microscopy [1, 2] allows the acquisition of

three-dimensional images with subcellular resolution every few seconds and during long periods of time, providing a link between the molecular, the cellular, and the tissue scales in the context of animal development. Therefore, live imaging is an ideal tool to investigate the molecular signals that determine cellular behavior. However, simultaneous tracking of cellular and molecular dynamics generates large data sets whose manual analysis is cumbersome and time consuming. Therefore, there is a need for methods that automate the quantitative examination of large collections of images, thus increasing the number of samples measured and the statistical power of the results.

Quantitative analysis of cellular and molecular dynamics from image data typically begins with the delineation of cells, also known as cell segmentation. Several packages exist for automated cell segmentation [3–7]. These tools fail at accurately delineating cells in images with low contrast or with signals that they were not designed for, such as electron microscopy images in software designed for fluorescence microscopy. In these cases, manual correction of the results is indispensable, and this has an impact on the ability to process images rapidly. Furthermore, many existing tools are limited to the analysis of cell behavior, and do not integrate the analysis of molecular dynamics, which must be done using additional software.

Automated cell segmentation is often based on region-growing method, in particular the watershed algorithm [8]. The watershed algorithm requires the identification of an initial seed point per cell. Seed points are grown simulating a flooding process that begins at the seeds and reaches pixels in an order that depends on the pixel value or on how that value changes locally (measured by the image gradient). Pixels are linked to the seed that caused their flooding, partitioning the image. The flooding process ends when water from a seed would reach pixels assigned to an adjacent seed. The seed detection step is therefore essential to obtain accurate segmentation results. Errors in seed detection can result in over-segmentation if there is more than one seed per cell, or under-segmentation if there is less than one seed per cell. The watershed algorithm works well to delineate cells in images in which cytoplasmic and cortical pixels have clearly different intensity values, and when the signal used to delineate the cells is continuous along the cell outline. Cells outlined by discontinuous signals can be segmented using active contours [9, 10], in which a curve is allowed to expand towards the cell boundary under conditions that limit its shape and deformability, thus preventing situations in which regions grown with the watershed algorithm would squeeze through a discontinuity on the cell cortex and invade an adjacent cells. However, active contour methods are slow, as they are based on the solution of the partial differential equations that dictate the motion of a curve evolving under external forces. Furthermore, active contours will stop in areas of strong cytoplasmic signal, which are mistaken for cell boundaries.

Semiautomated methods can be used to segment cells in images in which the contrast is not appropriate for fully automated segmentation. One of these methods is the LiveWire algorithm [11]. In the LiveWire algorithm, a "cost" is assigned to each pixel, with a lower cost associated with the pixels that are most likely to belong to the cell outline. This can be accomplished by setting the cost to be the inverse of the pixel value or of the local image gradient. The user moves the mouse around the perimeter of the cell and the algorithm calculates, in real time, the minimal cost path that follows the trajectory of the mouse using Dijkstra's optimal path search algorithm [12]. This results in accurate cell delineation with minimal user interaction.

To enable the quantitative, integrated analysis of cellular and molecular dynamics using image data, we have developed a platform for Scientific ImagE SegmenTation and Analysis (SIESTA) [5]. SIESTA integrates automated morphological and molecular analyses of cells. Furthermore, SIESTA incorporates tools that minimize the user interaction required to correct automated segmentation results, thus minimizing the time necessary to analyze multidimensional images. These tools include seed editing, which allows the user to correct seeds before watershed segmentation, rather than correcting entire cell outlines after the segmentation; seed copying across images to further minimize the number of seed corrections necessary; and semiautomated delineation of cell outlines based on the LiveWire algorithm. Once cells are segmented, SIESTA allows cell tracking and measurement of cell morphology and molecular dynamics. These measurements include quantification of asymmetries in protein distribution in the plane of the tissue, also known as planar cell polarity [13].

2 Materials

2.1 Software List

1. The Matlab (Mathworks Inc.) Compiler Runtime (MCR) version 8.2 (2013b) for Mac OSX can be downloaded from http://www.mathworks.com/supportfiles/downloads/R2013b/deployment_files/R2013b/installers/maci64/MCR_R2013b_maci64_installer.zip (*see* **Note 1**).

2. SIESTA (University of Toronto) for Mac OSX can be downloaded from http://individual.utoronto.ca/quantmorph/software.html.

2.2 Installation

1. Install the Matlab Compiler Runtime.

2. Uncompress the SIESTA zip file into your hard drive. This will create a new folder (siesta3) containing all the files necessary to run SIESTA.

3. Edit the file run_siesta3.sh in the siesta3 folder (*see* **Note 2**).

4. In line 13, MCRROOT="/Applications/MATLAB/MATLAB_Compiler_Runtime/v82/" substitute the path where you installed the Matlab Compiler Runtime.

5. Open a terminal window.

6. Change into the folder where you installed SIESTA (the folder that contains run_siesta3.sh). To do this, use this command

   cd full_path_where_you_installed_siesta

7. Run siesta by typing

   ./run_siesta3.sh

   Do not forget the dot and the slash, they are important!! If this did not work, make sure the run_siesta3.sh script can be executed by running

   sudo chmod 777 run_siesta3.sh

   (this may ask for your password to change the file permissions).

3 Methods

3.1 Cell Segmentation and Tracking

0. A video tutorial on how to use SIESTA is available (Video S1).

1. Open a time-lapse sequence using "Load grayscale image" (the keyboard shortcut is t) or "Load color image" (I) in the IO menu. You can select a multipage TIFF containing all the time points, or you can just click on one of the files belonging to a group of images named sequentially.

2. If you opened a color image, use the "Switch channels" (s) option from the IMAGE menu to switch to the channel that you want to use to segment the cells.

3. Click on "Find seeds ..." (S) in the IMAGE menu. Seeds are points that will be grown in subsequent steps using the watershed algorithm [8] to find the cell boundaries.

4. In the dialog, select the time points where you want to find seeds for the watershed algorithm (*see* **Note 3**).

5. Enter the XY resolution (pixel size in your images). The Z value should be left as 1.0.

6. During segmentation, the image is initially smoothened to reduce the noise introduced during image acquisition. This is accomplished using a Gaussian filter, which substitutes each pixel by the weighted average of the intensity value of its neighbors (Fig. 1a, b). The standard deviation of the Gaussian filter determines which neighbors are used and the degree of blurring introduced by the filter (Fig. 2), and is represented by the "Image smoothing" parameter in the "Find seeds ..." dialog in SIESTA.

7. SIESTA uses an adaptive threshold of the smoothened image to identify bright pixels (Fig. 1c). In contrast to absolute
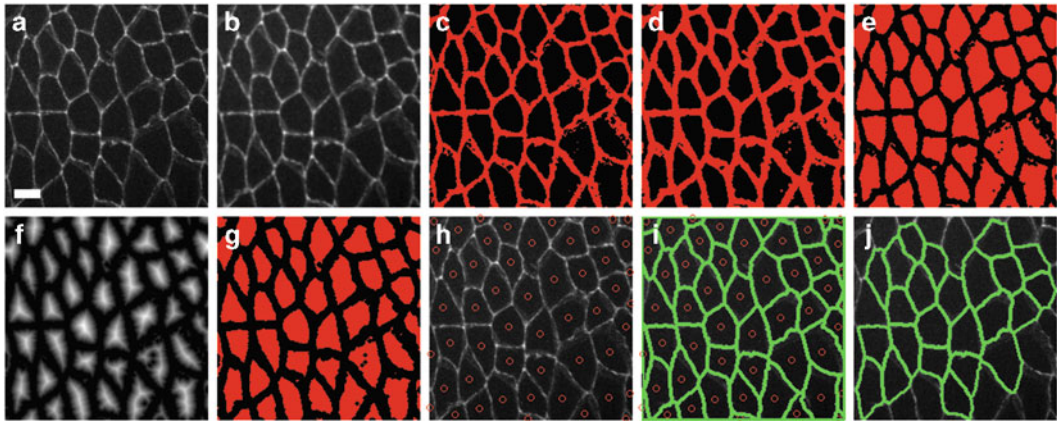
Fig. 1 Watershed-based cell segmentation. Images show the steps to segment all the cells that are completely included within an image. (**a**) Original image. Scale bar = 25 pixels. (**b**) After Gaussian filtering the image shown in (**a**) using $\sigma = 0.65$. (**c**) Adaptive threshold of the image shown in (**b**) using a 30 × 30 pixel window. The resulting image is a binary image (red = 1, black = 0). (**d**) Dilation of the image shown in (**c**). (**e**) Inversion of the image shown in (**d**). (**f**) Distance transform of the binary image shown in (**e**). (**g**) Local maxima of the distance transform shown in (**f**) using a cutoff value of 1.2. (**h**) The centroids of the objects shown in (**g**) are displayed as *red* circumferences on the original image. Tiny objects in (**g**) were filtered out using a minimum size threshold. (**i**) Result of running the watershed segmentation using the *red* circumferences shown in (**h**) as seeds. Watershed lines are indicated in green. (**j**) Watershed segmentation results after deleting polygons that touch the border of the image
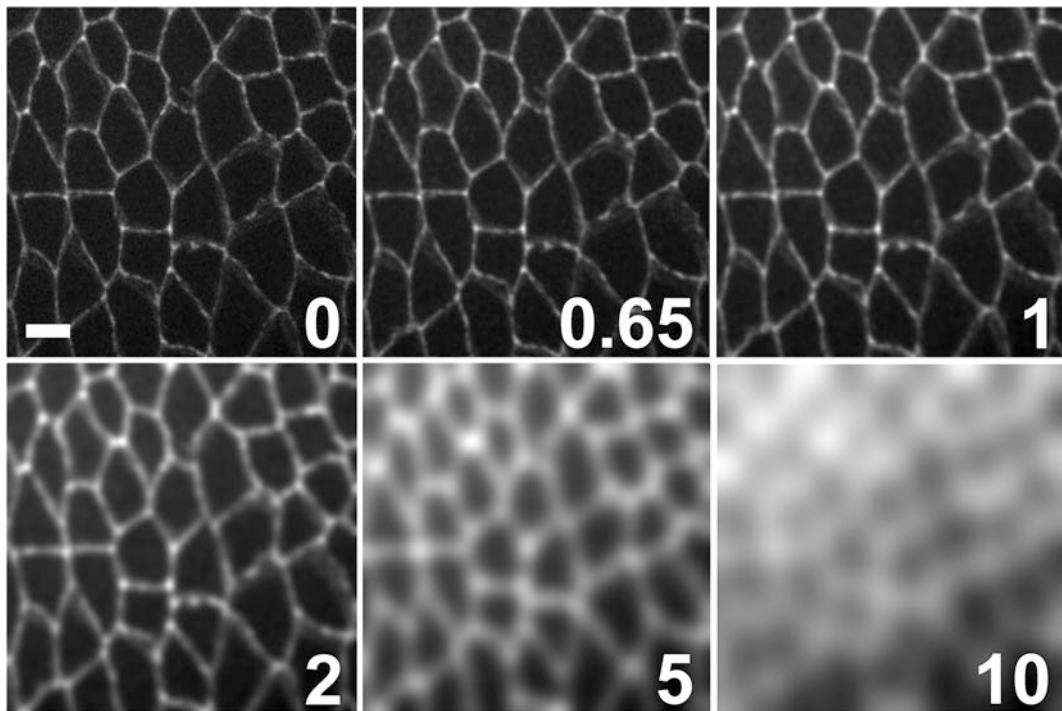
Fig. 2 Gaussian filtering for noise reduction. Numbers indicate the standard deviation (in pixels) of the Gaussian filter used for smoothing. Increasing Gaussian widths result in wider cell-cell interfaces, but also in blurrier images. Scale bar = 25 pixels
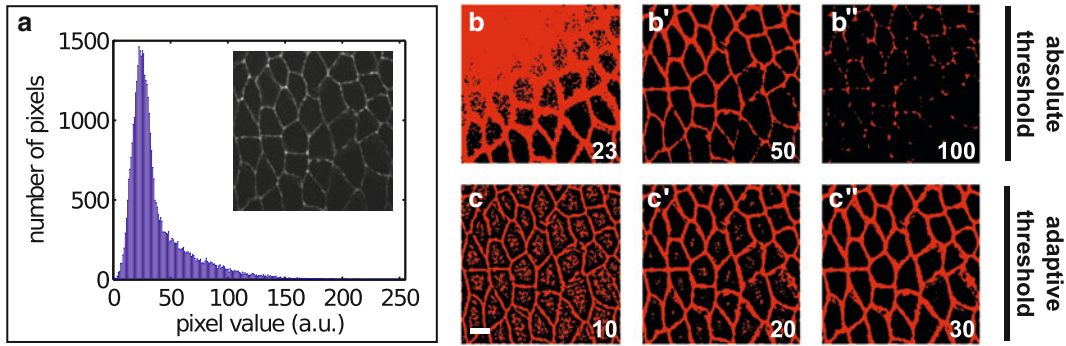
Fig. 3 Absolute vs. adaptive thresholds. (**a**) Histogram of gray values in the image shown as an inset. The mode (most frequent pixel value) is 23. (**b–b″**) Binary images resulting from the application of an absolute threshold to the image shown in (**a**). The threshold value is indicated in the lower right corner of each image. A unique threshold value cannot be used to distinguish junctional and cytoplasmic pixels in the upper left and lower right corners of the image, due to inhomogeneous sample illumination during image acquisition. (**c–c″**) Binary images obtained by applying an adaptive threshold to the image shown in (**a**). The window size used to calculate the local threshold is indicated in the lower right corner of each image. Scale bar = 25 pixels

thresholds, which set one cutoff value for the entire image based on the histogram of pixel values (Fig. 3a, b), the adaptive algorithm used by SIESTA sets an independent threshold value for each pixel in the image. For any given pixel, the threshold is determined by the average gray value of its neighboring pixels. Neighboring pixels are those included within a box of specific width and height and centered on the pixel in question (Fig. 3c). The adaptive threshold algorithm generates a binary image with only two possible pixel values, 0 and 1. A pixel is set to 1 if its gray value in the smoothened image is greater than the average value of its neighboring pixels, and to 0 if it is smaller. Pixels on bright structures, such as the cell outline, will have a value of 1 in the binary image, and dimmer pixels, such as those in the cytoplasm, will have a value of 0 (Fig. 1c). The binary image is then dilated to close small discontinuities in the bright structures (Fig. 1d).

8. The main parameter of the seed-finding algorithm [14] is the "Minimum distance seed-cortex." The thresholded image is inverted (Fig. 1e), and a distance transform is calculated to measure the shortest distance from each pixel to the regions of the image identified as bright by the adaptive threshold (Fig. 1f). The "Minimum distance seed-cortex" is used to threshold the distance transform and extract its local maxima (Fig. 1g) (*see* **Note 4**). The centers of each "connected component" (groups of pixels that maintain continuity) are used as seeds (Fig. 1h).

9. When most of the cells are assigned a single seed, use the editing tools in the ANNOTATION menu to manually correct

missing or extra seeds. SIESTA treats seeds as fiducial markers, represented as small, red circumferences. Select "Set fiducial markers" (f) from the annotation menu to go into fiducial-editing mode. Left click to add fiducials (seeds), and right click on a fiducial marker to remove it.

10. Once seeds are correct, they should be saved in an annotation file. To do this, click on "Save annotations ..." (a) in the IO menu. These annotations can later be loaded using "Load annotations ..." (L) from the same menu.

11. Seeds can be transferred to other time points using the options "Copy fiducial markers" (C) and "Paste fiducial markers" (V) in the ANNOTATION menu. You can move back and forth between time points using "Next image" (.), "Previous image" (,), and "Go to ..." (g) from the IO menu. You can move groups of fiducials by drawing a polyline (*see* **Note 5**) around them and selecting "Move fiducials in polyline" from the ANNOTATION menu. Left click on the polyline and drag it to move all the fiducials included in the polyline. Right click on the polyline to delete it (*see* **Note 6**).

12. Seeds can be expanded using the watershed algorithm (Fig. 1i) (*see* **Note 7**). To do this, select "Expand from these seeds ..." from the IMAGE menu. The default parameters should work for most images.

13. Edit the cells that were not segmented properly. To correct the segmentation of one cell, go into the polyline-drawing mode by selecting "Draw polyline" (y) from the ANNOTATION menu. Right click on the contour of the cell that you want to delete. You can zoom in using the options in the SIZES menu, or simply pressing z while the mouse is on the image. This last option will cycle through 100, 200, 300, and 400 % zooms of the image. When you are zoomed in, you can use the arrow key to move the image. Alternatively, select "Pan" from the ACTIONS menu to drag the image with the mouse.

14. Cells can be manually delineated using polylines (*see* **Note 5**). A more efficient solution is the LiveWire algorithm, which can be used to segment cells semiautomatically (Video S2). Select "LiveWire" from the ANNOTATION menu. Click with the left mouse button on the cell outline to start the LiveWire and move the mouse around the cell. The LiveWire uses Dijkstra's minimal path search algorithm to calculate the brightest path between the last point clicked and the current position of the mouse (Box 1). When you are satisfied with a segment, click on the left button to store it. Right-click to close the polyline, and middle-click to delete the previous segment stored. When you

Box 1
Pseudocode for Dijkstra's Minimal Path Search Algorithm
in a Weighted Graph

```
;; The path is initially empty.
path=empty

;; Each node in the graph is assigned an infinite distance value.
for each node, i,
    d_i=∞

;; The initial node is assigned a zero distance.
d_source=0

;; For all unprocessed nodes …
while there are unprocessed nodes

    ;; Take the unprocessed node with the smallest distance value
    ;; (in the first iteration this will be the initial node)
    i=unprocessed node with smallest d

    ;; If i is the final node, finish here.
    if i=target
        done!

    ;; For each unprocessed neighbor …
    for each unprocessed neighbor, j, of i
        ;; Update its distance to the sum of the distance at i and the distance from i to j.
        d=d_i+distance(i,j)

        ;; … only if the new distance is shorter than the current distance.
        ;; In that case, node i is part of the optimal path from the initial node to node j.
        if d < d_j
            d_j=d
            add i to path-to-j
```

are done, add a fiducial inside your cell if there is not one there already.

15. SIESTA tracks cells based on fiducials. Select "Track polylines (using fiducials) …" from the ANNOTATION menu. Watch the Matlab terminal for error messages (*see* **Notes 8** and **9**). The algorithm projects each fiducial onto the next time point in the sequence and finds the closest neighbor. Each fiducial is assigned a number or ID. Fiducial IDs will be reassigned such that corresponding fiducials have matching IDs. You can visualize fiducial IDs selecting "Toggle ids" in the ANNOTATION menu. Polylines will be assigned the ID of the fiducial they enclose.

3.2 Morphological and Molecular Analyses

1. To measure cells, select "Measure polylines" from the MEASUREMENT menu (*see* **Note 10**). Indicate the time points that you want to analyze. Select a file for storing the output. The measurements can be saved in .mat format, for Matlab, or in .csv format, which can be opened with a text

editor or in a spreadsheet. If you cancel here, the analysis will run, but only the results of the first image analyzed will be displayed on the screen.

2. NaN ("Not a Number") values in the measurement results indicate the presence of a fiducial with no assigned polyline in that time point.

3. In .csv format, the Center is given as $x1$, $y1$, $x2$, $y2$, ..., xn, yn, where 1, ..., n are the time points measured.

4. Area, perimeter, and length measurements are provided in pixel units.

5. LengthH and LengthV measure cell length along the horizontal and the vertical axes, respectively, by overlaying a grid of horizontal or vertical lines, 1 pixel apart, on the cell outline, and calculating the average length of the intersections between the lines and the cell outline.

6. LengthEllipseH and LengthEllipseV measure cell length along the horizontal and vertical axes, respectively, by fitting an ellipse to the cell outline and calculating the length of the intersection between the ellipse and a horizontal and a vertical axes going through the center of the ellipse.

7. Red/green/blue brightness (perimeter) measures the mean value of the pixels that are part of the cell outline (*see* **Note 11**).

8. Red/green/blue brightness (center) measures the mean value of the pixels that are inside the cell outline (*see* **Note 11**).

3.3 Quantification of Planar Cell Polarity

1. Open your image using "Load grayscale image" (t) or "Load color image" (I) from the IO menu (*see* **Note 12**).

2. If you opened a color image, use the "Switch channels" (s) option from the IMAGE menu to switch to the channel where you want to delineate cell outlines (or stay on the color image if you prefer to delineate cells there).

3. To quantify planar polarity, you need to draw a line or a "trajectory" on each cell interface. Select "Draw trajectory" (j) from the ANNOTATION menu (*see* **Note 13**).

4. Click once with the left mouse button to initialize the trajectory. Release the mouse button and move to the next point along the cell interface. Click on the left mouse button to set the current point as part of the trajectory. Click on the middle button to remove the last point that was set. Right-click to finish drawing the trajectory (*see* **Notes 14** and **15**).

5. To delete a trajectory, right-click on it.

6. When you are done drawing trajectories, use the "Switch channels" (s) option from the IMAGE menu to switch to the channel where you want to quantify polarity. You can also

switch to the color image to quantify the polarity of the three channels at once.

7. Select "Quantify signal polarity based on trajectories" from the MEASUREMENT menu, and choose a file to store the output. The measurements can be saved in .mat format, for Matlab, or in .csv format, which can be opened with a text editor or in a spreadsheet. If you cancel here, the analysis will run and the results will be displayed on the screen.

8. The output file contains the mean cytoplasmic brightness (measured generating a mask that excludes the drawn trajectories), the image mode (the most frequent pixel value), and the mean image brightness. These three values can be used to correct for background [15].

9. Also in the output file are the angle (in degrees, *see* **Note 16**), length (in pixels), and average red, green, and blue intensity value for each individual trajectory.

10. The output file contains the mean results obtained by grouping trajectories according to their angle, in 15° bins, and a similar analysis transforming all angles to the [0,90] degree range (e.g., 105° = 75°).

3.4 Representative Results

We have used automated cell segmentation and tracking to follow the cellular and molecular dynamics of axis elongation in *Drosophila* embryos [5]. Figure 4 shows the analysis of 94 cells in an embryo tracked for 8 min with a temporal resolution of 15 s. Our analysis revealed cycles of assembly and disassembly of networks formed by the motor protein non-muscle myosin II at the medial cortex of ectodermal cells (Fig. 4a–c). Medial myosin pulses were accompanied by oscillations of the apical area of the cells (Fig. 4b, d). Apical area oscillations were not associated with a reduction in cell area (Fig. 4f), in contrast with the oscillatory behaviors observed during mesoderm invagination [16]. These results showed that the oscillatory behaviors associated with medial myosin networks are not exclusive of cells undergoing apical constriction, and have opened the way to new investigations on the function and molecular regulators of oscillatory behaviors during axis elongation.

SIESTA can also measure asymmetries in the localization of molecules in the plane of the tissue [13, 17, 18]. Figure 5 shows an analysis of protein localization in a wild-type *Drosophila* embryo undergoing axis elongation, and in an embryo mutant for *bicoid, nanos* and *torso-like*, three transcription factors required for anterior-posterior axis specification and elongation. Embryos were stained for the PDZ domain protein Par-3 (red), which is thought to stabilize adherens junctions, and for myosin II (green) (Fig. 5a, b). In the wild-type embryo, Par-3 localized preferentially at cell interfaces within 0–45° with respect to the anterior-posterior
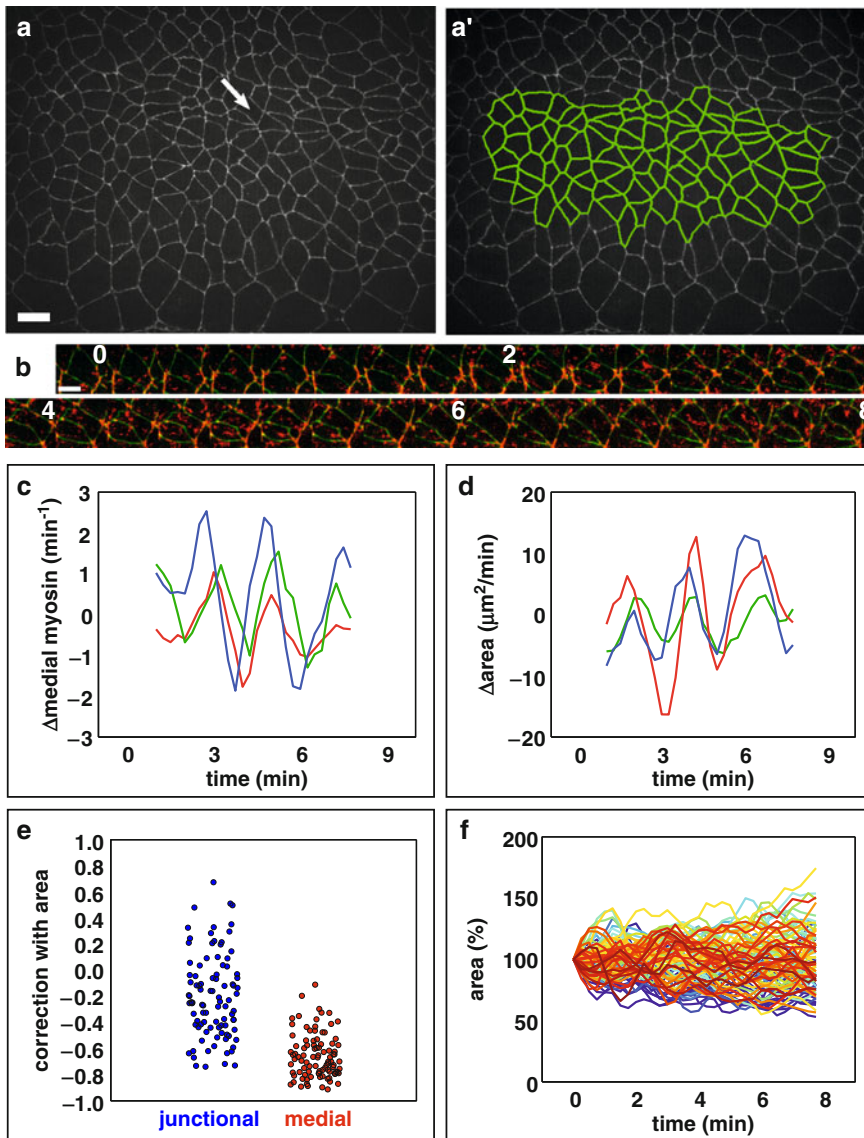
Fig. 4 Analysis of cellular and molecular dynamics in living *Drosophila* embryos by automated cell detection and tracking. (**a**) Ectodermal cells expressing the junctional marker E-cadherin:GFP in a stage 7 *Drosophila* embryo. The results of watershed-based, automated cell delineation applied to (**a**) are displayed as green polygons in (**a′**). The white arrow in (**a**) points at a cell tracked in (**b**). Anterior left, dorsal up. Scale bar = 10 μm. (**b**) Kymograph showing a cell expressing E-cadherin:GFP (green) and myosin:mCherry (red). Images were acquired every 15 s. The time with respect to the beginning of the movie is indicated in minutes. Anterior left, dorsal up. Scale bar = 5 μm. (**c**) Dynamics of myosin concentration at the medial cortex of three example cells during axis elongation in the embryo shown in (**a**) (each curve represents a different cell). The blue curve measures medial myosin dynamics in the cell shown in (**b**). (**d**) Apical area changes over time for the three example cells shown in (**c**). (**e**) Correlation of myosin changes in the junctional (blue) and medial (red) regions with respect to apical area changes for the cells delineated in (**a′**). Each dot represents a cell (n = 94). (**f**) Percent change of apical area over time for the cells delineated in (**a′**). Each curve represents a cell (n = 94)
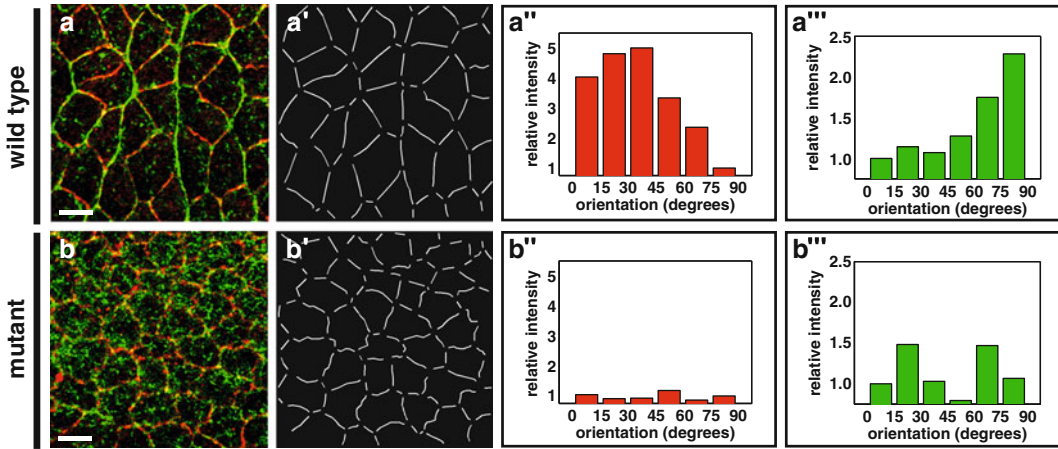
Fig. 5 Multicolor planar polarity measurements to compare wild-type and mutant embryos. (**a**, **b**) Epidermal cells in stage 7, wild-type (**a**) and *bicoid, nanos, and torso-like* triple mutant (**b**) embryos, immunostained for myosin (*green*) and Par-3 (*red*). Anterior left, dorsal up. Scale bar = 6 μm. (**a′**, **b′**) Cell outline annotations to quantify planar polarity in (**a**) and (**b**), respectively. (**a″**, **b″**) Quantification of Par-3 localization. Cell interfaces are classified according to their orientation with respect to the AP axis of the embryo. The average red fluorescence for each orientation is shown, normalized to the value of the interfaces with an inclination of 75–90° with respect to the AP axis. (**a‴**, **b‴**) Quantification of myosin localization. Fluorescence was normalized to the average value of the interfaces with an inclination of 0–15° with respect to the AP axis

(AP) axis of the embryo (Fig. 5a, a″) [19, 20], with a 4.6-fold enrichment with respect to interfaces perpendicular to the AP axis. Myosin localization was reciprocal to Par-3 (Fig. 5a‴) [19, 21, 20], with a 2.3-fold myosin enrichment at cell interfaces perpendicular to the AP axis of the embryo. In the *bicoid, nanos, torso-like* mutant, Par-3 and myosin localized uniformly around the apical cell cortex (Fig. 5b, b‴) [19], and myosin displayed an increase in the medial-to-junctional ratio, as we previously reported in living embryos (Fig. 5b) [5]. By immunostaining for different markers at different developmental stages, this analysis can be used to reconstruct the temporal sequence of events that leads from a cell that is molecularly symmetric to one that is spatially patterned, and to screen for defects in the asymmetric distribution of proteins in the cell.

4   Notes

1. The Matlab Compiler Runtime is required to run Matlab code packaged with the Matlab Compiler. This allows users to run Matlab code without having to buy a Matlab license (the Matlab Compiler Runtime is available free of charge).

2. run_siesta3.sh is the file that will be used to run SIESTA. It is a Unix shell script, a list of instructions for the operating system

indicating where are the different components necessary to run the program.

3. It is usually faster to find the right parameter values for the seed-finding algorithm on a single image before trying with multiple time points at once. Also, it is easier to find the right seeds for the first time point and then transfer them and adjust their position for all the subsequent time points using the tools described below.

4. Increase the value of the "Minimum distance seed-cortex" if you have too few seeds (some cells are not assigned seeds). Decrease this value if you have too many seeds (more than one seed per cell).

5. To draw a polyline, select "Draw polyline" in the ANNOTATION menu. Click on the left mouse button to start drawing. Each left click adds one vertex to the polyline. Close the polyline with a right click. Clicking the middle button while drawing deletes the last segment of the polyline.

6. You can also delete all seeds outside a polyline. Once the polyline is drawn, select "Delete fiducial markers outside polyline" in the ANNOTATION menu and click on the polyline to delete all the fiducials outside.

7. Cells that touch the image border are automatically deleted by SIESTA (Fig. 1i, j). Most segmentation errors occur with the most external layer of cells. Thus, it is a good practice to add extra seeds outside the group of cells that need to be correctly segmented.

8. Tracking in SIESTA will only work if the same number of fiducials is present in consecutive time points. An error message will be displayed otherwise. In that case, flip back and forth between the two time points indicated by the error message to identify the position of the missing/extra fiducials. Error messages during tracking may also indicate that two fiducials map onto the same one in the next time point. Simply look for the corresponding fiducial in the indicated time point and edit the two fiducials that map onto it from the previous time point.

9. Fiducial based tracking is simple and runs fast, but it requires that the temporal resolution of the movie is high enough that cells do not move too far from one time point to the next. If cells move over half a cell diameter between time points, tracking will not work.

10. The displayed channel or channels will be measured, so if you are using a color movie, switch to the color channel to measure all the channels at once. If your movie has two channels stored as independent files, you can analyze one, save the results, and

then open the second channel, load the annotation file, and analyze it.

11. These measurements will be affected by the width of the cell outline. The width of the cell outline can be determined using "Set brush diameter" under the OPTIONS menu. After changing the brush size, the visual appearance of the cell outlines will be updated when you move to a different time point.

12. Make sure you do not have images with sequential names in the same folder as the image that you are opening, as SIESTA will try to open all of them as a sequence.

13. Do not draw any trajectories that touch the border of the image, or SIESTA will return an error message when it runs the analysis.

14. Try to draw trajectories that do not include vertices where three or more cells meet, as these vertices can accumulate protein from multiple cell interfaces.

15. The width of the trajectories can be modified by selecting "Set brush diameter" under the OPTIONS menu. This will affect any new trajectories as well as trajectories that are already drawn, although the visual appearance of the trajectories will only be updated when you press sequentially on . and , to refresh the image.

16. Trajectories can consist of one or multiple segments. The angle of trajectories consisting of a single segment is the angle between the segment and a horizontal line extending to the right from the bottom end of the segment. For trajectories that contain multiple segments, the angle is calculated as the angle between a straight line connecting the end points of the trajectory and a horizontal line as above.

Acknowledgments

References

1. Krzic U, Gunther S, Saunders TE et al (2012) Multiview light-sheet microscope for rapid in toto imaging. Nat Methods 9 (7):730–733

2. Tomer R, Khairy K, Amat F et al (2012) Quantitative high-speed imaging of entire developing embryos with simultaneous multiview light-sheet microscopy. Nat Methods 9(7):755–763

3. Carpenter AE, Jones TR, Lamprecht MR et al (2006) Cell profiler: image analysis software for identifying and quantifying cell phenotypes. Genome Biol 7(10):R100

4. Aigouy B, Farhadifar R, Staple D et al (2010) Cell flow reorients the axis of planar polarity in the wing epithelium of Drosophila. Cell 142 (5):773–786

5. Fernandez-Gonzalez R, Zallen JA (2011) Oscillatory behaviors and hierarchical assembly of contractile structures in intercalating cells. Phys Biol 8(4):045005

6. Mashburn DN, Lynch HE, Ma X et al (2012) Enabling user-guided segmentation and tracking of surface-labeled cells in time-lapse image sets of living tissues. Cytometry A 81 (5):409–418

7. Rasband WS (1997) ImageJ. U.S. National Institutes of Health, Bethesda, MD

8. Vincent L, Soille P (1991) Watersheds in digital spaces: an efficient algorithm based on immersion simulations. IEEE T Pattern Anal 13(6):583–598

9. Kass M, Witkin A, Terzopoulos D (1987) Snakes - active contour models. Int J Comput Vision 1(4):321–331

10. Osher S, Sethian JA (1988) Fronts propagating with curvature dependent speed: algorithms based on Hamilton-Jacobi formulations. J Comput Phys 1988:12–49

11. Mortensen E, Morse B, Barrett W et al. (1992) Adaptive boundary detection using 'Live-Wire' two-dimensional dynamic programming. Paper presented at the Computers in Cardiology, Durham, NC, October 11–14, 1992.

12. Dijkstra E (1959) A note on two problems in connexion with graphs. Numer Math 1:269–271

13. Simões SM, Blankenship JT, Weitz O et al (2010) Rho-kinase directs Bazooka/Par-3 planar polarity during Drosophila axis elongation. Dev Cell 19(3):377–388

14. Fernandez-Gonzalez R, Simoes SM, Röper J et al (2009) Myosin II dynamics are regulated by tension in intercalating cells. Dev Cell 17 (5):736–743

15. Marcinkevicius E, Fernandez-Gonzalez R, Zallen J (2009) Q&A: quantitative approaches to planar polarity and tissue organization. J Biol 8 (12):103

16. Martin A, Kaschube M, Wieschaus E (2009) Pulsed contractions of an actin-myosin network drive apical constriction. Nature 457 (7228):495–499

17. Tamada M, Farrell DL, Zallen JA (2012) Abl regulates planar polarized junctional dynamics through β-catenin tyrosine phosphorylation. Dev Cell 22(2):309–319

18. Marcinkevicius E, Zallen JA (2013) Regulation of cytoskeletal organization and junctional remodeling by the atypical cadherin Fat. Development 140(2):433–443

19. Zallen J, Wieschaus E (2004) Patterned gene expression directs bipolar planar polarity in Drosophila. Dev Cell 6(3):343–355

20. Blankenship J, Backovic S, Sanny J et al (2006) Multicellular rosette formation links planar cell polarity to tissue morphogenesis. Dev Cell 11 (4):459–470

21. Bertet C, Sulak L, Lecuit T (2004) Myosin-dependent junction remodelling controls planar cell intercalation and axis elongation. Nature 429(6992):667–671

Chapter 8

A Multiplex Fluorescent In Situ Hybridization Protocol for Clonal Analysis of *Drosophila* Oogenesis

Lily S. Cheung and Stanislav Shvartsman

Abstract

Fluorescent in situ hybridization (FISH) is a common inmunohistochemical method used to examine the distribution of RNAs in tissue samples. In mosaic tissues composed of a mixed population of wild-type and loss-of- or gain-of-function mutant cells, FISH allows comparison of the effect of the perturbation on gene expression patterns in a mutant cell and its wild-type neighbors. Here, we provide a protocol for the detection of RNA in *Drosophila* mosaic follicular epithelia, where the mosaic analysis with a repressible cell marker (MARCM) technique is used for expression of transgenes.

Key words *Drosophila melanogaster*, Oogenesis, Follicle cells, Mosaic analysis with a repressible cell marker (MARCM), Fluorescent in situ hybridization (FISH)

1 Introduction

Drosophila melanogaster oogenesis is a classic model for the analysis of patterning and morphogenesis regulation by extracellular signaling pathways. In addition to the simple anatomy of the egg chamber, the large availability of transgenic tools for its manipulation allows the study of a number of developmental processes, many of which are conserved between flies and vertebrates. Moreover, this tractable system shares many of the morphogenetic events of larger organs under the control of some of the same regulatory networks, and has already provided great insight into the molecular mechanisms coordinating morphogenesis [1, 2].

One useful tool to prove the function of genes is the GAL4/UAS binary system for transgene expression. GAL4 encodes a protein identified in the yeast *Saccharomyces cerevisiae* as a regulator of genes induced by galactose. In *Drosophila*, many lines (known as "drivers"), where the GAL4-coding sequence has been stably incorporated into the genome under the control of *Drosophila* regulatory sequences (with tissue- and stage-specific expression), are reported and publicly available. GAL4 regulates transcription by

binding to four related 17 bp sites known as upstream activating sequences (UAS), and thus promoting transcription of nearby genes [3, 4]. Many lines with the coding sequences of *Drosophila* genes under the control of UAS are also publicly available.

An additional level of control of transgene expression can be achieved with the MARCM method [5, 6], which combines the FLP/FRT [7] system and the dominant GAL80 protein to inhibit activation of the GAL4/UAS system. The MARCM method can be used to prevent lethality due to off-target effects, and to allow comparison of gene expression in a mutant cell and its wild-type neighbors within the same tissue.

The FLP-recombinase and its target, the FRT sequence, can induce high-frequency mitotic recombination between FRT sites located on homologous chromosome arms to produce mosaics of homozygote mutant, heterozygote, and homozygote wild-type cells [7]. If a GAL80 sequence is incorporated distally to an FRT site, FLP-induced mitotic recombination removes GAL80 in a random group of cells which allows the transcription of UAS-regulated transgenes by GAL4 (Fig. 1a). Furthermore, the choice
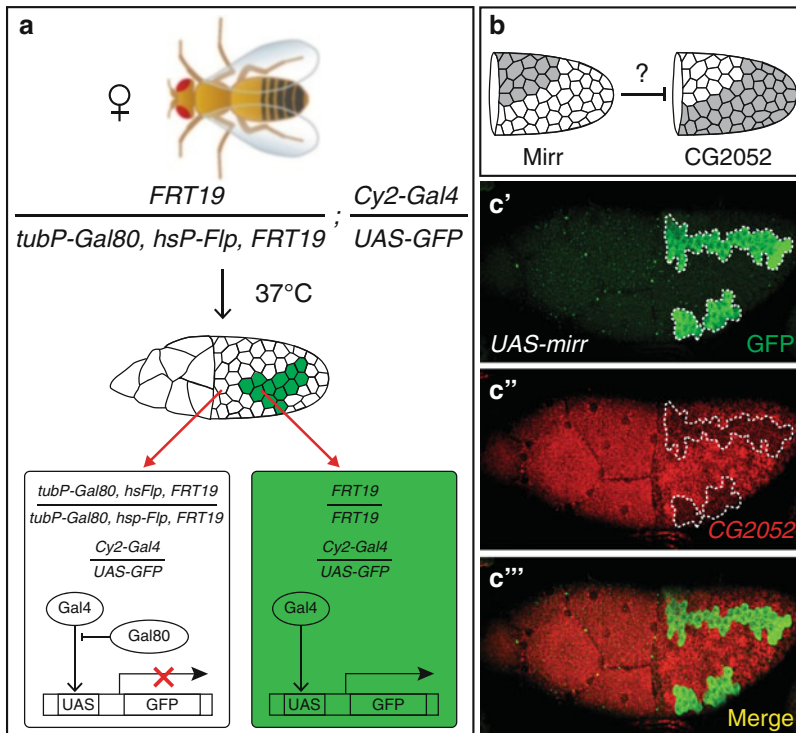
Fig. 1 The effect of a gene on a potential target can be tested by ectopic expression of the gene under UAS control. (**a**) Females with a *tubP-GAL80*, *FRT* in *trans* to an *FRT* site, an *hsP-FLP* recombinase, a *UAS-GFP*, and the oogenesis-specific *Cy2-GAL4* driver produce GFP-marked clones upon heat shock. (**b**) The effect of the transcription factor mirror (*mirr*) on another gene with complementary expression pattern can be assayed by introducing a *UAS-mirr* transgene [12, 13]. (**c–c'''**) Ectopic expression of *mirr* in ventral follicle cells produces downregulation of *Lin-29* (*CG2052*) RNA in GFP-marked clones (*dashed line*)

of oogenesis-specific Gal4 drivers [8] allows a more temporally restricted transgene expression.

In this chapter, we describe a procedure to induce MARCM clones in follicle cells during oogenesis, and to analyze the resulting changes in RNA expression using fluorescent in situ hybridization (FISH). The FISH protocol described below was adapted from that developed for *Drosophila* embryos, with further modification suggested in the author's laboratory website [9, 10]. This protocol can successfully detect medium-to-high levels of RNA. Other techniques allowing the detection of low levels of RNA through the use of amplification steps [11] are not covered here.

2 Materials

Prepare all solutions using nuclease-free water and molecular biology-grade reagents.

2.1 Labeled RNA Probe Preparation

1. Hydrolysis buffer: Dissolve sodium carbonate (Na_2CO_3) and sodium bicarbonate ($NaHCO_3$) in water to concentrations of 1.2 M and 0.8 M, respectively. Check for a final pH of 10. The solution can be prepared in advance and stored in aliquots at $-20\ ^\circ C$.

2. Stop buffer: Dilute sodium acetate buffer solution (3 M, pH 5, Sigma) to a final concentration of 0.2 M in water. Use sodium acetate buffer solution (3 M, pH 7, Sigma) to adjust the final pH to 6. The solution can be prepared in advance and stored in aliquots at $-20\ ^\circ C$.

3. Hybridization buffer: Mix 25 mL of formamide, 12.5 mL of SSC buffer (20×, Sigma), 12 mL of water, 500 µL of Salmon sperm DNA (10 mg/mL, Sigma), 50 µL of Tween-20 (Sigma), and 50 µL of a 50 mg/mL stock of heparin. To prepare the heparin stock, dissolve heparin sodium salt (Sigma) in water. The hybridization buffer can be prepared in advance and stored at $-20\ ^\circ C$.

4. in vitro transcription (IVT) reaction mix: Combine 2 µL of transcription buffer (10×, Roche Applied Science), 2 µL of DIG or Biotin RNA labeling mix (Roche Applied Science), 2 µL of RNase inhibitor (Roche Applied Science), 2 µL of nuclease-free water, and 2 µL of T3, T7, or SP6 RNA Polymerase (Roche Applied Science). Select the RNA polymerase that will produce antisense RNA from the template DNA. Use immediately after preparation.

5. DNAse I (Roche Applied Science).

6. RNeasy Mini Kit (Qiagen).

7. Microcentrifuge.

2.2 Ovary Sample Preparation	1. Isotherm incubator at 37 °C.
	2. Baker's yeast (MP Biomedicals).
	3. Stereo dissecting microscope, carbon dioxide pad, Pyrex glass spot plate, and Dumont forceps for dissection.
	4. Wide-bore pipet tips.
	5. Dissection solution: Dissolve Tween-20 in Grace's Insect Medium (1×, Invitrogen) to a final concentration of 0.02 %. The solution can be prepared in advance and stored at 4 °C.
	6. PBST wash solution: Dissolve Tween-20 in 1× Dulbecco's phosphate-buffered saline (PBS) to a final concentration of 0.02 %. The solution can be prepared in advance and stored at room temperature.
	7. Nutating mixer.
	8. 8 % formaldehyde fix solution: Mix 43 µL of formaldehyde (37 %), 157 µL of 1× PBS, and 600 µL of heptane. Use immediately after preparation.
	9. Methanol.
2.3 Hybridization of RNA Probes	1. Ethanol.
	2. Xylene.
	3. Methanol.
	4. 6 % formaldehyde fix solution: Dilute the formaldehyde (37 %) in 1× PBS to a final concentration of 6 % formaldehyde. Use immediately after preparation.
	5. Acetone.
	6. Benchtop incubating orbital shaker with Eppendorf tube holder.
2.4 Antibody Staining	1. Blocking solution: Mix 1 mL of the Western blocking reagent (WBR, 10×, Roche Applied Science) and 4 mL of 1× PBS. Store at 4 °C for up to 1 day.
	2. Sheep anti-DIG antibody (Roche Applied Science) or mouse anti-Biotin antibody (Jackson ImmunoResearch Lab) depending on the particular probe used.
	3. Alexa Fluor 488-conjugated rabbit anti-GFP antibody (Molecular Probes).
	4. Alexa Fluor-conjugated secondary antibodies (Molecular Probes).
2.5 Sample Mounting	1. Aqua Poly-Mount (PolySciences).
	2. Glass slide and glass cover slip.
	3. Wide-bore pipet tips.
	4. Clear nail polish.

3   Methods

3.1   Labeled RNA Probe Preparation

1. Amplify DNA template for the gene of interest by polymerase chain reaction (PCR) according to the instructions for the particular polymerase used. Add 10 µL of the PCR product to 10 µL of the IVT reaction mix. Incubate at 37 °C for 3 h.

2. Add 2 µL of DNase I and incubate at 37 °C for 30 min.

3. Purify the probe using the Qiagen RNeasy Mini Kit following the instructions for RNA cleanup.

4. Elute RNA from the Qiagen column with 40 µL of nuclease-free water.

5. Add 2 µL of hydrolysis buffer, and incubate at 60 °C for a time (in minutes) equal to $(L - 0.2)/(0.022 \times L)$ where L is the length of the DNA template in kb.

6. Add 40 µL of stop buffer to quench the hydrolysis.

7. Dilute the RNA probe solution in 200 µL of the hybridization buffer and store at −20 °C.

3.2   Ovary Sample Preparation

1. Prepare heterozygote flies carrying a *tubP-GAL80*, *FRT* in *trans* to an *FRT* site, as well as an oogenesis-specific *GAL4* driver, an *hsP-FLP* recombinase, and a *UAS-GFP* marker. Additionally, *UAS*-transgenic constructs can be incorporated to study their function (for example as in Fig. 1, *see* **Note 1**).

2. Heat-shock the flies for two consecutive days. Place vials with adult females and some male flies in an isotherm incubator set at 37 °C for 5 h each time (*see* **Note 2**). Transfer the flies to a fresh vial with standard cornmeal food.

3. Let the flies recover at room temperature, and on the fourth day add Baker's yeast to their food to promote oogenesis. Wait until the next day for dissection.

4. Anesthetize 10–20 female flies on a carbon dioxide pad.

5. Dissect ovaries in a glass spot plate with cold dissection solution. Separate each ovary in half, and transfer them to an Eppendorf tube using a wide-bore pipet tip (*see* **Note 3**).

6. Remove as much liquid from the sample as possible, and add the 8 % formaldehyde fix solution. Incubate for 20 min on a nutating mixer (*see* **Note 4**).

7. Rinse once and wash the fixed ovaries in PBST three times for 5 min each (*see* **Note 5**).

8. Dehydrate ovaries by washing successively in solution of 25, 50, and 75 % methanol in $1 \times$ PBS for 5 min each on a nutating mixer. Rinse once and store the ovaries in 100 % methanol at −20 °C for up to 3 months.

3.3 Hybridization ***of RNA Probes***	1. Rinse ovaries once and wash with ethanol for 5 min.

3.3 Hybridization of RNA Probes

1. Rinse ovaries once and wash with ethanol for 5 min.

2. Incubate in a solution of 90 % of xylene in ethanol for 1 h.

3. Rinse once and wash with ethanol for 5 min.

4. Rinse once and wash with methanol for 5 min.

5. Fix the dissected ovaries in an equal parts mixture of 6 % formaldehyde solution and methanol for 5 min.

6. Fix again in 6 % formaldehyde solution for 25 min.

7. Rinse once, and wash in PBST three times for 5 min each.

8. Separate ovaries into individual egg chambers (*see* **Note 6**).

9. Incubate in a solution of 80 % acetone in nuclease-free water at −20 °C for 10 min. Invert the tube once during incubation to improve permeabilization.

10. Rinse once, and wash in PBST three times for 5 min each.

11. Fix in 6 % formaldehyde solution for 25 min.

12. Rinse once, and wash in PBST three times for 5 min each.

13. Incubate in an equal parts mixture of hybridization buffer and PBST for 10 min.

14. Incubate sample in hybridization buffer at 60 °C for 2 h.

15. Dilute the RNA probe in hybridization buffer. Try several concentrations starting with a 1:10 dilution. Denature the probe by heating this solution to 80 °C for 4 min, and then quenching in ice for 1 min. Immediately after, add the probe solution to the sample and incubate at 60 °C overnight in an orbital shaker.

3.4 Antibody Staining

1. Rinse once, and wash in hybridization buffer three times at 60 °C for 1 h each.

2. Incubate in an equal parts mixture of hybridization buffer and PBST for 10 min.

3. Rinse once, and wash in PBST three times for 5 min each.

4. Incubate the sample in blocking solution for 30 min.

5. Dilute the primary antibodies in blocking solution. Try several concentrations starting with a 3:500 dilution for sheep anti-DIG, 1:100 for mouse anti-biotin, and 1:100 for rabbit anti-GFP. Add this antibody solution to the sample, and incubate at 4 °C overnight in a nutation mixer (*see* **Notes 7–9**).

6. Rinse once, and wash in PBST three times for 5 min each.

7. Incubate in blocking solution for 30 min.

8. Dilute the secondary antibodies in blocking solution. Try several concentrations starting with a 1:500 dilution. Add the probe solution to the sample and incubate for 2 h. Protect the sample from light (*see* **Note 10**).

9. Rinse twice, and wash in PBST two times for 20 min each.

10. Wash the sample in PBS for 20 min, and then remove as much of the wash liquid as possible.

3.5 Sample Mounting

1. Add an equal parts mixture of PBS and Aqua-Poly-Mount (i.e., in one drop of each for a 22 × 60 mm cover slip), and pipet several times to suspend the ovaries using a wide-bore pipet tip. Transfer the sample to a glass slide, and remove any bubbles. Place cover slip genteelly on the sample, and seal the edges with nail polish (*see* **Notes 11** and **12**). Store the slide at 4 °C, and protect from light. Wait for 1 day before imaging.

4 Notes

1. It is convenient to keep one stock with the *tubP-GAL80 FRT*, the *hsP-FLP* recombinase, the *GAL4* driver, and the *UAS-GFP* marker, and another stock with the FRT and the UAS-transgenic construct to be analyzed, that can be crossed multiple times to easily repeat experiments.

2. The duration and frequency of the heat shock affect the number and size of clones. The particular conditions described here produce several medium-size (2–10 cells) clones when combined with the *FRT19* site.

3. Keep the 0.02 % Tween-20 in Grace's medium solution in ice.

4. All fixation, wash, and incubation steps are done at room temperature unless otherwise specified.

5. In each of the rinse steps in this protocol, rinse refers to removing as much of the previous solution as possible, replacing it with PBST, and then removing the PBST, while in the wash steps, the samples are placed in nutation mixer for the indicated time before removal of the PBST. The duration of the wash steps is recommended, but can be extended.

6. The separation into individual egg chamber can also be performed after **step 7** of Subheading 3.2, before the dehydration step. If samples from different dissections will be combined into a single FISH, separating the egg chamber after **step 7** decreases the workload for the hybridization procedure.

7. Fluorescein-labeled probes can also be incorporated to monitor the expression of a third gene, combined with a commercial rabbit anti-fluorescein antibody. Because of fluorescein's green fluorescence, the secondary antibody used for its detection should be Alexa Fluor 488 conjugated. In our hands, dinitrophenyl-labeled probes produce nonspecific fluorescence.

8. Samples treated in this protocol retain negligible fluorescence from GFP; thus GFP can be detected with appropriate primary and secondary antibodies not conjugated to Alexa Fluor 488.

9. Because of the extensive sample treatment, the concentration of antibodies used for protein detection in this protocol is approximately double that required in conventional inmunostaining.

10. The DNA-binding dye DAPI can be added to this step to stain nuclei.

11. If the sample size is too small and will be analyzed with confocal microscopy, it is possible to mount the sample in between two cover slips to allow imaging of the sample from both sides. Place the sample on a cover slip and genteelly lay another cover slip of equal size on top. Let the liquid spread between the cover slips and wipe the edges to remove excess liquid. Seal the edges with nail polish, and set on a support that avoids contact with the nail polish. When imaging, tape the cover slip setup to a glass slide. As limitations, this arrangement is not adequate for epifluorescence or light microscopy, breaks easily, and should be handled with care.

12. If the ovaries show signs of shrinking, it is possible that the ratio of Aqua-Poly-Mount to PBS is too high. Increase the amount of PBS in subsequent experiments.

References

1. Horne-Badovinac S, Bilder D (2005) Mass transit: epithelial morphogenesis in the Drosophila egg chamber. Dev Dyn 232:559–574

2. Wu X, Tanwar PS, Raftery LA (2008) Drosophila follicle cells: morphogenesis in an eggshell. Semin Cell Dev Biol 19:271–282

3. Duffy JB (2002) GAL4 system in Drosophila: a fly geneticist's Swiss army knife. Genesis 34:1–15

4. Brand AH, Perrimon N (1993) Targeted gene expression as a means of altering cell fates and generating dominant phenotypes. Development 118:401–415

5. Lee T, Luo L (1999) Mosaic analysis with a repressible cell marker for studies of gene function in neuronal morphogenesis. Neuron 22:451–461

6. Wu JS, Luo L (2006) A protocol for mosaic analysis with a repressible cell marker (MARCM) in Drosophila. Nat Protoc 1:2583–2589

7. Xu T, Rubin GM (1993) Analysis of genetic mosaics in developing and adult Drosophila tissues. Development 117:1223–1237

8. Goentoro LA, Yakoby N, Goodhouse J, Schupbach T, Shvartsman SY (2006) Quantitative analysis of the GAL4/UAS system in Drosophila oogenesis. Genesis 44:66–74

9. Kosman D, Mizutani CM, Lemons D, Cox WG, McGinnis W, Bier E (2004) Multiplex detection of RNA expression in Drosophila embryos. Science 305:846

10. Kosman D (2003) Multiplex fluorescent mRNA in situ hybridization. http://people.biology.ucsd.edu/davek/. Accessed on 10 Jan 2013

11. Lecuyer E, Necakov AS, Caceres L, Krause HM (2008) High-resolution fluorescent in situ hybridization of Drosophila embryos and tissues. CSH Protoc 2008:pdb prot5019

12. Yakoby N, Bristow CA, Gong D, Schafer X, Lembong J, Zartman JJ, Halfon MS, Schupbach T, Shvartsman SY (2008) A combinatorial code for pattern formation in Drosophila oogenesis. Dev Cell 15:725–737

13. Yang CH, Simon MA, McNeill H (1999) Mirror controls planar polarity and equator formation through repression of fringe expression and through control of cell affinities. Development 126:5857–5866

Chapter 9

Active Cell and ECM Movements During Development

Anastasiia Aleksandrova, Brenda J. Rongish, Charles D. Little, and András Czirók

Abstract

Dynamic imaging of the extracellular matrix (ECM) and cells can reveal how tissues are formed. Displacement differences between cells and the adjacent ECM scaffold can be used to establish active movements of mesenchymal cells. Cells can also generate large-scale tissue movements in which cell and ECM displacements are shared. We describe computational methods for analyzing multi-spectral time-lapse image sequences. The resulting data can distinguish between local "active" cellular motion versus large-scale, tissue movements, both of which occur during organogenesis. The movement data also provide the basis for construction of realistic biomechanical models and computer simulations of in vivo tissue formation.

Key words Cell motility, Time-lapse imaging, Avian development, Computational analysis

1 Introduction

Tissue engineering, the controlled construction of tissues—that is, cells and their extracellular matrix (ECM) environment—is a promising avenue of future biomedical applications. To realize this possibility, the dynamic and mutually interdependent relationship between cells and ECM has to be understood. Changes in local cell and ECM organization have a clear impact on cell differentiation, cell signaling, and further downstream effects with direct medical importance; for example, the durability of heart leaflet implants [9] or treatments to reduce malignant cell invasion [7]. The large-scale tissue movements, which characterize early embryonic development, are not replicated by typical culture techniques. Thus the ability of cells to translocate in conjunction with their microenvironment is generally underappreciated—so much so that it is often taken for granted that cells inevitably crawl along ECM fibers in response to repulsive or attractive biochemical cues. Yet, if investigators are interested in measuring modes of active cell

locomotion, in situ, it is necessary to study cellular motion in the context of deformation of the surrounding ECM; i.e., as part of a composite tissue.

In the following sections we discuss experimental and computational techniques that we used to study ECM movements in live embryos, and the methods we used to compare cell and local ECM movement data to establish cell-autonomous motility relative to the ECM microenvironment.

2 Embryo Preparation

1. Fertilized wild-type or transgenic Tie1::H2B-YFP quail eggs (Coturnix coturnix japonica) are incubated in the humidified atmosphere at 37 °C.

2. Embryos are removed from the eggs and mounted on Whatman 52 filter paper rings (Whatman International, Maidstone, England) as described in [2, 11, 12].

3. Embryos are staged according to the classification developed by Hamburger and Hamilton (HH) [8].

4. For further manipulations, embryos are placed onto culture dishes [3, 2], typically with their ventral surface facing away from the culture support.

3 In Vivo Labeling of ECM Antigens

Fluorophore conjugation is an efficient method to covalently label antibodies or other molecules of interest [10, 12]. To visualize ECM antigens in living quail embryos we use anti-fibrillin-2 antibody JB3 and anti-fibronectin antibody B3D6 (both from Developmental Studies Hybridoma Bank, Iowa City, IA).

1. Antibodies are conjugated to fluorophores using AlexaFluor 488, 555, and 647 Antibody Labeling kits (Molecular Probes, catalog numbers A-20181, A20187, and A-20186) as per manufacturer's instructions. For microinjections, antibodies are solubilized in ePBS [11] at 1 μg/μL concentration.

2. For microinjection, embryos are oriented with their ventral (endodermal) surface up (away from the agar-albumen bed underlying the embryo in the culture dish).

3. The glass needle penetrates the endoderm at an acute angle (less than 45°).

4. Fluorophore-conjugated antibodies are delivered into the interstitial space by 6–20 pulses of 5–10 nl of antibody solution. Microinjections utilize a pneumatically driven Pico-Injector

(Harvard Apparatus, Holliston, MA) associated with a hydraulic micromanipulator assembly (Narishige Scientific Instrument Laboratory, Tokyo). Each pulse lasts for 10 ms and the applied pressure is 3.5–5.0 psi.

Notes: Antibody microinjection at HH6-7 provides more extensive labeling of fibronectin and fibrillin-2 constituents of the developing heart compared to the antibody delivery at earlier stages. Proteins, other than immunoglobulins, such as human serum fibronectin (BD Biosciences, catalog number 354008) can similarly be labeled with AlexaFluor fluorophores and delivered into the living quail embryos by the same method [1].

4   Cell Transfection

Lipofectamine 2000(c)-mediated delivery of plasmid DNA into the embryo can be used for cell transfection, as an alternative method to electroporation techniques. For example, myocardial progenitors can be selectively labeled by chicken Cardiac Myosin Light Chain 2 (cmlc2) promoter-driven GFP or RFP reporter constructs. Endodermal cells can be visualized by local exposure of the pCAAGS-GFP plasmid (a gift from Dr. Olivier Pourquie, Institute of Genetics and Molecular and Cellular Biology, Strasbourg, France).

1. Ten micrograms of plasmid DNA is diluted in endotoxin-free water and mixed with OptiMEM I Reduced Serum Medium (Invitrogen, catalog number 31985-062) to yield the 40–50 μL volume, and incubated at room temperature for 5 min.

2. After incubation, 20 or 30 μL of Lipofectamine 2000 Transfection Reagent (Invitrogen, catalog number 11668-027) was added to the OptiMEM-DNA mixture (1:2 or 1:3 DNA:Lipofectamine 2000 ratio), and the resulting solution was incubated for 20 min at room temperature to allow the DNA-transfection reagent complex to form.

3. The transfection complex containing solution is microinjected into the subendodermal space of quail embryos in 10–15, 5–10 nl pulses.

4. For localized reagent diffusion (such as labeling cells from a small area) the viscosity of the transfection mixture is increased by adding equal volume of 20 % solution of Pluronic F-127 (Sigma) in PBS. Twenty to forty microliters of the resulting solution is applied directly onto the targeted cell layer using a standard plastic-tipped 100 μL micropipette.

5. Following the exposure to transfection reagents, embryos are incubated at 37 °C for 3–4 h, at which time the reporter fluorescence becomes detectable.

Note: We achieved the best efficiency for the myocardial progenitor transfection when the DNA-Lipo2000 mixture was delivered during the time interval between late HH5 and early HH7.

5 Epifluorescence Time-Lapse Image Acquisition

To visualize tissue-level movements we subjected quail embryos containing fluorescent markers to long-term (4–16 h) wide field time-lapse imaging. Our automated microscopy system consists of a computer-controlled epifluorescent microscope (Leica DMRXA2, DM6000B or DMIRE2), equipped with a motorized stage and connected to a cooled digital CCD camera (QImaging Retiga-SRV). The details regarding custom software developed to operate the equipment are described in detail elsewhere [4, 11]. The most recent version of the software (TiLa) is available as an open-source code from the authors on request.

In the majority of our experiments we use a 10× objective (0.25 NA). Images are acquired in both epifluorescence and differential interference contrast (DIC) modes. One time point of the image sequence typically includes 4–8 images taken at slightly overlapping *xy* locations of the embryo ("tiles"), with 7–9 focal (*z*) planes in each tile. The length of the time interval between consecutive time points depends on the number of focal planes, tiles, and optical modes and is usually within the range of 2–20 min. The duration of a typical time-lapse image acquisition is usually between 4 and 16 h. However, embryos within the imaging chamber remain viable for extended periods of time, allowing for up to 48 h-long imaging experiments if required. Up to 12 embryos can be imaged per recording.

The design of the multi-well glass bottom imaging chamber used and steps required for its construction are illustrated in [11]. Within the imaging chamber embryos reside on a layer of albumen/agar/glucose mixture [13] on their dorsal side. This supporting layer is created just prior to mounting the embryos by pipetting 0.8–1 ml of warm albumen/agar/glucose solution into each well of the 12-well chamber, and allowing it to solidify for 20–30 min at room temperature. We utilize a custom-made thick-walled cardboard incubator that encloses the entire microscope to maintain the temperature of the imaging chamber mounted on the microscope stage within the 37–38.5 °C range throughout image acquisition (*see* ref. [12]).

Following the image acquisition, embryos can be fixed with 4 % paraformaldehyde in PBS with 0.05 % azide (PBSa) at 4 °C, and subsequently subjected to whole-mount immunolabeling and/or histological sectioning as described in [12, 1].

6   Particle Tracking

Manual or automated tracking procedures yield the location $\mathbf{x}_k(t_n)$ of object k at time points t_1, t_2, t_3, ..., t_n, corresponding to image frames I_1, I_2, ..., I_n. The displacement of the object k between two frames, e.g., t_1 and t_2, is thus

$$\Delta\mathbf{x}_k(t_1, t_2) = \mathbf{x}_k(t_1) - \mathbf{x}_k(t_2) \tag{1}$$

In practice, the time difference between t_1 and t_2 should be large enough so the displacements calculated in (1) are larger than the uncertainty of the positions x. For example, cell displacements smaller than the typical cell size are strongly affected by tracking details such as the definition of cell centroid.

7   Particle Image Velocimetry

Displacements of generic image features can be estimated by the analysis of the "optical flow." We use the following particle image velocimetry (PIV) algorithm [15] implemented in MatLab (Mathworks, Inc.):

1. The similarity of two image tiles, T_1 and T_2, each of the same size, $w \times w$, is characterized by their cross-correlation

$$C(T_1, T_2) = \frac{1}{w^2} \sum_{i=1}^{w} \sum_{j=1}^{w} h_1(i,j) h_2(i,j) \tag{2}$$

where $h_n(i, j)$ denotes the normalized brightness of the pixel (i, j) in image tile T_n. If the raw brightness values are denoted as $b_n(i, j)$, the normalization expresses these values relative to the average brightness

$$m_n = \frac{1}{w^2} \sum_{i=1}^{w} \sum_{j=1}^{w} b_n(i,j) \tag{3}$$

and scales the difference with the standard deviation

$$\sigma_n = \frac{1}{w} \sqrt{\sum_{i=1}^{w} \sum_{j=1}^{w} (b_n(i,j) - m_n)^2} \tag{4}$$

as

$$h_n(i,j) = \frac{b_n(i,j) - m_n}{\sigma_n}. \tag{5}$$

2. For an image pair, (I_1, I_2), typically taken from a sequence of images, the displacement of a certain image tile T_1 in image I_1 is

determined by maximizing the cross correlation $C(T_1, T_2)$ for all possible $w \times w$ subimage tiles T_2 within the image I_2:

$$C(T_1, T_2^*) \geq C(T_1, T_2) \tag{6}$$

Thus, by this procedure we identify T_2^* as the image tile in I_2 into which our original image tile T_1 moved and morphed.

3. To strike a balance between pattern specificity versus spatial resolution, the image tile T_2^* is selected in two steps. First, to increase pattern specificity, T_1 is enclosed in a larger tile, T_1', of a size of 64 pixels in image I_1. Its best fit pattern T_2' is selected according to the maximal cross correlation requirement (6). In the second step, the smaller (typically $w = 16$ pixels wide) T_2* is selected by restricting its possible location within T_2', instead of the whole image I_2.

4. The procedure yields the estimated displacement of the tile T_1 as

$$\Delta\mathbf{x} = C(T_2^*) - C(T_1) \tag{7}$$

where $C(T)$ denotes the coordinates of the center pixel of tile T.

5. Repeating the above steps for several tiles T_1, we obtain an array of estimated displacement vectors $\Delta\mathbf{x}(\mathbf{x})$ characterizing various image locations x (Fig. 1).

8 Image Registration

During time-lapse recordings living embryos shift position relative to the microscope objective; thus, an anatomical region of interest is often displaced by large-scale morphogenetic movements, an example being elongation of the vertebral axis. Thus, it is useful to relate the observed displacements to certain anatomical reference points. If the mean displacement of the reference points, $\Delta\mathbf{x}_{\mathrm{ref}}$, is established either by tracking or by PIV analysis, and rotational movements are negligible, we can easily express the displacements of our objects of interest within the frame of reference associated with the anatomical landmarks as

$$\Delta\mathbf{X}_k(t) = \Delta\mathbf{x}_k(t) - \Delta\mathbf{x}_{\mathrm{ref}}(t) \tag{8}$$

To reconstruct a trajectory within the anatomical frame of reference, these displacement values are accumulated as

$$\mathbf{X}_k(t_n) = \sum_{i=1}^{n-1} \Delta\mathbf{X}_k(t_i) \tag{9}$$
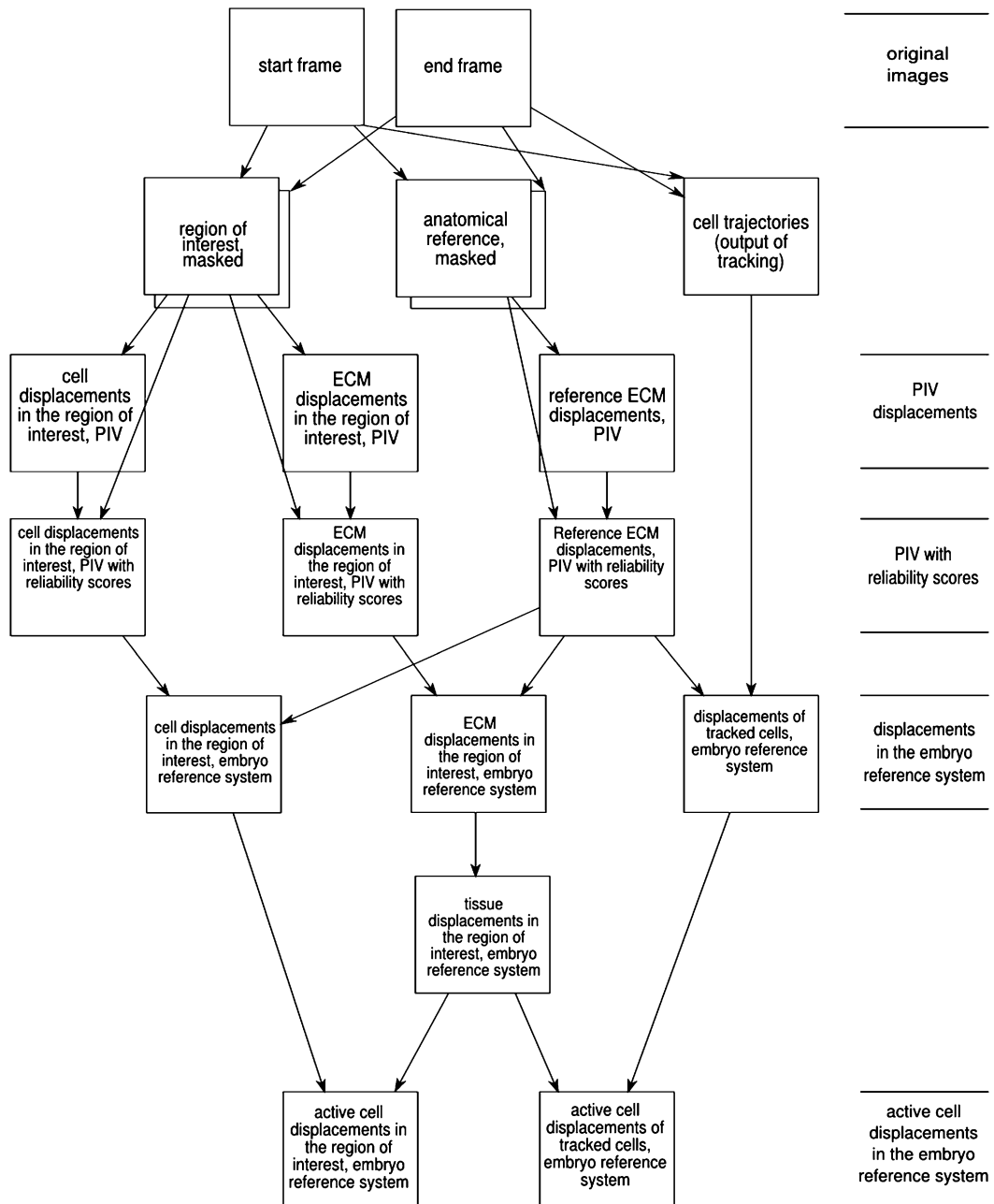
Fig. 1 Image processing workflow to analyze cell and ECM displacements. Image pairs characteristic for a certain developmental stage are selected. The two sets of images were acquired in multiple focal (*Z*) planes and multiple microscopy modes. By a manual masking procedure, image regions are selected that contain either the region of interest or the anatomical reference used later. PIV analysis gives displacement estimation for the various optical modes, thus for the investigated cell population and ECM. The PIV data are weighted by the local standard deviation of the immunofluorescence intensity, which is used as a reliability score. Displacements obtained from a region of interest are registered to an anatomical frame of reference by subtracting displacement vectors characterizing an anatomical reference. Local tissue movements are established from ECM displacements by filtering techniques. Finally, the comparison of cell and local tissue movements yields cell-autonomous displacements

9 Active Cell Motion Versus Tissue Motion

Using the same principle as in the previous section, we can define *active* cell displacements as displacements relative to the local ECM scaffold

$$\Delta \mathbf{X}_k^{\text{active}} = \Delta \mathbf{x}_k - \Delta \mathbf{x}_{\text{ECM}}. \tag{10}$$

This definition of active cell movement corresponds closely to the "conventional" in vitro scenarios where cellular motility occurs on a fixed two-dimensional surface or within (static) gels [6].

Fluorescent ECM tags can be used to map tissue movements in avian embryos [15, 16, 1]. This approach is motivated by the observation that, unlike cells, ECM filaments are passive tracers, incapable of active movements. This idea is backed by data showing that labeling of multiple distinct ECM glycoproteins, in a single specimen, yields similar motion patterns [17]; further, ECM filaments move similarly irrespective of their dorsal–ventral position [14]. Microinjected passive tracer particles, such as microbeads, are also convected similar to the ECM; thus for beads, or ECM, "independent" motion by these passive objects does not influence calculated active cellular displacements values [1].

The application of Eq. 10 requires that we have two displacement values *from the same location*: one for the cells of interest and one for the ECM scaffold. Thus it requires simultaneous imaging in multiple (at least two) optical modes, using two distinct fluorophores with no spectral overlap. In some experiments the traced cell population can be sparse and the ECM label highly nonuniform, Eq. 10. In such cases motion is evaluated only where both the cell and ECM signal are sufficiently strong. A practical way of characterizing fluorescence signal is the local standard deviation of brightness, σ, as defined in Eq. 4. Thus active cell movement data are available where the local σ is greater than a threshold value for both optical modes. While conceptually the ECM signal is better suited to act as a reference in Eq. 10, in practice we found that tissue movements are so dominant during early avian development that the optical flow derived from transmitted light DIC images yields highly similar displacement vectors [5]. This observation validates the concept that tissue flow can be quantified during early organ morphogenesis.

10 Subtracting Tissue Movements from Cell Locomotion

If a given object or pattern is located at the position $\mathbf{x}$ in image I_1, the corresponding location in image I_2 is $\mathbf{x} + \Delta \mathbf{x}$. From a number of such displacement vector data scattered within the field of view, a continuous displacement vector field can be calculated for

each pixel location $p = (i, j)$ by interpolation—for example, by fitting a thin plate spline for both the x and y components of the Δx displacement data. Of particular interest is the field $v_1(\mathbf{p})$, which maps the location $\mathbf{p}_1$ in the image I_1 forward in time to image I_2 as

$$\mathbf{p}_2 = \mathbf{p}_1 + \mathbf{v}_1(\mathbf{p}_1). \tag{11}$$

This interpolation spline allows us to define a transformed image $\mathbf{F}_1 I_2$ as

$$\mathbf{F}_1 I_2(\mathbf{p}) = I_2(\mathbf{p} + \mathbf{v}_1(\mathbf{p})). \tag{12}$$

Thus, image $\mathbf{F}_1 I_2$ is such a transform of image I_2 that each pixel is projected to the location it is moved *from* by the tissue flow $\mathbf{v}$. Therefore, in image $\mathbf{F}_1 I_2$ the tissue movements are eliminated by the transformation.

Similarly, the image I_n of the image sequence is transformed as

$$\mathbf{F}_1 \mathbf{F}_2 \ldots \mathbf{F}_{n-1} I_n = I_n(\mathbf{p} + \mathbf{v}_{n-1}(\mathbf{p}) + \mathbf{v}_{n-2}(\mathbf{p} + \mathbf{v}_{n_1}(\mathbf{p})) + \cdots) \tag{13}$$

to obtain a movie showing cell activities without tissue movements.

11   Tissue Flow as Low-Pass Filtered ECM Movement

Cells can actively remodel, pull, and drag the ECM. Thus, our definition according to which cells move relative to a conveyor-belt like ECM (i.e., active cell motion is the difference between local cell and ECM movements) is obviously an approximation. Statistical analysis of high temporal resolution recordings of ECM movements [14] indicated that local cell activity results in fluctuations that change quickly, with a correlation time less than a minute. In contrast, tissue movements can be identified as ECM movements that are persistent in time (autocorrelation time being in hours). This observation allows a more precise extraction of tissue movements by low-pass temporal filtering of the ECM displacement data. A practical possibility is a linear (or low order polynomial) fit by minimizing the expression

$$\Delta^2(\mathbf{x}) = \sum_t [\mathbf{v}(\mathbf{x}, t) - \mathbf{A}(\mathbf{x}) + \mathbf{B}(\mathbf{x})t]^2 \tag{14}$$

for each location $\mathbf{x}$.

References

1. Aleksandrova A, Czirók A, Szabó A, Filla MB, Hossain MJ, Whelan PF, Lansford R, Rongish BJ (2012) Convective tissue movements play a major role in avian endocardial morphogenesis. Dev Biol 363(2):348–361. doi:10.1016/j.ydbio.2011.12.036. http://dx.doi.org/10.1016/j.ydbio.2011.12.036

2. Chapman S, Collignon J, Schoenwolf G, Lumsden A (2001) Improved method for chick whole-embryo culture using a filter paper carrier. Dev Dyn 220:284–289

3. Cui C, Little CD, Rongish BJ (2009) Rotation of organizer tissue contributes to left-right asymmetry. Anat Rec (Hoboken) 292 (4):557–561. doi:10.1002/ar.20872. http://dx.doi.org/10.1002/ar.20872

4. Czirok A, Rupp PA, Rongish BJ, Little CD (2002) Multi-field 3d scanning light microscopy of early embryogenesis. J Microsc 206 (Pt 3):209–217

5. Czirok A, Rongish BJ, Little CD (2011) Vascular network formation in expanding versus static tissues: embryos and tumors. Genes Cancer 2(12):1072–1080. doi:10.1177/1947601911426774. http://dx.doi.org/10.1177/1947601911426774

6. Even-Ram S, Yamada KM (2005) Cell migration in 3d matrix. Curr Opin Cell Biol 17 (5):524–532. doi:10.1016/j.ceb.2005.08.015. http://dx.doi.org/10.1016/j.ceb.2005.08.015

7. Friedl P, Wolf K (2008) Tube travel: the role of proteases in individual and collective cancer cell invasion. Cancer Res 68 (18):7247–7249. doi:10.1158/0008-5472.CAN-08-0784. http://dx.doi.org/10.1158/0008-5472.CAN-08-0784

8. Hamburger V, Hamilton H (1951) A series of normal stages in the development of the chick embryo. J Morphol 88:49–92

9. Heydarkhan-Hagvall S, Schenke-Layland K, Dhanasopon AP, Rofail F, Smith H, Wu BM, Shemin R, Beygui RE, MacLellan WR (2008) Three-dimensional electrospun ecm-based hybrid scaffolds for cardiovascular tissue engineering. Biomaterials 29(19):2907–2914. doi:10.1016/j.biomaterials.2008.03.034. http://dx.doi.org/10.1016/j.biomaterials.2008.03.034

10. Little CD, Drake CJ (2000) Whole-mount immunolabeling of embryos by microinjection. Increased detection levels of extracellular and cell surface epitopes. Methods Mol Biol 135:183–189

11. Rupp PA, Czirok A, Little CD (2003) Novel approaches for the study of vascular assembly and morphogenesis in avian embryos. Trends Cardiovasc Med 13:283–288

12. Rupp PA, Visconti RP, Czirok A, Cheresh DA, Little CD (2008) Matrix metalloproteinase 2-integrin alpha(v)beta3 binding is required for mesenchymal cell invasive activity but not epithelial locomotion: a computational time-lapse study. Mol Biol Cell 19(12):5529–5540. doi:10.1091/mbc.E07-05-0480. http://dx.doi.org/10.1091/mbc.E07-05-0480

13. Streit A (2008) Ec culture: a method to culture early chick embryos. Methods Mol Biol 461:255–264

14. Szabó A, Rupp PA, Rongish BJ, Little CD, Czirók A (2011) Extracellular matrix fluctuations during early embryogenesis. Phys Biol 8 (4):045006. doi:10.1088/1478-3975/8/4/045006. http://dx.doi.org/10.1088/1478-3975/8/4/045006

15. Zamir EA, Czirok A, Rongish BJ, Little CD (2005) A digital image-based method for computational tissue fate mapping during early avian morphogenesis. Ann Biomed Eng 33:854–865

16. Zamir EA, Rongish BJ, Little CD (2008) The ecm moves during primitive streak formation--computation of ecm versus cellular motion. PLoS Biol 6(10):e247. doi:10.1371/journal.pbio.0060247. http://dx.doi.org/10.1371/journal.pbio.0060247

17. Czirok A, Zamir EA, Filla MB, Little CD, Rongish BJ (2006) Extracellular matrix macro assembly dynamics in early vertebrate embryos. Curr Top Dev Biol. 73:237–258

Part II

Culture Models of Morphogenesis

Chapter 10

3D Culture Assays of Murine Mammary Branching Morphogenesis and Epithelial Invasion

Kim-Vy Nguyen-Ngoc, Eliah R. Shamir, Robert J. Huebner, Jennifer N. Beck, Kevin J. Cheung, and Andrew J. Ewald

Abstract

Epithelia are fundamental tissues that line cavities, glands, and outer body surfaces. We use three-dimensional (3D) embedded culture of primary murine mammary epithelial ducts, called "organoids," to recapitulate in days in culture epithelial programs that occur over weeks deep within the body. Modulating the composition of the extracellular matrix (ECM) allows us to model cell- and tissue-level behaviors observed in normal development, such as branching morphogenesis, and in cancer, such as invasion and dissemination. Here, we describe a collection of protocols for 3D culture of mammary organoids in different ECMs and for immunofluorescence staining of 3D culture samples and mammary gland tissue sections. We illustrate expected phenotypic outcomes of each assay and provide troubleshooting tips for commonly encountered technical problems.

Key words 3D culture, Organotypic culture, Organoids, Extracellular matrix, Matrigel, Collagen I, Branching morphogenesis, Mammary epithelium, Immunofluorescence

1 Introduction

Mammary gland development occurs postnatally from a simple epithelial rudiment [1, 2]. During puberty, this rudiment undergoes stratification and initiates branching morphogenesis to form a network of epithelial tubes. The functional unit of elongation is a proliferative, multilayered front called the terminal end bud (TEB) [3, 4]. Behind the TEB, repolarization to a mature duct reestablishes a simple, bi-layered architecture, characterized by an inner layer of luminal epithelial cells and an outer layer of myoepithelial cells. These fundamental programs involve concurrent changes in

cell proliferation, migration, polarity, and tissue architecture and are modulated by signaling cues from stromal cells and the extracellular matrix (ECM) [5].

Because mammary epithelium develops within a fat pad with limited optical accessibility, various groups have used 3D culture to facilitate direct observation and manipulation of epithelial cell behaviors [6–14]. Cultures of primary mammary tissues were first developed half a century ago [15, 16], but the past decade has seen significant improvements in and increasing utilization of 3D culture models [17–20]. While many conventional methods rely on immortalized cell lines or primary single cells, we use freshly isolated, murine mammary epithelial ducts, which we term "organoids." The organoid assay arose from a series of papers published in the Bissell and Werb Labs [17–19, 21]. There are technical differences among the papers, but all involve mechanical disruption, enzymatic digestion, and differential centrifugation to separate mammary epithelial organoids from surrounding adipocytes and stromal cells. Purified organoids can be embedded in various ECMs to model distinct epithelial programs.

Our recent studies have revealed many of the cellular mechanisms driving epithelial morphogenesis and demonstrated that the ECM microenvironment regulates the migration and dissemination of mammary epithelial cells [17, 22–24]. Normal development in vivo occurs within a basement membrane, and we use Matrigel, a basement membrane-rich ECM, as an experimentally convenient model for the normal ductal microenvironment. Culture of organoids in basal medium, without supplemental growth factors, induces formation of simple, bi-layered cysts, while culture with growth factor induces a stereotyped program of branching morphogenesis. In contrast, cancer progression involves breaks in the basement membrane, and the microenvironment around a tumor is enriched in collagen I [25–30]. We demonstrated that collagen I-rich microenvironments induce a conserved program of invasion and dissemination in normal and malignant mammary epithelium [23]. Conversely, defined mixtures of Matrigel and collagen I can reproduce a more physiological organization of the elongating TEB [24].

Building on our previously published methods [17, 22, 23, 31, 33–35], this protocol seeks to provide a comprehensive guide to utilizing the mammary organoid assay (Fig. 1a). We introduce several variations on the assay in different ECMs and growth conditions that model different aspects of epithelial development and disease. We also provide optimized protocols for immunofluorescence staining of organoids in 3D embedded culture and of tissue sections of whole mammary glands.
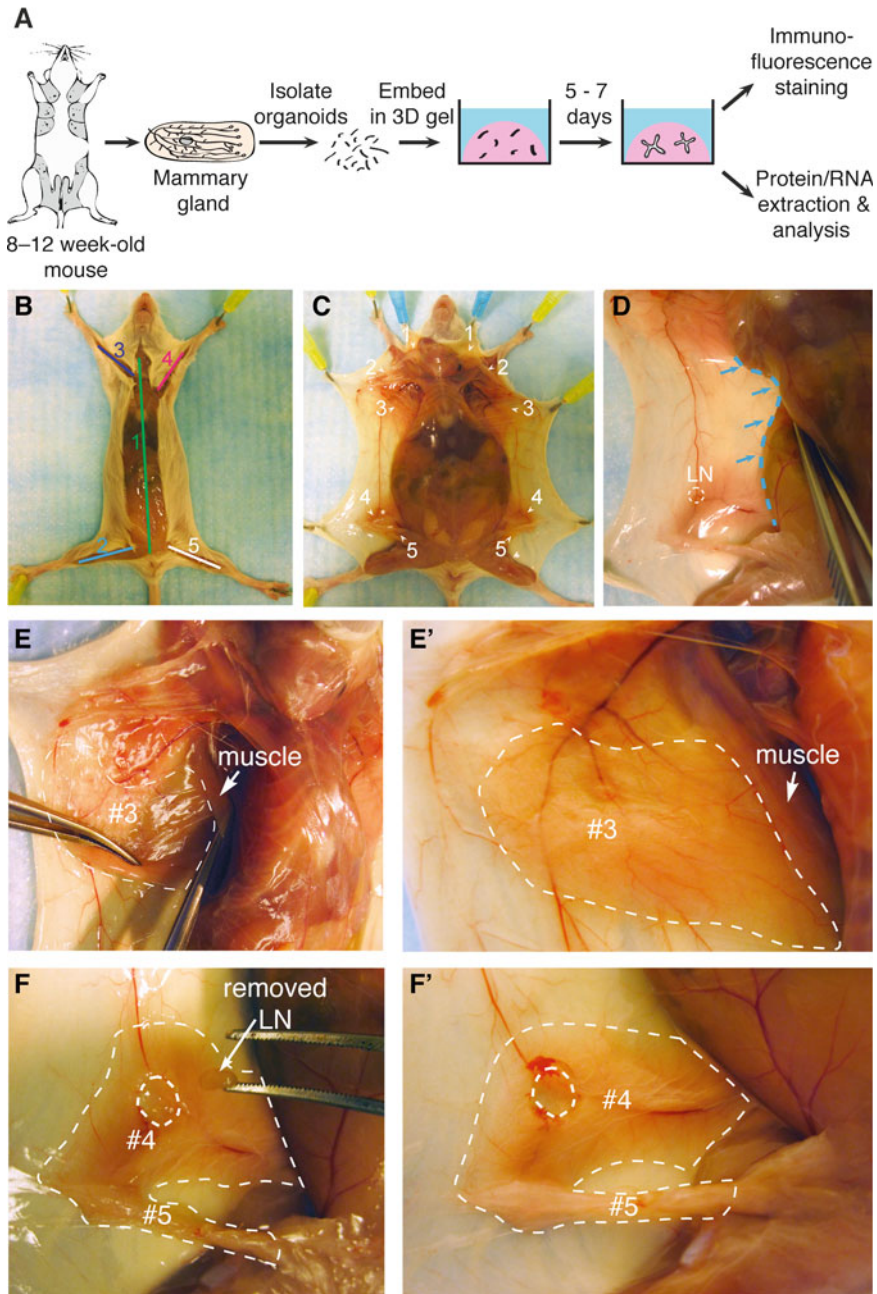
Fig. 1 Collection of mouse mammary glands for organoid isolation and 3D culture. (**a**) Schematic description of isolation and 3D culture of mouse mammary organoids. (**b**) Scheme for surgically accessing the mammary glands. Numbers indicate the order of cuts. (**c**) Locations of the ten mammary glands. (**d**) Expose glands #3, #4, and #5 by pushing back the abdomen (*blue dotted line*) with the back of the Graefe forceps. (**e–e′**) A thin layer of muscle partially covers gland #3 (**e**) and should be pushed back before dissection (**e′**). *Dotted line* in (**e′**) indicates the region of gland #3 to be collected. (**f**) Use the Graefe forceps to pluck out the lymph node in gland #4. *Dotted line* in (**f′**) indicates the approximate region of glands #4 and #5 to be collected (Color figure online)

2 Materials

2.1 Mice

We have successfully isolated and cultured organoids from mice ranging in age from E18.5 through 1.5 years. There are variations in response to growth factors with age and strain. All protocols below are optimized for FVB mice between 8 and 12 weeks of age. Once euthanized, mammary tissue is optimally isolated and cultured immediately, but successful organoid cultures have been established from mice sacrificed and then kept at 4 °C overnight.

2.2 Reagents

1. Collagenase solution in DMEM/F12: 2 mg/mL collagenase, 2 mg/mL trypsin, 5 % v/v fetal bovine serum (FBS), 5 μg/mL insulin, and 50 μg/mL gentamicin.

   (a) Collagenase from *Clostridium histolyticum* (Sigma C2139): Dissolve 1 g in 10 mL DMEM/F12, and make 200 μL aliquots. Store at −20 °C.

   (b) Trypsin: Dissolve 1 g in 10 mL DMEM/F12, and make 200 μL aliquots. Store at −20 °C.

2. Dulbecco's phosphate-buffered saline (DPBS, with Ca^{2+}, Mg^{2+}).

3. Phosphate-buffered saline (PBS, without Ca^{2+}, Mg^{2+}).

4. BSA solution: 2.5 % bovine serum albumin (BSA) in DPBS.

5. 2,000 U DNase (Sigma D4263): Dissolve in 1 mL of PBS, and make 40 μL aliquots. Store at −20 °C.

6. Organoid medium in DMEM/F12: 1 % penicillin/streptomycin and 1 % insulin-transferrin-selenium-X (ITS) (GIBCO 51500).

7. FGF2, 25 μg (Sigma F0291): Dissolve in 250 μL of PBS, and make 20 μL aliquots. Store at −20 °C.

8. Growth Factor Reduced Matrigel (Corning 354230).

9. Rat tail collagen I (Corning 354236).

10. DMEM 10×, low glucose.

11. 1.0 N NaOH.

12. 4 % paraformaldehyde (PFA) in DPBS.

13. OCT compound.

14. 0.5 % Triton X-100 in DPBS.

15. 10 % FBS in DPBS.

16. Mounting Medium (Sigma F4680-25ML).

17. Primary antibodies.

18. Secondary antibodies conjugated to fluorescent probes.

2.3 Instructions for Preparing Solutions

Prepare solutions as follows:

1. Collagenase solution (10 mL per mouse): Combine 9 mL DMEM/F12, 500 μL FBS, 5 μL insulin (10 mg/mL stock), 10 μL gentamicin (50 mg/mL stock), 200 μL collagenase (100 mg/mL stock), and 200 μL trypsin (100 mg/mL stock) in a 15 mL tube. Filter sterilize through a 0.2 μm filter into a new tube (Do not filter collagenase and trypsin stocks, the filter will get clogged). This solution should be made fresh for each experiment.

2. BSA solution: Combine 46 mL DPBS and 4.1 mL BSA (30 % stock solution). Filter sterilize, and store at 4 °C. This solution can be reused for several experiments if kept sterile but should be monitored for contamination.

3. Organoid medium: Remove 10 mL of DMEM/F12 from a 500 mL bottle of medium. Add 5 mL penicillin/streptomycin (10,000 units penicillin and 10 mg streptomycin/mL stock) and 5 mL ITS. For the branching morphogenesis assays (Subheadings 3.10.2 and 3.10.3) and the invasion assay (Subheading 3.10.4), supplement organoid medium with growth factor at the desired concentration. Diverse growth factors induce branching in the 1–10 nM range, including EGF ligands (EGF, TGF-α, amphiregulin, heregulin, neuregulin), FGF ligands (FGF2, FGF7), and HGF. We typically use 2.5 nM FGF2 for 8–12-week-old FVB mice. It is necessary to optimize the growth factor concentration for the specific age and strain of mouse.

2.4 Tools and Instruments

1. One Spencer Ligature scissors, delicate pattern (Fine Science Tools (FST) 14028–10): *For mouse exterior.*

2. One standard forceps, narrow pattern (FST 11003–12): *For mouse exterior.*

3. One Iris scissors, straight pattern (FST 14060–09): *For mouse interior (sterile).*

4. One Graefe forceps (FST 11051–10): *For mouse interior (sterile).*

5. Sterile scalpel, #10 blade.

6. Polystyrene Petri dish.

7. Benchtop incubator orbital shaker (Thermo Scientific MaxQ 4450).

8. Incublock™ microtube incubator with two blocks set to 37 °C (Denville Scientific Inc. I0540).

9. Ice bucket.

10. Centrifuge tubes, 15 and 50 mL.

11. Chambered coverglass, 2-well and 4-well (Nunc, Lab-Tek, Thermo Scientific).

12. SensoPlate, black, 24 W multiwell plate, glass bottom, sterile, w/lid (Greiner Bio-One 662892).

13. 24-Well glass plate cover (MatTek Corp P24GTOP-1.5-F).

14. Disposable base molds: $15 \times 15 \times 5$ mm, $24 \times 24 \times 5$ mm, and $30 \times 24 \times 5$ mm (Fisher Scientific).

15. Superfrost® Plus Gold precleaned microscope slides (Fisher Scientific 15-188-48).

16. Cover glass, 50×22 mm.

17. Orbital Shaker (Reliable Scientific, Inc.).

18. StainTray with black lid (Simport M920-2).

19. Cryostat.

3   Methods

3.1   Collecting Mouse Mammary Glands

Mice have five pairs of mammary glands located beneath the skin and outside the peritoneum. This section describes how to collect glands #3, #4, and #5 for organoid isolation and how to limit contamination by other tissues.

1. Generally, use female mice between 8 and 12 weeks old.

2. Sterilize the dissecting area with 70 % ethanol.

3. Sterilize the dissecting tools by heat in a glass bead sterilizer.

4. Euthanize the mouse in a CO_2-saturated chamber for 3–5 min followed by cervical dislocation.

5. Pin the mouse face up to a protected Styrofoam board.

6. Wet the mouse thoroughly with 70 % EtOH. Use the back of the standard forceps to smooth down the fur. Wipe away any feces with a 70 % EtOH-damp Kimwipe.

7. Use the standard forceps to grasp the skin above the groin.

8. Use the Spencer Ligature scissors to cut along the ventral midline from the groin to the chin (Fig. 1b). Be careful to cut only the skin and not the peritoneum underneath.

9. Make four incisions from the midline cut towards the four legs (Fig. 1b).

10. Use the standard forceps to pull back the skin one side at a time to expose the mammary glands (Fig. 1c). Use the dorsal side of the Graefe forceps to help separate the skin from the peritoneum (Fig. 1d).

11. Push back a thin yellow layer of muscle located on top of gland #3 to expose the mammary gland (Fig. 1e–e′).

12. Use the Graefe forceps to remove the inguinal lymph node located at the intersection of three blood vessels in gland #4 (Fig. 1f–f′).

13. Use the Graefe forceps and Iris scissors to grasp and pull out mammary glands #3, #4, and #5 from both right and left sides. Pool glands in a sterile Petri dish (Fig. 2a) (*see* **Note 1**).

3.2 Isolating Mammary Epithelial Organoids

Mammary epithelium is embedded inside a fat pad containing adipose tissue and collagen-rich stroma. This section describes how to purify fragments of mammary epithelium ("organoids") using enzymatic and mechanical digestion. All centrifugation speeds refer to a Sorvall Legend X1R benchtop swinging bucket centrifuge (1,500 rpm, 1,250 rcf). We have achieved similar results with 1,500 rpm spins in similar benchtop centrifuges from other manufacturers.

1. In a sterile hood, mince mammary glands with a scalpel, ~25–50 times per mouse, until the tissue relaxes (Fig. 2a, a′). Use a separate scalpel for each mouse type.

2. Use the scalpel to transfer the minced glands to collagenase solution in a 15 or a 50 mL tube (Fig. 2b). We use 10 mL of collagenase solution per mouse.

3. Shake the suspension at 110–150 rpm for 30–40 min (*see* **Note 2**) at 37 °C until the tissue breaks up into smaller pieces and is relatively dispersed (Fig. 2b′) but not overdigested (Fig. 2b″). We typically use a Thermo Scientific MaxQ 4450 for this purpose.

4. Spin the tube in a centrifuge at 1,500 rpm for 10 min at room temperature. The tube will have three layers: a fatty layer on top, an aqueous layer in the middle, and a red pellet of epithelium on the bottom (Fig. 2c).

5. Precoat (Fig. 3a) (*see* **Note 3**) a 15 mL tube with BSA solution. Use one tube per mouse type. For all subsequent steps, precoat all pipette tips and tubes with BSA solution prior to contact with mammary tissue (Fig. 3).

6. To recover additional epithelial tissue, use a BSA-coated pipette (Fig. 3b) to transfer the opaque fatty layer into the BSA-coated 15 mL tube. Add DMEM/F12 up to 10 mL. Pipette up and down vigorously to disperse the fatty layer (Fig. 2d). Spin the tube at 1,500 rpm for 10 min at room temperature. Aspirate the fat and supernatant, and save the pellet (Fig. 2e).

7. Aspirate (*see* **Note 4**) the aqueous layer in the tube with the original pellet.

8. Add 10 mL DMEM/F12 to the tube with the original pellet, and transfer to the 15 mL "fatty layer" tube (**step 6**). Pipette up and down vigorously to resuspend and combine the two pellets.
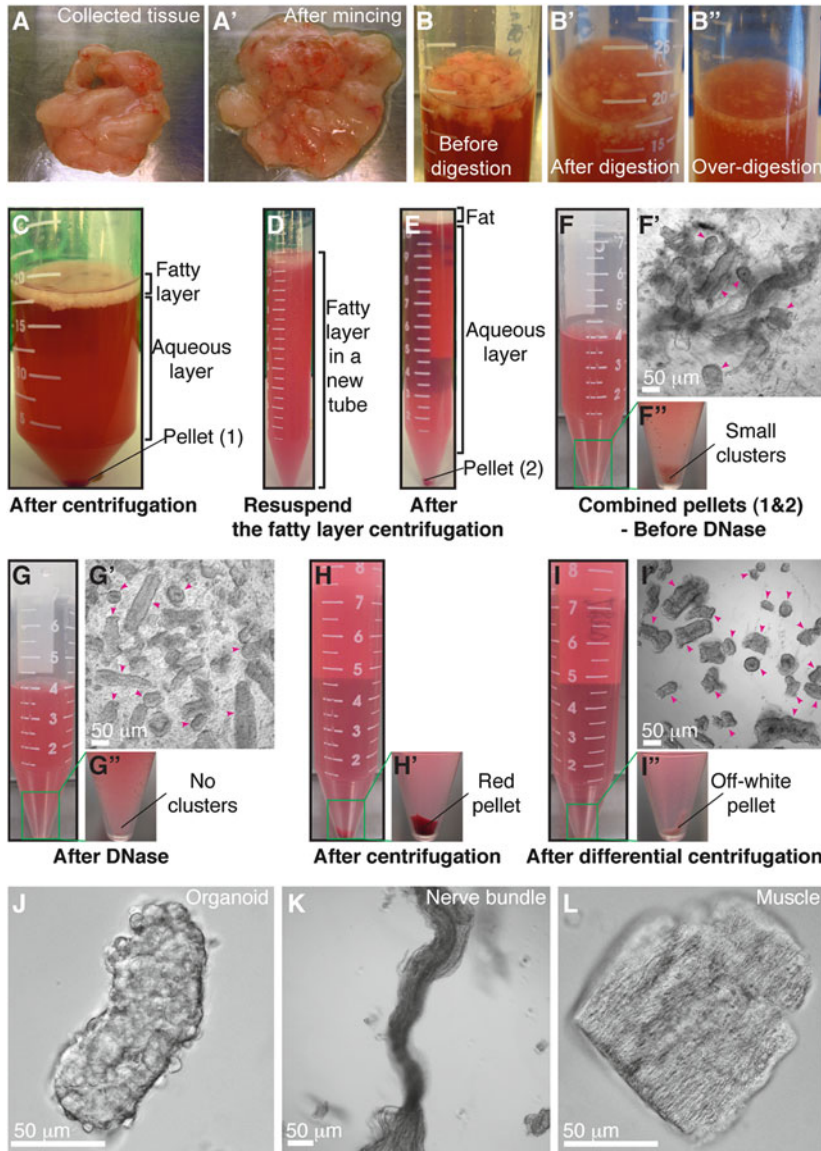
Fig. 2 Mammary organoid isolation. (**a–a′**) Collected mammary glands are pooled in a Petri dish (**a**) and minced until the tissue relaxes, typically 25–50 cuts (**a′**). (**b–b″**) Incubation in collagenase solution breaks up the fat pad (**b**) into smaller pieces that are relatively dispersed (**b′**). Too long of a digestion (**b″**) will cause organoids to be too small and not grow well. (**c**) Following incubation in collagenase solution, centrifugation separates the suspension into three layers, with a top opaque layer of fat and a pellet (#1) of epithelium and stroma. (**d**) The fatty layer is transferred to a new tube and resuspended in 10 mL DMEM/F12. (**e**) Centrifugation of the dispersed fatty layer recovers additional epithelium in the pellet (#2). (**f–f″**) The combined pellets from (**c**) and (**e**) are resuspended in 4 mL DMEM/F12 with DNase (**f**). Before DNase treatment, organoids (*pink arrowheads*) are loosely attached to each other and to stromal cells (**f′**), forming visible clusters in the tube (**f″**). (**g–g″**) DNase treatment causes organoids (*pink arrowheads*) to detach from one another (**g′**) and the clusters to disappear (**g″**). (**h–h′**) Centrifugation of the suspension in (**g**) results in a compact red pellet (**h′**). (**i–i″**) Differential centrifugation removes single cells from the suspension (**i′**) and results in an off-white pellet of purified epithelial organoids (**i″**). Organoids (*pink arrowheads*) may appear rounded and small or more elongated and even branched (**i′**). Larger organoids typically survive and branch more efficiently in our assays. (**j**) Close-up view of an organoid. (**k–l**) Non-epithelial tissues can be observed in the final suspension, including nerve bundles (**k**) and muscle (**l**) (Color figure online)
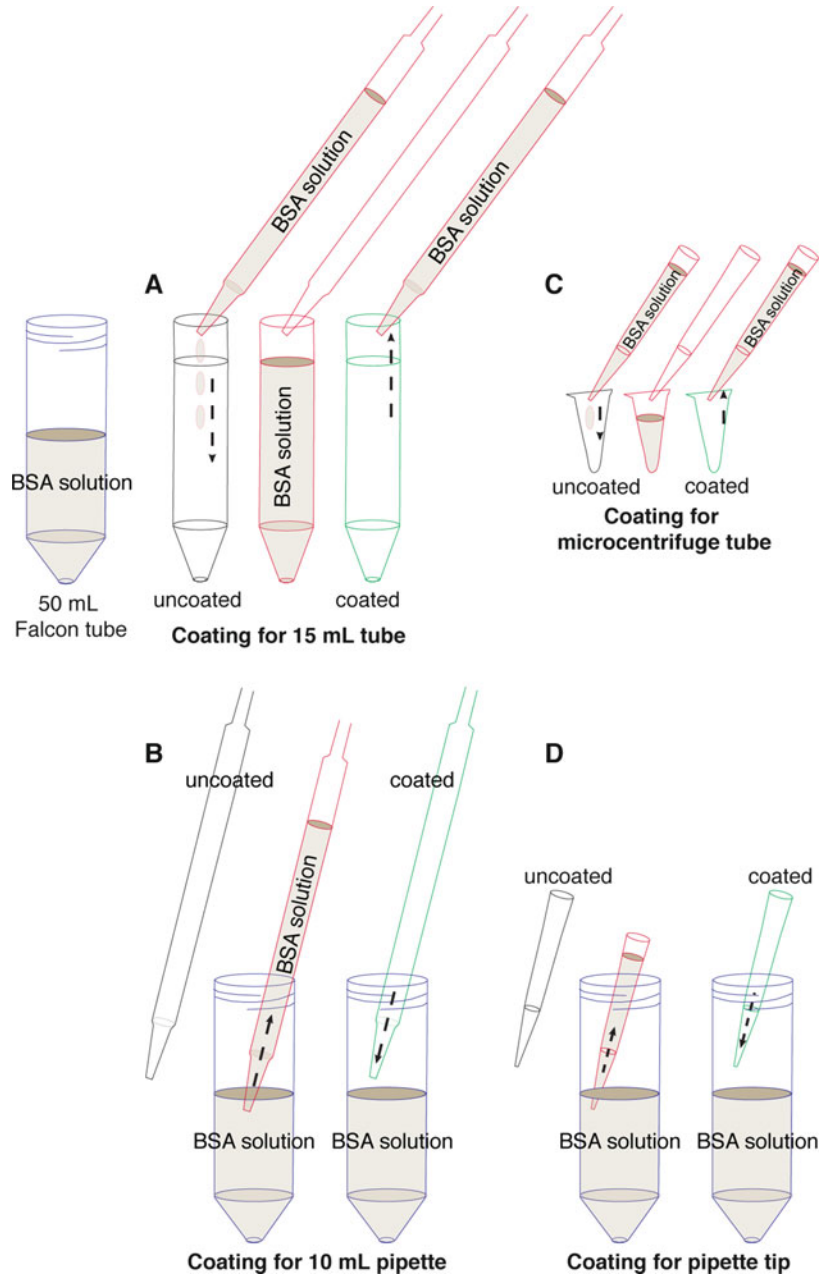
Fig. 3 Precoating tubes and pipette tips with BSA. Fresh tissue can adhere to uncoated plastic surfaces, and this protocol involves many pipetting steps. Accordingly, it is essential to precoat the plastic surfaces with BSA solution to maximize final organoid yield. (**a**) Precoat a 15 mL tube by filling the tube with BSA solution, inverting the tube to precoat the cap, and removing the BSA solution. (**b**) Precoat a 10 mL pipette tip by taking up BSA solution to fill the entire pipette and ejecting back out. (**c**, **d**) Use the same approach to precoat a microcentrifuge tube (**c**) and a small pipette tip (**d**) with BSA solution

9. Spin the tube at 1,500 rpm for 10 min at room temperature.

10. Aspirate the supernatant, and add up to 4 mL DMEM/F12 to the combined pellet (Fig. 2f). At this stage during isolation, the suspension contains small clusters of organoids and stromal cells attached to one another (Fig. 2f–f″).

11. Add 40 μL DNase (2 U/μL) into the 4 mL organoid suspension, and gently invert by hand for 2–5 min at room temperature to break up the clusters and detach organoids from single cells (Fig. 2g′–g″).

12. Add 6 mL of DMEM/F12, and pipette up and down thoroughly.

13. Spin tube at 1,500 rpm for 10 min at room temperature. The pellet should now appear red and more compact (Fig. 2h–h′).

    Next perform differential centrifugation to wash out enzymes and separate single stromal cells from the epithelial organoids. The protocol suggests aspiration of the supernatant assuming that the stromal cells will be discarded. If recovery of mammary stromal populations is desired, then transfer the supernatant after each spin to a 50 mL tube.

14. Aspirate the supernatant to the 0.5 mL mark.

15. Resuspend the pellet in 10 mL DMEM/F12, and mix thoroughly.

16. Pulse to 1,500 rpm, and stop the centrifuge 3–4 s after it reaches speed.

17. Repeat **steps 14–16** three more times (*see* **Note 5**).

18. The final pellet should be off-white and consist mostly of organoids, without single cells (Fig. 2i–i″, j). However, the organoid suspension may be contaminated with other tissue types, most commonly fiber bundles (Fig. 2k) and muscle (Fig. 2l).

3.3 Organoid Density Determination

This section describes how to determine the density of the organoid suspension and the overall yield.

1. Resuspend the pellet in 10 mL DMEM/F12 to form a homogeneous mixture (*see* **Note 6**).

2. Mix thoroughly (e.g., by rocking the tube by hand), and transfer 50 μL of the suspension to a 30 mm Petri dish. Count the number of organoids in this sample volume under a microscope (Fig. 2i′, j).

3. Calculate the total number of organoids collected according to the following formula. For example, if 20 organoids were counted in a 50 μL sample removed from a 10 mL total volume (9,950 μL remaining), then the total number of organoids would be $(20/50) \times 9{,}950 = 3{,}980$ organoids:

$$\text{Total number of organoids} = \frac{\text{Number of organoids}}{\text{Sample volume (e.g., 50 μL)}}$$
$$\times \text{ Remaining volume (e.g., 9950 μL)}$$

4. Calculate the organoid density (*see* **Note 7**), and readjust to 1,000 organoids/mL to simplify allocation to ECM gels.

5. Calculate the number of organoids and the respective volume of suspension required for each experiment.

6. Aliquot the required volumes of organoid suspension into BSA-coated 1.5 mL microcentrifuge tubes (Fig. 3c), and spin the tubes at 1,500 rpm for 5 min at room temperature.

7. Carefully remove the supernatant so as not to disturb the pellet (*see* **Note 8**).

8. Calculate the volume of ECM solution required to reach a final density of two organoids/μL (*see* **Note 9**).

3.4 Plating Mammary Organoids in Matrigel

Mammary epithelium develops in vivo within a basement membrane. 3D culture in Matrigel, a basement membrane-rich gel, recapitulates important features of epithelial development [17, 19, 22, 23]. This section describes how to embed organoids in 3D Matrigel.

1. Thaw Matrigel at 4 °C for 3–4 h prior to plating. If the Matrigel is put at 4 °C to thaw at the start of the prep, it will be ready to use by the end of the prep. During plating, always keep Matrigel on ice.

2. Use a plate with a cover glass bottom for time-lapse imaging.

3. Preincubate the plate at 37 °C for 5 min.

4. Set up the tissue culture hood in preparation for plating (Fig. 4a).

5. Set the heating block to 37 °C, and place the plate in direct contact with the block (Fig. 4b–c′) (*see* **Note 10**).

6. Add the required volume of liquid Matrigel to a microcentrifuge tube with organoids. Since Matrigel is quite viscous, first pipette up and down slowly a few times to coat the tip and ensure an accurate volume.

7. Keep the Matrigel-containing tube on ice or in a cold block. Resuspend the organoid pellet gently to avoid introducing air bubbles. Do not try to take up the entire volume into the pipette tip while mixing.

8. Plate the appropriate volume of Matrigel/organoid suspension into the wells according to the following table (Fig. 5a). Pipette up and down to resuspend the organoids before plating each sample, and pipette out only until the first stop.
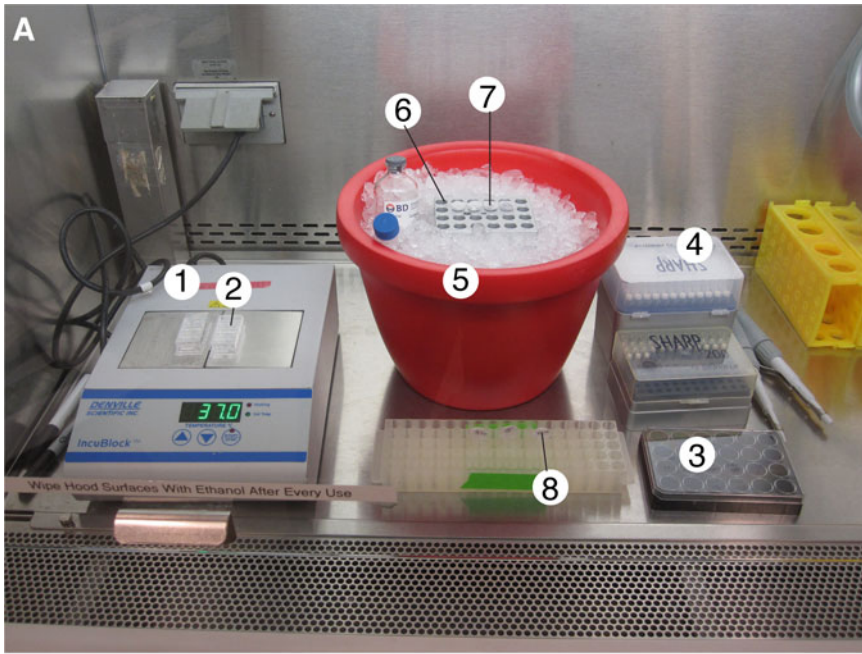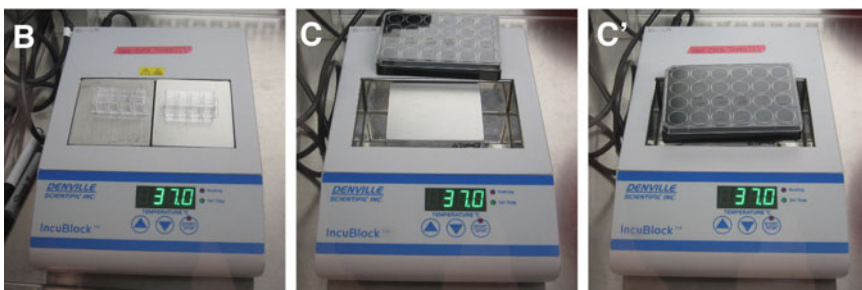
Fig. 4 Setting up the tissue culture hood for plating. (**a**) Sample layout of reagents, tools, and equipment used for plating 3D culture samples. (**b**) Heating block setup for plating in 2-well or 4-well chambers. (**c**, **c**′) To plate in a 24-well dish, remove one of the blocks from the heating block (**c**) to establish direct contact between the remaining block and the plate bottom (**c**′)

Type of plate	Volume of gel/well (µL)	Volume of medium/well (µL)
24-Well plate	50–150	750–1,000
4-Well chamber	50–75	750–1,000
2-Well chamber	150–300	1,500–2,000
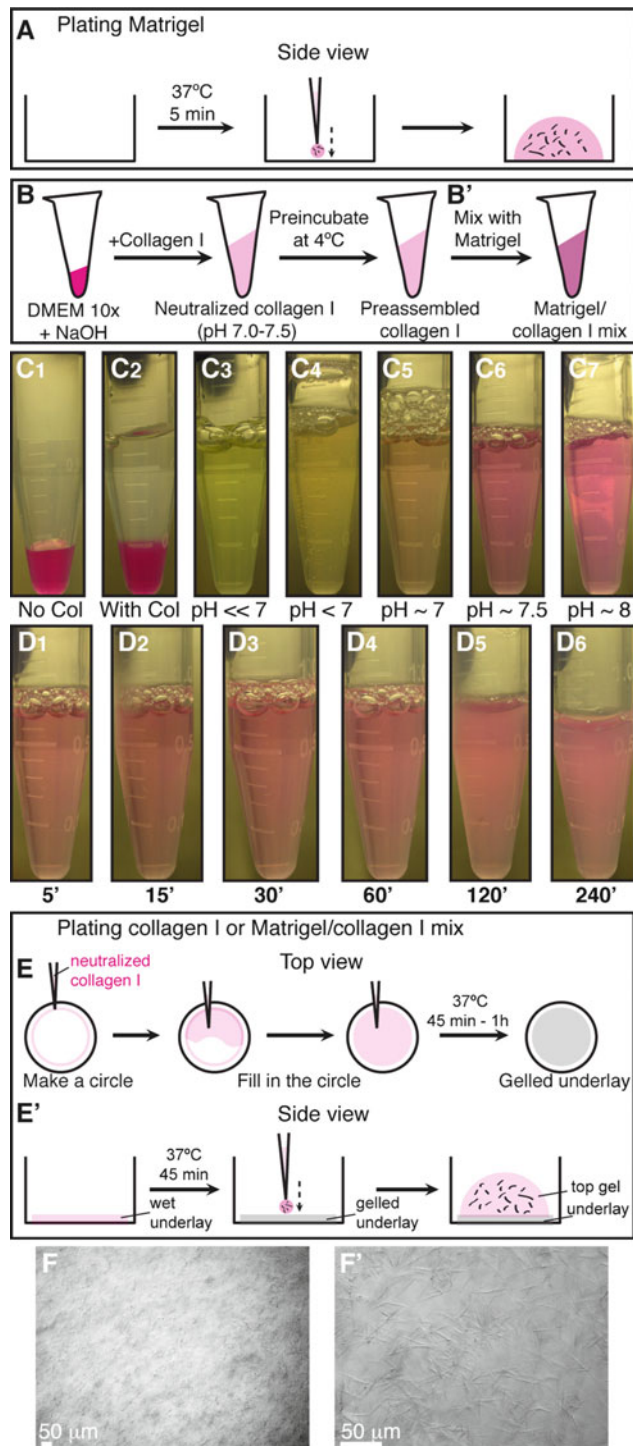
Fig. 5 Plating organoids in 3D Matrigel and collagen I. (**a**) Schematic description of plating organoids in Matrigel. (**b–b'**) Schematic description of preparing preassembled collagen I (**b**), which can be used alone or mixed with Matrigel (**b'**). (**c₁–c₇**) Color indicators for the pH of the collagen I solution during neutralization. (**d₁–d₆**) Decreasing transparency of the collagen I solution during preincubation on ice. (**e–e'**) Schematic description of plating organoids in 3D collagen I or in a mixture of Matrigel and collagen I. (**e**) Shows a top view for making an underlay on the cover glass. (**e'**) Shows a side view of how to plate the organoid/collagen I suspension on top of the gelled underlay. (**f–f'**) Representative DIC images of collagen I fibers at low (**f**) and high (**f'**) magnification (Color figure online)

9. Keep the plate on the heating block for several minutes to allow further gelation before returning it to the incubator.

10. Incubate the plate at 37 °C, 5 % CO_2, for 30–60 min.

11. Gently add pre-warmed organoid medium to the wells. For the cyst formation assay (Subheading 3.10.1), use basal medium without supplemental growth factors. For the branching morphogenesis assay (Subheading 3.10.2 and 3.10.3), supplement the medium with nanomolar concentrations of growth factor. A variety of growth factors may be used, including EGF ligands (EGF, TGF-α, amphiregulin, heregulin, neuregulin), FGF ligands (FGF2, FGF7), and HGF. We most commonly use 2.5 nM FGF2.

12. Add sterile water or PBS to the empty wells to prevent desiccation.

13. Label the wells. Return the plate to the incubator.

14. If the plate will be used for DIC imaging, use a glass plate cover for better image quality.

3.5 Preparing Collagen I Solution

Collagen I solubilized from rat tail is commonly used to study 3D migration of many cell types [32]. However, the properties of collagen I gels vary depending on multiple factors during preparation, such as temperature, pH, and collagen concentration. We demonstrated that the extent of collagen fiber assembly correlated strongly with invasive behavior [24]. This section describes how we prepare collagen I (Fig. 5b).

1. Rat tail collagen I is used to prepare a collagen solution according to the following formula. The steps below describe how to make a 250 μL solution. Scale up the volume as needed:

Total volume (μL)	250	500	1,000	2,000	5,000
1.0 N NaOH (μL)	8	16	32	64	160
DMEM 10× (μL)	25	50	100	200	500
Collagen I stock (μL)	217	434	868	1,763	4,340

2. Perform all steps on ice. To work with a large volume of collagen solution, use a 1,000 μL extra long pipette tip to avoid the collagen solution getting stuck to the filter barrier during pipetting.

3. First, combine 25 μL DMEM 10× and 8 μL NaOH, and mix well. The solution will turn a dark pink color (Fig. 5c$_1$).

4. Add 217 μL collagen I (Fig. 5c$_2$) (*see* **Note 11**). Since collagen I is quite viscous, pipette up and down slowly a few times to coat the pipette tip.

5. Mix the solution well until the color remains stable. When the pH changes from acidic → neutral → basic, the color changes from light green/yellow → light pink/orange → dark pink, respectively (Fig. 5c$_{3-7}$). The desired color is light pink or salmon, which corresponds to a pH of 7.0–7.5 (Fig. 5c$_6$) (*see* **Note 12**). The pH can be tested using pH strips.

6. Use DMEM 1× to adjust the neutralized collagen I solution to the desired collagen concentration (*see* **Note 13**). For the invasion assay (Subheading 3.10.4), we use a collagen concentration of 3 mg/mL.

3.6 Plating Mammary Organoids in Collagen I

Fibrillar collagen I, the most abundant structural protein in mammary glands, plays an important role in normal development as well as in breast cancer. Our previous studies have demonstrated that collagen I induces a conserved response of protrusive invasion in both normal and tumor organoids [23]. This section describes how to properly prepare preassembled collagen I and embed mammary organoids in a 3D gel.

1. Use a plate with a glass bottom for time-lapse imaging.

2. Use 20–30 μL of neutralized collagen to make a thin underlay on the cover glass of the well at room temperature (Fig. 5e). The underlay helps the top collagen/organoid suspension attach better to the cover glass.

3. Incubate the plate with the underlays at 37 °C until ready for plating.

4. Preincubate the neutralized collagen I solution (used for the top gel) at 4 °C for 60–120 min for preassembly [24] (*see* **Note 14**). The collagen I solution will turn cloudy and fibrous (Fig. 5d$_{1-6}$) (*see* **Note 15**), a state we term preassembled collagen I.

5. Set up the tissue culture hood in preparation for plating (Fig. 4a).

6. Set the heating block to 37 °C, and place the plate on top, in direct contact with the block (Fig. 4b–c′) (*see* **Note 10**).

7. Always keep the collagen I solution on ice. Add the desired amount of preassembled collagen I to the organoid pellet in a microcentrifuge tube. Since collagen I is quite viscous, first pipette up and down slowly a few times to coat the tip and ensure an accurate volume.

8. Keep the tube on ice or in a cold block. Resuspend the organoid pellet gently to avoid introducing air bubbles. Do not try to take up the entire volume into the pipette tip while mixing.

9. Plate the appropriate volume of collagen/organoid suspension (see table in Subheading 3.4) on top of the underlay (Fig. 5e′). Pipette up and down to resuspend the organoids before plating each sample, and pipette out only until the first stop.

10. Keep the plate on the heating block for several minutes to allow further gelation before returning it to the incubator (*see* **Note 16**).

11. Incubate the plate at 37 °C, 5 % CO_2, for 45–60 min. After gelation, collagen I fibrils are visible under the microscope at 10× and 40× (Fig. 5f–f′).

12. Gently add pre-warmed organoid medium supplemented with growth factor to the wells. A variety of growth factors may be used, including EGF ligands (EGF, TGF-α, amphiregulin, heregulin, neuregulin), FGF ligands (FGF2, FGF7), and HGF. We most commonly use 2.5 nM FGF2.

13. Add sterile water or PBS to the empty wells to prevent desiccation.

14. Label the wells. Return the plate to the incubator.

15. If the plate will be used for DIC imaging, use a glass plate cover for better image quality.

3.7 Plating Mammary Organoids in a Mixture of Matrigel and Collagen I

A mixture of Matrigel and collagen I represents a more physiological ECM microenvironment for mammary branching morphogenesis. The presence of collagen I significantly improves epithelial ductal elongation and myoepithelial coverage [24]. We do not observe epithelial protrusions into mixed Matrigel/collagen I gels [24]. This section describes how to properly prepare a mixture of Matrigel and preassembled collagen I and how to embed mammary organoids in this mixed matrix.

1. Prepare collagen I solution as described in Subheading 3.5.

2. Repeat **steps 1–4** in Subheading 3.6 to make underlays and prepare preassembled collagen I.

3. Combine Matrigel and preassembled collagen I at the desired ratio. Gently pipette up and down a few times to form a homogeneous solution (Fig. 5b′).

4. Always keep the mixed matrix solution on ice. Add the desired amount to the organoid pellet in a microcentrifuge tube.

5. Plate the mixed matrix/organoid suspension as described in **steps 5–15** in Subheading 3.6 (Fig. 5e′).

3.8 Immuno-fluorescence Staining of 3D Culture Samples

The thickness of 3D gels and the multicellular structure of mammary organoids often result in reduced antibody accessibility for immunofluorescence (IF) staining and poor visualization during imaging.

This section describes two methods for performing IF staining in 3D culture samples. First, fix gels as follows:

1. Remove organoid medium from the wells.

2. Fix samples with 4 % PFA for 10–15 min at room temperature (*see* **Note 17**) on an orbital shaker at 20 rpm.

3. Remove PFA, and wash samples 2–3× 10 min with DPBS.

From here, you can perform antibody staining directly in intact 3D gels or on cut sections on slides. The whole-gel staining works well with high-quality antibodies and probes such as phalloidin (stains for F-actin), smooth muscle actin (SMA), and keratin 14. For many other antibodies, staining sections on slides is preferable.

3.8.1 Staining Whole Gels

1. Permeabilize the gel with 0.5 % Triton X-100 for 30–60 min.

2. After permeabilization, immediately block samples with 10 % FBS (*see* **Note 18**) for 1–3 h at room temperature or overnight at 4 °C.

3. Remove the blocking solution, add primary antibody in 10 % FBS (*see* **Note 18**) at the desired ratio, and incubate for 2–3 h at room temperature or overnight at 4 °C.

4. Remove the primary antibody solution, and wash samples 3× 10 min with 10 % FBS in DPBS at room temperature.

5. Optional: Block the samples again with 10 % FBS for 30–60 min at room temperature.

6. Add secondary antibody in 10 % FBS (*see* **Note 18**) at the desired ratio, and incubate for 1–2 h at room temperature.

7. Wash 3× 10 min with DPBS at room temperature.

8. Store samples in DPBS at 4 °C, but remove DPBS before imaging. If the gel has detached from the cover slip, leaving the DPBS in the well causes the gel to wiggle or float and go out of focus.

3.8.2 Staining Sections on Slides

1. Gently detach the gel from the culture plate and transfer to a small disposable base mold (15 × 15 × 5 mm) filled with a thin layer of OCT.

2. Freeze the mold at −80 °C for 5–10 min.

3. Fill up the mold with OCT to cover the sample, and return to −80 °C for long-term storage.

4. During sectioning, store molds on dry ice. Set up the cryostat with OT at −20 °C and CT at −20 °C.

5. Remove an OCT block from its mold, and cut sections at 20–100 μm thickness.

6. Transfer sections to slides using a fine camel hair brush or a pair of forceps.

7. Keep slides at −80 °C for long-term storage.

8. For antibody staining, thaw slides at room temperature (*see* **Note 19**).

9. Wash slides 2–3× 10 min with DPBS to remove OCT.

10. Permeabilize with 0.5 % Triton X-100 for 30–60 min (*see* **Note 20**).

11. Wash 2× 10 min with DPBS to remove Triton.

12. Block slides with 10 % FBS for 2 h at room temperature or overnight at 4 °C.

13. Remove the blocking solution, add primary antibody in 10 % FBS, and incubate for 2–3 h at room temperature or overnight at 4 °C (*see* **Note 21**).

14. Wash 3× 10 min with 10 % FBS or DPBS.

15. Add secondary antibody in 10 % FBS, and incubate for 2 h at room temperature or overnight at 4 °C.

16. Wash 3× 10 min with DPBS.

17. Mount slides with mounting medium and 50 × 22 mm coverslips. Let the slides dry at room temperature in a dry StainTray or in a dark drawer before imaging.

3.9 Immuno-fluorescence Staining of Mammary Gland Tissue Sections

The opacity and thickness of the mammary fat pad limit the accessibility of mammary epithelium to whole-gland staining and imaging. This section describes how to perform IF staining in mammary gland tissue sections.

1. Collect mouse mammary glands #3 and/or #4, as described in Subheading 3.1, taking care to keep the entire gland intact (*see* **Note 22**). Spread out the gland on the bottom of a 1- or a 2-well chambered cover glass.

2. Fix the tissue with 4 % PFA for 4 h at room temperature or overnight at 4 °C.

3. Wash 3× 15 min with DPBS to remove PFA.

4. Transfer the gland to a medium (24 × 24 × 5 mm) or a large (30 × 24 × 5 mm) disposable base mold filled with a thin layer of OCT.

5. Freeze the mold at −80 °C for 5–10 min.

6. Fill up the mold with OCT to cover the gland, and return to −80 °C for long-term storage.

7. During sectioning, store molds on dry ice. Set up the cryostat with OT at −40 °C and CT at −30 °C.

8. Remove an OCT block from its mold, and cut sections at 50–200 μm thickness.

9. Transfer sections to slides using a fine camel hair brush or a pair of forceps.

10. Keep slides at $-80\,^{\circ}C$ for long-term storage.

11. Repeat **steps 8–17** in Subheading 3.8.2 for IF staining (*see* **Note 23**).

3.10 Assays

In vivo, mammary epithelium develops within a basement membrane surrounded by collagen-rich stromal tissue. The ability to manipulate the ECM microenvironment in 3D organotypic culture allows us to isolate the effects of individual matrix components on mammary epithelial cell behaviors. This section describes four assays that use different ECM compositions or growth conditions to model distinct epithelial programs (Fig. 6a).

3.10.1 Cyst Formation Assay

In 3D Matrigel in basal medium, mammary organoids reorganize from a multilayered fragment to establish a simple bi-layered epithelium with an internal lumen, termed a cyst (Figs. 6b and 7a). The extent of lumen formation varies with the initial size of the organoid and with the mouse strain (Fig. $7a_1$–a_4). The resulting morphologies include a minimal or a barely detectable lumen (Fig. $7a_1$), a partial lumen (Fig. $7a_2$), a complete lumen in a small cyst (Fig. $7a_3$), and a complete lumen in a large cyst (Fig. $7a_4$). Epithelial cells in the cyst always maintain a smooth basal surface with the ECM (Fig. $7a_{4'}$). We have observed that C57BL6 organoids form cysts with complete lumens (Fig. 6b) more efficiently than FVB organoids. Although the appearance of the lumen varies by light microscopy, immunofluorescence staining for SMA and F-actin can confirm the establishment of a simple bi-layered structure of internal luminal epithelial cells and basal myoepithelial cells (Fig. 8a). We use this assay to model the formation of mammary epithelial ducts in vivo (Fig. 8d).

3.10.2 Branching Morphogenesis Assay in Matrigel

In 3D Matrigel, nanomolar concentrations of growth factor induce mammary organoids to undergo branching morphogenesis (Fig. 6c). The branching program includes sequential steps of lumen clearing, stratification, bud initiation, and bud elongation (Fig. 6c) [17]. We observe variation in morphology depending on the extent of progression through this program. Organoids that only complete stratification or bud initiation (Fig. $7b_1$), or that form fewer than three buds (Fig. $7b_2$–b_4), are not scored as "branched" (Fig. 7b). Only organoids with three or more elongated buds are scored as "branched" (Fig. 7c). However, the morphology of branched organoids varies based on the initial size of the organoid, the mouse strain, and the types of growth factors added. Here, we present four examples of branching in Matrigel (Fig. $7c_1$–c_4). The first two show organoids with multiple multilayered, elongating buds without any regions of repolarization

Fig. 6 3D organotypic culture assays. (**a**) Schematic description of four assays that use different extracellular matrix compositions to model specific epithelial behaviors. (**b**–**e**) Representative frames of DIC time-lapse movies showing cyst formation in Matrigel in basal medium (**b**), branching morphogenesis in Matrigel induced by FGF2 (**c**), branching morphogenesis in a mixture of Matrigel and collagen I induced by FGF2 (**d**), and epithelial cell invasion into pure collagen I induced by FGF2 (**e**)

(Fig. 7c$_1$–c$_2$). In contrast, the second two show organoids that have reestablished simple epithelial architecture in the central lumen (Fig. 7c$_3$) or within buds (Fig. 7c$_4$). During bud elongation in Matrigel, the leading front of the bud is always non-protrusive (Fig. 7b$_{4'}$, c$_{4'}$). Notably, these buds lack or are incompletely covered by myoepithelial cells (SMA$^+$, Fig. 8b). These gaps in myoepithelial coverage can be observed in vivo, particularly in side branches of the mammary ductal tree (Fig. 8e).

3.10.3 Branching Morphogenesis Assay in a Mix of Matrigel and Collagen I

In a mixture of Matrigel and collagen I, mammary organoids undergo a similar program of branching morphogenesis to that in Matrigel alone, with several notable differences [24] (Fig. 6d). Branched organoids in the mixed matrix generally have fewer

Fig. 7 Phenotypic variability in assay outcomes. (**a**) Schematic description of a cyst. (**a₁–a₄**) DIC images showing variation in cyst morphology. (**a₄'**) An inset of (**a₄**) showing a smooth basal surface with Matrigel. (**b**) Schematic description of a stratified, unbranched organoid. (**b₁–b₄**) DIC images showing examples of stratified, unbranched organoids in Matrigel. (**b₄'**) An inset of (**b₄**) showing a smooth basal surface with Matrigel. (**c**) Schematic description of a branched organoid in Matrigel. (**c₁–c₄**) DIC images showing variation in branching morphology. (**c₄'**) An inset of (**c₄**) showing a smooth basal surface with Matrigel. (**d**) Schematic description of a branched organoid in a mixture of Matrigel and collagen I. (**d₁–d₄**) DIC images showing variation in branching morphology. (**d₄'**) An inset of (**d₄**) showing a smooth basal surface with the mixed matrix. (**e**) Schematic description of an organoid with protrusive tips in collagen I. (**e₁–e₄**) DIC images showing

buds, but the buds elongate much further into the ECM. We have demonstrated that ratios of 5:5 and 3:7 Matrigel to collagen I induce the highest average bud lengths [24]. Here, we present four examples of branching in the mixed matrices. Organoids may contain both short and long buds, without repolarization (Fig. $7d_1$) or with partial repolarization (Fig. $7d_2$, d_4). We also observe bifurcation at the ends of elongated buds (Fig. $7d_3$). As in Matrigel alone, the leading front of the bud is always non-protrusive (Fig. $7d_{4'}$). Importantly, a mix of 3:7 Matrigel to collagen I yields a high percentage of epithelial buds that maintain complete myoepithelial coverage throughout bud initiation and elongation (Fig. 8c). This phenomenon more closely models elongation of the terminal end bud in vivo (Fig. 8f).

3.10.4 Invasion Assay

Collagen I induces a conserved protrusive response in mammary epithelium (48 h, Fig. 6e). Organoids invade collectively into collagen I, with branches varying in shape and length, from short and thin (Fig. $7e_1$–e_2) to elongated and wide (Fig. $7e_3$–e_4). Initially, we observe extensive subcellular protrusions. However, these protrusions cease, and the epithelium reestablishes a smooth basal surface upon formation of a basement membrane between the epithelium and ECM (Fig. 6e) [23]. The extent of invasion and epithelial reorganization varies, even within the same organoid. At day 5 in culture, we observe both protrusive (*violet arrowheads*, Fig. $7e_{4'}$) and non-protrusive, round tips (*violet filled arrowheads*, Fig. $7e_1$–e_4) at the ends of multicellular invasive structures. We also observe single cell dissemination into collagen I (*blue arrowheads*, Fig. $7e_1,e_4$).

3.11 Technical Issues

Here we present several technical problems that we commonly encounter during 3D culture. First, epithelial organoids located very close to the cover glass tend to lose their 3D structure and spread out in 2D as sheets of cells (Fig. $7f_1$–f_2). Second, organoids may be surrounded by protrusive or stringy cells, which likely results from stromal or other non-epithelial cells attaching to organoids during their isolation (Fig. $7f_3$). Non-epithelial contaminating species appear distinct and behave differently from organoids.

◄

Fig. 7 (continued) variation in protrusive invasion. ($e_{4'}$) An inset of (e_4) showing protrusive tips into collagen I. (**f**) DIC images showing commonly observed technical issues. (f_1–f_2) Organoids lose their 3D organization in Matrigel (f_1) and collagen I gels (f_2) when they make contact with the cover glass. (f_3) Non-epithelial species (*red arrowheads*) attached to organoids may appear elongated and mesenchymal (ECM: Matrigel). (f_4) A group of dead cells beside a branching organoid (ECM: collagen I). (f_5) A cluster of elongated, non-epithelial cells (ECM: Matrigel). (f_6) A nerve bundle disseminating single cells into the surrounding matrix (ECM: Matrigel) (Color figure online)
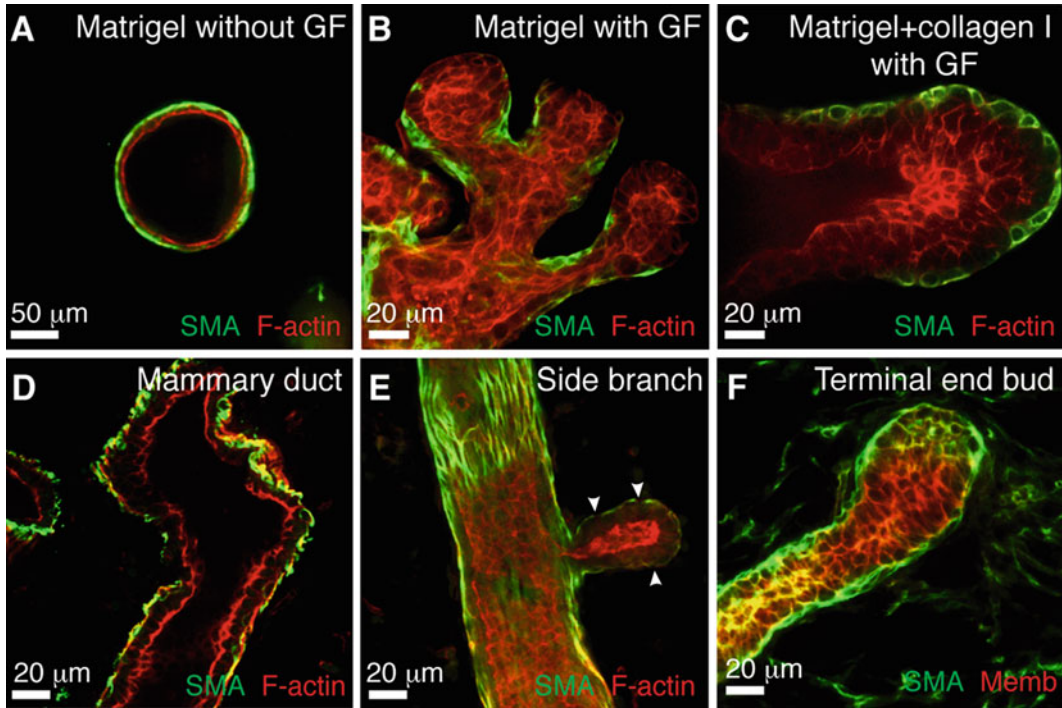
Fig. 8 Correlation between epithelial morphologies in 3D organotypic assays and in vivo. (**a–c**) Representative confocal images of a cyst in Matrigel (**a**), branched buds in Matrigel (**b**), and a stratified, elongating bud in a mixture of Matrigel and collagen I (**c**). (**d–f**) Representative confocal images from mammary gland tissue sections of a bilayered duct (**d**), a side branch (**e**), and a terminal end bud (**f**)

We have observed groups of dead cells (Fig. 7f$_4$), clusters of protrusive stromal cells (Fig. 7f$_5$), and nerve bundles (Fig. 7f$_6$), which tend to locally disseminate cells into the matrix.

4   Notes

1. Mammary gland #1 is very small. Mammary gland #2 is located in the neck and is hard to distinguish from other tissues. Generally, do not collect these glands so as to avoid contamination by other tissues (e.g., muscle or other epithelial glands) (Fig. 2l).

2. Incubation in collagenase solution can require up to 60 min to adequately break up the fat pad. Check the status of the suspension after 30 min of shaking. We have observed that inappropriate incubation times increase the amount of contaminating tissues in the final organoid suspension (Fig. 2k). If shaking is done in an incubator that is also used for bacterial cultures, wipe the outside of the tube with 70 % ethanol before bringing it into the tissue culture hood.

3. Always precoat new pipette tips and tubes with BSA solution to prevent organoids from sticking to the plastic. This precoating (Fig. 3) is critical to achieving a high final yield of organoids, especially with mice at younger ages or mice on a C57BL6 background.

4. Never aspirate the supernatant completely to avoid sucking up the pellet.

5. Carefully examine the pellet after each quick spin before aspirating the supernatant. If the organoids are not well pelleted, mix the suspension thoroughly again, and increase the centrifugation time.

6. The appropriate volume of DMEM/F12 to use for counting varies depending on the estimated yield. If the yield is low, add less medium. If the yield is high, dilute the suspension further 2–10×.

7. The yield varies significantly with mouse strain and age. We generally obtain 2,000–4,000 organoids per FVB mouse and 500–2,000 organoids per C57BL6 mouse.

8. Always check the pellet after every centrifugation. Be careful not to disturb the pellet when removing the supernatant. Use small pipette tips if necessary.

9. The optimal density of organoids in the gel differs for different ECMs and mouse strains. For example, C57BL6 organoids tend to be more contractile than FVB organoids when embedded in collagen I, resulting in contraction of the gel and detachment from the glass bottom if plated too densely.

10. In a 24-well plate, the glass bottom is slightly recessed from the edge of the plastic wall. When both blocks are present in the heating block (Fig. 4b), there is a small gap between the plate and the heating block surface, resulting in a temperature at the glass bottom less than 37 °C. To establish direct contact between the glass bottom and the heating block, remove one of the blocks, and set up the plate as in Fig. 4c–c'.

11. When preparing the collagen I solution, always wait for the solution to come down to the tip, and pipette it out completely. This is particularly important during collagen I neutralization to ensure an accurate volume and concentration of collagen.

12. Since the concentration and pH of rat tail collagen I vary among batches, adjust the pH using small volumes of collagen stock (up to 30 μL) or small amounts of 1.0 N NaOH (<0.5 μL).

    (a) If the adjustment requires addition of a large amount of collagen I stock, you will need to add more DMEM 10× to maintain ionic balance. However, this complicates

calculation of the final concentration of neutralized collagen solution.

(b) If you find that your collagen I stock is more basic, prepare the collagen solution with 7.0–7.5 μL of 1.0 N NaOH per 250 μL, and then adjust the final pH with small volumes of 1.0 N NaOH. This will avoid the need to add large volumes of collagen I stock to achieve the appropriate pH.

13. If you are concerned about the accuracy of the final collagen concentration, try to use the same pipette tip for mixing throughout neutralization and pH adjustment to limit the loss of collagen solution inside the pipette tip.

14. The preincubation time will determine the density of preassembled collagen fibrils. Due to batch variability in collagen stocks, the time required to obtain a gel with visible collagen fibrils varies considerably from 45 to 120 min. To examine the extent of fibril formation during preincubation, plate 30 μL of collagen solution onto a small Petri dish, let it gel for several minutes, and examine under the microscope.

15. If the neutralized collagen I solution is preincubated for more than 3–4 h on ice, it will become very cloudy and fibrous (Fig. 5d$_6$), and the resulting gel will be less transparent, impairing visibility during imaging.

16. Collagen I gels tend to detach from the cover glass when kept too long on the heating block. Therefore, if you have Matrigel and collagen I gels on the same plate, plate the Matrigel samples first and the collagen I samples last.

17. In PFA, Matrigel becomes very fragile, especially after more than 4 days in culture. To avoid disintegration of the gel, reduce the PFA concentration to 2 % with lighter shaking or incubate the gel with 4 % PFA for 8–10 min.

18. In our lab, we have identified two successful approaches for performing antibody staining that use slightly different solutions and incubation times. The first one, described in Subheadings 3.8 and 3.9, uses 10 % FBS in DPBS as both the blocking buffer and the dilution buffer for antibodies. The other method uses 10 % FBS and 1 % BSA in DPBS as a blocking buffer and 1 % FBS and 1 % BSA in DPBS as the dilution buffer for antibodies.

19. From this step on, slides are kept in a StainTray with a black lid filled with a shallow layer of water to prevent desiccation and photo-bleaching of fluorescent probes.

20. If you plan to stain for extracellular proteins, such as basement membrane components, permeabilize the samples before embedding into OCT and sectioning. Direct permeabilization on slides can extract too many of these proteins.

21. To conserve primary antibodies, especially ones that require a high concentration, use a PAP pen to draw a hydrophobic border around the section, and add primary antibody solution within this area.

22. For mice less than 4 weeks of age, we typically use only gland #4 and remove the fat pad distal to the lymph nodes. Since the glands at this age are very small, pool several glands into one OCT block for sectioning.

23. To improve antibody staining in mammary gland tissue sections, it is sometimes useful to significantly increase the incubation times. For example, we sometimes permeabilize with Triton X-100 for 1 h at room temperature; incubate with primary antibody for 48 h at 4 °C; and incubate with secondary antibody for 6 h at room temperature or overnight at 4 °C. In addition, for incubation with antibodies, it is preferable to draw a hydrophobic border around the tissue with a PAP pen to reduce the volume of solution required and to ensure that the tissue is always immersed in solution. Do not let samples air-dry.

Acknowledgements

References

1. Sternlicht MD (2006) Key stages in mammary gland development: the cues that regulate ductal branching morphogenesis. Breast Cancer Res 8:201

2. Hogg NA, Harrison CJ, Tickle C (1983) Lumen formation in the developing mouse mammary gland. J Embryol Exp Morphol 73:39–57

3. Williams JM, Daniel CW (1983) Mammary ductal elongation: differentiation of myoepithelium and basal lamina during branching morphogenesis. Dev Biol 97:274–290

4. Hinck L, Silberstein GB (2005) Key stages in mammary gland development: the mammary end bud as a motile organ. Breast Cancer Res 7:245–251

5. Sternlicht MD, Kouros-Mehr H, Lu P, Werb Z (2006) Hormonal and local control of mammary branching morphogenesis. Differentiation 74:365–381

6. Mroue R, Bissell MJ (2012) Three-dimensional cultures of mouse mammary epithelial cells. Methods Mol Biol 945:221–250

7. Vidi PA, Bissell MJ, Lelievre SA (2012) Three-dimensional culture of human breast epithelial cells: the how and the why. Methods Mol Biol 945:193–219

8. Griffith LG, Swartz MA (2006) Capturing complex 3D tissue physiology in vitro. Nat Rev Mol Cell Biol 7:211–224

9. Gudjonsson T, Ronnov-Jessen L, Villadsen R, Bissell MJ, Petersen OW (2003) To create the correct microenvironment: three-dimensional heterotypic collagen assays for human breast epithelial morphogenesis and neoplasia. Methods 30:247–255

10. Nelson CM, Bissell MJ (2005) Modeling dynamic reciprocity: engineering three-dimensional culture models of breast

architecture, function, and neoplastic transformation. Semin Cancer Biol 15:342–352

11. Nelson CM, Inman JL, Bissell MJ (2008) Three-dimensional lithographically defined organotypic tissue arrays for quantitative analysis of morphogenesis and neoplastic progression. Nat Protoc 3:674–678

12. Wozniak MA, Keely PJ (2005) Use of three-dimensional collagen gels to study mechanotransduction in T47D breast epithelial cells. Biol Proced Online 7:144–161

13. Provenzano PP, Eliceiri KW, Inman DR, Keely PJ (2010) Engineering three-dimensional collagen matrices to provide contact guidance during 3D cell migration. Curr Protoc Cell Biol Chapter 10:Unit 10 17

14. Debnath J, Muthuswamy SK, Brugge JS (2003) Morphogenesis and oncogenesis of MCF-10A mammary epithelial acini grown in three-dimensional basement membrane cultures. Methods 30:256–268

15. Ichinose RR, Nandi S (1964) Lobuloalveolar differentiation in mouse mammary tissues in vitro. Science 145:496–497

16. Ichinose RR, Nandi S (1966) Influence of hormones on lobulo-alveolar differentiation of mouse mammary glands in vitro. J Endocrinol 35:331–340

17. Ewald AJ, Brenot A, Duong M, Chan BS, Werb Z (2008) Collective epithelial migration and cell rearrangements drive mammary branching morphogenesis. Dev Cell 14:570–581

18. Simian M, Hirai Y, Navre M, Werb Z, Lochter A, Bissell MJ (2001) The interplay of matrix metalloproteinases, morphogens and growth factors is necessary for branching of mammary epithelial cells. Development 128:3117–3131

19. Fata JE, Mori H, Ewald AJ, Zhang H, Yao E, Werb Z, Bissell MJ (2007) The MAPK(ERK-1,2) pathway integrates distinct and antagonistic signals from TGFalpha and FGF7 in morphogenesis of mouse mammary epithelium. Dev Biol 306:193–207

20. Nelson CM, Vanduijn MM, Inman JL, Fletcher DA, Bissell MJ (2006) Tissue geometry determines sites of mammary branching morphogenesis in organotypic cultures. Science 314:298–300

21. Sternlicht MD, Sunnarborg SW, Kouros-Mehr H, Yu Y, Lee DC, Werb Z (2005) Mammary ductal morphogenesis requires paracrine activation of stromal EGFR via ADAM17-dependent shedding of epithelial amphiregulin. Development 132:3923–3933

22. Ewald AJ, Huebner RJ, Palsdottir H, Lee JK, Perez MJ, Jorgens DM, Tauscher AN, Cheung KJ, Werb Z, Auer M (2012) Mammary collective cell migration involves transient loss of epithelial features and individual cell migration within the epithelium. J Cell Sci 125:2638–2654

23. Nguyen-Ngoc KV, Cheung KJ, Brenot A, Shamir ER, Gray RS, Hines WC, Yaswen P, Werb Z, Ewald AJ (2012) The ECM microenvironment regulates collective migration and local dissemination in normal and malignant mammary epithelium. Proc Natl Acad Sci U S A 109:E2595–E2604

24. Nguyen-Ngoc KV, Ewald AJ (2013) Mammary ductal elongation and myoepithelial migration are regulated by the composition of the extracellular matrix. J Microsc 251 (3):212–223

25. Provenzano PP, Eliceiri KW, Campbell JM, Inman DR, White JG, Keely PJ (2006) Collagen reorganization at the tumor-stromal interface facilitates local invasion. BMC Med 4:38

26. Provenzano PP, Inman DR, Eliceiri KW, Knittel JG, Yan L, Rueden CT, White JG, Keely PJ (2008) Collagen density promotes mammary tumor initiation and progression. BMC Med 6:11

27. Conklin MW, Eickhoff JC, Riching KM, Pehlke CA, Eliceiri KW, Provenzano PP, Friedl A, Keely PJ (2011) Aligned collagen is a prognostic signature for survival in human breast carcinoma. Am J Pathol 178:1221–1232

28. Egeblad M, Rasch MG, Weaver VM (2010) Dynamic interplay between the collagen scaffold and tumor evolution. Curr Opin Cell Biol 22:697–706

29. Paszek MJ, Zahir N, Johnson KR, Lakins JN, Rozenberg GI, Gefen A, Reinhart-King CA, Margulies SS, Dembo M, Boettiger D, Hammer DA, Weaver VM (2005) Tensional homeostasis and the malignant phenotype. Cancer Cell 8:241–254

30. Levental KR, Yu H, Kass L, Lakins JN, Egeblad M, Erler JT, Fong SF, Csiszar K, Giaccia A, Weninger W, Yamauchi M, Gasser DL, Weaver VM (2009) Matrix crosslinking forces tumor progression by enhancing integrin signaling. Cell 139:891–906

31. Ewald AJ (2013) Isolation of mouse mammary organoids for long-term time-lapse imaging. Cold Spring Harb Protoc 2013

32. Wolf K, Alexander S, Schacht V, Coussens LM, von Andrian UH, van Rheenen J, Deryugina E, Friedl P (2009) Collagen-based cell migration models in vitro and in vivo. Semin Cell Dev Biol 20:931–941

33. Cheung KJ, Gabrielson E, Werb Z, Ewald AJ, "Collective invasion in breast cancer requires a

conserved basal epithelial program," Cell. 2013 Dec 19;155(7):1639–51

34. Shamir ER, Papallardo E, Jorgens DM, Coutinho K, Tsai WT, Aziz K, Auer M, Tran PT, Bader JS, Ewald AJ, "Twist1-induced dissemination preserves epithelial identity and requires E-cadherin," The Journal of Cell Biology. 2014 Mar 3;204(5):839–56.

35. Huebner RJ, Lechler T, Ewald AJ, "Mammary epithelial stratification occurs through symmetry breaking vertical divisions of luminal cells," Development. 2014 Mar;141(5):1085–94.

Chapter 11

Culture of Mouse Embryonic Foregut Explants

Felicia Chen and Wellington V. Cardoso

Abstract

The ability to culture embryonic organ rudiments and follow their development ex vivo has helped to understand how tissues are constructed and what cellular and biological events are important in this process. Here we outline a technique for isolation and ex vivo growth of foregut explants from E8.5 mouse embryos. This technique serves as a reliable tool for the analysis of the morphogenetic processes and signaling networks during early development of foregut derivatives, such as the lungs.

Key words Organ explant, Foregut culture, Development, Organogenesis, Mouse, Lung development

1 Introduction

The emergence of tissue engineering as a discipline requires a good understanding of tissue formation during embryonic development [1]. The ability to culture embryonic organ rudiments ex vivo and follow their development has emerged as an important tool to understand how tissues are constructed and what cellular and biological events are important in this process. Organ culture protocols developed over the past five decades allowed exploration of complex tissu interactions and provided invaluable insights into mechanisms that control morphogenesis and differentiation. These techniques have been widely used in the study of kidney, salivary gland, and gut-derived organs, such as the pancreas and lung [2–7].

Early in organogenesis, the gut endoderm is specified into distinct organ domains along the anterior-posterior axis of the gut tube, which then is roughly divided into three regions: the foregut (the most anterior or cranial), midgut, and hindgut (the most posterior or caudal). The foregut gives rise to the thyroid, lung, stomach, liver, and pancreas. In mice, thyroid and liver progenitors are specified as early as embryonic day E8.0 (approximately 4–6-somite stage).

However in organs, such as the lungs, specification occurs later around E9.0 and primordial buds form at E9.5 (20–25-somite stage) [8–10].

This protocol describes how to isolate and culture mouse embryonic foregut explants and follow the initial stages of organogenesis of some of its derivatives, with a particular focus on the lung. We have previously shown that the initial stages of lung development in foregut cultures recapitulate key early events observed in vivo [11–14]. The response of the foregut to agonists or inhibitors added directly to the culture medium or locally applied in the tissue using heparin beads can be studied with relative ease using this model. Mechanistic insights into the role of developmental pathways and how they interact can be readily obtained in many cases without the cost and time to generate genetically engineered animals. Moreover, this culture system allows studies of the development of the foregut derivatives in genetic models that result in early embryonic lethality shortly after E8.5 [14]. The combination of genetic and pharmacological manipulations using this system represents a robust approach to address developmental processes. In summary, ex vivo culture of the foregut is a powerful tool to dissect some of the early events that regulate organogenesis of foregut-derived structures.

2   Materials

All solutions, tools, and equipment used for dissection and culture should be sterilized to prevent contamination. Culture media should be aseptically prepared.

2.1   Isolation of Foregut from Embryonic Mice

1. Pregnant female mouse, gestational age day 8.5 (embryos approximately 6–18 somites).
2. Absorbent papers.
3. 70 % ethanol in a spray bottle.
4. Surgical scissors.
5. Forceps, Dumont #5, two pairs.
6. Petri dishes, 60 and 100 mm diameters.
7. Cold PBS, $1\times$, with calcium and magnesium.
8. Ice.
9. Laminar flow hood equipped with a dissecting microscope, magnification ranging from $0.8\times$ to $5\times$.
10. Tungsten needles, 0.25 mm diameter, secured in pin holders (Fine Science Tools).

2.2 Culture of Foregut Explants	1. Foregut culture medium: BGJb medium (Life Technologies) containing 0.02 % L-ascorbic acid, 100 units/ml penicillin, 100 μg/ml streptomycin, and 10 % fetal calf serum. Pass the medium through a 0.22 μm disposable filter. Store at 4 °C for up to 1 week.
	2. Micropipetter with tips (1,000 μl).
	3. 6-Well plate and collagen-coated transwell inserts, 0.4 μm pore size (Fisher Scientific #07-200-558).
	4. Medicine dropper with rubber bulb, 2 ml (glass to avoid sticking to the tissue).
	5. Incubator preset to 37 °C, 5 % CO_2, humidified.

3 Methods

3.1 Isolation of Foregut Explants

Euthanize the pregnant mouse by cervical dislocation (*see* **Note 1**).

1. Lay the mouse on its back on a few pieces of absorbent paper and soak its abdomen thoroughly with 70 % ethanol from a spray bottle (*see* **Note 2**).

2. Make a longitudinal cut in the abdomen and reflect the skin using surgical scissors and forceps (*see* **Note 2**). Cut the abdominal wall through the peritoneum to reveal the abdominal contents. Push the gut out of the way and locate the two horns of the uterus. Remove the uterus with the embryos by holding it at one end of the uterine horns and cutting along the mesometrium and the blood vessel connections on the dorsal side of the uterus.

3. Place the dissected uterus in a Petri dish on ice containing cold 1× PBS and transfer the Petri dish to a dissecting microscope in a biological laminar flow hood.

4. Insert the forceps at the nonvascular end of the uterus to create an opening and remove the muscular layer. Dissect the decidua to reveal the embryos.

5. Separate the placenta and yolk sac from each embryo (*see* **Note 3**).

6. Using a medicine dropper, move each embryo to an individual 60 mm Petri dish containing approximately 5 ml of cold PBS (*see* **Notes 4** and **5**).

7. Place the embryo on the dish with its dorsal side facing right. Identify the heart, foregut, somites, spinal cord, and the otic vesicles (*see* Fig. 1a). Separate the somites with the spinal cord from the foregut by doing a longitudinal incision using the
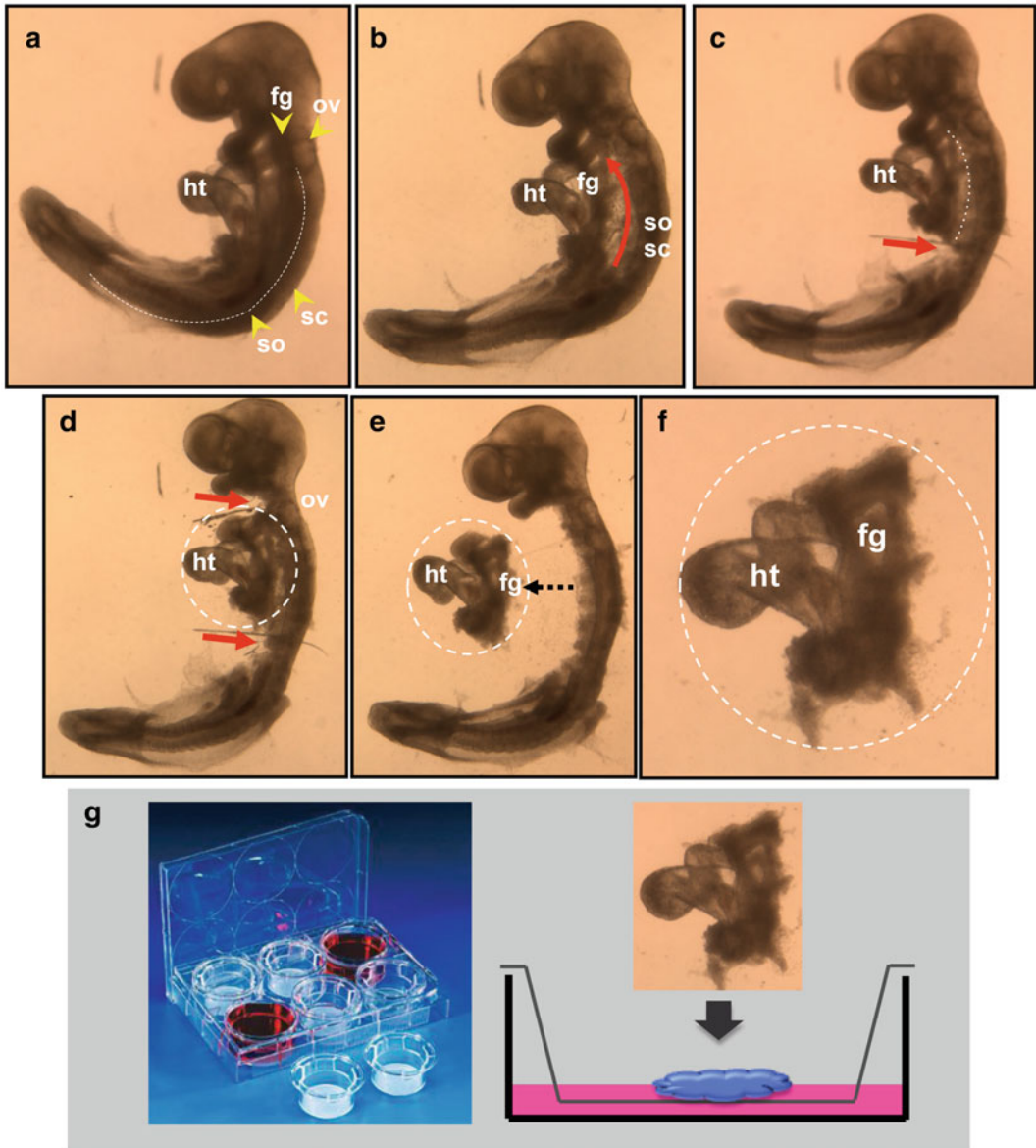
Fig. 1 Dissection and culture of mouse embryonic foreguts. (**a**) E8.5 embryo; *dashed line* representing somite (so) and spinal cord (sc) regions; *ov* otic vesicle, *fg* foregut, *ht* heart. (**b**–**f**) Stepwise isolation of the foregut explant; *red arrows* represent surgical incisions. (**g**) Culture of the foregut explant at the air–liquid interface in transwell filters

Tungsten needles (*see* Fig. 1b, **Note 6**). Transect the embryo slightly caudal to the inferior margin of the heart (*see* Fig. 1c), and again at the level of the otic vesicle (see Fig. 1d). The heart (on the left) remains attached to the foregut (*see* **Note 7**). The explant is now ready to be cultured (*see* Fig. 1e).

3.2 Culture of Foregut Explants	1. Prewarm the foregut culture medium to 37 °C.

1. Prewarm the foregut culture medium to 37 °C.

2. Moisten the transwell membrane insets with a minimal amount of culture medium.

3. Fill each well of the culture plates with 1.5 ml of culture medium and place the moistened transwell into the well.

4. Transfer the foregut explant onto the moistened transwell inset using the medicine dropper. Using Tungsten needles, place the explant with the heart lying on the left side of the foregut, not on top of it (*see* **Note 8**). Excess medium should be removed with a medicine dropper (*see* Fig. 1f, **Notes 9** and **10**).

5. Explants can be cultured for up to 5 days in a humidified 37 °C incubator with 5 % CO_2. Change the medium at the bottom of the well every 24 h and monitor the explant's growth under a dissecting or an inverted microscope daily. During the initial 24 h in culture the explant flattens and primordial buds form in the lung and pancreatic fields. At this time these structures are still difficult to visualize in live specimens. However by days 2–3 most of the organ primordia, including the stomach, can be promptly distinguished by morphology. By days 4–5 primary lung buds have elongated and in some cases secondary buds have started to form (usually in explants initially older than 8-somite stage). Both thyroid and pancreas (ventral and dorsal) primordia are prominent and the liver grows broadly at the posterior region of explant. At this time, strong rhythmic peristaltic movements are seen throughout the foregut, particularly prominent in the lung buds and the stomach. All organs can be recognized not only by morphology in live specimens but also by expression of characteristic markers of differentiation, when analyzed by in situ hybridization (ISH) or immunohistochemistry (*see* Fig. 2, **Note 11**).

4   Notes

1. Cervical dislocation can be performed by breaking the mouse's neck by applying firm pressure at the base of the skull while at the same time pulling the tail backward. Some animal facilities require the animal be anesthetized prior to cervical dislocation, so consult your institutional animal facility for guidelines.

2. These steps markedly reduce the risk of contaminating the dissection with bacteria or fungi from the mouse's skin and hair.

3. We find that it is much easier to separate the yolk sac from the embryo using Tungsten needles than forceps.
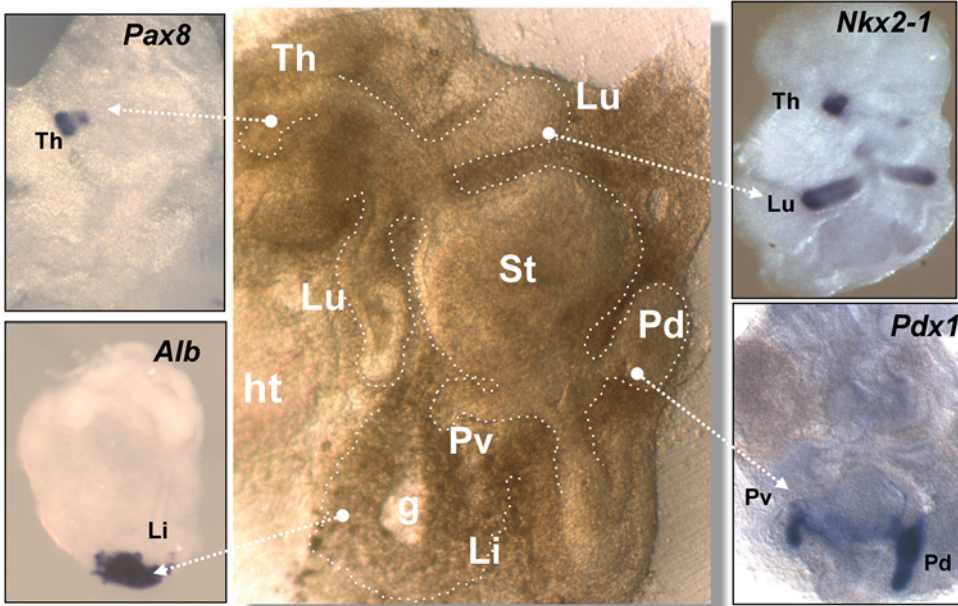
Fig. 2 Foregut organogenesis in vitro. At the center, whole-mount view of a live foregut explant in culture at around days 3–4. *Th* thyroid, *Lu* lungs, *St* stomach, *Gb* gall bladder, *Pv* ventral pancreas, *Pd* dorsal pancreas, *Li* liver, *g* prospective gallbladder. Lateral panels, whole-mount ISH of markers of cell fate markers in day-3 foregut cultures. Pax8 (Th), Albumin (Li), Nkx2-1 (Th, Lu), Pdx1 (Pv, Pd). Modified from ref. 11

4. The level of PBS should be just enough to cover the embryo to prevent adherence of tissue to the Tungsten needles and also minimize embryo motion during dissection.

5. While foregut explant from most E8.5 embryos can be cultured successfully, we find that those that are older than the 8-somite stage grow the best in culture. Explants from embryos younger than the 6-somite stage generally grow poorly in culture. Thus, the system is not optimized to culture foreguts prior to the specification of the thyroid and liver progenitors.

6. It is essential to dissect out and exclude the neighbor somite tissue as thoroughly as possible as it will overgrow in culture and obscure the foregut.

7. It is important to leave the heart attached to the foregut for the culture; explants tend to grow poorly or break apart during culture without the heart attached.

8. The mechanical forces generated by the pulsation of the heart can break the foreguts if the heart is placed on top of the foregut.

9. The explant should not be covered by medium; it grows best at the air–liquid interface, not when submerged.

10. When multiple explants are placed in the same filter, allow enough space for each explant to grow; otherwise they will fuse in culture. Up to nine foreguts can be cultured on each transwell filter.

11. Cultured explants at the desired time points can be harvested and stored for protein/RNA analysis (quick freeze or RNAlater [QIAGEN kit]) or processed for immunohistochemistry and in situ hybridization in whole-mount or histological sections (fixation with 4 % paraformaldehyde solution overnight at 4 °C). Methods for gene or protein analysis of these cultures are reported elsewhere [13, 14].

References

1. Lanza RP, Langer R, Vacanti J (2000) Principles of tissue engineering, 2nd edn. Academic, San Diego, CA

2. Barak H, Boyle SC (2011) Organ culture and immunostaining of mouse embryonic kidneys. Cold Spring Harb Protoc. doi:10.1101/pdb.prot5558

3. Taderera JV (1967) Control of lung differentiation in vitro. Dev Biol 16(5):489–512

4. Kratochwil K (1969) Organ specificity in mesenchymal induction demonstrated in the embryonic development of the mammary gland of the mouse. Dev Biol 20(1):46–71, PMID: 5795848

5. Wessells NK, Cohen JH (1967) Early pancreas organogenesis. Morphogenesis, tissue interactions, and mass effects. Dev Biol 15:237–270

6. Spooner BS, Wessells NK (1970) Mammalian lung development: interactions in primordium formation and bronchial morphogenesis. J Exp Zool 175(4):445–454, PMID: 5501462

7. Wessells NK (1970) Mammalian lung development: interactions in formation and morphogenesis of tracheal buds. J Exp Zool 175 (4):455–466, PMID: 5501463

8. Zorn AM, Wells JM (2009) Vertebrate endoderm development and organ formation. Annu Rev Cell Dev Biol 25:221–251, PMID: 19575677

9. Cardoso WV, Lu J (2006) Regulation of early lung morphogenesis: questions, facts and controversies. Development 133(9): 1611–1624

10. Morrisey EE, Hogan BL (2010) Preparing for the first breath: genetic and cellular mechanisms in lung development. Dev Cell 18 (1):8–23

11. Desai TJ, Malpel S, Flentke GR et al (2004) Retinoic acid selectively regulates Fgf10 expression and maintains cell identity in the prospective lung field of the developing foregut. Dev Biol 273:402–415

12. Desai TJ, Chen F, Lu J et al (2006) Distinct roles for retinoic acid receptors alpha and beta in early lung morphogenesis. Dev Biol 291:12–24

13. Chen F, Desai TJ, Qian J et al (2007) Inhibition of Tgf beta signaling by endogenous retinoic acid is essential for primary lung bud formation. Development 134:2969–2979

14. Chen F, Cao Y, Qian J et al (2010) A retinoic acid-dependent network in the foregut controls formation of the mouse lung primordium. J Clin Invest 120:2040–2048

Chapter 12

Investigating Human Vascular Tube Morphogenesis and Maturation Using Endothelial Cell-Pericyte Co-cultures and a Doxycycline-Inducible Genetic System in 3D Extracellular Matrices

Stephanie L.K. Bowers, Chun-Xia Meng, Matthew T. Davis, and George E. Davis

Abstract

Considerable progress has occurred toward our understanding of the molecular basis for vascular morphogenesis, maturation, and stabilization. A major reason for this progress has been the development of novel in vitro systems to investigate these processes in 3D extracellular matrices. In this chapter, we present models of human endothelial cell (EC) tube formation and EC-pericyte tube co-assembly using serum-free defined conditions in 3D collagen matrices. We utilize both human venous and arterial ECs and show that both cell types readily form tubes and induce pericyte recruitment and both ECs and pericytes work together to remodel the extracellular matrix environment by assembling the vascular basement membrane, a key step in capillary tube network maturation and stabilization. Importantly, we have shown that these events occur under serum-free defined conditions using the hematopoietic stem cell cytokines, SCF, IL-3, and SDF-1α and also including FGF-2. In contrast, the combination of VEGF and FGF-2 fails to support vascular tube morphogenesis or pericyte-induced tube maturation under the same serum-free defined conditions. Furthermore, we present novel assays whereby we have developed both human ECs and pericytes to induce specific genes using a doxycycline-regulated lentiviral system. In this manner, we can upregulate the expression of wild-type or mutant gene products at any stage of vascular morphogenesis or maturation in 3D matrices. These in vitro experimental approaches will continue to identify key molecular requirements and signaling pathways that control fundamental events in tissue vascularization under normal or pathologic conditions. Furthermore, these models will provide new insights into the development of novel disease therapeutic approaches where vascularization is an important pathogenic component and create new ways to assemble capillary tube networks with associated pericytes for tissue engineering applications.

Key words Endothelial cells, Pericytes, Tube formation, Three-dimensional extracellular matrix, Inducible gene expression, Hematopoietic stem cell cytokines, Serum-free defined conditions

1 Introduction

Understanding how blood vessels form and mature [1–12] is essential for our ability to properly treat a wide range of diseases and cancers where vascularization is a major pathogenic feature as well as develop applications for tissue bioengineering and regenerative medicine. Despite major advances in our understanding of vasculogenesis and sprouting angiogenesis [1, 2, 4, 7, 11, 13], much remains to be learned about the fundamental cell biology of key cell types within the vasculature (i.e., endothelial cells [ECs], pericytes, vascular smooth muscle cells) and cellular signaling processes that control how ECs form tubes (i.e., EC tubulogenesis); how they specialize into arteries, capillaries, veins, and lymphatics and how these unique vessels mature and eventually stabilize [14]. These morphogenic events stereotypically occur during vasculogenesis, angiogenesis, or pathologic neovascularization, and in the context of embryogenesis, wound healing, and tumor growth.

Progression through the various stages of blood vessel formation, maturation, and eventual stabilization requires proper communication between ECs and surrounding cells such as mural cells (e.g., pericytes and vascular smooth muscle cells) and parenchymal cells within given tissues, as well as the extracellular matrix (ECM), which all contribute to the molecular control of EC morphogenesis [1, 3, 7, 8, 11, 12, 15–17] (Fig. 1). These morphogenic events include tube formation, the establishment of apical-basal polarization, the deposition of the vascular basement membrane in a basal position, and the proper positioning of mural cells along the abluminal surface of EC tubes [2, 6, 8, 9, 18, 19]. EC-pericyte interactions, which are particularly critical in capillaries, are fundamentally important because capillaries represent the major vessels that deliver oxygen and nutrients to facilitate tissue development and homeostasis (Fig. 1). It is perhaps not a surprise that abnormalities of EC-pericyte interactions are noted in major human diseases such as diabetes and cancer [10, 20]. Thus, a molecular understanding of how ECs form capillary tube networks, become invested with pericytes, and then lead to functional capillaries which interface and sustain each unique tissue is a major requirement in the context of normal development, various human diseases, and the key area of tissue engineering.

ECs and pericytes during vascular morphogenic events are controlled by cell-specific responses to changes in the ECM as it is remodeled [3, 7, 8, 18, 19]. A critical and fundamental step in EC tubulogenesis is ECM degradation where ECs create vascular guidance tunnels [19] (Fig. 1). These EC-generated tunnels are matrix conduits and physical spaces within 3D matrices where EC tube formation and remodeling occur and where pericytes are recruited to the EC tube abluminal surface [18, 19, 21] (Fig. 1). Within
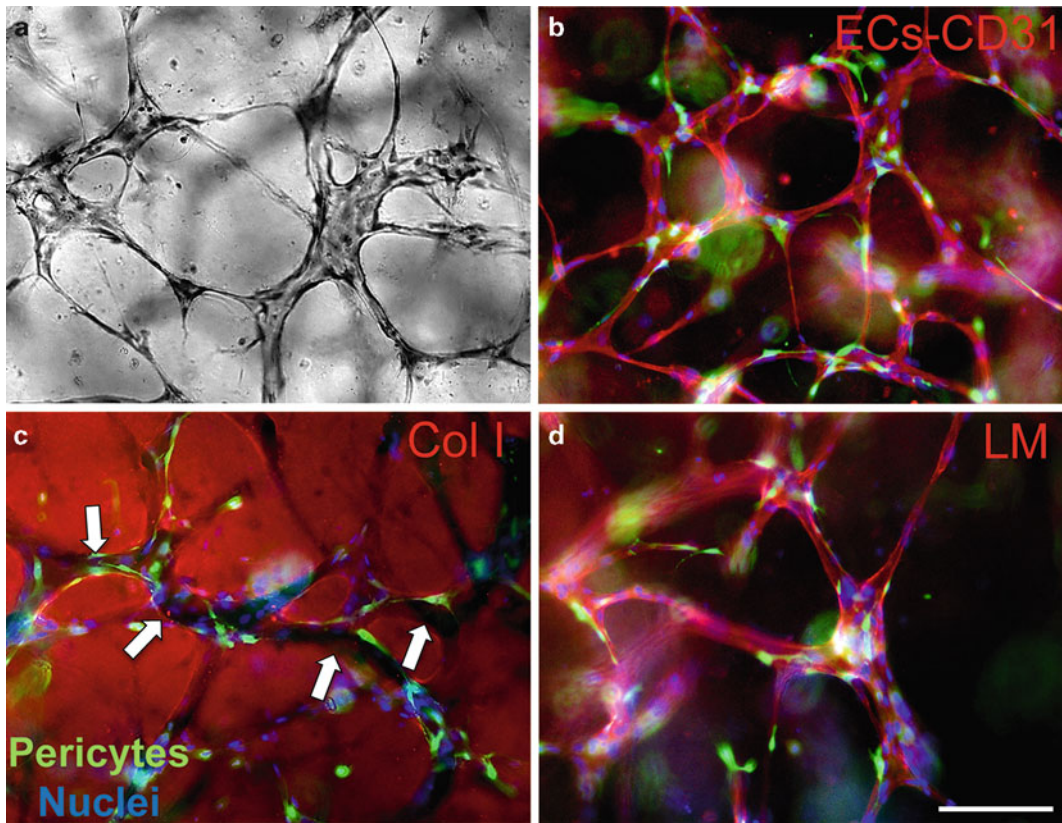
Fig. 1 EC-pericyte tube co-assembly in 3D collagen matrices under serum-free defined conditions. Using a serum-free, growth factor-defined 3D collagen matrix assay with hematopoietic stem cell cytokines (SCF, IL-3, SDF-1α) and FGF-2, human ECs (HUVECs) and pericytes co-assemble into vascular networks. After 96 h of culture, gels were fixed and stained with toluidine blue to visualize tube assembly as indicated by the light image (**a**). Representative immunofluorescence images show several important aspects of this multicellular tube co-assembly process. (**b**) GFP-labeled pericytes are shown to recruit to the abluminal surface of EC-lined tubes as indicated by immunostaining with anti-CD31 antibodies (shown in *red*). (**c**) EC tube formation generates vascular guidance tunnels which are revealed following immunostaining for collagen type I (Col I) matrix as they are created through EC-derived MT1-MMP-dependent proteolysis of this matrix (*arrows* indicate the border of the tunnels). After pericyte recruitment, both ECs and pericytes are observed within the tunnel spaces. (**d**) EC-pericyte tube co-assembly within vascular guidance tunnels results in vascular basement membrane matrix deposition as indicated by laminin (LM) staining on the EC tube abluminal surface and in between the two cell types. In each image, GFP-pericytes are shown in *green* while nuclei are *blue* following staining with Hoechst dye. *Bar* equals 50 μm

these spaces, both ECs and pericytes are highly migratory and together, they assemble the vascular basement membrane along the tube abluminal surface between the two cell types [8, 18]. Furthermore, they respond to this newly remodeled ECM through basement membrane-binding integrins including α5β1, α3β1, α6β1, and α1β1 [7, 18]. Importantly, these integrins do not appear to play a role in our collagen system when ECs are forming tubes in

the absence of pericytes and in this circumstance, the integrin α2β1 plays a critical role [7, 12, 18, 22, 23]. This past work demonstrates that not only do EC-pericyte interactions lead to vascular basement membrane matrix formation, but both cell types directly respond to this newly deposited matrix through integrins that recognize basement membrane matrix proteins [7, 8].

Pericytes represent a major regulator of EC tubulogenesis, tube remodeling, and vessel maturation events [8, 17, 18, 21]. For example, pericyte recruitment leads to more elongated and branched tubes which are narrower in diameter compared to EC tubes without pericytes under the same culture conditions [8, 18, 21]. Their timely recruitment to the developing vasculature assists with controlling vascular morphogenic events through cell-cell contacts, but also through their ability to regulate deposition of basement membrane which alters signaling events. These distinct signals delivered to both ECs and pericytes occur downstream of altered integrin signaling (through recognition of basement membrane instead of collagen type I) [7] but also are likely coupled to distinct integrin/growth factor co-signaling [24, 25] that uniquely occurs following adsorption of EC- and pericyte-derived growth factors to this matrix. Interestingly, past studies demonstrated the ability of bone morphogenic protein-4 (BMP-4) to specifically adsorb to collagen type IV [26], so this might be an example of a growth factor signal that would change when a vascular basement membrane is formed. Such a signal would likely be distinct when EC tubes form without pericytes or when there are abnormalities in EC-pericyte interactions that are known to be an issue in key diseases such as diabetes and cancer.

Many studies both in vitro and in vivo indicate that pericytes are capable of stabilizing EC-lined tubes and their presence reduces the possibility that such tube networks will regress [3, 8, 12, 17, 27, 28]. In several studies from our laboratory, pericyte-derived TIMP-3 played a key role in reducing vascular regression by suppressing EC-derived MMPs such as MMP-1 and MMP-10 which promote ECM degradation and vessel breakdown [17, 29–31]. Also, siRNA suppression of the pericyte-derived and ECM-binding matrix metalloproteinase inhibitor, TIMP-3, affects tube diameter and remodeling, in that EC tubes are much wider and have reduced collagen type IV assembly when pericyte TIMP-3 expression is reduced [18]. Furthermore, reduced pericyte coverage along vessels in the central nervous systems leads to disruptions of the blood–brain barrier [32, 33]. Thus, considerable evidence suggests that disruption of pericyte recruitment, retention, or survival on EC-lined tubes results in altered EC biology and a disorganized, unstable vasculature. Clearly, a wide range of events are involved in vascular morphogenesis and maturation which must be considered when designing or interpreting studies aimed to elucidate particular aspects of blood vessel formation or function.

A key point is that both in vitro and in vivo experimental approaches are necessary to address such questions and to ultimately develop a comprehensive understanding of these processes [1–3, 6, 7]. It is our view that both approaches are necessary together to make the key insights which will lead to effective new therapeutics to treat complex human diseases where the vasculature plays a major pathogenic role.

Many different in vivo models are currently employed to study the molecular mechanisms underlying vascular morphogenesis, maturation, and stabilization, including those in mice, zebrafish, and avian species [1]. A major advance in the utility of in vitro approaches to address such questions was the establishment of 3D matrix vascular morphogenic models using either isolated human ECs or pieces of tissues such as the rodent aorta [2, 6–8, 34–36]. These 3D matrix systems are of particular importance in the investigations of vascular morphogenesis since processes such as tubulogenesis and angiogenic sprouting occur only in a 3D matrix environment [2, 6, 23]. The use of 3D matrix assay systems has proved to be of particular importance because of their ability to recapitulate in vivo vascular network formation, which has led to increased understanding of the factors and signaling events that are required for these events [2, 6, 8, 18, 37].

In particular, our lab has developed and routinely utilizes a serum-free, factor-defined 3D matrix system using both collagen type I and fibrin matrices [2, 18, 21, 34, 37, 38]. Using this system, we have identified hematopoietic stem cell cytokines that promote human EC tubulogenesis in conjunction with fibroblast growth factor (FGF)-2, specifically the combination of stem cell factor (SCF), stromal-derived factor-1α (SDF-1α), and interleukin-3 (IL-3) [18, 21, 37, 38]. In addition, we have demonstrated that this system allows for an analysis of EC-pericyte interactions, where pericytes recruit to developing EC tubes, participate in deposition of basement membrane matrix, and travel within the tunnels created by ECs during EC tubulogenesis [8, 18, 21, 38]. As we show in this chapter, a range of techniques are employed to analyze cell-cell and cell-ECM relationships during vasculogenic tube assembly, including growth factor signaling, protein kinase cascades, GTPase regulation, and integrin signaling. A novel technique described here is the combination of our defined 3D matrix system with a gene-inducible lentiviral system, where a gene of interest can be regulated by ECs or pericytes (following addition of doxycycline) at a particular time in the tube formation or the maturation process. This experimental approach allows for a precise examination of the effects of particular genes and signaling pathways at distinct stages of vascular morphogenic and maturation events under serum-free defined conditions and in 3D extracellular matrices.
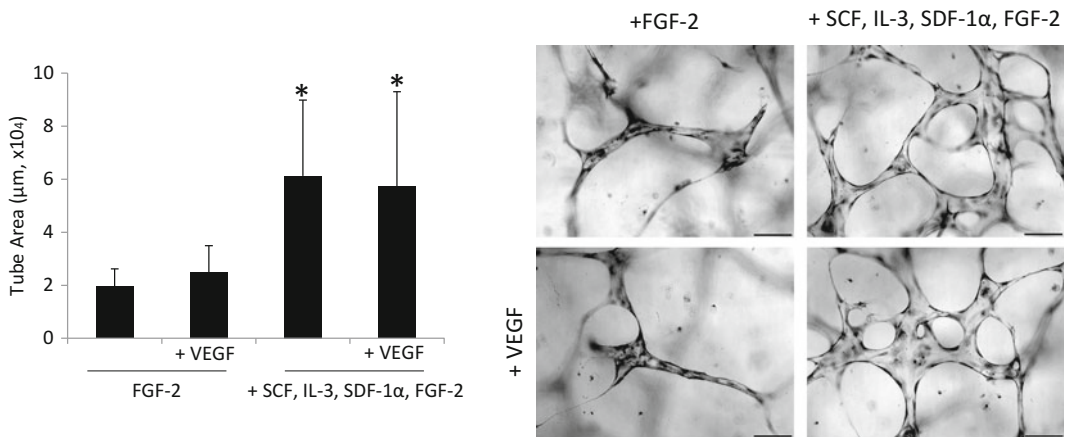
Fig. 2 Hematopoietic stem cell cytokines markedly stimulate human arterial ECs to form tubes in 3D collagen matrices under serum-free defined conditions. Using a serum-free, factor-defined system in 3D collagen matrices, human umbilical arterial endothelial cells (HUAECs) markedly assemble into EC-lined tubes in response to hematopoietic stem cell cytokines and FGF-2. Cultures were fixed, stained, and analyzed after 72 h in culture. Total tube area per image ($n = 25$/group) is averaged and plotted $\pm$ standard deviation in the *left panel*. Images on the *right panel* are representative of each of these culture conditions, where growth factors were added into the 3D collagen gel during the assay: FGF-2 alone; FGF-2 + VEGF; SCF, IL-3, SDF-1α + FGF-2; and SCF, IL-3, SDF-1α + FGF-2 + VEGF. These results are similar to what we have previously shown using HUVECs, and provide further evidence that the hematopoietic cytokines SCF, SDF-1α, and IL-3 synergize with FGF-2 to promote tubulogenesis in ECs, while VEGF addition to 3D cultures during the assay does not enhance tubulogenesis. The *asterisk* indicates significance at $p < 0.01$ compared to either FGF-2 alone or FGF-2 + VEGF. *Bar* equals 100 μm

Of importance to evaluate the utility of any model, in vivo or in vitro, is itsability to obtain detailed information concerning the molecular and functional behaviors of the cell types being examined. For example, what defines an EC as an EC, and a pericyte as a pericyte (Table 1)? Our serum-free, factor-defined 3D assay systems allow for such an analysis to take place and to define EC and pericyte behaviors from a functional and molecular perspective [1, 18, 21, 34, 37] (Table 1). One of the key abilities of ECs that is frequently overlooked is that they must be able to form tubes in 3D matrices (Figs. 1 and 2). This is a characteristic feature of all ECs, and thus, studies that create EC-like cells from induced pluripotent stem cells, for example, must demonstrate that the ECs are tubulogenic in a 3D matrix system such as those that we have described [2, 6].

In contrast, pericytes do not form tubes in any of our 3D matrix models (nor do vascular smooth muscle cells or fibroblasts), but pericytes readily recruit to EC-lined tubes by invading 3D matrices in a manner dependent on the presence of ECs [8, 17, 18, 21, 38]. In fact, using nuclear GFP-labeled pericytes, we demonstrated that pericytes, when cultured alone, showed minimal to no ability to directionally migrate/invade in 3D collagen matrices (their movement is MMP dependent), while the presence of ECs

Table 1
Functional properties of endothelial cells and pericytes during vascular morphogenesis and maturation

Endothelial cells	Pericytes
Key ability to form tubes in 3D collagen or fibrin matrices	Do not form tubes in 3D matrices, but invade as single cells
Create vascular guidance tunnels during EC tubulogenesis in 3D matrices; tunnels are created through ECM proteolysis that is mediated in large part by MT1-MMP	Pericytes invade in response to ECs in a manner dependent on PDGF-BB; recruitment to tubes results in more elongated and narrow EC tubes
ECs dramatically migrate in 3D matrices and co-assemble into tubes within vascular guidance tunnels	Pericytes express very high levels of PDGFRβ and utilize this receptor to invade toward EC tubes and migrate along the tube abluminal surface
There is minimal to no proliferation of ECs during tube formation in 3D matrices	Pericytes proliferate in response to ECs in manner dependent on PDGF-BB and HB-EGF in 3D matrices
ECs co-assemble with pericytes to create capillary vessels and generate a vascular basement membrane	Pericytes migrate along the EC tube abluminal surface within vascular guidance tunnels to facilitate basement membrane formation
Human ECs form tubes and sprout in response to the hematopoietic stem cell cytokines, SCF, IL-3, and SDF-1α, and FGF-2 under serum-free defined conditions	Human EC-pericyte tube co-assembly with accompanying basement membrane formation occurs in 3D matrices in response to hematopoietic cytokines

markedly increased the migration and directional movement of pericytes [8, 21]. Furthermore, we demonstrated that EC-derived PDGF-BB and HB-EGF were responsible for both pericyte movement and their ultimate ability to recruit to EC tubes [21]. In addition, pericytes proliferate during these events in a manner dependent on both the presence of ECs and PDGF-BB/HB-EGF [21]. Blockade of pericyte proliferation as well as recruitment to EC tubes by interfering with PDGF-BB/HB-EGF or their receptors led to abnormally wide EC tubes with markedly reduced basement membrane deposition in vitro or in vivo [21]. Thus, pericytes can be defined by their ability to invade/migrate and proliferate in response to ECs, recruit to EC tubes, and then regulate vascular basement membrane matrix formation in 3D matrices (Table 1). Pericytes also dramatically invade 3D collagen matrices in response to PDGF-BB under defined serum-free conditions due to their
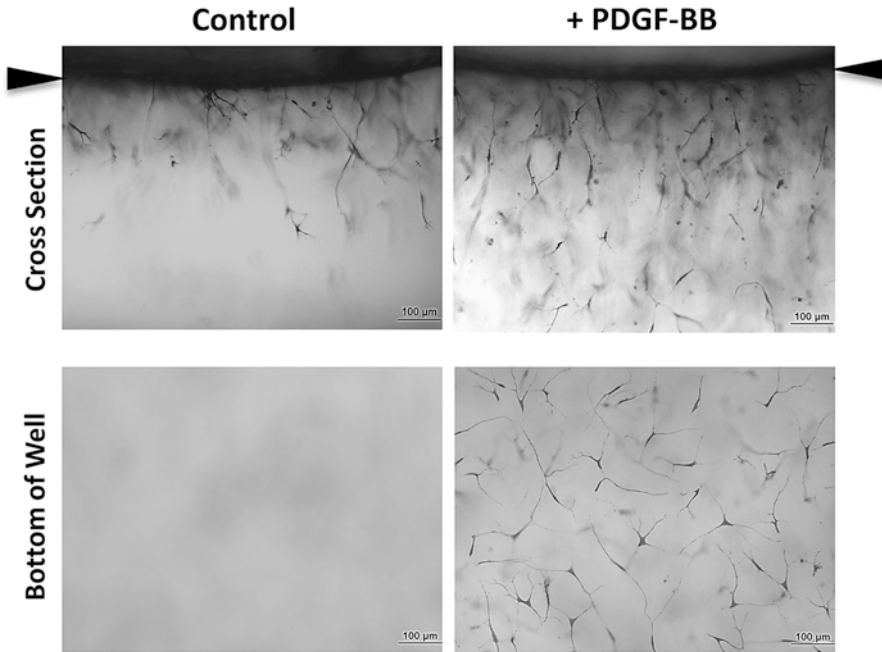
Fig. 3 Pericyte invasion of 3D collagen matrices is markedly stimulated by PDGF-BB under serum-free defined conditions. Human pericytes were seeded on the surface of 3D collagen gels which had no addition (control) or PDGF-BB at 200 ng/ml and after 72 h, cultures were fixed and stained with toluidine blue. Cultures were photographed on the bottom of the wells or were cross-sectioned and then photographed from the side. The invasion responses that are observed are MMP dependent in that the addition of GM6001 completely blocks the invasion response (not shown). *Arrowheads* indicate the monolayer surface. *Bar* equals 100 μm. Image analysis and quantitation can be performed on cross sections (*top panels*) for distance of invasion and number of pericytes below the monolayer. In addition, cultures can be imaged at the very bottom of the well, where fully invaded pericytes display a flattened phenotype (due to attachment to the plastic after invading through the entire depth of the collagen gel), and images analyzed for the number of invading pericytes per field. This assay can assist with a variety of analyses, where comparisons may be made among pericytes of different tissue origins (or other mural cells), those treated with chemicals or drugs to assess pericyte invasion signaling requirements, following transfection with siRNAs to test gene function or following upregulation of genes using our Dox-regulated system to assess their influence on pericyte invasive behavior in 3D matrices

high expression of PDGFRβ (Fig. 3). Also, in our hands, human vascular smooth muscle cells such as aortic smooth muscle cells weakly invade in response to PDGF-BB in 3D collagen matrices and fail to recruit to EC-lined tubes in our model systems, thus demonstrating a strong biological difference between pericytes and vascular smooth muscle cells (data not shown). We believe that these functional definitions of ECs versus pericytes are critical to augment the definition of these cell types in addition to genes and protein markers that are routinely used to define them (Table 1).
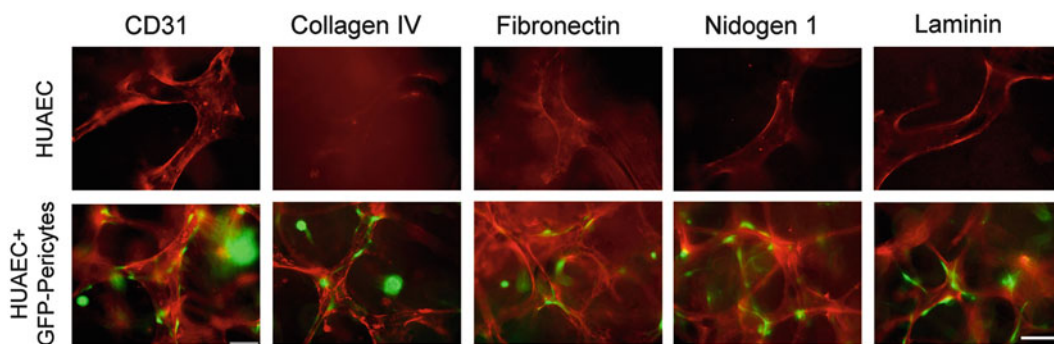
Fig. 4 Hematopoietic stem cell cytokines stimulate human arterial EC-pericyte tube co-assembly leading to vascular basement membrane matrix deposition in 3D collagen matrices. As we have shown for HUVEC-pericyte co-cultures, basement membrane deposition is markedly increased when pericytes are co-cultured with HUAECs in a serum-free, factor-defined 3D collagen matrix assay using hematopoietic stem cell cytokines and FGF-2. After 120 h, cultures are fixed with paraformaldehyde and immunostained for CD31 to label ECs or the indicated basement membrane proteins. The immunostaining protocol is performed in the absence of detergent so that we are only observing extracellularly deposited basement membrane proteins. GFP pericytes are shown in *green*, and CD31, collagen type IV, fibronectin, nidogen 1, and laminin are shown in *red. Bar* equals 100 μm

We have previously elucidated the synergistic effects of SCF, SDF-1α, IL-3, and FGF-2 to induce tube formation using human umbilical vein ECs (HUVECs) and to investigate EC-pericyte tube co-assembly [8, 18, 21, 37, 38] (Figs. 1, 2, and 4). We have also used this system to demonstrate a role of VEGF and FGF-2 (and their combination) as primers for tubulogenesis [37]. When ECs are treated with VEGF or FGF-2 (and in particular the combination) overnight prior to being used in a 3D assay, EC morphogenesis and tubulogenesis are strongly enhanced (i.e., in response to the hematopoietic cytokines, SCF, IL-3, and SDF-1α) [37]. However, if VEGF is added during the assay, either alone or in conjunction with FGF-2, tubulogenesis fails to occur [37]. The combination of SCF, SDF-1α, and IL-3 with FGF-2 strongly stimulates tube formation and adding VEGF to these factors during the tube formation assay has no additional effect [37]. This chapter describes the use of a new EC type, human umbilical arterial ECs (HUAECs) in 3D morphogenesis assays, and shows that HUAECs form tubes in our system very readily (Figs. 2 and 4). In addition, all of the observations with HUVECs appear to hold true for HUAECs also with regard to their ability to form tubes in response to hematopoietic cytokines and to stimulate pericyte recruitment with accompanying vascular basement membrane matrix assembly. We also describe a human pericyte-only invasion assay that will be useful in the characterization and definition of pericytes (Fig. 3). Finally, we describe a lentiviral gene-inducible system that, when used in conjunction with our serum-free, defined 3D matrix assay, can be used for the doxycycline-regulated expression of a wild-type
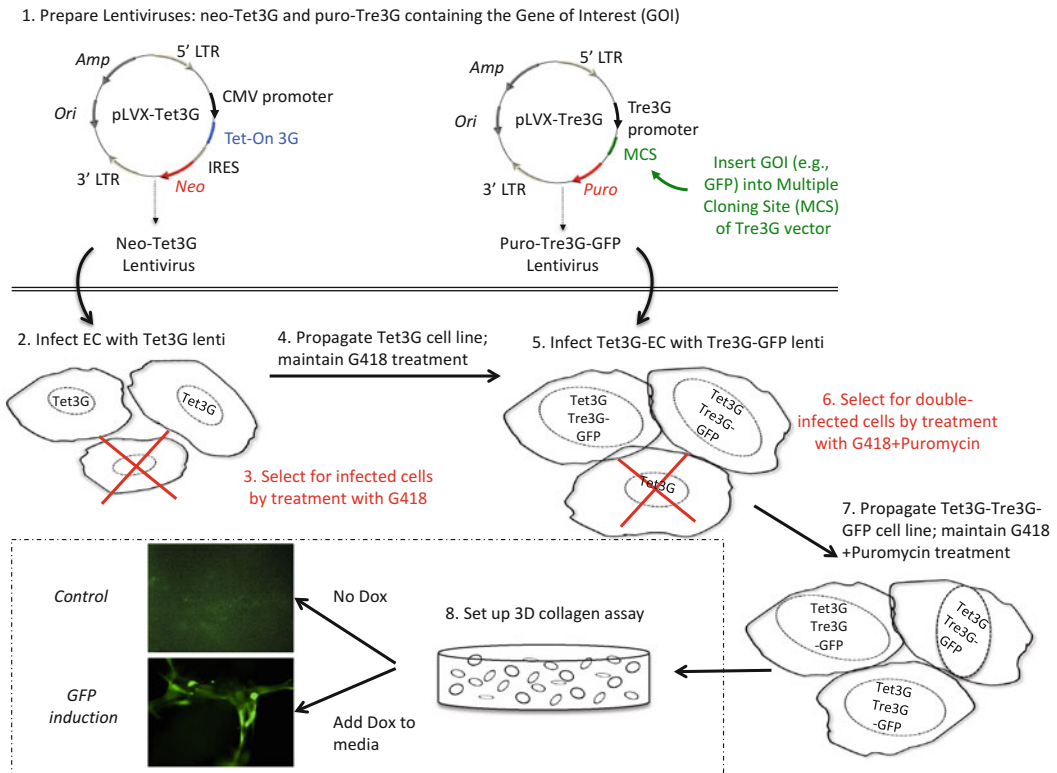
Fig. 5 Development of cell lines with doxycycline-inducible genes in ECs or pericytes using recombinant lentiviruses. This schematic illustrates how cell lines can be created to regulate the expression of specific genes of interest (GOI) in ECs, pericytes, or other cell types. (1) Recombinant lentiviruses are created for both the neo-Tet3G vector and a puro-Tre3G vector containing the GOI. The current example regulates the expression of GFP in ECs (see text for primer sequences that enable GFP cloning into the vector), but we have used this system with a variety of genes in ECs and pericytes alike. (2) Low-passage ECs (P2) are then infected with the Tet3G lentivirus. (3) After 3 days, G418 (geneticin) is added to the cell culture media to select for cells that have been infected with the Tet3G virus, killing all non-infected cells. (4) Cells are allowed time to grow back to near confluency while maintaining G418 selection, and propagated to provide enough cells to freeze down and split in order to continue with infection. (5) A confluent flask of Tet3G-ECs is infected with the Tre3G-GFP lentivirus prepared in [1]. (6) After 3 days, puromycin is added to the media (with existing G418 treatment) to select for cells that contain both the Tet3G and Tre3G-GFP vectors. (7) Cells are grown and propagated in the presence of both G418 and puromycin. (8) Once the cell line has been established and frozen down, a flask is used in the serum-free, defined 3D collagen matrix assay described in the text. A comparison between control cultures (No Dox) and doxycycline-treated cultures (+Dox, 5 μg/ml) is illustrated

or mutant gene of interest, in either ECs or pericytes (Figs. 5, 6, 7, and 8). In addition to investigating the role of particular genes at different stages of vascular morphogenesis and maturation, we may be able to utilize this approach to create ECs or pericytes with enhanced abilities to perform their functions for the purposes of bioengineering and regenerative medicine.
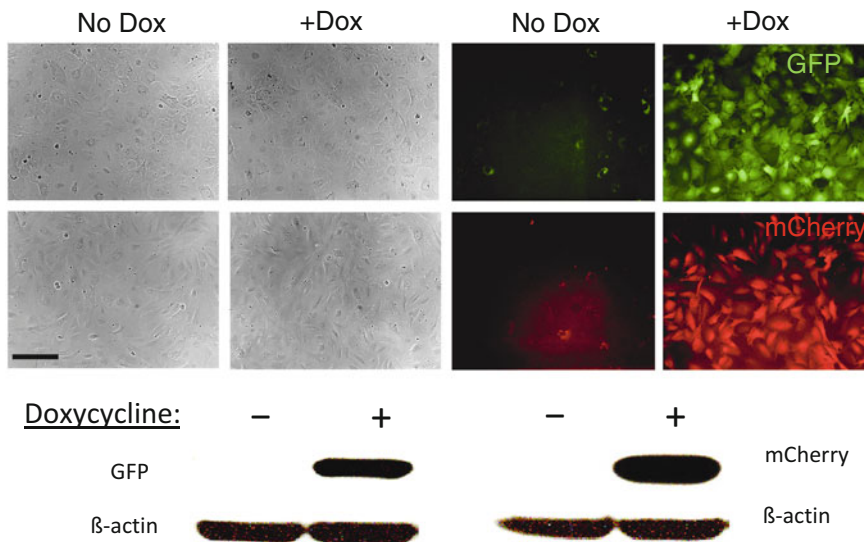
Fig. 6 Doxycycline-inducible expression of recombinant genes in human pericytes. An example of the efficiency of the doxycycline-inducible system is shown also for human pericytes. GFP and mCherry were cloned into a lentiviral vector system allowing for doxycycline (Dox)-inducible expression and stable pericyte cell lines were established. Dox was added or not and pericytes were photographed under fluorescence. For the *bottom panel*, lysates were prepared of these cultures and Western blots were performed to detect GFP or mCherry proteins. *Bar* equals 100 μm

2 Materials

The key materials necessary to perform these morphogenic assays include human endothelial cells and human pericytes, which are grown as we have described previously [18, 21, 34]. We perform morphogenic assays utilizing 3D rat tail collagen type I containing matrices and use recombinant growth factors and cytokines, which are added either into the collagen matrix or into the culture media, or both [34]. All of the assays are performed in half-area 96-well plates while immunostaining is performed by fixing the 3D collagen gels and staining the gels using methods similar to whole-mount staining of tissues or embryos [34, 39]. Cultures can also be stained with dyes such as toluidine blue, which facilitates our ability to assess and quantitate lumen and tube formation by photography and trace tube areas using Metamorph software [34].

2.1 Endothelial Cells and Pericytes

Human umbilical vein endothelial cells (HUVECs; Lonza) and human umbilical arterial cells (HUAECs; Cell Applications, Inc.) are grown from passages 2–6 using Medium 199 (Invitrogen) containing 20 % fetal calf serum, 400 μg/ml of bovine hypothalamic extract, and 100 μg/ml of heparin (Supermedia; *see* **Notes 1** and **2**). Flasks are pre-coated with 1 mg/ml of gelatin in PBS for at
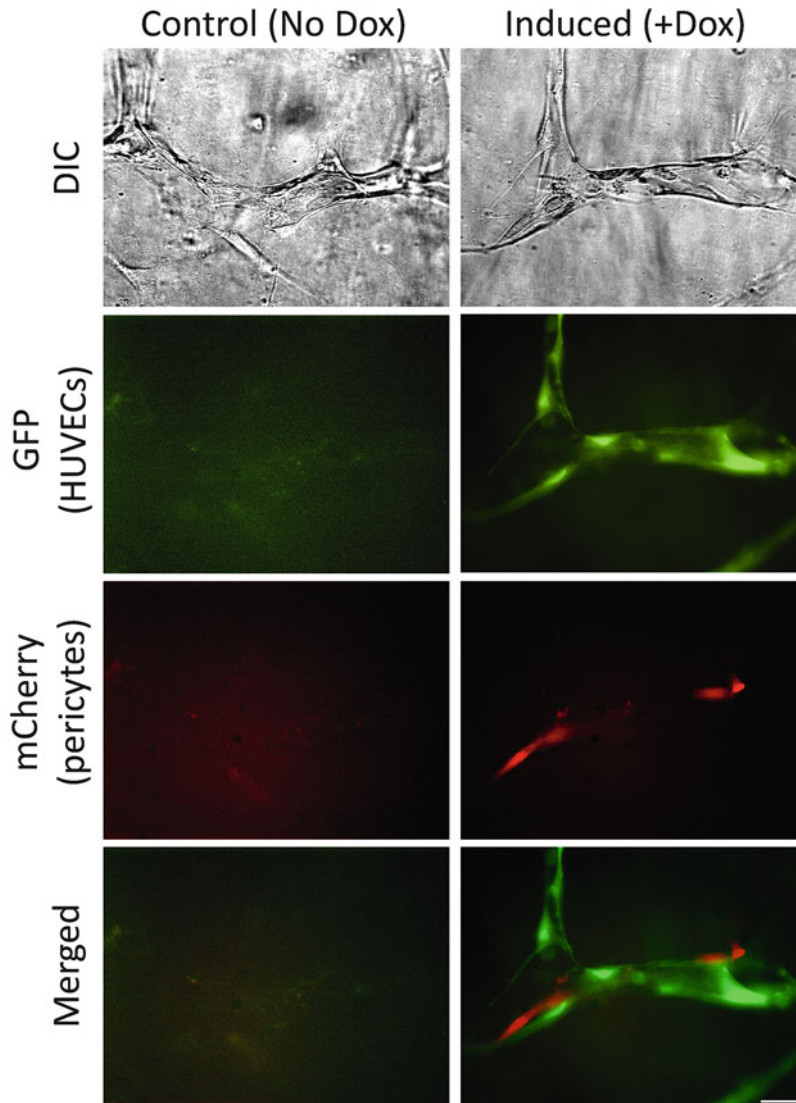
Fig. 7 Doxycycline-inducible expression of GFP and mCherry during EC-pericyte tube co-assembly in 3D collagen matrices. GFP and mCherry were cloned into ECs and pericytes, respectively, in the doxycycline-inducible system and were allowed to undergo tube morphogenesis under serum-free defined conditions with hematopoietic cytokines and FGF-2 in 3D collagen matrices for 72 h. At the beginning of the assay, cells were either left untreated (control; No Dox) or were induced with doxycycline (+Dox). Gels were then fixed in 2 % paraformaldehyde and imaged under fluorescence microscopy. Separate panels of DIC light images, fluorescent GFP and mCherry images, as well as merged overlay images are shown. *Bar* equals 50 μm

least 30 min at 25 °C. Human brain vascular pericytes (HBVP; ScienCell) are grown from passages 2–10 and grown in DMEM with 10 % fetal calf serum on gelatin-coated flasks. Pericytes were labeled with enhanced GFP using a recombinant lentivirus, or with inducible Tre3G-mCherry, as described below.
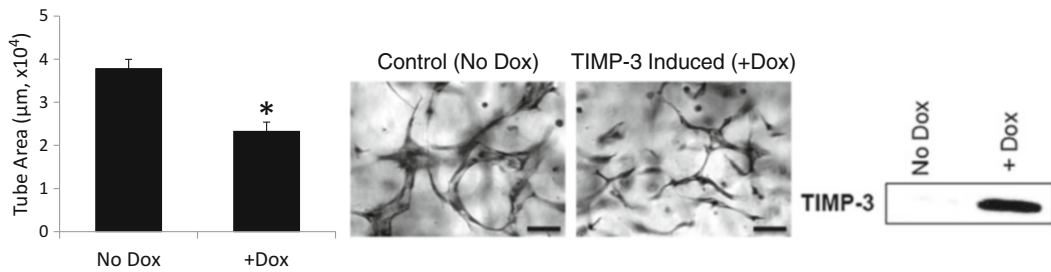
Fig. 8 Doxycycline-inducible expression of TIMP-3 in ECs markedly blocks tube formation in a serum-free, defined 3D collagen matrix assay. To provide a functional example of the efficiency of the inducible lentiviral transfection system, TIMP-3 expression was induced with doxycycline (Dox, 5ug/ml), or not (No Dox control). Cultures were fixed, stained with toluidine blue, photographed, and analyzed for EC tube area after 72 h ($n = 25$/group that is averaged and plotted $\pm$ standard deviation). Cells treated with or without Dox were examined for TIMP-3 expression by Western blot (*right panel*). The *asterisk* indicates significance at $p < 0.01$. *Bar* equals 100 μm

2.2 Rat Tail Collagen Type I	Collagen type I is purified from rat tails and lyophilized from a 0.1 % acetic acid solution in H_2O (sterile filtered). The collagen is resuspended in 0.1 % acetic acid in H_2O solution at a final concentration of 7.1 mg/ml and we obtain approximately 100 mg of collagen type I from one rat tail (*see* **Note 1**).
2.3 Reduced Serum Supplement II (RSII)	This supplement is made by mixing a combination of insulin, transferrin, selenium, and fatty acid-free bovine serum albumin (all obtained from Sigma) with added C18 oleic acid (obtained from Avanti Polar Lipids) which is prepared as described [34] and the mixture is frozen and stored at −20 °C. After thawing an aliquot, the RSII can be left at 4 °C for 1–2 months and utilized in the assay systems.
2.4 Recombinant Growth Factors, Cytokines, and Other Media Additives	Recombinant FGF-2 is obtained from Millipore, and SCF, IL-3, and SDF-1α are obtained from R&D Systems. Ascorbic acid is obtained from Sigma.
2.5 Culture Plates	Half-area 96-well tissue culture plates (Costar) are used in all experiments.
2.6 Lentivirus Production	Lentiviruses are generated using the ViraPower Lentiviral Expression system (Invitrogen) and utilize a lentiviral construct (pLenti6/V5 TOPO) with a blasticidin resistance gene (GFP-pericytes), or using the Lenti-X system (Clontech) or the lentiviral vector pLVX-Tre3G (puromycin selection) or pLVX-Tet3G (G418 selection) to be able to induce gene expression in ECs or pericytes. A lentiviral vector packaging system from Clontech is utilized along with 293FT cells (grown in DMEM with 10 % fetal calf serum) to make recombinant lentiviruses.

3 Methods

3.1 EC Tube Morphogenesis Assay in 3D Collagen Matrices Using HUAECs

This assay has been described for use with HUVECs; this report utilizes HUAECs in the exact same manner (Fig. 2). One T75 cm^2 flask of confluent human ECs is trypsinized, washed $1\times$ with 10 ml of Medium 199 (M199), and suspended at 10^7 cells/ml in M199 (these cells are gently mixed with a P200 tip to break up small clumps). They are then seeded at 2×10^6 cells per ml in 2.5 mg/ml of collagen type I suspended in M199. To make 1 ml of gel, 350 μl of 7.1 mg/ml type I collagen in 0.1 % acetic acid, 39 μl of $10\times$ M199, 2.1 μl of 5 N NaOH, and 409 μl of $1\times$ M199 are mixed together thoroughly via pipette. 200 μl of ECs are then added to this mixture, which is swirled on ice. The cell mixture is then placed on ice. The recombinant growth factors, SCF, IL-3, SDF-1α, and FGF-2, are then added at 200 ng/ml within the collagen matrix. 28 μl of gel is added per well and the plates are periodically tapped on each edge to make certain that the gels are evenly distributed in each well prior to polymerization. The plates are allowed to equilibrate in a CO_2 incubator for 30 min and then 100 μl of culture media is added. The culture media contains M199 with a 1:250 dilution of RSII supplement (which is added first to the media), and then 40 ng/ml of FGF-2 and 50 μg/ml of ascorbic acid are added. We add 125 μl of H_2O in every well surrounding the wells and also add 150 μl of H_2O in non-well areas that surround each of the wells to maintain humidity and to reduce potential dehydration of culture wells over time. Assays are allowed to proceed for 1, 3, or 5 days, at which time cultures are fixed with either 2 % paraformaldehyde in PBS or 3 % glutaraldehyde in PBS. For the 5-day culture time point, cultures are fed on day 3 by removing and replacing 60 μl of media with fresh media. Paraformaldehyde-fixed gels can be utilized to visualize fluorescence or perform immunostaining using various antibodies directed to CD31 or extracellular matrix proteins. Glutaraldehyde-fixed gels are typically stained with 0.1 % toluidine blue in H_2O, which is an excellent stain to visualize tubes using light microscopy.

3.2 EC-Pericyte Tube Co-assembly Assay in 3D Collagen Matrices

HUAECs or HUVECs are placed in collagen gels (2.5 mg/ml) at 2×10^6 cells/ml while pericytes are added at 0.4×10^6 cells/ml (Figs. 1 and 4). Also added to the gels are 200 ng/ml of SCF, IL-3, SDF-1α, and FGF-2, and 28 μl of the cell-gel mixture are added to the half-area 96-well plate as described above. After polymerization and equilibration for 30–60 min, M199 culture media (100 μl/well) is added per well, and contains a 1:250 dilution of RSII, 40 ng/ml of FGF-2, and 50 μg/ml of ascorbic acid. Cultures are typically allowed to proceed for 3 or 5 days of culture. For the 5-day culture time point, cultures are fed on day 3 by removing and replacing 60 μl of media with fresh media. Cultures are fixed with

either 2 % paraformaldehyde in PBS for immunostaining and fluorescence microscopy or 3 % glutaraldehyde in PBS to then stain with 0.1 % toluidine blue in H_2O.

3.3 Pericyte Invasion into 3D Collagen Matrices in Response to PDGF-BB

Collagen gels (2.5 mg/ml) are prepared as described above and contain 200 ng/ml of recombinant PDGF-BB, without the addition of cells. 28 μl of gel preparation is added per well in half-area 96-well plates as described above. Gels are allowed to polymerize and equilibrate the pH by placing them in a CO_2 incubator for 30–60 min. After this time, pericytes are seeded at 50,000 cells/well in M199 culture media (100 μl/well) that contains a 1:250 dilution of RSII, FGF-2 at 40 ng/ml, and ascorbic acid at 50 μg/ml. Cultures are allowed to incubate for 3 days of culture and then fixed with 3 % glutaraldehyde in PBS (140 μl per well). Fixed cultures are stained with 0.1 % toluidine blue in H_2O. For analysis, gels can be imaged by focusing on the very bottom of the well, where pericytes have migrated completely through the gel and have a flattened morphology (Fig. 3). Alternatively, gels can be bisected with a clean razor blade to visualize a cross section of pericyte invasion in 3D collagen matrices (Fig. 3). Pericytes readily invade in response to PDGF-BB, which is synthesized by ECs and directly appears to stimulate pericyte invasion toward EC-lined tubes. These properties can be utilized to define whether or not a cell behaves as a pericyte, or if a particular gene of interest affects PDGF-BB-induced pericyte invasive behavior in 3D matrices.

3.4 Priming of ECs with VEGF and FGF-2 to Activate EC Morphogenic Responses

T25 or T75 cm^2 flasks of HUAECs or HUVECs are cultured to confluence in Supermedia as described above, then washed 2× with 3 or 7 ml of base M199 media, respectively, and then co-cultured for 16–20 h in M199 media containing one of the following: (a) a 1:250 dilution of RSII only; (b) 1:250 RSII and VEGF-165 (40 ng/ml); (c) 1:250 RSII and FGF-2 (40 ng/ml), or (d) 1:250 RSII, VEGF-165 (40 ng/ml), and FGF-2 at 40 ng/ml. After this time, ECs are trypsinized and used for either the EC only or EC-pericyte co-culture assays as described previously and above. In all cases, EC morphogenic responses are strongly enhanced using this VEGF priming protocol. Our work suggests that the major morphogenic influence of VEGF is in priming and preparing ECs for morphogenic responses that are stimulated by the hematopoietic stem cell cytokines, SCF, IL-3, and SDF-1α [37].

We have shown that a key consequence of pericyte recruitment to HUVEC-lined tubes is the deposition of vascular basement membrane matrices (Fig. 1). Here, we recapitulate these findings using HUAECs which rapidly form tubes and also dramatically recruit pericytes to the abluminal surface of the tubes (Fig. 4). This recruitment results in markedly increased deposition of collagen type IV, fibronectin, nidogen 1, and laminin, which shows again

3.5 Analysis of Vascular Basement Membrane Deposition Resulting from EC-Pericyte Interactions During Tube Co-assembly in 3D Collagen Matrices

that EC-pericyte interactions lead to vascular basement membrane matrix assembly (Fig. 4).

EC-pericyte co-cultures are established in 3D collagen gels as described above and after 3 or 5 days of culture, cultures are fixed with 2 % paraformaldehyde. A critical point is that the immunostaining protocol for vascular basement membrane matrix assembly is performed in the absence of detergent, such that only extracellular staining is observed. We typically utilize unlabeled ECs and GFP-pericytes and thus stain for the vascular basement membrane components, laminin, fibronectin, collagen type IV, nidogen 1, nidogen 2, and perlecan, using AlexaFluor 594-conjugated secondary antibodies so that they are red in color (Fig. 4). To stain ECs, we typically utilize antibodies to CD31 and utilize the AlexaFluor-conjugated secondary antibody to stain them red (Figs. 1 and 4).

3.6 Lentiviral Infection of ECs or Pericytes with Doxycycline-Inducible Gene Vectors Facilitates Analysis of Genes of Interest During Specific Stages of Vascular Morphogenesis and Maturation

A critical addition to our serum-free, defined 3D matrix assays is the ability to regulate the expression of specific genes in an inducible fashion to address their functions at distinct times of the assay (Figs. 5, 6, 7, and 8). A requirement for such lentiviral experiments is that doxycycline (Dox) alone has no deleterious influence on the cell's functional ability to participate in morphogenic events in this system, which it does not (Fig. 7). For this inducible system, we have utilized a technique whereby ECs or pericytes are infected sequentially with lentiviruses; the first contains a Tet3G-ON vector, while the second carries a Tre3G-ON vector in which we have cloned a specific gene of interest (GOI) (Fig. 5). The Tet3G vector is selected with 500 μg/ml G418, and once selected cells have propagated (a maintenance dose of 200 μg/ml), the cells are infected with the Tre3G lentivirus, and selected using 1 μg/ml puromycin (a maintenance dose of 0.35 μg/ml) (*see* **Notes 3** and **4**).

Following the derivation of cell lines, assays of ECs alone or EC-pericyte co-cultures are performed exactly as described above. A schematic of the infection, selection, and assay process is illustrated (Fig. 5). A clear example of how genes are induced only when Dox (5 μg/ml) is added can be observed (Fig. 6). Pericytes carrying inducible GFP or mCherry are treated in 2D cultures with or without Dox overnight and cultures were photographed under light and fluorescence and were also lysed and Western blots performed to examine the degree of induction as well as the background expression of either GFP or mCherry (Fig. 6). A similar experiment was performed in the EC-pericyte co-culture morphogenesis assay where ECs are induced to express GFP, while pericytes are induced to express mCherry following addition of Dox. mCherry-labeled pericytes are observed following their recruitment to EC tubes which are labeled with GFP. Also, tube formation is not affected by Dox administration compared to control (Fig. 7). A specific functional example of this Dox-regulated system is illustrated by the induction of the MT1-MMP inhibitor, TIMP-3, in

ECs which results in markedly reduced EC tube formation compared to control (Fig. 8).

The sequences of the primers used for the GFP, mCherry, and TIMP-3 constructs for the inducible system are as follows:

GFP- UP- Not1: 5′-AGGCGGCCGCACCATGGTGAGCAAGG GCGAGGAGCTG-3′

GFP- DN- EcoR1: 5′-AGGAATTCTTACTTGTACAGCTCGTC CATG-3′

mCherry- UP- BamH1: 5′-AGGGATCCACCATGGTGAGCAAG GGCGAGGAG-3′

mCherry- DN- Not1: 5′-AGGCGGCCGCTTACTTGTACAGC TCGTCCATGCC-3′

TIMP-3- UP- BamH1: 5′-AGGGATCCACCATGACCCCTTGG CTCGGGCTCATC-3′

TIMP-3- DN- EcoR1: 5′-AGGAATTCTCAGGGGTCTGTGG CATTGATGATG-3′

4 Notes

1. Two key reasons for our success over the years in performing these EC tube morphogenesis assays are that we make our own bovine brain extract as well as make our own rat tail collagen type I preparations. In this way, we have an internal consistency (for more than 15 years) that is not dependent on variable commercial sources or availability issues.

2. For optimal assays, ECs should be of passages 2–6 and "Supermedia" growth media should be made and used to feed cells exactly as we describe. Because of different factors that are used in commercially available media, they may adversely impact the performance of the assays that we describe. This issue has not been assessed in detail; however, our assays are highly reproducible if performed as we describe, and they will work well each time an assay is established.

3. G418 selection is relatively mild, but the cell line used and virus titer will determine how quickly selection occurs, which is evidenced by patchy areas where cells have detached with a large increase in cell debris. It usually takes up to a week for selection to begin; it is recommended to utilize G418 at a dose of 400–600 μg/ml, and then use 200 μg/ml for maintenance feeding after selection has occurred. Depending on the virus titer, anywhere from 30 to 90 % of cells will die off.

4. ECs are highly sensitive to puromycin treatment, so it is important to find a balance between rapid selection and

getting the cells to a lower maintenance dose as quickly as possible. Conversely, pericytes are less sensitive, and the higher 1 μg/ml dose may need to be maintained for a longer period of time (3–5 days) before selection is observed. In our experience, a common observation for ECs or pericytes during puromycin selection is that cells will select very suddenly overnight, with a large amount (at least 50 %) of cell death within a period of 12 h.

References

1. Davis GE (2012) Molecular regulation of vasculogenesis and angiogenesis: recent advances and future directions. In: Homeister JW, Willis MS (eds) Molecular and translational vascular medicine. Springer, New York, NY, pp 169–206

2. Davis GE, Stratman AN, Sacharidou A, Koh W (2011) Molecular basis for endothelial lumen formation and tubulogenesis during vasculogenesis and angiogenic sprouting. Int Rev Cell Mol Biol 288:101–165

3. Davis GE, Stratman AN, Sacharidou A (2011) Molecular control of vascular tube morphogenesis and stabilization: Regulation by extracellular matrix, matrix metalloproteinases and endothelial cell-pericyte interactions. In: Gerecht S (ed) Biophysical regulation of vascular differentiation. Springer, New York, NY, pp 17–47

4. Holderfield MT, Hughes CC (2008) Crosstalk between vascular endothelial growth factor, notch, and transforming growth factor-beta in vascular morphogenesis. Circ Res 102:637–652

5. Nicosia RF, Zorzi P, Ligresti G, Morishita A, Aplin AC (2011) Paracrine regulation of angiogenesis by different cell types in the aorta ring model. Int J Dev Biol 55:447–453

6. Sacharidou A, Stratman AN, Davis GE (2012) Molecular mechanisms controlling vascular lumen formation in three-dimensional extracellular matrices. Cells Tissues Organs 195:122–143

7. Senger DR, Davis GE (2011) Angiogenesis. Cold Spring Harb Perspect Biol 3:a005090

8. Stratman AN, Davis GE (2012) Endothelial cell-pericyte interactions stimulate basement membrane matrix assembly: influence on vascular tube remodeling, maturation, and stabilization. Microsc Microanal 18:68–80

9. Iruela-Arispe ML, Davis GE (2009) Cellular and molecular mechanisms of vascular lumen formation. Dev Cell 16:222–231

10. Armulik A, Genove G, Betsholtz C (2011) Pericytes: developmental, physiological, and pathological perspectives, problems, and promises. Dev Cell 21:193–215

11. Adams RH, Alitalo K (2007) Molecular regulation of angiogenesis and lymphangiogenesis. Nat Rev Mol Cell Biol 8:464–478

12. Davis GE, Senger DR (2005) Endothelial extracellular matrix: biosynthesis, remodeling, and functions during vascular morphogenesis and neovessel stabilization. Circ Res 97:1093–1107

13. Xu K, Cleaver O (2011) Tubulogenesis during blood vessel formation. Semin Cell Dev Biol 22:993–1004

14. Swift MR, Weinstein BM (2009) Arterial-venous specification during development. Circ Res 104:576–588

15. Hynes RO (2007) Cell-matrix adhesion in vascular development. J Thromb Haemost 5 (Suppl 1):32–40

16. Astrof S, Hynes RO (2009) Fibronectins in vascular morphogenesis. Angiogenesis 12:165–175

17. Saunders WB, Bohnsack BL, Faske JB et al (2006) Coregulation of vascular tube stabilization by endothelial cell TIMP-2 and pericyte TIMP-3. J Cell Biol 175:179–191

18. Stratman AN, Malotte KM, Mahan RD, Davis MJ, Davis GE (2009) Pericyte recruitment during vasculogenic tube assembly stimulates endothelial basement membrane matrix formation. Blood 114:5091–5101

19. Stratman AN, Saunders WB, Sacharidou A et al (2009) Endothelial cell lumen and vascular guidance tunnel formation requires MT1-MMP-dependent proteolysis in 3-dimensional collagen matrices. Blood 114:237–247

20. Hammes HP (2005) Pericytes and the pathogenesis of diabetic retinopathy. Horm Metab Res 37(Suppl 1):39–43

21. Stratman AN, Schwindt AE, Malotte KM, Davis GE (2010) Endothelial-derived PDGF-BB and HB-EGF coordinately regulate pericyte recruitment during vasculogenic tube assembly and stabilization. Blood 116:4720–4730

22. Davis GE, Camarillo CW (1996) An alpha 2 beta 1 integrin-dependent pinocytic mechanism involving intracellular vacuole formation

and coalescence regulates capillary lumen and tube formation in three-dimensional collagen matrix. Exp Cell Res 224:39–51

23. Sacharidou A, Koh W, Stratman AN, Mayo AM, Fisher KE, Davis GE (2010) Endothelial lumen signaling complexes control 3D matrix-specific tubulogenesis through interdependent Cdc42- and MT1-MMP-mediated events. Blood 115(25):5259–5269

24. Somanath PR, Ciocea A, Byzova TV (2009) Integrin and growth factor receptor alliance in angiogenesis. Cell Biochem Biophys 53:53–64

25. Hynes RO (2009) The extracellular matrix: not just pretty fibrils. Science 326:1216–1219

26. Wang X, Harris RE, Bayston LJ, Ashe HL (2008) Type IV collagens regulate BMP signalling in Drosophila. Nature 455:72–77

27. Benjamin LE, Hemo I, Keshet E (1998) A plasticity window for blood vessel remodelling is defined by pericyte coverage of the preformed endothelial network and is regulated by PDGF-B and VEGF. Development 125:1591–1598

28. Benjamin LE, Golijanin D, Itin A, Pode D, Keshet E (1999) Selective ablation of immature blood vessels in established human tumors follows vascular endothelial growth factor withdrawal. J Clin Invest 103:159–165

29. Saunders WB, Bayless KJ, Davis GE (2005) MMP-1 activation by serine proteases and MMP-10 induces human capillary tubular network collapse and regression in 3D collagen matrices. J Cell Sci 118:2325–2340

30. Davis GE, Pintar Allen KA, Salazar R, Maxwell SA (2001) Matrix metalloproteinase-1 and −9 activation by plasmin regulates a novel endothelial cell-mediated mechanism of collagen gel contraction and capillary tube regression in three-dimensional collagen matrices. J Cell Sci 114:917–930

31. Davis GE, Senger DR (2008) Extracellular matrix mediates a molecular balance between vascular morphogenesis and regression. Curr Opin Hematol 15:197–203

32. Daneman R, Zhou L, Kebede AA, Barres BA (2010) Pericytes are required for blood–brain barrier integrity during embryogenesis. Nature 468:562–566

33. Armulik A, Genove G, Mae M et al (2010) Pericytes regulate the blood–brain barrier. Nature 468:557–561

34. Koh W, Stratman AN, Sacharidou A, Davis GE (2008) In vitro three dimensional collagen matrix models of endothelial lumen formation during vasculogenesis and angiogenesis. Methods Enzymol 443:83–101

35. Nakatsu MN, Hughes CC (2008) An optimized three-dimensional in vitro model for the analysis of angiogenesis. Methods Enzymol 443:65–82

36. Aplin AC, Fogel E, Zorzi P, Nicosia RF (2008) The aortic ring model of angiogenesis. Methods Enzymol 443:119–136

37. Stratman AN, Davis MJ, Davis GE (2011) VEGF and FGF prime vascular tube morphogenesis and sprouting directed by hematopoietic stem cell cytokines. Blood 117: 3709–3719

38. Smith AO, Bowers SLK, Stratman AN, Davis GE (2013) Hematopoietic stem cell cytokines and fibroblast growth factor-2 stimulate human endothelial cell-pericyte tube co-assembly in 3D fibrin matrices under serum-free defined conditions. PLoS One 8(12): e85147

39. Stratman AN, Kim DJ, Sacharidou A, Speichinger KR, Davis GE (2012) Methodologic approaches to investigate vascular tube morphogenesis and maturation events in 3D extracellular matrices in vitro and in vivo. In: Zudaire E, Cuttitta F (eds) The textbook of angiogenesis and lymphangiogenesis: methods and applications. Springer, Netherlands, pp 101–126

Chapter 13

Three-Dimensional Traction Force Microscopy of Engineered Epithelial Tissues

Alexandra S. Piotrowski, Victor D. Varner, Nikolce Gjorevski, and Celeste M. Nelson

Abstract

Several biological processes, including cell migration, tissue morphogenesis, and cancer metastasis, are fundamentally physical in nature; each implicitly involves deformations driven by mechanical forces. Traction force microscopy (TFM) was initially developed to quantify the forces exerted by individual isolated cells in two-dimensional (2D) culture. Here, we extend this technique to estimate the traction forces generated by engineered three-dimensional (3D) epithelial tissues embedded within a surrounding extracellular matrix (ECM). This technique provides insight into the physical mechanisms that underlie tissue morphogenesis in 3D.

Key words Micropatterning, Biomechanics, Engineered tissue

Abbreviations

2D	Two-dimensional
3D	Three-dimensional
BSA	Bovine serum albumin
DMEM	Dulbecco's modified Eagle's medium
DVC	Digital volume correlation
ECM	Extracellular matrix
EMT	Epithelial-mesenchymal transition
FBS	Fetal bovine serum
HBSS	Hanks' balanced salt solution
PBS	Phosphate-buffered saline
PDMS	Polydimethylsiloxane
TFM	Traction force microscopy

1   Introduction

1.1   History and Importance of Traction Force Microscopy (TFM)

Many fundamental biological processes are driven by an interplay between mechanical and biochemical signals, including cell proliferation [1], differentiation [2–4], and epithelial-mesenchymal transition (EMT) [5, 6]. Quantifying the mechanical forces that cells exert, however, and assessing their role in the vast array of molecular signaling networks that regulate cell behavior is a tremendous challenge. This is partially owing to the fact that mechanical loads act across hierarchical length scales. (For example, should we be measuring forces at the level of the cytoskeleton, the level of the organism, or somewhere in between?) In addition, cells are usually ill suited to traditional mechanical tests, as they are small and often mechanically inaccessible, both when embedded in a dense meshwork of ECM and when interconnected with neighboring cells in an intact epithelium.

Still, despite these challenges, significant progress has been made in the study of mechanical forces in biology with the advent of traction force microscopy (TFM). This technique involves cells (or tissues) cultured on or embedded within a flexible substratum that can deform in response to cell-generated tractions. If the mechanical properties of the substratum are well characterized, then the traction forces that generated the observed deformations can be calculated (*see* **Note 1**).

When TFM was first invented, deformations were restricted to two dimensions (2D), since cells were typically cultured on thin films [7–10]. TFM was later expanded to three-dimensional (3D) systems: first, by accounting for 3D deformations of the underlying substratum during 2D cell culture [11], and then later by studying individual cells embedded in 3D gels [12]. Single cells have been estimated to exert forces on the order of 10 nN on their surrounding substrata [11].

1.2   Recent Contributions

We were among the first to fully extend 3D TFM into a multicellular context. Engineered mammary epithelial tissues can be embedded within 3D collagen gels [13] containing fluorescently labeled polystyrene microspheres, which are used to track the deformations of the gel during culture and thereby estimate the traction stresses exerted by the developing tissues [14]. Here we present a detailed protocol for these experiments, which can be readily extended to other types of cells, gels, and tissues.

2   Materials

2.1   PDMS Stamps

1. Polydimethylsiloxane (PDMS) (Sylgard 184, Ellsworth Adhesives).

2. PDMS curing agent (Sylgard 184, Ellsworth Adhesives).

    3. Lithographically patterned silicon master.

    4. Plastic weigh boat.

    5. 100 mm Petri dishes (Fisher Scientific).

    6. 70 % (v:v) Ethanol.

    7. Razor blade.

2.2 Micropatterning Materials

Prepare collagen mixture on ice. Keep reagents at 4 °C.

1. 10× Hanks' balanced salt solution (HBSS).

2. Cell culture media: 1:1 Dulbecco's modified Eagle's medium: Ham's F12 Nutrient Mixture (DMEM/F12 (1:1), Hyclone) supplemented with 2 % fetal bovine serum (FBS), 5 μg/mL insulin, and 50 μg/mL gentamicin.

3. Phosphate-buffered saline (PBS).

4. 0.1 N NaOH.

5. Bovine type I collagen (non-pepsinized; Koken, Tokyo, Japan).

6. 1 μm diameter fluorescent polystyrene beads (Invitrogen).

7. 1 % (m:v) bovine serum albumin (BSA) in PBS. Store at 4 °C.

8. Curved stainless steel tweezers (#7 Dumont).

9. 35 mm tissue culture dishes (Fisher Scientific).

10. 15 mL conical tube (Fisher Scientific).

11. 1.5 mL Eppendorf Safe-Lock Tube (Eppendorf).

12. Circular #1 glass coverslips, 15 mm in diameter (Bellco Glass Inc.).

13. Vybrant DiI (or DiO) cell-labeling solution (Invitrogen).

14. 0.05 % 1× Trypsin–EDTA (Invitrogen).

15. 70 % (v:v) Ethanol.

16. Ice.

2.3 Confocal Fluorescence Microscopy

1. CCD camera attached to an inverted spinning disk confocal microscope.

2. 0.05 % (v:v) Triton X-100 in PBS.

2.4 Tracking Bead Displacements

1. Imaris, Version 7.6.3 (Bitplane).

2.5 Calculating Average Displacement Fields

1. MATLAB (The Mathworks).

2.6 Reconstructing Tissue Geometry

1. Inventor Professional (AutoDesk, Inc.).

2.7 Computing Traction Forces

1. COMSOL Multiphysics, Version 4.2a (COMSOL AB).

3   Methods

Here, we describe a 3D engineered tissue model used to quantify the traction forces exerted by tissues on their surrounding ECM (Fig. 1). Collagen matrices containing fluorescent beads with multiple tube-shaped cavities of defined geometry are created using a microlithography-based technique. The cavities are then seeded with epithelial cells labeled with fluorescent vital dye (DiI). The tissues and surrounding fluorescent beads are then imaged in 3D using confocal fluorescence microscopy both before and after treatment with Triton X-100. Bead displacements are tracked in 3D, and the resultant traction stresses are calculated using computational modeling.
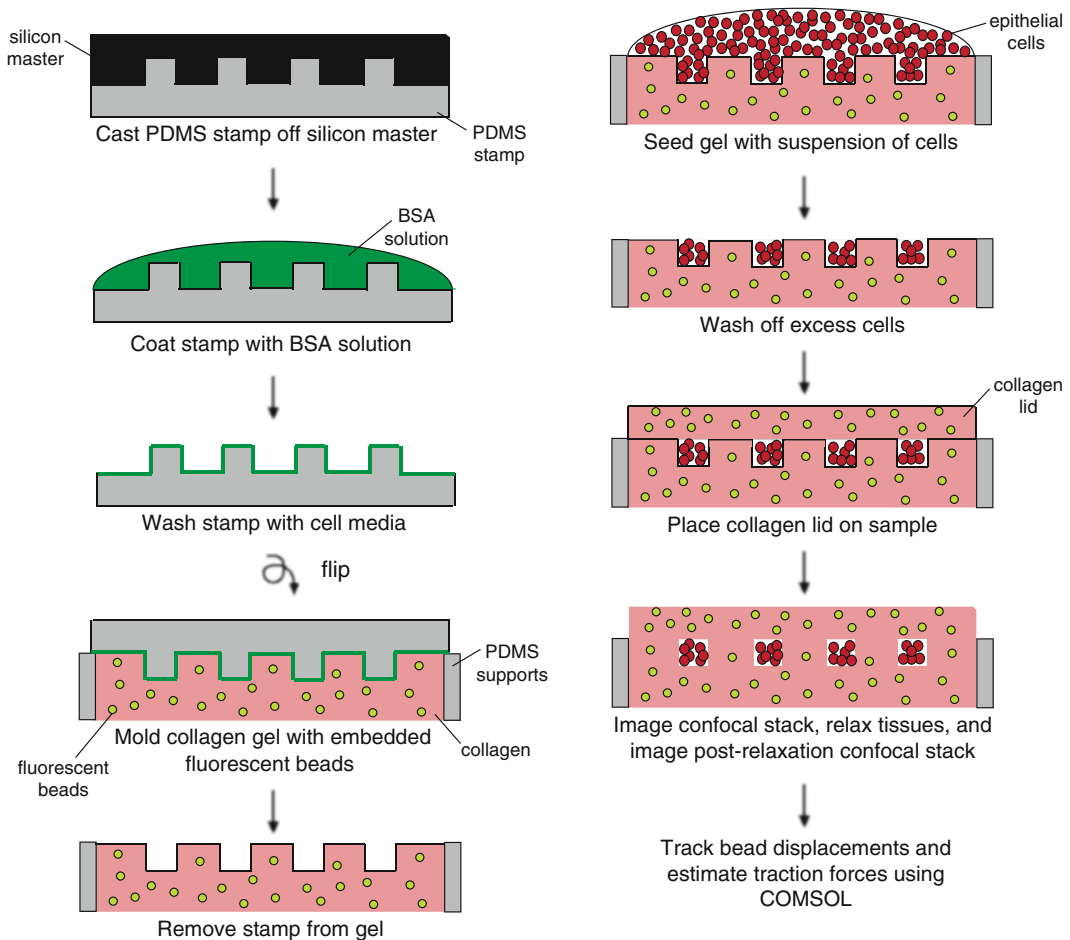
Fig. 1 Schematic of procedure for preparing samples

3.1 Preparation of PDMS Stamps for 3D Micropatterning

1. Mix the PDMS prepolymer and curing agent at a 10:1 (w:w) ratio. Aim for a total weight of approximately 60 g. Remove the entrapped air bubbles by degassing in a vacuum chamber (~15 min). Pour the bubble-free mixture onto a lithographically patterned silicon master in a large weigh boat. Cure the PDMS in an oven at 60 °C for at least 2 h.

2. Once the PDMS is cured, remove the rims from the weigh boat and carefully peel the PDMS from the silicon wafer, removing any PDMS on the bottom of the master. Using a clean razor blade, remove any excess PDMS from around the imprinted features, leaving the remaining PDMS in a circular shape.

3. Using a clean razor blade, cut the polymerized PDMS into stamps (~5 mm cubes), making one stamp for each sample. Place the stamps feature side up in a 100 mm Petri dish.

4. Create supports for the PDMS stamps by spreading 2–3 g of PDMS on a 100 mm Petri dish using a spin coater (*see* **Note 2**). Cure the PDMS as described above. Using a razor blade, cut out two (~5 mm square) supports per PDMS stamp and place the supports in the Petri dish containing the PDMS stamps.

5. In a biosafety cabinet (cell culture hood), sterilize stamps and supports by washing briefly with 70 % ethanol and aspirating the excess liquid. Allow residual ethanol to evaporate completely (~2 min).

3.2 Micropatterning of 3D Epithelial Tissues

1. In a biosafety cabinet, coat four PDMS stamps with approximately 200 μL of 1 % BSA in PBS (*see* **Note 3**). Leave the BSA-coated stamps at 4 °C for a minimum of 4 h to eliminate air bubbles.

2. Aspirate BSA from the four PDMS stamps.

3. Add cell culture media to the stamp surfaces, aspirate, and repeat (200 μL per four stamps per wash should be sufficient).

4. Using curved stainless steel tweezers, place the PDMS supports in the 35 mm tissue culture dishes (two supports per stamp, separated by a distance slightly less than the length of the stamp).

5. Wash four circular glass cover slips (15 mm in diameter, #1) with 70 % ethanol and aspirate the excess liquid. Place these in a 100 mm Petri dish.

6. In a chilled 1.5 mL Eppendorf tube, prepare a neutralized solution of collagen. Add 50 μL 10× HBSS, 30 μL 0.1 N NaOH, 30 μL cell culture media, and 400 μL of stock collagen for a final concentration of 4 mg/mL (*see* **Note 4**). Mix slowly by pipetting up and down; try not to introduce bubbles. If bubbles are introduced, centrifuge the mixture. If fluorescent beads are to be used for TFM, add them to the collagen mixture at this time at a high concentration (~4×10^8 beads/mL).

7. Distribute 200 μL of the collagen mixture evenly on the surfaces of the PDMS stamps (approximately 50 μL per stamp).

8. Using the curved tweezers, flip the stamps upside down onto the supports in the tissue culture dishes and place the dishes into the incubator at 37 °C for approximately 30 min. Add 50 μL of the collagen mixture onto each of the circular cover slips (these will be the collagen caps that are placed on top of the patterned tissues) and place these into the incubator at 37 °C for approximately 30 min.

9. Aspirate the media from a 100 mm tissue culture dish that is 40 % confluent with epithelial cells. Add 10 μL Vybrant DiI (or DiO) (Invitrogen) in 2 mL of fresh culture media to the tissue culture dish and incubate at 37 °C for 15 min.

10. After the incubation, aspirate the media containing DiI or DiO, wash the cells once with PBS, and trypsinize the cells using 2 mL of trypsin.

11. Add 8 mL of cell culture media to the trypsinized cells, place in a 15 mL conical tube, and centrifuge at 800 rpm for 5 min.

12. After the centrifugation step, aspirate the supernatant and resuspend the cells in 250–400 μL of cell culture media for a final cell concentration of ~10^6–10^7 cells/mL (*see* **Note 5**).

13. Remove the tissue culture dishes containing the PDMS stamps and collagen from the incubator and lift the PDMS stamps off of the collagen using the curved tweezers (*see* **Note 6**); the stamps can now be discarded.

14. Add 30 μL of cell suspension onto each collagen gel. While observing under a microscope, shake the dishes so that the cells settle into the patterned collagen (*see* **Note 7**).

15. After ~5 min (or whenever the cells have settled into the wells of the pattern), wash the stamps with 430 μL of cell culture media by tilting the tissue culture dish on its side and allowing the media to pour over the stamp (*see* **Note 8**). Aspirate the wash from the tissue culture dish and repeat.

16. Place the collagen containing the cells in the incubator at 37 °C for 15 min. Then, place the glass cover slips with collagen caps on top of the cell-containing gels so that the cells are completely embedded in collagen (Fig. 2). Place the dishes in the incubator at 37 °C again for 15 min.

17. Add cell culture media slowly (~2.5 mL) on top of the glass cover slip until the cell-containing gels are covered in media, and place the dishes in the incubator at 37 °C.

3.3 Confocal Time-Lapse Imaging of Fluorescent Bead Displacements and Tissue Morphogenesis

1. Monitor the positions of the fluorescent beads by collecting confocal stacks of the tissues: 120 images (spaced 1 μm apart).

2. Relax the tissues by adding 0.05 % Triton X-100 in PBS overnight.

3. Capture a second stack of post-relaxation images (120 images, 1 μm apart) of fluorescent beads the next day (*see* **Note 9**).
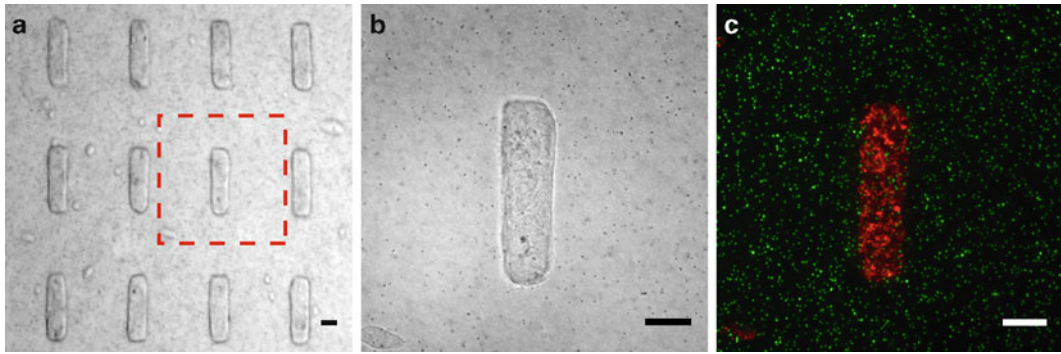
Fig. 2 (**a**) Bright-field image of micropatterned epithelial tissues. (**b**) Higher magnification view of micro-patterned tissue presented in (**a**). (**c**) Confocal fluorescence image (maximum z intensity) of tissue shown in (**b**); 1 μm diameter fluorescent microspheres (*green*), DiI-labeled cells (*red*). *Scale bars* = 50 μm

4. To account for experimental noise in the motion of the fluorescent beads, monitor the positions of the beads in cell-free collagen gels (*see* **Note 10**).

3.4 Tracking Bead Displacements

1. For each tissue, import 3D image stacks into Imaris (*see* **Note 11**). There should be two time points—before and after treatment with Triton X-100.

2. Correct for rigid body drift between image stacks.

   (a) Select Edit → Properties, and input voxel dimensions.

   (b) In Surpass view, use Spots filtering to select a region of beads far away from the tissue.

   (c) Track these spots using the Autoregressive Motion routine.

   (d) Highlight all tracks in the "Edit Track" window and select "Correct Drift." This should be largely rigid body motion (i.e., only translations and rotations).

   (e) In Surpass view, the newly drift-corrected image stack should appear.

3. Quantify 3D bead displacements in the entire imaging volume using the Spots filter and the Autoregressive Motion tracking routine (Fig. 3) (*see* **Note 12**).

4. Export the tracked displacements as a spreadsheet. The following quantities will be used for further analysis:

Track Position Start X	Track Position Start Y	Track Position Start Z	Track Displacement X	Track Displacement Y	Track Displacement Z
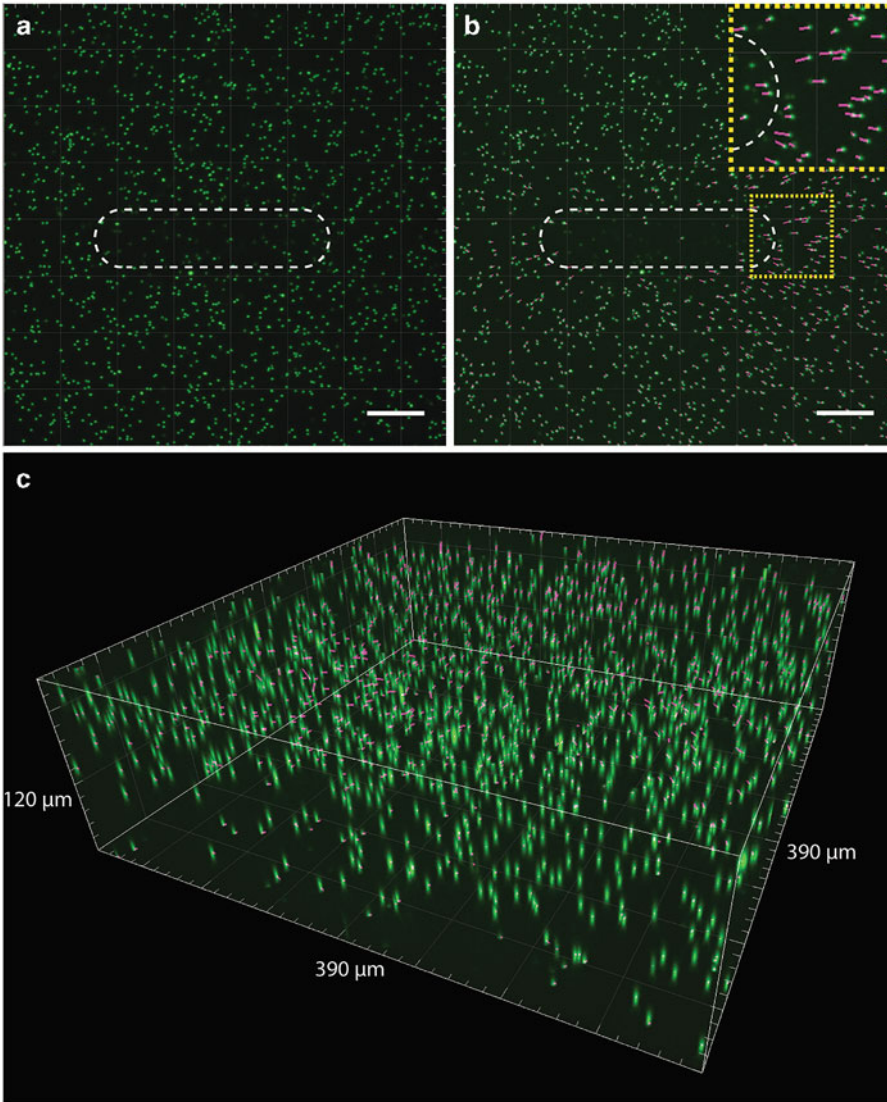
Fig. 3 (**a**) Maximum z intensity image of confocal stack showing fluorescent microspheres before treatment with Triton X-100; the epithelial tissue outline is indicated with a *white dashed line*. (**b**) Maximum z intensity image of confocal stack showing fluorescent microspheres after treatment with Triton X-100; bead displacements are shown in *purple*, and the tissue outline is indicated with a *white dashed line*. The *inset* shows a higher magnification view of the *boxed region*. (**c**) 3D reconstruction of bead trajectories shown in (**b**) with indicated dimensions. *Scale bars* = 50 μm

3.5 Computing Average Displacement Field (Using Data from Multiple Tissues)

1. Use the *griddata* subroutine in MATLAB to interpolate the exported displacement data across a 3D grid spanning the entire imaging volume. Use Track Position Start X, Y, Z to define a point cloud, and then interpolate each component of the displacement field (e.g., Track Displacement X) separately. These data are often fairly noisy (Fig. 4a).
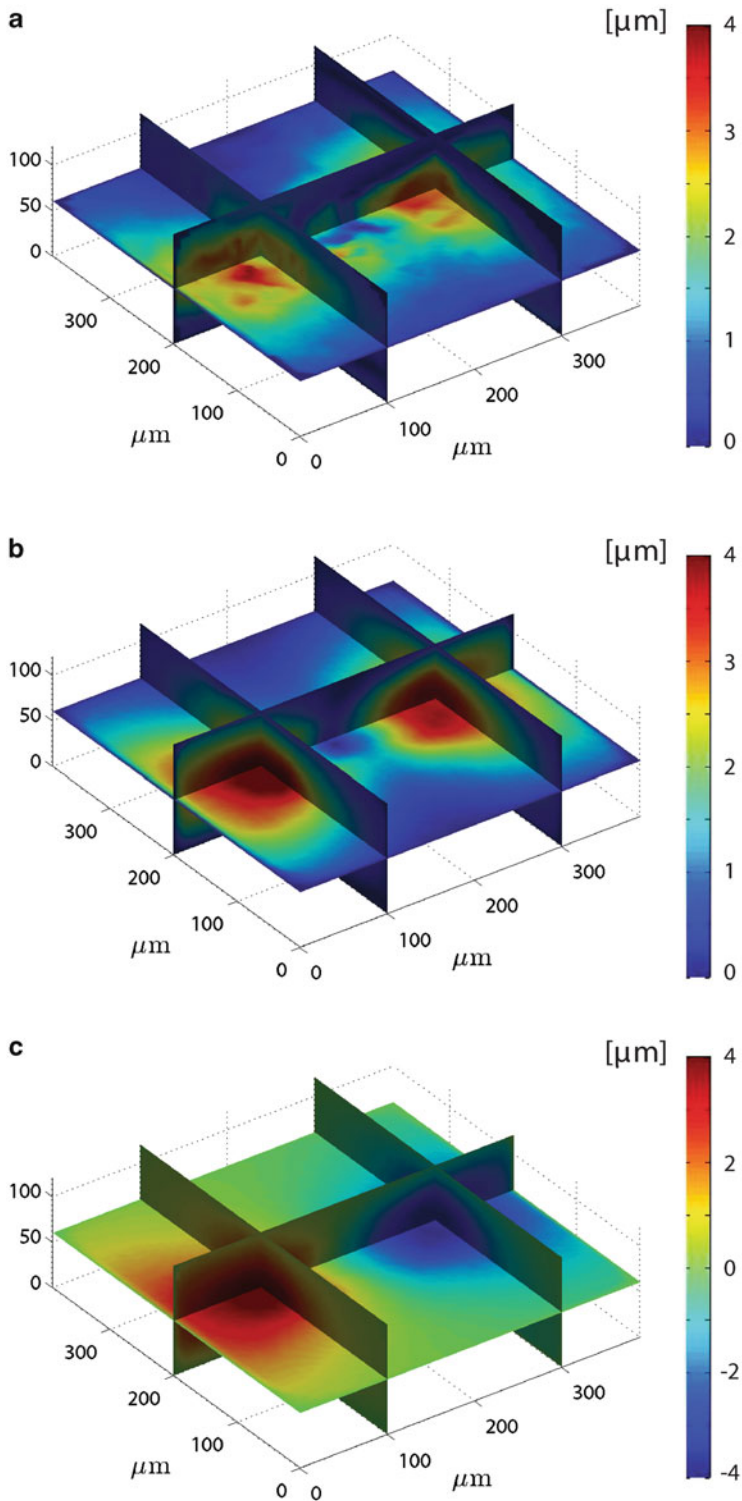
Fig. 4 (**a**) Plot of the interpolated total displacement field for a single tissue. (**b**) Plot of the interpolated total displacement field averaged over 20 tissues. (**c**) Plot of the averaged x component of the displacement field
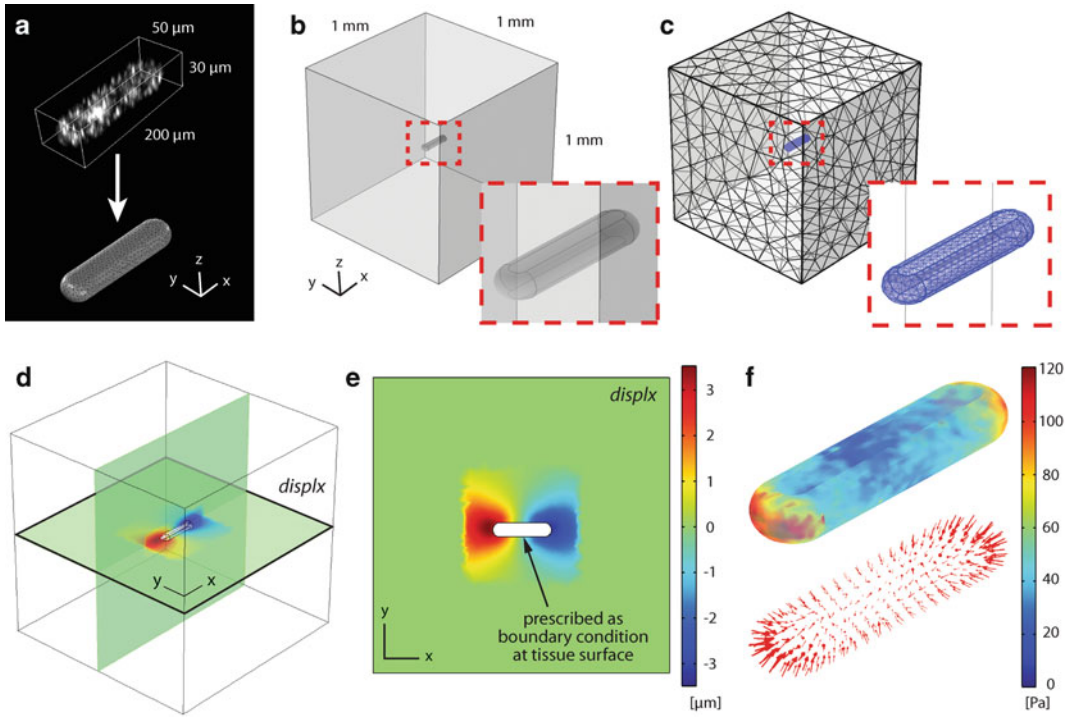
Fig. 5 (**a**) Tissue geometry was reconstructed in AutoDesk Inventor from measurements of fluorescently labeled tissues in Imaris. Adapted from [14]. (**b**) Model geometry used to compute traction forces in COMSOL Multiphysics. (**c**) Finite element mesh. (**d**, **e**) Imported displacement field prescribed as boundary condition along the surface of imported tissue geometry. Here, the x component of the displacement field "displx" is shown. (Compare to Fig. 4c.) (**f**) Model-computed traction stresses

2. To increase the signal-to-noise ratio, each component of the displacement field can be averaged across multiple tissues (Fig. 4b, c), but only if the displacement data from multiple tissues are properly aligned using the fluorescently labeled tissue geometry. Especially for small displacements, subtle alignment errors can produce significant artifacts in the averaged displacement field.

3. Ensure that the data for each component of the displacement field is organized in a format compatible with the finite element package used to compute the resultant traction forces.

3.6 Reconstructing and Exporting Tissue Geometry

1. Using Imaris, measure average morphological parameters (e.g., tissue length, height) for several fluorescently labeled tissues (Fig. 5a).

2. Use the measured parameters to draw a 3D surface in Auto-Desk Inventor Professional. Save the reconstructed geometry as an Inventor .ipt file (Fig. 5a).

3.7 Calculating Traction Forces

1. Construct a 3D finite element model to compute the traction forces exerted by the engineered tissues. Although other commercial software packages can be used, the following protocol employs COMSOL Multiphysics Version 4.2a (*see* **Note 13**).

   (a) Open COMSOL Multiphysics and create a New (File → New…) model file.

   (b) Select "3D" for Space Dimension, "Solid Mechanics (solid)" for Add Physics, and "Stationary" for "Select Study Type" (*see* **Note 14**). Click the "Finish" icon.

2. Create model geometry.

   (a) Click "Geometry 1" and specify the appropriate units for length.

   (b) Right-click "Geometry 1" in the Model Builder window, and click "Import." Under the "Geometry import:" pull-down menu, select "3D CAD file," then click "Browse…" to locate the Inventor .ipt file containing the exported tissue geometry, and click "Import" (*see* **Note 15**). Ensure that "Solids" and "Surfaces" are checked under "Objects to import" and that "Form solids" is selected under the "Import options" pull-down menu. (If the length units specified in the CAD file are correct, ensure that "From the CAD document" is selected from the "Length unit" pull-down menu.)

   (c) Right-click "Geometry 1" in the Model Builder window, and click "Block." Under the "Size and Shape" menu, select values for "Width," "Depth," and "Height" that are significantly larger than those of the imported tissue geometry. This block will represent the surrounding collagen gel. (The appropriate size will depend on how far the displacement field propagates into the gel. The displacements should all decay to zero before the outer boundary of the block. Here, we specified a cube with sides of 1 mm.) Click the "Build Selected" icon.

   (d) Right-click "Geometry 1" in the Model Builder window, and under the "Transforms" menu, click "Move." Under "Input objects:," click on the imported tissue geometry and click the "+" icon. Select "imp1" (i.e., the imported tissue geometry) and specify values for "x," "y," and "z" that move the tissue to a location within the surrounding gel that will coincide with the position of the tissue in the measured displacement field exported from Imaris. (The two must be aligned to ensure that the correct experimental displacements are interpolated along the model tissue surface.)

(e) Right-click "Geometry 1" in the Model Builder window, and under the "Boolean Operations" menu, click "Difference." Under "Objects to add," click on the block and click the "+" icon. Under "Objects to subtract," click on the imported tissue geometry and click the "+" icon.

(f) Right-click "Geometry 1" in the Model Builder window, and click "Build All." This final geometry (Fig. 5b) represents the geometry of collagen gel surrounding the tissue.

3. Import the (averaged) experimental displacements.

   (a) Right-click "Global Definitions" in the Model Builder window, and under the "Function" menu, select "Interpolation."

   (b) Under "Data Source," select "File" and click "Browse..." to locate the data file containing the x component of the averaged gel displacements. (Ensure that the units of the grid points specified in the imported displacements file match the units in the model.)

   (c) Select the appropriate data format and assign the function a name. (Here we use "displx".) Check the box for "Use space coordinates as arguments." Under the Extrapolation pull-down menu, select "Specific value" and input "0" for "Value outside range."

   (d) Repeat and create separate interpolation functions for the y and z components of the averaged gel displacements. (Here we name these functions "disply" and "displz," respectively.)

   (e) Right-click "Definitions" under "Model 1" in the Model Builder window, and select "Variables." Select "Boundary" from the "Geometric entity level" pull-down menu. Ensure that "Manual" has been selected from the "Selection" menu.

   (f) Select the surfaces bounding the imported tissue geometry and define the following variable:

   $$tract \; \mathrm{sqrt}\left(\mathrm{solid.Tax}^2 + \mathrm{solid.Tay}^2 + \mathrm{solid.Taz}^2\right)$$

4. Define mechanical properties and boundary conditions

   (a) Expand "Solid Mechanics (*solid*)" in the Model Builder window, and click "Linear Elastic Material Model 1."

   (b) Ensure that the entire model geometry is selected. Under the "Linear Elastic Model" menu, select "Isotropic" and specify the Young's modulus and Poisson's ratio as follows (*see* **Note 16**):

E	Young's modulus	User defined	750 Pa
ν	Poisson's ratio	User defined	0.2

(c) Right-click "Solid Mechanics (*solid*)" and select "Prescribed Displacement." Under "Boundary Selection," ensure that "Manual" is selected, and select the surfaces bounding the tissue by clicking on them individually and selecting "+" (Fig. 5d, e).

- Check the box next to "Prescribed in x direction" and input the following (*see* **Note 17**):

$$u_0 - \text{displx} * 10^{(-6)}$$

- Repeat for displacements in the y and z directions, using "disply" and "displz," respectively.

(d) Right-click "Solid Mechanics (*solid*)" and select "Fixed Constraint." Under "Boundary Selection," ensure that "Manual" is selected, and select each of the outer surfaces of the box representing the collagen gel.

5. Create model mesh.

(a) Right-click "Mesh 1" in the Model Builder window. Select "Free Triangular" under "More Operations."

(b) Under "Geometric entity level," ensure that "Boundary" is selected from the pull-down menu and that "Manual" is selected from the "Selection" menu.

(c) Select the surfaces bounding the imported tissue geometry.

(d) Right-click "Free Triangular 1" and select "Size." Under the "Predefined" list for "Element Size," select "Fine."

(e) Right-click "Mesh 1," and select "Free Tetrahedral." Ensure that "Remaining" is selected as the "Geometric entity level."

(f) Right-click "Free Tetrahedral 1" and select "Size." Under the "Predefined" list for "Element Size," select "Coarser."

(g) Right-click "Mesh 1" and select "Build All" (Fig. 5c).

6. Solve model and plot results.

(a) Right-click "Study 1" in the Model Builder window and select "Compute." Once the solution converges, results can be plotted in the "Results" tab. (Ensure that the scale factor for deformations in all plots is set to 1.)

(b) To plot traction stresses, right-click "Results" and create a "3D Plot Group." Right-click the "3D Plot Group" and select "Surface." Under "Expression," type "tract" (defined above) and click Plot (Fig. 5f).

(c) Ensure that model displacements reasonably reproduce those observed experimentally. If they do not, a more accurate description of the mechanical properties of the surrounding gel may be needed. Alternatively, nonlinear effects due to large deformations may likewise need to be included in the analysis.

4   Notes

1. It is important to note that forces are not measured directly here. Instead, they are calculated from the observed deformations of flexible substrata. The accuracy of the computed forces is thus highly dependent on the measured mechanical properties of these flexible materials, which are (typically) only characterized for a specific set of loading conditions. Moreover, simplifying assumptions such as material linearity, isotropy, and homogeneity are often assumed. These assumptions are often made for convenience and only approximate the actual behavior of real materials. The traction forces computed using TFM are thus only estimates.

2. The thickness of the supports will determine how close the epithelial tissues are to the bottom of the tissue culture dish.

3. In a biosafety cabinet, place four dots of BSA in the four corners of each stamp and one in the center, and then spread with a pipet tip so that BSA covers the entire stamp.

4. When using a new bottle of collagen (5 mg/mL), check the pH of the final mixture. The pH should be 8–8.5; adjust the volume of NaOH accordingly.

5. Err on the side of less media; a more concentrated cell suspension will promote faster and more homogeneous settling of the cells into the collagen cavities.

6. Gently lift the PDMS stamps off the collagen as vertically as possible so as not to disturb the pattern.

7. To improve settling of the cells into patterned wells, place the tissue culture dishes next to a bench top centrifuge set to 700 rpm. The vibrations from the centrifuge shake the cells into the collagen cavities.

8. It may be easier to wet the bottom support first so that the wash flows straight down.

9. The elastic recoil happens quickly after adding the detergent (as soon as the detergent diffuses in and lyses the cells). Full relaxation/viscous flow is complete after treating with detergent overnight.

10. This accounts for noise owing to bead movement (which is negligible in these dense gels) as well as for inaccuracies in the

Imaris tracking algorithm. In a single sample, signal-to-noise was typically 5:1, but averaging data from multiple samples attenuated the ratio to ~20:1.

11. Other (free) tracking applications are available. Their implementation, however, requires that the user is proficient with different programming languages (e.g., MATLAB). Examples include Crocker and Grier's 3D particle tracking algorithm [15], and Franck and colleagues' digital volume correlation (DVC) [16].

12. Filters (using quantities such as track length) can be used to screen errant tracks.

13. Although the steps outlined in this protocol are specific to COMSOL Multiphysics Version 4.2a, a similar workflow can be developed in both older and newer versions of the software.

14. In selecting a "Stationary" study type, we thereby neglect inertial effects, which are typically negligible in problems such as cell migration and tissue morphogenesis.

15. Several other CAD formats are compatible with COMSOL. If one would prefer not to use Inventor, consult the COMSOL Mulitphysics User's Guide for a list of these alternatives [17].

16. As only a first approximation, we assume linear elastic material properties for the surrounding collagen gel [14].

17. In our analysis, displacements were interpolated in micrometers and therefore converted into meters. The negative sign is owing to the fact that displacements were tracked from before to after treatment with Triton X-100—that is, from the deformed to the undeformed configuration of the gel, which here must be reversed.

Acknowledgements

References

1. Nelson CM, Jean RP, Tan JL, Liu WF, Sniadecki NJ, Spector AA, Chen CS (2005) Emergent patterns of growth controlled by multicellular form and mechanics. Proc Natl Acad Sci U S A 102(33):11594–11599

2. McBeath R, Pirone DM, Nelson CM, Bhadriraju K, Chen CS (2004) Cell shape, cytoskeletal tension, and rhoa regulate stem cell lineage commitment. Dev Cell 6 (4):483–495

3. Engler AJ, Sen S, Sweeney HL, Discher DE (2006) Matrix elasticity directs stem cell lineage specification. Cell 126(4):677–689

4. Lui C, Lee K, Nelson CM (2012) Matrix compliance and rhoa direct the differentiation of mammary progenitor cells. Biomech Model Mechanobiol 11(8):1241–1249

5. Gomez EW, Chen QK, Gjorevski N, Nelson CM (2010) Tissue geometry patterns epithelial-mesenchymal transition via intercellular mechanotransduction. J Cell Biochem 110(1):44–51

6. Lee K, Chen QK, Lui C, Cichon MA, Radisky DC, Nelson CM (2012) Matrix compliance regulates rac1b localization, nadph oxidase assembly, and epithelial-mesenchymal transition. Mol Biol Cell 23(20):4097–4108

7. Harris AK, Wild P, Stopak D (1980) Silicone rubber substrata: a new wrinkle in the study of cell locomotion. Science 208(4440):177–179

8. Lee J, Leonard M, Oliver T, Ishihara A, Jacobson K (1994) Traction forces generated by locomoting keratocytes. J Cell Biol 127(6 Pt 2):1957–1964

9. Dembo M, Oliver T, Ishihara A, Jacobson K (1996) Imaging the traction stresses exerted by locomoting cells with the elastic substratum method. Biophys J 70(4):2008–2022

10. Dembo M, Wang YL (1999) Stresses at the cell-to-substrate interface during locomotion of fibroblasts. Biophys J 76(4):2307–2316

11. Maskarinec SA, Franck C, Tirrell DA, Ravichandran G (2009) Quantifying cellular traction forces in three dimensions. Proc Natl Acad Sci U S A 106(52):22108–22113

12. Legant WR, Miller JS, Blakely BL, Cohen DM, Genin GM, Chen CS (2010) Measurement of mechanical tractions exerted by cells in three-dimensional matrices. Nat Methods 7 (12):969–971

13. Nelson CM, Inman JL, Bissell MJ (2008) Three-dimensional lithographically defined organotypic tissue arrays for quantitative analysis of morphogenesis and neoplastic progression. Nat Protocols 3(4):674–678

14. Gjorevski N, Nelson CM (2012) Mapping of mechanical strains and stresses around quiescent engineered three-dimensional epithelial tissues. Biophys J 103(1):152–162

15. Crocker JC, Grier DG (1996) Methods of digital video microscopy for colloidal studies. J Colloid Interface Sci 179(1):298–310

16. Franck C, Hong S, Maskarinec SA, Tirrell DA, Ravichandran G (2007) Three-dimensional full-field measurements of large deformations in soft materials using confocal microscopy and digital volume correlation. Exp Mech 47 (3):427–438

17. Comsol multiphysics user's guide (2011). Comsol 4.2a. COMSOL AB, Burlington, MA.

Part III

Manipulating Cells and Tissues In Vivo

Chapter 14

Probing Cell Mechanics with Subcellular Laser Dissection of Actomyosin Networks in the Early Developing *Drosophila* Embryo

M. Rauzi and P.-F. Lenne

Abstract

Laser dissection is a useful tool in developmental biology to probe mechanical forces from the subcellular to the tissue/embryo scale. During tissue morphogenesis, cells are equipped with networks of actomyosin that generate forces. Here we present a technique based on near-infrared (NIR) femtosecond (fs) pulsed laser dissection that allows subcellular ablation of actomyosin networks. This technique allows to selectively ablate actomyosin networks while preserving cell plasma membrane. The resulting relaxation of the remaining network after laser dissection is imaged and analyzed to deduce local forces responsible for tissue morphogenesis in the developing *Drosophila* embryo.

Key words Cell mechanics, Actomyosin network, Submicron dissection, Membrane preservation, IR femtosecond laser, High NA objective, Fast confocal imaging, Safety procedures

1 Introduction

Probing the cell mechanics in vivo is crucial to understand how cells and tissues acquire and maintain their shape. During the last decade, laser dissection by near-infrared (NIR) femtosecond (fs) pulses has proven to be an efficient tool to disrupt structures, which support mechanical tension in vitro and in vivo [1, 2]. It produces subcellular disruption with low collateral damage due to nonlinear absorption processes and localized plasma formation [3, 4]. Here we present the application of this technique to study subcellular mechanics of actomyosin networks in the early *Drosophila* embryo.

2   Materials

2.1   Safety Equipment

For safety reasons build the system in a dedicated room with controlled access. Use adapted light-protecting goggles (for the laser specified here below, with optical density (OD) 11 at 1,030 nm wavelength) (*see* **Note 1**).

2.2   Laser, Optical, and Mechanical Components

1. 1 W average power, 1,030 nm wavelength, 50 MHz, 200 femtosecond Yb::YAG solid state laser (Mikan, Amplitude Systèmes, Pessac, FRANCE) connected to its controller. Fs lasers at other NIR wavelengths could be used alternatively.

2. A mechanical shutter with diameter greater than the laser beam width and with a time cycle of opening/closing of a millisecond.

3. One Dichroic mirror for IR light reflection and visible light transmission (FF01-750/SP, Semrock).

4. Four coated mirrors for IR light reflation (*see* **Note 2**).

5. One light-polarizing prism, one polarization rotator $\lambda/2$ for 1,030 nm wavelength mounted on a computer-controlled mechanical rotating wheel.

6. A telescope composed of two lenses with IR coating for optimal IR light transmission (*see* **Note 3**).

7. A power meter with a head light detector adapted to >1 W light source.

8. IR visor and IR fluorescent paper disc that can be mounted on a lens holder for IR laser light alignment.

9. An inverted microscope (*see* **Note 4**) equipped with a nanometer precision moving stage and high numerical aperture (NA) high-magnification IR-corrected objective (e.g., Plan Apochromat $60\times$ water immersion NA 1.2 by Nikon, or C-Apochromat $63\times$ water immersion NA 1.2 by Zeiss having 65 % transmission at 1,030 nm).

10. A commercial spinning disc system coupled to the microscope for fast confocal imaging.

11. A periscope to elevate the optical path.

12. Rails to mount all optical components, lens and mirror holder, screws. The system should be mounted on an optic table.

2.3   Software and Controllers

1. Use LabView software to control all mechanical components and to read and plot the CCD frames captured during live acquisition.

2. Use an image-processing software (e.g., ImageJ) to process the images for force measurement.

3. Three controllers connected to the computer are necessary: (1) for controlling the opening and closing of the shutter; (2) for rotating the $\lambda/2$, thus modulating the intensity of the laser; and (3) for controlling the microscope stage to position the sample.

2.4 Sample Preparation Equipment

Two types of sample have to be prepared: the laser alignment sample and the biological sample (*Drosophila* melanogaster embryo).

2.4.1 Laser Alignment Sample

1. 0.17 mm glass cover slip.
2. 500 nm fluorescent polystyrene beads.

2.4.2 Biological Sample

1. 0.17 mm glass cover slip, bleach, heptane glue, and halocarbon oil. For more detailed information about the materials for embryo preparation for confocal imaging and laser dissection refer to [5].
2. For membrane preservation control after ablation use a caged fluorescein (0.9 kDa) UV uncageable (Molecular Probes).

3 Methods

All experiments are done at 22° room temperature. Pay special attention to safety procedure to avoid any eye, skin, and fire hazard. Here are presented just some of the major safety procedures. Do refer to more detailed information on the laser safety norms according to the European (EN 207/208/60825) or the American standards (ANSI Z136). Use the IR visor and the IR fluorescent paper disc to visualize the laser beam. Here we present as an experiment the ablation of junctional actomyosin. The laser surgery system presented in this method session is optimized for punctual ablation by fixing in space the ablating focal point and moving the sample with the microscope stage. A similar procedure can be applied for cell medial-apical actomyosin meshwork ablation [6].

3.1 Safety Procedures

1. Wear eye-protecting goggles when the laser is shooting.
2. Work as much as possible in bright room conditions while building the surgery system. Brightness reduces the NA of the eye and thus reduces the risk of eye hazard.
3. Do not wear a watch or any metal bracelets while setting up and using the system.
4. Avoid crossing with your eyes the plane on which the optic path mostly travels through by installing all controllers possibly above the optic table.
5. Design and build an optical path that travels as long as possible close (few centimeters) to the optic table.
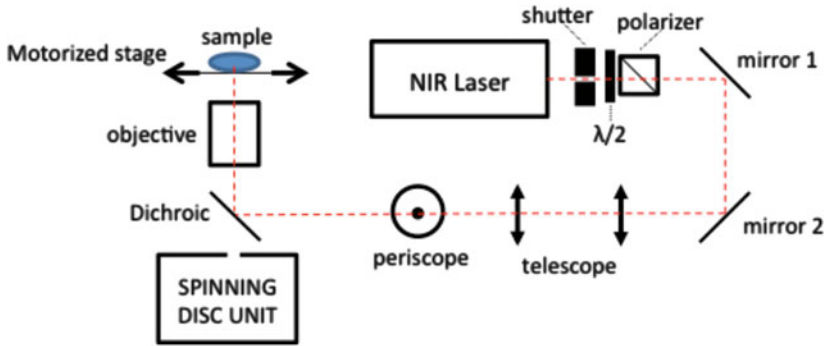
Fig. 1 Schematics of the laser dissection setup

6. Always keep your goggles on even when looking through the IR visor.

7. After setting up the laser dissection system, build a protection box (e.g., in metal to absorb IR light) around it to protect the user from IR laser light exposure.

3.2 Setting Up the Laser Dissection Optical Path

1. Position and fix to the optic table the microscope and the laser in a way that with two 90° reflections the beam is directed towards one lateral side of the microscope (*See* Fig. 1).

2. Position as close as possible in front of the laser exit and fix to the table the mechanical shutter (*see* **Note 5**).

3. Position after the shutter, align to the laser line, and fix the λ/2 and the polarizing prism as close as possible to the laser. These two optical elements in conjunctions constitute the laser beam attenuator. If you follow the optic path, the λ/2 should come first and then the polarizer. Nevertheless when installing the attenuator you should first position the prism, mounted on a manual rotator, and orient it in order to have maximal light transmission (*see* **Note 6**). Position the λ/2 in front of the polarizer. Both optical components should be aligned with the laser line.

4. Place two mirrors to reflect the beam towards the microscope with two 90° reflections. These two mirrors are mounted on mirror holders equipped with at least two screws representing the two degrees of freedom of movement per holder (four degrees of freedom in total) used to align the laser into the telescope. Do not place the mirrors too close to one another for a more efficient alignment of the telescope (*see* **step 6**).

5. Place and fix the telescope on a rail and align it more over with the two times reflected beam. The telescope is composed of two lenses that expand the beam to a width equal to the diameter of the back aperture of the objective (*see* **Note 7**). The lens with smallest focal length should come first.

6. To align the beam to the telescope put two irises aligned in front of the two lenses of the telescope. Use the four reflecting degrees of freedom given by the two mirrors to align the beam to the center of the two lenses (*see* **Note 8**).

7. Place, align, and fix the periscope bringing upwards the optical path closer to the back aperture of the objective. The two mirrors of the periscope are mounted in a way that their long axis is lying on the inclination of the mirror in order to reflect the full expanded beam.

8. Place the dichroic mirror underneath the back aperture of the objective with a ~45° angle in order to reflect the beam coming from the periscope into the objective.

9. The dichroic is also mounted on a holder having at least two degrees of freedom of movement. Use these degrees of freedom along with the ones of the mirrors mounted on the periscope to align the laser beam into the objective (*see* **Note 9**).

3.3 Alignment Sample Preparation

Make a single layer of 500 nm fluorescent beads over a cover slip (*see* **Note 10**).

3.4 Focal Ablation Spot Alignment

1. Use the alignment sample to focus the IR light onto the same focal plane as the imaging system. While imaging the monolayer of beads let the IR laser shutter open with laser at full power (1 W) and move back and forth the lens of the telescope with greater focal length until the laser beam ablates the monolayer. Since the power is very high a big cluster of beads is ablated.

2. Reduce gradually the power and the time exposure and find gradually the optimal position of the lens of the telescope for successful bead ablation. By moving such lens you are changing the depth at which the IR laser is focused by the objective. You should finally find the optimal conditions (laser power and telescope lens position) necessary to ablate one single bead with few milliseconds laser exposure time.

3. Reduce further the laser power: the bead will just bleach. Check if the bead was ablated or bleached by passing from fluorescence confocal imaging to bright-field diffraction imaging.

3.5 Computer Communication with the External Mechanical Devices

Use LabView software to communicate and control the opening/ closing of the shutter; the $\lambda/2$ angular position does modulate the laser power and the microscope stage to position the desired region of the sample in the focus of the objective.

3.6 Biological Sample Preparation

1. Collect *Drosophila* embryos after 4 h of egg laying in order to perform the ablation experiments during embryo gastrulation. Bleach the embryos and wash them with water.

2. Transfer the embryos over a solid substrate of agar gel. Align and orient the embryos.

3. Take a cover slip and spread some heptane glue over it. Glue the embryos onto the cover slip by gently pressing the glue side of the cover slip against the agar.

4. Put few drops of halocarbon oil over the embryos sticking on the cover slip. For more detailed information about the methods for embryo preparation for confocal imaging and laser dissection refer to [5].

3.7 Laser Dissection Experiments of Actomyosin Bundles

1. Use *Drosophila* embryos expressing MyoII tagged with fluorescent protein (i.e., GFP) to visualize MyoII or actin-binding protein (like utrophin or moesin) tagged with a fluorescent protein to visualize actin.

2. Displace the microscope stage by using the LabView software over a bundle of actomyosin at the cell junction (usually situated at 5 μm depth from the surface of the embryo).

3. Expose the bundle to 3–5 ms of laser light with an average power of 370 mW on the back aperture of the objective. Control the exposure time by controlling the shutter open/closing time and control the laser intensity by rotating the $\lambda/2$ and by checking the power with the power meter.

4. Use the confocal spinning disc for live imaging of the ablation of the bundle and of its relaxation by capturing 1 frame/s (*see* Fig. 2a, b).

3.8 Probing Cell Membrane Integrity After Laser Ablation

1. To control cell membrane integrity after ablation inject the caged fluorescein in the embryo yolk during the stage of cellularization while cells are still open at their basal side (for injection *see* ref. 7). The caged fluorescein will diffuse in all cells of the embryo.

2. Focus the objective in the center of one of the two cells sharing the ablated actomyosin junction. Uncage the fluorescein by using the same IR laser source used for ablation. Reduce the laser power to 40 mW at the back aperture of the objective (~10-fold less than the power used for ablation) (*see* **Note 11**). If the ablation has perforated the membrane you will notice that both cells sharing the ablated junction will emit fluorescent signal from their cytoplasm (*see* Fig. 3b). If the membrane has been preserved only one cell will highlight (*see* Fig. 3b and **Note 12**).
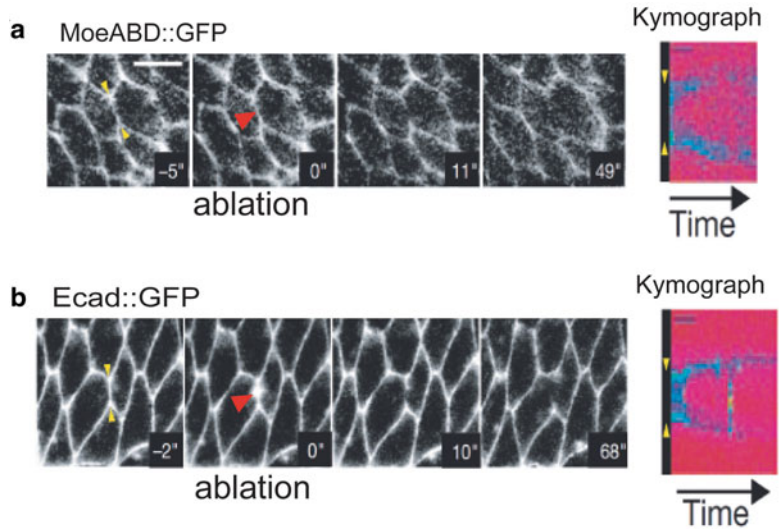
Fig. 2 A punctual ablation in the center of a cell junction depletes actin (**a**) and E-cadherin (**b**). Kymographs show the distribution of each protein along the ablated junction in function of time and the relaxation of the junction. Adapted from ref. 2
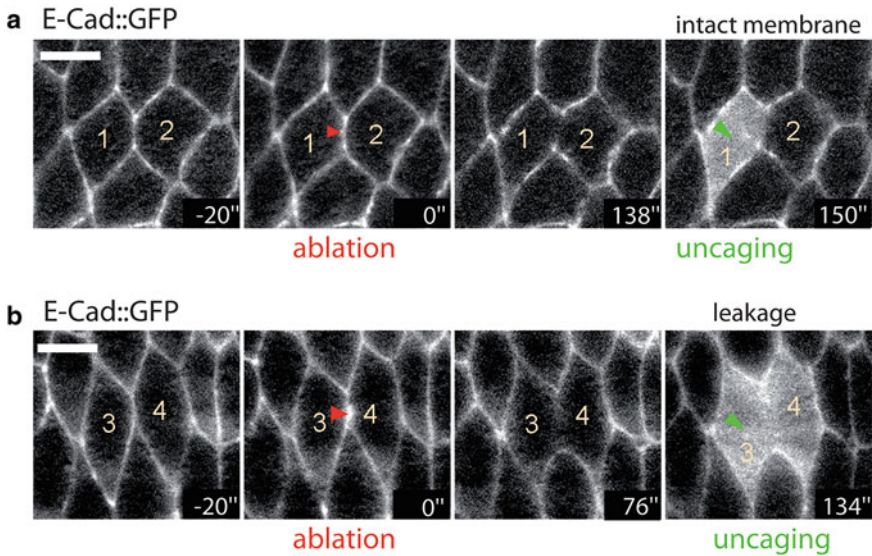
Fig. 3 Control of the membrane preservation after ablation. All cells are loaded with a caged probe used to detect possible holes in the cell membrane after performing laser ablation. (**a**) After ablation (*red arrowhead*), no leakages are detected between cells 1 and 2 since the caged probe, uncaged (*green arrowhead*) in cell 1, does not diffuse out from the cell. (**b**) Using higher laser power or longer laser exposure time is possible to form holes in the cell membrane. After laser ablation, the caged molecule is uncaged (*green arrowhead*) in cell 3 and it leaks in the neighboring cell 4: this experiment shows that the ablation has damaged the contacting membrane of both cells 3 and 4. Adapted from ref. 2 (Color figure online)
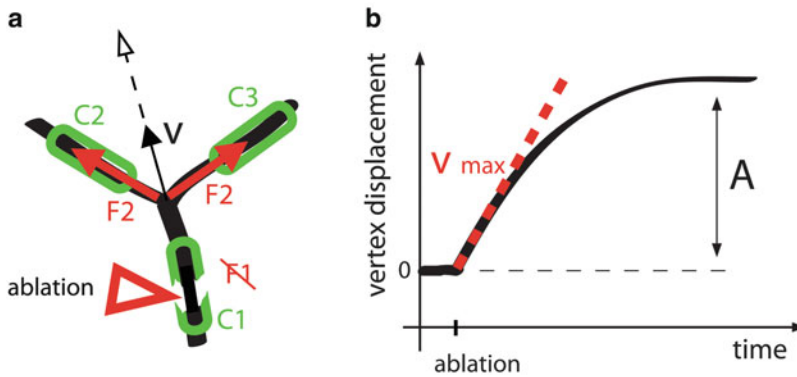
Fig. 4 (**a**) Cartoon representing a three-way cell vertex. A contractile element (C, *green*) produces a cortical force along the junction (F, *red*). After ablating C1, F1 is null and the vertex moves at a certain speed v. (**b**) Plot showing the vertex displacement after ablation in function of time. Vertex speed is maximal (*v*_max) shortly after ablation. At longer time scales, the vertex reaches an asymptotic distance

3.9 Image Analysis for Force Measurement

Open the confocal spinning disc image time lapse of an ablation experiment. Measure the increase over time of the displacement of a vertex of the ablated junction. Measure the slope of the obtained curve just after ablation. This value will give you an estimate of the tension acting on the junction (*see* Fig. 4a, b and **Note 13**).

4   Notes

1. For laser dissection noncommercial systems, like the one presented here, wear eye-protecting goggles before turning on the laser. The laser presented in this method section is a 4-class laser (highest class of danger). Respect this and all additional standard safety procedures for such laser class.

2. Choose accurately the size of the two mirrors that are placed after the telescope, mounted on the periscope. The minor axis should be at least as long as the diameter of the back aperture of the objective used and the major axis should be at least twice as long. The same is for the dichroic mirror.

3. For safety reason one lens should have negative focal length in order to expand the beam without focusing the laser beam before reaching the back aperture of the objective. By focusing the laser the intensity increases and thus the safety procedure gets stricter. Focusing the laser beam can in addition produce plasma in the air, and this would drastically reduce the laser power after the plasma in addition to producing undesired acoustic noise and emitting wide-spectrum light. The focal length of the lenses is chosen in a way that the beam will completely cover the back aperture of the objective (*see* Subheading 3).

4. Inverted Nikon microscopes are generally very suited for laser coupling since they have free accessible space below the back aperture of the objective.

5. The moving part of the mechanical shutter is usually shaped as an iris and when it closes it can leave a small aperture in the center. Do misalign the center of the shutter from the laser beam line in order to have full blocking of the beam when the shutter is closed and still full transmission of the beam when the shutter is open. Do place the shutter with the most reflecting side towards the laser. Give to the shutter an angle so that the reflected part of the beam is reflected not towards to the exit of the laser. Do place a beam block element (made of black metal with a long cavity that avoids the beam to escape) absorbing the light reflected by the mechanical shutter.

6. The efficiency of the $\lambda/2$ of rotating the polarization of the laser light is <100 %. If the polarizer is not oriented along the laser light polarization the maximal transmission of the attenuator is reduced. By turning the polarizing prism and placing the power meter after it you will find the optimal orientation when you will detect maximum power. Check for both the $\lambda/2$ and the polarizer which is the side facing the beam.

7. Choose two lenses having focal length f1 and f2 so that |f1/f2| gives the wanted expanding beam factor. For a beam of 1 mm in diameter and an objective with back aperture of 8 mm you need an expansion factor of 8 (thus, e.g., f1 = 240 mm and f2 = -30 mm). You should then place the two lenses at a distance equal to |f1|−|f2|. Do not choose lenses with focal length smaller than 30 or 25 mm: these short focal length lenses tend to degrade the properties of the laser beam. Use plano-convex lenses, for instance, and remember to position the convex region of both lenses towards the outside of the telescope where the beam is parallel.

8. Use the mirror reflecting the first to align the beam on the first iris/lens of the telescope and the following mirror to align the beam on the second lens. Repeat the alignment in cycles always using the same procedure until reaching perfect alignment.

9. Use an IR fluorescent paper or a mirror mounted on a holder that can be screwed in the place of the objective. This will allow you to see with the IR visor the cross section of the expanded beam and to center it moving the dichroic mirror and the periscope mirrors.

10. To make a single layer of beads dilute the beads in water, then transfer some drops of the solution onto the cover slip, and let it dry slowly. When the water is evaporated the beads will end up forming a monolayer attached to the cover slip.

11. The caged fluorescein is typically uncageable with a UV light source (333 nm). NIR femtosecond pulsed laser can also be used by exploiting a 3-NIRphoton absorption process. Plasma formation in water is instead a higher order [4, 5] multiphoton absorption process.

12. The caged fluorescein is a very small molecule that diffuses 270 $\mu m^2/s$ in water. This is an optimal probe to detect even very short transient holes in the cell membrane. For further control uncage the fluorescein in one cell before ablating one of its junctions.

13. Consider a vertex from which three junctions (L1, L2, and L3) radiate. Three forces can be considered acting on each junction (F1, F2, and F3). These forces reflect the contribution of the actomyosin contractile units (C1, C2, and C3). By considering the system in a quasi-equilibrium state, the resultant of the three forces is null. If now C1 is ablated, F1 can be considered null. In this way the system is driven out of equilibrium and the resultant of forces can be written as $\overrightarrow{F}_{tot} = \overrightarrow{F}_2 + \overrightarrow{F}_3 + \mu \overrightarrow{v}$, where μ is the drag coefficient and $\overrightarrow{v}$ is the speed of vertex displacement. Shortly after ablation a maximum speed is reached that can be written as $v_{\max} = \left\| \overrightarrow{F}_2 + \overrightarrow{F}_3 \right\|_{t=0^+} / \mu$.

Acknowledgement

References

1. Kumar S, Maxwell IZ, Heisterkamp A et al (2006) Viscoelastic retraction of single living stress fibers and its impact on cell shape, cytoskeletal organization, and extracellular matrix mechanics. Biophys J 90:3762–3773

2. Rauzi M, Verant P, Lecuit T et al (2008) Nature and anisotropy of cortical forces orienting Drosophila tissue morphogenesis. Nat Cell Biol 10:1401–1410

3. Niemz MH (2004) Laser-tissue interaction: fundamentals of microscopy. Springer, Berlin

4. Glezer EN, Mazur E (1997) Ultrafast-laser driven micro-explosions in transparent materials. Appl Phys Lett 71:882–884

5. Cavey M, Lecuit T (2008) Imaging cellular and molecular dynamics in live embryos using fluorescent proteins. Methods Mol Biol 420:219–238

6. Rauzi M, Lenne PF, Lecuit T (2010) Planar polarized actomyosin contractile flows control epithelial junction remodelling. Nature 468:1110–1114

7. Pilot F, Philippe JM, Lemmers C et al (2006) Spatial control of actin organization at adherens junctions by a synaptotagmin-like protein Btsz. Nature 442:580–584

Chapter 15

UV Laser Ablation to Measure Cell and Tissue-Generated Forces in the Zebrafish Embryo In Vivo and Ex Vivo

Michael Smutny, Martin Behrndt, Pedro Campinho, Verena Ruprecht, and Carl-Philipp Heisenberg

Abstract

Mechanically coupled cells can generate forces driving cell and tissue morphogenesis during development. Visualization and measuring of these forces is of major importance to better understand the complexity of the biomechanic processes that shape cells and tissues. Here, we describe how UV laser ablation can be utilized to quantitatively assess mechanical tension in different tissues of the developing zebrafish and in cultures of primary germ layer progenitor cells ex vivo.

Key words Zebrafish—UV laser ablation, Mechanical tension, Force generation, Actomyosin cortex, Epiboly, Enveloping layer (EVL), Yolk syncytial layer (YSL), Mesoderm cells

1 Introduction

Morphogenesis is intrinsically a mechanical process where tissues and cells move and deform due to mechanical forces generated in a local microenvironment [1, 2]. Recent studies have provided both experimental and theoretical insight into the molecular and cellular mechanisms by which a complex network of mechanically coupled cells drive tissue morphogenesis by generating forces that are transmitted to neighboring cells, which in turn actively respond to those local forces by modifying transcriptional and posttranslational processes involved in cell shape and fate specification [3–5].

Visualization and measuring of biological forces has been a major challenge. In the last decade, significant advances have been made to develop tools for probing cell mechanics, such as micropipette aspiration, atomic force microscopy, magnetic tweezers, traction force microscopy, and laser ablation [6]. Clearly, to understand the complexity of biomechanic properties of living organisms, it is also necessary to complement qualitative measurements with

quantitative data analysis to enable a precise description of an observed phenomenon [7].

In this section we focus on laser-tissue interactions to visualize tensions within tissues and cells of the developing zebrafish embryo in vivo and ex vivo. Pulsed lasers allow severing of biological tissues with a precision in the range of hundreds of nanometers and provide a powerful tool to locally perturb molecular structures within a single cell or even a subcellular compartment [8, 9]. Depending on the main light parameters several distinct laser-tissue interactions can be achieved, amongst them photochemical interactions, thermal interactions, photoablation, plasma-induced ablation, and photodisruption. In this review, we exclusively describe experimental methods using plasma-induced laser ablation of biological tissue. For in-depth theoretical and technical information on the other abovementioned categories of laser-tissue interactions, we refer the reader to recent excellent reviews on these and related topics [5, 10].

Plasma is formed at high light power densities (exceeding $1,000 \text{ W/cm}^2$) in solids and in fluids, and a nonlinear absorption phenomenon occurs (optical breakdown) that leads to mechanical shock waves in the tissue due to energy absorption of the plasma itself [11]. In principle, plasma can be generated by near-infrared (NIR) and ultraviolet (UV) radiation and both methods have been successfully applied to produce very fine ablations in biological material. In this section, we deal solely with plasma-induced UV laser ablation. Important features of plasma-induced laser ablation are that it needs to be performed on samples that are nonpigmented, like transparent embryonic tissues, and that ablations can be used as a noninvasive tool for ablating biological structures in living embryos without affecting cellular and developmental processes.

This chapter provides protocols to monitor, measure, and analyze tension within the cortex of cells and intercellular forces between cells of the developing zebrafish embryo both in vivo and ex vivo. The zebrafish embryo has proven to be an excellent model to study tissue morphogenesis and offers some key advantages over other vertebrate organisms, such as its quick and external development and optical transparency making it easily accessible to various imaging tools. Moreover, there are multiple transgenic lines available to visualize the actomyosin network in cells of different tissues within the developing embryo.

In the following, we explain in detail how to prepare embryos for high-speed fluorescence imaging on an inverted microscope equipped with a spinning disc, and how an attached UV laser cutter can be used to generate ablations in the enveloping layer (EVL) and in the yolk syncytial layer (YSL) of the developing zebrafish embryo, and on cultured mesoderm germ layer progenitor cells. The EVL is a simple squamous epithelium that spreads together with the underlying deep cells and the YSL over the spherical yolk

to ultimately seal the embryo on the vegetal side [12, 13]. The YSL constitutes a thin multinucleated cytoplasmic layer at the surface of the yolk cell directly beneath the blastoderm and undergoes epiboly movements simultaneously with the EVL, which is connected to the YSL at its margin [13, 14]. Force generation produced by a contractile actomyosin network within the YSL has been previously identified as a critical regulator of EVL epiboly movements [15, 16].

Finally we focus on force generation in ex vivo cultures of primary mesoderm germ layer progenitor cells. Mesoderm progenitor cells undergo collective migration during zebrafish gastrulation, a process that seems to be controlled by the mechanical properties of these cells [17, 18].

2 Materials

2.1 Embryos

1. Wild-type embryos of TL (Tupfel Long fin) background.

2. Transgenic embryos:

   GFP-tagged Lifeact—*Tg*(*actb2:lifeact-GFP*).

   RFP-tagged Lifeact—*Tg*(*actb2:lifeact-RFP*).

   GFP-tagged non-muscle myosin 2 regulatory light chain—*Tg* (*actb2:myl12.1-GFP*).

   mCherry-tagged non-muscle myosin 2 regulatory light chain—*Tg*(*actb2:myl12.1-mCherry*).

   GFP under the *goosecoid* gene promoter—*Tg*(*gsc:GFP*).

2.2 Media

1. $1 \times$ E3 medium:

   5 mM NaCl, 0.17 mM KCl, 0.33 mM $CaCl_2$, 0.33 mM $MgSO_4$. Make a $1 \times$ E3 fresh from a $60 \times$ stock solution.

2. $1 \times$ Danieau's buffer:

   58 mM NaCl, 0.7 mM KCl, 0.4 mM $MgSO_4$, 0.6 mM Ca $(NO_3)_2$, 5 mM HEPES pH 7.2. Prepare each component as a $100 \times$ stock solution, except for NaCl, which should be $50 \times$ concentrated. Add 5 ml of a mixture of 10,000 units penicillin/ ml and 10,000 µg/ml of streptomycin to 1,000 ml of solution when preparing a $1 \times$ buffer.

3. Dulbecco's modified Eagle's medium/nutrient F12 ham mixture (DMEM/F12):

   15.6 g of phenol-free DMEM/F12 powder was dissolved in H_2O, calibrated to pH 7.7, sterile filtered, and stored at 4 °C.

2.3 Dechorionating and Mounting Embryos

1. Stereomicroscope equipped with transmitted and ultraviolet (UV) light.

2. Glass petri dishes (100×15 mm).

3. Two sharp forceps (Dumont no. 5).

4. Plastic Pasteur pipettes (3.5 ml).

5. 150 mm Glass Pasteur pipettes.

6. Stock of 1 % low-melting-point agarose (LMP) dissolved in 1×
   E3 media or 1× Danieau's buffer. Heat solution in microwave
   until it is completely dissolved, aliquot in 1 ml in Eppendorf
   tubes, and store them at 4 °C.

7. Heating block at 70 °C.

8. Heating block at 40 °C.

9. Matek glass-bottom cell culture dishes (35 mm).

2.4 Spinning Disk with UV Laser Cutter Setup

The setup is shown in Fig. 1. The UV laser cutter is based on a
previously described layout [16, 19].

1. Axio Observer Z1 (Zeiss) inverted microscope with a Plan Apo
   water-immersion objectives (40 × 1.2 NA, 63 × 1.2 NA).

2. Confocal spinning disk unit (Andor Revolution Imaging
   System, Yokogawa CSU-X1).

3. Passively Q-switched solid-state 355 nm UV-A laser (Power-
   chip, Teem Photonics).

4. Acousto-optic power modulator (AOM, AA.MQl l0-43-UV,
   Pegasus Optik).

5. Variable zoom beam expander (Sill Optics).

6. Pair of high-speed galvanometric mirrors (Lightning DS,
   Cambridge Technology) with a telecentric f-theta objective
   (Jenoptik).
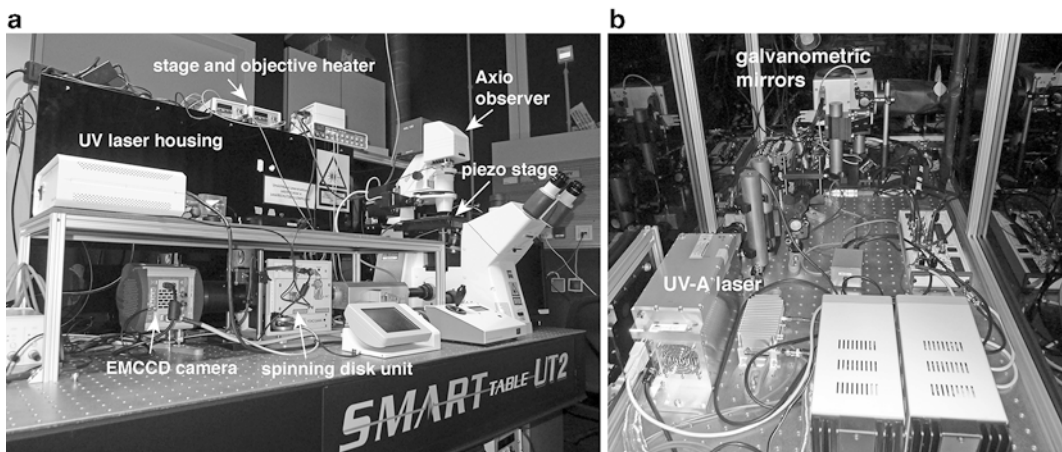
Fig. 1 Setup of the microscope with UV laser cutter. (**a**) Axio Observer Z1 inverted microscope with spinning disk unit; (**b**) UV laser setup inside the housing

7. Motorized stage (MS 2000, ASI) with a piezoelectric actuator.

8. iXon DU-897-BV EMCCD camera (Andor Technology).

9. Custom-built stage heater and objective heater.

10. Computer-controlled custom-built software for cutting in 3D (LabView, National Instruments).

2.5 Preparation and Culturing of Induced Mesoderm Cells

1. Microinjection setup is described elsewhere [20].

2. Cyclops synthetic mRNA (100 pg).

3. Casanova *morpholino* (2 ng, Genetools).

4. Fibronectin from bovine plasma (Sigma-Aldrich).

5. Bovine Serum Albumins (Sigma-Aldrich): Prepare a 50 mg/ml solution in PBS, filter sterile, and keep aliquots at 4 °C.

6. Stereoscope equipped with transmitted and ultraviolet (UV) light.

7. Matek glass-bottom culture dish.

3 Methods

3.1 UV Laser Ablation of the Actomyosin Cortex In Vivo

3.1.1 Obtaining Embryos

To image the actomyosin cortex in the YSL and EVL tissue throughout the course of UV laser ablation procedure, zebrafish transgenic embryos expressing GFP-tagged myosin 2 regulatory light chain or GFP-tagged Lifeact can be used. Expression of the transgene needs to be provided maternally for imaging during gastrulation. To visualize the EVL cell membrane, inject the embryos with *GPI-RFP* mRNA (50 pg).

1. Set up one male and female adult zebrafish of the respective transgenic line per water-filled container box in the evening before the experiment and keep them separated by a mesh of metal or plastic overnight.

2. Next morning put the male and female adult fish together for mating and collect transgenic embryos after the fish have laid.

3. For UV laser ablation of the EVL actomyosin cortex inject *GPI-RFP* mRNA into one-cell stage of transgenic embryos (microinjection setup explained in [20]).

4. Transfer injected embryos into plastic petri dishes.

5. Keep uninjected embryos for control of developmental stages in 1× E3 media.

6. Keep the embryos in a plastic dish containing 1× E3 media at 25–31 °C (*see* **Note 1**).

7. After 2 h, sort out unfertilized eggs and embryos that look sick using a pipette tip and remove them with a plastic Pasteur pipette.

3.1.2 Dechorionating Embryos

For imaging of embryos, the chorions have to be removed before mounting. Here we describe manual dechorionation, which is less invasive for the embryo than enzymatic removal of the chorion. Dechorionated embryos are very sensitive and react with plastic and air; hence care has to be taken not to damage the embryos. For subsequent handling of the embryos use glassware (glass petri dishes) and metalware (forceps) to prevent any damage.

1. Transfer previously selected embryos with a plastic pipette into a glass petri dish containing Danieau's buffer for dechorionation.

2. Use two sharp forceps to make small holes into the chorion and very gently peel off the chorion without injuring the embryo.

3. Remove the floating chorions and eventually damaged embryos from the petri dish and incubate embryos at the desired temperature until mounting.

3.1.3 Handling and Mounting Embryos in Agarose Solution

When using a glass Pasteur pipettes to transfer dechorionated embryos, make sure that the ends of the pipettes have no sharp edges. For time-lapse imaging of living embryos, it is necessary to embed the embryos in a mounting media that is rigid enough to immobilize the embryo while still allowing sufficient flexibility and enough oxygen diffusion for the embryo to develop normally. For imaging embryos on an inverted scope, mount them against a glass cover slip of a Matek dish in an LMP agarose-containing solution.

1. Prepare fire-polished pipettes by quickly moving the front edge of the pipette through a flame of a Bunsen burner to smoothen the edge (*see* **Note 2**).

2. Before mounting the embryos melt 1 % LMP agarose solution at 70 °C for at least 30 min.

3. Transfer the LMP agarose solution to a heating block at 40 °C.

4. Start with the mounting when the embryos are in the desired stage of development.

5. Use the glass Pasteur pipette and slowly suck up to ten dechorionated embryos from the glass dish.

6. Transfer embryos into the Eppendorf tube that contains the melted agarose solution at 40 °C by diluting the agarose as little as possible with additional Danieau's medium. Discard the remaining Danieau's medium from the glass Pasteur pipette.

7. Carefully suck up the embryos from the agarose solution in the Eppendorf tube using the glass Pasteur pipette.

8. Transfer the embryos with the agarose solution from the pipette onto a glass cover slip of a Matek dish. Make sure that the embryos are not touching air when transferred and that the embryos settle down completely on the glass cover slip (*see* **Note 3**).

9. Carefully orient the embryos with a hair loop or a forceps so that the region desired for imaging is facing the cover slip (*see* **Note 4**).

10. Wait for a few minutes until the agarose is solidified and cover with 1× Danieau's solution.

3.1.4 UV Laser Ablation and High-Speed Imaging of the Actomyosin Cortex of the YSL and EVL During Epiboly

The UV laser cutter is based on a previously described layout [16, 19] and detailed technical information about laser nanodissection for biological tissues can be found elsewhere [21]. In brief, a pulsed laser beam operating at a wavelength of 355 nm enables diffraction-limited dissection of the actomyosin cortex. The response of the cortex to the perturbation can be visualized with high spatial-temporal resolution by coupling the ablation system to an inverted spinning disk setup with an ultrasensitive iXon EMCC camera. A custom-designed LabView software allows for simultaneous control of the image acquisition and UV laser ablation systems.

EVL epiboly movements during zebrafish gastrulation are thought to be driven by EVL cell division, motility, and cell–cell rearrangements, and through pulling by an actomyosin ring within the YSL. To investigate how the actomyosin ring within the YSL pulls on the EVL margin, we perform cortical laser ablations of the YSL actomyosin ring in living embryos [16]. Furthermore, to determine how the EVL responds to pulling forces from the YSL actomyosin ring, we utilize cortical laser ablations to map tension distribution within the EVL.

UV Laser Ablation of the Actomyosin Cortex Within the YSL

1. Set temperature on the stage heater as well as objective heater to 28.5 °C.

2. Transfer the embryos mounted on the glass-bottom Matek dish into the dish holder of the temperature chamber (*see* **Note 5**).

3. Use a low-magnification objective to confirm the developmental stage of the embryos.

4. Switch to high-resolution objective (63×) and focus with respective laser and filter settings onto the bright actomyosin structure within the YSL close to the EVL margin in one embryo.

5. As the actomyosin ring is a thin structure, one z plane is sufficient to image the ablation response and acquire images fast (acquisition time 380 ms, loop time 500 ms).

6. Draw the desired ROI using the LabView software along which the cortex will be ablated, e.g., a 20 μm long line 20 μm away from the EVL margin and perpendicular to it (Fig. 2a).

7. UV ablation will be performed point-wise along the line. Therefore adjust the settings of the UV laser for pulse
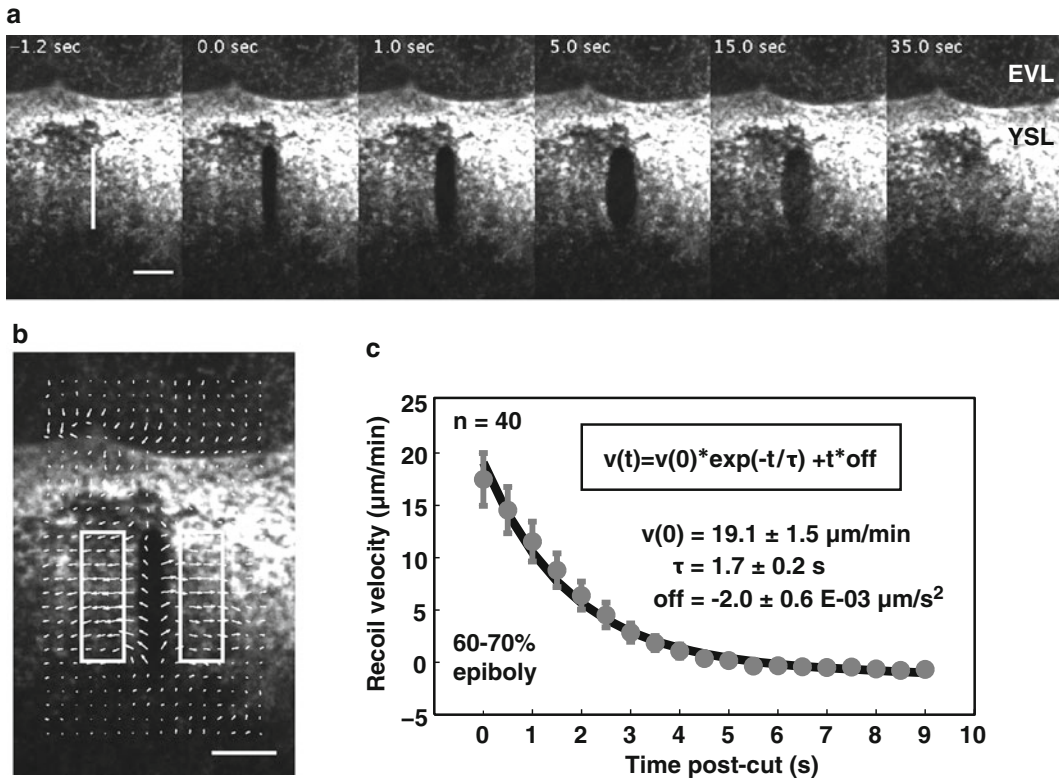
Fig. 2 Laser ablation within the YSL actomyosin ring. (**a**) Image sequence of a *Tg*(*actb2*:*myl12.1-eGFP*) embryo labeling myosin-2 at 70 % epiboly, which has been ablated along a 20 μm long line (*white solid line*) perpendicular to the EVL margin. Fast recoil of the actomyosin network in response to the cut is followed by regrowth of the cortex within the cut opening. Cortex recovery and the lack of visible wound response serve as a control that the plasma membrane has not been permanently damaged. (**b**) PIV analysis produces the 2D velocity field (*white arrows*) of the recoiling actomyosin network. Rectangles (*white solid line*) adjacent to the cut indicate the region, in which components orthogonal to the cut line are averaged to yield the mean recoil velocity for a given time point. (**c**) The average recoil velocity curve for perpendicular cut in embryos at 60–70 % epiboly decays exponential with time. The experimental data (*gray dots*) are fitted using an exponential function (*solid black line*) with linear offset to determine the initial recoil velocity v(0) and the characteristic decay time τ. Error bars denote the error of the mean at 95 % confidence

repetition rate, number of pulses per ablation point, ablation point density, and UV laser intensity for optimal ablation of the cortex (*see* **Note 6**).

8. While the images are being acquired, initialize UV ablation along the designated ROI. During the ablation procedure (e.g., for a 20 μm line with the respective settings: 1.2 s) image acquisition is temporarily paused, but it should cover at least 5 s of the unperturbed cortex before the cut and enough frames afterwards to clearly see the subsequent cortex recovery (>1 min).
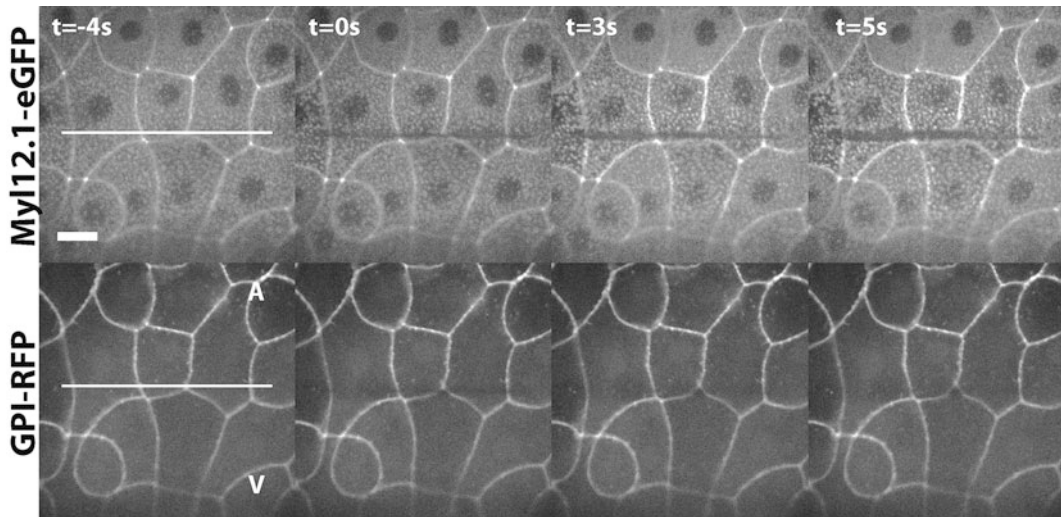
Fig. 3 Laser ablation within the apical actomyosin cortex of the EVL. Image sequence of a 60 % epiboly *Tg* (*actb2:myl12.1-eGFP*) embryo that was injected with *GPI-RFP* mRNA to label the cell membrane (*down*). The apical actomyosin cortex was ablated along 100 μm long line (*white solid lines*), which was placed at about 3–6 cell rows away from the margin and parallel to it. Opening of the actomyosin cortex (*up*) in response to the ablation without affecting the cell membrane integrity (*down*). Animal pole (A) is up and vegetal pole (V) is down. *Scale bar*, 20 μm

9. Switch to a new embryo within the same dish and continue with **steps 3–8**.

10. After cutting all embryos of the dish check once more for the developmental stage to confirm the time window in which the ablation experiments were conducted.

UV Laser Ablation of the Actomyosin Cortex Within the EVL

1. Proceed as indicated in **steps 1** and **2** for UV laser ablation of the actomyosin cortex within the YSL (Subheading UV Laser Ablation of the Actomyosin Cortex Within the YSL).

2. Use a low-magnification objective to confirm the developmental stage of the embryos and the EVL margin location that will serve as a reference when cutting close to the margin.

3. Switch to a high-resolution objective (40×) and focus with respective laser and filter settings onto the apical actomyosin EVL cortex in one embryo.

4. In order to visualize the ablation response in the whole depth of the EVL, acquisition of three z planes per channel (488 and 561 nm wavelengths) is sufficient and also allows for fast image acquisition (acquisition time 100 ms per z plane, loop time per frame 1,000 ms).

5. Draw the desired ROI using the LabView software along which the cortex will be ablated, e.g., a 100 μm long line 3–6 cell rows distant from the EVL margin and parallel to it (Fig. 3) (*see* **Note 7**).

6. UV ablation will be performed point-wise along the line. Therefore adjust the UV laser settings (for details and advice *see* Subheading UV Laser Ablation of the Actomyosin Cortex Within the YSL) for optimal ablation of the cortex.

7. While the images are acquired, initialize UV ablation along the designated ROI. During the ablation procedure (e.g., for a 100 μm line with the respective settings: 3 s) image acquisition is temporarily paused. Nevertheless, image acquisition should cover at least 5 s of the unperturbed cortex before the cut and enough frames afterwards to clearly see the subsequent cortex opening and membrane integrity in response to the cut (>30 s) (*see* **Note 8**).

8. Switch to a new embryo within the same dish and continue with **steps 3–7**.

9. After cutting all embryos of the dish, check once more for the developmental stage to confirm the time window in which the ablation experiments were conducted.

3.2 UV Laser Ablation of Cell–Cell Interfaces of Mesoderm Cells Ex Vivo

Embryos injected with *cyc* mRNA and *cas morpholino* oligonucleotides ubiquitously express *goosecoid*, a marker of the anterior axial mesoderm. To analyze actomyosin dynamics in mesoderm-induced cells, use embryos from crosses of male *Tg*(*gsc*:*GFP*) with female *Tg*(*actb2*:*lifeact-RFP*) or female *Tg*(*actb2*:*Myl12.1-mCherry*).

3.2.1 Obtaining Mesoderm Progenitor Cells from Zebrafish Embryos

1. Inject a mixture of *cyc* mRNA and *cas morpholino* into one-cell-stage fertilized transgenic embryos (microinjection setup explained in [20])

2. Transfer injected embryos into plastic petri dishes and incubate embryos in 1× E3 at 25–31 °C.

3. Keep uninjected embryos in 1× E3 media to control the developmental stage.

4. Once control embryos reach 30 % epiboly, discard those embryos that do not exhibit characteristic phenotype of mesoderm-induced embryos, such as disorganized blastoderm not initiating epiboly.

5. Dechorionate embryos as explained in Subheading 3.1.2 of this chapter.

6. At 50 % epiboly, check embryos for GFP-expressing cells. Discard embryos that show partial or no expression of GFP (*see* **Note 9**).

7. Transfer around 30 GFP-positive embryos gently with a glass pipette (as described in Subheading 3.1.3) into a 15 ml Falcon tube (*see* **Note 10**).

8. Remove excess media above the embryos with a pipette and carefully add 2 ml of pre-warmed (28 °C) DMEM/F12 media.

9. Remove excess media and wash twice with DMEM/F12 media.

10. Dissociate embryos by pipetting the embryos up and down. This will lead to shearing of the embryos and subsequent release of the embryonic cells into the DMEM/F12 media (*see* **Note 11**).

11. Spin cell suspension for 3 min at $600 \times$ g at room temperature.

12. Wash cell pellet twice with 2 ml DMEM/F12 media.

13. Remove excess media and resuspend mesoderm cells in 200–250 μl of DMEM/F12 media.

14. Keep cells at 28 °C until transferring them to a culture dish.

3.2.2 Culturing of Mesoderm Cells In Vitro

In order to produce larger aggregates of mesoderm cells in vitro, cells have to be cultured in clusters on a glass cover slip coated with fibronectin.

1. Make a fresh dilution of fibronectin in sterile H_2O to a final concentration of 200 μg/ml.

2. For one Matek dish glass cover slip add 50 μl fibronectin solution and spread it out to coat the cover slip.

3. Air-dry the cover slip at room temperature until liquid is completely evaporated (~1–2 h).

4. Block fibronectin by applying 300 μl of BSA onto the fibronectin-covered area and incubate for at least 30 min at room temperature (for longer storage keep at 4 °C).

5. Wash fibronectin twice with pre-warmed DMEM/F12 media and add 3 ml of DMEM/F12 media to the dish.

6. Take 3–5 μl of mesoderm cell suspension prepared in Subheading 3.3.1 and place ~50 cells as a cluster onto the fibronectin substrate. Use a stereoscope with transmitted light to check the placement and distribution of the cells on the fibronectin substrate.

7. Allow cells to adhere to the substrate by incubating them for at least 90 min at 28 °C.

3.2.3 UV Laser Ablation of Cell–Cell Interfaces Between Migrating Mesoderm Cells In Vitro

Mesoderm cells have been shown to undergo directed cell migration as a collective during gastrulation in the zebrafish embryo [17, 18]. Cooperative migratory behaviors require both cohesion and force application at the cell–cell interface, such as tugging forces generated by the actomyosin network on cadherin adhesion receptors of neighboring cells [22]. In order to visualize forces between cells, we use UV laser ablation (for setup *see* Subheading 3.1.4) to sever interfaces between cohesive polarized cells in vitro.
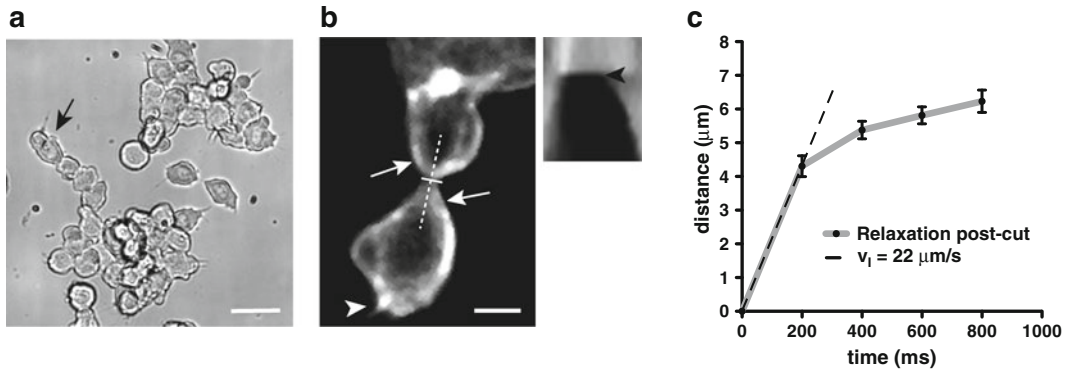
Fig. 4 Laser ablation of cultured mesoderm progenitor cells. (**a**) DIC image showing several clusters of mesoderm progenitor cells spread on fibronectin substrate. A leader cell migrates away from the cluster (*arrow*) and is followed by other cells, thereby creating a chain-like cell pattern. *Arrow bar* equals 50 μm. (**b**) Polarized leader cell making contact at its rear to a follower cell before laser ablation. Actomyosin is enriched adjacent to the cell–cell contact area (*arrows*) and at the leading edge of the leader cell (*arrowhead*). A kymograph was created from a line (*dashed line*) perpendicular to the cut area (*full line*) and relaxation of the actomyosin-labeled cell cortex was followed after the cut (*black arrowhead* in kymograph indicates cut frame). *Arrow bar* equals 5 μm. (**c**) The graph shows the distance of relaxation after laser ablation measured over time from five different cuts. The tension at the cell interface was calculated by linear-regression analysis (*dashed line*) of the initial relaxation velocity (v_l). Error bars represent standard error of the mean

1. Check mesoderm cells 2 h after incubation on the stereoscope for polarized cells migrating out of the cluster in random directions (Fig. 4a) (*see* **Note 12**).

2. Mount the Matek dish on a heated motorized piezo stage on an inverted spinning disc microscope and use a $63\times$ objective and transmitted light to focus on an area where polarized cells form a continuous chain (*see* **Note 13**).

3. Briefly check soluble GFP expression of the cells by using a 488 nm excitation laser with ~25 % laser power (laser output power 2.5 mW) to ensure mesoderm fate of cells (LP 488 emission filter).

4. Switch the laser line to 561 excitation laser and adjust the laser power to ~20 % (laser output power 2.5 mW) to visualize actin (RFP-tagged Lifeact) or myosin 2 (mCherry-tagged myosin 2 light chain) in the cells (LP 568 emission filter) (*see* **Note 14**).

5. Use the ROI function of the LabView software to draw a line along the cell–cell contact area to define the position of the cut (Fig. 4b). As the contact area between polarized mesoderm cells on a substrate is a thin structure, usually one z plane is sufficient to image the relaxation of the cortex after ablation (*see* **Note 15**).

6. For UV laser ablation, set the pulse rate of the laser to 1 kHz, set the area density along the line to 1 shot/μm^2, adjust four pulses per shot, and adjust the laser intensity to sever contacts (*see* **Note 16**).

7. For high-speed image acquisition (200 ms frame rate, 150 ms exposure time), start recording a few seconds before the ablation and continue imaging for several seconds after the ablation to observe complete recoil recovery (*see* **Note 17**).

8. Observe the behavior and morphology of the cells for several minutes after laser ablation (*see* **Note 18**).

3.3 Analysis

3.3.1 Analysis of Laser Cuts for Measurement of Cortical Tension in the YSL and EVL

Laser ablation can be used to visualize cortical tension in vivo, because locally disrupting a cortical actomyosin network under tension will lead to immediate recoil of adjacent cortical material. Importantly, the initial recoil velocity in response to the cut is proportional to the mechanical tension, under which the actomyosin network was before the ablation [19]. The proportionality factor is related to the viscous properties of the cortex and often not known. It is therefore important to keep in mind that the measure of cortical tension by laser ablation techniques is always a relative one. Meaningful insight into the mechanical properties of the cortex under study can only be gained by comparative laser ablation experiments. For instance, conducting laser ablation for different orientations of laser cuts will enable to characterize the degree of anisotropy of tension within the cortex. Comparing laser ablation results in the presence or the absence of specific components of regulatory pathways can help to unravel the molecular basis of tension generation.

As outlined above the analysis of laser ablation experiments is based on quantifying the recoil velocity of the cortex in response to the cut. For laser ablation in the YSL actomyosin ring or the apical cortex of the EVL, recoil movement of the actomyosin network can be well captured using particle image velocimetry (PIV). In contrast to the classical application of PIV, where injection of tracer particles allows for visualization of flows in fluid or gases, structural contrast in the actomyosin network of the YSL/EVL is sufficient to apply PIV directly on these images. As depicted in Fig. 2b, PIV analysis yields the 2D velocity field (vector arrows) of the recoiling actomyosin network. Averaging the velocity component, which is orthogonal to the cut line, in two rectangular regions adjacent to the ablation site, produces the outward recoil velocity as a function of time. The mean recoil velocity for laser ablation experiments in multiple embryos is characterized by an exponential decay (Fig. 2c). Fitting the experimental data therefore with an exponential function allows to determine the initial outward velocity, which is proportional to the tension before the cut, and a characteristic decay time, which depends on the viscoelastic material properties of the cortex [16, 19].

3.3.2 Analysis of Tension at the Cell–Cell Interface

Although the actomyosin cortex of a cell is treated as an active viscoelastic material, the cortex shows elastic behavior on short time scales [19]. Cortical elastic tension of a cell is comparable to the tension of a spring and the mechanical energy of a cell and the tension at interfaces are dependent on the cell deformations, like stretching [23]. We assume that highly polarized migrating mesoderm cells in culture generate actomyosin-dependent forces at the cell–cell interface and the release of these forces by laser ablation results in an elastic relaxation between cells and recoil of the cortex.

We represent one way to quantitatively analyze intercellular forces by measuring the relaxation of the actomyosin cortex shortly after laser ablation and extraction of the initial relaxation velocity [23]. Briefly, a kymograph was used from a line scan perpendicular to the cut position to represent pre- and post-cut states of the cell contact area (Fig. 4b). We utilized fluorescence of the actomyosin cortex to visualize relaxation of intercellular tension from the kymograph analysis and estimated the relaxation distance (d) for several hundreds of milliseconds post-cut (t). As the relaxation velocity reaches a maximum immediately after the cut, the initial relaxation velocity (v_I) can be calculated from the initial slope of the distance against the time plot through the origin (Fig. 4c). Thus fitting the relaxation data at the maximum speed displacement with a linear function can be utilized to derive the initial displacement velocity, which relates to mechanical forces occurring at the cell–cell interface before the ablation.

4 Notes

1. In order to conduct multiple rounds of ablation experiments at the same developmental stage on one day, put the fish together at different times in the morning and do different rounds of injection. In addition or alternatively, incubate embryo batches at slightly different temperatures.

2. Take care when you melt the glass capillary not to make the glass diameter too small for the embryos to pass through. Use a diameter ($\approx$1 mm) that creates a large enough opening to allow a dechorionated embryo to pass through without deforming it.

3. Larger agarose droplets allow for more time to orient the embryos. If the time is not sufficient, consider using solutions with less dissolved agarose (e.g., 0.7 % or 0.5 % LMP agarose).

4. Depending on the time that the mounting as well as subsequent steps take, anticipate the epiboly movement, when orienting the embryo for instance for laser ablation of the YSL actomyosin ring or of EVL cells close to the leading edge.

5. Preferentially, set the temperature at least 30 min prior to starting the experiment in order to allow for thermal equilibration.

6. Optimal ablation of the cortex for tension measurement is characterized, by efficiently disrupting the cortex without causing additional wound response, e.g., through permanently damaging the plasma membrane. Such wounding could lead to outflow of yolk material and interfere with the tension measurements. As a quality control for the ablation of the YSL actomyosin ring, adjust therefore the cutting parameter to achieve clear disruption of the cortex (characterized by fast and homogeneous opening of the cortex in response to the cut) with subsequent recovery of the cortex within the opening, indicative of an intact plasma membrane. Cuts that are followed by a wound response, e.g., visible by an accumulation of F-actin or myosin for wound closure, should be discarded from the tension measurements. In our experience, more pulses per ablation point and a higher density of ablation points along the designated line lead to better and more reproducible cutting results. To minimize the time it takes to conduct a cut without compromising on ablation performance the following settings proved a good balance: 1 kHz pulse repetition rate, 25 pulses per ablation point, and an ablation point density of 2 pts/μm. With these settings the intensity of the UV laser has to be fine-tuned for optimal cutting conditions as characterized above. To account for possible variation in laser intensity, cortical tension measurements for different conditions have to be conducted alternating with control conditions on the same day.

7. If necessary move the stage so that the EVL margin comes into the field of view, and then draw the desired ROI along the EVL margin. Afterwards, slowly, move back to your desired cut location while counting how many cell rows distant the EVL margin is. For cuts at the animal pole (AP) there is no need to check for the EVL margin, given that it should be equidistant in all directions and, thus, the cut orientation is not relevant. Nonetheless, as an internal control, alternate the cut orientation in between the different AP cuts. We chose 100 μm length cut in order to cut along the cortex of 3 to 4 EVL cells, thus probing tension across the whole tissue rather than assessing the tension at one cell–cell junction alone.

8. Optimal ablation of the cortex for cuts in the EVL has to be determined similar to cuts within the YLS (*see* **Note 6**). Cuts that illicit cortical opening in conjunction with permanent cell membrane rupturing, recognizable by loss of the GPI-RFP labeling in the cut opening, should be discarded from analysis. Thus, for the ablation of the EVL actomyosin cortex, adjust the cutting parameters to achieve clear disruption of the cortex without damaging the cell membrane [5]. We used the following settings to ablate the EVL cortex: 1 kHz pulse repetition

rate, 25 pulses per ablation point, and an ablation point density of 1 pts/μm. With these settings the intensity of the UV laser has to be fine-tuned for optimal cutting conditions as characterized above. Note that EVL cells on which the cortical laser ablation was performed displayed apoptosis and were actively extruded from the epithelium.

9. If microinjection was performed optimally, mesoderm-induced embryos usually show *gsc*::GFP expression in all of the cells.

10. Make sure to transfer embryos with enough liquid to cover them and check that the embryos sink to the bottom of the Falcon tube to prevent them to stick to the sidewall of the tube.

11. Do not produce air bubbles during the pipetting, as contact to air can damage embryos and cells.

12. Usually, we observed that cells migrate outwards of the cluster and form a chain-like pattern with a leader cell up front, while the cell that migrates out of the cluster at last still displays physical contact to the cluster (Fig. 4a).

13. Stage unit and objective should be preheated to 28 °C at least 30 min before imaging for thermal equilibration.

14. Note: We observed that actomyosin accumulated adjacent to the contact area between two neighboring cells, indicating increased local tension surrounding the junctions (Fig. 4b).

15. Cell–cell contacts of cultured mesoderm cells are very dynamic and can vary in cell height and width. For optimal cuts find highly polarized cells that display reduced cell height at the cell interface. We found that cells with a contact area of more than 5 μm width could not be successfully separated with a single cut. For tension measurements, we considered only single cuts that led to an immediate and complete separation of the cell contact as successful cuts. Save the xy positions of the cut line for post-processing.

16. The settings described here are recommendations based on our experience with cultured mesoderm cells. For other cell types and culture conditions, these settings would have to be optimized empirically.

17. For fast relaxation times within seconds, keep the frame in hundreds of milliseconds and the exposure as short as possible to increase the time resolution of the relaxation. Image acquisition was continued during ablation and the cut frame(s) should be clearly visible in the movie. Under our conditions, a complete cut was usually achieved in 200–400 ms.

18. Cells that exhibit permanent severe membrane damage should be discarded from the measurements. Signs of continuous membrane damage include constant cell blebbing, detachment of the cell from the substrate, or leakage of cytoplasm into the

media (visible by fluorophore leakage). Therefore the cut conditions have to be empirically determined for different cell and culture conditions (*see* also **Note 6**).

Acknowledgements

References

1. Ingber DE (2006) Cellular mechanotransduction: putting all the pieces together again. FASEB J 20:811–827

2. Keller R, Shook D, Skoglund P (2008) The forces that shape embryos: physical aspects of convergent extension by cell intercalation. Phys Biol 5:015007

3. Cai Y, Sheetz MP (2009) Force propagation across cells: mechanical coherence of dynamic cytoskeletons. Curr Opin Cell Biol 21:47–50

4. Lecuit T, Lenne P-F, Munro E (2011) Force generation, transmission, and integration during cell and tissue morphogenesis. Annu Rev Cell Dev Biol 27:157–184

5. Rauzi M, Lenne P-F (2011) Cortical forces in cell shape changes and tissue morphogenesis. Curr Top Dev Biol 95:93–144

6. Vogel V, Sheetz M (2006) Local force and geometry sensing regulate cell functions. Nat Rev Mol Cell Biol 7:265–275

7. Oates AC, Gorfinkiel N, González-Gaitán M et al (2009) Quantitative approaches in developmental biology. Nat Rev Genet 10:517–530

8. Colombelli J, Reynaud EG, Stelzer EHK (2007) Investigating relaxation processes in cells and developing organisms: from cell ablation to cytoskeleton nanosurgery. Methods Cell Biol 82:267–291

9. Colombelli J, Solon J (2012) Force communication in multicellular tissues addressed by laser nanosurgery. Cell and tissue research. Springer, Berlin

10. Niemz MH (2007) Laser-tissue interactions. Fundamentals and applications, 3rd edn. Springer, Berlin

11. Vogel A, Venugopalan V (2003) Mechanisms of pulsed laser ablation of biological tissues. Chem Rev 103:577–644

12. Kimmel CB, Ballard WW, Kimmel SR et al (1995) Stages of embryonic development of the zebrafish. Dev Dyn 203:253–310

13. Kane D, Adams R (2002) Life at the edge: epiboly and involution in the zebrafish. Results Probl Cell Differ 40:117–135

14. Siddiqui M, Sheikh H, Tran C et al (2010) The tight junction component Claudin E is required for zebrafish epiboly. Dev Dyn 239:715–722

15. Köppen M, Fernández BG, Carvalho L et al (2006) Coordinated cell-shape changes control epithelial movement in zebrafish and Drosophila. Development 133:2671–2681

16. Behrndt M, Salbreux G, Campinho P et al (2012) Forces driving epithelial spreading in zebrafish gastrulation. Science 338:257–260

17. Arboleda-Estudillo Y, Krieg M, Stühmer J et al (2010) Movement directionality in collective migration of germ layer progenitors. Curr Biol 20:161–169

18. Diz-Muñoz A, Krieg M, Bergert M et al (2010) Control of directed cell migration in vivo by membrane-to-cortex attachment. PLoS Biol 8:e1000544

19. Mayer M, Depken M, Bois JS et al (2010) Anisotropies in cortical tension reveal the physical basis of polarizing cortical flows. Nature 467:617–621

20. Carvalho L, Heisenberg C-P (2009) Imaging zebrafish embryos by two-photon excitation time-lapse microscopy. Methods Mol Biol 546:273–287

21. Colombelli J, Grill SW (2004) Ultraviolet diffraction limited nanosurgery of live biological tissues. Rev Sci Instrum 75:472–478

22. Weber GF, Bjerke MA, DeSimone DW (2012) A mechanoresponsive cadherin-keratin complex directs polarized protrusive behavior and collective cell migration. Dev Cell 22:104–115

23. Rauzi M, Verant P, Lecuit T et al (2008) Nature and anisotropy of cortical forces orienting Drosophila tissue morphogenesis. Nat Cell Biol 10:1401–1410

Measurement of Intercellular Cohesion by Tissue Surface Tensiometry

Ramsey A. Foty

Abstract

Intercellular adhesion plays a vital role in many biological processes including embryonic development, malignant invasion, and wound healing, and can be manipulated to generate complex structures in tissue engineering applications. Accurate measurement of the strength of intercellular adhesion is not trivial and requires methods rooted in sound physical principles. Tissue surface tensiometry (TST) rigorously quantifies intercellular cohesive energy of 3D tissue-like aggregates under physiological conditions. TST utilizes a custom-built tensiometer to compress 3D spheroids between parallel plates. The resistance to the applied force and changes in aggregate geometry are applied to the Young-Laplace equation, generating a measurement of apparent surface tension. We describe all components comprising the tensiometer and provide step by step instructions of all the key steps involved in generating spherical aggregates. We explain how tissue surface tension is calculated and provide a statistical analysis of a sample data set from 12 aggregates.

Key words Cell adhesion, Tissue liquidity, Surface tension, Tissue surface tensiometry, Parallel plate compression

1 Introduction

Differences in the strength of cell-cell adhesion have been demonstrated to specify relative spatial positioning between cells and tissues, in vitro [1–3] and in vivo [4–6], reviewed in [7]. Methods adopted by biologists to measure cell adhesion generally fall into three categories—distractive, kinetic, and thermodynamic [8]. *Distractive procedures* measure the forces required to separate adhering cells from each other. Interpretation of this force is difficult since it may represent separation of adhesion receptors, extraction of receptors from membranes, extraction of membranes from cells, or a combination thereof. To further complicate

interpretation, distractive methods must also consider the rate of application of the distractive force since this can significantly affect the peak "force of distraction" [8]. *Kinetic measurements* [9, 10] are used to assess the rate of cell aggregation in stirred suspensions. Such measurements present at least three serious obstacles to their use to measure the strengths of cell-cell adhesions. First, forward reaction rates are limited not by free energies of the reaction but by activation energies [11]. Thus aggregation rate cannot be used as a measure of intercellular adhesive strength or affinity. Second, the shear force employed in comparing the aggregation rates of different cell populations may itself create the functional equivalent of an activation energy barrier preventing the aggregation of one population of mutually adhesive cells while permitting that of another and thus creating a misleading impression of adhesive specificity [12]. Third, since cell adhesions mediated by cadherins, for example, become greatly strengthened during the hour or so following their initiation [13], the rate of initial cell attachment cannot measure the strengths of mature, physiologically relevant adhesions. *Thermodynamic measurements* of cell-cell adhesion, carried out under equilibrium conditions free of kinetic artifacts, of energy dissipation due to transient cell deformations [14], and of the possibility of receptor "pullout" [15, 14], none of which influences the steady-state adhesion itself, are ideal since they measure an adhesive free energy rather than a force or a rate.

The method described here, tissue surface tensiometry (TST), was developed to generate rigorous measurements of intercellular binding energy in 3D tissue-like spheroids under physiological conditions. TST is grounded in the concept of tissue liquidity. The concept that certain tissues behave like "living liquids" was originally posited by Malcolm Steinberg in the 1960s to explain the "rounding-up" and "sorting-out" behaviors displayed by avian and amphibian embryonic tissues (reviewed in [16]). The concept has more recently been applied to teleost germ layer tissues [3], various cancer cell lines [17–20], and genetically engineered cells [12, 2]. Briefly, mutually cohesive cells, if prevented from adhering to a substrate, will spontaneously assemble into clusters. Over time, these clusters will "round up" to form spheres (Fig. 1a, Movie 1 at SpringerExtras.com). They do so to minimize their surface area to volume ratio ratio and thus adhesive free energy. TST employs a custom-built instrument (Fig. 2) to compress spherical cellular aggregates between parallel plates to which they cannot adhere. A chart recorder is used to monitor the applied force, and a dissecting microscope is used to capture images of aggregate geometry. Aggregates are compressed (Fig. 1b) until they reach a shape and force equilibrium, whereupon measurements of aggregate geometry and the force of resistance at equilibrium are applied to the Young-Laplace equation (Eq. 1) [21], producing numerical values of apparent tissue surface tension. Each aggregate is then
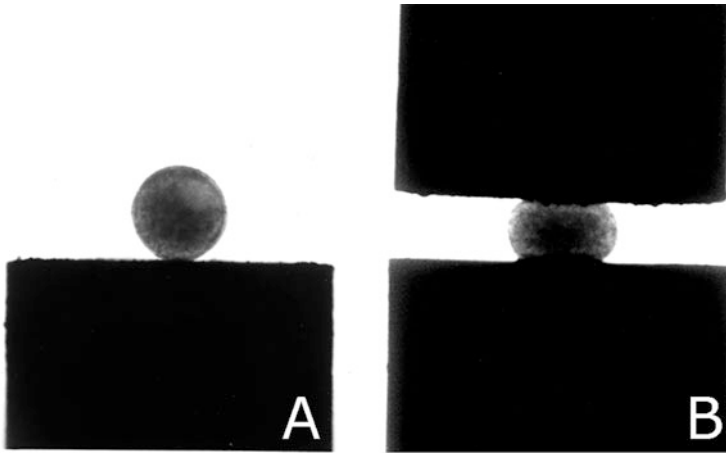
Fig. 1 Aggregate of chick embryonic liver. Image of an aggregate positioned on the lower compression plate, which has been coated with poly-HEMA to prevent attachment and spreading (**a**). The same aggregate undergoing parallel plate compression (**b**)
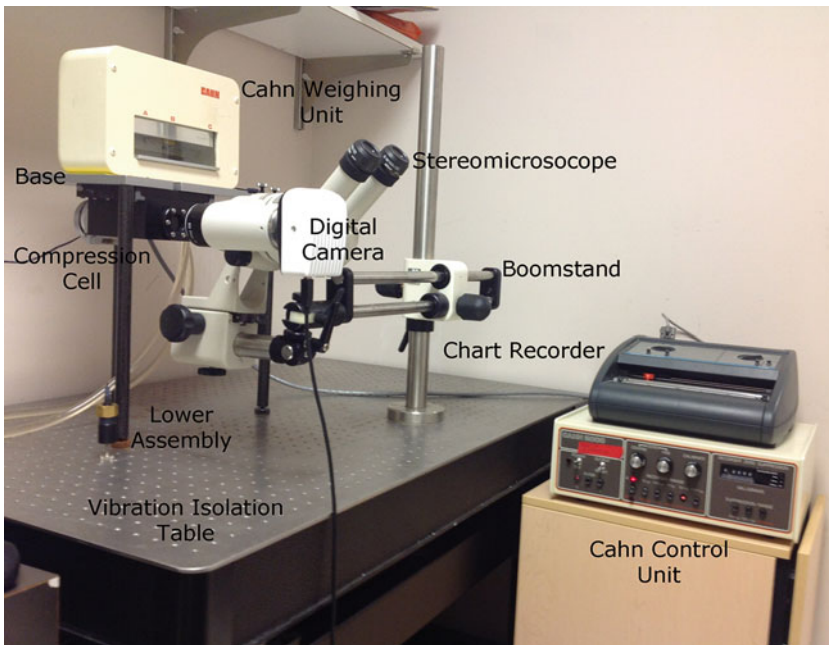
Fig. 2 The tissue surface tensiometer. The instrument comprises a number of commercially available components including the Cahn electronic balance weighing unit and controller, a chart recorder, a stereomicroscope, digital camera, and boom stand, all positioned on a vibration isolation table. The base, compression cell, and the lower assembly are custom-built

decompressed and allowed to round up for some time, whereupon it is subjected to a second, greater compressive force. After aggregates have reached a second force and shape equilibrium, surface tension is again calculated. Only measurements in which surface tension is independent of the applied force, as would be expected of a liquid system, are used calculate the average surface tension for any aggregate type. In this context, tissue surface tension represents a physically rigorous assessment of aggregate cohesion. We will describe, in detail, the components comprising the tissue surface tensiometer and various methods used to generate spherical aggregates. We will provide a step-by-step description of how the data are generated and analyzed. Where necessary, we will point out potential pitfalls and provide solutions to overcome them:

$$\sigma = \frac{F}{\pi R_3^2} \left(\frac{1}{R_1} + \frac{1}{R_2} \right)^{-1} \tag{1}$$

2 Materials

2.1 The Tissue Surface Tensiometer

1. *The compression cell* (Fig. 3) is composed of two machine-milled Delrin chambers. The inner chamber (IC) sits in a groove in the base of the outer chamber (OC). Both chambers contain two round quartz-glass viewing windows to facilitate visualization of the aggregate. The lid, also composed of Delrin, has a series of stainless steel screws that when tightened compress a rubber gasket that effectively seals the chamber. The OC contains two ports that are connected to the inlet and outlet valves of a Haake DC10 circulating water pump, and thus serves to regulate the temperature of the inner chamber (IC). The bottom of the inner chamber contains a tapped hole that accepts the lower assembly (LA). The LA (Fig. 4) screws into the base of the inner chamber and is used to (a) position the aggregate in the inner chamber, (b) seal the bottom of the inner chamber, (c) elevate the aggregate to initiate compression, and (d) control the distance between the parallel plates and hence the compression of the aggregate. The central core (CC) of the assembly is adjustable. The tip of the central core is composed of smooth Teflon and acts as the lower compression plate (LCP). The upper compression plate (UCP) is a Teflon cylinder 15 mm long that hangs from the balance arm (B) by a thin nickel-chromium wire (*see* **Note 1**).

2. *The Cahn C-2000 Recording Balance and flat-bed chart recorder.* The C-2000 is a very sensitive weight and force measurement instrument, and is essentially a force to current converter. It works on the null-balance principle. The fulcrum of the balance arm has an armature and torque motor within a
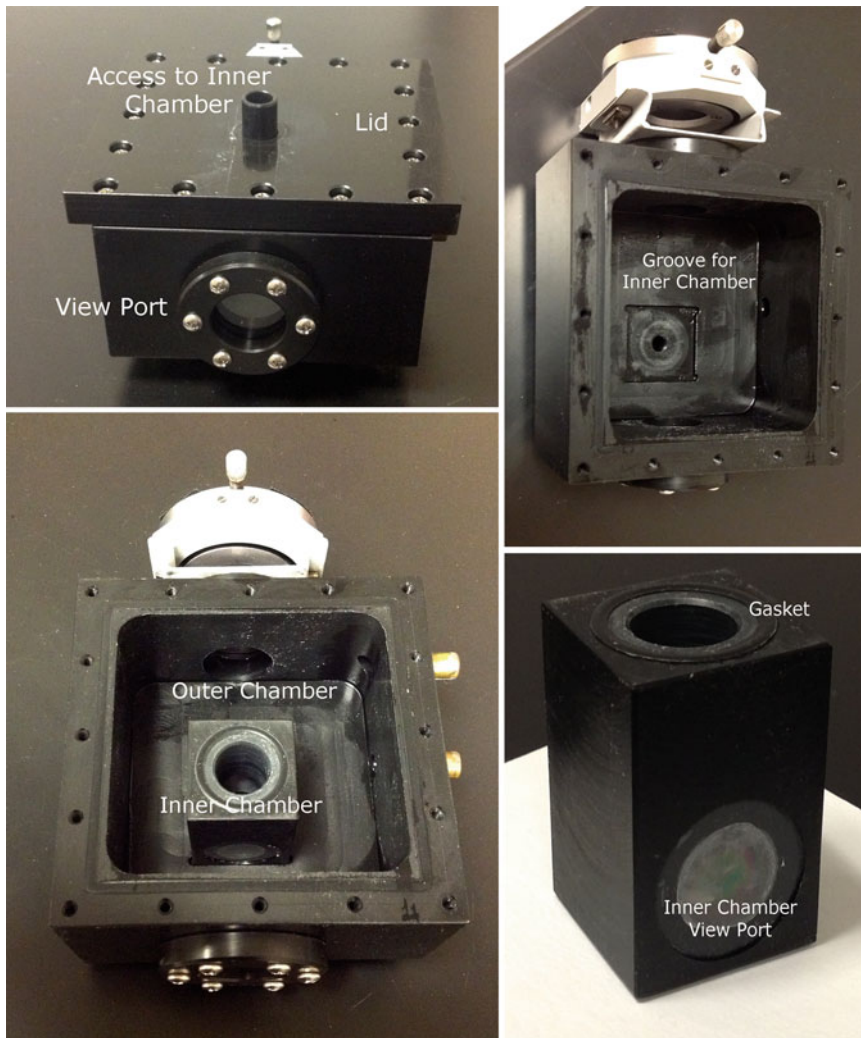
Fig. 3 The compression cell. The cell comprises two chambers: an outer is connected to a circulating water bath that serves to regulate the temperature of the inner chamber (IC). The IC fits into a groove in the base of the outer chamber. When the lid is fastened, rubber gaskets compress, effectively sealing each of the chambers. Both chambers contain view ports to allow for visualization of the aggregate

permanent magnetic field. When the balance is operating, it continuously modulates the current passing through the electromagnetic assembly, which in turn maintains the balance arm in the horizontal position. When an object is suspended from the balance arm, the voltage, which the balance applies to keep the arm in the horizontal position, is proportional to the object's weight at that moment. The balance is composed of a control unit where all controls and outputs are contained, and the weighing unit, which detects the actual weight or force. The weighing unit is connected to the control unit by an
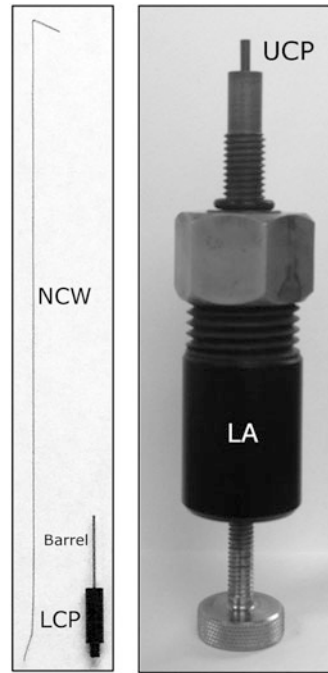
Fig. 4 The upper and lower compression plates. The upper plate comprises a flame-straightened nickel-chromium wire attached to a Delrin cylinder, which acts as the upper compression plate. The barrel of a 30-gauge needle is inserted into the Delrin cylinder and serves to connect the wire. The end of the wire is slightly kinked so as to provide friction between the I.D. of the barrel and the wire. The upper part of the wire is bent at a 45° angle to connect the wire to the "A" loop of the balance arm. The lower assembly (LA) houses the adjustable inner core that serves as the lower compression plate (LCP)

interconnect cable. The control unit connects to a Servogor 102 potentiometric flat-bed chart recorder (*see* **Note 2**).

3. *The base unit.* The unit is composed of an 18 × 8 × ½ (*L* × *W* × thickness) inch steel plate to which three 12 in. long, ¾ diameter legs are attached by stainless steel screws. The bottom of each leg contains an adjustable footpad to level the base unit. The base serves to house the compression cell. The weighing unit of the Cahn balance sits on top of the base and is connected to it by an aluminum plate that is fastened to an *x–y* manipulator.

4. *The stereomicroscope, boom stand, and digital camera.* To visualize the aggregate, a Nikon SMZ-10A stereoscopic dissecting microscope connected to an Infinity 2 B&W digital camera is mounted on a Digital Imaging Instruments boom stand. To capture an image of the aggregate, the camera is connected to a PC running Infinity software. An LED light source is used to illuminate the aggregate.

5. *Vibration isolation*. The setup including the base unit with attached compression cell, the weighing unit of the Cahn balance, and the stereomicroscope/boom stand/camera combination are positioned on a TMC vibration isolation table connected to a compressed air cylinder.

2.2 Other Equipment/Supplies

1. *Orbital shaker water bath with gassing hood*. Lab-Line model 3445 orbital water/bath shaker with a Plexiglass gassing hood. The hood is connected to a COBE gas mixer. Pressurized CO_2 and air are mixed in the COBE unit and flushed through the gassing hood. A Fyrite gas analyzer is used to monitor CO_2 concentration and adjustments to airflow are made until a 5 % CO_2 concentration is achieved. The shaker also houses a platform to hold 32 clamps sized for 10 ml custom-designed round-bottom glass flasks.

2. *Shaker flasks*. These are 10 ml capacity, 1¼ in. diameter, 2 5/8 in. height, 1¼ in. DeLong neck shake flasks and were custom-ordered from Bellco Glass Inc. Catalogue # 2511-S0001, factory order # PROD015056. The round-sided design prevents tissue fragments from converging at the center of the flask and helps to avert their cohesion. Stainless steel vent caps were used as closures.

2.3 Reagents

1. *Poly(2-hydroxyethylmethacrylate)* (*poly-HEMA*). The reagent is supplied as a solid (Sigma, P-3932) and must be dissolved in 100 % methanol. The stock solution is prepared by dissolving 100 mg of poly-HEMA in 10 ml of methanol and rotating for 2–3 days at room temperature. This solution is used to coat both the UCP and LCP prior to TST.

2. *Compression medium*. Since TST is performed in room air, it is necessary to employ a CO_2-independent medium. The basal medium is available from Gibco Life Technologies and is provided as a 1× liquid. The medium contains a unique buffering system composed of mono- and dibasic phosphate and β-glycerophosphate. It contains a small amount of sodium bicarbonate to support essential bicarbonate-dependent functions. The basal medium must be supplemented with L-glutamine, 10 % fetal calf (or horse) serum, and a mixture of antibiotics/antimycotics. The medium must be degassed prior to use (*see* **Note 3**).

3. *Standard tissue culture reagents*. Basal medium (DMEM, RPMI etc.), fetal calf serum, and other additives, including L-glutamine, nonessential amino acids, and antibiotic/antimycotics, should be carefully chosen to optimize cell growth. Other reagents required to passage cells include trypsin/EDTA, phosphate-buffered saline (HBSS), Hanks' balanced salts solution (HBSS), and DNase.

3   Methods

The following will provide a detailed description of the four major steps associated with tissue surface tensiometry: (1) generation of spherical aggregates for compression, (2) setting up of the compression cell and tensiometer, (3) aggregate compression, and (4) data analysis.

3.1   Generation of Spherical Aggregates

Various cultured cell types have been successfully used to generate spherical aggregates. To establish the methodology, it is advisable to start with a cell line that readily forms spherical aggregates and that is easy to grow and maintain. Rat-2 fibroblast cells are suitable candidates for spheroid formation using either the hanging drop or the centrifuged sheet method (*see* **Note 4**). All steps should be performed under aseptic conditions using a laminar-flow hood, sterile solutions, and lab-ware. A video describing the process can be found in [22].

To generate spheroids by the hanging drop method:

1. Culture cells in DMEM/10 % FCS/antibiotics/antimycotics until they achieve 80–90 % confluence. We typically grow cells in 10 cm dishes.

2. Wash cell monolayers twice with PBS and then add 2 ml of trypsin/EDTA until cells detach.

3. Stop the trypsinization by adding 2 ml of complete medium, and then transfer cells into a 15 ml conical centrifuge tube.

4. Add 40 μl of a 10 mg/ml DNase solution and incubate at room temperature (RT) for 5 min (*see* **Note 5**).

5. Centrifuge cells at $80 \times g$ for 4 min at RT and wash the pellet twice with PBS.

6. Resuspend the washed cells in 1 ml of complete medium and count the cells using either a hemocytometer or an automated cell counter (BioRad TC10).

7. For the hanging drop method, adjust the concentration to 4×10^6 cells/ml in complete medium (*see* **Note 6**).

8. To create a hydration chamber for incubation of the hanging drops, remove the lid from a 60 mm tissue culture dish and pipet 5 ml of HBSS into the bottom of the dish.

9. To create hanging drops, pipet up to twenty 10 μl drops of the cell suspension onto the underside of the lid, making sure that drops are kept sufficiently apart so as not to touch.

10. Re-invert the lid and replace it onto the HBSS-filled bottom. Allow the drops to sit at RT for at least 30 min or until cells have had a chance to pool at the bottom of the drop.

11. Transfer the dish to a tissue culture incubator set at 37 °C/95 % humidity/5 % CO_2 and incubate until spheroids form (*see* **Note 7**).

3.2 Setting Up of the Compression Cell

1. *Coating the UCP and LCP with poly-HEMA.* To prevent adhesion and spreading of aggregates on the UCP and LCP, the plates must first be coated with a thin layer of poly-HEMA. It is easier to coat the plates when visualized through a stereo-microscope. The plates must first be cleaned using 95 % ethanol. It is convenient to load 1 ml tuberculin syringes fitted with 30-gauge needle with 95 % ethanol or with the stock solution of poly-HEMA. To clean the plates, a small droplet of ethanol is placed directly on top of the surface of the plate and allowed to rest there for approximately 15 s. The edge of a Kimwipe should then be used to wick off excess ethanol. This should be repeated three times, at which point the surface of the plate should be allowed to air-dry for a few minutes. To coat the plates, a small drop of poly-HEMA stock solution is deposited onto the surface. The edge of a Kimwipe is then used to wick off excess poly-HEMA (*see* **Note 8**). The plates are then allowed to air-dry for a few minutes.

2. *Connecting the UCP to the nickel-chromium wire.* The UCP is composed of a Teflon cylinder 15 mm long into which the barrel of a 30-gauge needle with nominal I.D. of 0.14 mm is inserted (Fig. 4). The inner diameter of the barrel is just small enough to provide friction between it and the nickel-chromium wire. The wire has an optimal outer diameter of 0.127 mm. It is available from Consolidated Electronic Wire and Cable Corporation (Part # 36 BNC). The wire must be heat-straightened (*see* **Note 9**) prior to use. To prepare the UCP/wire combination for attachment to the balance arm, the end of the wire that fits into the barrel of the UCP must be very slightly bent to increase friction between the wire and the barrel. This is best achieved by applying a little pressure using the edge of a razor blade approximately 10 mm from the end of the wire. Care must be taken not to overbend the end of the wire as this will make it difficult to pass the wire into the barrel. The other end of the wire must also be bent at a 45° angle to produce a sharp bend that will attach to the loop of the balance arm (Fig. 4). We typically use two razor blades to produce a 45° bend approximately 10 mm from the end of the wire. The wire is connected to the UCP by threading the slightly kinked end of the wire into the barrel of the connector until it reaches the end. The overall length of UCP/wire must be empirically determined so as to provide the best possible visualization of the UCP and the LCP within the viewing window when aggregates are under compression.

3. *Filling the compression cell.* Screw the lower assembly (LA) into base of the inner compression chamber (ICC) and hand tighten. The LCP has a rubber o-ring to seal the connection between the LA and the ICC. Ensure that the vibration

isolation table is activated. Turn on the circulating water bath and allow the temperature of the ICC to reach 37 °C. Once temperature is achieved, pipet 12.5 ml of the compression medium into the top of the ICC. Do this slowly so as to avoid forming of any air bubbles or protein froth. Allow the compression medium to equilibrate to temperature for approximately 15 min. To further eliminate air bubbles, repeatedly raise and lower the LCP. After three cycles, bubbles should no longer escape. Any bubbles that adhere to the UCP should be dislodged using a Pasteur pipet and a rubber bulb.

3.3 Loading the Aggregates

Aggregates are loaded by first transferring them to a 35 mm tissue culture dish containing approximately 5 ml of compression medium. Individual aggregates are then aspirated halfway up the tip of a Pasteur pipette fitted with a silicone bulb. The pipette is transferred to the inner chamber, and the tip positioned above the LCP. The aggregate is then expelled onto the LCP by very gently squeezing the bulb. Alternatively, the aggregate is allowed to fall by gravity onto the LCP. A hair loop is then used to position the aggregate onto the middle of the LCP and the LCP is lowered into the central core. The UCP is transferred gently into the ICC, making sure that it is positioned well away from the LCP. On occasion, it may be necessary to remove and replace the UCP/wire combination so as to dislodge any air bubbles that may have formed. The balance weighing unit is then positioned above the compression cell, making sure to align the hole in the base of the weigh unit over the nickel-chromium wire without bending it.

3.4 Attaching the UCP to the Balance Arm

The arm of the balance has three loops. The right side contains the "C" or the tare loop. The tare loop connects to a saddle and weigh pan. The left arm contains the "A" and "B" loops. The UCP/wire combination must be attached to the "A" loop. To do so, fine tweezers are used to grasp the top of the wire near the 45° bend and suspending the wire through the "A" loop (*see* **Note 10**). The weight of the UCP/wire combination suspended from the "A" loop must then be balanced with the tare loop.

3.5 Establishing a Pre-compression UCP Weight Baseline

In order to determine precisely how much force/weight is applied to compress the aggregate and the force at shape equilibrium, it is first necessary to establish a pre-compression weight baseline for the UCP. Doing so requires setting certain control switches on the Cahn balance control unit and on the chart recorder. The control unit settings should be "power" on, filter set to zero, recorder range set to 10 mg, and suppression range set to zero. The chart recorder should be connected to the Cahn unit using the 10 mV output/input ports, and the paper speed set to 6 cm/h. When ready, the toggle switch on the control unit labeled "short" should be switched to "output." At this point, the pen on the chart

recorder will deflect to some position on the chart paper. To zero this position, small pieces of aluminum foil should be either added to or removed from the tare loop/saddle to position the pen as close as possible to the 0 mark on the chart paper (*see* **Note 11**). The coarse and fine adjustments on the Cahn control unit can then be turned to fine-tune the position of the pen at the zero point of the chart paper.

3.6 Aligning the LCP, Aggregate, and UCP

Once a zero baseline for the UCP has been established, the LCP, aggregate, and UCP must be positioned relative to one another so as to optimize visualization for image capture. Whereas the LCP and aggregate are held in place, the UCP is free to move in an *x,y* plane. The UCP should be adjusted to align directly above the LCP, with the aggregate positioned as close to the center of the LCP as possible. If aligned properly, the UCP and LCP will be parallel to one another and the aggregate will be positioned between them. Illumination must be optimized to generate high-contrast images. Care should be taken to focus carefully so as to optimize clarity of both parallel plates and the aggregate. At this point, a pre-compression image of the aggregate and plates should be captured using the attached digital camera and image capture software.

3.7 Aggregate Compression

Compression is initiated by raising the LCP using the adjustable knob at the base of the lower assembly. The LCP is raised until the aggregate becomes compressed between the LCP and UCP. Compression effectively reduces the weight of the LCP, causing the pen on the chart recorder to deflect proportionally to the weight change (*see* Movie 2 *at SpringerExtras.com*). The degree of compression must be determined empirically for each aggregate/tissue type (*see* **Note 12**). Apparent UCP weight change is continuously recorded on a strip chart recorder, achievement of shape equilibrium being denoted by the leveling off of the Cahn balance's voltage output. Aggregate images at this first force/shape equilibrium are captured, whereupon, the force is released and aggregates are allowed to "relax" for at least 30 min (*see* Movie 3 *at Springerextras.com*). A second, greater compression is then applied and the aggregate is again allowed to reach a second shape and force equilibrium (*see* **Note 13**). A second set of images and force tracings are recorded. Images of the compressed aggregates are analyzed using ImageJ as described below. A video describing the procedure can be found in [23].

3.8 Calculation of Aggregate Surface Tension

At shape equilibrium, the surface tension of an aggregate of cells compressed between parallel plates to which it does not adhere can be obtained from the Young-Laplace equation (Eq. 1), where σ is cohesivity, F is the force acting to compress the aggregate, $\pi r^2{}_3$ is the area of the surface of the aggregate upon which force F is exerted, and R_2 and R_3 are, respectively, the radius of the equator
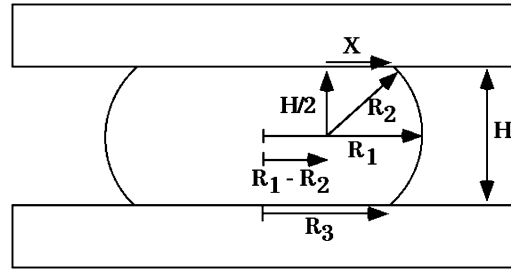
Fig. 5 Geometry of a compressed sphere. Diagram of a liquid droplet compressed between two parallel plates to which it adheres poorly, at shape equilibrium. R_1 and R_2 are the two primary radii of curvature, at the droplet's equator and in a plane through its axis of symmetry, respectively. R_3 is the radius of the droplet's circular area of contact with either compression plate. H is the distance between upper and lower compression plates. X is one side of a right-angled triangle with hypotenuse R_2 extending to a point of contact between the droplet's surface and either compression plate. R_1, R_2, and H are used to calculate R_3, using Eq. 2. The Young-Laplace equation (Eq. 1) is then used to calculate aggregate surface tension (σ)

of the compressed aggregate and the radius of an arc defining its surface profile normal to the compressing plates and extending between them (Fig. 5). To measure the changes in aggregate shape, images are opened in ImageJ. The scale is set using the diameter of the LCP, namely 1.69 mm. The line tool is used to measure aggregate diameter (D_1) and the height between the parallel plates (H). D_2 is measured by superimposing a circle that best aligns with the circular edges of the compressed aggregate and extracting R_2. Since R_3 is difficult to visualize accurately, H is used in Eq. 2 to calculate R_3. Applying these measurements to the Young-Laplace equation generates numerical values of *apparent* tissue surface tension. Upon reaching equilibrium and calculation of σ_1, aggregates are decompressed and allowed to approach a second equilibrium and σ_2 is calculated as described above. A minimum of ten aggregates, each being subjected to a double compression, are required to generate a data set:

$$R_3 = (R_1 - R_2) + \sqrt{(R_2)^2 - \left(\frac{H}{2}\right)^2} \qquad (2)$$

3.9 Confirmation of Aggregate Liquidity

The calculated surface tension of a liquid aggregate, when subjected to two different compressions, will remain constant. Accordingly, the means of σ_1 and σ_2 when compared by a paired t-test must not be significantly different. For liquid aggregates the ratio of σ_2/σ_1 will approach 1 and will be less than the ratio of the applied force at each successive compression (F_2/F_1). In contrast, the calculated

Table 1
Sample data set of TST measurements for 12 aggregates

Agg. #	σ_1 (dynes/cm)	σ_2 (dynes/cm)	σ_2/σ_1	F_2/F_1	Volume mm^3
1	11.9	13.1	1.10	1.59	0.031
2	13.1	14.1	1.08	1.44	0.087
3	17.5	15.9	0.908	1.48	0.065
4	12.5	10.6	0.848	1.87	0.074
5	15.4	13.3	0.864	1.46	0.108
6	14.6	14.8	1.01	2.20	0.042
7	13.0	14.6	1.12	1.88	0.097
8	17.2	17.9	1.04	1.56	0.102
9	17.5	16.0	0.914	1.56	0.045
10	13.6	13.6	1.00	1.61	0.087
11	17.5	16.0	0.91	1.62	0.042
12	13.6	13.6	1.00	2.20	0.108

surface tension of an elastic aggregate will obey Hooke's law and increase proportionately to the applied force. For elastic aggregates the ratio of σ_2/σ_1 will not approach 1 but will instead equal F_2/F_1. Any aggregates that do not follow these rules must be eliminated from the data set since they do not represent a true liquid surface tension (*see* **Note 14**). Only measurements in which surface tension is independent of the applied force are used to calculate average σ for aggregate type. The surface tension of liquid aggregates will also be independent of aggregate size. The relationship of aggregate surface tension and volume is analyzed by regression analysis and the correlation coefficient must approach zero. For a more visual demonstration of the liquid-like properties of aggregates, *see* **Note 15**.

3.10 A Sample Data Set

Results of TST data for a sample data set of 12 aggregates, each subjected to two successive compressions, can be found in Table 1. For this cell line, the average surface tension was calculated to be 14.6 ± 0.4 dynes/cm (*see* **Note 16**). In order to represent a true surface tension, confirmation of aggregate liquidity is required. For liquid aggregates, σ calculated at compression 1 must be similar to that calculated at a second, greater compression 2. A paired t-test generated a p-value of 0.414, indicating that σ_1 and σ_2 were not significantly different (Table 2, Fig. 6a, b). For liquid aggregates, the ratio of surface tensions obtained at two different degrees of compression (σ_2/σ_1) must approach 1. As seen in Table 2, σ_2/σ_1

Table 2
Statistical analysis of TST data for confirmation of aggregate liquidity

σ_1 (dynes/ cm) $\pm$ s.e.m.	σ_2 (dynes/ cm) $\pm$ s.e.m.	t-test, σ_1 vs. σ_2, p	σ_2/σ_1	F_2/F_1	t-test, σ_2/σ_1 vs. F_2/F_1, p	σ vs. Volume, r^2
14.8 ± 0.6	14.5 ± 0.5	0.414	0.98 ± 0.03	1.71 ± 0.08	<0.0001	0.0128
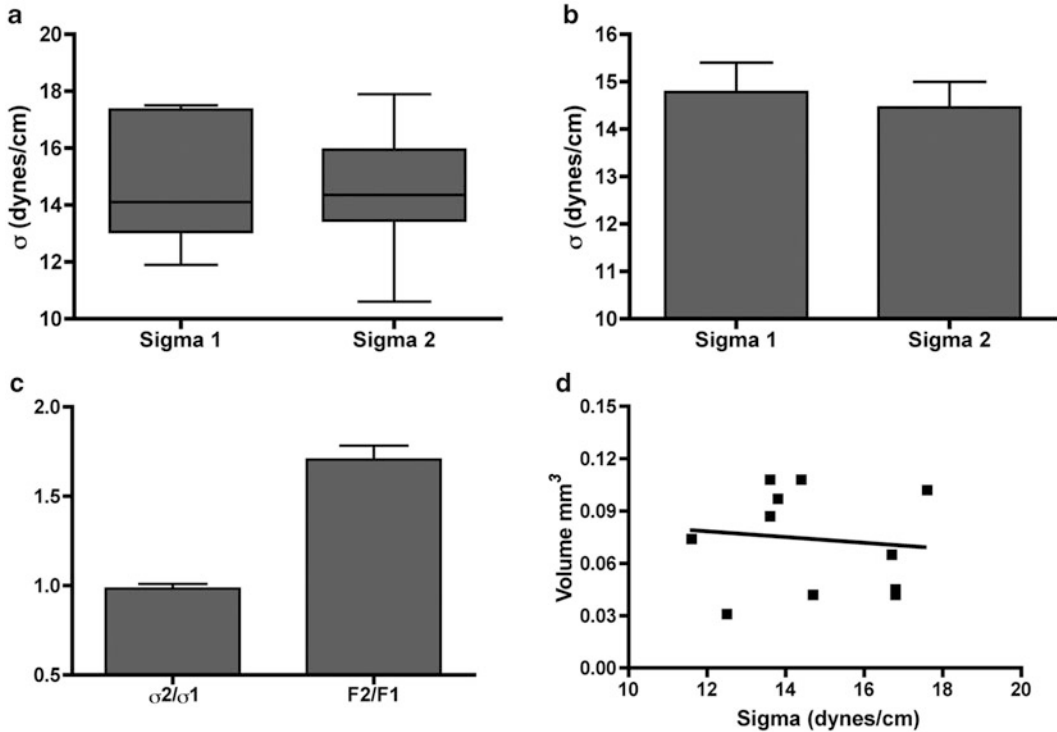
Fig. 6 Confirmation of aggregate liquidity. Surface tension measurements can only be considered valid if the means of σ_1 and σ_2 are not significantly different. A box plot (**a**) and bar graph (**b**) of sample data show that this is indeed the case. The surface tension of liquid aggregates must also be independent of the applied force (**c**) and of size (**d**)

was 0.98. That ratio must also be significantly different than the ratio of the applied force F_2/F_1, calculated here as 1.71. A paired t-test confirmed that the ratio of σ_2/σ_1 was significantly different than that of F_2/F_1 ($p < 0.0001$, Table 2, Fig. 6c). For liquid aggregates, surface tension must also be independent of aggregate size. Regression analysis was performed to test this relationship and generated a correlation coefficient r^2 of 0.0128 (Table 2, Fig. 6d), indicating no relationship between these two parameters. Collectively, the data confirm that a σ value of 14.6 ± 0.4 dynes/cm represents a true surface tension.

4   Notes

1. The chambers were custom-built by a skilled machinist and were designed to eliminate the possibility of leaks between the inner and outer chambers, or between the outer chamber and the environment. The inner chamber should be cleaned after every run by flushing first with distilled water, then with 1 % H_2O_2, and finally with 70 % ethanol. The compression cell should be cleaned once/month by dismantling the unit and soaking the components overnight in 2 % SDS. After thoroughly rinsing with distilled water, each component should be misted with 70 % ethanol and allowed to air-dry.

2. The balance must be kept away from any sources of vibration or drafts. Large temperature fluctuations must also be avoided.

3. Air bubbles can significantly affect this method and steps must be taken to ensure that their presence is minimized, or at best eliminated. Accordingly, degassing the compression medium is of paramount importance. This can be accomplished by simply placing the complete medium at 37 °C in a water bath overnight, or actively degassing the medium by applying a vacuum. For the latter, 50 ml of compression medium is placed in a 250 ml vacuum flask and the flask is plugged with a rubber stopper. The flask is then connected to house vacuum for 5 min with gentle agitation. Once small air bubbles disappear, the vacuum should be slowly released. The medium should then be immediately loaded into the compression cell.

4. An alternative method to generate spherical aggregates from tissue culture is to generate a single-cell suspension and adjusting the concentration to 1×10^6 cells/ml. Three milliliters can then be transferred to 13×100 mm borosilicate glass round-bottom centrifuge tubes (Bellco Glass Inc. Part # 2012-01310). Cells are then centrifuged into a thin sheet and incubated overnight. The cohesive sheet can then be transferred to a 35 mm culture dish and cut into 1 mm fragments using micro-scalpels. These fragments are then transferred to shaker flasks containing 3 ml of tissue culture medium and incubated under tissue culture conditions with orbital shaking at 80–90 rpm until spheroids form. Spherical aggregates can also be generated from embryonic tissues as per the methods described in [1] and [3].

5. DNase is added to prevent nonspecific clumping when damaged cells release DNA into the medium.

6. Cell concentration must be empirically determined for each cell type. Smaller cells typically require a higher cell concentration than larger cells. For example, whereas RAT2 cells that are ~6 μm in diameter require a concentration of

4–6×10^6 cells/ml to form 200 μm diameter aggregates, MLL cells that are between 14 and 16 μm in size require a lower concentration, 2.5×10^6 cells/ml, to generate such aggregates.

7. The time required for spheroids to round up must be empirically determined for each cell type. Some can take as little as 2 h, whereas others may require 4–5 days. For longer incubations in hanging drop cultures, it may be necessary to "feed" each drop by adding another 10 μl of tissue culture medium. Alternatively, cell clusters can be transferred to shaker flasks and incubated as described in **Note 4**.

8. Care must be taken to remove just enough poly-HEMA to leave a thin coating. Removing too much may not prevent adhesion, whereas leaving too much may generate a thick gel that will peel off the surface of the compression plates.

9. The nickel-chromium wire is heat-straightened by hanging a 15 in. length from a retort stand and clamping a small binder clip to the end. A Bunsen burner is then quickly run up and down the length of the wire until the wire glows red. The straightened wire can then be cut into appropriate lengths.

10. Operators sometime experience difficulty when hanging the UCP/wire combination because the wire tends to adhere by surface tension to the sides of the aperture at the top of the inner chamber. To resolve this, care must be taken not to over- or underfill the inner chamber. Any liquid adhering to the sides of the aperture should be dried using a cotton swab.

11. The pen can be zeroed at any position on the chart paper, and not necessarily on the 0 mark. However, if the operator wished to position the pen at any specific point, this should be accomplished by adding or removing small pieces of aluminum foil at the tare loop and not by using the coarse or the fine adjustment knobs on the Cahn balance. The balance tends to exhibit less zero drift when adjusted mechanically rather than electronically.

12. Some aggregates require very little force to significantly change shape, whereas others can be subjected to a large compressive force without appreciably changing shape. Determining how much force to apply at first and second compression will vary with aggregate type. Too small a compression will not sufficiently change aggregate shape. Accordingly, cells within the aggregate may not become sufficiently compressed and will not rearrange to dissipate the applied force. Conversely, too large a compression may require massive cell rearrangement, and in the extreme may cause aggregates to rupture. In either case, it is unlikely that the surface tension calculated will be a true surface tension.

13. The time for aggregates to reach shape and force equilibrium varies with aggregate type and must be determined empirically.

Some aggregates reach equilibrium within an hour, whereas others may take up to 8 h. It is advisable to err on the side of caution and allow the aggregate more time to reach equilibrium, particularly during the first compression. Aggregates should also be allowed to relax for some time between compressions. This too will vary with aggregate type. Typically, softer aggregates tend to require less time to relax prior to second compression than do tighter aggregates.

14. For any two successive compressions, the ratio of σ_2/σ_1 will likely never be exactly 1.0. This is because aggregates seldom reach a true force or shape equilibrium. Viscosity interferes and prevents aggregates from reaching an absolute equilibrium state. Accordingly, the operator must use his/her judgment to determine what is an acceptable difference between σ_2 and σ_1 that would still denote a liquid aggregate. We typically assume that a 10 % difference is acceptable, although for larger aggregates, a larger difference, perhaps up to 15 %, is also tolerable. What is more important is that the data set as a whole reflects liquidity by demonstrating that the means of σ_1 and σ_2 are not statistically different.

15. Aggregates display both viscoelastic and liquid-like properties. When initially compressed, aggregates behave as an elastic solid. That is, if aggregates are compressed between parallel plates, and the force is immediately released, they almost immediately "spring" back into their original shape (Movie 4 at SpringerExtras.com). If, however, aggregates are clamped between parallel plates and held under compression for several hours, they do not "spring" back into a sphere once decompressed. Rather, the aggregate surfaces in contact with the parallel plates remain flat, and only round back up after several hours in culture (Movie 5 at SpringerExtras.com). This behavior led to the assertion that aggregates, upon compression, behave as elastics on short time scales and viscous liquids on longer time scales.

16. Since σ_1 and σ_2 were not significantly different, the average σ value was calculated by pooling all the data.

Acknowledgements

References

1. Foty RA, Pfleger CM, Forgacs G, Steinberg MS (1996) Surface tensions of embryonic tissues predict their mutual envelopment behavior. Development 122(5):1611–1620

2. Foty RA, Steinberg MS (2005) The differential adhesion hypothesis: a direct evaluation. Dev Biol 278(1):255–263

3. Schotz EM, Burdine RD, Julicher F, Steinberg MS, Heisenberg CP, Foty RA (2008) Quantitative differences in tissue surface tension influence zebrafish germ layer positioning. HFSP J 2(1):42–56

4. Hackett-Jones EJ, Landman KA, Newgreen DF, Zhang D (2011) On the role of differential adhesion in gangliogenesis in the enteric nervous system. J Theor Biol 287:148–159

5. Kragl M, Knapp D, Nacu E, Khattak S, Maden M, Epperlein HH, Tanaka EM (2009) Cells keep a memory of their tissue origin during axolotl limb regeneration. Nature 460(7251):60–65

6. Wada N (2011) Spatiotemporal changes in cell adhesiveness during vertebrate limb morphogenesis. Dev Dyn 240(5):969–978

7. Foty RA, Steinberg MS (2013) Differential adhesion in model systems. WIREs Dev Biol 2:631–645

8. Steinberg M (1964) The problem of adhesive selectivity in cellular interactions. In: Locke M (ed) Cellular membranes in development 22nd symposium of the society for the study of development and growth. Academic, New York, NY, pp 321–366

9. Moyer WA, Steinberg MS (1976) Do rates of intercellular adhesion measure the cell affinities reflected in cell sorting and tissue spreading configurations. Dev Biol 52:246–262

10. Nose A, Nagafuchi A, Takeichi M (1988) Expressed recombinant cadherins mediate cell sorting in model systems. Cell 54:993–1001

11. Glasstone S, Laidler KJ, Eyring H (1941) The theory of rate processes; the kinetics of chemical reactions, viscosity, diffusion and electrochemical phenomena. McGraw-Hill Book Company, Inc., New York, NY

12. Duguay D, Foty RA, Steinberg MS (2003) Cadherin-mediated cell adhesion and tissue segregation: qualitative and quantitative determinants. Dev Biol 253(2):309–323

13. Chu YS, Thomas WA, Eder O, Pincet F, Perez E, Thiery JP, Dufour S (2004) Force measurements in E-cadherin-mediated cell doublets reveal rapid adhesion strengthened by actin cytoskeleton remodeling through Rac and Cdc42. J Cell Biol 167(6):1183–1194

14. Bell GI (1978) Models for the specific adhesion of cells to cells. Science 200(4342):618–627

15. Evans E, Berk D, Leung A (1991) Detachment of agglutinin-bonded red blood cells I. Forces to rupture molecular-point attachments. Biophys J 59:838–848

16. Steinberg MS (1996) Adhesion in development: an historical overview. Dev Biol 180(2):377–388

17. Foty RA, Steinberg MS (1997) Measurement of tumor cell cohesion and suppression of invasion by E- or P-cadherin. Cancer Res 57(22):5033–5036

18. Jia D, Dajusta D, Foty RA (2007) Tissue surface tensions guide in vitro self-assembly of rodent pancreatic islet cells. Dev Dyn 236(8):2039–2049

19. Sabari J, Lax D, Connors D, Brotman I, Mindrebo E, Butler C, Entersz I, Jia D, Foty RA (2011) Fibronectin matrix assembly suppresses dispersal of glioblastoma cells. PLoS One 6(9): e24810

20. Winters BS, Shepard SR, Foty RA (2005) Biophysical measurement of brain tumor cohesion. Int J Cancer 114(3):371–379

21. Davies JT, Rideal EK (1963) Interfacial phenomena. Academic, New York, NY

22. Foty R (2011) A simple hanging drop cell culture protocol for generation of 3D spheroids. J Vis Exp (51)

23. Butler CM, Foty RA (2011) Measurement of aggregate cohesion by tissue surface tensiometry. J Vis Exp (50)

Chapter 17

Quail-Chick Chimeras and Eye Development

Sinu Jasrapuria Agrawal and Peter Y. Lwigale

Abstract

The quail-chick chimera is a stable and precise labeling technique that allows tracing of definite cells and their progeny without interfering with normal development of two related avian species. This technique utilizes the transplantation of quail tissues into chick embryo or vice versa. The region of interest (graft) is removed from the donor and replaced in the stage-matched host embryo. The quail-chick chimeras can be analyzed by immunolabeling donor-derived cells with species-specific antibodies, or by differential staining of the nucleus. The use of the quail-chick chimera technique is valuable to eye development studies since its formation involves coalition of tissues from different embryonic origins: the ectoderm, neuroectoderm, and neural crest cells derived from the interaction between the ectoderm and neural ectoderm. This chapter describes the protocols for using quail-chick chimeras to identify neural crest- and ectoderm-derived components of the eye. This technique can be used in combination with molecular biology techniques in functional studies to determine the cellular and tissue interactions involved in eye development.

Key words Quail-chick chimera, Neural crest cells, Neural tube, Eye development

1 Introduction

The quail-chick chimera is a powerful technique to identify embryonic territories that contribute to organ formation during development. It is also widely used for mapping cell fate of neural crest cells and neural primordium at different stages of embryonic development [1–3]. During the first days of incubation, when most of the important events in embryogenesis take place, the size of the quail and chick embryos and the chronology of their development differ only slightly, which facilitates "cut-and-paste" transplantation of tissues between the two species. Transplantation of donor tissues into host embryos to generate chimeras is performed in ovo, thus permitting analysis of chimeras until late stages of development or after hatching.

Eye development studies are a perfect candidate for the quail-chick chimera technique, since it is formed from three distinct embryonic origins (ectoderm, neuroectoderm, and neural crest cells). The lens and ocular epithelium are of ectodermal origin.

The optic cup (future retina) forms as a result of invagination of the neuroectoderm (optic vesicles) in the region of the diencephalon. The neural crest cells originate from the dorsal neural tube, migrate into the periocular region, and give rise to majority of the remaining ocular tissues including the cornea, iris, sensory nerves, ciliary body, and mesenchyme of the eyelid [4–8]. Therefore quail-chick chimeras for studying ocular development can be generated using grafts from the cranial ectoderm, neural tube, or dorsal neural tube prior to neural crest migration. The eyes of chimeras generated after grafting any of these tissues can be analyzed at various stages of development using different identification techniques. Earlier analyses were based on differential staining of the nucleus by Feulgen and Rossenback nuclear staining [6, 9], but recently immuno-labeling of quail cells using the quail-specific nuclear antibody (QCPN) has gained popularity [2, 4, 8, 10].

With the recent advances in molecular techniques, quail-chick chimeras can be easily used in combination with electroporation to perform gain- or loss-of-function studies in the avian embryos. Quail-chick chimeras can also be used to study stem cell potential of tissues. An example of such study is the injection of stromal keratocytes isolated from quail corneas into chick embryos [8]. In this chapter we provide a protocol for using quail-chick chimeras to trace the tissue origin of the avian eyes.

2   Materials

2.1   Egg Incubation

1. Fertilized eggs from Japanese quail (*Coturnix coturnix japonica*) and White Leghorn chick (*Gallus gallus domesticus*) are used (*see* **Note 1**).

2. Ventilated and humidified incubators equipped with timed programmers are useful to obtain very precise stages of development (*see* **Note 2**).

3. Cardboard egg holders (in which they are transported).

2.2   Preparation of Donor Grafts (Quail) and Host Embryos (Chick)

1. 70 % ethanol for sterilization.

2. Disposable syringes (1- or 5-mL) and hypodermic needles (18½ G and 26½ G).

3. Transparent tape (5 cm in width).

4. Microsurgical instruments including fine scissors, AA forceps (Swiss Dumont no. 5), tungsten needles or pulled glass needles (*see* **Note 3**), curved iris forceps. All instruments should be sterilized with 70 % ethanol before use.

5. Physiological buffers: Sterile phosphate buffer saline (PBS) or sterilized Ringer's solution. Phosphate-buffered saline: Dissolve 138 mM NaCl, 2.7 mM KCl, 8.1 mM $Na_2HPO_4 \cdot H_2O$,

1.4 mM KH$_2$PO$_4$, 90 μM CaCl$_2$·2H$_2$O, 49 μM MgCl$_2$·6H$_2$O, in Milli-Q water and adjust the pH to 7.4. Sterilized Ringer's Solution: Dissolve 123 mM NaCl, 1.5 mM CaCl$_2$, 5 mM KCl, 81 μM Na$_2$HPO$_4$, 14 μM KH$_2$PO$_4$ in Milli-Q water and adjust the pH to 7.4. Supplement the buffers with Penicillin/Streptomycin antibiotics: final concentration 100 μg/mL penicillin and 100 μg/mL streptomycin.

6. 1 mL Pasteur pipettes and parafilm.

7. India ink diluted 1:10 in sterile Ringer's solution containing antibiotics.

8. Stereomicroscope equipped with magnification (5× to 40×) and gooseneck light source.

2.3 Histological Analysis of the Chimeric Embryos

1. 4 % paraformaldehyde for fixation of the tissues.

2. Paraffin histology (*see* **Note 4**).

3. Microscope equipped with digital cameras and imaging software.

3 Methods

A video showing detailed instructions of a similar technique applied to unilateral dorsal neural tube grafts is available at http://www.jove.com/video/3622/ [11].

3.1 Incubation of Eggs

1. Wash the eggs with tepid water to remove debris.

2. Chick eggs are arranged horizontally on the cardboard egg holder. With the eggs in horizontal position, pencil-mark the highest point of the surface with an "X." This region corresponds to the site where the future embryo will be localized. Quail eggs are incubated with the blunt side up.

3. Eggs are incubated for 29–30 h at 38 °C in a humidified and ventilated incubator (*see* **Note 5**). Turn on rocking function. The operations described here are performed with stage 8 and stage 9 embryos [12].

3.2 Preparation of Eggs for Dissection and Windowing

1. Experiments should be carried out under relatively sterile conditions, in a clean separate room. Eggshells are cleaned with 70 % ethanol (*see* **Note 6**).

2. Eggs are placed onto an individual egg holder (*see* **Note 7**). Using AA forceps make a small hole in the eggshell near the pointed end of the egg.

3. Remove about 3 mL of albumin from the egg, using 18½ G hypodermic needle and 5 mL syringe (*see* **Note 8**). This lowers

the yolk level and separates the blastoderm from the eggshell membrane.

4. The hole is wiped with 70 % ethanol and sealed with a small piece of transparent tape.

5. Using AA forceps, tap another hole onto the upper surface of the chick egg, in the region of the egg marked "X." Insert one end of the curved iris forceps into the hole parallel to the eggshell, pinch off the shell to create a ~2 cm diameter window in the eggshell. The fertilized embryo appears as an opaque disc on top of the yolk (*see* **Note 9**).

6. Inject a small amount of India ink beneath the blastoderm to increase visual contrast and assist with the staging of the embryo. Use a 1 mL syringe and 26½ G hypodermic needle, bent at an angle of 45° at the base of the needle, with the bevel facing up. Puncture the yolk membrane outside the perimeter of the blastoderm and slide the tip of the needle beneath the embryo, close to the surface of the yolk but not in the embryonic layers. Inject just enough ink to outline the embryo, and then carefully withdraw the needle (*see* **Note 10**).

7. Embryos are staged according to Hamburger and Hamilton (HH) [12] under stereomicroscope with fiber optic gooseneck light source.

8. To prevent dehydration and/or contamination of the embryo, 2–3 drops of sterile Ringer's solution are added on the embryo surface. Temporarily, seal the window with parafilm stretched over the surface of the egg. Stage all the eggs before proceeding to the transplantation (*see* **Note 11**).

3.3 Prepare the Donor (Quail) Graft Tissue

1. Use curved iris forceps to open quail eggs in the blunt end region that forms the top surface during incubation. With fine scissors, make four cuts outside the embryo (*see* **Note 12**).

2. Use curved iris forceps to carefully lift the embryo from the yolk and transfer it to Petri dish containing Ringer's solution. Gently remove the transparent vitelline membrane with fine forceps.

3. Transfer the quail embryos into fresh Ringers' solution. The embryos are kept at room temperature throughout the duration of the grafting procedure. For proper grafting, the donor and host embryos are strictly stage-matched. Under the microscope, the quail embryo is then excised at the region of interest (*see* Subheading 3.5). Depending on the needs of the experiment, this region may be a complimentary region of the host (chick) neural tube or from a different region near the ectoderm.

3.4 Prepare the Host (Chick) Embryo to Receive the Graft

1. Remove the parafilm from the chick egg. Using a tungsten needle, make a small hole in the vitelline membrane above the desired region of the embryo.

2. To prevent dehydration of the exposed embryo, add a drop of the sterile Ringer's solution and repeat as required.

3. Use a pulled glass needle to extirpate the tissues from the desired region of the host embryo.

3.5 The Grafts

1. *Neural Tube transplantation*: To target presumptive ocular neural crest, make bilateral incisions in the dorsal neural tube between the rostral diencephalon and metencephalon region (Fig. 1a, arrowheads) of a stage 9 chick embryo. After the two edges of the dorsal neural tube are detached, make a perpendicular cut in the diencephalic region followed by an identical cut in the metencephalic region (Fig. 1a, asterisks). Use a pulled glass micropipette with Ringers' solution to aspirate and discard the detached dorsal neural tube explant. Make similar dissection in a stage-matched quail embryo and use a micropipette to transfer the dorsal neural tube explant to the prepared chick host. Use the pulled glass needle to orient the graft and gently insert it in the extirpated neural tube region of the chick.

2. *Ectoderm Transplantation*: Use stage 8 quail and chick embryos to target ocular ectoderm. At this stage the embryo is relatively flat and ideal for ectoderm grafts (Fig. 1g). Prior to dissection, the chick and quail embryos are prepared as described in the neural tube grafts above. Dissect the ectoderm from the rostral region of the embryo by making incisions adjacent to the neural fold and lateral region of the embryo (Fig. 1g, arrowhead), followed by anterior and posterior incisions (Fig. 1g; asterisks). Use glass needle to gently tease the ectoderm from the underlying cranial mesenchyme. Remove the detached ectoderm from the chick embryo using a micropipette and discard. Dissect an identical region from the quail embryo. Any loose cranial mesenchyme can be scrapped from the explant using a tungsten needle (*see* **Note 13**). Use a micropipette to transfer the explant to the chick host. Use a glass needle to orient and tuck the explant underneath the edges of the host ectoderm. This prevents dislodging of the explant.

3.6 Sealing the Eggs

1. Add 2–3 drops of Ringer's solution to the egg (away from the graft region to prevent dislodging explant) and seal with Scotch tape. Make sure that the tape seals the entire region of the windowed egg, to prevent dehydration and contamination of the embryo. Following transplantation, eggs can be kept at
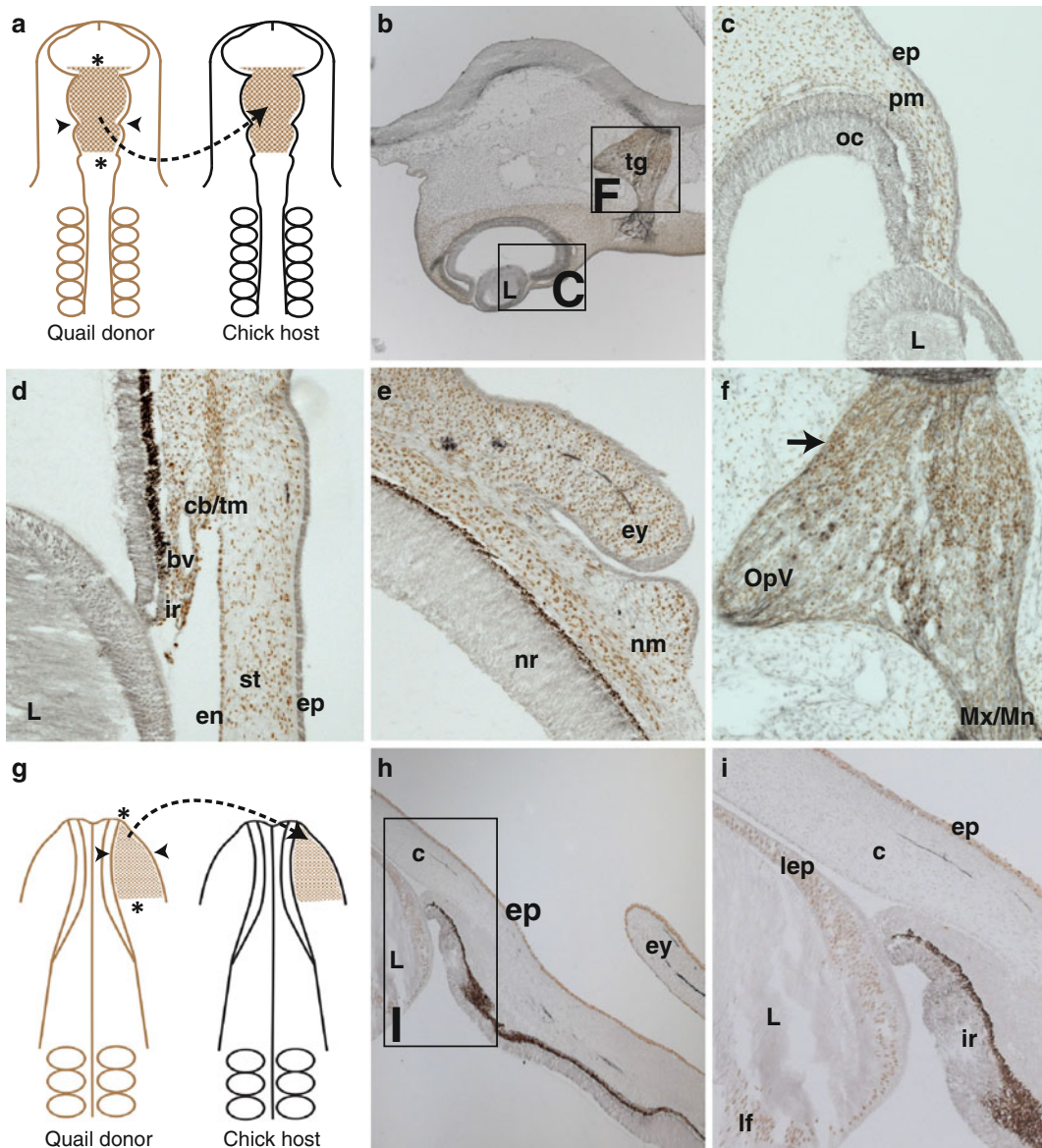
Fig. 1 Localization of quail-derived cells in quail-chick chimeras following neural tube and ectoderm transplantation. (**a**) Schematic showing bilateral dorsal neural tube transplantation from stage 9 quail into stage-matched chick host. *Black arrowheads* represent the region of incisions in the dorsal neural tube between the rostral diencephalon and metencephalon and *asterisks* represent the extent of the cuts in the diencephalic and metencephalic region respectively. (**b**, **c**) Analysis of a cross section through chimera collected at E4 shows quail neural crest-derived cells (*brown*) localized in the periocular mesenchyme (pm) and trigeminal ganglion. The epithelium (ep), optic cup (oc), and lens (l) are chick-derived (*grey*). (**d**) At E9, quail neural crest-derived cells are localized in the region of the presumptive ciliary body/trabecular meshwork (cb/tm), corneal endothelium (en), stroma (st), iris (ir), and around the ocular blood vessel (bv). (**e**) Also at E9, quail neural crest-derived cells are in the mesenchyme of the nictitating membrane (nm) and eyelids (ey). (**f**) High magnification of the trigeminal ganglion showing quail neural crest-derived neurons (large cells) in the proximal region (*arrow*) and glia (small cells) distributed throughout the ganglion. (**g**) Schematic showing unilateral transplantation of cranial ectoderm (shaded in *brown*) from stage-8 quail donor into stage-matched chick host. *Arrowheads* and *asterisks* indicate the boundaries of the grafted tissue. (**h**, **i**) A cross section through the eye of a chimera collected at E9 shows quail ectoderm-derived cells in the lens epithelium (lep), lens fiber (lf), corneal epithelium (ep), and eyelid epithelium

room temperature until all chimeric embryos are created (we usually do not exceed 10 h).

2. Incubate eggs until desired stages. Make sure the "rocking" function is turned off while incubating the chimeras (*see* **Note 14**).

3.7 Analysis of Chimeric Embryos

1. Quail-chick chimeras can be analyzed at different stages of development depending on the experiment. For eye development studies, embryos can be analyzed at embryonic day (E)3, which corresponds to the rudimentary eye stage when neural crest mesenchyme surrounds the optic cup, and the lens vesicle is detached from the overlying ectoderm (Hay and Revel, 1969).

2. To collect chimeras during early stages of development (E3–E4), cut the embryo away from the yolk with four large cuts outside the boundaries of the blastoderm. Between E5 and later stages, embryos can be lifted from the egg using curved forceps.

3. Transfer the embryo to a Petri dish containing Ringer's solution. Take care to minimize air exposure to prevent dehydration.

4. Under stereomicroscope, remove any unwanted tissues using #5 forceps or fine scissors. For eye development, we simply detach the head from the rest of the embryo at early stages, and for later stages, we remove the eyeballs.

5. Transfer embryos or dissected tissues to ice cold 4 % paraformaldehyde and fix overnight at 4 °C.

6. Prepare the samples and embed for paraffin sectioning. Alternatively, samples can be embedded in gelatin for cryosectioning.

7. Immunostain with QCPN supernatant antibody (diluted 1:1) following standard protocols.

3.8 Analysis of Quail-Chick Chimeras for Neural Crest and Ectoderm Contribution to the Eye

Sections of quail-chick chimeras collected at desired time points can be immunostained and visualized using fluorescent secondary antibodies or stained with 3,3′-Diaminobenzidine (DAB). Here we show DAB stained sections showing contrast between the quail-derived cells (brown) in the chick host (grey). Examination of a neural tube grafted quail-chick chimera at E4 reveals quail-derived cells in the periocular region that surrounds the optic cup of the rudimentary eye (Fig. 1b, c). The quail neural crest-derived cells from the grafted dorsal neural tube region also contribute to the trigeminal ganglion (Fig. 1b), where they give rise to neurons (large cells) in the proximal region (Fig. 1f, arrow) and glia (small cells) throughout the ganglion. Sensory nerve projections into the eye originate from the trigeminal ganglion. Both neural crest- and

placode-derived axons project into most ocular tissues, except for the cornea, which is innervated by only the neural crest-derived nerves [10]. During eye development, some of the quail neural crest-derived cells migrate between the ectoderm and lens to form the cornea stroma and endothelium (Fig. 1d). The cells that remain in the periocular region form the iris stroma, ciliary body, trabecular meshwork, and also contribute pericytes to the ocular blood vessels. The quail neural crest-derived cells in the distal region of the eye contribute to the mesenchyme of the nictitating membrane and eyelids (Fig. 1e), and later contribute to the musculature of these tissues.

The quail ectoderm grafts in the cranial region followed in an E9 chimera show that the ectoderm gives rise to the lens (epithelium and fiber cells, Fig. 1h, i). Quail ectoderm-derived cells also contribute to the epithelium of the cornea, conjunctiva, and to the eyelid (Fig. 1h, i).

4 Notes

1. For neural crest grafts, a nonpigmented chick strain can be chosen to use the heavily pigmented quail strain as the marker. Freshly laid eggs are stored no later than a week at 15 °C.

2. Incubators must be set at temperature 38 °C and humidity regulated to 45 % (first two-thirds of incubation time), 75 % (last one-third of incubation time and hatching).

3. Pulled glass needles are generated from silicon glass capillary tubes that have been pulled under heat with a needle pulling apparatus.

4. After fixation samples are passaged through a series of increasing concentration of ethanol in PBS (50, 70, 90, and 100 %). Samples are cleared in Histosol, then embedded in paraffin. These blocks of paraffin containing samples are sectioned (8–10 μm) using a microtome.

5. For HH stage 8 incubation time ranges from 27 to 29 h and for HH stage 9 incubation times range from 29 to 33 h at 38 °C. Chick and quail embryos were staged according to conventionally used developmental tables [12–14].

6. Spray and wipe off the ethanol quickly with a Kimwipe to avoid absorption through the eggshell.

7. For individual egg holders, we use small Petri dish (size 35 × 10 mm for quail and 60 × 15 mm for chick) lined with folded Kimwipes (to provide cushion to the eggs).

8. Care should be taken to insert the needle vertically into the hole, with the bevel facing the pointed end of the egg; this prevents damaging of yolk when albumin is withdrawn.

9. Fertilized eggs are identified by presence of a blastoderm on the surface of the yolk. If a white spot is observed, the egg is unfertilized and should be discarded.

10. Injecting too much ink could be lethal. Also care should be taken to avoid injecting any air bubbles beneath the embryo, as this can be a source of contamination.

11. Eggs continue to develop at the room temperature but the rate of development is very slow.

12. The four cuts should make a rectangular shape and all ends must meet to permit extraction of the embryo.

13. Alternatively, tissue can be incubated briefly in dispase to loosen and remove the mesenchyme. In this case, the tissue must be rinsed extensively in Ringers' solution containing bovine serum albumin (BSA) to inactivate the enzyme prior to grafting.

14. Avoid sudden jerking movements while transferring the eggs to the incubator as this might dislodge the explants. Eggs may be gently turned by hand two times a day to increase the viability. Also, the incubator humidity must be raised from 45 to 75 %.

References

1. Catala M, Teillet MA, De Robertis EM et al (1996) A spinal cord fate map in the avian embryo: while regressing, Hensen's node lays down the notochord and floor plate thus joining the spinal cord lateral walls. Development 122:2599–2610

2. Douarin L (1982) The neural crest. Cambridge University Press, Cambridge

3. Le Douarin NM (1993) Embryonic neural chimaeras in the study of brain development. Trends Neurosci 16:64–72

4. Creuzet S, Vincent C, Couly G (2005) Neural crest derivatives in ocular and periocular structures. Int J Dev Biol 49:161–171

5. Hay ED, Revel JP (1969) Fine structure of the developing avian cornea. Monogr Dev Biol 1:1–144

6. Johnston MC, Noden DM, Hazelton RD et al (1979) Origins of avian ocular and periocular tissues. Exp Eye Res 29:27–43

7. Lwigale PY, Bronner-Fraser M (2009) Semaphorin3A/neuropilin-1 signaling acts as a molecular switch regulating neural crest migration during cornea development. Dev Biol 336:257–265

8. Lwigale PY, Cressy PA, Bronner-Fraser M (2005) Corneal keratocytes retain neural crest progenitor cell properties. Dev Biol 288:284–293

9. Gabe M (1968) Techniques histologiques. Masson, Paris

10. Lwigale PY (2001) Embryonic origin of avian corneal sensory nerves. Dev Biol 239:323–337

11. Griswold SL, Lwigale PY (2012) Analysis of neural crest migration and differentiation by cross-species transplantation. J Vis Exp 60:1–8

12. Hamburger V, Hamilton HL (1951) A series of normal stages in the development of the chick embryo. J Morphol 88:49–92

13. Eyal-Giladi H, Kochav S (1976) From cleavage to primitive streak formation: a complementary normal table and a new look at the first stages of the development of the chick. I. General morphology. Dev Biol 49:321–337

14. Zacchei AM (1961) Lo sviluppo embrionale della quaglia giaponese. Archivi Anatomica 66:36–62

Part IV

Emerging Models of Tissue Morphogenesis

Chapter 18

Studying Epithelial Morphogenesis in *Dictyostelium*

Daniel J. Dickinson, W. James Nelson, and William I. Weis

Abstract

The discovery of polarized epithelial tissue in the social amoeba *Dictyostelium discoideum* establishes this classical model organism as a novel system for the study of epithelial polarity and morphogenesis. *D. discoideum* grows as single cells and is easily maintained in cell culture. Starvation of the cells triggers a multicellular developmental process that culminates with the formation of a fruiting body, whose normal morphogenesis is dependent on a polarized epithelium located at the apex of the developing structure. Here, we discuss techniques for genetic manipulation and imaging of multicellular *D. discoideum*, with a focus on methods that have facilitated the study of the epithelial tissue in this organism.

Key words Cell polarity, *Dictyostelium*, Epithelium, Immunofluorescence, Microscopy, Morphogenesis, Multicellularity, RNAi

1 Introduction

A simple epithelium, comprising a monolayer of structurally and functionally polarized cells, is the basic unit of organization of animal body plans. Epithelial cells have biochemically distinct apical and basolateral plasma membrane domains and a polarized organization of the secretory pathway and cytoskeleton. An epithelium is the first differentiated tissue to appear during embryonic development, and the coordinated rearrangement of epithelial cells is a major contributor to tissue and organism morphogenesis [1, 2]. In mature epithelial organs, the epithelium is organized into a tube, with the apical surface facing the lumen [3].

The social amoeba *Dictyostelium discoideum* is a classical model system for the study of cell motility, cell–cell interactions, evolution, and morphogenesis [4]. *Dictyostelium* multicellular development is triggered by starvation, which induces aggregation of individual amoebae to form a mound, then a slug, and finally a fruiting body (Fig. 1a). *D. discoideum* offers several unique advantages as a model system for the study of morphogenesis. The amoebae grow as single cells that can be handled with ease similar
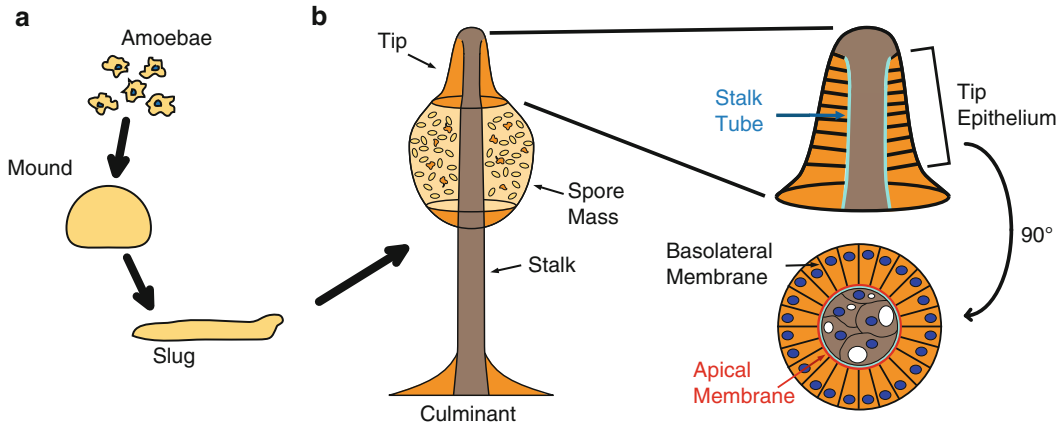
Fig. 1 Epithelial polarity in social amoebae. (**a**) The *D. discoideum* developmental process. Starvation triggers the aggregation of individual amoebae to form a mound, which then elongates to form a slug. After a period of migration, the slug develops into a fruiting body. The process of fruiting body formation is called culmination, and an immature fruiting body is called a culminant. (**b**) The fruiting body consists of a rigid stalk supporting a collection of spores. Stalk formation is orchestrated by the tip, which consists of a polarized epithelium surrounding the stalk at the apex of the culminant. The epithelial cells are polarized, with the apical surface adjacent to the stalk. Adapted from [8]

to mammalian tissue culture cells, but with considerably less cost. Multicellular development takes only 24 h and can be induced at will by simply subjecting the cells to starvation. Techniques for genetic and biochemical manipulation of cells are well established, and modern approaches for genomic analysis and high-resolution imaging are increasingly being adopted. Finally, the phylogenetic position of the social amoebae as an outgroup to the opisthokonts (animals + fungi) [5] makes *D. discoideum* an informative model for comparative studies [6, 7].

The final stage of *D. discoideum* development is called culmination and results in the formation of a mature fruiting body. At the onset of culmination, a polarized epithelium appears which is essential for normal fruiting body morphogenesis (Fig. 1b) [6, 8]. The organization and polarity of the epithelium require homologues of β-catenin and α-catenin, which are also essential for epithelial integrity in animals. This epithelial tissue is located in a region called the tip (Fig. 1b), which was classically known as an organizing center for morphogenesis [9, 10]. Our recent work has revealed how the tip epithelium contributes to *D. discoideum* culmination. Tip epithelial cells secrete cellulose and extracellular matrix proteins directionally to form the rigid exterior of the stalk [6], while at the same time, apical actomyosin contractility in the tip epithelium regulates stalk diameter [8]. Importantly, directional protein secretion, apical actomyosin contractility, and a requirement for β- and α-catenin are conserved properties of epithelial tissues in both *D. discoideum* and metazoans.

The experimental tractability of *D. discoideum* and the similarities between *D. discoideum* and metazoan epithelia make *D. discoideum* an attractive simple model system for the study of epithelial polarity and morphogenesis. Here, we provide a suite of methods to facilitate the investigation of *D. discoideum* culmination. These methods allow the investigator to obtain homogenous expression of fluorescent protein fusions, to disrupt gene function with temporal specificity using RNA interference, and to examine the developmental process at subcellular resolution using confocal microscopy. Basic techniques for culture, maintenance, and transformation of *D. discoideum* cells are not covered here due to lack of space, but the reader is referred to recent methods articles that discuss these techniques in detail [11, 12].

2   Materials

2.1   Cell Growth and Transformation with Fluorescent Protein Fusions

1. HL5 Medium: Dissolve 7 g Proteose Peptone No. 2 (BD), 7 g Proteose Peptone No. 3 (BD), 7 g Yeast Extract, 1.5 g KH_2PO_4, and 0.5 g Na_2HPO_4 in 950 mL of water, adjust pH to 6.5 and autoclave. Before use, add 50 mL filter-sterilized 27 % Glucose (final concentration 1.35 %) and 10 mL of a tissue culture-grade 100× Penicillin-Streptomycin solution; also add selective drugs if needed (see below). Store at 4 °C after addition of antibiotics.

2. G418: Prepare a 100 mg/mL (active concentration) stock solution, filter sterilize, and store at −20 °C.

3. Hygromycin B: Can be purchased as a 50 mg/mL stock solution, which can be stored at 4 °C indefinitely. Alternatively, prepare a stock solution from powder, filter sterilize, and store at 4 °C.

4. Genes of interest are cloned into one of the pDM expression vectors [13] or another appropriate *Dictyostelium discoideum* expression vector.

2.2   Development of D. discoideum Under Controlled Conditions

1. Development Buffer (DB): Prepare a solution of 5 mM Na_2HPO_4, 5 mM KH_2PO_4, adjust pH to 6.5 and autoclave. The solution may be stored at room temperature, but should be cooled to 4 °C before use. Also, autoclave stock solutions of 1 M $MgCl_2$ and 1 M $CaCl_2$. Immediately before use, add $MgCl_2$ and $CaCl_2$ to a final concentration of 2 mM each (*see* **Note 1**).

2. Whatman No. 3 filter paper.

3. 25 mm black Nuclepore filters with 0.2 μm pores (Whatman). Before the experiment, wash the filters by placing them in a

beaker of boiling water with gentle stirring for 10–20 min. The stirring should be vigorous enough to discourage the filters from sticking to the sides of the beaker, but not so vigorous that the filters contact the stir bar. The filters will tend to float to the surface and to stick to each other; use forceps to separate them and push them down into the water. Boiled filters may be stored indefinitely in a clean petri dish.

2.3 RNA Interference

1. Hairpin construct targeting the gene of interest (see below for vector construction).

2. Doxycycline hyclate, stored in powder form in a desiccator at 4 °C (*see* **Note 2**).

3. Antibody recognizing the protein of interest on a western blot, for characterization of the efficacy of knockdown.

2.4 Whole-Mount Immunofluorescence of Culminants

1. Fixation solution: 4 % formalin in histology-grade ethanol. May be stored at 4 °C for several months.

2. Blocking solution: 10 % bovine serum albumin (BSA), 5 % goat serum (*see* **Note 3**), 1 % saponin (*see* **Note 4**), 0.02 % sodium azide, in phosphate buffered saline (PBS). May be stored at 4 °C for several months.

3. Antibody solution: 3 % BSA, 5 % goat serum (*see* **Note 3**), 0.5 % saponin (*see* **Note 4**), 0.02 % sodium azide in PBS. May be stored at 4 °C for several months.

4. Primary antibodies recognizing the protein of interest. The primary antibody should recognize a single band (corresponding to the protein of interest) on a western blot; if nonspecific bands are observed, affinity purify the antibody.

5. Secondary antibodies appropriate for the species of primary antibody being used, labeled with fluorophores suitable for the microscope to be used.

6. Fluorescently labeled phalloidin.

7. Calcofluor white M2R (also known as fluorescence brightener 28) for cellulose staining (optional).

8. PBST: PBS containing 0.1 % (v/v) Tween 20.

9. Vectashield mounting medium (Vector Labs). Vectashield containing DAPI can be purchased if nuclear staining is desired. Add 200 μg/mL (final concentration) of calcofluor to the mounting medium if staining of cellulose in the stalk tube is desired.

10. Nail polish for sealing slides.

3 Methods

3.1 Obtaining Homogenous Expression of Fluorescent Fusion Proteins

Transformation of *D. discoideum* with plasmid DNA is a rapid and efficient procedure [12], but transgenes introduced in this manner are typically expressed at variable levels and in only a subset of cells (*see*, e.g., [13]). For experiments using single cells this is not a problem, as one can choose to analyze only the cells that express a transgene at the desired level. However, for the study of morphogenesis it is often desirable to achieve equal levels of fluorescent protein expression in all cells in a multicellular structure. In addition, one often wishes to compare the localization of a fluorescent protein in different mutant backgrounds, and for this it is important that the transgene be expressed at equivalent levels in different cell lines (which must be independently transformed). Here, FACS sorting of transformed *D. discoideum* cells is used to achieve homogenous and reproducible transgene expression levels.

1. Place 10 mL of HL5 axenic medium in a 10 cm tissue culture dish, and inoculate with *D. discoideum* cells from a frozen stock or from spores (*see* **Note 5**).

2. When the cells are >80 % confluent, remove the medium. Resuspend the cells in a few mL of medium by squirting them off the bottom of the dish with a pipet, and transfer to a 15 cm dish with 20 mL of fresh medium (or split between two 10 cm dishes).

3. Allow the cells to grow to near confluence. A total of at least 3×10^7 cells are needed for one transformation experiment.

4. Transform two batches of 10^7 cells each with the desired DNA construct of interest, using electroporation [12]. Also electroporate a control sample with no DNA. After transformation, allow the cells to recover in the absence of selective drugs overnight.

5. Replace the medium with fresh medium containing selective drugs (*see* **Notes 6** and **7**).

6. Examine the cells daily and look for the appearance of drug-resistant clones only on the transformed plates (colonies should not appear on the control plate). Substantial cell death should be apparent within 24–48 h after addition of selective medium.

7. Change the medium every 48 h until colonies appear (usually within 4–10 days after the addition of selective medium). When changing the medium, rock the plate gently from side to side to dislodge dead cells and remove them with the old medium.

8. Once the colonies are large (several hundred cells), resuspend the cells in fresh medium and allow them to distribute evenly over the surface of the culture dish. This allows the cells to
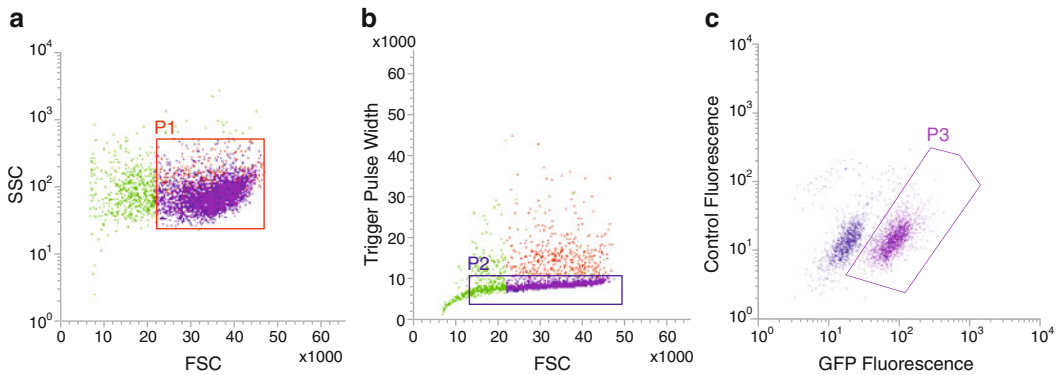
Fig. 2 FACS sorting to obtain homogenous expression of fluorescent protein fusions. (**a**) Forward-scatter (FSC) versus side-scatter (SSC) plot. The P1 gate is used to eliminate dead cells. (**b**) Pulse width versus FSC plot. The P2 gate is used to eliminate cell doublets and other aggregates. (**c**) Fluorescence intensity plot showing GFP fluorescence on the *x*-axis. The fluorescent protein-expressing cells can be easily separated from the non-expressing cells. Here the P3 gate was used to isolate all expressing cells, but a narrower gate could be used to select cells with a particular expression level if desired. GFP fluorescence was detected using a 488 nm excitation laser and a 525/50 bandpass emission filter. "Control fluorescence" is the background fluorescence measured using a 488 nm excitation laser and a 692/40 bandpass emission filter

grow to confluence without becoming overcrowded in the centers of the colonies.

9. When the cells are nearly confluent (but not overcrowded), resuspend and transfer the cells to a conical tube. Spin for 5 min in a clinical centrifuge to pellet the cells and resuspend in 1 mL fresh medium (*see* **Note 8**).

10. Purify fluorescent protein-expressing cells using a Fluorescence Activated Cell Sorter. We use three gates to isolate a pure population:

    (a) A forward-scatter (FSC) gate is used to eliminate dead cells, which are present in relatively large numbers due to the selection (Fig. 2a).

    (b) A pulse width gate is used to eliminate cell doublets and any higher-order aggregates (Fig. 2b).

    (c) Finally, a fluorescence intensity gate is used to isolate cells expressing the transgene (Fig. 2c).

    Collect 10^5–10^6 expressing cells into a sterile tube. After sorting is complete, transfer the cells to fresh medium for further growth.

11. As soon as possible after sorting, freeze some of the sorted amoebae for later use or long-term storage [11].

12. For experiments, maintain the sorted cells in medium with selective drugs. The cells should be passaged in axenic medium for no more than 3 weeks (*see* **Note 5**); transgene expression levels and homogeneity of expression will gradually decline during this time.

3.2   Development of D. discoideum Under Controlled Conditions

A key advantage of studying morphogenesis in *D. discoideum* is that the investigator can induce multicellular development at will. The following procedure is used to prepare multicellular structures for microscopy. Modifications are described in Subheading 4 that adapt the procedure for biochemical experiments.

1. Grow cells of the desired strain in axenic culture to 50–80 % confluence. Do not use 100 % confluent or overgrown cells for this procedure, since overgrowth triggers starvation responses that give some cells a "head start" on development. An 80 % confluent 10 cm tissue culture dish will typically yield enough cells for 2–3 samples.

2. Prepare DB by adding $CaCl_2$ and $MgCl_2$ (*see* Subheading 2) and place on ice; 100 mL is enough for a typical experiment (*see* **Note 9**).

3. Prepare a petri dish with four layers of Whatman No. 3 filter paper in the bottom. Soak the filters with enough DB to saturate them. Let stand for 2–3 min at room temperature to ensure that the filters are fully saturated, then aspirate the excess DB and gently smooth the filter paper to squeeze out any large air bubbles.

4. Wet a washed Nuclepore filter briefly with DB and place it shiny side down on the saturated filter paper (*see* **Note 10**).

5. Remove the medium from the cells and wash twice by gently adding ~6 mL DB (for a 10 cm dish), taking care not to dislodge the cells. Then resuspend the cells in a third portion of DB by using a pipet to squirt the cells off the bottom of the dish. Use a graduated pipet to transfer the cell suspension to a conical tube on ice and note the total volume.

6. Remove a 10 μL aliquot of the cell suspension and transfer to a Neubauer hemocytometer for cell counting.

7. Centrifuge the cell suspension for 5 min in a clinical centrifuge at 4 °C to pellet the cells. While the cells are spinning, count the cell aliquot in the hemocytometer to determine the cell density, and calculate the total number of cells.

8. Resuspend the cell pellet in ice-cold DB to a density of 4×10^7 cells/mL.

9. Pipet 125 μL of the cell suspension onto each Nuclepore filter. To distribute the cells evenly, start in the center of the filter and move the pipet tip in a spiral while dispensing the cell suspension. Use the pipet tip to spread the liquid over most of the surface of the filter (but avoid wetting all the way to the edges, since this will cause the cell suspension to flow off of the Nuclepore filter and onto the filter paper below).

10. Let the dish stand undisturbed for a few minutes until the liquid is absorbed, then seal the plate with parafilm and place in the dark.

11. Monitor development periodically with a dissecting microscope. Mounds are typically observed 8–12 h after plating, slugs at 15–18 h, and culminants at 20–24 h (the timing will vary somewhat from strain to strain).

3.3 RNA Interference During Multicellular Development

RNA interference offers an alternative to gene disruption for rapidly investigating gene function in *D. discoideum*. We have improved upon existing protocols for RNAi [14] by driving expression of the knockdown construct under an inducible promoter. A key advantage of this approach is that cells can be challenged by depleting a protein of interest and assayed immediately thereafter, thus avoiding the confounding effects of secondary mutations that can sometimes arise during the lengthy selection procedure required to generate a knockout. This approach also allows temporal control of gene disruption, which allows one to study the developmental roles of genes that have essential functions in vegetative cells and to avoid the lethality that would be caused by constitutive knockdown or gene deletion.

1. *Construct design and construction*: Use BLAST [15] to align the DNA sequence of the gene of interest against the entire *D. discoideum* genome [16]. Identify the longest contiguous region of the gene that has low homology to other genes in the genome—this region will be used to generate an RNA hairpin (*see* **Note 11**).

2. Clone two copies of the hairpin region in opposite orientations into the doxycycline-inducible expression vector pDM310 (Fig. 3) [17]. Also include a spacer region of 300–500 bp between the two inverted repeats—this spacer does not contribute to knockdown, but allows the inverted repeat to be stable in *E. coli* (Fig. 3) (*see* **Notes 12** and **13**).

3. Transform cells with the hairpin construct and grow up a pool of transformants (*see* **Notes 7** and **14**).

4. *Gene depletion during multicellular development*: Grow cells to 60–80 % confluence and split 1:4 into medium containing 10 μg/mL doxycycline to induce expression of the hairpin (*see* **Note 2**). Prepare a control plate of cells in parallel, lacking doxycycline. Allow cells to grow overnight in the presence of doxycycline (*see* **Note 15**).

5. Develop the cells as directed in Subheading 3.2, adding 10 μg/mL doxycycline to the DB used for all steps. Process the control sample in parallel, taking care not to expose the control cells to doxycycline at any step in the procedure.
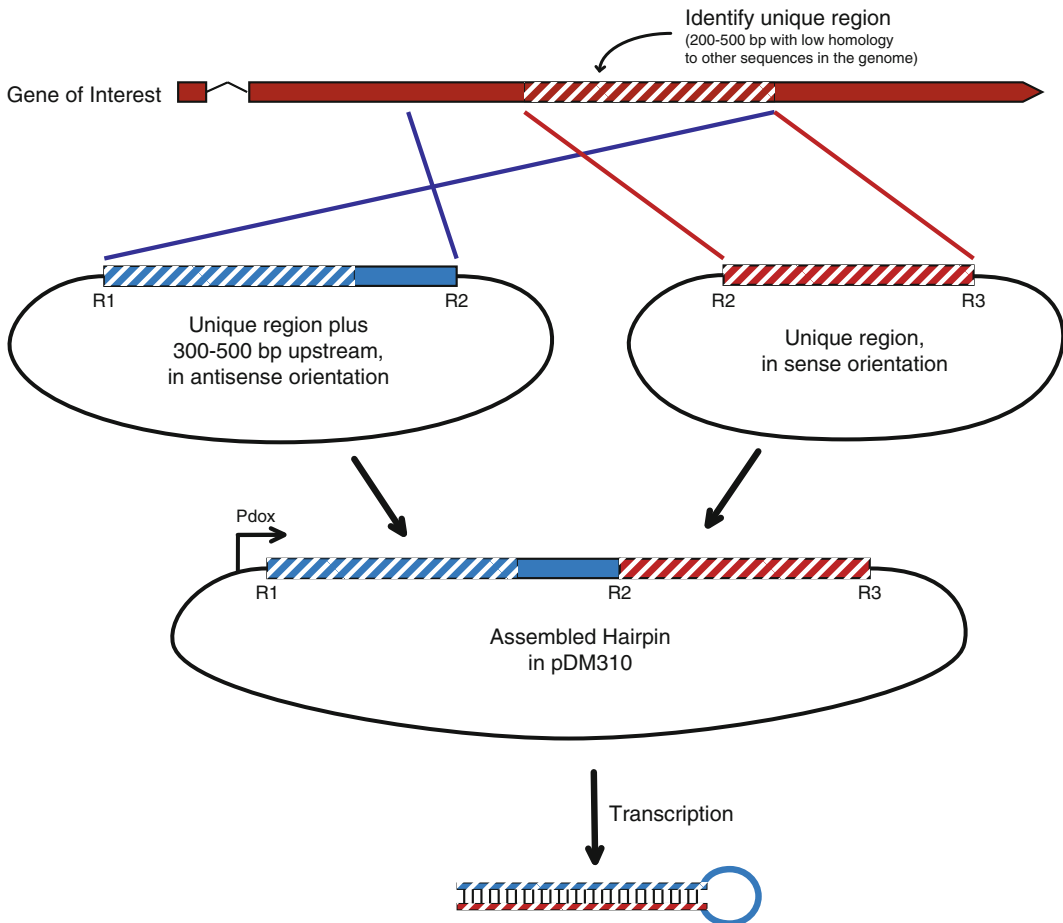
Fig. 3 Construct design for RNA interference in *D. discoideum*. Using BLAST analysis of the gene of interest, a region with low homology to other genomic regions (at least four mismatches in every 20 bp stretch) is selected. This unique region is cloned in the sense orientation into any convenient plasmid, and unique restriction sites (R2 and R3) are introduced. The unique region plus several hundred bp of flanking sequence (*see* **Note 12**) is cloned in an antisense orientation into another vector, flanked by unique restrictions sites (R1 and R2). After sequence verification, the two pieces are combined in pDM310 to produce the final hairpin construct. "Pdox" indicates the doxycycline-inducible promoter

6. Collect samples at different time points and test for depletion of the target protein by western blotting or immunofluorescence. If stronger knockdown is desired, retransform the hairpin construct and select at a higher G418 concentration (*see* **Note 7**) and/or isolate clonal cell populations and identify clones with more efficient knockdown (*see* **Note 14**).

7. Once a cell population with the desired level of knockdown is obtained, it should be frozen as soon as possible for storage. Maintain cells in axenic culture for no more than 3 weeks after isolation (*see* **Note 5**); in our hands, the efficiency of knockdown gradually declines over this window.

3.4 Whole-Mount Immunofluorescence of Culminants

Our primary assay for the study of morphogenesis in *D. discoideum* is immunofluorescence of fixed specimens, which allows both visualization of protein localization (using either a specific antibody or fluorescent protein fusions as described in Subheading 3.1) and examination of the morphology of culminants under various mutant or RNAi conditions. For numerous examples of images produced using this method, please *see* [6, 8].

We note that although high-resolution live imaging of the slug stage of *D. discoideum* development is possible [18], it is unclear whether culmination can occur under the conditions that were used to achieve subcellular resolution. In the future, it will be important to develop methods for high-resolution live imaging of the tip epithelium during culmination.

1. Develop cells as described in Subheading 3.2. If desired, induce dsRNA expression as described in Subheading 3.3. Monitor development with a dissecting microscope.

2. When the desired developmental stage is reached, use forceps to transfer the Nuclepore filter to a 6 cm dish or to one well of a six-well plate. Immediately add ~2 mL of cold (4 °C) fixation solution to the filter (try to do this gently, but as quickly as possible so that the filter doesn't dry out). The best way to add the fixative is to pipet it dropwise directly onto the center of the filter. Some structures will dissociate from the filter, but some should remain attached.

3. Place the sample at 4 °C and incubate for 1 h.

4. Remove the fixative and wash the filter three times for 5–10 min each with ~2 mL PBS. Use forceps to gently push the filter down so that it sinks in the PBS rather than floating on top. Do not rush this washing step—if culminants are not adequately rehydrated, they will not stain well. At this stage, the samples may be stored for up to a few days in PBS containing 0.02 % sodium azide.

5. Aspirate the PBS and transfer the filter to a sheet of parafilm placed in a humidified box. Add 500 µL blocking solution (the culminants should be completely submerged) and incubate for 2–3 h at room temperature.

6. Dilute primary antibodies in antibody solution just before use. The optimal concentration will depend on the antibody, but we typically use ten times the concentration that works for western blotting as a starting point for further optimization.

7. Aspirate the blocking solution and replace with 250 µL of primary antibody solution. Incubate with primary antibodies overnight at 4 °C.

8. Aspirate the primary antibody solution and wash three times for 5 min each with PBST.

9. Dilute secondary antibodies in antibody solution just before use. We use a 1:100 dilution as the starting point for most secondary antibodies. Also add fluorescently labeled phalloidin (use a 1:200 dilution as a starting point). We include phalloidin in all of our experiments, because it serves as a useful counterstain that outlines the cells.

10. Aspirate the PBST and replace with 250 µL of secondary antibody/phalloidin solution. Incubate with secondary antibodies for 2–3 h at room temperature in the dark.

11. Aspirate the secondary antibody/phalloidin solution and wash three times for 5 min each with PBST, then twice for 5 min each with PBS (without Tween).

12. Transfer the filter to a glass slide and aspirate any residual PBS. Place a drop of Vectashield in the center of the filter, then place a coverslip on top (avoid air bubbles). Aspirate the excess mounting medium, then seal the edges of the coverslip with nail polish.

13. Acquire images using a laser scanning confocal microscope. We use a $63\times$, 1.4 *NA* objective for routine imaging at subcellular resolution. Techniques for acquiring high-quality images using a confocal microscope are beyond the scope of this chapter; consult with experts or core facility staff at your institution for help if needed.

4   Notes

1. Add $CaCl_2$ and $MgCl_2$ immediately before use, and do not store DB after divalent cations have been added. Calcium from $CaCl_2$ gradually precipitates as calcium phosphate, which lowers both the calcium and phosphate buffer concentrations in solution and adversely affects reproducibility.

2. Doxycycline stability in aqueous solutions varies widely depending on pH, temperature, and light exposure; however, its half life has been reported to be as short as 24 h under some conditions. Therefore, to ensure reproducible results, we store doxycycline exclusively in powder form and dissolve it in water immediately before use.

3. We use secondary antibodies produced in goat, and so the addition of goat serum to the blocking and antibody solutions helps reduce background. If using secondary antibodies produced in a different species, substitute the appropriate serum.

4. Saponin is ideal for permeabilizing culminants, which are rather fragile and require a gentle detergent. Saponin also works well for aggregation streams. For mounds and slugs, which are denser and thicker, use of a stronger detergent (e.g., Triton X-100) may give better results.

5. When studying multicellular development in *Dictyostelium discoideum*, it is crucial to regularly start new cultures from frozen stocks or spores, in order to ensure a stable phenotype over time. There are two reasons for this: first, since *Dictyostelium* grows as single cells, there is no selective pressure to maintain normal multicellular development when the cells are grown continuously in axenic culture; and second, since *D. discoideum* cells are haploid, any mutations that arise during axenic growth can immediately generate phenotypes once the cells are developed. For these reasons, we maintain cells in axenic culture for no more than 3 weeks after isolation before discarding them and starting new cultures from frozen stocks. Because generating transgenic strains for imaging can take 1–3 weeks, we always start the process with a fresh batch of cells.

6. The choice of selective drug influences the copy number of the transformed plasmid, and hence the expression level of the transgene [12, 19]. We routinely use hygromycin selection to express fluorescent fusion proteins, because it results in moderate plasmid copy number [20]; for example, we have used a hygromycin-resistant vector to express GFP-myosin at near-endogenous levels [8]. G418 selection produces higher copy number [19], and so we typically reserve its use for situations where overexpression is desired (including expression of RNAi constructs). We avoid the use of blasticidin resistance as a selectable marker for fluorescent protein fusions because blasticidin is typically used for gene disruption in *D. discoideum*, and consequently many useful mutant strains are already blasticidin-resistant.

7. Plasmid copy number (and hence transgene expression level) can be influenced to some extent by the concentration of selective drugs used [19]. Since the activity of drugs can vary somewhat between different lots and manufacturers, it is good practice to perform a dose-response study by incubating untransformed cells in the presence of different concentrations of the drug of choice. For fluorescent fusion protein expression, we typically use the minimum drug concentration that is required to kill 100 % of untransformed cells (10 μg/mL G418 or 50–60 μg/mL Hygromycin in our hands). For RNAi, it is useful to generate and test cell lines at several different G418 concentrations, as the degree of knockdown can correlate with drug concentration.

8. There have been anecdotal reports of autofluorescence from *Dictyostelium* cells grown in HL5 medium, which in principle could interfere with FACS sorting. However, autofluorescence has not been a problem in our hands. It is critical to sort cells under fed conditions (i.e., resuspended in medium, not in buffer) because starvation induces rapid cell aggregation that interferes with cell sorting.

9. Because of the low salt concentration and relatively weak buffering conditions, development in DB is somewhat asynchronous (i.e., different aggregates develop at slightly different rates). For microscopy this asynchrony is convenient, as it ensures that a range of stages are present in a single sample. For biochemistry, however, more synchronous development is desirable, especially if one wishes to compare the abundance of a protein, mRNA, or protein complex between different developmental stages. More synchronous development can be achieved by using Sussman's LPS buffer (8 mM Na_2HPO_4, 32 mM KH_2PO_4, 20 mM KCl, pH 6.5, with 2 mM $MgCl_2$ and 2 mM $CaCl_2$ added just before use) in place of DB [21].

10. For biochemistry, use Whatman #50 filter paper in place of a Nuclepore filter. We routinely purchase 42.5 mm diameter filters and cut them into quarters; one quarter holds 5×10^6 cells in 125 μL (the same as a Nuclepore filter). This number of cells is sufficient for performing a western blot.

11. To exclude the possibility of nonspecific gene knockdown, there should be no fewer than four mismatches in any 20-nucleotide window of the chosen region [22]. We have had success with a 170 bp hairpin region, but longer hairpins may increase the likelihood of achieving knockdown.

12. It is often convenient to derive the spacer region from an adjacent portion of the gene of interest, as shown in Fig. 3; however, it may also be derived from unrelated vector sequence.

13. Sequencing and PCR of the assembled hairpin construct are usually impossible, since the hairpin folds rapidly when the DNA is denatured (which prevents primer annealing). Therefore, we recommend cloning and sequencing each half of the hairpin separately, and then subcloning (without PCR) to assemble the full hairpin construct. Alternatively, a gateway cloning strategy could be used, as has been done in other systems [23, 24]. Regardless of the cloning strategy, it is helpful to include unique restriction sites that can be used to identify the correct hairpin construct by restriction mapping.

14. The simplest way to avoid clonal selection artifacts is to work with a pool of transformants. However, this sometimes results in ineffective knockdown, presumably because not enough of the cells express the hairpin construct at high levels. We recommend testing depletion of the protein of interest using a pool of transformants first. If the desired reduction in protein levels is not achieved, isolate single clones by serial dilution into 96-well plates, and test these to identify clones with strong knockdown. If clonal populations are used, at least three independent clones should be assayed to ensure that all show a similar phenotype.

15. For genes whose expression is strongly upregulated during development, induction of hairpin expression for 12–24 h before initiating development increases the efficiency of knockdown (probably because it allows time for the hairpin RNA to accumulate before the gene of interest becomes active). However, for genes that have important functions in both vegetative growth and development, hairpin induction during the growth phase may be toxic. If this is the case, hairpin expression can be induced later, at the onset of development; we have observed target protein depletion under these conditions. We have also attempted to achieve temporal control of gene expression by adding doxycycline after the onset of development, but we were unable to induce expression when doxycycline was added at or after the mound stage (approximately 8 h after the onset of starvation). This is probably because the doxycycline does not diffuse efficiently through multicellular structures.

Acknowledgements

References

1. Keller R (2002) Shaping the vertebrate body plan by polarized embryonic cell movements. Science 298:1950–1954

2. St Johnston D, Sanson B (2011) Epithelial polarity and morphogenesis. Curr Opin Cell Biol 23:540–546

3. Bryant DM, Mostov KE (2008) From cells to organs: building polarized tissue. Nat Rev Mol Cell Biol 9:887–901

4. Kessin RH (2001) *Dictyostelium*. Cambridge University Press, Cambridge

5. Baldauf SL (2003) The deep roots of eukaryotes. Science 300:1703–1706

6. Dickinson DJ, Nelson WJ, Weis WI (2011) A polarized epithelium organized by beta- and alpha-catenin predates cadherin and metazoan origins. Science 331:1336–1339

7. Dickinson DJ, Nelson WJ, Weis WI (2012) An epithelial tissue in Dictyostelium challenges the traditional origin of metazoan multicellularity. Bioessays 34:833–840

8. Dickinson DJ, Robinson DN, Nelson WJ, Weis WI (2012) α-catenin and IQGAP regulate myosin localization to control epithelial tube morphogenesis in Dictyostelium. Dev Cell 23:533–546

9. Bonner JT (1944) A descriptive study of the development of the slime mold Dictyostelium discoideum. Am J Bot 31:175–182

10. Raper KB (1940) Pseudoplasmodium formation and organization in Dictyostelium discoideum. J Elisha Mitchell Sci Soc 56:241–282

11. Fey P, Kowal AS, Gaudet P, Pilcher KE, Chisholm RL (2007) Protocols for growth

and development of Dictyostelium discoideum. Nat Protoc 2:1307–1316

12. Gaudet P, Pilcher KE, Fey P, Chisholm RL (2007) Transformation of Dictyostelium discoideum with plasmid DNA. Nat Protoc 2:1317–1324

13. Veltman DM, Akar G, Bosgraaf L, Haastert PJMV (2009) A new set of small, extrachromosomal expression vectors for Dictyostelium discoideum. Plasmid 61:110–118

14. Kuhlmann M, Popova B, Nellen W (2006) RNA interference and antisense-mediated gene silencing in Dictyostelium. Methods Mol Biol 346:211–226

15. Altschul SF, Madden TL, Schäffer AA, Zhang J, Zhang Z, Miller W, Lipman DJ (1997) Gapped BLAST and PSI-BLAST: a new generation of protein database search programs. Nucleic Acids Res 25:3389–3402

16. Eichinger L, Pachebat JA, Glöckner G, Rajandream M-A, Sucgang R, Berriman M, Song J, Olsen R, Szafranski K, Xu Q, Tunggal B et al (2005) The genome of the social amoeba Dictyostelium discoideum. Nature 435:43–57

17. Veltman DM, Keizer-Gunnink I, Haastert PJMV (2009) An extrachromosomal, inducible expression system for Dictyostelium discoideum. Plasmid 61:119–125

18. Dormann D, Weijer CJ (2006) Visualizing signaling and cell movement during the multicellular

stages of dictyostelium development. Methods Mol Biol 346:297–309

19. Pang KM, Lynes MA, Knecht DA (1999) Variables controlling the expression level of exogenous genes in Dictyostelium. Plasmid 41:187–197

20. Egelhoff TT, Brown SS, Manstein DJ, Spudich JA (1989) Hygromycin resistance as a selectable marker in Dictyostelium discoideum. Mol Cell Biol 9:1965–1968

21. Sussman M (1987) Cultivation and synchronous morphogenesis of Dictyostelium under controlled experimental conditions. Methods Cell Biol 28:9–29

22. Effler JC, Kee Y-S, Berk JM, Tran MN, Iglesias PA, Robinson DN (2006) Mitosis-specific mechanosensing and contractile-protein redistribution control cell shape. Curr Biol 16:1962–1967

23. Johnson NM, Behm CA, Trowell SC (2005) Heritable and inducible gene knockdown in C. elegans using Wormgate and the ORFeome. Gene 359:26–34

24. Wesley SV, Helliwell CA, Smith NA, Wang MB, Rouse DT, Liu Q, Gooding PS, Singh SP, Abbott D, Stoutjesdijk PA, Robinson SP et al (2001) Construct design for efficient, effective and high-throughput gene silencing in plants. Plant J 27:581–590

Chapter 19

Primary Cell Cultures of Regenerating Holothurian Tissues

Samir A. Bello, Ricardo J. Abreu-Irizarry, and José E. García-Arrarás

Abstract

The ability to culture different cell types is essential for answering many questions in developmental and regenerative biology. Studies in marine organisms, in particular echinoderms, have been limited by the lack of well-described cellular culture systems. Here we describe a cell culture system, for normal or regenerating holothurian cells, that allows cell characterization by immunohistochemistry and scanning electron microscopy. These cell cultures can now be used to perform multiple types of experiments in order to explore the cellular, biochemical, and genomic aspects of echinoderm regenerative properties.

Key words Echinoderm, Sea cucumber, Primary cell culture, Regeneration, Gastrointestinal tract, Immunohistochemistry, Scanning electron microscopy

1 Introduction

Echinoderms stand out among the group of animals known for their remarkable regenerative properties. Members from different classes of the Echinodermata can regenerate, both as adults or larvae, a large number of tissues and organs. Well-known examples include the regeneration of spines by sea urchins, arm regeneration by sea stars and brittle stars, and the regeneration of viscera by holothurians. The latter has been exploited in our laboratory using the species *Holothuria glaberrima* as a model system to study not only intestinal regeneration following evisceration but also nervous system regeneration following radial nerve transection [1–4].

Investigators using novel model systems need to develop many of the tools for modern molecular biology analyses, tools that are readily available for most classical model organisms. Echinoderm studies, in particular, are limited by the lack of a well-described technique for culturing cells or tissues from adult organisms. In fact, the culture of primary cells from marine invertebrates has been one of the limiting factors not only to study regeneration in echinoderms but also for the study of different processes in several animal groups. Initial attempts have been done previously where

investigators have been able to grow explants and cells from crinoid arms [5, 6] and different tissues of asteroids [7, 8]. Other investigators, using cells from regenerating tissues of the sea cucumber *Apostichopus japonicus*, established cell cultures where different cell activities could be identified [9]. We have built upon these previous studies and have established a culture system that is amenable for the maintenance of dissociated cells of holothurians. Cells in these cultures can be identified using the same markers applied to in vivo tissues, namely immunohistochemical and morphological analyses.

Tissue cultures provide a unique tool where many cellular events and processes can be characterized. Moreover, these cultures will provide a tool for the development of techniques and methodology such as gene transfections, single cell transcriptomics, and lineages studies, among others, that are hitherto unavailable to study regeneration in adult echinoderms.

2   Materials

Prepare all solutions using ultrapure water and analytical-grade reagents. Diligently follow all waste disposal regulations when disposing waste materials. All cell culture procedures must be carried out under sterile conditions in a laminar flow hood.

2.1   Sea Cucumber Collection and Evisceration

1. Potassium chloride (KCl): 0.35 M solution in distilled water. Add 250 mL of distilled water in a 500 mL beaker. Weight 6.5 g KCl and transfer to the beaker. Mix using a magnetic stirrer and store at room temperature (RT).

2.2   Sea Cucumber Disinfection and Gut Dissection

1. Anesthetic solution: 1,1,1-Trichloro-2-methyl-2-propanol hemihydrate (chlorobutanol, Sigma), 0.2 % in natural sea water (SW). Add 950 mL of filtered SW in a glass beaker. Weigh 2 g chlorobutanol and transfer to the beaker. Stir for about 45 min until solubilized. Make up to 1 L with SW. Store at 4 °C.

2. Sodium hypochlorite: 10 % solution in water.

3. Ethanol: 95 % solution in water.

4. Antibiotic/antifungal solution (*see* **Note 1**): Penicillin/Streptomycin (300 U/mL and 300 μg/mL, respectively), neomycin (150 μg/mL), and amphotericin B (7.5 μg/mL) in filtered SW. Add 1.5 mL of the concentrated penicillin/streptomycin solution (10,000 U penicillin and 10 mg/mL streptomycin), 750 μL of the concentrated neomycin solution (10 mg/mL), and 150 μL of the amphotericin B stock solution (2.5 mg/mL) to 45 mL of SW in a 50 mL tube. Adjust the pH to 7.7. Complete to 50 mL with SW and sterilize by filtration (0.22 μm filters). Store at 4 °C.

2.3 Gut Rudiment Dissociation and Cell Culture

1. Calcium and Magnesium Free Artificial Sea Water Solution (CMFSS) [10]: Weight 0.8 g potassium chloride (KCl), 25.5 g sodium chloride (NaCl), 3.0 g sodium phosphate dibasic (Na_2HPO_4), 3.0 g glucose, and 2.86 g (4-(2-hydroxyethyl)-1-piperazineethanesulfonic acid) HEPES and transfer to a 1 L beaker. Add 950 mL of ultrapure water and mix by magnetic stirring. Adjust the pH to 7.7 and complete to 1 L with ultrapure water. Sterilize by filtration (0.22 μm filters) and store at RT (*see* **Note 2**).

2. Collagenase Type IA (Sigma): 0.125 % in CMFSS [9] supplemented with antibiotics (200 U/mL penicillin, 200 μg/mL streptomycin, 100 μg/mL neomycin) and antifungal (5 μg/mL amphotericin B). Add 45 mL of CMFSS in a 50 mL tube. Add 1 mL of the concentrated penicillin/streptomycin solution (10,000 U penicillin and 10 mg/mL streptomycin), 500 μL of the concentrated neomycin solution (10 mg/mL neomycin), and 100 μL of the amphotericin B stock solution (2.5 mg/mL) in the 50 mL tube. Weight 62.5 mg of collagenase type IA and transfer to the 50 mL tube. Adjust the pH to 7.7. Complete to 50 mL with CMFSS and sterilize by filtration (0.22 μm filters). Aliquot 5 mL of the solution in 15 mL tubes and store at −20 °C until use.

3. L-15 Medium (Leibovitz, Sigma): conditioned for marine species adding salts to the original composition [11, 12]. Weight 6.9 g L-15 powder, 6.25 g NaCl, 3.12 g glucose, 1.58 g magnesium sulfate ($MgSO_4$), 172 mg KCl, 96 mg sodium bicarbonate ($NaHCO_3$), 1.33 g magnesium chloride ($MgCl_2$), 150 mg L-glutamine, 745 mg calcium chloride dihydrate ($CaCl_2 \cdot 2H_2O$) and transfer to a 500 mL beaker. Complete to 500 mL with ultrapure water. Mix by magnetic stirring. Sterilize by filtration (0.22 μm filters). Store at 4 °C in a bottle wrapped in aluminum foil.

4. Cell culture medium: L-15 medium conditioned for marine species supplemented with antibiotics (100 U/mL penicillin, 100 μg/mL streptomycin, 50 μg/mL gentamicin), antifungal (2.5 μg/mL amphotericin B), 1× MEM nonessential amino acids, 1 mM sodium pyruvate, 1.75 mg/mL α-tocopherol acetate, 1 μg/mL hydrocortisone, 1× ITS (Insulin, Transferrin, and sodium Selenite), 2 % Fetal Bovine Serum, 10 % cell-free coelomic fluid (*see* **Note 3**). Add 500 μL of penicillin/streptomycin stock solution (10,000 U penicillin and 10 mg/mL streptomycin), 250 μL of gentamicin stock solution (10 mg/mL), 50 μL of amphotericin B stock solution (2.5 mg/mL), 500 μL of MEM nonessential amino acid stock solution (100×), 500 μL of sodium pyruvate stock solution (100 mM), 50 μL of α-tocopherol-acetate stock solution (17.5 mg/mL), 100 μL of hydrocortisone stock solution

(500 μg/mL), 500 μL of the ITS (Insulin, Transferrin, and sodium Selenite) stock solution (100×), 1 mL of fetal bovine serum (FBS, Sigma), and 5 mL of sea cucumber cell-free coelomic fluid in a 50 mL tube. Transfer L-15 medium conditioned for marine species to the 50 mL tube to complete 45 mL. Mix gently by inversion of the tube. Adjust the pH to 7.7–7.8 using sodium hydroxide (NaOH) 1 N. Complete to 50 mL adding L-15 medium. Sterilize by filtration (0.22 μm filters). Store at 4 °C in a bottle wrapped in aluminum foil (*see* **Note 4**).

5. Sea cucumber cell-free coelomic fluid: The method that we apply to obtain the cell-free coelomic fluid was described by Zhao et al. [13] with some modifications. Briefly, we wash the animals in clean SW to remove particles attached to the animal skin. Then, a person holds the animal on a sterile dissecting pan while another person cut its oral side (where the tentacles are present) using a sterile razor blade. The animal is raised and squeezed so that the coelomic fluid squirts into a sterile beaker which is on ice. Transfer the coelomic fluid to 50 mL tubes and centrifuge at 2,000 × g × 10 min at 4 °C to remove the cells. Transfer the supernatant to clean tubes. Sterilize by filtration (0.22 μm filter). Aliquot the supernatant in 5 mL aliquots and store at −20 °C. A new aliquot of coelomic fluid must be used every time culture medium is prepared (*see* **Note 5**).

6. Trypan blue dye (Sigma): 0.4 % solution in CMFSS. Sterilize by filtration (0.22 μm membranes). Store at RT.

2.4 Cell Identification by Indirect Immuno-histochemistry

1. Lab-Tek™ II Chamber Slide System, 8 wells per slide (0.7 cm²/well) (Thermo Fisher Scientific). Each pack of glass slides includes a slide separator system to remove the polystyrene chamber.

2. Poly-L-lysine (Sigma): 0.01 % solution in water.

3. Paraformaldehyde (PFA, Sigma): 4 % in filtered SW (*see* **Note 6**).

4. Blocking solution: Normal goat serum (Sigma) diluted 1:50 in PBS containing 0.01 % sodium azide (NaN$_3$).

5. Triton X-100 (Sigma): 0.1 % solution in PBS.

6. Phosphate Buffered Saline (PBS): 0.1 M. Weight 8 g NaCl and 13.4 g sodium phosphate dibasic heptahydrate (NaH$_2$PO$_4$·7 H$_2$O) and transfer to a 1 L beaker. Add 800 mL to the beaker and mix using a magnetic stirrer. Adjust the pH to 7.4. Complete to 1 L with ultrapure water.

7. RIA buffer: Weight 7.06 g potassium phosphate dibasic (K$_2$HPO$_4$), 1.29 g potassium phosphate monobasic (KH$_2$PO$_4$), 9 g NaCl, 5 g bovine serum albumin (BSA), 0.1 g sodium azide (NaN$_3$) and transfer to a 1 L beaker. Add 800 mL to the beaker

and mix using a magnetic stirrer. Adjust the pH to 7.4. Complete to 1 L with ultrapure water. Aliquot in bottles wrapped in aluminum foil and store at −20 °C.

8. Monoclonal antibody Meso 1 [14]: diluted 1:20 in RIA buffer. This antibody was developed in mouse in our laboratory and specifically labels the mesothelial cells from the mesentery and the gut rudiment of holothurians.

9. Monoclonal anti-β tubulin antibody (Sigma, clone 2-28-33): diluted 1: 500 in RIA buffer. This antibody was prepared from sea urchin sperm axonemes. It labels neuron-like cells and nerve bundles in the mesothelium and connective tissue of normal and regenerating mesenteries in *H. glaberrima* [15]. Aliquot 10 μL of the anti-β tubulin antibody in microtubes. Store at −20 °C. Immediately before use add 990 μL of the RIA buffer to a microtube to obtain a stock solution (1:100). Transfer 100 μL of the stock solution (1:100) to a new tube and add 400 μL of the RIA buffer to obtain a working solution of 1:500 in RIA buffer.

10. Secondary antibody: Goat anti-mouse conjugated with the fluorophore Cy3 (GAM-Cy3, Jackson Immuno Research Laboratories) diluted 1:1,000 in RIA buffer. Aliquot 10 μL of the GAM-Cy3 solution in microtubes. Store at −20 °C. Immediately before use, add 990 μL of the RIA buffer to a microtube to obtain a stock solution (1:100). Transfer 100 μL of the stock solution (1:100) to a new tube and add 900 μL of the RIA buffer to obtain a working solution of 1:1,000 in RIA buffer.

11. Phalloidin-Fluorescein Isothiocyanate (FITC) labeled (Sigma): diluted 1:1,000 solution in RIA buffer. Prepare the stock solution (1:100) and the working solution (1:1,000) as indicated for the GAM-Cy3 antibody.

12. Mounting media: buffered glycerol solution containing 2 μg/mL 4′,6-diamidino-2-phenylindole (DAPI) (Sigma). To make a 5 mg/mL DAPI stock solution (14.3 mM), dissolve the contents of one vial (10 mg) in 2 mL of ultrapure water. Then prepare a 1 mg/mL DAPI working solution adding 200 μL of stock solution to 800 μL of ultrapure water. To prepare the mounting media add 100 μL of the DAPI working solution (1 mg/mL) to 24.9 mL of 0.1 M PBS in a 50 mL tube. Finally add 25 mL of glycerol to the same 50 mL tube and mix. Wrap in aluminum foil and store at 4 °C.

2.5 Cell Identification by Scanning Electron Microscopy

1. Round German glass coverslips (Electron Microscopy Sciences): 8 mm in diameter, 0.16–0.19 mm in thickness.

2. 24-well Cell Culture Plate (BD Falcon): tissue culture-treated polystyrene, flat-bottom with lid.

3. Glutaraldehyde (Sigma) (*see* **Notes 6** and **7**): 2 % solution in 85 % natural SW. Mix 85 mL of natural SW with 15 mL of distilled water to obtain 100 mL of 85 % natural SW. To prepare 100 mL of the 2 % glutaraldehyde solution, mix 96 mL of 85 % natural SW with 4 mL of 50 % glutaraldehyde. The final osmolality is 1.1 Osm.

4. Osmium Tetroxide (OsO_4, Electron Microscopy Sciences): 1 % in natural SW with the contribution of glucose. Add 0.37 g of glucose to 6 mL of natural SW. To produce 8 mL of 1 % OsO_4 mix the 6 mL of natural SW containing glucose with 2 mL of 4 % OsO_4 (*see* **Notes 6** and **7**).

5. Ethanol (Sigma): 25, 40, 50, 60, 70, 80, 90, 100 % solutions in distilled water.

6. Hexamethyldisilazane (HMDS, Electron Microscopy Sciences): diluted in ethanol at 25 %, 50 %, 75 %, and pure (100 %).

7. Carbon adhesive tabs (Electron Microscopy Sciences): 12 mm in diameter.

8. Aluminum mounts (Electron Microscopy Sciences): stubs of 12.2 mm in diameter.

3   Methods

3.1   Sea Cucumber Collection and Evisceration

1. Collect sea cucumbers of the species *Holothuria glaberrima* (*see* **Note 8**) and maintain them in the laboratory in sea water aquaria with constant oxygenation.

2. Eviscerate the sea cucumbers by injecting 0.35 M KCl (3–5 mL) into the coelomic cavity. During evisceration sea cucumbers expel most of their viscera (gut, hemal vessels, gonads, and part of the respiratory trees) through the cloaca in approximately 5 min. After evisceration, return the animals to the aquaria and allow them to regenerate for 5 days.

3.2   Sea Cucumber Disinfection and Gut Dissection

1. Immerse ten of the sea cucumbers which have regenerated their gastrointestinal tract for 5 days in 500 mL beakers containing 250 mL of anesthetic solution (prewarmed to RT) for 45 min at RT.

2. Decontaminate the sea cucumber surface immersing the animals one at a time in a 10 % sodium hypochlorite solution for 1 min, 95 % ethanol for 5 min, and a quick rinse in sterile ultrapure water.

3. Put the animals, ventral side up, on an autoclaved vinyl pad in a dissecting pan. The ventral side can be identified by the presence of the ambulacral feet. Cut with scissors along the

longitudinal line that separates the dorsal and ventral axis. In *Holothuria glaberrima* this line rests at the boundary between the ventral side and the side without ambulacral feet (dorsal). To decrease the risk of contamination, make the cut from about 1 cm from the mouth (surrounded by a crown of tentacles) to approximately 1 cm from the cloaca. Once the body wall is opened, hold down the sea cucumber using push-pins. Dissect the gut rudiments under the stereoscopic microscope using fine tweezers and spring scissors. The gut rudiment may be recognized at day 5 of regeneration because in *H. glaberrima* it appears as a pink thickening at the free end of the mesenterium.

4. Collect the gut rudiments of ten sea cucumbers in 10 mL of the antibiotic/antifungal solution in a 15 mL tube and keep on ice.

5. Wash the gut rudiments with fresh antibiotic/antifungal solution twice for 30 min at 4 °C.

3.3 Gut Rudiment Dissociation and Cell Culture

1. Cut the gut rudiments into small pieces of approximately 1 mm^3 on a sterile glass petri dish using a scalpel with #12 blades in the laminar flow hood. Transfer the pieces to 5 mL of 0.125 % collagenase in a 15 mL tube using a sterile dissecting needle.

2. Incubate the pieces in a water bath with constant agitation (15 rpm) (*see* **Note 9**) for approximately 2 h at 28 °C. Check for the presence of remaining tissue pieces after 1 h of incubation, the length of the dissociation will depend on the amount of tissue.

3. Centrifuge the cell suspension at low speed ($300 \times g$, 4 °C) for 1 min to form a pellet with the tissue that remains nondissociated. Transfer the supernatant containing the cell suspension to a new 15 mL tube and discard the pellet (nondissociated tissue pieces).

4. Pass the cell suspension through a sterile cell strainer (mesh size 70 μm) placed on a 50 mL tube to remove large cell aggregates.

5. Centrifuge the cell suspension at $900 \times g$ for 10 min at 4 °C, discard the supernatant containing the collagenase solution. Resuspend the cells in 5 mL of CMFSS supplemented with antibiotics and centrifuge again ($900 \times g$, 10 min, 4 °C) to wash the cells and to eliminate the cell debris.

6. Resuspend the cells in 1 mL of CMFSS (*see* **Note 10**). Perform trypan blue exclusion test to estimate the number of cells in suspension and their viability. Transfer 20 μL of the cell suspension to a microcentrifuge tube and add 20 μL trypan blue dye (0.4 % in CMFSS) (*see* **Note 11**). Mix and load
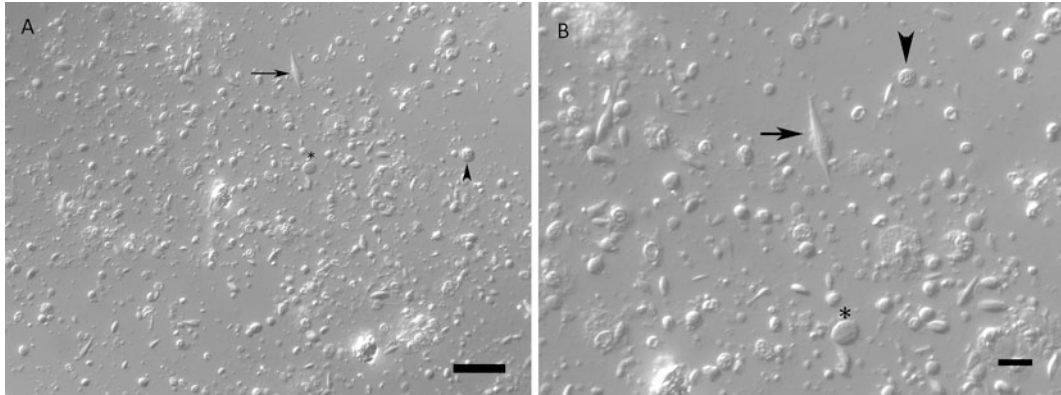
Fig. 1 Cells from regenerating gut rudiments (5 days post-evisceration) of the sea cucumber *Holothuria glaberrima* after 5 days in culture observed by phase contrast microscopy. Various cell sizes and morphologies can be observed, among them are *spherical* (*arrowhead*), *oval*-(*asterisk*), and *spindle*-shaped structures (*arrow*). Scale: (**a**) = 30 μm, and (**b**) = 10 μm

approximately 10 μL of the cell suspension by capillary action in each side of a hemocytometer and count the cells under an inverted microscope. Dead cells will stain blue.

7. Count the number of live and dead cells in each of the four corner squares of the hemocytometer. To estimate the cell concentration in a milliliter of CMFSS follow the formula: (total live cells/4) $\times$ Dilution Factor (DF) $\times$ 10^4. As an example, if you counted on average 80 cells in the four squares of the hemocytometer and used the DF mentioned in 6, then the formula will be: $80 \times 2 \times 10^4 = 1.6 \times 10^6$ cells/mL of CMFSS. The cell viability is determined by: (total live cells)/(total live cells + total dead cells). Following the dissociation protocol mentioned previously, the cell viability should be >80 %.

8. Seed the cells on 8-well glass slides treated with poly-L-lysine (*see* **Note 12**) at a cell density of 6×10^4 cells/cm^2, diluting the cell suspension in the supplemented cell culture medium. Add 300 μL of culture medium per well.

9. Incubate the cells in a modular incubator chamber (Billups-Rothenberg Inc) at RT. Change the culture medium every 3–5 days to reduce the risk of contamination (*see* **Note 4**). Check your cultures daily under an inverted microscope to check the cell morphology and possible contamination. Figure 1 shows an example of a 5 day cell culture observed by phase contrast microscopy.

3.4 Cell Identification by Indirect Immuno- histochemistry

1. After culturing cells on glass slides for the previously determined length of time, discard the culture medium and wash carefully the cultures with 300 µL of filter sterilized SW (*see* **Note 13**) per well. Add 300–500 µL of 4 % paraformaldehyde solution for 24 h (*see* **Note 14**) at 4 °C to fix the cells. After fixation rinse the cultures twice with filtered SW for 5 min each. At this point you can store the cultures in SW with 0.01 % sodium azide (NaN_3) at 4 °C.

2. Add 300 µL of normal goat serum (diluted 1:50) in each well and incubate for 1 h at RT to block the nonspecific binding of the primary antibodies.

3. Discard the normal goat serum. Add 300 µL of 0.1 % triton X-100 in 0.1 M of Phosphate Buffered Saline (PBS) for 10 min at RT to each well (*see* **Note 15**). Wash twice carefully with 0.1 M PBS for 10 min each.

4. Incubate the cells overnight (ON) at 4 °C with the primary antibody(ies) at the appropriate dilution in RIA buffer (*see* **Note 16**). The primary antibody may be monoclonal (generally raised in mice) or polyclonal (generally raised in rabbits) or a mix of both. As an example, we have used the monoclonal antibody Meso-1 [14] or the monoclonal antibody β-tubulin. For the 8-well glass slides with a surface area of 0.7 cm^2/well, we use at least 100 µL of the primary antibody solution per well. Keep in mind that this solution must completely cover the cells.

5. After incubation with the primary antibody, wash cultures thrice carefully with 0.1 M PBS for 10 min each.

6. Incubate the cultures with the secondary antibody, conjugated with a fluorophore, and diluted in RIA buffer for 1 h at RT in the dark. In this case, we have used the goat anti-mouse antibody conjugated with the fluorophore Cy3 (GAM-Cy3) diluted 1:1,000 in RIA buffer. To label SLSs (*see* **Note 17**) incubate the samples with phalloidin-FITC. The samples can be simultaneously labeled with GAM-Cy3 and phalloidin-FITC. Transfer 100 µL of the GAM-Cy3 and 100 µL of the phalloidin-FITC stock solutions (1:100) in a microtube and add 800 µL to obtain a working solution (diluted 1:1,000) of secondary antibody and phalloidin. Use at least 100 µL of the working solution per well.

7. After incubation with the secondary antibody and phalloidin-FITC, wash cultures thrice carefully with 0.1 M PBS for 10 min each.

8. Carefully remove the polystyrene medium chamber using the slide separator included in each pack of the glass slides. Mount each slide adding mounting media and a 24 × 55 mm coverglass (VWR), sealing the borders with nail polish and drying under a blower. The DAPI is used to stain the cell nuclei.
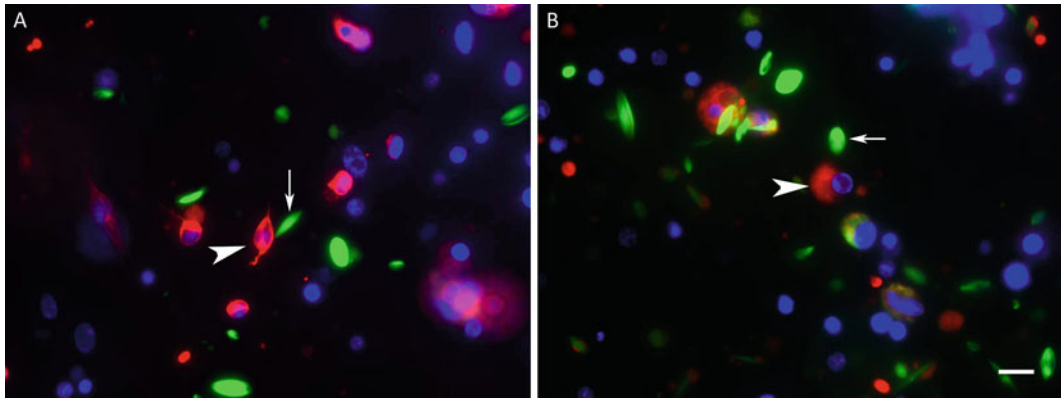
Fig. 2 Anti-β-tubulin and Meso-1 immunoreactivity of primary cell cultures from regenerating gut rudiments (5 days post-evisceration) of the sea cucumber *Holothuria glaberrima* after 5 days in culture. (**a**) Anti-β-tubulin labels (*red*) *spherical* and *oval*-shaped cells some of which exhibit cell projections (*arrowhead*). (**b**) Meso-1 labels (*red*) *spherical* cells (*arrowhead*). Phalloidin labels (*green*) *spindle*-like structures (*arrow*) that lack nuclei in (**a**) and (**b**). Cell nuclei are labeled with DAPI (*blue*). Scale = 10 μm

9. Examine the slides using a microscope equipped with the appropriate filters (*see* **Note 18**).

   Figure 2 shows a 5 day primary cell culture from a regenerating gut of *H. glaberrima* displaying cells immunoreactive for β-tubulin (Fig. 2a) and Meso-1 (Fig. 2b).

3.5 Cell Identification by Scanning Electron Microscopy (See Note 7)

1. Proceed to gut rudiment dissociation as indicated in Subheading 3.2 from **steps 1**–**7**. Then seed the cells on round glass coverslips treated with poly-L-lysine (*see* **Note 12**) at a cell density of 1×10^5 cells/cm^2. The 8 mm round coverslips fit inside the 24 well plates. Dilute the cell suspension in the supplemented cell culture medium. Add 500 μL of culture medium per well (*see* **Note 19**) and incubate the cells as in 3.3.9.

2. After culturing cells on glass slides for the previously determined length of time, discard the culture medium and wash carefully the cultures with 500 μL of filtered SW (*see* **Note 13**) per well. Add 300–500 μL of 2 % glutaraldehyde in filtered SW. Incubate for 2 h at 4 °C. Discard the glutaraldehyde and incubate in 500 μL of filtered SW ON at 4 °C.

3. Post-fix the cells adding 300–500 μL of 1 % osmium tetroxide (OsO_4) in SW (*see* **Note 13**) for 2 h at RT. Wash specimens in sterile distilled water with two rapid washes.

4. Dehydrate the cultured cells in graded ethanol (25, 40, 50, 60, and 70 %) for 10 min each; (80, 90 %) twice for 10 min each, and 100 % ethanol thrice for 10 min each.

5. Chemically dry the samples using Hexamethyldisilazane (HMDS, Electron Microscopy Sciences) (*see* **Note 20**)
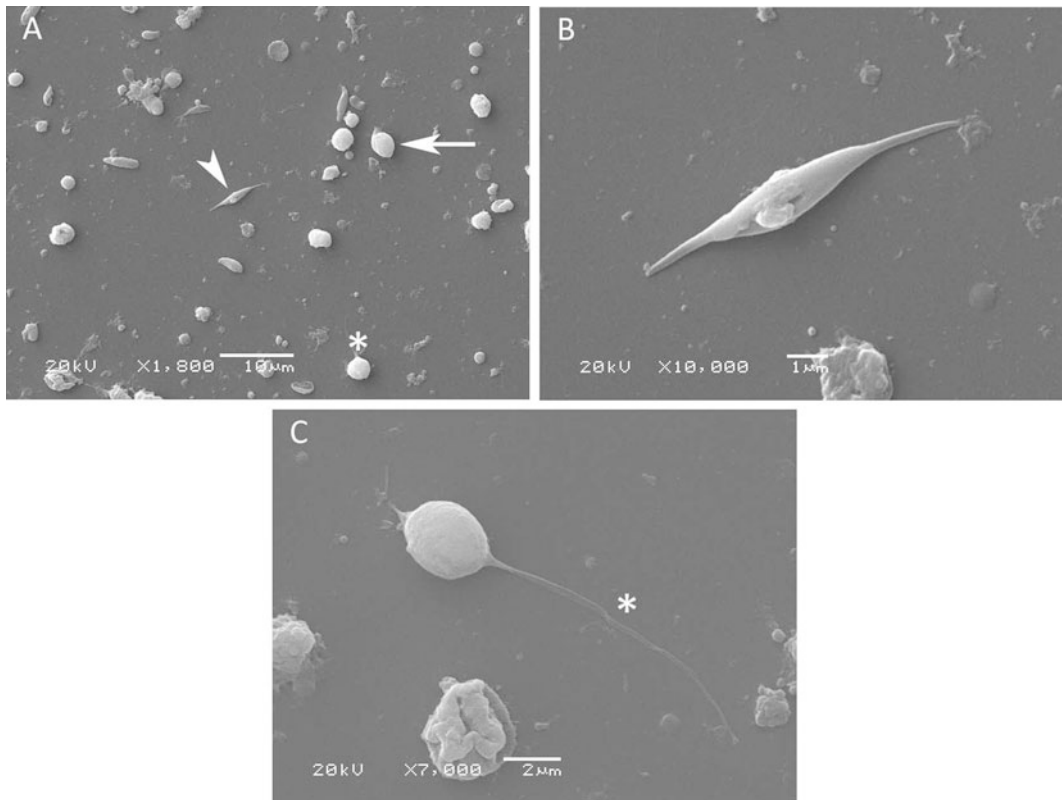
Fig. 3 Cell morphology of cultured cells from regenerating gut rudiments (5 days post-evisceration) of the sea cucumber *Holothuria glaberrima* after 5 days in culture shown by Scanning Electron Microscopy. *Spherical* (*asterisk*), *ovoid*-shaped (*arrow*), and *spindle*-shaped (*arrowhead*) structures are observed in (**a**). Higher magnification of *spindle*-like structures (**b**) and an *ovoid*-shaped cell with a cell projection (*asterisk*) (**c**) are shown. Scale: (**a**) = 10 μm, (**b**) = 1 μm, and (**c**) = 2 μm

incubating successively with 25, 50, and 75 % HMDS in 100 % ethanol for 10 min each. Finally, wash thrice the samples with 100 % HMDS for 10 min each. Let the third wash in HMDS to evaporate ON in a clean protected place at RT.

6. Put a carbon adhesive tab on each stub (Electron Microscopy Sciences, 12.2 mm in diameter) with fine tweezers and proceed to mount the sample. This is done carefully picking the glass coverslips from the 24 well plates with fine tweezers one at a time and placing them on the adhesive tab with the poly-L-lysine (cell) side facing up. If you are not sure, check the coverslips under the stereoscopic microscope.

7. Coat the samples with a layer of 25 nm of gold and then examine them with a scanning electron microscope (JEOL JSM 6480 LV) using variable magnifications.

Figure 3 shows a 5 day primary cell culture from a regenerating gut of *H. glaberrima* displaying cells with different morphologies by Scanning Electron Microscopy.

4   Notes

1. The antibiotic/antifungal solution concentration is three times higher compared to that in cell culture medium and is used to disinfect the dissected tissues. Diluted antibiotic and antifungal solutions are heat labile, thus, it is recommended to store the SW supplemented with antibiotics/antifungal at 4 °C until use.

2. There are different formulations to prepare calcium and magnesium free artificial sea water. The formulation presented here is the one reported by Van der Merwe et al. [10].

3. Cell-free coelomic fluid is used as a growth factor source in our cell culture protocol.

4. Antibiotics and antifungal lose their activity in culture medium in approximately 3–5 days. Additionally, supplements such as L-glutamine also lose their activity in a few days in culture. Thus, it is recommended to add the supplements to the L-15 medium the same day or the day before the cells are cultured, and to change the culture medium every 3–5 days. The L-15 supplemented medium can be stored up to 2 weeks at 4 °C. Some of the supplements used to enrich our culture medium are used as reported by Odintsova et al. [9].

5. We obtain the coelomic fluid from sea cucumbers from the species *Holothuria mexicana*, that, due to their size contain a higher volume of coelomic fluid per animal when compared to *Holothuria glaberrima*.

6. Prepare and manipulate the paraformaldehyde, glutaraldehyde, and osmium tetroxide (OsO$_4$) solutions carefully under the fume or chemical hood since these solutions and their vapors are highly hazardous by inhalation or skin contact. Use personal protective equipment: chemical goggles, disposable nitrile gloves, disposable laboratory coat, and closed-toed shoes. Before manipulation of these solutions read the corresponding Material Safety Data Sheet. The used paraformaldehyde, glutaraldehyde, and osmium tetroxide solutions should be disposed as hazardous waste.

7. The recipe to prepare the glutaraldehyde and the osmium tetroxide solutions, as well as the protocol to fix and dehydrate the cell monolayers for scanning electron microscopy was kindly provided by Dr. Cristiano Di Benedetto from the University of Milan, Bioscience Department (personal communication).

8. We work with the species *Holothuria glaberrima* because of their high availability in nearby coastal areas, however, the procedure described here could be used with other species of holothurians, such as *Holothuria mexicana*.

9. Prewarming the collagenase solution for approximately 5 min at 28 °C in the water bath previous to tissue incubation, as well as the agitation during incubation, accelerate the dissociation of the tissue.

10. We have observed that cells from regenerating tissues tend to clump more when compared to cells from nonregenerating sources. Thus, it may be necessary to pass again the cell suspension at this time through a cell strainer (mesh size 70 μm) to eliminate the cell aggregates so as to be able to quantify the cells.

11. You must dilute the trypan blue in CMFSS to obtain the same osmolality as the medium in which the cells are resuspended, otherwise the cells will lyse. We have tried resuspending cells in culture medium but this increases the cell clumping.

12. Poly-L-lysine coated glass slides and coverslips are prepared by incubating each well of the 8-well glass slides with 200 μL and each coverslip in 24-wells plates with 500 μL of 0.01 % poly-L-lysine solution ON; then the excess solution is removed and the wells are washed in sterile ultrapure water. The slides and coverslips are dried and sterilized exposing them to UV light ON in a laminar flow hood. These can be stored dry for up to a year at RT if protected from dust.

13. We use filtered natural sea water but artificial sea water can also be used to wash the cells.

14. Initially, we fixed the cells in 4 % PFA for only 10 min at 4 °C, but after completing the immunohistochemistry protocol we observed that most cells had detached from the well surface. Thus, we increased the length of the fixation to 24 h, which increased the number of attached cells remaining after the immunohistochemistry protocol.

15. Triton X-100 is used to permeate the cell membrane to facilitate the entrance of the primary antibody into the cells. If the antigen is on the external side of the membrane it might not be necessary to incubate the cells with Triton X-100.

16. We centrifuge (13,000 × g for 2 min) the primary antibody solutions prior to their addition to cells to eliminate any particulate present from the solution. Most of the antibodies used in our lab are produced by our group and correspond to ascites or hybridoma supernatants which contain suspended particles. These particles may increase the background in your samples if they are not eliminated at this point.

17. A cellular process involved in gut regeneration in holothurians is cell dedifferentiation [14]. Specifically, when muscle cells dedifferentiate they condense their contractile apparatus into vesicles termed spindle-like structures (SLSs). These structures

may be visualized labeling the SLSs which contain actin with the phalloidin conjugated with the fluorophore FITC or Rhodamine. Phalloidin is a fungal toxin that is well-known to bind to actin filaments.

18. In our laboratory, cell cultures are examined and photographed using a Nikon Eclipse E600 fluorescent microscope equipped with FITC, R/DII and DAPI filters, and a Spot RT3 digital camera (Diagnostic Instruments, Inc.). Images were recorded using the Spot Basic software (version 4.7; Diagnostic Instruments, Sterling Heights, MI), and Image J (version 1.37; NIH, Bethesda, MD).

19. The 8 mm glass coverslips float in small volumes of poly-L-lysine or cell culture medium. We have observed that 500 µL is a suitable volume to maintain the coverslips on the bottom of the 24-well plates.

20. An alternative method to dry the cells is the critical point drying which requires a specialized device (Critical Point Dryer), liquid carbon dioxide (CO_2), and amyl acetate. In our lab, the chemical-drying works well with the holothurian cells.

Acknowledgements

References

1. García-Arrarás JE, Estrada-Rodgers L, Santiago R et al (1998) Cellular mechanisms of intestine regeneration in the sea cucumber, *Holothuria glaberrima Selenka* (Holothuroidea: Echinodermata). J Exp Zool 281:288–304

2. Garcia-Arraras JE, Greenberg MJ (2001) Visceral regeneration in holothurians. Microsc Res Tech 55:438–451

3. San Miguel-Ruiz JE, Maldonado-Soto AR, García-Arrarás JE (2009) Regeneration of the radial nerve cord in the sea cucumber *Holothuria glaberrima*. BMC Dev Biol 9:3

4. Mashanov V, García-Arrarás JE (2011) Gut regeneration in holothurians: a snapshot of recent developments. Biol Bull 221:93–109

5. Candia Carnevali MD, Bonasoro F, Patruno M, Thorndyke MC (1998) Cellular and molecular mechanisms of arm regeneration in crinoid echinoderms: the potential of arm explants. Dev Genes Evol 208:421–430

6. Di Benedetto C (2011) Progenitor cells and regenerative potential in echinoderms. An in vivo and in vitro approach. Lambert Academic Publishing, Saarbrucken

7. Sharlaimova NS, Pinaev GP, Petukhova OA (2010) Comparative analysis of behavior and proliferative activity in culture of cells of coelomic fluid and of cells of various tissues of the sea star *Asterias rubens L.* isolated from normal and injured animals. Cell Tissue Biol 4:280–288

8. Sharlaimova NS, Petukhova OA (2012) Characteristics of populations of the coelomic fluid and coelomic epithelium cells from the starfish *Asterias rubens L.* able attach to and spread on various substrates. Cell Tissue Biol 6:176–188

9. Odintsova NA, Dolmatov IY, Mashanov VS (2005) Regenerating holothurian tissues as a source of cells for long-term cell cultures. Mar Biol 146:915–921

10. Van der Merwe M, Auzoux-Bordenave S, Niesler C, Roodt-Wilding R (2010) Investigating the establishment of primary cell culture from different abalone (Haliotis midae) tissues. Cytotechnology 62:265–277

11. Schacher S, Proshansky E (1983) Neurite regeneration by Aplysia neurons in dissociated cell culture: modulation by Aplysia hemolymph and the presence of the initial axonal segment. J Neurosci 3:2403–2413

12. Sahly I, Erez H, Khoutorsky A et al (2003) Effective expression of the green fluorescent fusion proteins in cultured Aplysia neurons. J Neurosci Methods 126:111–117

13. Zhao Y, Wang DO, Martin KC (2009) Preparation of Aplysia sensory-motor neuronal cell cultures. J Vis Exp 28:1355

14. Garcia-Arraras JE, Valentin-Tirado G, Flores JE et al (2011) Cell dedifferentiation and epithelial to mesenchymal transitions during intestinal regeneration in *H. glaberrima*. BMC Dev Biol 11:61–77

15. Tossas-Robles KE (2012) Temporal study of the regeneration of the enteric nervous system of the sea cucumber *Holothuria glaberrima*. In: Regeneration of the enteric nervous system of the sea cucumber *Holothuria glaberrima* using tubulin and others neuronal markers. Doctoral Thesis, University of Puerto Rico, Rio Piedras Campus, p 119

Part V

Computational Models of Tissue Morphogenesis

Large-Scale Parameter Studies of Cell-Based Models of Tissue Morphogenesis Using *CompuCell3D* or *VirtualLeaf*

Margriet M. Palm and Roeland M.H. Merks

Abstract

Computational, cell-based models, such as the cellular Potts model (CPM), have become a widely used tool to study tissue formation. Most cell-based models mimic the physical properties of cells and their dynamic behavior, and generate images of the tissue that the cells form due to their collective behavior. Due to these intuitive parameters and output, cell-based models are often evaluated visually and the parameters are fine-tuned by hand. To get better insight into how in a cell-based model the microscopic scale (e.g., cell behavior, secreted molecular signals, and cell-ECM interactions) determines the macroscopic scale, we need to generate morphospaces and perform parameter sweeps, involving large numbers of individual simulations. This chapter describes a protocol and presents a set of scripts for automatically setting up, running, and evaluating large-scale parameter sweeps of cell-based models. We demonstrate the use of the protocol using a recent cellular Potts model of blood vessel formation model implemented in *CompuCell3D*. We show the versatility of the protocol by adapting it to an alternative cell-based modeling framework, *VirtualLeaf*.

Key words Cellular Potts model, *CompuCell3D*, *VirtualLeaf*, Angiogenesis, Cell-based model, Parameter study, Quantification

1 Introduction

To study the mechanisms of tissue morphogenesis, it is often useful to see a tissue as a swarm of interacting cells that follow a set of stereotypic or stochastic rules, which would be determined ultimately by their genome. The decisions of the cells are then guided by present and past interactions with adjacent cells and the micro-environment. In this view, tissue morphogenesis is a problem of collective cell behavior, in which tissues emerge, sometimes via non-intuitive mechanisms, from stereotypic or stochastic rules that the individual cells follow.

A useful computational tool for studying collective cell behavior is *cell-based modeling* [1, 2]. The inputs to a cell-based model are the behavioral rules that cells follow. The output of a cell-based

model is the tissue morphogenesis that follows indirectly from the collective behavior of the individual cells. Cell-based models have been applied to a wide range of problems in developmental biology, including somitogenesis [3], tumor development [4–7], liver regeneration [8], plant development [9, 10], epithelial branching [11], cystogenesis [12], and angiogenesis and vasculogenesis [13–18]. In many cell-based models cell behavior is described at a phenomenological level, based on experimental observations. More recent approaches have introduced detailed models of genetic networks guiding cell behavior; *see*, e.g., refs. 3, 19. These studies demonstrate the utility of cell-based modeling for elucidating the mechanisms of development.

Because most cell-based simulations cannot be solved analytically, insight into their behavior must be obtained using computer simulation. Individual simulations with visual output can give some initial intuition about the behavior and parameter sensitivity of the model. To obtain a more systematic overview of the range of behaviors the model can exhibit, and its sensitivity to parameters, it becomes necessary to rerun the simulation many times for different parameters, and, in case of stochastic models, to obtain statistical measures of the model results by rerunning many random instantiations of the model. If values for the model parameters cannot be determined experimentally, we must test the model for a range of experimentally plausible parameter values [14, 20]. And where parameter values are partly known, systematic parameter studies help predict the response of the system to pharmaceutical treatments [17, 18] or evaluate the behavior of a tissue. Thus, systematic parameter studies are a central tool for analyzing cell-based modeling.

As cell-based models become more complex and take longer to run, performing such parameter studies can become a challenging problem both in terms of computational power and in terms of data management. Here, we describe a protocol and release a set of Python scripts to automatically set up, run, and analyze large parameter sweeps of cell-based models on desktop machines, computational clusters, or in the cloud. Although the protocol and parts of the scripts can be used with any kind of simulation tool that can be started from the command line, we illustrate the protocol in detail with a simulation of vasculogenesis (blood vessel formation; [13, 21]), developed using the cell-based simulation package *CompuCell3D* [22]. *CompuCell3D* is an implementation of the cellular Potts model (CPM) [23, 24], a widely used cell-based simulation method. The CPM is a lattice-based technique that simulates the stochastic, amoeboid motility of biological cells in response to local cues from adjacent cells and diffusive signals, in this way making predictions on collective cell behavior. To illustrate that the parameter sweep can be applied to any kind of simulation tool with a command-line interface, we also show how to adapt the

Python scripts to set up, run, and analyze a parameter sweep for *VirtualLeaf* [9], which is an alternative cell-based modeling technique.

2 Materials

The following materials and prior knowledge are required for using and extending the code provided in this protocol.

2.1 Python

To use *CompuCell3D*, and to run the *CompuCell3D* extensions and parameter sweep scripts presented in this chapter, you will use the programming language Python.

1. Download and install the latest version of the Python 2.x branch (*see* **Note 1**) from http://www.Python.org/download/. Alternatively, Linux users can install Python using their package manager.

2. Familiarize yourself with Python (*see* **Note 2**). We recommend http://en.wikibooks.org/wiki/Non-Programmer's_Tutorial_for_Python_2.6 for readers with no programming experience and http://docs.Python.org/2/tutorial/ for readers with programming experience in other programming languages.

2.2 Cloud Computing

Because cell-based simulation models typically take dozens of minutes to hours to complete, depending on the technique you use and the complexity of the model, we recommend using a computer cluster or a cloud computing service to run multiple simulations in parallel. You can acquire access to a computing cluster via your institute or use online services, like *Amazon Webservices* (http://aws.amazon.com). If you want to use a computer cluster, familiarize yourself with its usage.

2.3 CompuCell3D

CompuCell3D [7] offers an easy-to-use graphical user interface for setting up and running simulations. *CompuCell3D* is designed as a modular framework and can therefore easily be extended, either using Python or C++.

1. The Python scripts provided in this chapter require the most recent Numpy version. Download Numpy from http://sourceforge.net/projects/numpy/files/ and install it (*see* **Note 3**) before installing *CompuCell3D*. This will prevent *CompuCell3D* from installing an older release of Numpy.

2. Download a suitable *CompuCell3D* installer from http://www.compucell3d.org/SrcBin. Currently installers are available for Ubuntu Linux OS X (10.6, 10.8, and 10.9), and Windows. If there is no installer for your operating system, build *CompuCell3D* from the source http://www.compucell3d.org/CompilingCC3D (*see* **Note 4**). When you are installing *CompuCell3D* on a cluster, you may also need to compile

CompuCell3D because of the absence of suitable installers or because you are not allowed to run an installer from your account. During the installation of *CompuCell3D* you must specify the installation directory; in the remainder of this chapter we refer to this directory as CC3DPATH.

3. Familiarize yourself with the CPM [23, 24] and with *CompuCell3D*. A step-by-step tutorial explaining the CPM and how to set up and run simulations with *CompuCell3D* can be found in [22] and an overview of the functions of *CompuCell3D* can be found in the reference manual [25]. The *CompuCell3D* installation includes a variety of example models, which can be found in the directory "Demos" located in the installation directory of *CompuCell3D*.

2.4   CC3DSimUtils   As supplementary material to this book chapter, we provide a Python module *CC3DSimUtils*. This module can be used to visualize and analyze simulation results, and to set up simulations with *CompuCell3D*.

1. Download the supplementary material from http://persistent-identifier.org/?identifier=urn:nbn:nl:ui:18-22500 and extract it.

2. Create a project directory at any location. In this directory we will store all code, simulation scripts, and results. We will refer to the path of this directory as PROJECTPATH.

3. Create a directory named "src" in PROJECTPATH.

4. Get CC3DSimUtils.zip from the supplementary materials and copy it to the "src" directory. Make sure that the directory containing *CC3DSimUtils* is named "CC3DSimUtils". In the subdirectory "doc" of "CC3DSimUtils" you will find the documentation of *CC3DSimUtils* ("html/CC3DSimUtils.html").

5. Tell Python about the location of *CC3DSimUtils*. For a Python script that will be executed from the root of PROJECTPATH, insert the following commands to the beginning of the Python script:

```
import sys
sys.path.append("src/")
```

Alternatively, experienced users can add the path to *CC3DSimUtils* to the system variable PYTHONPATH.

6. Install the following packages, which are required for *CC3DSimUtils* (*see* **Note 5**):

   • **Scipy**: http://sourceforge.net/projects/scipy/files/ (*see* **Note 3**)
   • **Python imaging library (PIL)**: www.pythonware.com/products/pil/
   • **Mahotas**: http://luispedro.org/software/mahotas (*see* **Note 6**)
   • **Pymorph**: http://luispedro.org/software/pymorph

Installation instructions for these packages can be found at their websites. Alternatively, use a Python package manager, such as setup_tools or pip. For example:

```
>> pip install pymorph
```

3   Methods

We illustrate the use of *CC3DSimUtils* using a model of vascular network formation based on the cellular Potts model, which is implemented in *CompuCell3D*. The model is described in detail elsewhere [13, 21]. Briefly, the model captures the self-organization of endothelial cells into vascular network-like structures, based on the following assumptions: (a) endothelial cells have an elongated shape, they (b) adhere to one another, and (c) they move and rotate randomly [21]. In a variant of the model, chemotaxis speeds up network formation and increases the stability of the networks [13, 21].

Overall, the presented workflow is as follows. We first organize the project directory with several subdirectories that will hold all code, simulation scripts, simulation data, images, and analysis results. We then run the model once and analyze the dynamics of network formation. Next, we use this model as the basis for a parameter study: We show how to set up, perform, and evaluate a parameter study using *CompuCell3D* and *CC3DSimUtils*. Finally, we illustrate the versatility of the parameter sweep protocol by adapting the Python scripts to the alternative cell-based modeling framework *VirtualLeaf* [9].

3.1   Organize Project Directory

To organize the simulations, we create a project directory in which you store simulation and analysis scripts, raw simulation data, simulation images, and analysis results. The structure of this directory is based on the structure suggested by Noble [26].

1. Create a project directory at any location, if you have not yet done so in Subheading 2.3. From now on we will refer to the path to the project directory with PROJECTPATH. This directory will be used for all examples in this section.

2. Create the following subdirectories:

   - "src": Holds all non-executable codes, such as the *CC3DSimUtils* module.
   - "bin": Holds all executable codes, such as analysis scripts.
   - "scripts": Holds all simulation scripts that will be used with *CompuCell3D*.
   - "log": Holds text files that list parameter values and random seeds for automatically generated simulations.

- "data": Holds all raw simulation data.
- "images": Holds all images that show the configuration of cells resulting from a simulation.
- "results": Holds all data files and images resulting from analysis methods.

3.2 Run the CompuCell3D *Model from the Command Line*

We run a simulation of the blood vessel formation model using the command line interface of *CompuCell3D*. By running *CompuCell3D* from the command line we can bypass the graphical user interface, which reduces simulation time. Furthermore, using the command line enables us to use a computer cluster, because clusters are usually unable to run a graphical interface. All commands provided in this section are designed to be executed from the root of the PROJECTPATH. When we refer to directories, we refer to subdirectories of PROJECTPATH.

1. Get the file "steppables.zip" from the supplementary materials and extract it to the "src" directory.

2. Get "longcells_chem.zip" from the supplementary materials and extract it to the "scripts" directory. The zip file contains three files: a CC3DML file (".xml"), and Python file (extension ".py"), and a "*CompuCell3D*" file (extension ".cc3d"). Together, these three files specify a single *CompuCell3D* simulation. Change the variable `projectpath` on line 5 of "longcells_chem.py" (in subdirectory "longcells_chem" of the "scripts" directory) to your PROJECTPATH. Windows users can use either the slash (/) or two backslashes (\cr) in path definitions.

3. Run the simulation by typing the following in a terminal emulator (Linux and OS X) or Command Prompt (windows) (*see* **Notes 7–9**):

   Linux and OS X

   ```
   >>CC3DPATH/runScript.sh --noOutput -i
   PROJECTPATH/scripts/longcells_chem.cc3d
   ```

   Windows

   ```
   >>CC3DPATH\runScript.bat --noOutput --i
   PROJECTPATH\scripts\longcells_chem.cc3d
   ```

   >>This may take up to ~45 min.

4. Next we plot the simulation results, and combine the images for a number of time steps in a single figure. Get "longcells_chem_draw.py" and "default.ctb" from the supplementary materials. Save "longcells_chem_draw.py" in the "bin" directory and "default.ctb" in your PROJECTPATH. Run "draw_longcells_chem.py" (*see* **Note 10**):
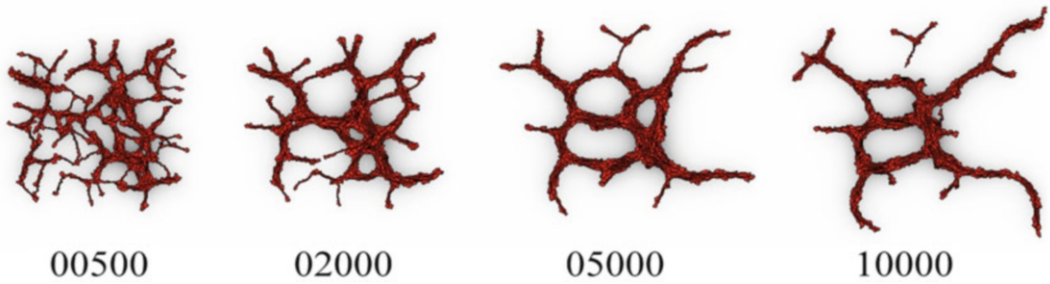
Fig. 1 Morphologies at 500, 2,000, 5,000, and 10,000 time steps, for a simulation with "longcells_chem"

```
>>python bin/longcells_chem_draw.py
```

The directory "longcells_chem" (subdirectory of "images") contains the morphologies of consecutive time steps, and the "results" directory contains a collage similar to Fig. 1 ("longcells_chem.png") of the morphologies for 500, 2,000, 5,000, and 10,000 simulations steps combined. The morphologies are created with the function `makeImages` from *CC3DSimUtils*. This function draws images using the data files generated by the simulation. The function `stackImages` from *CC3DSimUtils* can be used to combine any set of images of the same size. See the *CC3DSimUtils* documentation for further details.

3.3 Analyzing a Single CompuCell3D Simulation

Now we have a set of simulation results and images. We next present a series of methods to quantify these simulation results.

1. Calculate the compactness of the vascular network simulations. The compactness is defined as $\frac{A_{\text{cells}}}{A_{\text{hull}}}$ with A_{cells} the total area of the largest connected component and A_{hull} the area of the convex hull. The convex hull can be seen as the smallest "gift wrapping" around an object. Get "longcells_chem_compactness.py" from the supplementary materials, save it in the "bin" directory, and run with

```
>>python bin/longcells_chem_compactness.py
```

The "results" directory will contain a tab-separated text file, "longcells_chem_compactness.data", which lists the compactness for every time step measured. A plot of this data should look similar to Fig. 2.

2. Analyze where the elongated cells align with one another and where defects in alignment occur. To do so, we first quantify and visualize the relative orientations of the cells. Calculate an angle θ between the cell at a pixel $\overrightarrow{x}$ and the average orientation in the neighborhood of $\overrightarrow{x}$. The orientation of a cell, $\overrightarrow{v}$, is the
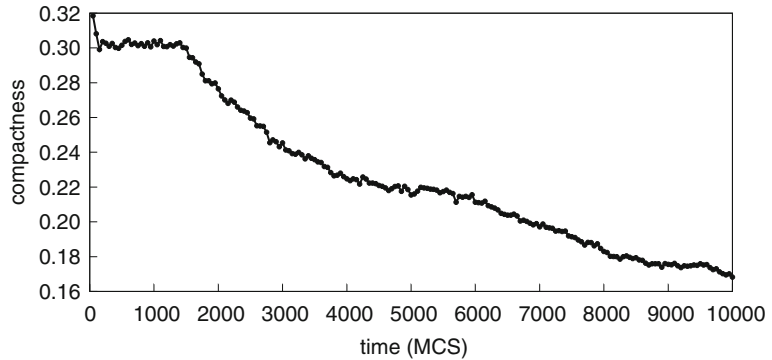
Fig. 2 Time evolution of the compactness for a single simulation of "longcells_chem"

orientation of the long axis of that cell. Assuming that cells are close to elliptic, we can approximate $\overrightarrow{v}$ by the orientation of the eigenvector corresponding to the largest eigenvalue of the cell's inertia tensor. For a cell C, defined as the set of pixels with coordinates $\overrightarrow{x} = \{x_1, x_2\}$ that the cell occupies, the inertia

tensor is defined as $I(C) = \begin{pmatrix} \sum\limits_{\overrightarrow{x} \in C} x_2{}^2 & -\sum\limits_{\overrightarrow{x} \in C} x_1 x_2 \\ -\sum\limits_{\overrightarrow{x} \in C} x_1 x_2 & \sum\limits_{\overrightarrow{x} \in C} x_1{}^2 \end{pmatrix}$.

The average cell orientation within a disk of radius r centered on $\overrightarrow{x}$ is called the *director*: $\overrightarrow{n}(\overrightarrow{x}, r) = \left\langle \overrightarrow{v}(\sigma(\overrightarrow{y})) \right\rangle_{\left\{ \overrightarrow{y} \in \mathbf{Z}^2 : \left| \overrightarrow{x} - \overrightarrow{y} \right| < r \right\}}$. The angle θ between the cell orientation $\overrightarrow{v}$ and the director $\overrightarrow{n}$ is a measure for local cell alignment: $\theta(\overrightarrow{x}, r) = \cos^{-1}\left(\frac{\left| \overrightarrow{n}(\overrightarrow{x}, r) \cdot \overrightarrow{v}(\sigma(\overrightarrow{x})) \right|}{\left| \overrightarrow{n}(\overrightarrow{x}, r) \right| \left| \overrightarrow{v}(\sigma(\overrightarrow{x})) \right|} \right)$. Get "longcells_chem_alignment.py" from the supplementary materials, save it to the "bin" directory, and then run with

```
>>python bin/longcells_chem_alignment.py
```

This script calculates θ for $r = 3$ at each pixel and plots it on the morphology. The script stores the resulting images in the subdirectory "longcells_chem" of "images". It also creates a collage similar to Fig. 3 ("longcell_chem_reldir_r=3.png" in "results"), which combines plots of θ for $r = 3$ at time steps 500, 2,000, 5,000, and 10,000.

3. The 2D nematic order parameter $S(r) = \left\langle \cos\left(2\theta\left(\overrightarrow{X}(\sigma), r \right) \right) \right\rangle_{\sigma}$, with $\overrightarrow{X}(\sigma)$ the center of mass of cell σ, quantifies the degree of local alignment in a morphology with a number between 0 and 1. $S(r) \to 1$ for cells aligning with one other on overage over a
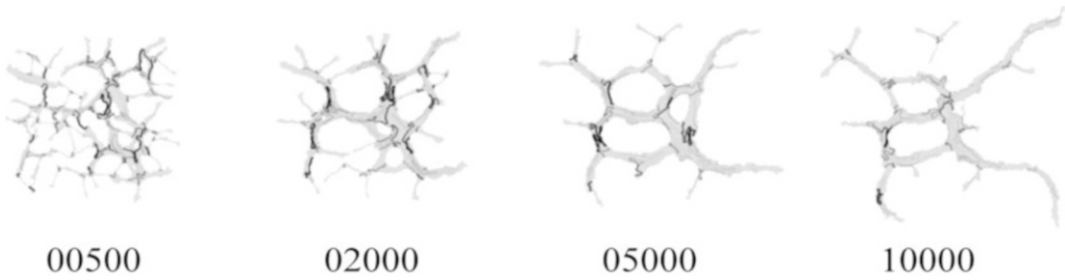
Fig. 3 Angle θ between cells and the local director (for $r = 3$) mapped on the morphologies at 500, 2,000, 5,000, and 10,000 time steps, for a simulation with "longcells_chem"
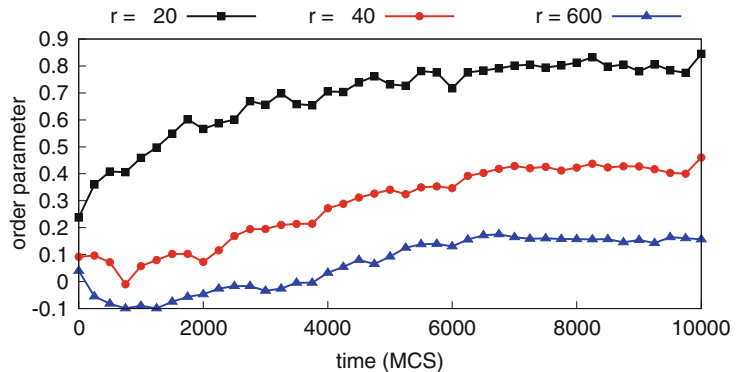

Fig. 4 Time evolution of the order parameter for radii 20, 40, and 600 (global) for a single simulation of "longcells_chem"

distance r, and $S(r) \rightarrow 0$ for cells with random orientations. Get "longcells_chem_orderparameter.py" from the supplementary materials and save it in the "bin" directory. Run the script with

```
>>python bin/longcells_chem_orderparameter.py
```

This script produces a file, named "longcells_chem_orderparameter.data", in the "results" directory that contains the order parameter for radii 20, 40, and 600 for every 250th time step. Note that radius $r = 600$ the disk covers the whole 400×400 simulation domain, so $S(600)$ becomes a *global order parameter*. Plotting the evolution of the order parameters should result in an image similar to Fig. 4.

3.4 Setting Up and Running a Parameter Sweep with CompuCell3D

We showed how to set up, run, and analyze a single simulation using *CompuCell3D* and *CC3DSimUtils*. To gain insight into how specific parameters affect the model behavior, a model should be simulated repeatedly with different parameter values. In case of a stochastic model, such as the CPM, the simulation for each parameter value should be repeated multiple times to obtain good statistics.

Here we show how to set up and run such a parameter sweep. First, we create a *driver* script that runs and analyzes a single simulation. Next, we show how to automatically create the simulation scripts for each parameter value and simulation repeat. In this example we vary the surface tension and turn chemotaxis on or off.

1. Get "driver.py" from the supplementary materials and save it as a subdirectory of PROJECTPATH called "bin". The driver script runs a simulation (Subheading 3.2) and analyzes the simulation results (Subheading 3.3). Change the variables `projectpath` and `cc3dpath` in "driver.py" such that `projectpath` points to your PROJECTPATH and `cc3dpath` points to your CC3DPATH. For example, to run the driver script for "longcells_chem.cc3d" run the driver script with

   ```
   >>python bin/driver.py longcells_chem
   ```

   The concept of collecting all operations concerning a single simulation in one driver script can be applied to any modeling method that can be invoked from the command line.

2. (For cluster users) When a driver script is used on a cluster, you may also include commands to compress and pack the data to facilitate data transfer to your desktop machine. The command `system` in the Python module "os" can call the compression utilities from your driver script. To create a compressed archive containing all files starting with "longcells_chem" and ending with ".data", append the following line to the driver script:

   ```
   os.system("tar --czf data_longcells_chem_001-1.
   tar.gz longcells_chem_001-1*.data")
   ```

3. To automatically set up the simulation, we use template simulation scripts. Get "templates.zip" from the supplementary materials and extract it in the root of PROJECTPATH. This will create a new folder named "templates" and in it you find four files: "longcells_chem.py", "longcells_chem.xml", "longcells_nochem.py", and "longcells_nochem.xml". The first two files serve as templates for the simulations with chemotaxis and the second two files serve as templates for the simulations without chemotaxis.

4. Automatically generate the scripts needed to run a *CompuCell3D* simulation. Get "preprocess.py" from the supplementary materials, save it in the "bin" folder, and run with

   ```
   >>python bin/preprocess.py
   ```

   For each parameter value specified in "preprocess.py" this script creates for each repeat a *CompuCell3D* script, and a directory containing a CC3DML script and Python script in the "scripts" directory. For each simulation repeat a unique random seed is generated to ensure that each simulation is

different (*see* **Note 11**). Each simulation is identified by an automatically generated simulation name, constructed as [description]_[number]-[repeat]. We use the [description] to differentiate between simulations with and without chemotaxis: "longcells_chem" and "longcells_nochem". The three-digit simulation [number] is used to link a simulation to a parameter value. The [repeat] is a number that is used to set apart the simulation repeats. Besides the scripts for *Compu-Cell3D*, "preprocess.py" also generates log files (in the directory "log") that store the parameter values ("longcells_1-10.sim") and the random seeds ("longcells_1-10_10x.seed"). "preprocess.py" is specific for changing the surface tension in a set of templates. For other *CompuCell3D* models and/or other parameter sets, adapt "preprocess.py" using the functionality in the *Experiment* class of *CC3DSimUtils*. See the *CC3DSimUtils* documentation for more details.

5. (For cluster users) The simulations become faster if you save the simulation results on a section of the file system local to the node you are running on (often called "scratch space"), and move the data to your home directory when the simulation is finished. Point the variable `datapath` in "preprocess.py" to the scratch space, and add commands to the driver to copy the data back to your home directory. For this we recommend using the Python standard library modules *os* and *shutil*.

6. (For cluster users). The script "preprocess_cluster.py" automatically generates the job scripts needed to schedule the simulations on cluster using PBS [27]. Get "preprocess_cluster.py" from the supplementary materials to the "bin" directory, create a directory "clusterscripts" in PROJECTPATH, and run "preprocess_cluster.py":

```
>>python bin/preprocess_cluster.py
```

After running the script, there will be a number of PBS scripts in the "clusterscripts" directory and should look like the following:

```
#PBS -S/bin/bash
#PBS -lnodes=1
#PBS -lwalltime=8:00:00
cd $HOME
python driver.py longcells_chem_001-1 > log/
longcells_chem_001-1.out 2> log/longcells_chem_
001-1.err &
...
python driver.py longcells_chem_001-8 > log/
longcells_chem_001-8.out 2> log/longcells_chem_
001-8.err &
wait
```

Submit the job script with "qsub" to add the run to the queue on the cluster. Each PBS script contains 8 jobs and requests an 8-core node (*see* **Note 12**). To change these parameters, change the variables `cores` and `ppn` in "preprocess_cluster. py". You may also need to modify the function `createPBS` in "CC3DPipeline.py" in *CC3DSimUtils* to fit the hardware and scheduling software of the cluster you are using.

7. When all simulations are finished we have a collection of raw data files, data analysis results, and images. For each simulation all data files should be located in the "data" directory, in a subdirectory with the simulation name, for example: "PRO-JECTPATH/data/longcells_chem_001-1/". Similarly, the images are expected to be in a subdirectory with the simulation name in the directory "images": "PROJECTPATH/images/longcells_chem_001-1/". If this is not the case, move your data files and/or images to these locations.

3.5 Analyzing a CompuCell3D Parameter Sweep

After running the parameter sweep we have raw data, data analysis results, and images for each simulation. Here we show how to collect and present this data.

1. Create a *morphospace*, a collage of simulated morphologies as a function of one or two simulation parameters. Get "postprocess_morphospace.py" from the supplementary materials, save it to the "bin" directory, and run it with

   ```
   >>python bin/postprocess_morphospace.py
   ```

   Now, you should find an image named "longcells_1-10_morphospace_100000.png" in the "results" folder, which should look similar to Fig. 5. The morphospace is created
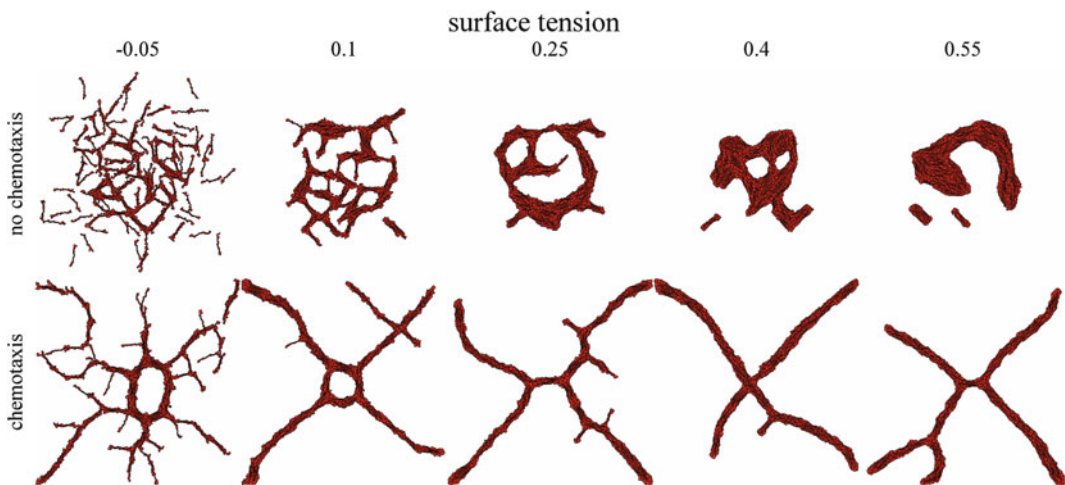

Fig. 5 Morphospace showing the effects of varying surface tensions with and without chemotaxis
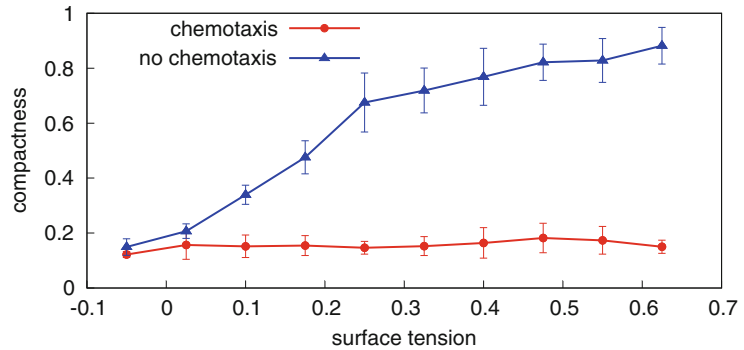
Fig. 6 Compactness for simulations with and without chemotaxis, plotted against the surface tension. The compactness was calculated at 100,000 time steps, and for each parameter the simulation was repeated 10 times (error bars represent standard deviation)

with the function `morphImages`, from *CC3DSimUtils*. See the *CC3DSimUtils* documentation for more details.

2. Calculate the compactness as a function of the surface tension. Get "postprocess_compactness.py" from the supplementary materials and save it in the "bin" directory. Run it with

```
>>python bin/postprocess_compactness.py
```

The script collects the compactness at the last time step of each simulation repeat for each tested parameter value and it calculates the mean and standard deviation over the simulation repeats. The results can be found in "longcells_chem_1-10_10x_compactness.data" (simulations with chemotaxis) and "longcells_nochem_1-10_10x_compactness.data" (simulations without chemotaxis) in the "results" directory. Plotting this data should result in a plot similar to Fig. 6.

3. Quantify the degree of cell alignment by calculating the mean and standard deviation of the order parameter. Get "postprocess_orderparameter.py" from the supplementary materials, save it into the "bin" directory, and run the script with

```
>>python bin/postprocess_orderparameter.py
```

This script calculates the mean and standard deviation of the order parameter $S(r, t)$ as a function of time for radii $r = 20$ and $r = 40$, and the global order parameter ($r = 600$) for all simulation repeats of one surface tension. The results can be found in "longcells_chem_003_10x_orderparameter.data" and "longcells_nochem_003_10x_orderparameter.data", in the "results" directory. With the data in these files we generated the plot in Fig. 7 for simulations of 1,000,000 time steps. Note that to reduce simulation time the scripts presented in this chapter produce only 100,000 time steps.
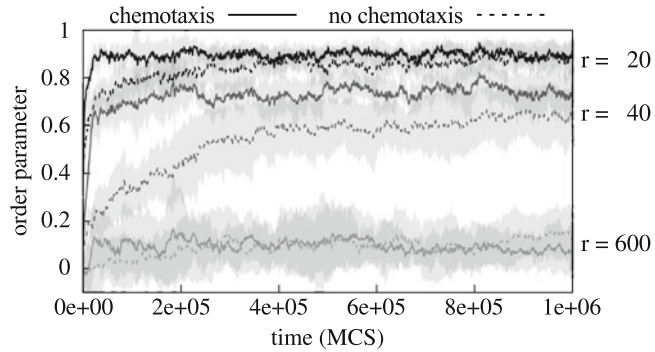
Fig. 7 Time evolution of the order parameter for radii 20, 40, and 600 (global). Each line represents the average order parameter of ten simulations and the *grey areas* represent the standard deviation

4. To relate cell motility to the degree of cell alignment, we detect clusters of aligned cells in the morphology. We loosely define a "cluster" as a set of cells aligned with the local director, $\theta(\overrightarrow{x}, r) < \theta^*$, with $\theta^\star$ a threshold value. Clusters are separated from other clusters by regions with values of $\theta(\overrightarrow{x}, r) > \theta^*$ (dark gray regions in Fig. 3). More formally, clusters are detected as follows:

   (a) Define a binary matrix B of dimensions equal to the simulation domain.

   (b) Assign a value of $B(\overrightarrow{x}) = 1$ to all cell pixels $\overrightarrow{x}$ for which $\theta(\overrightarrow{x}, r)\theta^*$, with $\theta^\star$ a threshold value and $B(\overrightarrow{x}) = 0$ for all other pixels.

   (c) In B detect all connected components larger than 50 pixels. A set of cells forms a cluster if each cell overlaps with the same connected component in B for 50 % of its area or more.

5. To study how aggregation of aligned cells in clusters affects cell behavior we measured the translation and rotation of the cells as a function of cluster size. The translational diffusion coefficient D_t quantifies the translational motility of cells. It is derived from the *mean squared displacement* (MSD) of a cell: $\left\langle \left| \overrightarrow{X}(\sigma, t) - \overrightarrow{X}(\sigma, 0) \right|^2 \right\rangle_\sigma = 4 D_t t$. The rotational diffusion coefficient D_r is derived from the *mean squared rotation* (MSR) of a cell: $\langle (\alpha(\sigma, t) - \alpha(\sigma, 0))^2 \rangle_\sigma = 2 D_r t$.

6. Calculate the translational and rotational diffusion coefficients. Get "postprocess_diffusion.py" from the supplementary materials, save it in the "bin" directory, and run the script with

```
>>python bin/postprocess_diffusion.py
```
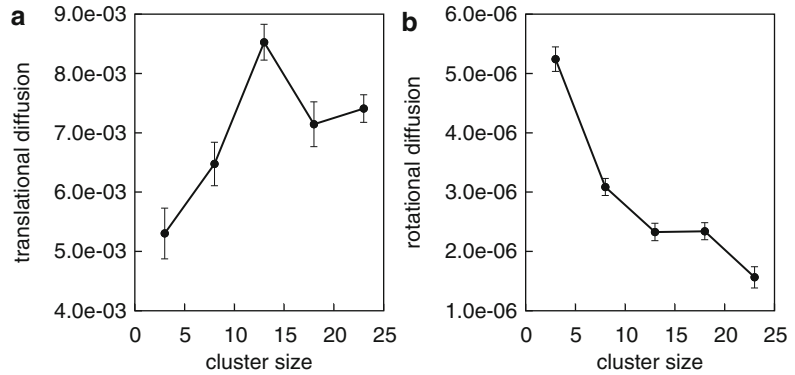
Fig. 8 Diffusion coefficients as a function of the cluster size. (**a**) Translation diffusion coefficient and (**b**) rotational diffusion coefficient. These diffusion coefficients were calculated from ten simulations of 250,000 time steps. The error bars represent the standard error of the estimates of the least square fit

This script creates time series of the MSD and the MSR of each cell as a function of the cluster size and uses those time series to calculate the translational and rotational diffusion coefficients. First, cells are binned according to cluster size for each time step, with a bin size of five cells and the first bin running from two to five cells. Then, the MSD and MSR of each cell are split into chunks of ten consecutive time steps, during which that cell belonged to the same cluster size bin. Using these binned chunks the translational and rotational diffusion coefficients are calculated with a least square fit of, respectively, the MSD and MSR. The diffusion coefficients, together with the standard error of the estimate of the fit, are stored in "longcells_no-chem_003_10x_diffusion.data" in the "results" directory. In Fig. 8 we plot the translational and rotational diffusion coefficients calculated using data from time step 500 to 250,000 (similar to our previous work [21]). As mentioned before, the scripts presented in this chapter only produce 100,000 time steps in order to reduce simulation time.

3.6 Adapting the Protocol to Alternative Simulation Packages

The scripts described in Subheadings 3.4 and 3.5 can be adapted to any simulation package that is (1) invoked from the command line and (2) for which model parameters are specified in a text file. As an example, we show how to use the scripts used in Subheadings 3.4 and 3.5 to set up, run, and analyze for the cell-based, vertex-based modeling framework *VirtualLeaf* [9, 28]. A model in the *Virtual-Leaf* is defined by the so-called *plugin* and the model parameters are defined in the so-called *leaf* file. With the *leaf* file and the *plugin*, *VirtualLeaf* can be invoked from the command line. Thus, *VirtualLeaf* meets both of the requirements of the parameter sweep protocol.

1. Create a project directory for your *VirtualLeaf* project (as described in Subheading 3.1).

2. Adapt "driver.py" to run and analyze *VirtualLeaf* simulations.

   (a) To run the simulation, "driver.py" uses the function `os.system` (on line 26), which attempts to execute its argument on the command line. For example, for *a VirtualLeaf* model defined in "plugin.cpp" and the parameters defined in "leaf.xml", this argument must be (*see* **Note 13**) as follows:

   ```
   /path/to/VirtualLeaf/bin/VirtualLeaf --b --l leaf.
   xml -m libplugin
   ```

   Assign the path to the VirtualLeaf executable to `execpath` (line 7) and assign the executable name, i.e., "VirtualLeaf" to `executable` (lines 10–11). Next, define a new variable named `plugin`, before line 26, that points to the plugin in which your model is defined (e.g., 'libplugin'). Now, change line 26 to the following:

   ```
   os.system('execpath+/+executable+  --b  --l
   '+projectpath+/scripts/+id+.xml --m '+plugin)
   ```

   (b) Remove the commands on line 28 and further, and replace them with calls to your own analysis functions.

3. Create a template *leaf* file for your model that contains the default parameter values for your model.

4. Create a new Python script to automatically generate *leaf* file, based on "preprocess.py".

   (c) Copy line 1 of "preprocess.py" to import the necessary Python libraries.

   (d) Create a function `buildLeafFile` to change specific parameter values in a template *leaf* file. Because *leaf* files are based on XML, you can use "Experiment.py" as an example on how to adapt an XML file using Python. Besides changing specific parameter values, `buildLeafFile` also assigns a random seed, sets the intervals at which the simulation generates graphical and numerical output, and sets the filenames and location of the output. As with the *CompuCell3D* simulations, model output files should be identified by the simulation description, simulation number, and repeat number: description_number-repeat, and be stored in a directory with the same name in the "data" directory of PROJECTPATH.

   (e) Define a variable `projectpath` (see line 47 of "preprocess.py"):

   ```
   projectpath = [PROJECTPATH]
   ```

   replacing [PROJECTPATH] for your PROJECTPATH.

(f) Define the parameters of the parameter sweep. These are `simname` for the simulation description, `offset` for the first simulation number, `repeats` for the number of repeats, and `rep0` for the first repeat number (see lines 51–58 of "preprocess.py"). For example:

```
simname = 'leaf'
offset = 1
repeats = 10
rep0 = 1
```

(g) Set the simulation time (`simtime`) and the frequency at which output is generated (`savefreq`) (see lines 59–62 of "preprocess.py"). For example:

```
simtime = 1000
savefreq = 25
```

(h) Create a list of parameter values, named `par`, that will be tested in the parameter sweep (see line 64 of "preprocess. py").

(i) Create output files for simulation settings and seeds, and write the file headers (see lines 70–76 of "preprocess.py"):

```
runid   =   simname+'_'+str(offset)+'-'+str
    (offset+len(par)-1)
# open log file for parameter values
out = open('log/'+runid+'.sim','w')
out.write('#id\tPARAMETERNAME')
# open log file for random seeds
sout   =   open('log/'+runid+'_'+str(repeats)
    +'x''.seed','w')
sout.write('#id\tseed')
```

(j) Iterate over the parameters and the simulation repeats (see lines 79–101 of "preprocess.py"). The outer loop is used to write the tested parameter values to the log files. In the inner loop the random seed is generated and the *leaf* file is created:

```
seeds = []
for i,p in enumerate(par):
  out.write('\n'+name+'_'+string.zfill(i
      +offset,3)+'\t'+str(p)+'\n')
  for n in range(rep0,repeats+rep0):
    simid   =   name+'_'+string.zfill(i+off-
      set,3)+'-'+str(n)
    seed = random.randint(1,10**9)
```

```
# check if seed is unique
while seed in seeds:
    seed = random.randint(1,10**9)
seeds.append(seed)
sout.write('\n'+simid+'\t'+str(seed))
#--- Create leaf file ---#
buildLeafFile(...)
```

5. Adapt "preprocess_cluster.py" to create a set of scripts for the PBS job scheduler.

   (a) Change numlist (line 7) such that it represents the ranges from the lowest simulation number to the highest simulation number.

   (b) Change replist (line 9) such that it represents the range from the lowest repeat number to the highest repeat number.

   (c) Replace basename (line 13) with your simulation description.

   (d) Change cores (line 17), ppn (line 19), and runtime (line 21) to fit the type of node, number of processors per node, and simulation time you will request on the cluster.

   (e) Replace line 25 with

   ```
   joblist = [name+'_'+string.zfill(num,3)+'-
       '+str(n) for name in simnames for num in
       numlist for n in replist]
   ```

6. Depending on the analysis performed in the driver script, create your own set of post-process scripts. For this, you can use post-process scripts from Subheading 3.5 as examples:

   • "postprocess_morphospace.py" can be used as an example for creating morphospaces.

   • "postprocess_compactness.py" can be used as an example to collect values for one time point per simulation, and mapping that data on parameter values.

   • "postprocess_orderparameter.py" can be used as an example on how to collect time course data for multiple simulations.

4   Notes

1. There are two Python branches: Python 2.x and Python 3.x, which are not fully compatible. All codes supplied with this chapter and *CompuCell3D* are compatible with Python 2.6 and new versions of the Python 2.x branch.

2. Python uses indentations to delimit blocks of codes. In code that is copied from different sources, indentation may be broken due to different indentation lengths or mixing of tabs and spaces. See http://www.Python.org/dev/peps/pep-0008/#indentation and http://www.Python.org/dev/peps/pep-0008/#tabs-or-spaces for more information on how to correctly indent your code.

3. Windows users should install the Numpy or the Scipy version that fits with your Python version. First check your Python version:

```
>>python --V
```

Note the first two digits of the Python version, e.g., 2.7. Now go to the download page of Numpy or Scipy and select the latest version. Here you should find an installer that ends with your python version, e.g., "numpy-x.y.z-win32-superpack-python27.exe".

4. When you compile *CompuCell3D*, always check the *CompuCell3D* website for the most recent instructions and dependencies. Here we list some extra instructions for the compilation of *CompuCell3D*.

   • The *CompuCell3D* developers recommend to use "cmake-gui"; for systems without a graphical user interface the "cmake curses gui", also known as "ccmake", can be used as an alternative.

   • Ensure that you compile *CompuCell3D* with the "release" flag because omitting this flag significantly increases simulation time. The "release" flag can be set with the "cmakegui" or "ccmake".

5. *CC3DSimUtils* needs freetype fonts for the labels on images. You may need to install freetype (http://www.freetype.org/download.html) and/or to change the variable `fontpath` in the function definitions of `makeImage`, `stackImages`, and `morphImages` (all in "ImageUtils.py" in *CC3DSimUtils*).

6. For windows users we strongly recommend to download the installer for Mahotas at http://www.lfd.uci.edu/~gohlke/pythonlibs/. Building the source of Mahotas, for example using pip, is not recommended.

7. *CompuCell3D* interprets all paths relative to its own path. Therefore, when running a simulation using runScript.sh you should specify the full path to the simulation file, for example.

   • Windows: `C:\Users\username\project_name\scripts\script.cc3d`

- Linux:`/home/username/project_name/scripts/
  script.cc3d`
- OS X:`/Users/username/project_name/scripts/
  script.cc3d`

8. On windows, running `runScript.bat` changes the working directory to the CC3DPATH. Make sure to change it back to the PROJECTPATH afterwards.

9. In this model we use a connectivity constraint to ensure that each cell consists of single connected component. Calculating the connected components is computationally expensive; therefore *CompuCell3D* checks only for local connectivity by checking if a cell is a single connected component within a small neighborhood. This can cause pixels to become *frozen*, because any change in their neighborhood breaks local connectivity. We fixed this by adding an extra test to the connectivity constraint for pixels that fit the pattern of a frozen pixel. We used this fixed connectivity constraint for all our simulations.

   This plugin ("ConnectivityFroNo.zip") can be downloaded from the supplementary materials and compiled as a part of the *CompuCell3D* developer zone; see the CC3D developers' manual [29] for instructions.

10. On Windows the Python installation directory may not be in the $PATH; this results in an error like the following:

    'Python is not recognized as an internal or external command, operable program or batch file.

    Adding the installation directory of Python to your $PATH system variable should solve this problem.

11. Random seeds are used to initialize a random generator. Every time a random generator is initialized with the same results, it returns the same sequence of pseudo-random numbers. Thus, if we run a *CompuCell3D* simulation twice with identical seeds, we get identical results. If no random seed is provided, *CompuCell3D* uses the current time to generate a random seed. When multiple simulations are started at the same moment, for example on a computer cluster, they will get the same seed. Thus, predefining random seeds has two advantages: (1) the results are reproducible and (2) the random seeds in parameter sweep are unique.

12. It is often more efficient to leave one core of a node idle. This core is then reserved for system processes while the remaining nodes are reserved for user processes, i.e., the simulations. To do so, set `ppn` (processes per node) in "preprocess_cluster.py" to one less than there are `cores` (number of cores of the requested node).

13. Due to a bug in the current version of *VirtualLeaf* (1.0.1), if *VirtualLeaf* is invoked with both a *leaf* file and a *plugin* in which another *leaf* file is defined, the *leaf* file defined in the *plugin* will be used. To correct this problem, add the following code to "virtualleaf.cpp' after the line with

```
"model_catalogue.InstallFirstModel();",
```
and recompile:

```
  if (leaffile){

    main_window->Init(leaffile);

}
```

Acknowledgments

References

1. Merks RMH, Glazier JA (2005) A cell-centered approach to developmental biology. Phys A 352:113–130

2. Anderson ARA, Chaplain MAJ, Rejniak K (2007) Single-cell-based models in biology and medicine. Birkhäuser Verlag, Basel

3. Hester SD, Belmonte JM, Gens JS et al (2011) A multi-cell, multi-scale model of vertebrate segmentation and somite formation. PLoS Comput Biol 7:e1002155

4. Drasdo D, Höhme S (2003) Individual-based approaches to birth and death in avascular tumors. Math Comput Model 37:1163–1175

5. Alarcón T, Byrne HM, Maini PK (2005) A multiple scale model for tumor growth. Multiscale Model Simul 3:440–475

6. Kim Y, Stolarska MA, Othmer HG (2007) A hybrid model for tumor spheroid growth in vitro I: theoretical development and early results. Math Models Methods Appl Sci 17:1773–1798

7. Macklin P, Edgerton ME, Thompson AM et al (2012) Patient-calibrated agent-based modelling of ductal carcinoma in situ (DCIS): from microscopic measurements to macroscopic predictions of clinical progression. J Theor Biol 301:122–140

8. Hoehme S, Brulport M, Bauer A et al (2010) Prediction and validation of cell alignment along microvessels as order principle to restore tissue architecture in liver regeneration. Proc Natl Acad Sci U S A 107:10371–10376

9. Merks RMH, Guravage M, Inzé D et al (2011) VirtualLeaf: an open-source framework for cell-based modeling of plant tissue growth and development. Plant Physiol 155:656–666

10. Hamant O, Heisler MG, Jönsson H et al (2008) Developmental patterning by mechanical signals in Arabidopsis. Science 322:1650–1655

11. Hirashima T, Iwasa Y, Morishita Y (2009) Dynamic modeling of branching

morphogenesis of ureteric bud in early kidney development. J Theor Biol 259:58–66

12. Engelberg JA, Datta A, Mostov KE et al (2011) MDCK cystogenesis driven by cell stabilization within computational analogues. PLoS Comput Biol 7:e1002030

13. Merks RMH, Brodsky SV, Goligorksy MS et al (2006) Cell elongation is key to in silico replication of in vitro vasculogenesis and subsequent remodeling. Dev Biol 289:44–54

14. Merks RMH, Perryn ED, Shirinifard A et al (2008) Contact-inhibited chemotaxis in de novo and sprouting blood-vessel growth. PLoS Comput Biol 4:e1000163

15. Bauer AL, Jackson TL, Jiang Y (2007) A cell-based model exhibiting branching and anastomosis during tumor-induced angiogenesis. Biophys J 92:3105–3121

16. Bauer AL, Jackson TL, Jiang Y (2009) Topography of extracellular matrix mediates vascular morphogenesis and migration speeds in angiogenesis. PLoS Comput Biol 5:e1000445

17. Kleinstreuer N, Dix D, Rountree M et al (2013) A computational model predicting disruption of blood vessel development. PLoS Comput Biol 9:e1002996

18. Scianna M, Munaron L, Preziosi L (2011) A multiscale hybrid approach for vasculogenesis and related potential blocking therapies. Prog Biophys Mol Biol 106:450–462

19. Andasari V, Roper RT, Swat MH et al (2012) Integrating intracellular dynamics using CompuCell3D and Bionetsolver: applications to multiscale modelling of cancer cell growth and invasion. PLoS One 7:e33726

20. Daub JT, Merks RMH (2013) A cell-based model of extracellular-matrix-guided endothelial cell migration during angiogenesis. Bull Math Biol. doi:10.1007/s11538-013-9826-5

21. Palm MM, Merks RMH (2013) Vascular networks due to dynamically arrested crystalline ordering of elongated cells. Phys Rev E 87:012725

22. Swat MH, Thomas GL, Belmonte JM et al (2012) Multi-scale modeling of tissues using CompuCell3D. In: Asthagiri AR, Arkin AP (eds) Computational methods in cell biology. Academic, Waltham, MA, pp 325–366

23. Glazier JA, Graner F (1993) Simulation of the differential adhesion driven rearrangement of biological cells. Phys Rev E 47:2128–2154

24. Graner F, Glazier JA (1992) Simulation of biological cell sorting using a two-dimensional extended Potts model. Phys Rev Lett 69:2013–2016

25. Swat MH, Belmonte J, Heiland RW et al (2012) CompuCell3D Reference Manual Version 3.6.2. http://www.compucell3d.org/BinDoc/cc3d_binaries/Manuals/CompuCell3D_Reference_Manual_v.3.7.2.pdf. Accessed 2 May 2013

26. Noble WS (2009) A quick guide to organizing computational biology projects. PLoS Comput Biol 5:e1000424

27. Henderson R (1995) Job scheduling under the portable batch system. In: Feitelson D, Rudolph L (eds) Job scheduling strategies for parallel processing. Springer, Berlin, pp 279–294

28. Merks RMH, Guravage MA (2013) Building simulation models of developing plant organs using VirtualLeaf. In: De Smet I (ed) Plant organogenesis. Springer, New York, pp 333–352

29. Swat MH, Cickovski T, Glazier JA et al (2009) Developers' documentation for CompuCell3D. http://www.compucell3d.org/BinDoc/cc3d_binaries/Manuals/Developers_Documentation_v3.4.1.pdf Accessed 2 May 2013

Chapter 21

Simulating Tissue Morphogenesis and Signaling

Dagmar Iber, Simon Tanaka, Patrick Fried, Philipp Germann, and Denis Menshykau

Abstract

During embryonic development tissue morphogenesis and signaling are tightly coupled. It is therefore important to simulate both tissue morphogenesis and signaling simultaneously in *in silico* models of developmental processes. The resolution of the processes depends on the questions of interest. As part of this chapter we introduce different descriptions of tissue morphogenesi s. In the simplest approximation tissue is a continuous domain and tissue expansion is described according to a predefined function of time (and possibly space). In a slightly more advanced version the expansion speed and direction of the tissue may depend on a signaling variable that evolves on the domain. Both versions will be referred to as "prescribed growth." Alternatively tissue can be regarded as incompressible fluid and can be described with Navier-Stokes equations. Local cell expansion, proliferation, and death are then incorporated by a source term. In other applications the cell boundaries may be important and cell-based models must be introduced. Finally, cells may move within the tissue, a process best described by agent-based models.

Key words Tissue dynamics, Signaling networks, In silico organogenesis

1 Introduction

During biological development signaling patterns evolve on dynamically deforming and growing domains. The tissue dynamics affect signaling by advective transport, molecular dilution, and separation of signaling centers and because of the cellular responses to mechanical stress and others. Tissue properties and cellular behavior, such as cell division and differentiation, in turn are all controlled by the signaling system. To understand the control of tissue growth and organ development both aspects, signaling and tissue mechanics, need to be analyzed simultaneously. Computational modeling and experimentation are increasingly combined (Fig. 1) to achieve an integrative understanding of such complex processes [1].

Modeling the mechanochemical interactions mathematically leads to systems, whose numerical solution is challenging. In this review, we present general methods to formulate, couple, and solve
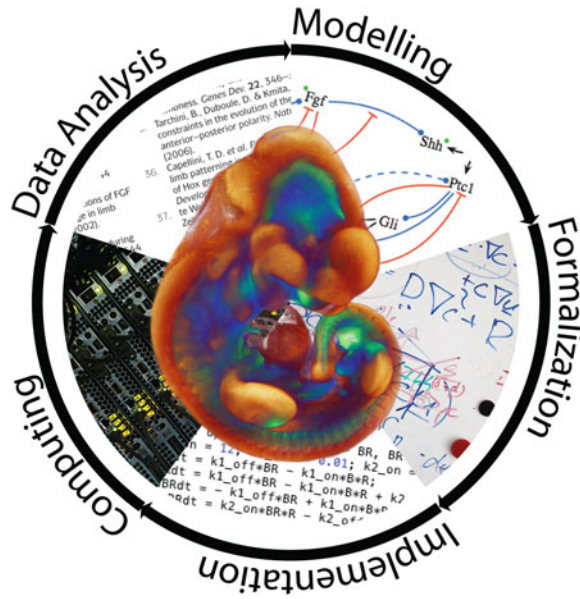
Fig. 1 *In silico* models of tissue morphogenesis and signaling. Models are formulated based on available data. The formalized models then need to be implemented and solved. Model solutions are subsequently compared to available and newly generated data. Models are updated until a good match is achieved

morphogenetic models. The chapter is organized as follows: In Subheading 2 we describe how signaling networks can be modeled on growing and deforming domains using a continuous, deterministic approach. In Subheading 3, different tissue models will be introduced and applications and limitations will be highlighted.

2   Signaling Models on Moving Domains

Growth can have a significant impact on patterning processes as the growing tissue transports signaling molecules, and molecules are diluted in a growing tissue. In the following we discuss the impact of growth on the spatiotemporal distribution of signaling factors. Let $c_i(\overrightarrow{x}, t)$ denote the spatiotemporal concentration of a component $i = 1, \ldots, N$ that can diffuse and react in a volume Ω; $\overrightarrow{x}$ is the spatial location, and t the time. The total temporal change of $c_i(\overrightarrow{x}, t)$ in the volume Ω must then be equal to the combined changes in the domain due to diffusion and reactions, i.e.,

$$\frac{\mathrm{d}}{\mathrm{d}t} \int_{\Omega} c_i(\overrightarrow{x}, t) \mathrm{d}V = \int_{\Omega} \left\{ -\nabla \cdot \overrightarrow{j} + R(c_k) \right\} \mathrm{d}V \qquad (1)$$

where $\overrightarrow{j}$ denotes the diffusion flux and $R(c_k)$ the reaction term, which may depend on the components c_k, $k = 1, \ldots, N$. The molecule c_i will diffuse from regions of higher concentration

to regions of lower concentration, and we thus have according to Fick's law

$$\vec{j} = -D_i \nabla c_i(\vec{x}, t)$$

which, in case of a constant domain Ω, leads to the well-known reaction-diffusion equation, i.e.,

$$\int_\Omega \left\{ \frac{dc_i}{dt} - D_i \Delta c_i - R(c_k) \right\} dV = 0$$

$$\frac{\partial c_i}{\partial t} = D_i \Delta c_i + R(c_k) \tag{2}$$

If the domain is evolving in time, then the Leibniz integral rule cannot be directly applied. We therefore map the time-evolving domain Ω to a stationary domain $\Omega_{\vec{\xi}}$ using a time-dependent mapping. $\vec{\xi}$ denotes the spatial coordinate in the stationary domain. For the left-hand side of Eq. (1) we then obtain, using the Reynolds transport theorem,

$$\frac{d}{dt} \int_{\Omega_t} c_i(\vec{x}, t) d\Omega = \frac{d}{dt} \int_{\Omega_{\vec{\xi}}} c_i\left(\vec{x}\left(\vec{\xi}, t\right), t\right) |J| d\Omega$$

$$= \int_{\Omega_{\vec{\xi}}} \left[\frac{dc_i}{dt} |J| + c_i \frac{d|J|}{dt} \right] d\Omega$$

$$= \int_{\Omega_{\vec{\xi}}} \left[\frac{\partial c_i}{\partial t} + \vec{u} \cdot \nabla c_i + c_i \nabla \cdot \vec{u} \right] |J| d\Omega$$

$$= \int_{\Omega_t} \left[\frac{\partial c_i}{\partial t} + \nabla \cdot \left(c_i \vec{u} \right) \right] d\Omega$$

where J with $\dot{J} = J \nabla \vec{u}$ denotes the Jacobian and $\vec{u} = \partial \vec{x} / \partial t$ the velocity field. We thus obtain as reaction-diffusion equation on a growing domain

$$\left. \frac{\partial c_i}{\partial t} \right|_{\vec{x}} + \nabla \cdot \left(c_i \vec{u} \right) = D_i \Delta c_i + R(c_i) \tag{3}$$

where $|_{\vec{x}}$ indicates that the time derivative is performed while keeping $\vec{x}$ constant. The terms $\vec{u} \cdot \nabla c_i$ and $c_i \nabla \cdot \vec{u}$ describe advection and dilution, respectively. If the domain is incompressible, i.e., $\nabla \cdot \vec{u} = 0$, the equations further simplify.

It should be noted that this deterministic reaction-diffusion equation only describes the mean trajectory of an ensemble.

Whenever the molecular population of the least prevalent compound is small, the advection-diffusion equation is not a good description and stochastic techniques need to be used.

2.1 The Lagrangian Framework

In growing tissues cells move. It can be beneficial to take the point of view of the cells and follow them. This is possible within the Lagrangian framework. To illustrate the differences between the Eulerian and Lagrangian framework consider a river. The Eulerian framework would correspond to sitting on a bench and watching the river flow by. In the Lagrangian framework we would sit in a boat and travel with the river.

Accordingly, at time $t = 0$ we now label a particle by the position vector $\vec{X} = \vec{x}(0)$ and follow this particle over time. At times $t > 0$, the particle is found at position $\vec{x} = \psi(\vec{X}, t)$. Here $\vec{x}$ is the spatial variable in the Eulerian framework and $\vec{X}$ is the spatial variable in the Lagrangian framework. If initially distinct points remain distinct throughout the entire motion then the transformation possesses the inverse $\vec{X} = \psi^{-1}(\vec{x}, t)$. Any quantity F (e.g., a concentration $F = c_i$) can therefore be written either as a function of Eulerian variables $(\vec{x}, t)$ or Lagrangian variables $(\vec{X}, t)$. To indicate a particular set of variables we thus write either $F = F(\vec{x}(\vec{X}, t), t)$ as the value of F felt by the particle instantaneously at the position $\vec{x}$ in the Eulerian framework or $F = F(\vec{X}, t)$ as the value of F experienced at time t by the particle initially at $\vec{X}$ (Lagrangian framework).

In the Lagrangian framework we now need to determine the change of the variable F following the particle, while in the Eulerian framework we were determining $\partial F / \partial t|_{\vec{x}}$, the rate of F apparent to a viewer stationed at the position $\vec{x}$. The time derivative in the Lagrangian framework is also called the material derivative:

$$\frac{\mathrm{d}F}{\mathrm{d}t} = \frac{\mathrm{d}F\left(\vec{x}\left(\vec{X}, t\right), t\right)}{\mathrm{d}t} = \frac{\partial F\left(\vec{X}, t\right)}{\partial t} \tag{4}$$

and follows as

$$\underbrace{\frac{\mathrm{d}F\left(\vec{X}, t\right)}{\mathrm{d}t}}_{\text{Lagrangian}} = \left.\frac{\partial F}{\partial t}\right|_{\vec{x}} + \frac{\partial F}{\partial x_k}\underbrace{\frac{\partial x_k\left(\vec{X}, t\right)}{\partial t}}_{u_k}$$

$$= \underbrace{\left.\frac{\partial F}{\partial t}\right|_{\vec{x}} + \vec{u} \cdot \nabla F}_{\text{Eulerian}} \tag{5}$$

Note that the advection term $\vec{u} \cdot \nabla F$ vanishes in the material derivative as compared to the Eulerian description. We can now also write the Eulerian spatial derivatives in terms of the Lagrangian reference frame using the Jacobian of the transformation:
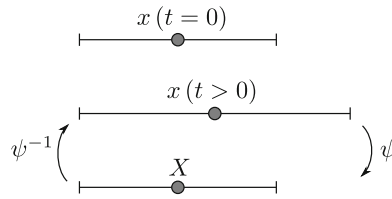
Fig. 2 Mapping to a stationary domain. A one-dimensional domain is stretched. A point on the domain, initially at $x(t = 0)$, is advected and later found at position x $(t > 0)$. At all times, the Eulerian coordinate system can be mapped to a stationary domain using a mapping function ψ, and vice versa using its inverse ψ^{-1}. On the stationary domain, the point stays at the same position for all times and thus can be labeled by X

$$J = \frac{\partial(X_1, X_2, X_3)}{\partial(x_1, x_2, x_3)} \tag{6}$$

Geometrically, $|J|$ represents the dilation of an infinitesimal volume as it follows the motion:

$$dX_1 dX_2 dX_3 = |J| \, dx_1 dx_2 dx_3 \tag{7}$$

Example—*Uniform Growth*: The benefit of working in a Lagrangian reference frame is directly apparent in case of a uniformly growing domain. In case of uniform growth in one spatial dimension we have $x = L(t)X$, where $L(t)$ is the time-dependent length of the domain. We then have

$$\frac{\partial X}{\partial x} = \frac{1}{L(t)} \quad u = \dot{L}(t)X \quad u = \dot{L}(t)X \tag{8}$$

Since the stretching factor $L(t)$ is independent of the spatial position, the Lagrangian reference frame X corresponds to a stationary domain. As reaction-diffusion equation on an uniformly growing domain we then obtain a rather simple formula, i.e.,

$$\frac{dc}{dt} + \frac{\dot{L}(t)}{L(t)}c = D\frac{1}{L(t)^2}\frac{\partial^2 c}{\partial X^2} + R(c) \tag{9}$$

where $c = c(X, t)$. The principle is summarized in Fig. 2. We have used this approach in a 1D model of bovine ovarian follicle development (Iber and De Geyter, under review).

2.2 Arbitrary Lagrangian-Eulerian (ALE) Method

The arbitrary Lagrangian-Eulerian (ALE) method is a generalization of the well-known Eulerian and Lagrangian domain formulations [2]. In the Eulerian framework, the observer does not move with respect to a reference frame (Eq. 3). Large deformations can be described in a simple and robust way, but tracking moving boundaries can lead to nontrivial problems. In the Lagrangian framework, on the other hand, the observer moves according to the local velocity field. The convective terms are zero because the
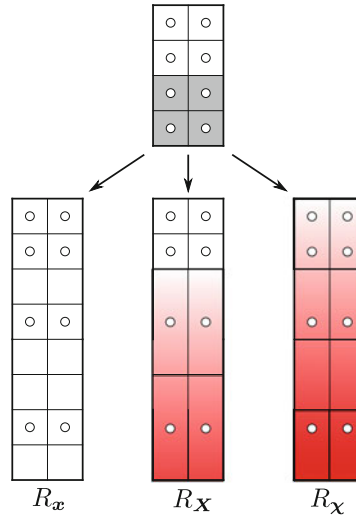
Fig. 3 Reference frame paradigms. The *grey-shaded* material of the initial domain is stretched threefold. Material particles (*circles*) are attached to the continuum. In the Eulerian domain $R_{\vec{x}}$ the mesh does not move as opposed to the Lagrangian domain $R_{\vec{X}}$ and ALE domain $R_{\vec{\chi}}$. The *red* color denotes the magnitude of mesh velocity $\vec{v}$. In the Lagrangian domain, the mesh velocity coincides with the material velocity field $\vec{u}$, whereas in the ALE domain the mesh velocity can be chosen arbitrarily

relative motion to the material vanishes locally, and the equations simplify substantially (Eq. 5). However, this comes at the expense of mesh distortions when facing large material deformations.

In the ALE framework, finally, the observer is allowed to move freely and describe the equations of motions from his or her viewpoint. This allows for the flexibility to deform the mesh according to, e.g., moving boundaries, but also for the possibility to freely remodel the mesh independent of the material deformations. Although the problem of mesh distortion is much reduced as compared to the Lagrangian formulation, remeshing might still be required when confronted with complex deformations. The three paradigms are visualized in Fig. 3.

In the ALE framework, the reaction-diffusion equation reads

$$\left.\frac{\partial c_i}{\partial t}\right|_{\vec{x}} + \vec{w} \cdot \nabla c_i + c_i \nabla \cdot \vec{u} = D_i \Delta c_i + R(c_i) \qquad (10)$$

where $\partial_t c_i|_{\vec{x}}$ denotes the time derivative with fixed $\vec{x}$ coordinate. $\vec{w} = \vec{u} - \vec{v}$ is the convective velocity (i.e., the relative velocity between the material and the ALE frame) and $\vec{v}$ the mesh velocity. In the case of $\vec{v} \equiv \vec{u}$, i.e., the mesh is attached to the material, the Lagrangian formulation (Eq. 5) is recovered. On the other hand, when setting $\vec{v} = 0$, we get back the Eulerian formulation (Eq. 3). In between, the mesh velocity $\vec{v}$ can be chosen freely, which can be exploited to being able to track large deformations.

3 Tissue Models

3.1 Prescribed Growth

The development of mechanistic models of tissue growth is challenging and requires detailed knowledge of the gene regulatory network, mechanical properties of the tissue, and its response to physical and biochemical cues. If these are not available but the expansion of the tissue has been described, a phenomenological approach can be used to prescribe the geometry based on observations.

In "prescribed growth models" an initial domain and a spatio-temporal velocity or displacement field are defined. The domain with initial coordinate vectors $\vec{X}$ is then moved according to this velocity field $\vec{u}(\vec{X}, t)$, i.e.,

$$\frac{\partial \vec{X}(t)}{\partial t} = \left. \frac{\partial \vec{x}}{\partial t} \right|_{\vec{X}} = \vec{u}\left(\vec{X}, t\right) \tag{11}$$

3.1.1 Model-Based Displacement Field

The velocity field $\vec{u}\left(\vec{X}, t\right)$ can be captured in a functional form that represents either the observed growth or signaling kinetics. In the simplest implementation the displacement may be applied only normal to the boundary, i.e., $\vec{u} = \mu \vec{n}$, where $\vec{n}$ is the normal vector to the boundary and μ is the local growth rate. We studied such models in the context of organ development and found that the patterning on the developing lung and limb domains depends on the growth speed [3–6].

Growth processes often depend on signaling networks that evolve on the tissue domain. The displacement field $\vec{u}(\vec{X}, t)$ may thus be dependent on the local concentration of some growth or signaling factor. We then have $\vec{u} = \mu(c)\vec{n}$ where c is the local concentration of the signaling factor. These approaches can be readily implemented in the commercially available finite element solver COMSOL Multiphysics; details of the implementation are described in [7, 8]. Figure 4 shows as an example a 2D sheet that deforms within a 3D domain according to the strength of the signaling field normal to its surface, i.e., $\vec{u} = \mu c_1^2 c_2 \vec{n}$,
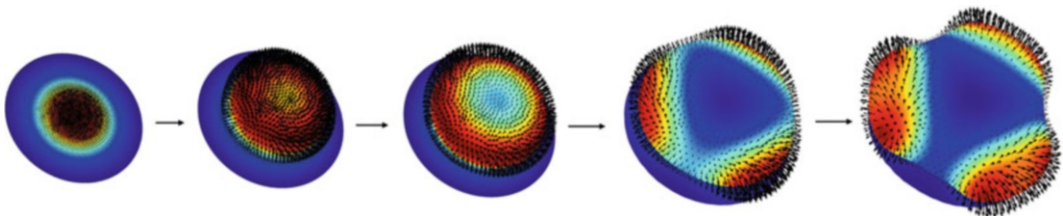

Fig. 4 "Prescribed" domain growth under the control of a signaling model. The deformation of the domain is controlled by a Turing-type signaling model (Eq. 12) according to $\vec{u} = \mu c_1^2 c_2 \vec{n}$. The *red* and *blue* regions denote areas with high and low concentration of $c_1^2 c_2$; the *arrows* denote the velocity field

where c_1 and c_2 are the two variables that are governed by the Schnakenberg-type Turing model:

$$\frac{\partial c_1}{\partial t} + \nabla \cdot \left(c_1 \overrightarrow{u} \right) = \Delta c_1 + \gamma \left(a - c_1 + c_1^2 c_2 \right)$$

$$\frac{\partial c_2}{\partial t} + \nabla \cdot \left(c_2 \overrightarrow{u} \right) = \mathrm{d} \Delta c_2 + \gamma \left(b - c_1^2 c_2 \right) \tag{12}$$

a, b, γ, and d are constant parameters in the Turing model.

3.1.2 Image-Based Displacement Field

The displacement field may also be obtained from experimental data. To obtain the displacement field from data, tissue geometries need to be extracted at sequential time points as shown for lung development in Fig. 5a, b. This requires the following steps: (1) staining of the tissue of interest, (2) imaging of the tissue at distinct developmental time points, (3) image segmentation, (4) meshing of the segmented domain, and (5) warping (morphing) of images at various developmental stages. Subsequently a mathematical regulatory network model can be solved on the deforming physiological domain. In the following we discuss the different steps in detail.
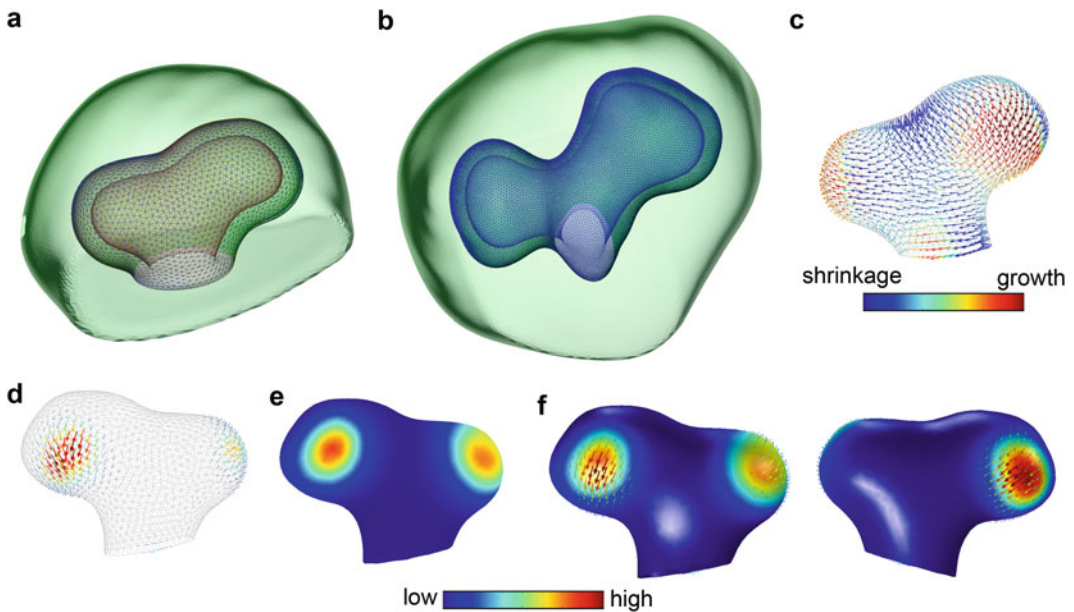

Fig. 5 Image-based displacement fields. (**a** and **b**) The segmented epithelium and mesenchyme of the developing lung at two consecutive stages. (**c**) The displacement field between the two stages in *panels* (**a**) and (**b**). (**d**) The growing part of the lung. The *colored vectors* indicate the strength of the displacement field. (**e**) The solution of the Turing model (Eq. 12) on the segmented lung of the stage in *panel* (**a**). (**f**) Comparison of the simulated Turing model (*solid surface*) and the embryonic displacement field (*arrows*). The image processing was carried out in AMIRA; the simulations were carried out in COMSOL Multiphysics 4.3a. The *panels* in the figure have been reproduced from Menshykau et al., submitted

**3D Image and Meshes
of Tissue**

In the first step we need to obtain 3D imaging data of the tissue of interest. In case different substructures are of interest, the tissue needs to be labeled accordingly. The staining and imaging technique of choice depends on the tissue, the substructure of interest, and the desired resolution. Available techniques have been reviewed in depth before [9].

Once the imaging data has been obtained these need to be processes computationally to obtain the 4D datasets. Several image processing software packages are available to perform these steps, e.g., Amira or Imaris. If multiple image recordings of the organ or the tissue are available at a given stage, then the 3D images can be aligned and averaged. The alignment procedure is a computationally nontrivial problem. In Amira a number of iterative hierarchical optimization algorithms (e.g., QuasiNewton) are available as well as similarity measures (e.g., Euclidean distance) to be minimized. Averaging is subsequently performed by averaging pixel intensities of corresponding pixels in multiple datasets of the same size and resolution. This helps to assess the variability between embryos and identifies common features. It also reduces variability due to experimental handling, but averaging of badly aligned datasets can result in loss of biologically relevant spatial information. It is therefore suggested to run the alignment algorithm several times, starting with different initial positions of the objects, which are to be aligned.

The next step is to perform image segmentation. During image segmentation the digital image is partitioned into multiple subdomains, usually corresponding to anatomic features and gene expression regions. A variety of algorithms are available for image segmentation, most of which are based on differences in pixel intensity.

To carry out finite element method (FEM)-based simulations of the signaling networks, segmented images are subsequently converted into meshes of sufficient quality. The quality of the mesh can be assessed according to the following two parameters: mesh size and the ratio of the sides of the mesh elements. The linear size of the mesh should be much smaller than any feature of interest in the computational solution; that is, if the gradient length scale in the model is 50 μm then the linear size of the mesh should be at least several times less than 50 μm. Additionally, the ratio of the length of the shortest side to the longest side should be 0.1 or more. To confirm the convergence of the simulation, the model must be solved on a series of refined meshes.

**Calculating
the Displacement Field**

To simulate the signaling models on growing domains we need to determine the displacement fields between the different stages. The displacement field between two consecutive stages can be calculated by morphing two subsequent stages onto each other. In other

words we are looking for a function which returns a point on a surface at time $t + \Delta t$ which corresponds to a point on a surface at time t.

The landmark-based Bookstein algorithm [10], which is implemented in Amira, uses paired thin-plate splines to interpolate surfaces over landmarks defined on a pair of surfaces. The landmark points need to be placed by hand on the two 3D geometries to identify corresponding points on the pair of surfaces. The exact shape of the computed warped surface therefore depends on the exact position of landmarks; landmarks must therefore be placed with great care. While various stereoscopic visualization technologies are available this process is time consuming and in parts difficult for complex surfaces such as the epithelium of the embryonic lung or kidney, in particular if the developmental stages are further apart.

Once the correspondence between two surfaces has been defined, a displacement field can be calculated by determining the difference between the positions of points on the two surface meshes as illustrated for the embryonic lung sequence in Fig. 5c; panel d highlights the growing part of the lung.

Simulation of Signaling Dynamics Using FEM

To carry out the FEM-based simulations the mesh and displacement field need to be imported into a FEM solver. To avoid unnecessary interpolation of the vector field, the displacement field should be calculated for exactly the same surface mesh as was used to generate the volume mesh. A number of commercial (COMSOL Multiphysics, Ansis, Abaqus, etc.) and open (Free-FEM, DUNE, etc.) FEM solvers are available. Figure 5e shows the solution of the Schnakenberg Turing model (Eq. 12) on the segmented lung of the stage in panel a. The distribution of the simulated Turing pattern coincides with the embryonic displacement field as shown as arrows (Fig. 5f).

3.2 Continuous Models

In an alternative approach tissue is treated as an incompressible fluid with fluid density ρ, dynamic viscosity μ, internal pressure p, and fluid velocity field $\overrightarrow{u}$. Tissue can then be described by the Navier-Stokes equation:

$$\rho\left(\partial_t \overrightarrow{u} + \left(\nabla \cdot \overrightarrow{u}\right)\overrightarrow{u}\right) = -\nabla p + \mu\left(\Delta \overrightarrow{u} + \frac{1}{3}\nabla\left(\nabla \cdot \overrightarrow{u}\right)\right) + \overrightarrow{f} \quad (13a)$$

$$\rho\nabla \cdot \overrightarrow{u} = \omega S \quad (13b)$$

where ωS denotes the local mass production rate, which is composed of contributions from proliferation, S_{prol}, and increase in cell volume by cell differentiation, S_{diff} (Fig. 6). ω is the molecular mass of cells [kg/mol]. The impact of cell signaling on tissue morphogenesis can be implemented via the source term $S = S_{\mathrm{prol}} + S_{\mathrm{diff}}$ in that S can depend on the local concentration of growth or

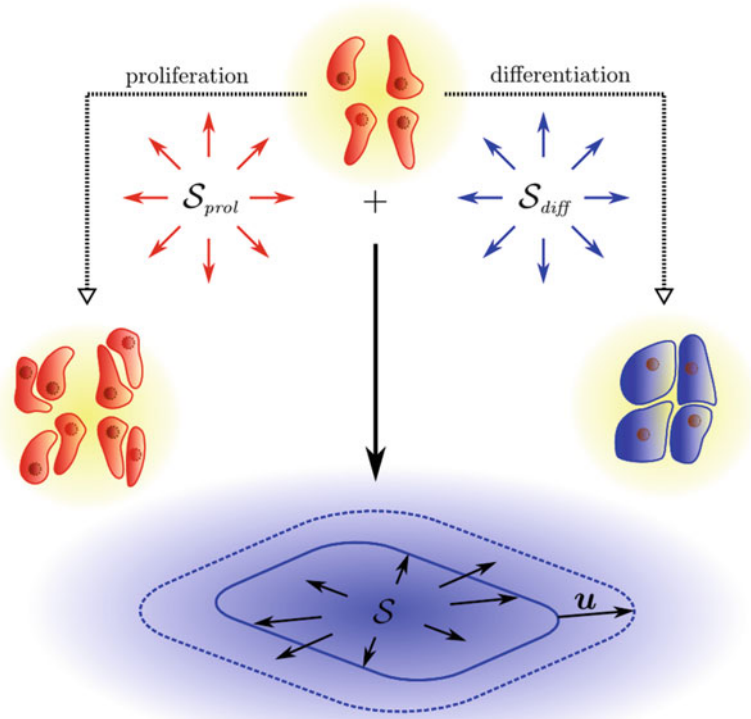**Fig. 6** Tissue as an incompressible fluid. Proliferating cells (shown in *red*) may divide, which is modeled as a local mass source S_{prol} (*left path*). As a result of differentiation, the cells increase in volume and lead to a local mass source S_{diff} (*right path*). Both mechanisms induce a velocity field $\vec{u}$ in the fluid

differentiation factors. $\vec{f}$ denotes the external force density and may, e.g., originate from cellular structures which exert force on the fluid.

The dynamic viscosity μ of embryonic tissue is approximately $\mu \approx 10^4$ Pa s [11], some 10^7-fold higher than for water, and the mass density of the tissue is $\rho \approx 1,000$ Pa s. Using a characteristic reference length L and a characteristic reference speed U, the non-dimensional Reynolds number $\mathrm{Re} = \rho L U / \mu$ is estimated to be of the order 10^{-14} in typical embryonic tissue. The Reynolds number characterizes the relative importance of inertial over viscous forces, whereby the latter are dominant in tissue mechanics. After non-dimensionalization, the Navier-Stokes Eq. (13a) reads (for the now non-dimensional variables $\vec{u}$ and p)

$$\mathrm{Re}\left(\partial_t \vec{u} + \left(\nabla \cdot \vec{u}\right)\vec{u}\right) = -\nabla p + \Delta \vec{u} + \frac{1}{3}\nabla\left(\nabla \cdot \vec{u}\right) \qquad (14)$$

Since Re is very small, the left-hand side of Eq. (14) can be neglected, resulting in the well-known Stokes equation for creeping flow. The Navier-Stokes equations can be numerically solved using

finite difference methods (FDM), finite element methods (FEM), finite volume methods (FVM), spectral methods, particle methods, and Lattice-Boltzmann methods (LBM) [12].

The Navier-Stokes description has been used in simulations of early vertebrate limb development [13], and, in an extended anisotropic formulation, has been applied to Drosophila imaginal disc development [14]. In case of the limb the applicability of an isotropic Navier-Stokes model to tissue growth has been challenged by experimental measurements [15]. To that end Boehm and collaborators determined the proliferation rates inside the limb and used the measured rates as source terms in the isotropic Navier-Stokes tissue model. They then compared the predicted shapes to measured shapes and noticed large discrepancies. They subsequently solved the inverse problem to obtain S from the measured shapes and found that S needed to also take negative values, and that the expansion was larger than expected from the measured proliferation rates. Limb expansion thus must result from anisotropic processes that also involve cell migration from the flank.

3.3   Cell-Based Tissue Models

All approaches described above neglect that tissues are an ensemble of cells. While many effects that result from cell-cell interactions can be described also with continuous differential equations, cell-based tissue models permit a detailed, mechanistic description of the process that relates more easily to the biophysical measurements, and that can help to understand how observed macroscopic properties may emerge from the microscopic interactions. Such cell-based simulations also allow simulations to explore signal readouts on a discrete cell level where receptors can diffuse on the surface of a cell but not between cells.

Most cell-based models are hybrid models that capture the discrete, individual nature of cells and which also include partial differential equations (PDEs) that give a continuous description of signaling pathways or availability of nutrients. These models have the advantage that they integrate biological processes happening on different scales; that is, they describe signaling processes within cells and forces between cells and observe effects on a multicellular level.

There are two general ways for how to define cells: lattice-based approaches where a cell occupies a certain number of lattice entities, e.g., squares or hexagons, and off-lattice approaches where cells can occupy an unconstrained area/volume in the 2D/3D space.

3.3.1   Viscoelastic Cell Model

Elastic cellular components such as the membrane and cell junctions play a key role in the cellular dynamics. The core idea of the viscoelastic cell model, introduced in [16–18], is to divide the viscous and elastic properties and represent these by a viscous fluid and massless elastic structures, respectively. The latter are modeled as elastic networks, which exert forces on the fluid. The fluid, on the other hand, exerts force on the elastic structures, which leads to a
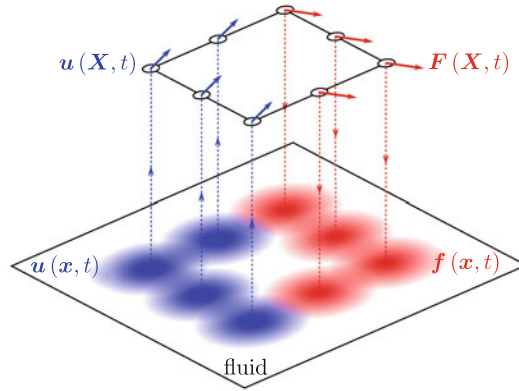
Fig. 7 Immersed boundary method. The geometry is discretized into nodes at positions $\vec{X}$. The force density $\vec{F}(\vec{X}, t)$, hosted by the node, is distributed to the local fluid neighborhood using a delta Dirac kernel function. The nodes are moved according to the local velocity $\vec{u}(\vec{X}, t)$, which is computed from the fluid velocity $\vec{u}(\vec{x}, t)$ using the same kernel function

classic fluid-structure-interaction (FSI) problem. A well-known technique to solve FSI problems is the immersed boundary (IB) method [19], which is illustrated in Fig. 7. The boundary is discretized into computational boundary nodes, which spread the force to their local neighborhood defined by a delta Dirac kernel function. Apart from the forcing term $\vec{f}$ in Eq. (13a), the fluid does not "see" the boundary, which significantly facilitates the numerical solution of the problem. The boundary nodes are subsequently moved in a Lagrangian manner according to the local velocity field.

Although the high computational costs limit this approach to intermediate problem sizes (up to few thousand cells) as compared to continuous cell-density representations and models with rudimentary cell representations, the simulation parameters, e.g., membrane elasticity and interstitial fluid and cytoplasm viscosity, can be inferred directly from biophysical measurements, as opposed to more abstract approaches. The method has been deployed to study, amongst others, tumor growth and ductal carcinoma development [16], growth of the trophoblast bilayer [17], and formation of epithelial hollow acini [20, 21].

3.3.2 Cellular Potts Model

One important example for a lattice-based method is the Monte Carlo-based Cellular Potts Model (CPM) [22], which is implemented in the modeling framework CompuCell3D [23]. CompuCell3D models both cell behavior and signaling dynamics by coupling the CPM module to a PDE module for diffusible signaling factors.

In the CPM framework every cell is represented by a set of lattice sites $\vec{i}$. Cell expansion is represented by an increase of lattice

sites per cell. As one cell expands another cell will shrink by one lattice site. If both cell types represent cells in the tissue the overall tissue size stays constant. Tissue growth can be achieved by introducing one cell type that represents the medium and that subsequently loses lattice sites to the cells in the tissue. Cell movement is achieved by a shift of the cell-specific lattice sites (identified by the cell index $\sigma(\vec{i})$) along the lattice. Each cell belongs to a specified cell type with index $\tau(\sigma(\vec{i}))$. Cells can secret, interact with, and respond to the diffusible signaling factors.

CompuCell3D implements a variant of the Metropolis Monte Carlo method. In every time step of the model, also called Monte Carlo sweep, on average every lattice site can attempt a transition to a different state. Thus in case of N lattice sites, during each sweep N lattice sites $\vec{i}$ and a neighboring lattice site $\vec{j}$ are chosen at random. If the cell indices $\sigma(\vec{i})$ and $\sigma(\vec{j})$ are different then a new configuration is proposed in which the neighboring lattice site becomes part of the originally chosen cell; that is, its cell index changes to $\sigma(\vec{j}) = \sigma(\vec{i})$. Every proposed new configuration is accepted with the probability

$$P = \min\left(1, \exp\left(-\frac{\Delta E}{kT}\right)\right) \qquad (15)$$

This means that proposed moves which lower the energy $(\Delta E < 0)$ are always accepted, while moves, which increase the energy $(\Delta E > 0)$, are accepted with a probability that depends on the energy difference ΔE and the energy-scaling factor kT. The energy of a configuration includes different energy terms, e.g., adhesion is calculated by the sum of the contact energies per unit area $J(\tau, \tau')$, which depends on the cell types that are in contact. In case of cell types with high adhesive forces, represented by low contact energies, cell clusters will emerge as these minimize the overall contact energy (Fig. 8).

The energy scaling factor kT controls how easily energetically unfavorable configurations are accepted. If kT is very large, moves will easily be accepted and the effects of the move on the total energy will not pose much of a constraint. If kT is very low, on the other hand, moves that increase the total energy are very unlikely to be accepted and the system will likely be trapped in a local energy minimum instead of converging to an optimal global energy minimum.

The definition of cells, movement, and growth is rather simplistic in the CPM framework. While this may not be appropriate for all cell-based biological problems, the CPM framework has the great advantage of being relatively easy to implement. It avoids many computational problems of more sophisticated cell-based models, e.g., the boundaries of cells are clearly defined and cells cannot overlap due to the lattice structure.
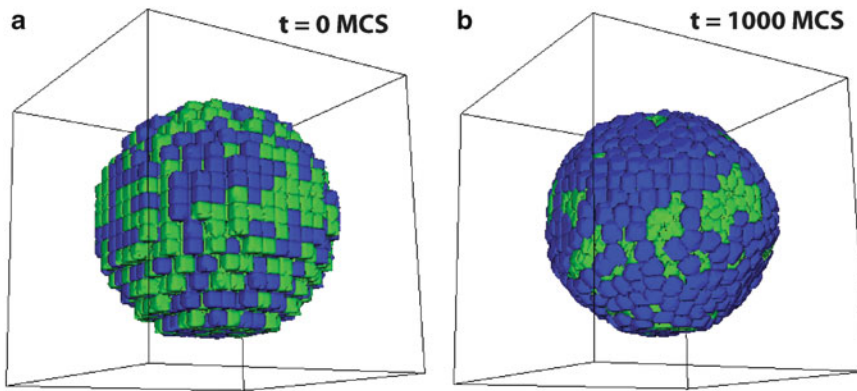
Fig. 8 Cellular Potts model. A typical CPM simulation of cell sorting using CompuCell3D. (**a**) Random initial configuration with two different cell types depicted in *blue* and *green*. Both cell types share the same properties, but the contact energy between cells of the same cell type is lower compared to the contact energy between mixed cell types. (**b**) After 1,000 MCS cells of a given type have clustered together to minimize the total energy, resulting in a patch of *blue* cells on one side of the sphere; the total number of cells per cell type is unchanged

3.3.3 Agent-Based Models

Finally agent-based models can be used when cells take a more active role in moving in the tissue. It is then possible to consider the cells as interacting agents that move according to certain rules and that may serve as sources and sinks for extracellular proteins that then diffuse in the extracellular space. Time delays and nonlinear responses can readily be incorporated. Agent-based cellular automata were originally introduced by John von Neumann and Stanislaw Ulam to study how complex biological behaviors might emerge from simple local rules. While agent-based models offer a great flexibility in encoding many details this comes at a heavy computational cost that limits the number of agents (cells) that can typically be followed. Agent-based models have been particularly popular in immunology where many behaviors depend on small cohorts of individual cells rather than tissues [24]. We have previously used agent-based models to model the germinal center reaction during an immune response with some 10,000 cells [25]. Parallel computing now permits the simulation of much larger systems and agent-based methods are also used in simulating morphogenetic processes during development [26].

Acknowledgment

References

1. Iber D, Zeller R (2012) Making sense-data-based simulations of vertebrate limb development. Curr Opin Genet Dev 22:570–577

2. Donea J, Huerta A, Ponthot J, Rodriguez-Ferran A (2004) Arbitrary Lagrangian-Eulerian methods. In: Encyclopedia of computational mechanics. Wiley, New York, pp 1–38

3. Probst S, Kraemer C, Demougin P, Sheth R, Martin GR, Shiratori H, Hamada H, Iber D, Zeller R, Zuniga A (2011) SHH propagates distal limb bud development by enhancing CYP26B1-mediated retinoic acid clearance via AER-FGF signalling. Development 138:1913–1923

4. Menshykau D, Kraemer C, Iber D (2012) Branch mode selection during early lung development. PLoS Comput Biol 8:e1002377

5. Cellière G, Menshykau D, Iber D (2012) Simulations demonstrate a simple network to be sufficient to control branch point selection, smooth muscle and vasculature formation during lung branching morphogenesis. Biol Open 1:775–788

6. Badugu A, Kraemer C, Germann P, Menshykau D, Iber D (2012) Digit patterning during limb development as a result of the BMP-receptor interaction. Sci Rep 2:991

7. Germann P, Menshykau D, Tanaka S, Iber D (2011) Simulating organogenesis in COMSOL. Proceedings of COMSOL conference, pp 1–5

8. Menshykau D, Iber D (2012) Simulation organogenesis in COMSOL: deforming and interacting domains. Proceedings of COMSOL conference, Milan

9. Gregg CL, Butcher JT (2012) Quantitative in vivo imaging of embryonic development: opportunities and challenges. Differentiation 84:149–162

10. Bookstein FL (1989) Principal warps: thin-plate splines and the decomposition of deformations. IEEE Trans Pattern Anal Mach Intell 11:567–585

11. Forgacs G, Foty RA, Shafrir Y, Steinberg MS (1998) Viscoelastic properties of living embryonic tissues: a quantitative study. Biophys J 74:2227–2234

12. Chen S, Doolen GD (1998) Lattice Boltzmann methods for fluid flows. Annu Rev Fluid Mech 30:329–364

13. Dillon R, Gadgil C, Othmer HG (2003) Short- and long-range effects of Sonic hedgehog in limb development. Proc Natl Acad Sci U S A 100:10152–10157

14. Bittig T, Wartlick O, Kicheva A, González-Gaitán M, Jülicher F (2008) Dynamics of anisotropic tissue growth. New J Phys 10:063001

15. Boehm B, Westerberg H, Lesnicar-Pucko G, Raja S, Rautschka M, Cotterell J, Swoger J, Sharpe J (2010) The role of spatially controlled cell proliferation in limb bud morphogenesis. PLoS Biol 8:e1000420

16. Dillon R, Owen M, Painter K (2000) A single-cell-based model of multicellular growth using the immersed boundary method. Contemporary Mathematics 466:1–15

17. Rejniak KA, Kliman HJ, Fauci LJ (2004) A computational model of the mechanics of growth of the villous trophoblast bilayer. Bull Math Biol 66:199–232

18. Rejniak KA (2007) An immersed boundary framework for modelling the growth of individual cells: an application to the early tumour development. J Theor Biol 247:186–204

19. Peskin CS (2002) The immersed boundary method. Acta Numerica. 11:479–517

20. Rejniak KA, Anderson AR (2008) A computational study of the development of epithelial acini: I. Sufficient conditions for the formation of a hollow structure. Bull Math Biol 70:677–712

21. Rejniak KA, Anderson AR (2008) A computational study of the development of epithelial acini: II. Necessary conditions for structure and lumen stability. Bull Math Biol 70:1450–1479

22. Graner F, Glazier J (1992) Simulation of biological cell sorting using a two-dimensional extended Potts model. Phys Rev Lett 69:2013–2016

23. Izaguirre JA, Chaturvedi R, Huang C et al (2004) CompuCell, a multi-model framework for simulation of morphogenesis. Bioinformatics (Oxford, England) 20:1129–1137

24. Bauer AL, Beauchemin CAA, Perelson AS (2008) Agent-based modeling of host-pathogen systems: the successes and challenges. Inf Sci 179:1379–1389

25. Meyer-Hermann ME, Maini PK, Iber D (2006) An analysis of B cell selection mechanisms in germinal centers. Math Med Biol 23:255–277

26. Thorne BC, Bailey AM, DeSimone DW, Peirce SM (2007) Agent-based modeling of multicell morphogenic processes during development. Birth Defects Res C Embryo Today 81:344–353

Chapter 22

Elasticity-Based Targeted Growth Models of Morphogenesis

Patrick W. Alford

Abstract

Embryonic tissue mechanics play an important role in regulating morphogenesis during organ formation, both in a bottom-up sense, where changes in gene expression drive mechanical shape changes, and in a top-down sense, where perturbations in tissue mechanics feed back to drive changes in gene expression. In growing tissues that can generate internal forces and have complex geometries, like those in the embryo, it can often be difficult to empirically determine the mechanical state of the tissue, let alone the relationships between gene expression and mechanical behavior. Mathematical models can be used to fill this gap. Here, we discuss elasticity-based models for growing tissues with a specific focus on targeted growth in embryonic tissues.

Key words Growth, Remodeling, Morphogenesis, Elasticity

1 Introduction

Mechanical forces have long been understood to play a key role in embryo morphogenesis. Large shape changes that occur during organogenesis are generated entirely by the cells in the embryo, so mechanical behavior of those cells must be tightly regulated to yield the appropriate tissue architecture. Further, numerous experiments, in which embryonic tissues are cut or portions are removed, have suggested that the cells adaptively respond to a loss of tension to return the tissue to some mechanical equilibrium [1–3]. More recently, it has also been shown that the mechanical environment can affect differentiation of progenitor cells [4] and phenotype expression of differentiated cells [5]. Taken together, these results suggest that mechano-adaptation, i.e. the process by which cells sense and refine their mechanical environment, plays a defining role in morphogenesis necessary to form organs.

To truly understand the interaction between tissue mechanics, gene expression, and mechano-adaptive feedback, it is first necessary to know the stresses in the tissue. However, for nonlinear materials that generate force internally, such as embryonic tissues,

this is not as straight forward as measuring the strain and using Hooke's Law, as might be done with traditional engineering materials. Thus, it is necessary to develop computational models that can be used in concert with experimental data to determine the full stress state of the tissue.

Though tissue stresses can be informative, the true goal of the biomechanician is to determine the mechanisms by which the stress is produced, the stimulus for this stress production, and the resulting change in cellular behavior as a result of the stress. Computational models can also be used to determine governing laws for mechano-adaptation, providing insight into the role mechanics play in regulating biological processes and driving morphogenesis.

In recent years, many mathematical models aiming to explain shape changes and pattern formation phenomena in embryos have been proposed. Many of these focus on modeling individual cells [6, 7] to capture the mechanics of cellular reorganization, while others model each cytoskeletal component, representing the cells or tissue as a network of springs and dashpots [8, 9]. In this chapter, we will not discuss these discrete models, but will instead focus on continuum models for morphogenesis. A variety of innovative continuum models have been proposed [10–12]. Here, we will primarily discuss models using elasticity-based nonlinear volumetric growth theory and targeted growth theory, with applications in basic morphogenesis.

2   Theory

To model the evolving stress and strain in morphogenesis, we will use a large-deformation, nonlinear elasticity approach. This assumes that the length scale of interest is large compared to its discrete components and the material can be considered a continuum. Thus, for our applications, the tissue is treated as a uniform material, not a set of discrete cells. To solve any elasticity problem, it is necessary to determine the strain-displacement relations, the relationship between stress and strain, known as the constitutive relations, and force equilibrium. Here, we will briefly describe the basics of this approach and how it must be modified to accommodate tissue growth, primarily by modifying the strain-displacement and constitutive relations.

2.1   Elasticity of Non-growing Bodies

In this section, we will very briefly summarize the key concepts of nonlinear elasticity necessary for the growth models presented in the following section. For a more complete description of nonlinear elasticity, the reader is referred to the excellent texts of Taber [13] and Holzapfel [14].

Suppose a body B undergoes some deformation, composed of a combination of translation, rotation, stretching, and shearing,
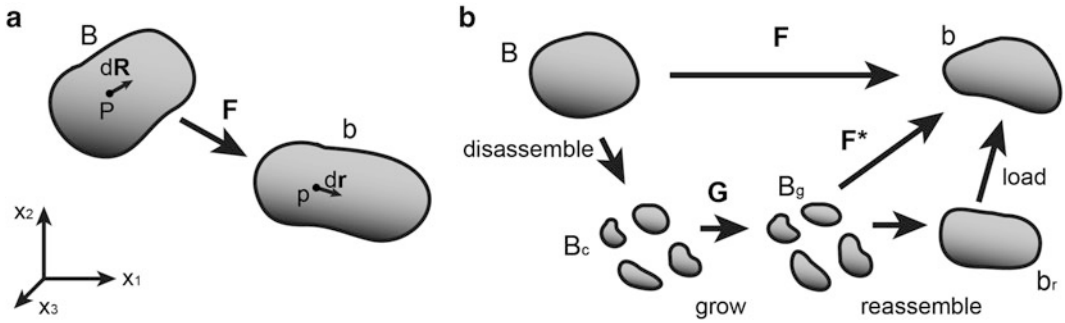
Fig. 1 Schematic representation of deformation in (**a**) non-growing and (**b**) growing bodies

resulting in the body b (Fig. 1). There exists a differential vector d**R** located at point P in B, which, following the deformation, is transformed into d**r**, located at point p in b. The tensor that fully describes the deformation of d**R** into d**r** is the deformation gradient tensor **F**, defined as

$$\boldsymbol{F} \cdot \mathrm{d}\boldsymbol{R} = \mathrm{d}\boldsymbol{r}. \tag{1}$$

In a non-growing body, one can assume one-to-one point mapping, meaning for every point P and vector d**R** in B, there exists a single point p and d**r** in b and a unique **F** that describes their deformation. Green strain, i.e. strain with respect to the reference undeformed body B, is given by

$$\boldsymbol{E} = \frac{1}{2}\left(\boldsymbol{F}^T \cdot \boldsymbol{F} - \boldsymbol{I}\right) = \frac{1}{2}(\boldsymbol{C} - \boldsymbol{I}) \tag{2}$$

where **C** is the right Cauchy-Green tensor, defined as $\boldsymbol{C} = \boldsymbol{F}^T \cdot \boldsymbol{F}$.

The relationship between stress and strain is defined by the strain-energy density function, W. Normally, W must be determined empirically for the material being deformed. If W is known, for a non-growing body, the Cauchy stress tensor (true stress) **σ** is given by

$$\boldsymbol{\sigma} = \frac{1}{J}\boldsymbol{F} \cdot \frac{\partial W}{\partial \boldsymbol{E}} \cdot \boldsymbol{F}^T = \frac{1}{J}\boldsymbol{F} \cdot \frac{\partial W}{\partial \boldsymbol{C}} \cdot \boldsymbol{F}^T, \tag{3}$$

where $J = \det(\boldsymbol{F})$ is the change in volume during deformation.

Finally, by Newton's second Law, every point p in the body b must be in force equilibrium, given by

$$\overline{\nabla} \cdot \boldsymbol{\sigma} + \boldsymbol{f} = \rho\boldsymbol{a}, \tag{4}$$

where $\overline{\nabla}$ is the gradient operator with respect to the deformed reference frame, **f** is the local body force, ρ is the material density, and **a** is the acceleration. For most problems in development, deformation is relatively slow and body forces, such as gravity, can be ignored, so equilibrium can be given by the simplified expression

$$\overline{\nabla} \cdot \boldsymbol{\sigma} = 0. \tag{5}$$

2.2 Elasticity of Growing Bodies

In a growing body, the one-to-one mapping assumption made above does not hold, since through biological processes, such as cell proliferation or ECM production, mass can be created within the body. To account for this, Rodriguez et al. [15] developed a formulation in which deformation is considered in two distinct steps; a growth deformation, where volume is added or subtracted from the material, and an elastic deformation, where mechanical loads cause shape change, as detailed above.

Figure 1b demonstrates how this two-step process can be modeled. Let B be the stress-free growth-free body and b be the deformed and grown body. The total observable deformation from B to b is given by F. However, we can define intermediate states in the deformation that parse deformation due to growth from deformation due to mechanical load. Suppose that the body B is disassembled into infinitesimally small pieces to give body B_c, in which each piece is still unconstrained and stress free. (In the case of a tissue, these could be individual cells or cytoskeletal components.) Next, each piece undergoes some volumetric growth, characterized by the growth tensor G. Because each piece is unconstrained, after growth, each is still stress-free. However, when the pieces are reassembled, giving body b_r, differential growth between the pieces would require a deformation be applied to fit the pieces together. This reassembly deformation can result in a stress, even when there is no external load. This load-free stress is known as residual stress. Additional loads due to external forces or boundary conditions transform b_r into b. The deformation F^*, from the grown zero-stress configuration B_g to the final configuration b is the combination of the deformation due to external loads and the post-growth reassembly and is called the elastic deformation.

The elastic deformation is a function of both the observed deformation and the growth deformation and is given by

$$F^* = F \cdot G^{-1}, \qquad (6)$$

and the elastic Green strain, or strain with respect to the post-growth zero-stress configuration (B_g, Fig. 1a) is given by

$$E^* = \frac{1}{2}(C^* - I), \qquad (7)$$

where

$$C^* = F^{*T} \cdot F^* = G^{-T} \cdot C \cdot G^{-1}. \qquad (8)$$

Stress in the growing body is a function of elastic deformation, such that

$$\sigma = \frac{2}{J^*} F^* \cdot \frac{\partial W}{\partial C^*} \cdot F^{*T}. \qquad (9)$$

Therefore, the stress in the body is now a function of both the deformation applied by the body's surroundings and the deformation generated internally by growth. Equilibrium in the growing body is determined as in the non-growing body (Eqs. 4 and 5).

3   Application

3.1 Applying Growth Theory to Basic Tissue Morphogenesis

As an example of this growth theory, we will demonstrate how it can be employed to study basic shape change in tissue sheets. Let the tissue be an initially unbent, plane strain beam, whose x_1-axis is oriented along its length and x_2-axis is oriented through the beam's thickness (Fig. 2). The tissue is initially 100 μm long and 2.5 μm thick. The beam is fixed at both ends, so that the ends cannot move in the x_1 direction. The strain-energy density function is given by a modified Neo-Hookean description,

$$W = \frac{\mu}{2}\left(I_1^* - 3\right) - \mu \log(J^*) + \frac{\nu\mu}{1-2\mu}\log\left(J^*\right)^2, \qquad (10)$$

where μ is the shear modulus, ν is the Poisson's ratio, $J^* = \det(\boldsymbol{F}^*)$ and I_1^* is the first strain invariant of the elastic deformation, given by

$$I_1^* = \mathrm{tr}(\boldsymbol{C}^*). \qquad (11)$$

For all models presented in this chapter, μ and ν are given by 50 kPa and 0.45, respectively. Note: Embryonic tissues are both nonlinear [16] and viscoelastic [17], so a simple Neo-Hookean model is unlikely to be appropriate for most morphogenesis problems. The appropriate strain-energy density function will vary by tissue.
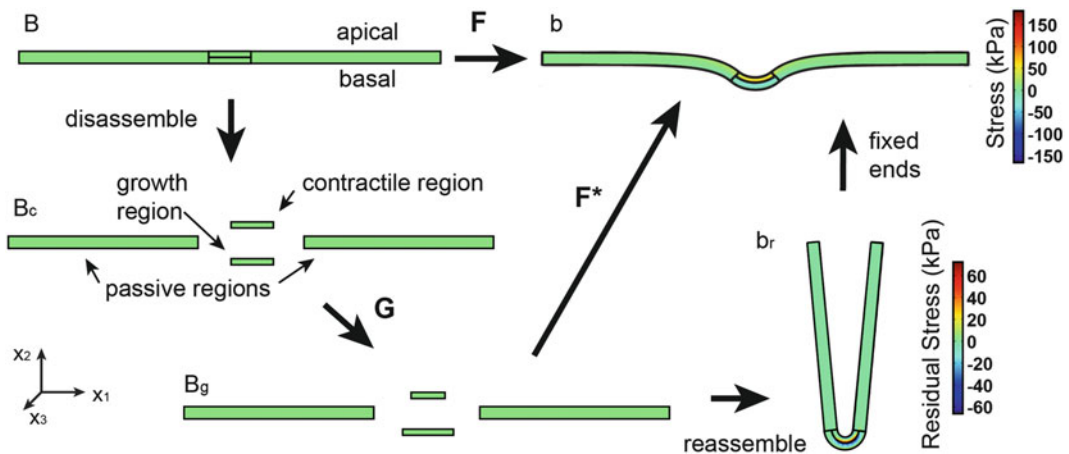

Fig. 2 Schematic representation of deformation in a tissue sheet. The tissue is represented initially as a straight beam. Differential growth in the central region, combined with fixed-end boundary conditions, results in an invagination

The tissue is subdivided into four regions (Fig. 2); two initially passive regions, one central basal growing region, and one central apical contracting region. The two central regions are each 10 µm long and half the tissue height.

We assume that all growth occurs only in the x_1-direction, such that

$$\boldsymbol{G} = \mathrm{diag}\big[\lambda_\mathrm{g}, 1, 1\big], \tag{12}$$

where λ_g is defined as the growth stretch ratio and characterizes the zero-stress change in length in the x_1-direction due to growth. In the two passive outer regions, $\lambda_\mathrm{g} = 1$, in the apical inner region, contraction is represented by negative growth, or shortening, given by $\lambda_\mathrm{g} = 0.8$, and in the basal inner region $\lambda_\mathrm{g} = 1.2$. If the four regions are disassembled (B_c) and the growth is applied to the central regions, those regions grow shorter or longer, according to the assigned λ_g, but their stress remains zero (B_g, Fig. 2). When the pieces are reassembled, the apical shortening and basal growth cause the central region to bend and generate residual stress at the junction between the two layers (b_r, Fig. 2). In b_r, the passive tissue is displaced but still predominantly stress free. Finally, the fixed-end boundary conditions are applied, limiting the bending in the central region and resulting in increased stress in all regions. The result is shape change and stress generated entirely by internal forces. In this simple case, local apical construction and basal expansion yields a shape change akin to initial stages of invagination.

Additional prescribed growth can drive further shape changes. Suppose that, following the invagination initiation in Fig. 2, the two central regions maintain their growth profiles, while the initially passive outer regions begin to grow uniformly longer in the x_1 direction (Fig. 3). Due to the initial bias caused by the central region differential growth, the growth does not result in simple compression, but instead induces the sheet to fold further (Fig. 3a, b). During the folding the stress in the tissue sheet will also evolve (Fig. 3c, d). For example, in this case, the stress on the basal surface of the tissue in the initially passive regions starts in tension, following the initial invagination, but goes into compression with increasing growth, while increased growth in the outer regions allows the central region to more closely approximate the load-free residual stress in b_r (Fig. 2). This prescribed growth approach can be a powerful tool when used in correlation with observed tissue deformation to determine the stresses in embryonic tissues with complex architectures [18–20].

3.2 Targeted Growth

Though prescribed growth can generate shape changes seen during development, the theory does not capture the adaptive nature of embryonic tissues. Regeneration of form and function following incision in or removal of tissue suggests that the tissue is not simply
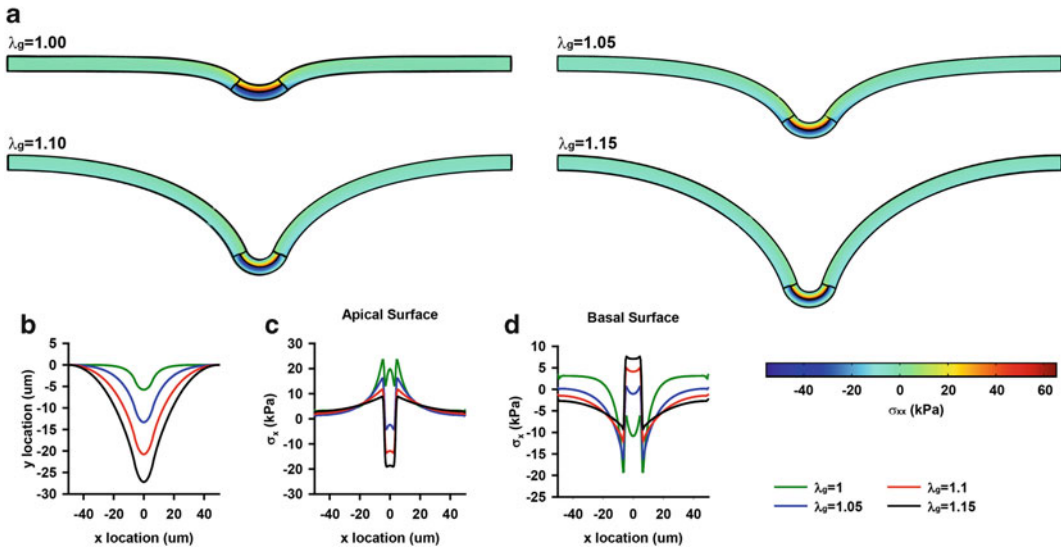
Fig. 3 Prescribed growth model of sheet folding. (**a**) After the initial differential growth-induced bending (Fig. 2), uniform growth (indicated by λ_g value) in the outer regions causes sheet folding. (**b**) Lateral tissue displacement as a function of location. (**c**) Cauchy stress (σ_{11} component) on the apical surface of the tissue. (**d**) Cauchy stress on the basal surface of the tissue

growing a prescribed amount, but is actively responding to it stress state. Targeted growth models suppose that we can define physical laws that describe how tissue growth behavior is both influenced and directed by mechanical environment.

Fung hypothesized that all tissues have one or more homeostatic stress states and that perturbation away from these stresses causes the tissue to grow and remodel to bring the tissue back to homeostasis [21]. Fung proposed that this mechano-adaptive growth could be characterized with a stress-dependent growth law with the form

$$\frac{\dot{\lambda}_g}{\lambda_g} = c(\sigma - \overline{\sigma}_1)^{k_1}(\sigma - \overline{\sigma}_2)^{k_2}(\sigma - \overline{\sigma}_3)^{k_3}, \tag{13}$$

where $\dot{\lambda}_g = \frac{\partial \lambda_g}{\partial t}$ is the time derivative of the growth stretch ratio, c, k_1, k_2, and k_3 are constants, and $\overline{\sigma}_1$, $\overline{\sigma}_2$, and $\overline{\sigma}_3$ are the target stresses at which the tissue is in homeostasis. Subsequent researchers have simplified this law to a linear relationship given by [12]

$$\frac{\dot{\lambda}_g}{\lambda_g} = \frac{1}{T}(\sigma - \overline{\sigma}), \tag{14}$$

where T is a constant that characterizes the rate of the adaptive growth. This law prescribes that in regions where the tissue stress is greater than the target stress, $\dot{\lambda}_g$ will be greater than zero and the tissue will grow longer, by cell proliferation, convergent extension, etc., in order to decrease the strain on each individual cell.
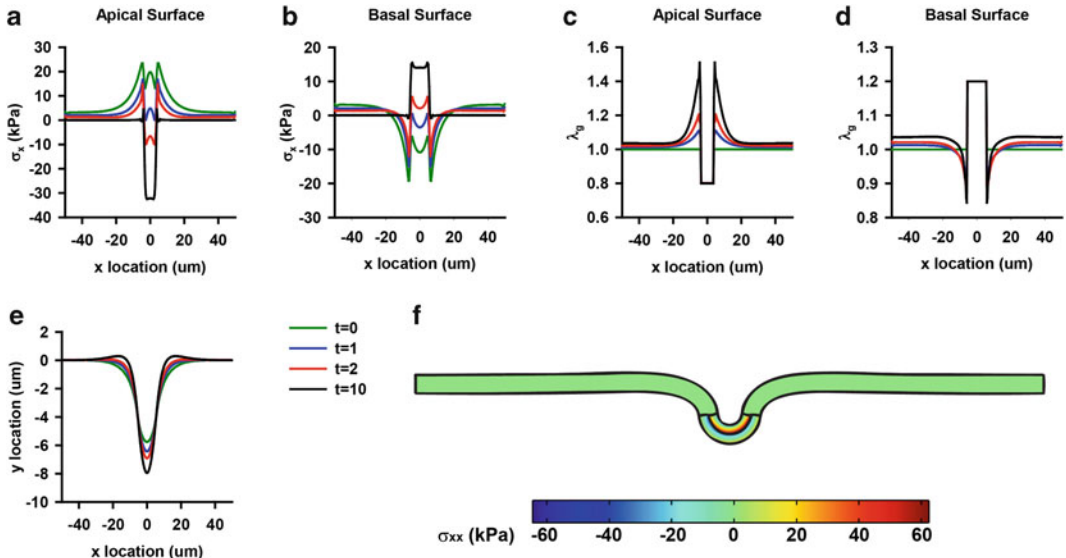
Fig. 4 Targeted growth model of sheet folding and invagination. (**a** and **b**) Cauchy stress on (**a**) apical and (**b**) basal surfaces of the tissue. (**c** and **d**) Stress-induced growth (λ_g) on the (**c**) apical and (**d**) basal surfaces of the tissue. (**e**) Lateral tissue displacement as a function of location. (**f**) Final equilibrium tissue geometry

In regions where the stress is below the target stress, $\dot{\lambda}_g$ will be negative and the tissue will grow shorter, via cytoskeletal contraction, apoptosis, etc., increasing the stress back to homeostasis.

Figure 4 demonstrates how targeted growth, following the initial invagination depicted in Fig. 2, can result in more local shape change than the globally prescribed growth in the previous section. After the initial central differential growth, we assume that the two central regions maintain their growth profiles, while the two initially passive regions undergo targeted growth, with the stress that influences growth being the σ_{11} component of the Cauchy stress tensor, i.e. the force in the x_1-direction on the face perpendicular to the x_1-direction in the undeformed body. Let $\bar{\sigma} = 0$ and $T = 2e5$ Pa $\cdot$ t (where t is unitless time). At time $t = 0$, nearest the central region, the stress on the apical side of the tissue is greater than the target stress (Fig. 4a), while the stress on the basal side is lower than the target stress (Fig. 4b). This stress mismatch induces differential growth, with the apical region near the central region growing longer ($\lambda_g > 1$) and the basal region growing shorter ($\lambda_g < 1$), which results in local bending of the tissue (Fig. 4c, f). With time, the stress in the responsive regions reaches the target stress and the tissue returns to equilibrium (Fig. 4a, b). In the example shown here, this targeted growth results in local bending, with the initial small central bending progressing toward an invagination (Fig. 4f).

This targeted growth method has been used to successfully model a number of biological growth problems, including cardio-vascular adaptation [22, 23], tumor growth [24, 25], and skin growth [26].

3.3 Moving the Target

The targeted growth model presented above has proven particularly useful for modeling mature tissues, where it is reasonable to assume that the tissue has an absolute, non-evolving target stress [22, 23, 27]. In embryos, however, gene and protein expression are rapidly changing, suggesting that the target stress may also be changing. Recently, additional growth laws, which take into account the evolving cell population, have been considered. Here, we will briefly discuss these more advanced methods.

Hyper-Restoration. Based on meticulous experiments perturbing the stress in embryonic tissue mid-development, Beloussov and colleagues hypothesized that changes in tissue stress can induce changes in target stress [2, 28–31]. More specifically, they hypothesized that if the stress in a developing tissue is perturbed, the cells in the tissue respond to restore it, but overshoot in their response. This overshoot subsequently induces a stress in the surrounding tissue, to which it responds (and overshoots). Belousov termed this behavior hyper-restoration and posited that it is a primary player in mechanically-mediated morphogenesis.

Recently, Taber formalized Belousov's theory by incorporating it into the growth theory presented above with an additional equation that gives the rate of change of the target stress as a function of tissue stress, such that [32, 33]

$$\dot{\bar{\sigma}} = -a(\sigma - \bar{\sigma}), \tag{15}$$

where $\dot{\bar{\sigma}}$ is the rate of change of the target stress and a is a positive constant. By tying target stress evolution to stress perturbation, this theory captures the hypothesized stress overshoot and mimics the embryonic shape changes observed by Beloussov and others [32], However, the complex spatially and temporally evolving target stress is difficult to empirically verify.

Phenotype-Dependent Growth. It stands to reason, that if the target stress is to change, it would do so through measurable gene and protein expression changes. So, while the target stress is itself difficult to measure, it may be possible to indirectly determine the target stress using cell phenotype expression.

We have recently developed a model for phenotype-dependent growth, wherein the phenotype distribution of the cells populating a tissue is dependent on the stress [34] and the growth behavior is dependent on the phenotype distribution. For example, suppose there are two phenotypes that a cell might take on, each with a distinct growth rate (T, Eq. 12) and target stress, and that the likelihood of the cell switching from phenotype A to phenotype B

increases with a greater perturbation away from the target stress. This relation could be characterized by stress-dependent phenotype laws, such as

$$\dot{\phi}_A = -a|\sigma - \overline{\sigma}_A| \text{ and } \phi_A + \phi_B = 1, \tag{16}$$

where ϕ_i is the fraction of cells of phenotype i, $\dot{\phi}_i$ is the rate of change of the fraction of the cells of phenotype i, and a is a positive constant.

One can imagine the target stress evolving with the embryo as the cells mature through stress-induced phenotype switching from pluripotent to terminally differentiated. Following some phenotype switches, the target stress might change in such a way that the overshoot observed by Beloussov could occur, while other switches could lead tissues to a homeostatic stress, indicative of mature tissue. Though this model has, as yet, not been employed for studies of embryonic morphogenesis, it has been used to model simple engineered vascular tissue adaptation to acute stress. In this case, protein and RNA expression were used to validate the model and suggest that the model assumptions are valid [34]. This simple model system suggests that a similar approach could be successfully used to study the relationships between tissue stress and phenotypic maturation during development.

4   Perspectives

Here, we have presented several elasticity-based targeted growth models, a small subset of the mathematical modeling techniques that have been employed to study morphogenesis in embryos. These models have been used to provide significant insight into the mechanics of embryonic tissues as well as a platform for testing provocative hypotheses connecting tissue stress and shape change. Current targeted growth models primarily assume a fairly direct relationship between stress perturbation and growth response. However, these physical growth laws often downplay the complexity of biological processes. Some recent models, such as the hyper-restoration and phenotype-dependent models presented here, portend the next step in tissue growth modeling by providing a framework for connecting cell signaling and gene expression to physical shape change. This next generation of models promises to be a useful tool for understanding the role of mechanics in embryogenesis.

5   Notes

All models presented here were developed using COMSOL Multi-physics 4.2 finite element software. Actual implementation of the growth in COMSOL requires some additional details beyond those

presented in the main text. In COMSOL, the stress calculated as a function of the strain energy density is the second Piola-Kirchoff stress s, defined as

$$s = \frac{1}{J} F^{-1} \cdot \sigma \cdot F^{-T};   \tag{17}$$

thus, within COMSOL, it is the second Piola-Kirchoff equation that must be manipulated, as in Eq. 9, such that

$$s = 2 \frac{J}{J^*} \frac{\partial W}{\partial C}.   \tag{18}$$

The software then calculates Cauchy stress and solves for equilibrium using this modified stress formulation. *See* refs. 23, 32 for additional details.

In addition, stresses calculated within COMSOL are with respect to the global reference frame, so rotation of the element will yield changes in the normal stresses reported. Since the stress of interest in our example problem is the one initially oriented along the tissue length and orientation of the tissue rotates significantly during growth (*see* Fig. 4e, f), the stress must be rotated into the new orientation. If stress in the global reference frame is given by σ_g and the tissue has rotated into a deformed reference frame given by $(x_{1'}, x_{2'}, x_{3'})$, then the stress component $\sigma_{1'1'}$ is given by

$$\sigma_{1'1'} = e_{1'} \cdot \sigma_g \cdot e_{1'}   \tag{19}$$

where $e_{1'}$ is the unit vector parallel to the $x_{1'}$ axis, which can be found by

$$e_{1'} = \frac{F \cdot e_1}{|F \cdot e_1|}   \tag{20}$$

where e_1 is the unit vector parallel to the global x_1-axis. This $\sigma_{1'1'}$ stress is the stress used for the targeted growth in Eq. 14.

References

1. Moore AR, Burt AS (1939) On the locus and nature of the forces causing gastrulation in the embryos of *Dendraster excentricus*. J Exp Zool 82(1):159–171

2. Beloussov LV, Lakirev AV, Naumidi II, Novoselov VV (1990) Effects of relaxation of mechanical tensions upon the early morphogenesis of *Xenopus laevis* embryos. Int J Dev Biol 34(4):409–419

3. Latacha KS et al (2005) Role of actin polymerization in bending of the early heart tube. Dev Dyn 233(4):1272–1286

4. Engler AJ, Sen S, Sweeney HL, Discher DE (2006) Matrix elasticity directs stem cell lineage specification. Cell 126(4):677–689

5. Peyton SR, Kim PD, Ghajar CM, Seliktar D, Putnam AJ (2008) The effects of matrix stiffness and RhoA on the phenotypic plasticity of smooth muscle cells in a 3-D biosynthetic hydrogel system. Biomaterials 29 (17):2597–2607

6. Chen HH, Brodland GW (2000) Cell-level finite element studies of viscous cells in planar aggregates. J Biomech Eng 122(4):394–401

7. Drasdo D, Loeffler M (2001) Individual-based models to growth and folding in one-layered tissues: intestinal crypts and early development. Nonlinear Anal 47(1):245–256

8. Odell GM, Oster G, Alberch P, Burnside B (1981) The mechanical basis of morphogenesis. 1. Epithelial folding and invagination. Dev Biol 85(2):446–462

9. Ingber DE (2003) Tensegrity I. Cell structure and hierarchical systems biology. J Cell Sci 116 (7):1157–1173

10. Ambrosi D et al (2011) Perspectives on biological growth and remodeling. J Mech Phys Solids 59(4):863–883

11. Munoz JJ, Conte V, Miodownik M (2010) Stress dependent morphogenesis: continuum mechanics and system of trusses. In: Koppel A, Oja J (eds) Continuum mechanics. Nova Publishers, Hauppauge, pp 223–243

12. Taber LA (1998) Biomechanical growth laws for muscle tissue. J Theor Biol 193 (2):201–213

13. Taber LA (2004) Nonlinear theory of elasticity: applications in biomechanics. World Scientific Pub, London, 416

14. Holzapfel GA (2000) Nonlinear solid mechanics: a continuum approach for engineering. Wiley, London

15. Rodriguez EK, Hoger A, McCulloch AD (1994) Stress-dependent finite growth in soft elastic tissues. J Biomech 27(4):455–467

16. Zamir EA, Taber LA (2004) Material properties and residual stress in the stage 12 chick heart during cardiac looping. J Biomech Eng 126(6):823–830

17. von Dassow M, Strother JA, Davidson LA (2010) Surprisingly simple mechanical behavior of a complex embryonic tissue. PLoS One 5 (12)

18. Voronov DA, Alford PW, Xu G, Taber LA (2004) The role of mechanical forces during dextral rotation during cardiac looping in the chick embryo. Dev Biol 272(2):339–350

19. Varner VD, Voronov DA, Taber LA (2010) Mechanics of head fold formation: investigating tissue-level forces during early development. Development 137(22):3801–3811

20. Ramasubramanian A et al (2013) On the role of intrinsic and extrinsic forces in early cardiac s-looping. Dev Dyn 242(7):801–816

21. Fung YC (1991) What are the residual stresses doing in our blood vessels? Ann Biomed Eng 19(3):237–249

22. Alford PW, Humphrey JD, Taber LA (2008) Growth and remodeling in a thick-walled artery model: effects of spatial variations in wall constituents. Biomech Model Mechanobiol 7(4):245–262

23. Alford PW, Taber LA (2008) Computational study of growth and remodelling in the aortic arch. Comput Methods Biomech Biomed Engin 11(5):525–538

24. Tracqui P (2009) Biophysical models of tumour growth. Rep Prog Phys 72(5)

25. Stylianopoulos T et al (2012) Causes, consequences, and remedies for growth-induced solid stress in murine and human tumors. Proc Natl Acad Sci U S A 109 (38):15101–15108

26. Tepole AB, Ploch CJ, Wong J, Gosain AK, Kuhl E (2011) Growing skin: a computational model for skin expansion in reconstructive surgery. J Mech Phys Solids 59(10):2177–2190

27. Gleason RL, Taber LA, Humphrey JD (2004) A 2-D model of flow-induced alterations in the geometry, structure, and properties of carotid arteries. J Biomech Eng 126(3):371–381

28. Beloussov LV, Dorfman JG, Cherdantzev VG (1975) Mechanical stresses and morphological patterns in amphibian embryos. J Embryol Exp Morphol 34(3):559–574

29. Belintsev BN, Beloussov LV, Zaraisky AG (1987) Model of pattern formation in epithelial morphogenesis. J Theor Biol 129 (4):369–394

30. Beloussov LV, Saveliev SV, Naumidi II, Novoselov VV (1994) Mechanical stresses in embryonic tissues: patterns, morphogenetic role, and involvement in regulatory feedback. Int Rev Cytol 150:1–34

31. Beloussov LV, Louchinskaia NN, Stein AA (2000) Tension-dependent collective cell movements in the early gastrula ectoderm of *Xenopus laevis* embryos. Dev Genes Evol 210 (2):92–104

32. Taber LA (2008) Theoretical study of Beloussov's hyper-restoration hypothesis for mechanical regulation of morphogenesis. Biomech Model Mechanobiol 7(6):427–441

33. Taber LA (2009) Towards a unified theory for morphomechanics. Philos Trans A Math Phys Eng Sci 367(1902):3555–3583

34. Alford PW et al (2011) Blast-induced phenotypic switching in cerebral vasospasm. Proc Natl Acad Sci U S A 108(31):12705–12710

INDEX